UNIVERSIDADE FEDERAL DO RIO DE JANEIRO

LARA DE OLIVEIRA ARINELLI

MODELING OF NATURAL GAS PROCESSING OPERATIONS: Multiphase and Multi-reactive Sound Speed, Supersonic Separator and Membrane Permeation

RIO DE JANEIRO

2019

Lara de Oliveira Arinelli

MODELING OF NATURAL GAS PROCESSING OPERATIONS: Multiphase and Multi-reactive Sound Speed, Supersonic Separator and Membrane Permeation

Tese de Doutorado apresentada ao Programa de Pós-Graduação em Engenharia de Processos Químicos e Bioquímicos, Escola de Química, Universidade Federal do Rio de Janeiro, como parte dos requisitos necessários à obtenção do título de Doutora em Ciências.

Orientadores:

Prof. José Luiz de Medeiros, D.Sc.

Prof. Ofelia de Queiroz Fernandes Araújo, Ph.D

RIO DE JANEIRO

2019

FICHA CATALOGRÁFICA

A711m

Arinelli, Lara de Oliveira
Modeling of Natural Gas Processing Operations: Multiphase and Multi-reactive Sound Speed, Supersonic Separator and Membrane Permeation / Lara de Oliveira Arinelli. -- Rio de Janeiro, 2019.
368 f.

Orientador: José Luiz de Medeiros.
Coorientadora: Ofélia de Queiroz Fernandes Araújo.
Tese (doutorado) - Universidade Federal do Rio de Janeiro, Escola de Química, Programa de Pós Graduação em Engenharia de Processos Químicos e Bioquímicos, 2019.

1. Velocidade do Som Multifásica e Multi reativa. 2. Separador Supersônico. 3. Permeação em Membranas. 4. Processamento Offshore de Gás Natural. 5. Gás Natural Rico e Ultra-Rico em CO2. I. de Medeiros, José Luiz, orient. II. Araújo, Ofélia de Queiroz Fernandes, coorient. III. Título.

Lara de Oliveira Arinelli

MODELING OF NATURAL GAS PROCESSING OPERATIONS: Multiphase and Multi-reactive Sound Speed, Supersonic Separator and Membrane Permeation

Tese de Doutorado apresentada ao Programa de Pós-Graduação em Engenharia de Processos Químicos e Bioquímicos, Escola de Química, Universidade Federal do Rio de Janeiro, como parte dos requisitos necessários à obtenção do título de Doutora em Ciências.

Aprovado em

_____

José Luiz de Medeiros, D.Sc., UFRJ
(Orientador – Presidente)

_____

Ofélia de Queiroz Fernandes Araújo, Ph.D., UFRJ
(Orientadora)

_____

Ana Paula Santana Musse, D.Sc., Petrobras

_____

Carlos André Vaz Junior, D.Sc., UFRJ

_____

Frederico de Araújo Kronemberger, D.Sc., UFRJ

_____

Luiz Fernando Lopes Rodrigues Silva, D.Sc., UFRJ

_____

Victor Rolando Ruiz Ahón, D.Sc., UFF

AGRADECIMENTOS

Agradeço aos meus pais, Simone e Roberto, pelo apoio e incentivo durante todas as etapas da minha vida. Ao meu avô, Walter, que não está mais aqui, mas tenho certeza que estaria muito orgulhoso, como sempre. À toda minha família, obrigada por estarem sempre comigo.

Aos meus orientadores, profs. José Luiz e Ofélia, agradeço pelos diversos ensinamentos, conselhos, paciência e confiança.

Aos meus colegas de trabalho pela parceria e troca de conhecimentos.

Aos meus amigos pela compreensão nas ausências, e força para seguir em frente.

A todos que de alguma forma me auxiliaram nessa jornada, obrigada.

RESUMO

ARINELLI, Lara de Oliveira. **Modelagem de Operações de Processamento de Gás Natural: Velocidade do Som Multifásica e Multi-Reativa, Separador Supersônico e Permeação em Membranas.** Rio de Janeiro, 2019. Tese (Doutorado em Engenharia de Processos Químicos e Bioquímicos) – Escola de Química, Universidade Federal do Rio de Janeiro, 2019.

Os ajustes de ponto de orvalho de água e hidrocarbonetos são etapas importantes no condicionamento de gás natural offshore, devido a problemas de garantia de escoamento para o transporte via gasodutos. Os processos de desidratação evitam a formação de hidratos em tubulações. A remoção de C3+ evita a condensação de hidrocarbonetos mais pesados, além de contribuir para aumentar a produção de óleo ou gerar matéria-prima petroquímica. No contexto dos campos de petróleo e gás no Pré-Sal, o processamento de gás é um fator decisivo, considerando os aspectos da produção em campos de águas ultra-profundas a 200 km da costa, com alta razão gás/óleo e alto teor de CO_2. Portanto, a produção de petróleo está atrelada a uma enorme produção de gás natural, com $\%CO_2$ entre 10-80%mol, acarretando desafios de processamento e pesquisas por novas tecnologias, dadas as limitações de espaço e peso da plataforma. As análises de consumo energético, econômicas e ambientais são úteis para determinar se as alternativas de processo, além de serem tecnicamente viáveis, são lucrativas e minimizam emissões de CO_2. Estes aspectos são abordados obtendo-se soluções para: (i) modelagem termodinâmica de velocidade do som multifásica/multi-reativa via extensões de operação unitária para HYSYS, PEC-UOE e REC-UOE, e ASPEN-PLUS, AMPEC; (ii) modelagem rigorosa termodinâmica de separador supersônico via extensões HYSYS, SS-UOE, e ASPEN-PLUS, AMSSO; (iii) modelagem de módulo de permeação em membranas via extensão HYSYS, MP-UOE; (iv) simulação de processamento offshore de gás natural com separadores supersônicos para alto (45% mol) e ultra-alto (68% mol) teores de CO_2, em comparação com tecnologias convencionais; (v) avaliações técnicas, energéticas, econômicas e ambientais estabelecendo a superioridade de alternativas com separador supersônico para processamento de gás natural visando a produzir gás combustível para geração de energia e CO_2 para recuperação avançada de petróleo. Outras aplicações de separadores supersônicos também foram investigadas.

Palavras-chave: velocidade do som multifásica; velocidade do som multi-reativa; separador supersônico; permeação em membranas; processamento offshore de gás natural; gás natural rico em CO_2.

ABSTRACT

ARINELLI, Lara de Oliveira. **Modeling of Natural Gas Processing Operations: Multiphase and Multi-Reactive Sound Speed, Supersonic Separator and Membrane Permeation**. Rio de Janeiro, 2019. Thesis (Doctorate in Chemical and Biochemical Processes Engineering) – School of Chemistry, Federal University of Rio de Janeiro, 2019.

Water and hydrocarbon dew-point adjustments are important steps in offshore natural gas conditioning, due to flow assurance issues for gas transportation via pipelines. Dehydration processes avoid hydrate formation in pipelines. C3+ removal prevents heavier hydrocarbons condensation, besides increasing oil production or generating petrochemical feedstocks. In the context of the Pre-Salt oil and gas fields, gas processing is a decisive factor, considering the production aspects at ultra-deep-water fields 200 km from coast, with high gas/oil ratios and high CO_2 content. Therefore, oil production is tied to a huge natural gas production, with 10-80%mol %CO_2, which entails processing challenges and new technology research, given the platform limitations of space and weight. Power consumption, economic and environmental assessments are crucial for determining if process alternatives, besides technically feasible, are lucrative and minimize CO_2 emissions. These aspects are approached obtaining solutions for: (i) modeling of thermodynamic multiphase and multi-reactive sound speed via unit operation extensions for HYSYS PEC-UOE and REC-UOE and for ASPEN-PLUS AMPEC; (ii) modeling of thermodynamically rigorous supersonic separator via HYSYS extension SS-UOE and ASPEN-PLUS extension AMSSO; (iii) modeling of membrane permeation modules via HYSYS extension MP-UOE; (iv) simulation of offshore gas processing with supersonic separators for high (45%mol) and ultra-high (68%mol) CO_2 content in comparison with conventional technologies; (v) technical, energy, economic and environmental assessments to establish the superiority of supersonic separator alternatives for natural gas processing aiming at producing fuel-gas for power generation and CO_2 for enhanced oil recovery. Other applications of supersonic separator were also investigated.

Keywords: Multiphase sound speed; multi-reactive sound speed; supersonic separator; membrane permeation; offshore natural gas processing; CO_2-rich natural gas.

CONTENTS

INDEX OF FIGURES

INDEX OF TABLES

CHAPTER I – INTRODUCTION

I.1. Contextualization and Motivations

Considering the recent concerns about climate change from global warming consequence, there is an urgent need to reduce greenhouse gas emissions, particularly CO_2. Therefore, the world's energy matrix is currently undergoing a transition process, where the participation of renewable sources is highlighted. However, renewable technologies still face some challenges associated with resource availability, transmission, and high associated value. In this scenario, natural gas (NG) becomes an important medium-term solution, since despite being a fossil fuel, it has the lowest CO_2 emission rate when compared to oil and coal. According to BP Statistical Review of World Energy, global primary energy consumption grew at a rate of 2.9% in 2018, the fastest since 2010, led by natural gas (40%) and renewables. NG production increased by 5.2% in 2018, while its consumption rose by 5.3%, one of the highest growth rates since 1984 (British Petroleum, 2019).

More than 10% of proven NG reserves contain high CO_2 content, ranging from 15%mol to 80%mol (Burgers et al., 2011; British Petroleum, 2019). In this context, the CO_2 capture process is not only important for NG specification, but also contributes significantly to CO_2 mitigation, being an essential step of carbon capture and storage (CCS) systems. One possible destination for the separated CO_2 is its reinjection in wells for enhanced oil recovery (EOR). In the case of non-associated gas fields, CO_2 can be sent via pipeline to nearby fields, or it can be stored in depleted fields or aquifers, as is in some fields in Indonesia and Australia (Burgers et al., 2011).

The discovery of new oil and gas reservoirs in the Brazilian Pre-Salt has expanded the horizon of the national oil and gas industry, raising it to a new level in the international market (Ernst & Young Terco, 2014). Lula field in Santos Basin is currently the largest oil and gas producer in Brazil, producing about 1.5 million barrels of equivalent oil per day, which is more than half of Petrobras' total production. Moreover, Mero field, located in ultra-deep waters of the Santos Basin (Libra block), is the most promising Pre-Salt field due to the huge reservoir magnitude and production potential (Petrobras, 2019).

Furthermore, over the next five years, 13 new production systems are expected to start operation by Petrobras, which will guarantee a 5% growth in production by 2023, with expected total investment of US$ 68.8 billion in oil and gas exploration and production (E&P) (Petrobras,

2019). Therefore, the outlook for Brazil's oil and gas sector is extremely promising. On the other hand, the current environmental concerns appeal to reducing greenhouse gas emissions. Hence the industry must search for process solutions to reduce environmental impact while still maintaining economic feasibility.

On the other hand, the Pre-Salt discoveries brought new challenges associated with their exploration and production, mainly due to high gas/oil ratio and high CO_2 content in the reservoirs. In Libra field, for example, huge amounts of associated gas with $\%CO_2 > 40\%mol$ are reported (Arinelli et al., 2017). Thus, there is constant need for studies and search of new technologies involving Pre-Salt E&P, as each field has unique characteristics that require solutions with high performance and lowest possible cost.

One of the major obstacles in the global NG sector is its difficulty in transporting it from production areas to consumption points. In Brazil, this issue is even more problematic, since most of the reserves are in offshore fields, some in ultra-deep waters, located more than 200 km from the coast. In this scenario, the best and most efficient form of gas transport would be to use high pressure subsea pipelines linking offshore platforms with onshore facilities. However, the presence of contaminants in raw NG may hinder the flow in subsea pipelines. Water, for example, can form hydrocarbon hydrates under conditions of high pressure and low temperatures, which are common in subsea pipelines, leading to hydrate accumulations and duct obstruction. The presence of liquids by condensation of heavier hydrocarbons (C3+) would be another problematic factor. Acid gases (H_2S and CO_2) may have issues associated with pipeline corrosion, reduction of the useful capacity of NG transmission lines, and environmental problems generated by their combustion. Therefore, it is crucial that NG undergoes a primary purification process at the topside of production platforms, which usually involves dew points adjustment and acid gas removal steps.

For NG water dew point (WDP) and hydrocarbon dew point (HCDP) adjustments, a new technology has been considered in the industry: the supersonic separator (SS). Fig. I.1 shows the SS device commercialized by two manufacturers – Twister BV and ENGO Engineering. In terms of benefits, SS operation implies significantly low footprint required, as it can perform WDP and HCDP adjustments simultaneously in a single compact unit operation. Moreover, there is no use of chemicals, and thus no need for recovery systems and make-up costs. In addition, there is usually a gain relative to the reduction in power consumption required for the

same water removal service when compared to conventional process (Arinelli et al., 2017). SS operation consists of accelerating the gas at supersonic velocities, promoting significant expansion and cooling, and consequent condensation. Thus, to correctly model the supersonic flow, it is necessary to calculate with accuracy the sound speed along the separator for the multiphase fluid. The sound speed calculation method directly affects the separator performance in terms of separation capacity and pressure recovery (de Medeiros et al., 2017). Moreover, the sound speed is not only an important parameter for supersonic separation. There are several other applications in the scopes of aeronautics and propulsion of spacecraft/rockets that involve the occurrence of chemical reactions under supersonic conditions.

According to SS manufacturers, NG hydrates in the SS separation section are not issues, as the short residence time of milliseconds in the device is not sufficient for nucleation of hydrates, given its slow kinetics (Twister BV, 2019). However, the two-phase condensate (containing water and HCs) ejected by SS can form gas hydrates in downstream processing. Therefore, the condensates are directed to an LTX separator with bottom heating to ≈20ºC, preventing hydrate formation (Arinelli et al., 2017).

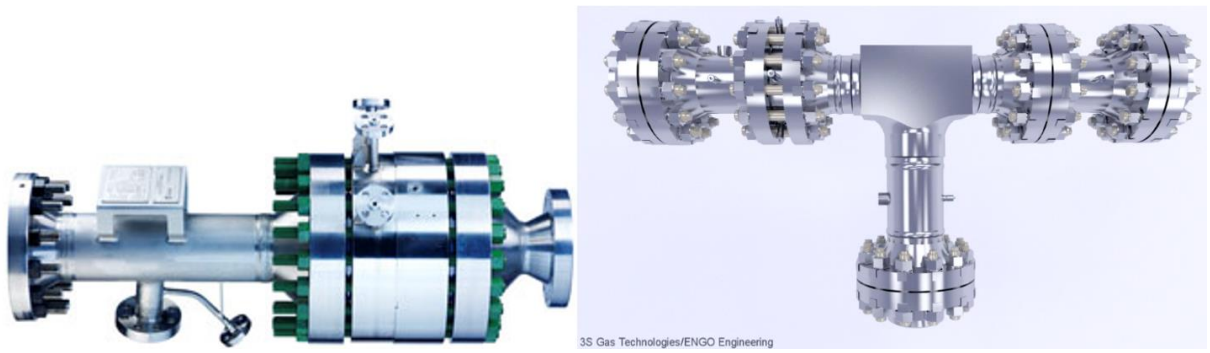

(a) **(b)**

Figure I. 1. Supersonic separator device: (a) Twister®; (b) ENGO 3S-Technology. Sources: Twister BV (2017) and ENGO Engineering (2019).

SS is not widely used in the NG conditioning industry yet, but the technology has been increasingly studied and addressed worldwide in both the theoretical and practical fields. Several projects were carried out in pilot plants by Twister BV with the aim of testing and demonstrating the technology for HCDP/WDP in the Netherlands, as well as other two in Nigeria, one in Brazil and one in Colombia. In 2003, the first commercial Twister SS system was installed by Shell Sarawak on platform B11 in Malaysia for dehydration of non-associated

sour NG, producing dry gas for transportation to an onshore NGL plant. With more than 10 years of operation, there has been no shutdowns, no hydrate formation, and savings of about 25% in weight and 23% in investment costs when compared to conventional TEG absorption (Twister BV, 2019).

The first industrial application of ENGO 3S technology started operation in 2004 at a NG processing plant in Western Siberia, consisting of two 3S devices conditioning 1.1 $MMSm^3/d$ of gas each (Alfyorov et al., 2005). In 2013, a unit with two 3S devices was also put into industrial operation in Talimi Field, China, by PetroChina. ENGO announces that since 2012 it has been promoting projects to develop 3S technology in several countries such as Russia, Brazil, Thailand and China. In June 2019, ENGO delivered to Yargeo, a subsidiary of Novatek, two 3S separators for a project of associated NG conditioning prior to the gas re-injection back into Yarudeiskoye oil field. The 3S application developed by ENGO Engineering provides effective re-injection of dry gas and additional project monetization through higher NGL recovery (increase of 50%) (ENGO Engineering, 2019).

Among the technologies for NG decarbonation, the most suitable for medium to high levels of CO_2 in the raw gas is membrane permeation (MP). Some advantages of MP when compared to other options available on the market for the same separation service are: low unit cost, modularity, simplicity of installation, no chemicals needed, and less weight and footprint required. But the most famous MP drawback is the trade-off selectivity versus specific capacity (flow rate per MP area); i.e., high selective MP can only operate at low specific capacities and vice-versa. MP units are commercialized in two main group types: hollow-fiber membranes (HFM) and spiral-wound membranes (SWM). Fig. I.2. shows two examples of membranes manufactured by Honeywell UOP (Separex - SWM) and by Schlumberger (CYNARA - HFM).

In view of the Brazilian Pre-Salt scenario, Petrobras started to invest in membrane permeation process for offshore CO_2 removal from NG. FPSO (Floating, Production, Storage and Offloading) platforms were commissioned with UOP-developed Separex® membrane systems to treat NG produced in Lula field (Honeywell, 2012). Several other projects with Separex were reported for Santos Basin FPSOs (UOP, 2013). Furthermore, in late 2014, BW Offshore announced the use of Separex® in an FPSO unit off the coast of Scotland in Great Britain, which is the first North Sea FPSO to use MP separation for NG conditioning. In 2017, UOP reported the successful operation of Separex® at the Virginia Indonesia Co plant, allowing the

use of NG as fuel-gas produced by its own process units via MP processing (UOP, 2017). With respect to CYNARA, operating facilities have been stablished in the USA, Canada, Southeast Asia and Argentina, being responsible for the largest installed membrane plant for NG decarbonation in terms of volume in the world, besides being the world leader in applications for EOR (Schlumberger, 2019).

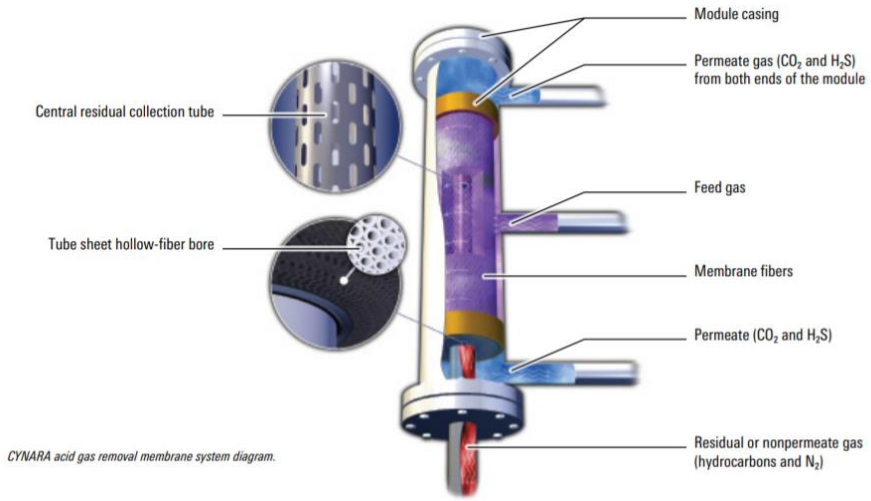

(a)

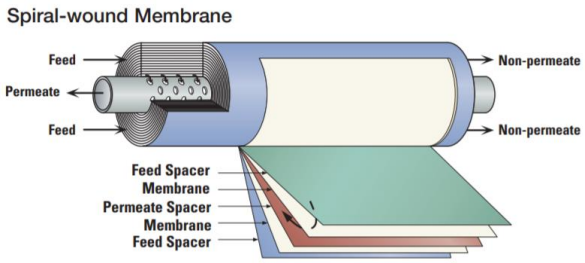

(b)

Figure I. 2. Membrane permeation devices: (a) CYNARA (HFM); (b) Separex (SWM). Sources: Schlumberger (2019) and UOP (2019).

On the other hand, the supersonic separator technology is also gaining ground in the field of NG decarbonation. The major gain in the use of SS would be the production of a high-pressure liquid CO_2-rich stream (de Medeiros et al., 2019). Such a possibility would represent a huge gain relative to the reduction in mechanical power required for injection when compared to MP, where low-pressure permeated CO_2 requires a huge and expensive compression train for the same purpose (Arinelli et al., 2019). In 2015, Twister BV announced a collaboration agreement with Petronas Carigali to provide a Twister® demo module for offshore CO_2 separation from

NG for the pilot project of K5 offshore Sarawak field to test new technology solutions for gas processing (Twister BV, 2015). In 2018, Twister BV has delivered a Crystallizer vessel that operates at cryogenic temperatures as a part of Sarawak K5 joint program for qualification testing in order to prove the concept of melting CO_2 solids and producing liquid CO_2 ready for reinjection (Twister BV, 2018).

Taking SS operation into consideration, other applications involving the separation of condensables from a gas phase may arise. An example is the air pre-purification unit (PPU) for oxygen production, in order to remove water, CO_2 and other impurities prior to the cryogenic separation step (Brigagão et al., 2019). The conventional process employs a temperature swing adsorption step on an activated alumina bed followed by a molecular sieve bed for dehydration and CO_2 removal, respectively. An alternative process adopts a low-pressure SS unit to pre-dehydrate the gas, greatly reducing the adsorption dehydration service, which is highly intensive in energy consumption (Brigagão et al., 2019).

Another application is in the recovery of thermodynamic hydrate inhibitor (THI) injected into the wellheads to avoid hydrate formation and ensure the flow in the riser to the production platforms. The multiphase fluid reaching the topside process goes through a three-phase separation step, extracting a liquid phase rich in THI, water, and salts, a second liquid phase, rich in C3+, and a gas phase containing a fraction of vaporized THI, that would be lost. A new processing proposal is to send NG from the three-phase separation step to an SS unit with pre-injection of water to enhance THI extraction, followed by a small atmospheric distillation step for water recovery (Teixeira et al., 2018). This process combination dramatically reduces THI loss in the final gas, while treating NG in terms of water and hydrocarbon dew points.

Another proposal of SS application is in the dehydration of CO_2 captured in post-combustion absorption process with alkanolamines for CCS. Considering a high capacity offshore NG processing plant, the produced gas can be used as fuel to generate electricity for the platform and/or for export (Interlenghi et al., 2019). In this case, after the combustion process, the flue gas must undergo a CO_2 capture process in order to reduce carbon emissions. Generally, the absorption process in alkanolamines is used for this purpose. After absorption, CO_2 is saturated with water, and if the destination is for EOR, this stream should be dehydrated, which can be accomplished with SS for minimal pressure drop, diminishing compression costs for injection (Teixeira et al., 2019).

Whether in the case of new production platform designs or in units already in operation, process simulation becomes an imperative tool for offshore engineering. The commercial simulation software provides a wide variety of attributes, such as a broad list of components, thermodynamic and phase equilibrium models, unit operations, stream properties, etc., which allow the investigation of process feasibility for future projects or for improvements of existing plants. On the other hand, emerging technologies are often not openly available in commercial simulation software, such as HYSYS. This is the case of MP and SS units. Hence, it is necessary to implement external unit operation extensions (UOEs) via Visual Basic programming to enable their application in the simulation environment for analysis of NG conditioning processes.

I.2. The Present Work and Achievements

As stated in Sec. I.1, to ensure accurate thermodynamic modeling of SS operation, it is necessary to precisely calculate the sound speed property of multiphase streams. The thermodynamic model for calculating the sound speed in multiphase fluids can also be implemented in HYSYS as an UOE, in order to become an available tool for simulation. Moreover, sound speed calculation in multi-reactive streams is a field in expansion, which can also be included in reactive process simulations through UOE's programming. The determination of rigorous thermodynamic multiphase multi-reactive sound speed was addressed in **CHAPTER II**.

Rigorous thermodynamic equations for the determination of sound speed were developed via a steady-state, unidimensional, horizontal, adiabatic, frictionless, multiphase and multi-reactive equilibrium plug-flow. The model makes a correspondence between the plug-flow element and an equilibrium closed system, which has only two equilibrium state coordinates and where mass and energy flow balances are processed. Two extensions for estimating the sound speed property via HYSYS were presented: for multiphase sound speed (PEC-UOE), and for multiphase multi-reactive sound speed (REC-UOE). Then, the performances of both PEC-UOE and REC-UOE were demonstrated for different multiphase and/or multi-reactive scenarios in comparison with literature data, using PR-EOS for high-pressure and/or multiphase applications and ideal gas behavior for low-pressure gas phase cases. Multiphase examples were solved by PEC-UOE for oil and gas fluids, while multi-reactive multiphase sound speeds were predicted by REC-UOE for NG pyrolysis and for two-phase methanol oxidation to

formaldehyde. PEC-UOE for HYSYS was also translated to an Aspen-Modeler analogue for ASPEN-PLUS as AMPEC.

In view of the successful results of PEC-UOE, REC-UOE and AMPEC, these extensions were registered in the Brazilian Patent and Trademark Office (Appendix T.5, Appendix T.6, and Appendix T.14, respectively), and the content of **CHAPTER II** was published in the Journal of Natural Gas Science and Engineering (Appendix T.8).

Following the correct attainment of sound speed, a rigorous thermodynamic model for the supersonic separator was approached as another extension for HYSYS: SS-UOE. SS-UOE for HYSYS was also translated to an Aspen-Modeler analogue as AMSSO. Besides, a short-cut lumped model calibrated with real offshore operation data was also developed for simulation of membrane permeation units in HYSYS: MP-UOE. HYSYS Extension SS-UOE and Aspen-Modeler AMSSO were registered in the Brazilian Patent and Trademark Office (Appendix T.7 and Appendix T.15, respectively). Works with ASPEN-PLUS extensions AMPEC and AMSSO are still under development for future publications.

CHAPTER III contemplates the methodologies and algorithms of both extensions SS-UOE and MP-UOE, including a comparison with literature data for SS-UOE. Afterwards, MP-UOE and SS-UOE were used for simulations of offshore CO_2-rich NG (45%mol CO_2) processing in HYSYS with PR-EOS. A conventional process comprising dehydration by TEG absorption, C3+ removal by JT expansion and NG decarbonation via MP was compared with alternatives involving SS for WDP/HCDP + MP for CO_2 removal, and TEG+JT for WDP/HCDP + SS for CO_2 removal. In the case of SS use for WDP/HCDP adjustments, a two-vessel scheme was added to the flowsheet in order to represent the LTX, with heating in the bottom. Simulations were evaluated in terms of technical and power consumption performances.

Considering the relevance of such results, **CHAPTER III** content culminated in a publication in the Journal of Natural Gas Science and Engineering (Appendix T.9). Other related works are presented in Appendix T.1 (Proceedings of PSE-2015 Conference, held in Copenhagen, Denmark), Appendix T.2 (Proceedings of OTC-Brazil 2015, held in Rio de Janeiro, Brazil) and Appendix T.3 (Proceedings of Rio Oil and Gas 2016, held in Rio de Janeiro, Brazil). The latter granted two awards: honorable mention for the presentation in 2016 Rio Oil & Gas Conference (Appendix T.33), and Plínio Catanhede 2018 award for best technical work published by IBP

in technology and innovation theme between 2016 and 2018 (Appendix T.34). Moreover, the CO_2-rich NG conventional processing and the alternative comprising SS for WDP/HCDP adjustments followed by MP for NG decarbonation were assessed via Monte-Carlo analysis in a more recent work, published in the Journal of Natural Gas Science and Engineering (Appendix T.29). Some results of this paper were summarized in Sec. VI.5 of **CHAPTER VI**.

On the other hand, MP-UOE extension has been improved since 2017, originating two new extensions: MPx-UOE and MPd-UOE. MPx-UOE contemplates the same permeation lumped short-cut method from MP-UOE, yet adopting energy balances for each stream, instead of only overall MP balance. MPd-UOE is a distributed model that divides the membrane unit in smaller cells, consecutively applying MPx-UOE method for each cell, enabling the attainment of fluid profiles through the unit. The description of MPx-UOE and MPd-UOE algorithms, and some technical results and sensitivity analyses via HYSYS simulation were presented in **CHAPTER VII**. The content of **CHAPTER VII** is material of submissions in 2019 for future publications.

Since in **CHAPTER III** the supersonic separators outperformed the conventional WDP/HCDP process, and demonstrated potential for CO_2 removal, a more complete analysis involving environmental and economic assessments was carried out in **CHAPTER IV**. In this study, an innovative process configuration with two SS units in series (1st for WDP/HCDP and 2nd for NG decarbonation) was investigated and compared with two alternatives from **CHAPTER III** via HYSYS simulations with PR-EOS. Moreover, the molar flow rate of CO_2-rich raw NG (45%molCO_2) was doubled to 12 MMSm³/d to represent a more realistic scenario considering the new discoveries in Brazilian Pre-salt with high GOR. NG was treated to produce fuel-gas (≈20%molCO_2) for consumption in the platform and exportation to other facilities, generating a revenue source, while the separated CO_2 was compressed and injected for EOR, also contributing to revenues in the form of an oil recovery factor. The content of **CHAPTER IV** was published in the Journal of Cleaner Production (Appendix T.27), while other associated works are available in Appendix T.17 (Proceedings of Brazilian Congress of CO_2 2018, held in Rio de Janeiro, Brazil), and in Appendix T.20 (Proceedings of SDEWES 2018, held in Palermo, Italy). This material also granted an award for best paper in capture theme presented in the Brazilian Congress of CO_2 2018 (Appendix T.35). Another related published paper in the Materials Science Forum is shown in Appendix T.30.

Nevertheless, the CO_2 content in NG reservoirs can achieve higher values, up to 80%mol of CO_2. Therefore, the successful application of SS observed in the first chapters must also be evaluated for CO_2 ultra-rich raw NG streams. **CHAPTER V** addressed this issue, considering a new scenario: a huge hub for high-pressure CO_2 ultra-rich (68%molCO_2, ≈50 MMSm³/d) gas processing from various wells. In this work, the process was simulated from the initial topside high-pressure separation area, producing oil, water, and gas that follows to conditioning. Four process alternatives were assessed, one with more conventional SS+MP configuration, and other three adopting an SS-SS process, yet with variations concerning recycle of condensates to the high-pressure separator and the operation for gas depressurization before SS. Due to the ultra-high CO_2 content, only a small portion of the dry gas is destined for fuel-gas production to generate power for consumption by the hub, while most of dry CO_2 ultra-rich gas is mixed with separated CO_2 (from fuel-gas) for compression and injection for EOR. Technical, power consumption, environmental and economic assessments were conducted for comparison of the process alternatives. Simulations were handled in HYSYS with PR-EOS, yet additional simulations of SS units with CPA-EOS were carried out for the sake of comparison between the thermodynamic models. In addition, another validation of SS-UOE with literature data was also included.

The content of **CHAPTER V** was published in the Journal of Natural Gas Science and Engineering (Appendix T.26). Moreover, the same processing scenario was approached in another publication in the Journal of Cleaner Production (Appendix T.28), where a classic conventional NG process contemplating molecular sieve for dehydration, JT expansion for C3+ removal, and MP for NG decarbonation was compared in terms of environmental and economic performances with the base case of **CHAPTER V**. Some results of such paper were presented in Sec. VI.4 of **CHAPTER VI.** Other associated work is shown in Appendix T.13 (Proceedings of SDEWES-LA 2018, held in Rio de Janeiro, Brazil).

Innovative applications for SS were also investigated, leading to other co-authored papers that were summarized in **CHAPTER VI**. As for air dehydration in pre-purification units (PPU), the use of SS was investigated in a paper published by the Separation and Purification Technology journal (Sec. VI.3, first page in Appendix T.23). The new SS-PPU process handles practically all dehydration service in SS, leaving only a small portion of water (together with CO_2 and HCs) to be removed via a smaller temperature-swing adsorption (TSA) unit. The utilization of

a SS step followed by a small TSA step (SS-TSA alternative) outperformed on economic grounds the traditional full TSA (FULL-TSA) PPU process. This innovative air pre-purification process originated a patent, which was deposited in the Brazilian Patent and Trademark Office (Appendix T.11). Other associated co-authored works involving SS-PPU are available in Appendix T.19 (Proceedings of Brazilian Congress of CO_2 2018, held in Rio de Janeiro, Brazil), and in Appendix T.22 (Proceedings of SDEWES 2018, held in Palermo, Italy). Another related co-authored paper published in the Materials Science Forum is shown in Appendix T.32.

SS use for thermodynamic hydrate inhibitor (THI) recovery from gas phase was assessed in two publications, one in the Journal of Natural Gas Science and Engineering (Sec. VI.1, first page in Appendix T.16), and another in the Journal of Environmental Management (Sec. VI.2, first page in Appendix T.25), which also approached a new application of SS for CO_2 dehydration. The first comprises the assessment of SS for THI (methanol, ethanol or MEG) recovery from NG, with an innovative strategy of pre-injection of water in SS feed, while simultaneously treating the NG stream in terms of WDP and HCDP. This new process, so-called SS-THI-Recovery, also originated a patent, deposited in the Brazilian Patent and Trademark Office (Appendix T.10). The second SS-THI-Recovery publication contemplated the environmental and economic assessments of conventional topside processing, in comparison with SS-THI-Recovery process for methanol, with addition of a post-combustion capture plant followed by CO_2 dehydration in SS for compression and injection to EOR. Other associated co-authored works involving SS-THI-Recovery are available in Appendix T.18 (Proceedings of Brazilian Congress of CO_2 2018, held in Rio de Janeiro, Brazil), and in Appendix T.21 (Proceedings of SDEWES 2018, held in Palermo, Italy). In addition, another co-authored paper published in the Materials Science Forum is shown in Appendix T.31.

Concerning the use of MEG as THI in offshore NG processing and the recovery process from the liquid aqueous phase separated topside, technical implications and exergy analysis were assessed in a co-authored paper (Appendix T.4), which was later extended to derive an international book, published by Springer (Appendix T.12). Moreover, multiphase and multi-reactive sound speeds, SS processing of CO_2-rich NG, thermodynamic modeling, CO_2 freeze-out, MP and SS-THI-Recovery contents of Chapters II and III and of Sec. VI.1 were also extended to originate a landmark international book published by Springer (Appendix T.24).

In the light of the variety of publications originated, this Thesis has achieved significant results, contributing to the literature of supersonic separators, membrane permeation, offshore NG processing and CO_2 mitigation with insights and innovations for scientific technological advances.

I.3. Thesis Structure

The content of this Thesis is organized into eight chapters, wherein each chapter from II to VII presents one or more main contributions of this research matter that was published (or to be published) in a recognized international scientific journal. Consequently, Chapters from I to VII have their own specific nomenclature, abbreviations, bibliographic review, methods and conclusions.

CHAPTER I introduces the subject of this Thesis, contextualizing and discussing key aspects of the research lines, and demonstrating the motivations, achievements and structure of the Thesis.

CHAPTER II addresses multiphase and/or multi-reactive sound speed calculation. Rigorous formula for the thermodynamic sound speed was derived via a steady-state, unidimensional, horizontal, adiabatic, frictionless, multiphase and multi-reactive equilibrium plug-flow. PEC-UOE and REC-UOE were developed for calculating the multiphase multi-reactive sound speed by HYSYS. Multiphase examples were solved by PEC-UOE for oil and gas fluids, including a supersonic separator for simultaneous adjustments of NG WDP/HCDP. Multi-reactive multiphase sound speeds were also predicted in supersonic reactors for NG pyrolysis and for two-phase methanol oxidation to formaldehyde.

CHAPTER III investigates supersonic separation for both WDP/HCDP adjustments or for decarbonation of a CO_2-rich raw NG stream (%CO_2≈45%mol) in offshore rigs. A conventional process comprising dehydration by TEG absorption, C3+ removal via JT expansion, and CO_2 capture in MP was compared with two SS process alternatives: (i) SS for WDP/HCDP + MP for CO_2 removal; and (ii) TEG+JT for WDP/HCDP + SS for CO_2 removal. Decarbonated NG was used as fuel-gas for power generation at the platform and for exportation, while separated CO_2 was compressed and injected for EOR. For simulations in HYSYS, two UOEs were developed to represent SS and MP: SS-UOE and MP-UOE. MP-UOE is a short-cut model with real data calibration; while SS-UOE contemplates a rigorous thermodynamic SS model,

applying PEC-UOE for determination of sound speed. In the case of SS for WDP/HCDP adjustments, a two-vessel scheme was added to the flowsheet in order to represent the LTX, with heating in the bottom and direct contact heat exchange between phases in the top. Technical and power consumption assessments were carried out for comparison of process alternatives. The chapter also includes an SS-UOE validation with literature data.

CHAPTER IV explores some gaps left by **CHAPTER III**: another SS-based process alternative comprising two SS units in series for full conditioning of raw CO_2-rich NG was approached, and environmental and economic assessments were also conducted to fully understand the gains of each case. In this chapter, the conventional processing case of raw CO_2-rich NG and the SS+MP alternative case from **CHAPTER III** were revisited for comparison with the new SS-SS alternative. Molar flow rate of raw CO_2-rich NG was also increased to represent a more realistic offshore scenario. Fuel-gas exportation and CO_2 injection were considered revenue sources for the process alternatives, the latter represented by an oil recovery factor.

CHAPTER V extends the investigations of the previous chapters for high-pressure CO_2 ultra-rich NG streams in an offshore high-capacity processing hub. In this work, the simulation flowsheets start with the multiphase oil/gas/water high-pressure separation topside, where oil and water are produced, and high-pressure gas is sent for conditioning steps. Four process alternatives were assessed all applying SS for WDP/HCDP. The first uses MP for NG decarbonation, while the other three use SS, with process variations related to recycle of condensates to high-pressure separator, and depressurization operation (JT valve or turbo-expander) for the SS feed. Only a small fraction of dry gas is deviated for fuel-gas production (for hub power consumption only), while the main dry gas stream is mixed with the separated CO_2 stream (from fuel-gas) for compression and injection for EOR. The alternatives were compared in terms of technical, power consumption, environmental and economic performances. The revenue sources in this scenario contemplate the oil recovery factor for injected CO_2, and an additional oil production relative to lowest production case.

CHAPTER VI presents additional co-authored research publications that use PEC-UOE, SS-UOE and MP-UOE for a variety of new applications assessed via simulations. Innovative SS applications were addressed, such as for THI recovery from NG in offshore platforms (SS-THI-Recovery), involving water pre-injection in SS feed, and air dehydration in pre-purification

systems for oxygen production (SS-PPU) in low pressure SS. Moreover, the content of **CHAPTER V** was explored in a co-authored publication for the same scenario of high-pressure NG processing with ultra-high CO_2 content, comparing the base case of that chapter with a classic conventional process comprising molecular sieve, JT expansion and MP. All these publications involve full technical, environmental and economic analyses. Content of **CHAPTER III** was also explored in another co-authored publication adopting Monte-Carlo analysis of platform designs under stochastic inputs (flow rate, gas-to-oil ratio and $\%CO_2$ of the main oil-gas-water feed) based on the conventional process (TEG dehydration, JT expansion and MP CO_2 removal) and the SS-MP process, both for processing raw CO_2-rich NG.

CHAPTER VII contemplates unpublished results for MP-UOE improvements, which originated two new software: MPx-UOE and MPd-UOE. MPx-UOE has the same methodology of MP-UOE, however adopting energy balances for each retentate and permeate streams in MP. On the other hand, MPd-UOE is a distributed model for parallel flow MP units, that divides the MP unit into smaller equally sized cells, applying the MPx-UOE algorithm for each cell consecutively. Results of MPx-UOE were evaluated for different MP stage configurations, while MPd-UOE stream profiles through the membranes were depicted for two stages serial configuration. Sensitivity analyses were also conducted in both models to understand the impact of an energy balance input parameter and of the MPd-UOE distribution.

CHAPTER VIII brings an overview of this work, with concluding remarks about the results achieved in this Thesis.

By last, Appendices A, B, C and D comprehend published Supplementary Materials belonging to the sound speed study conducted in CHAPTER II. Analogously, Appendices E, F, G, H and J involve published Supplementary Materials contemplating CO_2 freeze-out considerations, SS-UOE and MP-UOE algorithms, SS-UOE comparison with literature data, and SS simulation flowsheets belonging to CHAPTER III. Appendix K shows published Supplementary Materials with economic analysis methodology from CHAPTER IV. Appendix L, M, N, O, P, Q, R and S represent published Supplementary Materials with discussions about SS signatures, SS-UOE validation, SS-UOE simulation with CPA-EOS, HYSYS flowsheets, and analogous tables and figures of the process alternatives other than the base case depicted in CHAPTER V. Finally, Appendix T gathers the entire production derived from this Thesis, organized chronologically,

encompassing published papers, conference proceedings, books, software registrations, and pending patents, and by last, the awards received, namely:

Appendix T.1 – Dynamic Simulation and Analysis of Slug Flow Impact on Offshore Natural Gas Processing: TEG Dehydration, Joule-Thomson Expansion and Membrane Separation. Proceedings of 12th International Symposium on Process Systems Engineering and 25th European Symposium on Computer Aided Process Engineering, 2015.

Appendix T.2 – Performance Analysis and Comparison of Membrane Permeation versus Supersonic Separators for CO_2 Removal from a Plausible Natural gas of Libra Field, Brazil. Proceedings of Offshore Technology Conference Brazil (OTC Brazil), 2015.

Appendix T.3 – Performance Analysis and Comparison of Membrane Permeation versus Supersonic Separators for CO_2 Removal from a Plausible Natural gas of Libra Field, Brazil. Proceedings of Rio Oil & Gas Expo and Conference, 2016.

Appendix T.4 – Exergy Analysis of Monoethylene Glycol Recovery Processes for Hydrate Inhibition in Offshore Natural Gas Fields. Journal of Natural Gas Science and Engineering, 35, 798-813, 2016.

Appendix T.5 – HEPEC (Hysys Extension Phase Equilibrium Sound Speed). Registered software BR 512017000629-6, in 20/06/2017.

Appendix T.6 – HEREC (Hysys Extension Reactive Equilibrium Sound Speed (C)). Registered software BR512017000628-8, in 20/06/2017.

Appendix T.7 – HESSO (Hysys Extension Supersonic Separator Operation). Registered software BR512017000627-0, in 20/06/2017.

Appendix T.8 – Speed of sound of multiphase and multi-reactive equilibrium streams: a numerical approach for natural gas applications. Journal of Natural Gas Science and Engineering, 46, p. 222-241, 2017.

Appendix T.9 – Offshore Processing of CO_2 Rich Natural Gas with Supersonic Separator versus Conventional Routes. Journal of Natural Gas Science and Engineering, 46, p. 199-221, 2017.

Appendix T.10 – Processo para Recuperar Inibidores Termodinâmicos de Hidratos de Cargas de Gás Natural Utilizando Separador Supersônico Simultaneamente Ajustando Ponto de Orvalho de Hidrocarbonetos e Ponto de Orvalho de Água do Gás Final. Brazilian Patent Application BR 102017015092-5, deposited in 13/07/2017.

Appendix T.11 – Purificação do ar para fracionamento criogênico com separador supersônico de baixa pressão. BR Patent Application 102017027727-5, deposited in 21/12/2017.

Appendix T.12 – Monoethylene Glycol as Hydrate Inhibitor in Offshore Natural Gas Processing: From Fundamentals to Exergy Analysis. SpringerBriefs in Petroleum Geoscience & Engineering, SPRINGER, 2018.

Appendix T.13 – Technological alternatives for high CO_2 natural gas processing aiming offshore production of gas associated giant oil fields. 1st Latin-American Conference on Sustainable Development of Energy Water and Environment Systems (LA-SDEWES), 2018.

Appendix T.14 – AMPEC (Aspen Model of Phase Equilibrium Sound Speed (C)). Registered software BR512018001031-8, in 26/06/2018.

Appendix T.15 – AMSSO (Aspen Model of Supersonic Separator Operation). Registered software BR512018001032-6, in 26/06/2018.

Appendix T.16 – Recovery of thermodynamic hydrate inhibitors methanol, ethanol and MEG with supersonic separators in offshore natural gas processing. Journal of Natural Gas Science and Engineering, Vol. 52, p. 166-186, 2018.

Appendix T.17 – CO_2 rich natural gas processing: technical, power consumption and emission comparisons of conventional and supersonic separator technologies. Proceedings of 4th Brazilian Congress on CO_2 in the Oil, Gas and Biofuels Industries, 2018.

Appendix T.18 – Offshore natural gas conditioning and recovery of methanol as hydrate inhibitor with supersonic separators: increasing energy efficiency with lower CO_2 emissions. Proceedings of 4th Brazilian Congress on CO_2 in the Oil, Gas and Biofuels Industries, 2018.

Appendix T.19 – CO_2 emission and energy assessments of a novel pre-purification unit for cryogenic air separation using supersonic separator. Proceedings of 4th Brazilian Congress on CO_2 in the Oil, Gas and Biofuels Industries, 2018.

Appendix T.20 – CO_2 Rich Natural Gas Offshore Processing with Supersonic Separator: CO_2 Capture, Energy and Economic Assessments. Proceedings of 13th Conference on Sustainable Development of Energy Water and Environment Systems (SDEWES), 2018.

Appendix T.21 – Economic leverage of thermodynamic hydrate inhibitor recovery from raw natural gas with supersonic separator: post-combustion capture of 43% of CO_2 emissions preserving offshore gas plant profitability. Proceedings of 13th Conference on Sustainable Development of Energy Water and Environment Systems (SDEWES), 2018.

Appendix T.22 – Exergy analysis of a novel air pre-purification unit for cryogenic fractionation based on low-pressure supersonic separator combined with finishing adsorption step. Proceedings of 13th Conference on Sustainable Development of Energy Water and Environment Systems (SDEWES), 2018.

Appendix T.23 – A new concept of air pre-purification unit for cryogenic separation: low-pressure supersonic separator coupled to finishing adsorption. Separation and Purification Technology, 215, p. 173-189, 2019.

Appendix T.24 – Offshore Processing of CO_2-Rich Natural Gas with Supersonic Separator. Multiphase Sound Speed, CO_2 Freeze-Out and HYSYS Implementation. SPRINGER, 2019.

Appendix T.25 – Economic Leverage Affords Post-Combustion Capture of 43% of Carbon Emissions: Supersonic Separators for Methanol Hydrate Inhibitor Recovery from Raw Natural Gas and CO_2 Drying. Journal of Environmental Management, Vol. 236, pp. 534-550, 2019.

Appendix T.26 – Carbon capture and high-capacity supercritical fluid processing with supersonic separator: Natural gas with ultra-high CO_2 content. Journal of Natural Gas Science and Engineering, Vol. 66, p. 265-283, 2019.

Appendix T.27 – Supersonic separator for cleaner offshore processing of natural gas with high carbon dioxide content: Environmental and economic assessments. Journal of Cleaner Production, v. 233, p. 510-521, 2019.

Appendix T.28 – Supersonic separator for cleaner offshore processing of supercritical fluid with ultra-high carbon dioxide content: economic and environmental evaluation. Journal of Cleaner Production, 234, p. 1385-1398, 2019.

Appendix T.29 – Automatized Monte-Carlo analysis of offshore processing of CO_2-rich natural gas: Conventional versus supersonic separator routes. Journal of Natural Gas Science and Engineering, 69, 102943, 2019.

Appendix T.30 – CO_2 Rich Natural Gas Processing: Technical, Power Consumption and Emission Comparisons of Conventional and Supersonic Technologies. Materials Science Forum, 965, p. 79-86, 2019.

Appendix T.31 – Offshore Natural Gas Conditioning and Recovery of Methanol as Hydrate Inhibitor with Supersonic Separators: Increasing Energy Efficiency with Lower CO_2 Emissions. Materials Science Forum, Vol. 965, pp 97-105, 2019.

Appendix T.32 – CO_2 emission and energy assessments of a novel pre-purification unit for cryogenic air separation using supersonic separator. Materials Science Forum, 965, p. 59–67, 2019.

Appendix T.33 – Honorable Mention for the presentation of the technical work “Investigation of Technical Feasibility of Supersonic Separation for CO_2 removal from a plausible Libra Field Natural Gas” in the 2016 Rio Oil & Gas Conference, IBP.

Appendix T.34 – 2018 Plínio Catanhede Award for best technical work published by IBP in technology and innovation theme between 2016 and 2018 for the work “Investigation of Technical Feasibility of Supersonic Separation for CO_2 removal from a plausible Libra Field Natural Gas”, presented in the 2016 Rio Oil & Gas Conference.

Appendix T.35 – Best Paper Award in “Capture” theme for the work “CO_2 rich natural gas processing: technical, power consumption and emission comparisons of conventional and supersonic separator technologies” presented in the 2018 Brazilian Congress of CO_2 in the Industry of Oil, Gas and Biofuels, IBP.

Abbreviations

C3+ Propane and Heavier Alkanes; E&P Exploration and Production; EOR Enhanced Oil Recovery; HCDP Hydrocarbon Dew-Point; HFM Hollow-Fiber Membranes; JT Joule-Thomson; LTX Anti-Hydrate Separator; $MMSm^3/d$ Millions of Standard m^3 per day; MP Membrane-Permeation; NG Natural Gas; NGL Natural Gas Liquids; PR-EOS Peng-Robinson Equation-of-State; SS Supersonic Separator; SWM Spiral-Wound Membranes; TEG Triethylene Glycol; UOE Unit Operation Extension; WDP Water Dew-Point.

References

Alfyorov, V.; Bagirov, L.; Dmitriev, L.; Feygin, V.; Imayev, S.; Lacey, J. R. Supersonic nozzle efficiently separates natural gas components. Oil and Gas Journal Data Book, 53-58, 2005.

Arinelli, L. O.; Trotta T. A. F.; Teixeira, A. M.; de Medeiros, J. L.; Araújo, O. Q. F., Offshore Processing of CO_2 Rich Natural Gas with Supersonic Separator versus Conventional Routes, Journal of Natural Gas Science and Engineering, 46, p. 199-221, 2017. http://dx.doi.org/10.1016/j.jngse.2017.07.010.

Arinelli, L. O.; Teixeira, A. M.; de Medeiros, J. L.; Araújo, O. Q. F. Supersonic separator for cleaner offshore processing of natural gas with high carbon dioxide content: Environmental and economic assessments, Journal of Cleaner Production, v. 233, p. 510-521, 2019. doi: https://doi.org/10.1016/j.jclepro.2019.06.115

Brigagão, G. V.; Arinelli, L. O.; de Medeiros, J. L.; Araújo, O. Q. F. A new concept of air pre-purification unit for cryogenic separation: low-pressure supersonic separator coupled to finishing adsorption, Separation and Purification Technology, 215, p. 173-189, 2019. doi: https://doi.org/10.1016/j.seppur.2019.01.015

British Petroleum, BP Statistical Review of World Energy – 2019, 68th Edition, BP, London, United Kingdom, 2019. Available at: https://www.bp.com/content/dam/bp/business-sites/en/global/corporate/pdfs/energy-economics/statistical-review/bp-stats-review-2019-full-report.pdf

Burgers, W. F. J.; Northrop, P. S.; Kheshgi, H. S.; Valencia, J. A. Worldwide Development Potential for Sour Gas, Energy Procedia, Vol. 4, pp 2178-2184, 2011. doi: https://doi.org/10.1016/j.egypro.2011.02.104

de Medeiros, J. L.; Arinelli, L. O.; Araújo, O. Q. F. Speed of sound of multiphase and multi-reactive equilibrium streams: a numerical approach for natural gas applications, Journal of Natural Gas Science and Engineering, 46, p. 222-241, 2017. doi: 10.1016/j.jngse.2017.08.006

de Medeiros, J. L.; Arinelli, L. O.; Teixeira, A. M.; Araújo, O. Q. F. Offshore Processing of CO2-Rich Natural Gas with Supersonic Separator. Multiphase Sound Speed, CO_2 Freeze-Out and HYSYS Implementation, SPRINGER, 2019. doi: 10.1007/978-3-030-04006-2 / ISBN: 978-3-030-04005-5

Ernst & Young Terco. “Perspectivas para a indústria de Petróleo e Gás no Brasil: Uma análise das lições aprendidas no Mar do Norte e da retomada de licitações em 2013”, Ernst & Young Terco Brasil, 2014.

ENGO Engineering – Energy Gas Oil. ENGO 3S-Technology, 2019. Available at: http://www.engo3s.com/3s-tehnology

Honeywell. Honeywell UOP technology is used to clean natural gas on FPSO vessels, Membrane Technology - News, pp. 5, January 2012.

Interlenghi, S. F.; Silva, R. P. F.; de Medeiros, J. L.; Araújo, O. Q. F. Low-emission offshore Gas-To-Wire from natural gas with carbon dioxide: Supersonic separator conditioning and post-combustion decarbonation. Energy Conversion and Management, 195, 1334-1349, 2019. doi: https://doi.org/10.1016/j.enconman.2019.05.096

Petrobras, Exploração e Produção de Petróleo e Gás: Pré-Sal, 2019. Available at: http://www.petrobras.com.br/pt/nossas-atividades/areas-de-atuacao/exploracao-e-producao-de-petroleo-e-gas/pre-sal/

Schlumberger. CYNARA Acid Gas Removal membrane systems, 2019. Available at: https://www.slb.com/-/media/files/osf/product-sheet/cynara-ps

Teixeira, A. M.; Arinelli, L. O.; de Medeiros, J. L.; Araújo, O. Q. F. Recovery of thermodynamic hydrate inhibitors methanol, ethanol and MEG with supersonic separators in offshore natural gas processing, Journal of Natural Gas Science and Engineering, 52, 166-186, 2018. doi: 10.1016/j.jngse.2018.01.038

Teixeira, A. M.; Arinelli, L. O.; de Medeiros, J. L.; Araújo, O. Q. F. Economic leverage affords post-combustion capture of 43% of carbon emissions: Supersonic separators for methanol hydrate inhibitor recovery from raw natural gas and CO_2 drying, Journal of Environmental Management, 236, 534-550, 2019. doi: 10.1016/j.jngse.2018.01.038

Twister BV. Twister BV Selected by Petronas to Provide CO_2 Separation Offshore Demonstration Module for Petronas Carigali Sdn Bhd, 2015. Available at: http://twisterbv.com/news/twister-bv-selected-by-petronas-to-provide-co2-separation-offshore-demonstration-module-for-petronas-carigali-sdn-bhd/

Twister BV. Twister® Supersonic Separator, 2017. Available at: http://twisterbv.com/products-services/twister-supersonic-separator/

Twister BV. Offshore Dehydration: Shell (SSB) B-11, Malaysia, 2019. Available at: https://www.twisterbv.com/offshore-dehydration-shell-ssb-b-11-malaysia/

UOP. Petrobras selects Honeywell's UOP membrane technology. Filtration + Separation, pp. 4, 2013.

UOP. Separex enables natural gas producer to fuel wellhead equipment. Membrane Technology - News, pp. 2, February 2017.

UOP. UOP Separex Membrane Elements Datasheet, 2019. Available at: https://www.uop.com/?document=uop-separex-membrane-elements-datasheet&download=1

CHAPTER II – SPEED OF SOUND OF MULTIPHASE AND MULTI-REACTIVE EQUILIBRIUM STREAMS: A NUMERICAL APPROACH FOR NATURAL GAS APPLICATIONS

This paper was published in Journal of Natural Gas Science and Engineering, 46, 222-241, 2017. doi: 10.1016/j.jngse.2017.08.006 (Appendix T.8).

Speed of Sound of Multiphase and Multi-Reactive Equilibrium Streams: A Numerical Approach for Natural Gas Applications

José Luiz de Medeiros[*], *Lara de Oliveira Arinelli and Ofélia de Queiroz F. Araújo*

Escola de Química, Federal University of Rio de Janeiro, P.O. Box 68.594, 21941-972, Rio de Janeiro, RJ, Brazil

[*] *jlm@eq.ufrj.br*

Abstract

A method is presented for calculating the thermodynamic sound speed of multiphase multi-reactive streams. A rigorous formula for the thermodynamic sound speed is developed via a steady-state, unidimensional, horizontal, adiabatic, frictionless, multiphase and multi-reactive equilibrium plug-flow. The main theoretical point is a correspondence between a multiphase multi-reactive plug-flow element and an Equilibrium Closed System (ECS), which has only two equilibrium state coordinates. Momentum and energy flow balances are processed via the ECS framework allowing the sound speed derivation for complex streams. The method uses ECS thermodynamic properties provided by multiphase *Flash*(*P*,*T*) of HYSYS 8.8 simulator. Unit Operation Extensions (UOE) are developed for calculating the multiphase multi-reactive sound speed by HYSYS. HYSYS solves the multiphase multi-reactive equilibria, including liquid water separation, to feed the ECS sound speed formula with required properties. The sound speed is also investigated in the critical neighborhood via the Landau Model approach to prove that it does not exhibit $\pm\infty$ singularities at the critical point, despite the critical lambda-shape $\pm\infty$ singularities of $\overline{C}_P$ and (*T*,*P*) derivatives of the density. Multiphase examples are solved by the sound speed UOEs for simultaneous adjustments of water and hydrocarbon dew points of natural gas with supersonic separator. Multi-reactive multiphase sound speeds are also predicted in supersonic reactors for natural gas pyrolysis (GTL) and for two-phase methanol oxidation to formaldehyde.

Keywords: Thermodynamic Sound Speed; Multiphase Sound Speed; Multi-Reactive Sound Speed; Supersonic Separator; Landau Model Sound Speed; Natural Gas Pyrolysis.

II.1. Introduction

The thermodynamic single-phase speed of sound (*c*) is an equilibrium thermodynamic property with application in areas of industrial and military interest like aeronautics, supersonic flight, spacecraft propulsion and fluid transportation. In the specific case of multiphase systems, there are also technology fields of application demanding estimation of the multiphase thermodynamic speed of sound (*c*) such as aeronautics (e.g. supersonic flight through spray clouds and vapor cones (Wilkinson, 2012; Turner, 2009), spacecraft propulsion (e.g. steam nozzle nuclear engines (Mcmurtrey, 1964), natural gas (NG) conditioning in supersonic separators (SS) for simultaneous Water Dew Point Adjustment (WDPA) and Hydrocarbon Dew Point Adjustment (HCDPA) of raw NG (Schinkelshoek and Epsom, 2008; Machado et al., 2012; Yang et al., 2014; Cao and Yang, 2015; Secchi et al., 2016), CO_2 capture from dry combustion exhaust gases with SS (Hammer et al., 2014), choke-valve control for damping severe oil-gas slug flow in offshore production systems demanding estimation of choked multiphase sonic discharges (Ehinmowoa et al., 2016), and assessment of oil-gas reservoirs in geological formations by analyzing the propagation of seismic waves and its relationship with the multiphase sound speed of reservoir oil-gas-water fluids (Nichita et al., 2010).

In NG conditioning with SS, raw pressurized NG is accelerated to supersonic Mach Numbers (*Ma>1*) expanding through converging-diverging nozzles. Low temperatures and pressures are materialized during a few milliseconds of residence time, sufficient to produce condensation or freezing of liquids like water and C3+. Consequently, the pertinent sound speed to be used in SS equipment executing WDPA+HCDPA with NG is typically a three-phase *c* of a cold gas carrying a mist of water and C3+. In the case of SS for CO_2 capture from dry exhaust gas, the supersonic flow is cold enough to precipitate CO_2 as dry ice, i.e. the pertinent sound speed is a two-phase *c* of a cold gas with pulverized dry ice (Hammer et al., 2014).

Multiphase *c* is also important in safety studies of sonic discharges of two-phase jets from ruptures on pipelines and storage vessels with pressurized light liquids (or supercritical fluids) like ethane, propane, butane and CO_2 (Leung and Grolmes, 1987). Concerning accidental discharges of light liquids, the situation is aggravated if the ejected two-phase fluid readily reacts with air and/or water. This is the case of ruptures on pressurized storage vessels or pipelines of highly reactive light liquids e.g. ethylene, ethylene oxide and vinyl chloride (Crowl and Louvar, 2002). With such reactive fluids, the two-phase sonic discharge may develop

chemical reactions of partial polymerization triggered by free radicals from O_2 or multiple reactions with water. Such chemical reactions are fast and highly exothermic, potentially subsequently entailing combustion and explosion in air. These examples may require the calculation of the discharge flow rate using two-phase multi-reactive *c*.

In connection with aeronautics and spacecraft propulsion, multi-reactive gas expansion through nozzles also would involve the estimation of the multi-reactive *c*, for example, in the design of post-combustors of rockets and supersonic aircraft where a supersonic hot gas receives the injection of more fuel and/or oxidant creating a hypersonic multi-reactive flow (Libby, 1962; Shandor et al., 1963). However, in this particular field it is not uncommon to find works that merely estimate *c* via the ideal gas formula with changing composition along the flow path according to reaction coordinate (Powers and Paolucci, 2005). The truth is that the thermodynamic sound speed of reactive non-equilibrium systems can only be correctly calculated under the assumption of chemical equilibrium. Therefore, it seems to be incorrect to simply adapt an equilibrium single-phase *c* formula to a non-equilibrium reactive stream.

Indeed, the gamut of applications where there is simultaneity of supersonic flow and chemical reactions is expanding rapidly beyond the field of rocket and aircraft propulsion. Recent patents explore the design of supersonic reactors (SR) for fast chemical reactions. The objective is to expose reactants to very short reactor times of a few milliseconds in order to alter product selectivity by impeding undesirable secondary reactions. Recent patents (Raniere and Schuman, 1988; Bedard et al., 2014) developed methods to conduct SR pyrolysis of NG at $Ma=2$ above 1000^oC for producing olefins and acetylene, while GTL experiments (Romm and Somorjai, 2002) have been reported on low pressure SR pyrolysis of NG to produce olefins and higher hydrocarbons up to C_{21} with contact times of *1-100 ms* above 1000^oC. Cheng (2000) describes a method for conducting highly spontaneous chemical reactions in two-phase SR – e.g. oxidation of methanol to formaldehyde with O_2 – taking advantage of the very low *c* in gas-liquid streams with low gas content (*c* is minimal at $\approx 10^{-3}$ gas/liquid mass ratios) and using the normal shock at supersonic $Ma>1$ to finely divide gas bubbles rapidly increasing mass transfer and conversion without parallel undesirable reactions.

In order to address reliable modeling in above examples, the thermodynamic speed of sound *c* is an essential property that must be calculated with precision in single-phase as well as in multiphase multi-reactive streams. Accurate *c* is necessary to calculate sonic discharge flow

rates and, in SS and SR examples, to allow calculation of *Ma* in any flow point as *Ma=v/c*, where *v* is the velocity of the multiphase multi-reactive stream. Calculation of multiphase *c* is critical in SS design for WDPA+HCDPA of raw NG, as the correct positioning of vanes for collecting condensate depends on *Ma* of the multiphase stream in the diverging section. If condensate is not adequately collected at the appropriate supersonic *Ma*, the downstream incoming normal shock front will destroy all the attained separation by re-vaporizing condensates, undesirably retaining them in the gas product. This aspect is important for designing SS for WDPA+HCDPA of raw NG saturated with water, because it is very easy to oversize SS using excessive high pressure in the gas feed, excessive supersonic *Ma* and low temperature in the separation section, low backpressure, consequently requiring excessive power to compress the feed and SS NG product. The best SS design is a very low-profile one which just accelerates the gas to minimal supersonic *Ma*, condensing only the necessary water and C3+, using minimal pressure feed, maximum temperature separation section, maximum backpressure and minimal requirement of power to accomplish the service. This tight design can only be addressed with a correct stipulation of a not too high *Ma* in the separation section, which demands a good estimation of *c* for three-phase streams, one of them aqueous. The water content in the humid raw NG is always below 0.5% mol. But its withdrawal to a final content of 10-50 ppm is necessary to transport NG via long distance, high pressure, ultra-deep subsea pipelines without forming gas hydrates that could clog the line with time. High-depth subsea NG pipelines constitute the transport solution commonly adopted in oceanic oil and gas enterprises as in Libra field, Brazil (OGJ, 2014).

II.1.1. Multiphase Sound Speed in the Literature

The literature has works focusing on determination of sound speed *c* for two-phase or multiphase streams. There are empirical methods that compose the sound speed of pure component phases to obtain the two-phase counterpart (Wood, 1930). Others adapt the old two-phase method of Wood with a better estimation – via up-to-date EOS – of *c* for each phase, but completely ignore the formal thermodynamic aspects related to phase equilibrium and give no information when three or more phases are involved (Secchi et al., 2016). Nichita et al. (2010) presented a thermodynamic method to determine *c* for VLE systems using two-phase analogues of PVT properties and isobaric heat capacity, which are estimated after solving the VLE by a flash routine. Numerical derivatives under VLE in terms of *T* (at constant *P*) and *P* (at constant *T*) are used in conjunction with a *Flash*(*P*,*T*) routine to estimate the VLE analogues of

isothermal compressibility, isobaric expansivity, and isobaric heat capacity. Castier (2011) also explored a thermodynamic approach to determine the multiphase *c* using conservation constraints of volume, entropy, and species number of moles, the derivatives of thermodynamic properties, and the solution of a linear system, where the properties and their first order derivatives were calculated by a Mathematica-based package. This latter method is evidently a generalization of the former in the sense that it can cover multiphase streams with three or more phases, while the former handles only VLE streams. In fact, the differences of both approaches can be scrutinized here via a more plain presentation than the originally used in Castier (2011). It is just differential calculus, but in Castier (2011) the reader is left with an overwhelming "image of the tree", to the detriment of the "forest perspective". The following brief explanation, on the other hand, is centered "on the forest" and is also intended to allow the perception of the differences of both approaches to the present work. Castier (2011) considers a multiphase equilibrium with *np* phases, *nc* species and total mol fractions vector $\underline{Z}$. Let $\underline{\theta}$ be the *(np+np.nc) x 1* vector of all phase equilibrium variables containing *np* phase fractions and *np.nc* component mol fractions. Let $\underline{\Omega}$ be the *(np+np.nc) x 1* vector of all phase equilibrium constraints containing *nc.(np-1)* fugacity equalities, *nc* species balances and *np* normalizations of component mol fractions. Let Ψ be a scalar multiphase equilibrium intensive property per unit of mass or volume (e.g. ρ) or per mol (e.g. $\overline{H}$, $\overline{S}$, $\overline{C}_P$). According to Duhem's Theorem this multiphase equilibrium can be specified with ($T,P,\underline{Z}$), whereas the respective system of *np+np.nc* phase equilibrium constraints is written as in Eq. (II.1). It should be noticed that the intensive property Ψ is explicit in terms of ($\underline{\theta},T,P$) as in Eq. (II.2), with implicit dependence of $\underline{\theta}$ on ($T,P,\underline{Z}$) via Eq. (II.1). The square Jacobian of $\underline{\Omega}$ relative to $\underline{\theta}$ ($\underline{\underline{J}}$), the vector differential coefficients $\underline{\Omega}_T$, $\underline{\Omega}_P$ and the scalar differential coefficients Ψ_T, Ψ_P are defined in Eq. (II.3), where the gradient $\underline{\nabla}_\theta(.)$ is understood at constant ($T,P,\underline{Z}$).

$$\underline{\Omega}(\underline{\theta},T,P,\underline{Z})=\underline{0} \tag{II.1}$$

$$\Psi=\Psi(\underline{\theta},T,P) \quad , \quad \underline{\theta}=\underline{\theta}(T,P,\underline{Z}) \tag{II.2}$$

$$\underline{\underline{J}}=\left[\underline{\nabla}_\theta \underline{\Omega}^t\right]^t,\ \underline{\Omega}_T=\left(\frac{\partial \underline{\Omega}}{\partial T}\right)_{\underline{\theta},P,\underline{Z}},\ \underline{\Omega}_P=\left(\frac{\partial \underline{\Omega}}{\partial P}\right)_{\underline{\theta},T,\underline{Z}},\ \Psi_T=\left(\frac{\partial \Psi}{\partial T}\right)_{\underline{\theta},P},\ \Psi_P=\left(\frac{\partial \Psi}{\partial P}\right)_{\underline{\theta},T} \tag{II.3}$$

To make explicit the dependence of $\underline{\theta}$ on (*T*,*P*), under constant $\underline{Z}$, Eq. (II.1) is differentiated on both sides in Eq. (II.4). One then gets Eqs. (II.5). The differential coefficients of the scalar multiphase intensive property $\Psi(\underline{\theta},T,P)$ subjected to the phase equilibrium (i.e. subjected to $\underline{\theta}(T,P,\underline{Z})$) are then obtained in Eq. (II.6), which allows to write the total differential of Ψ with (*T*,*P*) under phase equilibrium and constant $\underline{Z}$ in Eq. (II.7).

$$d\underline{\Omega} = \underline{\underline{J}}.d\underline{\theta} + \underline{\Omega}_T.dT + \underline{\Omega}_P.dP = \underline{0} \tag{II.4}$$

$$\left(\frac{\partial\underline{\theta}}{\partial T}\right)_{P,\underline{Z}} = -[\underline{\underline{J}}]^{-1}\underline{\Omega}_T \quad , \quad \left(\frac{\partial\underline{\theta}}{\partial P}\right)_{T,\underline{Z}} = -[\underline{\underline{J}}]^{-1}\underline{\Omega}_P \tag{II.5}$$

$$\left(\frac{\partial\Psi}{\partial T}\right)_{P,\underline{Z}} = -(\underline{\nabla}_\theta\Psi)^t[\underline{\underline{J}}]^{-1}\underline{\Omega}_T + \Psi_T \quad , \quad \left(\frac{\partial\Psi}{\partial P}\right)_{T,\underline{Z}} = -(\underline{\nabla}_\theta\Psi)^t[\underline{\underline{J}}]^{-1}\underline{\Omega}_P + \Psi_P \tag{II.6}$$

$$d\Psi = \{-(\underline{\nabla}_\theta\Psi)^t[\underline{\underline{J}}]^{-1}\underline{\Omega}_T + \Psi_T\}.dT + \{-(\underline{\nabla}_\theta\Psi)^t[\underline{\underline{J}}]^{-1}\underline{\Omega}_P + \Psi_P\}.dP \tag{II.7}$$

Eqs. (II.6) and (II.7) are written for the total molar entropy in Eqs. (II.8) and (II.9). With Eq. (II.9), and constant entropy imposed ($d\bar{S} = 0$), the differential coefficient of temperature with *P* at constant $\bar{S}$ and $\underline{Z}$, and under phase equilibrium, is obtained in Eq. (II.10).

$$\left(\frac{\partial\bar{S}}{\partial T}\right)_{P,\underline{Z}} = -(\underline{\nabla}_\theta\bar{S})^t[\underline{\underline{J}}]^{-1}\underline{\Omega}_T + \bar{S}_T \quad , \quad \left(\frac{\partial\bar{S}}{\partial P}\right)_{T,\underline{Z}} = -(\underline{\nabla}_\theta\bar{S})^t[\underline{\underline{J}}]^{-1}\underline{\Omega}_P + \bar{S}_P \tag{II.8}$$

$$d\bar{S} = \{-(\underline{\nabla}_\theta\bar{S})^t[\underline{\underline{J}}]^{-1}\underline{\Omega}_T + \bar{S}_T\}.dT + \{-(\underline{\nabla}_\theta\bar{S})^t[\underline{\underline{J}}]^{-1}\underline{\Omega}_P + \bar{S}_P\}.dP \tag{II.9}$$

$$\left(\frac{\partial T}{\partial P}\right)_{\bar{S},\underline{Z}} = -\left\{\frac{-(\underline{\nabla}_\theta\bar{S})^t[\underline{\underline{J}}]^{-1}\underline{\Omega}_P + \bar{S}_P}{-(\underline{\nabla}_\theta\bar{S})^t[\underline{\underline{J}}]^{-1}\underline{\Omega}_T + \bar{S}_T}\right\} \tag{II.10}$$

The differential of any multiphase intensive equilibrium property Ψ with *P* at constant $\bar{S}$ and $\underline{Z}$, under phase equilibrium, can be written with Eq. (II.7) in the form shown in Eq. (II.11).

$$\left(\frac{\partial\Psi}{\partial P}\right)_{\bar{S},\underline{Z}} = \{-(\underline{\nabla}_\theta\Psi)^t[\underline{\underline{J}}]^{-1}\underline{\Omega}_T + \Psi_T\}.\left(\frac{\partial T}{\partial P}\right)_{\bar{S},\underline{Z}} - (\underline{\nabla}_\theta\Psi)^t[\underline{\underline{J}}]^{-1}\underline{\Omega}_P + \Psi_P \tag{II.11}$$

Castier (2011) uses an analogue of the classical Eq. (II.12) for the multiphase thermodynamic sound speed *c*. Therefore, with $\Psi = \rho$ in Eq. (II.11), and with Eq. (II.10), the multiphase equilibrium sound speed is numerically obtained with Eqs. (II.12) and (II.13).

$$c = \frac{1}{\sqrt{\left(\frac{\partial \rho}{\partial P}\right)_{\bar{S},\underline{Z}}}} \tag{II.12}$$

$$\left(\frac{\partial \rho}{\partial P}\right)_{\bar{S},\underline{Z}} = -\{-(\underline{\nabla}_\theta \rho)^t [\underline{\underline{J}}]^{-1} \underline{\Omega}_T + \rho_T\}.\left\{\frac{-(\underline{\nabla}_\theta \bar{S})^t [\underline{\underline{J}}]^{-1} \underline{\Omega}_P + \bar{S}_P}{-(\underline{\nabla}_\theta \bar{S})^t [\underline{\underline{J}}]^{-1} \underline{\Omega}_T + \bar{S}_T}\right\} - (\underline{\nabla}_\theta \rho)^t [\underline{\underline{J}}]^{-1} \underline{\Omega}_P + \rho_P \tag{II.13}$$

From the standpoint of a solved multiphase equilibrium at (*T*,*P*,$\underline{Z}$), the respective multiphase thermodynamic sound speed is obtained with some objects exported by the phase equilibrium solver; namely, $\underline{\underline{J}}$, $\underline{\Omega}_T$,$\underline{\Omega}_P$, $\underline{\nabla}_\theta \rho$, $\underline{\nabla}_\theta \bar{S}$, ρ_T, ρ_P, $\bar{S}_T$, $\bar{S}_P$. Such objects are straightforwardly obtained with a residual property routine and ideal gas heat capacities. If the Jacobian inverse is not available, the numerical burden of this approach is the creation of such differential objects and the Jacobian inverse in Eq. (II.13) (or equivalently, solving a linear system).

In Nichita et al. (2010) the sound speed calculation also starts with Eqs. (II.12) and (II.13). But Eq. (II.13) is shortened to Eq. (II.14) by using Eqs. (II.6) and (II.10) with $\Psi = \rho$.

$$\left(\frac{\partial \rho}{\partial P}\right)_{\bar{S},\underline{Z}} = \left(\frac{\partial \rho}{\partial T}\right)_{P,\underline{Z}} \cdot \left(\frac{\partial T}{\partial P}\right)_{\bar{S},\underline{Z}} + \left(\frac{\partial \rho}{\partial P}\right)_{T,\underline{Z}} \tag{II.14}$$

It can be shown (Sec. II.2.3) that the second factor in the RHS of Eq. (II.14) is given by Eq. (II.15). With Eqs. (II.14) and (II.15), one obtains Eq. (II.16), the *c* analogue used by Nichita et al (2010), where M_M is the molar mass (kg/mol) of the multiphase fluid, $\rho(T,P,\underline{Z})$ is the multiphase equilibrium density and $\bar{C}_P$ is the multiphase equilibrium isobaric heat capacity, via Eq. (II.6a), with $\Psi = \bar{H}$ in Eq. (II.17). These authors calculated *c* with Eq. (II.16) by estimating the phase equilibrium derivatives of ρ and $\bar{C}_P$ numerically with a VLE *Flash*(*P*,*T*) routine. Therefore five calls to VLE *Flash(P,T)* are executed: (i) one at (*T*,*P*,$\underline{Z}$) with subsequent calculation of the multiphase $\rho(T,P,\underline{Z})$, $\bar{H}(T,P,\underline{Z})$; (ii) two at ($T \pm \delta T$,*P*,$\underline{Z}$) for

$\rho(T \pm \delta T, P, \underline{Z})$, $\overline{H}(T \pm \delta T, P, \underline{Z})$; and (iii) two at ($T$,$P \pm \delta P$,$\underline{Z}$) for $\rho(T, P \pm \delta P, \underline{Z})$, $\overline{H}(T, P \pm \delta P, \underline{Z})$. Eq. (II.16) then gives c with the RHS's of Eqs. (II.18), (II.19), (II.20).

$$\left(\frac{\partial T}{\partial P}\right)_{\hat{S},\underline{Z}} = -\left(\frac{T.M_M}{\rho^2.\overline{C}_P}\right).\left(\frac{\partial \rho}{\partial T}\right)_{P,\underline{Z}} \tag{II.15}$$

$$c = \frac{1}{\sqrt{\left(\frac{\partial \rho}{\partial P}\right)_{T,\underline{Z}} - \left(\frac{T.M_M}{\overline{C}_P.\rho^2}\right).\left(\frac{\partial \rho}{\partial T}\right)^2_{P,\underline{Z}}}} \tag{II.16}$$

$$\overline{C}_P(T, P, \underline{Z}) = \left(\frac{\partial \overline{H}}{\partial T}\right)_{P,\underline{Z}} \tag{II.17}$$

$$\left(\frac{\partial \rho}{\partial P}\right)_{T,\underline{Z}} = \frac{\rho(T, P + \delta P, \underline{Z}) - \rho(T, P - \delta P, \underline{Z})}{2.\delta P} \tag{II.18}$$

$$\left(\frac{\partial \rho}{\partial T}\right)_{P,\underline{Z}} = \frac{\rho(T + \delta T, P, \underline{Z}) - \rho(T - \delta T, P, \underline{Z})}{2.\delta T} \tag{II.19}$$

$$\overline{C}_P = \left(\frac{\partial \overline{H}}{\partial T}\right)_{P,\underline{Z}} = \frac{\overline{H}(T + \delta T, P, \underline{Z}) - \overline{H}(T - \delta T, P, \underline{Z})}{2.\delta T} \tag{II.20}$$

In the context of VLE, the approach of Nichita et al. (2010) with five *Flash(P,T)* calls could be a little more CPU consuming than Castier's approach with just one *Flash(P,T)* and a matrix inversion in Eq. (II.13), despite the fast convergence of the secondary *Flash(P,T)* calls of the former as δT and δP are small and initializations are good. In terms of accuracy, there is no reason to suppose that these approaches perform distinctly, if δT and δP are adequately chosen. However, there is a problematic situation where the method of Nichita et al. (2010) is unfeasible, namely, when the VLE locus is 1D, i.e. a curve on plane (P,T), as in pure component loci or in constant composition homogeneous azeotrope loci. In such cases, the VLE analogues in the LHS of Eqs. (II.18), (II.19) and (II.20) are not defined on any (P,T) of the 1D locus, and if tried, they respectively diverge erratically to $+\infty$, $-\infty$ and $+\infty$, albeit the plain finitude of the two-phase c and its absolutely non-singular character. Moreover, both approaches will probably face problems within VLE loci in the vicinity of multicomponent critical points, the former because the two-phase analogues in the LHS of Eqs. (II.18), (II.19), (II.20) respectively diverge

to $+\infty$, $-\infty$, $+\infty$, and the latter because the Jacobian in Eq. (II.13) becomes singular without inverse, albeit the plain absence of singularity of *c* of critical phases. As explained in Sec. II.2.4, it is an amazing fact that *c* is totally free of $\pm\infty$ singularities at critical points, despite the well-known 2nd order critical point singularities of the properties on LHS's of Eqs. (II.18), (II.19), (II.20). Thus, to calculate *c* of critical phases it is a valid strategy to approach the critical point of fluid $\underline{Z}$ at (P_c,T_c) via an asymptotic path on the exterior of the VLE dome; i.e. on the single-phase supercritical fluid (SCF) domain with $T\text{-}Tc \rightarrow 0^+$.

II.1.2. Multiphase Multi-Reactive Sound Speed in the Literature

It seems that there is no previous work focusing on definition/calculation of the thermodynamic multiphase multi-reactive sound speed *c*. In every sought instance of reactive flow, *c* was always calculated at a given point in the non-equilibrium multi-reactive flow by using a single-phase *c* formula and substituting the reactive (*T*,*P*) and flow composition at that point. This expedient is used indiscriminately in supersonic burning flow through rocket nozzles with the ideal gas *c* formula (Powers and Paolucci, 2005). It must be stressed that such calculations did not address the true thermodynamic *c*, an equilibrium property that requires equilibrium thermodynamics to be accessed.

II.1.3. Outline of the work

This work attempts a unified approach to define and calculate the thermodynamic sound speed for multiphase multi-reactive streams. In Sec. II.2 the thermodynamic multiphase multi-reactive *c* is obtained by means of a steady-state, 1D, multiphase, multi-reactive, isentropic plug-flow, applying correspondence between plug-flow fluid elements and Equilibrium Closed Systems (ECS), enabling the description of state changes along the 1D plug-flow path in terms of (*P*,*T*). Sec. II.4.2 discusses theoretical aspects of *c* with pure fluid Landau Model (Landau, 1969), proving that *c* does not have $\pm\infty$ singularities at critical points, excepting a discontinuous change. Sec. II.3 implements multi-reactive multiphase *c*. As multiphase multi-reactive equilibria demand professional algorithms, species data and an arsenal of EOS's property methods, developments were oriented to use the thermodynamic framework of HYSYS 8.8 and its multiphase flash and reactor algorithms. Unit Operation Extensions (UOE) were created for calculating *c* within HYSYS. Sec. II.4 presents UOEs results for multiphase and multi-reactive *c*. Sec. II.5 addresses Conclusions.

II.2. Sound Speed of Multiphase Multi-reactive Streams

The sound speed (*c*) of multiphase, multicomponent, multi-reactive streams can be directly accessed provided thermodynamic equilibrium is assured. The derivation is straightforward. The final formulae are absolutely general. Any particular situation, deriving from this context, can simply use the same formulation if equilibrium is a valid premise, even if only a single-phase exists without chemical reactions.

II.2.1. Multiphase Multi-Reactive Steady-State, 1D, Horizontal, Adiabatic, Frictionless Equilibrium Plug-Flow

Let a multiphase, multi-reactive steady-state, 1D, horizontal, adiabatic, frictionless equilibrium plug-flow of a multicomponent fluid. Let the following premises: [P1] 1D axial, steady-state plug-flow on a horizontal, frictionless and adiabatic pipe, with varying section flow area *A(x)*, where *x* is the axial position on the flow path and is its unique independent variable. The pipe does not have lateral inlets or outlets of material, so that the flow has a constant mass flow rate *q* (kg/s) by steady-state. [P2] Strict Thermodynamic Equilibrium – mechanical, chemical and phase equilibria at each point *x* on the flow path. [P3] Along the flow path, there is a set of *nc* species, which is the union of all possible sets of species that can represent the stream composition at all points *x* on the flow path. [P4] Phases are sufficiently mutually dispersed. Under stratified, annular, slug and churn multiphase flows, the representation as plug-flow must prevail, which is an essential point here. Therefore, the formalism does not assume any of these multiphase flow regimes, but even in the circumstance of any of them, the important point is that *T, P*, axial velocity and component fugacities exist and are single-valued within an element of multiphase, multi-reaction fluid at each axial position *x*, i.e. profiles $T(x), P(x), v(x), \underline{\hat{f}}(x)$ are steady-state equilibrium-established on flow path. [P5] The 1D flow must have an initial point at *x=0*, where each plug-flow fluid element (i.e. a cylindrical fluid element with infinitesimal length and section area *A(x)* at *x*), was "prepared with" a global mol fractions *ncx1* vector $\underline{Z}$ with, perhaps, some of its components as zero. [P6] In view of [P1] and [P5], each moving plug-flow fluid element on flow path does not mix with neighbor fluid elements, so it behaves as an *Equilibrium Closed System* (ECS) with constant mass, but with changing properties per mass unit like $\hat{V} = \overline{V} / M_M$, $\hat{H} = \overline{H} / M_M$, $\hat{S} = \overline{S} / M_M$, $\hat{C}_P = \overline{C}_P / M_M$, $\hat{U} = \overline{U} / M_M$ or associated with a mass unit like ρ, Ξ_P, Ξ_T, all understood as multiphase

properties. [P7] The flow path dependent variables are only $T(x),P(x)$. The flow velocity $v(x)$ and thermodynamic multiphase properties of each volume element on flow path – $\hat{V}, \hat{H}, \hat{S}, \hat{C}_P, \hat{U}, \rho, \Xi_P, \Xi_T, \underline{\hat{f}}$ – respond as multiphase equilibrium functions of dependent variables $T(x),P(x)$ and preparation vector $\underline{Z}$. Therefore, one can write Eqs. (II.21), (II.22) and (II.23).

$$\hat{V}(T,P,\underline{Z}),\ \hat{H}(T,P,\underline{Z}),\ \hat{S}(T,P,\underline{Z}),\ \ \rho(T,P,\underline{Z})\ ,\ T(x),\ P(x) \tag{II.21}$$

$$\Xi_T(T,P,\underline{Z})=\left(\frac{\partial\rho}{\partial T}\right)_{P,\underline{Z}},\ \ \Xi_P(T,P,\underline{Z})=\left(\frac{\partial\rho}{\partial P}\right)_{T,\underline{Z}},\ \ \hat{C}_P(T,P,\underline{Z})=\left(\frac{\partial\hat{H}}{\partial T}\right)_{P,\underline{Z}} \tag{II.22}$$

$$v(x)=q/(A(x).\rho(T(x),P(x),\underline{Z})) \tag{II.23}$$

With so many attributes, the steady-state multiphase, multi-reactive, 1D, horizontal, adiabatic, frictionless equilibrium plug-flow has to be referred with a shorter characterization. This flow is adiabatic, frictionless and under equilibrium, therefore it is isentropic. So it will be referred here as steady-state 1D isentropic plug-flow; the multiphase, multi-reactive equilibrium attributes are implicitly understood. The assumptions of horizontal, frictionless and adiabatic 1D steady-state plug-flow are only necessary because the sound speed is the ultimate objective. They are not intended as particularizations of multiphase flow.

Fig. II.1 sketches the steady-state 1D isentropic plug-flow with flow direction as the positive direction of *x* axis. The flow is also a 1D steady-state compressible flow, primarily because any fluid phase is ultimately compressible; secondarily because even if really incompressible phases are present, the existence of vapor phase turns the multiphase flow into compressible. If the flow velocity *v(x)* is high – as in supersonic flow or near a normal shock – the hypothesis of mutual phase dispersion is reasonable.

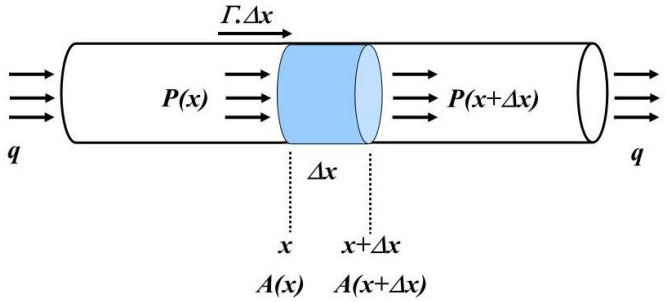

Figure II. 1. Multiphase, Multicomponent and Multi-Reactive Steady-State, 1D Isentropic Plug-Flow with Variable Flow Section.

Horizontal momentum, mass and energy enter in the plug-flow element Δx in Fig. II.1 through the flow section at x and leave through the section at $x+\Delta x$. Since the flow is steady, q is constant along the flow path, i.e. the rate of mass entering the element (q) is equal to the rate of mass leaving it (q). Shear stress term is absent due to the frictionless premise. The gravitational momentum term is not in Fig. II.1 because, as the flow is horizontal, the action of gravity, restricted to the vertical direction, is cancelled by the resultant of all normal wall reactions on the element Δx. Similarly, there is no change of potential gravitational energy of the fluid through Δx, therefore the gravitational term is absent in the energy balance. The horizontal momentum and energy balances of Δx are written in Eqs. (II.24) and (II.25), where the LHS's represent terms entering the element at x, while the RHS's represent terms leaving it at $x+\Delta x$. Units are strictly SI. In Eq. (II.24) the rate of horizontal momentum entering the element has three contributions: the transfer of momentum by the flow pressure at x, the horizontal reaction force of the wall (Fox et al., 2004) on the element according to Eq. (II.26) – it only exists when the flow section changes; i.e. it is positive when the flow section expands and negative when it contracts – and the rate of momentum carried by the moving material $q.v$ at x. In Eq. (II.25) energy is carried by the flow as enthalpy and as kinetic energy. Extensive thermodynamic properties are written per mass unit (i.e. specific properties), a convenience because q is constant at steady-state.

$$P(x).A(x)+\Gamma.\Delta x+\left(\frac{q^2}{\rho.A}\right)_x = P(x+\Delta x).A(x+\Delta x)+\left(\frac{q^2}{\rho.A}\right)_{x+\Delta x} \tag{II.24}$$

$$q.\left(\hat{H}+\frac{1}{2}\left(\frac{q}{\rho.A}\right)^2\right)_x = q.\left(\hat{H}+\frac{1}{2}\left(\frac{q}{\rho.A}\right)^2\right)_{x+\Delta x} \tag{II.25}$$

$$\Gamma.\Delta x = \frac{P(x)+P(x+\Delta x)}{2}.\frac{dA}{dx}.\Delta x \tag{II.26}$$

Eqs. (II.27), (II.28) and (II.29) are obtained by applying the limit $\Delta x \to 0$ after dividing Eq. (II.26) by Δx and dividing the subtraction RHS-LHS of Eqs. (II.24) and (II.25) by Δx.

$$\frac{d(P.A(x))}{dx} - \Gamma(x) + \frac{d(q^2/\rho.A(x))}{dx} = 0 \tag{II.27}$$

$$\frac{d}{dx}\left(q.\left(\hat{H} + \frac{1}{2}\left(\frac{q}{\rho.A}\right)^2\right)\right) = 0 \tag{II.28}$$

$$\Gamma(x) = P(x).\frac{dA}{dx} \tag{II.29}$$

After substituting Eq. (II.29) in Eq. (II.27), executing the derivatives and using constant q, the momentum and energy balances of the steady-state 1D isentropic plug-flow are written as in Eqs. (II.30) and (II.31), respectively. To proceed further, the spatial derivatives of thermodynamic properties $\rho(x)$, $\hat{H}(x)$ are necessary.

$$\frac{dP}{dx} - \left(\frac{q}{\rho A}\right)^2 \frac{d\rho}{dx} - \frac{q^2}{\rho A^3}\frac{dA}{dx} = 0 \tag{II.30}$$

$$\frac{d\hat{H}}{dx} - \left(\frac{q}{\rho A}\right)^2 \left(\frac{1}{\rho}\frac{d\rho}{dx} + \frac{1}{A}\frac{dA}{dx}\right) = 0 \tag{II.31}$$

II.2.2. Multiphase and Multi-Reactive Equilibrium Closed System (ECS)

Let a multiphase, multi-reactive *Equilibrium Closed System* (ECS) with state coordinates (*T,P)* and preparation vector of *nc* mol fractions $\underline{Z}$. As stated in Premise [P3], $\underline{Z}$ comprises all species that existed in ECS history (but not necessarily at ECS creation; i.e. may have $Z_i=0$); i.e., $\underline{Z}$ refers to all species that could be formed by all conceivable heat and work effects on ECS with the atoms loaded in its creation. Since ECS has constant mass and atoms (nuclear processes discarded), it is convenient that its extensive properties be defined per mass unit ($\rho, \hat{V}, \hat{H}, \hat{S}, \hat{C}_P$). ECS evolves with variable $\rho, \hat{V}, \hat{H}, \hat{S}, \hat{C}_P$ that change by heat and work effects on its boundaries according to the fundamental ECS relationships, which prescribe only two

equilibrium state coordinates (e.g. T,P). In the ECS, only the preparation $\underline{Z}$ has significance as composition. Since ECS is multi-reactive its current equilibrium composition can differ from $\underline{Z}$, but this has no importance at all, because the relevant ECS composition data is $\underline{Z}$, an invariant that molds its chemical history.

To obtain the complete differentials of density and specific enthalpy of ECS on plane (T,P), fundamental relationships are written for ECS under constant $\underline{Z}$. The final forms are Eqs. (II.32) and (II.33). Appendix A discloses the pertinent intermediate steps.

$$d\rho = \Xi_T.dT + \Xi_P.dP \qquad , \ \Xi_P = \left(\frac{\partial\rho}{\partial P}\right)_{T,\underline{Z}} \quad , \qquad \Xi_T = \left(\frac{\partial\rho}{\partial T}\right)_{P,\underline{Z}} \tag{II.32}$$

$$d\hat{H} = \hat{C}_P.dT + \frac{1}{\rho}\left(1 + \frac{T.\Xi_T}{\rho}\right).dP \tag{II.33}$$

II.2.3. Traveling Fluid Element of Steady-State 1D Isentropic Plug-Flow as ECS

Now it is possible to establish a correspondence between a traveling isentropic plug-flow fluid element of constant mass and preparation $\underline{Z}$, with a state-changing ECS with the same preparation $\underline{Z}$ and same mass. This is possible because the 1D plug-flow element does not mix with neighbor elements, so it is really an ECS since the 1D plug-flow occurs under equilibrium. The isentropic plug-flow fluid element only experiences changes of velocity and of $\rho,\hat{V},\hat{H},\hat{C}_P$ associated with mechanical transfers at its boundaries. No heat flux is present because the flow is adiabatic (and isentropic). With this correspondence, the differential property changes of ECS in Eqs. (II.32) and (II.33) can be divided by a differential change of axial position of the plug-flow element (Δx) giving the derivatives of density and specific enthalpy of the fluid with axial flow position in Eqs. (II.34) and (II.35).

$$\frac{d\rho}{dx} = \Xi_T\left(\frac{dT}{dx}\right) + \Xi_P\left(\frac{dP}{dx}\right) \tag{II.34}$$

$$\frac{d\hat{H}}{dx} = \hat{C}_P\left(\frac{dT}{dx}\right) + \frac{1}{\rho}\left(1 + \frac{T.\Xi_T}{\rho}\right)\frac{dP}{dx} \tag{II.35}$$

With Eqs. (II.34) and (II.35), the momentum and energy balances of the steady-state 1D isentropic plug-flow in Eqs. (II.30) and (II.31) are put as in Eqs. (II.36) and (II.37).

$$\left(1-\left(\frac{q}{\rho A}\right)^2 \Xi_P\right)\frac{dP}{dx}-\left(\left(\frac{q}{\rho A}\right)^2 \Xi_T\right)\frac{dT}{dx}-\frac{q^2}{\rho A^3}\frac{dA}{dx}=0 \tag{II.36}$$

$$\left(1-\left(\frac{q}{\rho A}\right)^2 \Xi_P+\frac{T\Xi_T}{\rho}\right)\frac{dP}{dx}+\left(\rho\hat{C}_P-\left(\frac{q}{\rho A}\right)^2 \Xi_T\right)\frac{dT}{dx}-\frac{q^2}{\rho A^3}\frac{dA}{dx}=0 \tag{II.37}$$

The steady-state 1D isentropic plug-flow will turn into sonic (*choked*) – marked * – on a segment of pipe with invariant flow section (*dA/dx = 0*). At the sonic condition Eqs. (II.36), (II.37) acquire the forms in Eqs. (II.38), (II.39), where *c* is the sound speed in Eq. (II.40).

$$\left(1-\left(\frac{q^*}{\rho.A}\right)^2 \Xi_P\right)\left(\frac{dP}{dx}\right)^*-\left(\frac{q^*}{\rho.A}\right)^2 \Xi_T\left(\frac{dT}{dx}\right)^*=0 \tag{II.38}$$

$$\left(1-\left(\frac{q^*}{\rho.A}\right)^2 \Xi_P+\frac{T.\Xi_T}{\rho}\right)\left(\frac{dP}{dx}\right)^*+\left(\rho.\hat{C}_P-\left(\frac{q^*}{\rho.A}\right)^2 \Xi_T\right)\left(\frac{dT}{dx}\right)^*=0 \tag{II.39}$$

$$c=\frac{q^*}{\rho.A} \tag{II.40}$$

Keeping Eq. (II.38) and subtracting Eq. (II.38) from (II.39), the sonic conditions of the steady-state 1D isentropic plug-flow become Eqs. (II.41) and (II.42). Now, Eqs. (II.41) and (II.42) are two linear and homogeneous algebraic equations for the sonic gradients of temperature and pressure *(dT/dx)**, *(dP/dx)**. These equations are not redundant and have a non-zero determinant. Consequently, both gradients have to be uniquely zero at the choked condition of the steady-state 1D isentropic plug-flow as written in Eq. (II.43).

$$\left(1-\left(\frac{q^*}{\rho.A}\right)^2 \Xi_P\right)\left(\frac{dP}{dx}\right)^*-\left(\frac{q^*}{\rho.A}\right)^2 \Xi_T\left(\frac{dT}{dx}\right)^*=0 \tag{II.41}$$

$$\frac{T.\Xi_T}{\rho}\left(\frac{dP}{dx}\right)^*+\rho.\hat{C}_P\left(\frac{dT}{dx}\right)^*=0 \tag{II.42}$$

$$\left(\frac{dP}{dx}\right)^*=\left(\frac{dT}{dx}\right)^*=0 \tag{II.43}$$

Albeit both zero, *T* and *P* gradients at sonic condition have a non-zero limiting ratio, shown in Eq. (II.44) by dividing them. The limiting ratio is in fact an ECS thermodynamic property, the

derivative of pressure with temperature at constant specific entropy ($\hat{S}$). By dividing Eqs. (II.41), (II.42) by *(dT/dx)** and using the identity in Eq. (II.44), the two sonic conditions are rewritten as in Eqs. (II.45) and (II.46).

$$\left(\frac{dP}{dx}\right)^{*} / \left(\frac{dT}{dx}\right)^{*} = \left(\frac{dP}{dT}\right)^{*} = \left(\frac{\partial P}{\partial T}\right)_{\hat{S},\underline{Z}} \tag{II.44}$$

$$\left(1 - \left(\frac{q^{*}}{\rho.A}\right)^{2} \Xi_{P}\right)\left(\frac{\partial P}{\partial T}\right)_{\hat{S},\underline{Z}} = \left(\frac{q^{*}}{\rho.A}\right)^{2} \Xi_{T} \tag{II.45}$$

$$\left(\frac{T.\Xi_{T}}{\rho}\right)\left(\frac{\partial P}{\partial T}\right)_{\hat{S},\underline{Z}} + \rho.\hat{C}_{P} = 0 \tag{II.46}$$

With Eqs. (A.3) and (A.5), it is easily shown that Eq. (II.46) is a well-known ECS thermodynamic identity useful to calculate the ECS $\hat{C}_{P}$. The other condition, Eq. (II.45), can be solved to give the sonic velocity *c* of a multiphase, multi-reactive equilibrium stream in Eq. (II.47).

$$c = \frac{q^{*}}{\rho.A} = \sqrt{\frac{\left(\frac{\partial P}{\partial T}\right)_{\hat{S},\underline{Z}}}{\Xi_{T} + \Xi_{P}\left(\frac{\partial P}{\partial T}\right)_{\hat{S},\underline{Z}}}} = \frac{1}{\sqrt{\Xi_{T}\left(\frac{\partial T}{\partial P}\right)_{\hat{S},\underline{Z}} + \Xi_{P}}} \tag{II.47}$$

With Eq. (II.32) for equilibrium changes of ECS density, one obtains Eq. (II.48), which, by its turn, allows recasting the ECS sonic speed Eq. (II.47) as the classical Eq. (II.49). With Eq. (II.46) the ECS sound speed Eq. (II.47) is also valid as in Eq. (II.50a).

$$d\rho = \Xi_{T}.dT + \Xi_{P}.dP \;\; \{\underline{Z}\, const. \;\Rightarrow\; \left(\frac{\partial \rho}{\partial P}\right)_{\hat{S},\underline{Z}} = \Xi_{T}\left(\frac{\partial T}{\partial P}\right)_{\hat{S},\underline{Z}} + \Xi_{P} \tag{II.48}$$

$$c = \frac{q^{*}}{\rho.A} = \frac{1}{\sqrt{\left(\frac{\partial \rho}{\partial P}\right)_{\hat{S},\underline{Z}}}} \tag{II.49}$$

$$c = \frac{q^{*}}{\rho.A} = \frac{1}{\sqrt{\Xi_{P} - (T/\rho^{2})\Xi_{T}^{2}/\hat{C}_{P}}} \tag{II.50a}$$

A compact formula for *c* is also obtained by using the ECS difference of heat capacities in Eq. (II.50b). With Eq. (II.50b) in Eq. (II.50a), one gets a fourth ECS *c* formula in Eq. (II.50c).

$$\hat{C}_P - \hat{C}_V = (T/\rho^2)\Xi_T^2/\Xi_P \tag{II.50b}$$

$$c = \sqrt{(\hat{C}_P/\hat{C}_V)/\Xi_P} \tag{II.50c}$$

For non-reactive systems, Eqs. (II.50a), (II.50b) and (II.50c) can also be written in molar forms as in Eqs. (II.50d), (II.50e) and (II.50f), respectively. The Mach Number, for reactive or non-reactive flows, follows in Eq. (II.50g).

$$c = \frac{1}{\sqrt{\Xi_P - (M_M T/\rho^2)\Xi_T^2/\overline{C}_P}} \tag{II.50d}$$

$$\overline{C}_P - \overline{C}_V = (M_M T/\rho^2)\Xi_T^2/\Xi_P \tag{II.50e}$$

$$c = \sqrt{(\overline{C}_P/\overline{C}_V)/\Xi_P} \tag{II.50f}$$

$$Ma = \frac{q/(\rho.A)}{c} \tag{II.50g}$$

In the case of a single-phase non-reacting ideal gas (marked $'$), the classical sound speed of ideal gas (c') can be recovered from Eq. (II.50f) as in Eq. (II.51). c' increases monotonously with *T*.

$$\Xi'_P = \frac{M_M}{R.T}\ ,\ \frac{\overline{C}'_P(T)}{\overline{C}'_V(T)} = \gamma'(T) \Rightarrow c' = \frac{q^*}{\rho'.A} = \sqrt{\frac{\gamma' RT}{M_M}} \tag{II.51}$$

The practical superiority of Eqs. (II.50a) and (II.50c) over Eq. (II.49) is that they use only common properties $\hat{C}_P$, $\hat{C}_V$ and PVT properties (ρ, Ξ_T, Ξ_P), which are easily calculated by process simulators for single-phase or multiphase and/or multi-reactive streams via *Flash(P,T)* – reactive or not. On the other hand, the ECS derivative in Eq. (II.49) depends on more specialized algorithms *Flash(P,S),* which also exist in simulators, but are inferior in terms of robustness compared with *Flash(P,T),* especially in multi-reactive multiphase mode.

II.2.4. Further Aspects of the Sound Speed

Thermodynamic properties can be roughly divided into three groups: (i) pure PVT properties; (ii) pure thermal properties; and (iii) mixed properties. Pure PVT properties are related only to PVT relationships and are all calculable via an EOS, like Residual and Excess properties, density (ρ), its differential coefficients (Ξ_T, Ξ_P) and fugacity and activity coefficients. Purely thermal properties are recognizable by their strict solely dependence on temperature and composition, like the enthalpy, internal energy and heat capacities of ideal gas and some liquids and solids. Mixed properties results from PVT and thermal behaviors of matter, encompassing first order integral properties ($\overline{H}, \overline{S}, \overline{G}$) and heat capacities ($\overline{C}_P, \overline{C}_V$) of non-ideal gases, common liquids and solids.

The sound speed (c) of real (multiphase or single-phase) fluids is a mixed property, but for ideal gases it is a thermal property by Eq. (II.51). Some qualitative aspects of c can be appreciated via Eq. (II.50a). Firstly, Ξ_P (a PVT facet of c) must dominate Eq. (II.50a) because the mixed term on the right is positive and must be always less than Ξ_P. Secondly, Ξ_P and ρ both have individually inverse effect on c, i.e. other things constant, c decreases as ρ increases; and c decreases as Ξ_P increases (i.e. as the hardness of the material, related to the inverse of Ξ_P, decreases). Therefore, very hard, but not too dense, materials like diamond, exhibit the highest c of $\approx 10^4 m/s$. Conversely, c can be very low ($<20\ m/s$) on low gas content ($\approx 0.1\%w/w$) air-water systems with high ρ and high Ξ_P. Temperature can have both effects on c depending on its effect on ρ, Ξ_P and $\hat{C}_P$. In gases ρ is low, as T increases Ξ_P decreases and c increases; but on liquids ρ is high, as T increases, ρ decreases, but Ξ_P increases and c decreases.

In the critical vicinity the analysis of Eq. (II.50a) or (II.50d) is nebulous because Ξ_P, Ξ_T, $\overline{C}_P$ diverge, respectively, to $+\infty$, $-\infty$ and $+\infty$ by 2nd order phase transition at the critical point. To assess the behavior of c on the critical neighborhood an asymptotic treatment is developed for pure fluid based on the Landau Model (LM) of phase transitions (Landau, 1969). LM is applied in the two neighborhoods of the pure fluid critical point: (i) in the upper subcritical vapor-liquid equilibrium (VLE) dome; and (ii) in the lower supercritical fluid (SCF) domain;

II.2.4.1. Landau Model in the Upper Subcritical VLE Dome of Pure Fluid

LM is not recognized for its accuracy. It is its usefulness as a prototype classical model that matters; i.e. LM behaves asymptotically as any other classical model (e.g. PR-EOS). In fact, the strict LM with its characteristic singular potential is not adopted here. Instead, it is used a 4th order expansion of the molar Helmholtz free energy of pure fluid, $\overline{A}(T,v)$, where T and v are temperature and molar volume. To strictly use LM, the generation function of the Legendre transform of $\overline{A}(T,v)$ would have to be taken as singular potential. The price of using $\overline{A}(T,v)$ is a pressure equality that has to be added under phase equilibrium. With $T<T_c$, $T-T_c \to 0^-$, $v \approx v_c$, the objective is to obtain the asymptotic behavior of c in the VLE dome near the critical point (T_c,v_c). Appendix B does the mathematics. The main results correspond to Eqs. (B.13a) to (B.13m) which collectively show that c is monotonous in the VLE critical neighborhood with a finite limit at (T_c , v_c).

II.2.4.2. Landau Model in the Lower Supercritical Fluid (SCF) Domain of Pure Fluid

The sound speed is now examined for the pure fluid in its lower supercritical fluid (SCF) domain in the critical neighborhood ($T>T_c$, $T-T_c \to 0^+$, $v \approx v_c$) with LM. Appendix C solves the algebra. The final result is Eq. (C.5a) which represents the asymptotic behavior of the sound speed c for $T>T_c$, $T-T_c \to 0^+$, $v \approx v_c$, showing that c does not exhibit singularities as $T-T_c \to 0^+$, $v \approx v_c$. The limiting critical (finite) value of c at $T=T_c^+$, $v = v_c$ is given by Eq. (C.5b).

II.2.4.3. LM Results: Pure Fluid in the Critical Neighborhood

Graphical results are provided for the LM pure fluid on both sides of the critical neighborhood: the VLE side ($T-T_c \to 0^-$, Appendix B) and the SCF side ($T-T_c \to 0^+$, Appendix C). As this work focuses on several aspects of the sound speed, besides its prediction by classical models, the objective here is to check the existence of critical point singularities of c according to LM. The motivation has to do with the fact that c is a 2nd order thermodynamic property and several 2nd order properties related to c exhibit 2nd order phase transition at the critical point with the characteristic lambda-shape divergence ($\overline{C}_P(T_c,v_c) \to +\infty$, $\Xi_T(T_c,v_c) \to -\infty$, $\Xi_P(T_c,v_c) \to +\infty$). Results are limited to pure fluid LM with one (SCF) or two (VLE) phases.

In Sec. II.4 more general scenarios are built with PR-EOS. All necessary objects were developed in Appendices B and C. To generate numbers with some intuitive appeal, LM parameters have to be specified accordingly. Table II.1 presents LM parameters and critical properties of a hypothetical fluid.

Table II. 1. Parameters of Hypothetical Fluid for Landau Model.

Molar Mass and Critical Parameters of Hypothetical Fluid (R=8.314 J/mol.K)				
Molar Mass	T_c	P_c	v_c	$\overline{C}_V^c = \overline{C}_V(T_c, v_c)$
0.044 kg/mol	*304 K*	72.10^5 *Pa*	3.10^{-4} m^3/mol	*30 J/mol.K*

Landau Model Parameters Based on Eq. (B.1a) with Eqs. (C.1a), (C.1b), (C.1c)			
$A_0(T)$		$A_{01} = -\overline{C}_V^c / 6$ *J/mol.K*	$A_{02} = -\overline{C}_V^c / (2.T_c)$ $J/mol.K^2$
$A_1(T)$	A_{10}= -P_c J/m^3	A_{11}=-R/v_c $J/m^3.K$	$A_{12}=A_{11}/10$ $J/m^3.K^2$
$A_2(T)$	A_{20}= 0 $J.mol/m^6$	$A_{21}=(R/2)/v_c^2$ $J.mol/m^6.K$	$A_{22}=A_{21}/10$ $J.mol/m^6.K^2$
$A_3(T)$	A_{30}= 0 $J.mol^2/m^9$	$A_{31}=-(2R/3)/v_c^3$ $J.mol^2/m^9.K$	
$A_4(T)$	$A_{40}=A_{21}/72.10^{-10}$ $J.mol^3/m^{12}$	$A_{41}=(3R/2)/v_c^4$ $J.mol^3/m^{12}.K$	

Fig. II.2 depicts several profiles generated with LM for subcritical (Appendix B) and supercritical (Appendix C) temperatures in the critical neighborhood of ± 2 *K*. In all cases the fluid is on a subcritical or a supercritical path towards the critical point with total molar volume on the line of rectilinear diameters, i.e. fixed at $v = v_c$. In the subcritical dome this corresponds to a vapor fraction also fixed at $\beta=0.5$ according to Eqs. (B.12c), (B.12d) and (B.13g). Profiles v_L, v_V and Δv versus T for $T<T_c$, $T - T_c \to 0^-$ are seen in Fig. II.2A. Fig. II.2B depicts similar plots for the VLE temperature derivatives of v_L, v_V and Δv, which diverge to $\pm\infty$ according to Eqs. (B.12c), (B.12d) and (B.13c). Similar $T<T_c$ profiles of molar entropy of saturated phases ($\overline{S}_L, \overline{S}_V$) and $\Delta\overline{S} = \overline{S}_V - \overline{S}_L$ are shown in Fig. II.2C. Vapor pressure profiles ($T<T_c$) are shown in Fig. II.2D calculated by Eqs. (B.13a), (B.13b) and their mean, all asymptotically merging as critical point approaches. Fig. II.2E depicts interesting properties for $T<T_c$; namely, the Clausius-Clapeyron coefficient $\Delta v / \Delta\overline{S}$ (Eq. B.13e), the isentropic differential coefficient of the vapor fraction $(\partial\beta / \partial T)_{\overline{S}}$ (Eq. B.13i) and the isentropic derivative of density with pressure $(\partial\rho / \partial P)_{\overline{S}}$ (Eq. B.13j). The latter is used to obtain c in the VLE subcritical dome via Eq. (B.13m). In the VLE dome $\overline{C}_P$, Ξ_T, Ξ_P are not defined as T cannot be changed at constant P and vice-versa, without losing the VLE. But c is perfectly defined. It is inaccessible via Eqs. (II.50d) or (II.50f), of course, but can be accessed via the isentropic derivative of the two-phase

density with pressure, using VLE temperature as $T^{SAT}(P)$. Despite the subcritical profiles in Fig. II.2 are following a path with constant $\beta=0.5$, this is not an imposition when the derivative $(\partial\beta/\partial T)_{\bar{S}}$ is taken at each point on the path; only constant $\bar{S}$ is. The two-phase sound speed given by Eq. (B.13m) smoothly increases in Fig. II.2F until approximately a limit of *100 m/s*, when it jumps through a discontinuity to about *180 m/s* on the SCF limit. In other words, there is no $\pm\infty$ singularity of *c* at critical points of classical fluids. On the SCF side ($T>T_c$) Eq. (C.5a) gives a monotonically decreasing sound speed as $T-T_c \to 0^+$ until the critical point limit in Eq. (C.5b) is reached, despite the SCF singularities $\bar{C}_P(T_c,v_c) \to +\infty$, $\Xi_T(T_c,v_c) \to -\infty$, $\Xi_P(T_c,v_c) \to +\infty$ in Eqs. (C.3a), (C.3b) and (C.3c).

Fig. II.3 confirms LM results in the SCF neighborhood of equimolar NG of CH_4 and CO_2 using classical PR-EOS with binary interaction parameter (BIP) $k_{CH4\text{-}CO2}=0.1$. For this NG its bubble and dew loci and critical point are located, defining on plane *T x P* the VLE dome. The exterior of the dome is swept by a dense grid of radials orthogonal to the dome penetrating into the single-phase fluid with temperatures from *-150ºC* up to *75ºC* and pressures up to *180 bar*. The radials are traversed by contours with constant distance from the dome. On this 2D grid single-phase properties are depicted via a color mapping into the jet palette of MATLAB (The Mathworks) comprising 64 tonalities on RGB scale. Color mappings are rendered for $\bar{C}_P(T,P)$ (*kJ/mol.K*), $\Xi_P(T,P)$ (*kg/m^3.bar*), $\Xi_T(T,P)$ (*kg/m^3.K*) and the sound speed *c(T,P)* (*m/s*) respectively on Figs. II.3A, II.3B, II.3C and II.3D, in all cases extending from the dome boundary (inclusive) until the outer periphery of the single-phase grid. The sound speed is calculated via Eq. (II.50d) with strict SI units. The SCF half of the 2nd order transitions of $\bar{C}_P(T,P)$, $\Xi_P(T,P)$ and $\Xi_T(T,P)$ are perceived as 2D "flames" emanating from the dome, on the SCF near the critical point in Figs. II.3A, II.3B and II.3C, respectively where $\bar{C}_P(T,P)$, $\Xi_P(T,P)$ and $\Xi_T(T,P)$ exhibit abrupt changes for small variations of (*T,P*). Counterpointing these singular behaviors, the sound speed *c(T,P)* is seen in Fig. II.3D without any sign of singularity on the SCF, behaving smoothly (excepting the inner dome discontinuity) and completely deprived of abrupt changes and $\pm\infty$ gradients. This is a colorful 2D confirmation of the pattern exhibited by the LM pure fluid on the SCF side of Fig. II.2F. The behavior of *c* on both sides of the critical neighborhood will be revisited in Sec. II.4 using the UOEs developed in this work.

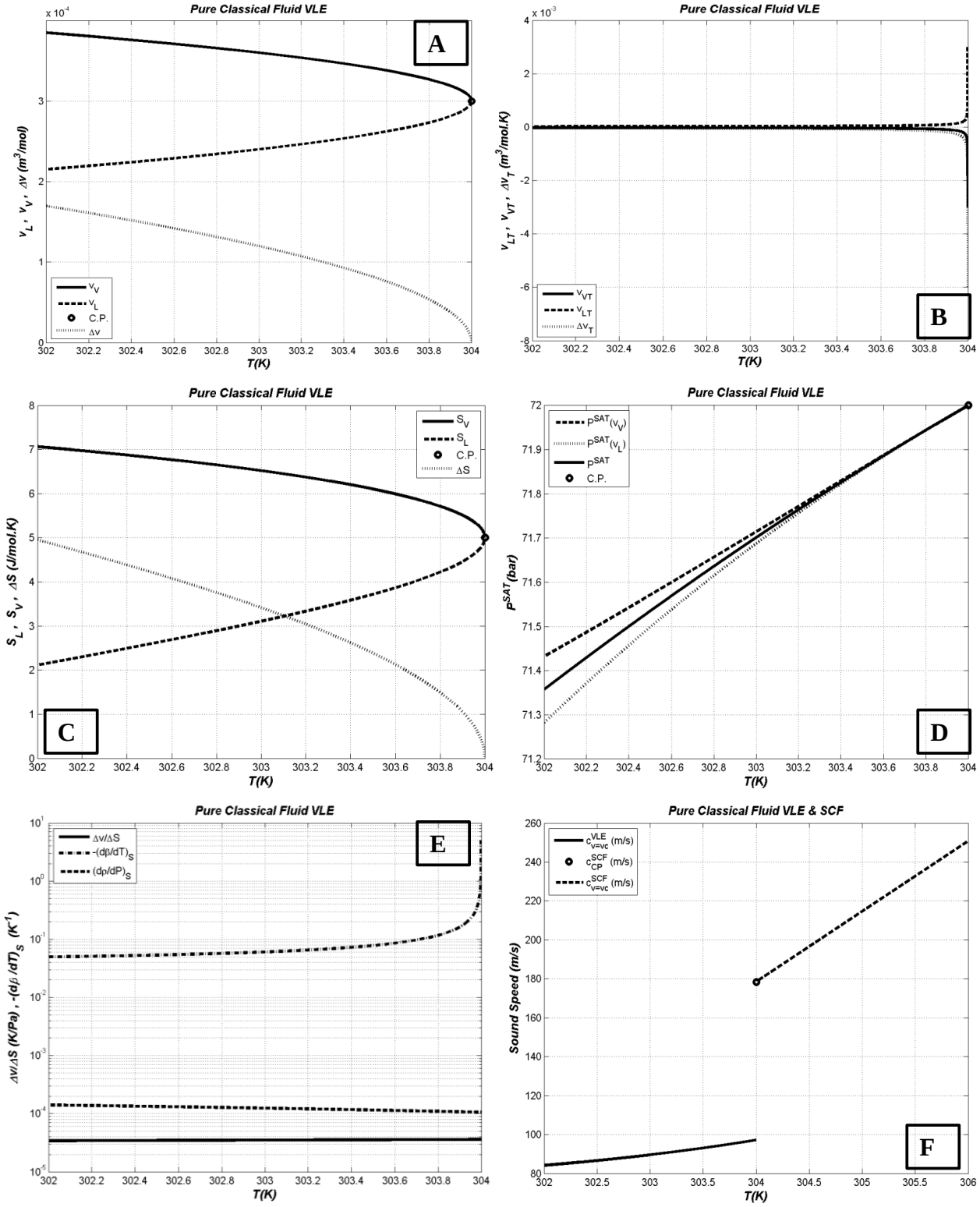

Figure II. 2. LM & Critical Neighborhood: (A) v_L, v_V, Δv vs T ($T<T_c$); (B) dv_L/dT, dv_V/dT, $d\Delta v/dT$ vs T ($T<T_c$); (C) $\bar{S}_L, \bar{S}_V, \Delta\bar{S}$ vs T ($T<T_c$); (D) $P^{SAT}(v_L)$, $P^{SAT}(v_V)$, P^{SAT} vs T ($T<T_c$); (E) $\Delta v/\Delta S$, $-(d\beta/dT)_S$, $(d\rho/dP)_S$ vs T ($T<T_c$); (F) c^{VLE} vs T ($v=v_c$, $T<T_c$), $c^{SCF}(v=v_c, T=T_c)$, c^{SCF} vs T ($v=v_c$, $T\geq T_c$).

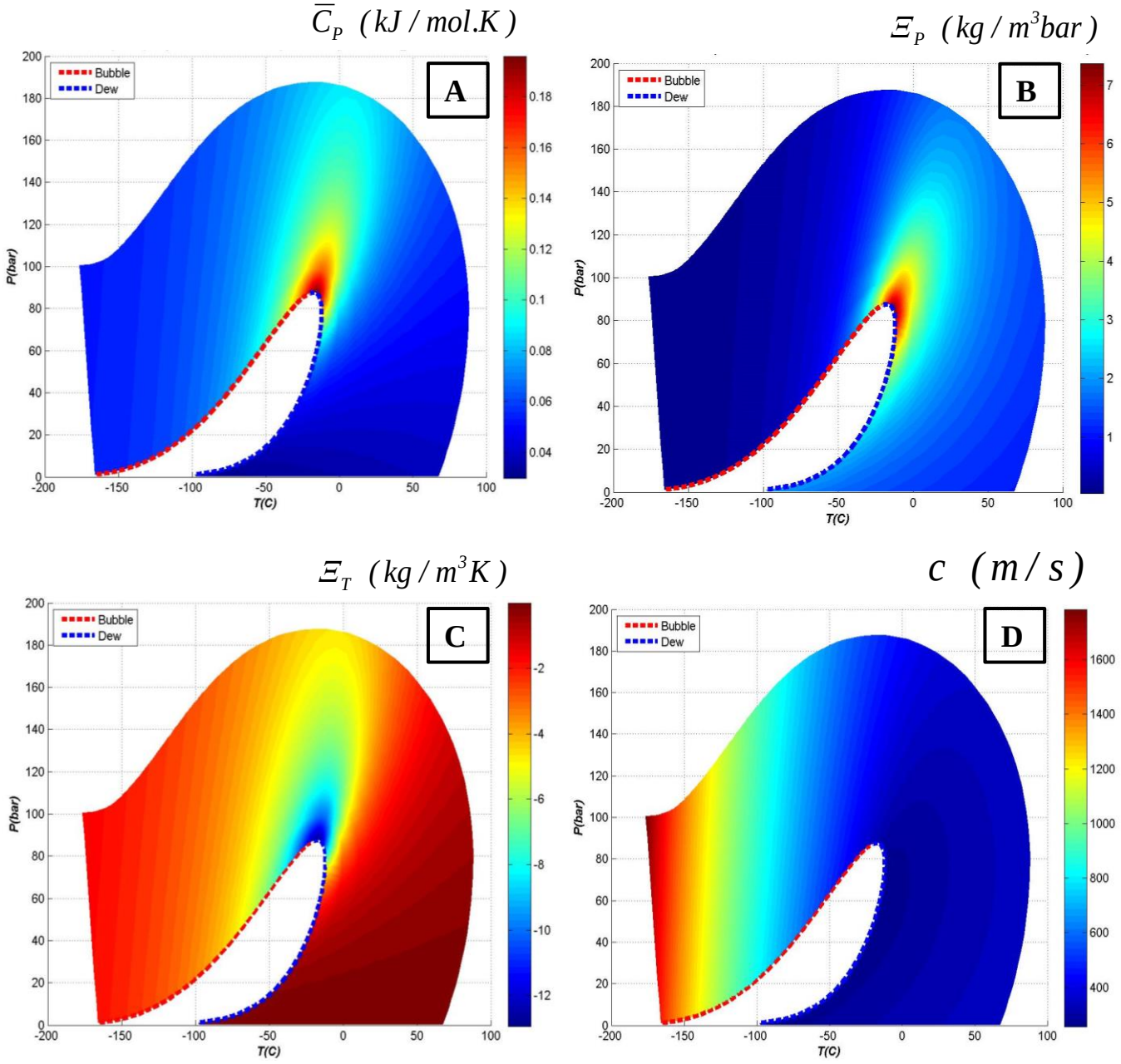

Figure II. 3. Binary NG *50%mol* CH_4 + *50%mol* CO_2 with PR-EOS: Bubble & Dew Curves and Critical Neighborhood via Color Mapping of Single-Phase Properties: *(A)* $\overline{C}_P\ (kJ/mol.K)\ vs(T,P)$; *(B)* $\Xi_P\ (kg/m^3 bar)\ vs(T,P)$; *(C)* $\Xi_T\ (kg/m^3 K)\ vs(T,P)$; *(D)* $c\ (m/s)\ vs(T,P)$.

II.3. Implementation of Multiphase Multi-Reactive Sound Speed

The multiphase multi-reactive sound speed *c* is numerically calculated by two Unit Operation Extensions (UOE) developed for HYSYS 8.8, namely: (i) PEC-UOE for (multi) phase equilibrium *c* without chemical reactions; and (ii) REC-UOE for (multi) reactive and (multi) phase equilibrium *c*. PEC-UOE and REC-UOE are portable DLLs that run with any EOS in the HYSYS palette of thermodynamic models and are attached to HYSYS PFDs that require calculation of *c*. This is the case of PFDs with Supersonic Separators (SS) and Supersonic Reactors (SR), both requiring *c* to access the stream *Ma*, important to assert throat and normal shock locations, critical items in SS and SR designs. PEC-UOE and REC-UOE can be also used in transient simulations of discharges of multiphase and/or multi-reactive fluids from ruptures on storage vessels or on high pressure pipelines.

II.3.1. UOE for Phase-Equilibrium Sound Speed: PEC-UOE

PEC-UOE adopts a basis of 1 mol of multiphase fluid at (T,P,$\underline{Z}$), where $\underline{Z}$ is the vector of total mol fractions. Eq. (II.50d) is applied to the Duhem's snapshot of the multiphase stream (T,P,$\underline{Z}$). The three multiphase ingredients Ξ_T, Ξ_P and $\overline{C}_P$ are calculated at (T,P,$\underline{Z}$) via numerical central-point derivatives of multiphase ρ and $\overline{H}$ by calling *Flash(P,T)* as done in Nichita et al. (2010). The difference is that the highly resilient HYSYS *Flash(P,T)* tool is used, which can smoothly treat single-phase, critical phase and multiphase with aqueous phase scenarios. HYSYS *Flash(P,T)* is not an unit operation, therefore it can be called for a given stream in the current PFD from a UOE without demanding the opening of a new PFD, which is a necessary time-consuming step in the case of calling classical unit operations that also handle multiphase streams (e.g. expander). This feature makes the calculations very fast. Five calls to HYSYS *Flash(P,T)* are executed: (i) one call at (T,P,$\underline{Z}$) – which also serves as initialization to subsequent calls – for calculating the multiphase $\rho(T,P,\underline{Z})$, $\overline{H}(T,P,\underline{Z})$, $M_M(T,P,\underline{Z})$ at the base point; (ii) two calls at ($T\pm\delta T$,P,$\underline{Z}$) for calculating $\rho(T\pm\delta T,P,\underline{Z})$, $\overline{H}(T\pm\delta T,P,\underline{Z})$; and (iii) two calls at (T,$P\pm\delta P$,$\underline{Z}$) for calculating $\rho(T,P\pm\delta P,\underline{Z})$, $\overline{H}(T,P\pm\delta P,\underline{Z})$. Eq. (II.50d) is then solved for *c* with $\rho(T,P,\underline{Z})$, $M_M(T,P,\underline{Z})$ and Eqs. (II.52a), (II.52b), (II.52c).

$$\Xi_P(T,P,\underline{Z}) = \frac{\rho(T,P+\delta P,\underline{Z}) - \rho(T,P-\delta P,\underline{Z})}{2.\delta P} \tag{II.52a}$$

$$\Xi_T(T,P,\underline{Z}) = \frac{\rho(T+\delta T,P,\underline{Z}) - \rho(T-\delta T,P,\underline{Z})}{2.\delta T} \tag{II.52b}$$

$$\overline{C}_P(T,P,\underline{Z}) = \frac{\overline{H}(T+\delta T,P,\underline{Z}) - \overline{H}(T-\delta T,P,\underline{Z})}{2.\delta T} \tag{II.52c}$$

II.3.2. UOE for Multiphase, Multi-Reactive Equilibrium Sound Speed: REC-UOE

REC-UOE adopts a basis of 1 kg of multiphase, multi-reactive ECS at (*T*,*P*,$\underline{Z}$), where $\underline{Z}$ is the vector of total mol fractions for ECS preparation defined in Sec. II.2.1. $\underline{Z}$ can be any known composition state of the stream on the reactive flow path, provided that all possible species existing in some point of this path are represented in it. It is irrelevant whether (*T*,*P*,$\underline{Z}$) corresponds or not to an chemical equilibrium state, because the subsequent ECS treatment will assure it. Eq. (II.50a) is applied to the ECS equivalent snapshot of the multiphase, multi-reactive stream (*T*,*P*,$\underline{Z}$). The three ECS ingredients $\Xi_T, \Xi_P, \hat{C}_P$ are calculated via central-point numerical derivatives of the ECS properties ρ and $\hat{H}$ by calling HYSYS reactive *Flash(P,T)* – known as HYSYS Gibbs Reactor (HGR). HGR generates a complete set of chemical reactions to represent the stoichiometry at (*T*,*P*,$\underline{Z}$). If only a subset of the complete set of reactions has to be used, HGR accepts it as specification. HGR can smoothly treat ECS multi-reactive scenarios with single-phase, critical phase and multiphase with aqueous phase. As before, five calls to HGR are executed: (i) one call at (*T*,*P*,$\underline{Z}$) for the ECS analogues $\rho(T,P,\underline{Z})$, $\hat{H}(T,P,\underline{Z})$ at the base point, also serving as initialization for subsequent calls; (ii) two calls at (*T*±δ*T*,*P*,$\underline{Z}$) for $\rho(T\pm\delta T,P,\underline{Z})$, $\hat{H}(T\pm\delta T,P,\underline{Z})$; and (iii) two calls at (*T*,*P*±δ*P*,$\underline{Z}$) for $\rho(T,P\pm\delta P,\underline{Z})$, $\hat{H}(T,P\pm\delta P,\underline{Z})$. Eq. (II.50a) is then solved for *c* with $\rho(T,P,\underline{Z})$ and Eqs. (II.53a), (II.53b), (II.53c). However, as HGR is formally a HYSYS unit operation, REC-UOE must open temporary HYSYS PFDs to perform HGR calculations, i.e. REC-UOE is much slower than PEC-UOE.

$$\Xi_P(T,P,\underline{Z}) = \frac{\rho(T,P+\delta P,\underline{Z}) - \rho(T,P-\delta P,\underline{Z})}{2.\delta P} \tag{II.53a}$$

$$\Xi_T(T,P,\underline{Z}) = \frac{\rho(T+\delta T,P,\underline{Z}) - \rho(T-\delta T,P,\underline{Z})}{2.\delta T} \tag{II.53b}$$

$$\hat{C}_P(T,P,\underline{Z}) = \frac{\hat{H}(T+\delta T,P,\underline{Z}) - \hat{H}(T-\delta T,P,\underline{Z})}{2.\delta T} \tag{II.53c}$$

II.4. Results

The multiphase multi-reactive sound speed *c* is calculated exclusively using HYSYS extensions PEC-UOE and REC-UOE. Comparisons are provided for some major examples of multiphase *c* in the literature. Applications in NG processing and conversion are addressed. To the authors' knowledge, there are no approaches in the literature addressing the reactive or critical sound speed, either in single-phase or multiphase scenarios. Unless stated otherwise, species critical constants, ideal gas molar isobaric heat capacities and PR-EOS BIPs, are from HYSYS 8.8. CPU times refer to a PC notebook running HYSYS 8.8 with license server on MS Windows-10, 64 bits, Intel Core i5-4210U @1.70 GHz, 6GB RAM.

II.4.1. Prudhoe Bay NG

The literature has results of *c* for Prudhoe Bay NG using PR-EOS (Nichita et al., 2010; Castier, 2011). This NG has the following %mol composition: CH_4 (*83.3310%*), C_2H_6 (*9.6155%*), C_3H_8 (*3.5998%*), iC_4H_{10} (*0.3417%*), nC_4H_{10} (*0.4585%*), iC_5H_{12} (*0.0403%*), nC_5H_{12} (*0.0342%*), nC_6H_{14} (*0.0046%*), nC_7H_{16} (*0.003%*), nC_8H_{18} (*0.001%*), toluene (*0.0002%*), N_2 (*1.4992%*), O_2 (*0.0008%*) and CO_2 (*1.0738%*). PR-EOS is used with all BIPs set to zero as in original sources. Sound speed is evaluated with PEC-UOE from *130 K* up to *270 K* at *10 bar*, *30 bar*, *50 bar* and *70 bar*. Fig. II.4 shows the *P x T* VLE dome for this NG with isobaric paths for *c* demonstration. An isothermal path at the critical temperature is added for Sec. II.4.3. On each isobaric path *c* is calculated at 285 temperatures crossing single-phase liquid, two-phase VLE and single-phase vapor, with CPU time of ≈5s per isobar. Fig. II.5 depicts the four isobaric *c* profiles with characteristic points sampled from Nichita et al. (2010). There is good agreement with Nichita et al. (2010), despite some small differences in bubble point and dew point sound speeds, which we attribute to some small divergence in pure component ideal gas heat capacity terms, component critical constants, PR-EOS and VLE numerical implementations and possible

differences of machine configuration. On each isobar, the large discontinuities in *c* occur near the bubble points, between the point where the VLE dome is touched on the left and the subsequent two-phase point with low vapor content. The minimal *c* on each isobar occurs at the minimal temperature with minimal non-zero vapor fraction, giving, as stated in Sec. II.2.4, the combination of highest density and highest compressibility that drastically damps *c*. Inside the VLE dome *c* increases monotonously with temperature in response to isobaric increase of vapor fraction gradually lowering the two-phase density. Perceptible increases of isobaric slopes occur at the dew points where the denser VLE dome is left behind.

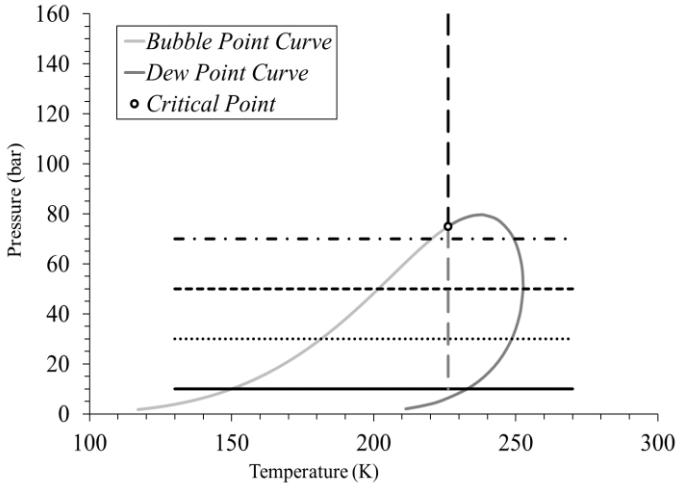

Figure II. 4. Prudhoe Bay NG: VLE Dome on Plane *P x T* with Isobaric Paths and Critical Isotherm Path for Calculating the Thermodynamic Sound Speed.

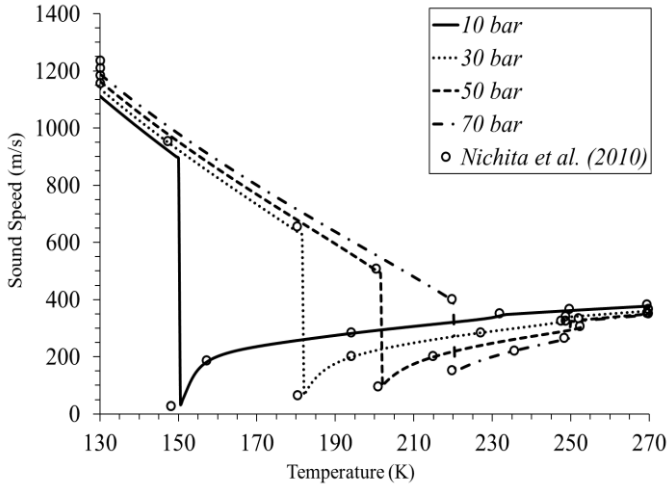

Figure II. 5. Prudhoe Bay NG: Thermodynamic Sound Speed Calculated on Isobaric Paths with Characteristic Points from Nichita et al. (2010).

II.4.2. Reservoir Oil with Water

Nichita et al. (2010) calculated *c* at 344.26K and high pressures of a Reservoir Oil with 10 HC species and 10 HC fractions with no water present. The corresponding mol fractions, critical constants and PR-EOS BIPs are available in Nichita et al. (2007). These authors also reported the use of PR78 modified alpha-function in the PR-EOS for HC fractions with acentric factors above 0.491. The molar masses and the coefficients of ideal gas isobaric heat capacity for the HC fractions are in Table II.1 of Castier (2011). The Reservoir Oil problem was put in a more challenging version (Castier, 2011) by adding water so that a *5%,* mol fraction of water results, while the other 20 mol fractions are reduced to *95%* of their original values. Castier also extended the range of pressures from *0.01 bar* up to *350 bar* keeping the temperature at *344.26 K*. The PR-EOS BIPs of water with all components were set to zero. It is reported that below *11.7 bar* the system is in VLE with vapor and oil phases, with a minimum (two-phase) *c* located at *6.4 bar*. At *11.7 bar* a third aqueous phase appears in the system, which is now in VLLE, with no perceptible effect on *c*. At *162.5 bar* the aqueous phase disappears, so that the system is back to VLE, again without major changes on *c*. At *276.1 bar,* vapor phase collapses and the system is now single-phase, with a discontinuity in *c* from *450 m/s* to *1048 m/s*.

Figs. II.6 and II.7 depict the isothermal profile of thermodynamic sound speed calculated by PEC-UOE at *344.26 K* on 3400 points from *0.01 bar* to *350 bar* for the Reservoir Oil with Water, allocating 29s of CPU. Sampled points from Castier (2011) are also plotted. The calculations used BIPs and characterization of HC fractions described above with the PR78 directive set in HYSYS for PR-EOS. The agreement with Castier's points is generally good, if taken into account the heavy load of characterizing parameters and algorithm idiosyncrasies that influence results. The agreement is very good on the low pressure side with a minimum *c* at *6.44 bar*. On the high pressure side some differences appear, especially above *260 bar*. The discontinuity of *c* at the bubble point transition occurs at *267.1 bar* below the reported value of *276.1 bar*. However, this divergence seems to be related only to the determination of the high pressure bubble point and not to the *c* values per se.

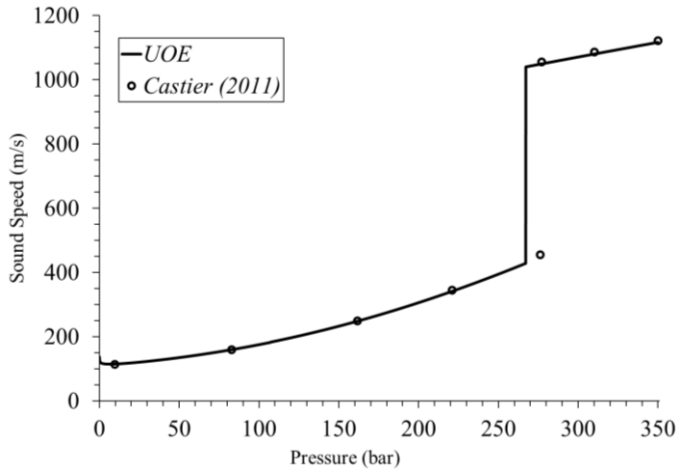

Figure II. 6. Reservoir Oil with Water: Isothermal Profile of Thermodynamic Sound Speed Calculated by PEC-UOE with Sampled Points from Castier (2011).

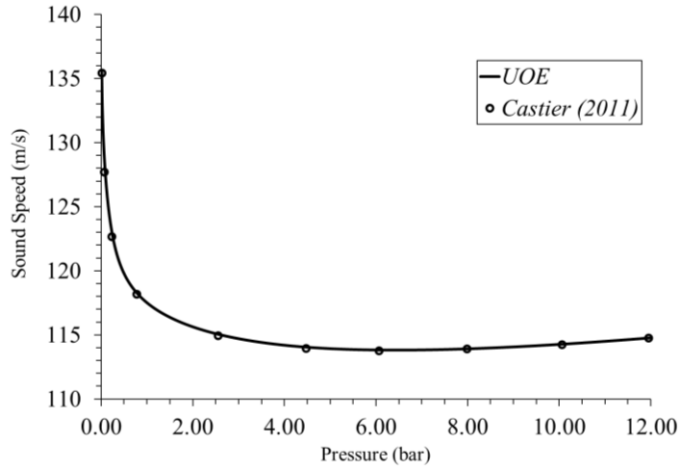

Figure II. 7. Reservoir Oil with Water: Low Pressure Side of the Isothermal Profile of Thermodynamic Sound Speed by PEC-UOE with Points from Castier (2011).

II.4.3. Prudhoe Bay NG: Critical Point Transition of Sound Speed

The Prudhoe Bay NG is back to analysis with the same characterization and PR-EOS BIPs. Its *P x T* VLE dome is in Fig. II.4, with the critical point located at *74.97 bar* and *226.2 K*. Besides the determination of the multiphase *c*, the present work is also committed with the determination of *c* at non-standard conditions like across critical transitions and in reactive systems. In this case, our focus is on the behavior of *c* across the critical transition of this fluid on its critical isotherm. The critical point is approached with two opposed isothermal paths at

T_c=*226.2 K*: (i) inside the VLE dome ($P<P_c$); and (ii) from the single-phase SCF ($P\geq P_c$). All calculations were done with PEC-UOE. Eqs. (II.52a), (II.52b) and (II.52c) were used to determine $\Xi_P(T,P,\underline{Z})$, $\Xi_T(T,P,\underline{Z})$, $\overline{C}_P(T,P,\underline{Z})$ on both paths and *c* was calculated by Eq. (II.50d) with them. Fig. II.8 depicts profiles of *c*, $\Xi_P(T,P,\underline{Z})$, $\Xi_T(T,P,\underline{Z})$ and $\overline{C}_P(T,P,\underline{Z})$ on both sides of the critical neighborhood versus pressure. Some properties were scaled or changed units to be accommodated on the same vertical axis in Fig. II.8. The three lambda-shape transitions of $\Xi_P(T,P,\underline{Z})$, $\Xi_T(T,P,\underline{Z})$, $\overline{C}_P(T,P,\underline{Z})$ are seen as they diverge at $P=P_c$, respectively to $+\infty$, $-\infty$, $+\infty$, on both sides of the critical neighborhood following asymmetric patterns. On the other hand, *c* does not exhibit $\pm\infty$ critical divergences, confirming the results in Sec. II.2.4.3 with the analytical LM and with the color mapping on the SCF neighborhood of the equimolar CO_2-CH_4 NG. The unique effect on *c* as the critical point is crossed is a discontinuity of *162 m/s*. On the two-phase path *c* decreases as *P* increases towards P_c because, as seen in Fig. II.4, the vapor fraction decreases as the dome left border is approached, leading gradually to higher densities with high compressibility, due to the presence of a vanishing vapor, resulting a combination that damps *c*. On the SCF path, *c* is initially high due to low compressibility at high *P*. As *P* decreases at T_c, the compressibility increases with approximately constant (high) density, reducing *c*. Each path has 6500 calculation points with 50s of CPU time.

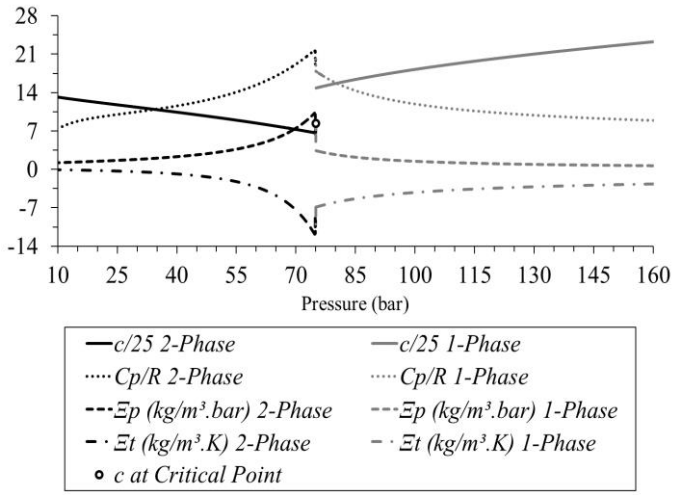

Figure II. 8. Sound Speed Calculated at $T=T_c$ on the Critical Neighborhood of Prudhoe Bay NG: In the Subcritical Side ($P<P_c$) and in the SCF Side ($P\geq P_c$).

II.4.4. Sound Speed Profile in Supersonic Separator with Humid CO_2 Rich Natural Gas

This example portraits the utilization of a battery of supersonic separators (SS) to process a water saturated NG with high CO_2 content. SS operation is designed to accomplish two simultaneous targets in the final NG: WDPA and HCDPA; i.e. the raw gas has to be dehydrated and has to be stripped of a part of its C3+ producing NGL. Data of the raw NG feed, NG product and extracted two-phase condensate are shown in Table II.2. All calculations are executed by PEC-UOE with HYSYS 8.8 using PR-EOS with HYSYS BIPs.

A full discussion on SS modeling is beyond the present scope and is available elsewhere (Arinelli et al., 2017). Therefore aspects of SS modeling are not disclosed here. The intent is only to demonstrate calculation of *c* through a NG separation operation that demands accurate determination of *c* under three-phase VLLE. It must be noticed that water could be captured as ice in the low temperature SS separation section, but the ordinary PR-EOS modeling can only see it as a super-cooled liquid. Despite this limitation, the enthalpy error involved is of low magnitude – super-cooling enthalpy of liquid water at $-40^oC \approx -3\ kJ/mol$ versus the low enthalpy of freezing $\approx -6\ kJ/mol$ plus the sub-cooling enthalpy of ice at $-40^oC \approx -1.3 kJ/mol$ – relatively to the high condensation enthalpy of water ($\approx -41\ kJ/mol$) plus other sensible heat effects ($\approx -3\ kJ/mol$). Table II.2 reports flow compositions along SS: feed composition is valid until the SS separation section where the two-phase condensate is withdrawn, prior to normal shock; whereas the final gas composition is valid from the normal shock point until SS discharge. All SS profiles (T,P,c,Ma) versus SS axial position (x) are available. Fig. II.9 sketches a typical SS nozzle and its design parameters with linear wall profiles, not showing the separation section located at $x=L^{Shock}$ where flow attains the specified supersonic *Ma* at normal shock (Ma^{Shock}). Here, SS was specified with $Ma^{Shock}=1.5$ so that a not too high feed pressure is required. A not too high Ma^{Shock} also implies a low degree of SS irreversibility, so that a good pressure recovery is achieved: final gas is discharged at *41.33 bar* for this *50 bar* feed. WDPA+HCDPA services specify a SS battery with 6 SS nozzles, each one with the following design for $Ma^{Shock}=1.5$: $D_I=0.08m$, $D_O=0.05m$, $D_T=0.04m$, $\alpha=15^o$, $\beta=2.75^o$, $L_C=0.091m$, $L_D=0.135m$, $L=0.226m$, $L^{Shock}=0.126m$, $L^{Diffuser}=0.1m$. The SS nozzle was designed and simulated by another HYSYS UOE: SS-UOE (Arinelli et al., 2017). SS-UOE uses PEC-UOE for calculating the multiphase *c* along SS. Results of interest are shown in Figs. II.10, II.11, II.12 and II.13. Fig. II.10 depicts

T and *c* profiles versus *x*, while Fig. II.11 shows profiles *P* and *Ma* versus *x*. There are two notable points in Figs. II.10 and II.11. The first is the throat location (*x=0.091m*) where $Ma \rightarrow 1^-$, $dT/dx \rightarrow -\infty$, $dP/dx \rightarrow -\infty$, $dv/dx \rightarrow +\infty$, $dc/dx \rightarrow -\infty$, $dMa/dx \rightarrow +\infty$, which are perfectly explainable via multiphase multi-reactive 1D isentropic flow and ECS formalism of Sec. II.2.3, but such proofs were deferred to Supplementary Materials (Appendix D) on behalf of space limitations. The second is the normal shock location (*x=0.126m*) where the supersonic flow suddenly collapses via a discontinuous adiabatic increase of *T*, *P*, *c* and entropy accompanying the *Ma* transition to subsonic. The minimal *T* (*-38.28°C*), *P* (*15.05 bar*) and *c* (*261.62 m/s*) are achieved at $Ma^{Shock}=1.5$, just before separation of two-phase condensate (Table II.2). Fig. II.12 depicts %mol of condensed water and %mol of condensed HC+CO_2 versus *x* showing that water is practically *100%* condensed, while HC+CO_2 species condensed only *1.2912%mol* until the withdrawal point (*x=0.126m*). Fig. II.12 shows that HC+CO_2 condensation starts weakly at *x=0.015m* where heavy species C7+ (with boiling points similar to water) start condensing and then becomes more intense at *x=0.08m* where less heavy, but more present, C3+C4 start condensation as flow temperature falls. Fig. II.13 shows state changes of the flow depicting two VLE domes on plane *P x T* with SS path superimposed. The larger VLE dome belongs to the raw NG, whose WDP curve lies outside the dome. The slender VLE dome refers to the final NG with adjusted WDP and HCDP. The SS (*P,T*) path starts at the WDP curve as the raw NG is water-saturated, i.e. water condenses from the outset (confirmed in Fig. II.12). More intense HC+CO_2 precipitation starts after SS path had crossed the HCDP curve on the larger dome, where a sudden big negative change of inclination of the *c* profile is seen in Fig. II.10 due to a sudden density increase as three-phase flow is formed more intensely at *x=0.08m* corresponding in Fig. II.12 to a more intense condensation of HC+CO_2. In Fig. II.13 SS (*P,T*) path has two branches: the first is the expansion path ending at $Ma^{Shock}=1.5$, *T=-38.28°C, P=15.05 bar, c=261.62 m/s*; the second initiates with rectilinear shock-jump back to *T=15.22°C, P=32.97 bar, c=299.90 m/s*, followed by subsonic diffuser recompression up to *T=31.57°C, P=41.33 bar* and *c=308.48 m/s*.

Table II. 2. Stream Data: SS with Humid CO_2 Rich NG.

Item	*Unit*	*Raw NG*	*Two-Phase Condensate*	*Final NG*
CO_2	%mol	43.92	27.33	44.17
CH_4	%mol	49.91	6.61	50.56
C_2H_6	%mol	2.99	3.90	2.98
C_3H_8	%mol	2.00	12.98	1.83
i-C_4H_{10}	%mol	0.30	5.30	0.22
n-C_4H_{10}	%mol	0.20	4.94	0.13
i-C_5H_{12}	%mol	0.20	8.84	0.07
n-C_5H_{12}	%mol	0.10	5.04	0.03
n-C_6H_{14}	%mol	0.10	6.32	0.01
n-C_7H_{16}	%mol	0.05	3.34	0.00
n-C_8H_{18}	%mol	0.03	2.03	0.00
n-C_9H_{20}	%mol	0.01	0.68	0.00
n-$C_{10}H_{22}$	%mol	0.01	0.68	0.00
H_2O	ppm mol	1784*	120,100.0	18.39
Flow Rate	$MMsm^3/d$	5.12	0.075	5.045
Temperature	^oC	35	-38.28	31.57
Pressure	bar	50	15.05	41.33

** at WDP*

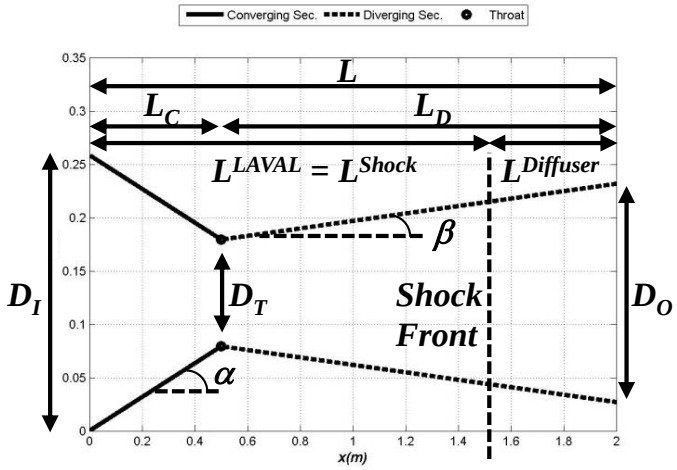

Figure II. 9. SS Geometric Parameters (illustrative axes values).

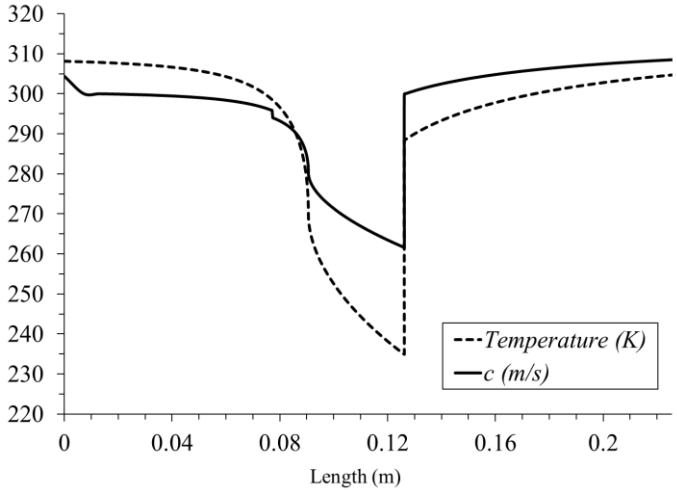

Figure II. 10. SS Profiles: Temperature (*K*) and Sound Speed (*m/s*) vs SS Axial Position (*m*).

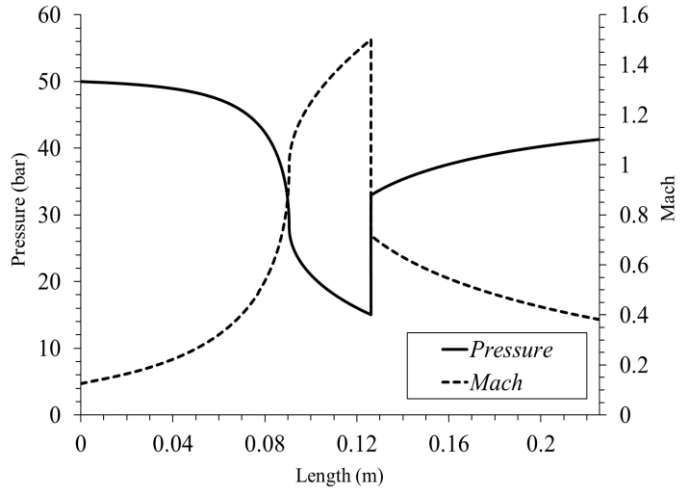

Figure II. 11. SS Profiles: Pressure (*bar*) and Mach vs SS Axial Position (*m*).

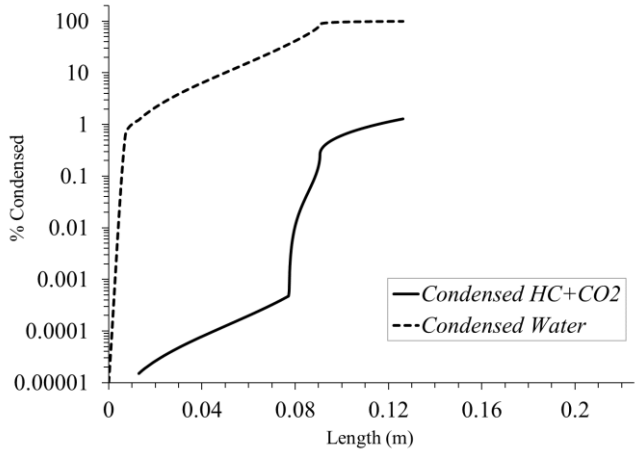

Figure II. 12. SS Profiles: %Condensed H_2O and %mol Condensed $HC+CO_2$ vs Axial Position (*m*).

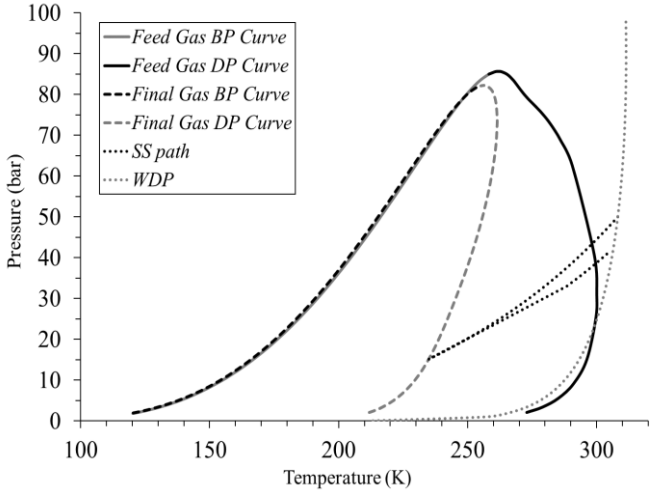

Figure II. 13. Plane *P x T*: (i) VLE Diagram of Raw NG with WDP Curve; (ii) SS Path; and (iii) VLE Diagram of Final NG.

II.4.5. Sound Speed in Two-Phase Reactive Stream O_2-Methanol

This example refers to a patent (Cheng, 2000) describing a SR to increase selectivity of methanol oxidation to formaldehyde by inhibiting over-oxidations. Gas O_2 and liquid CH_3OH are fed to a SR at *1 bar* with sub-stoichiometric molar ratios *10/90* and *30/70* as two-phase streams. The valid set of chemical reactions is solely Eq. (II.54). Fig. II.14 depicts the temperature influence on *c* assuming reactive and non-reactive conditions for *10/90* and *30/70* feeds. Reactive cases were calculated with REC-UOE, while the non-reactive ones with PEC-UOE (PR-EOS and HYSYS BIPs). Non-reactive profiles are *≈800X* as faster as the reactive

counterparts, both with 60 points: 1.5s against 1200s of CPU time. For non-reactive *10/90* feed, *c* is initially very low due to low gas content entailing high two-phase density and high two-phase compressibility. The gradient discontinuities on both non-reactive profiles at *331 K* (*30/70*) and *337 K* (*10/90*) signalize the respective dew points with O_2 gas, confirmed by Fig. II.15 with molar vapor fraction equilibrium profiles. From this point on, *c* increases practically linearly with temperature as in any low pressure gas. On the other hand, in the reactive cases gradient discontinuities are postponed to *355 K* (*30/70*) and *351 K* (*10/90*) due to water reaction product in Eq. (II.54) and absence of O_2 in the equilibrium stream, increasing the reactive dew points as shown in Fig. II.15.

$$CH_3OH(g) + (1/2)O_2(g) = H_2CO(g) + H_2O(g) \quad \text{(II.54)}$$

The reactive *c*'s are very different from the non-reactive analogues and higher above the reactive dew points. As vapor phases are approximate ideal gases, the equilibrium reactive gas has a lower molar mass giving a higher *c* via Eq. (II.51). Fig. II.16 depicts the *10/90* feed and its chemical equilibrium composition profiles versus *T*. The equilibrium mixture for this very spontaneous reaction has no O_2 and is practically invariant with *T* below *425 K*.

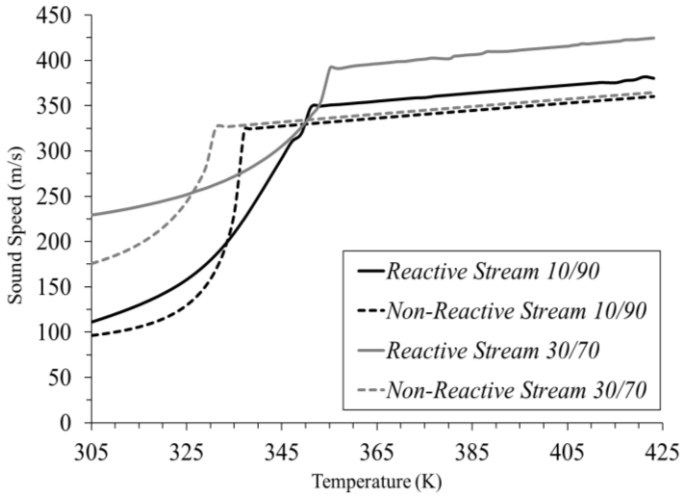

Figure II. 14. Sound Speed for Two-Phase O_2-CH_3OH Feed versus *T*: Reactive and Non-Reactive *10/90* and *30/70* Feeds.

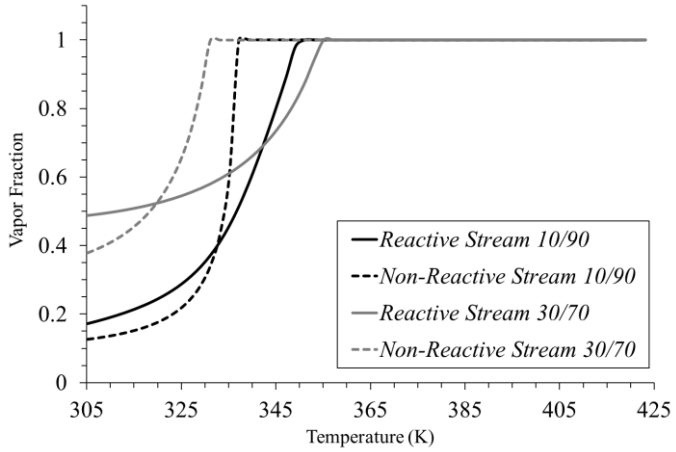

Figure II. 15. Molar Vapor Fractions for Two-Phase O_2-CH_3OH Feed versus *T*: Reactive and Non-Reactive *10/90* and *30/70* Feeds.

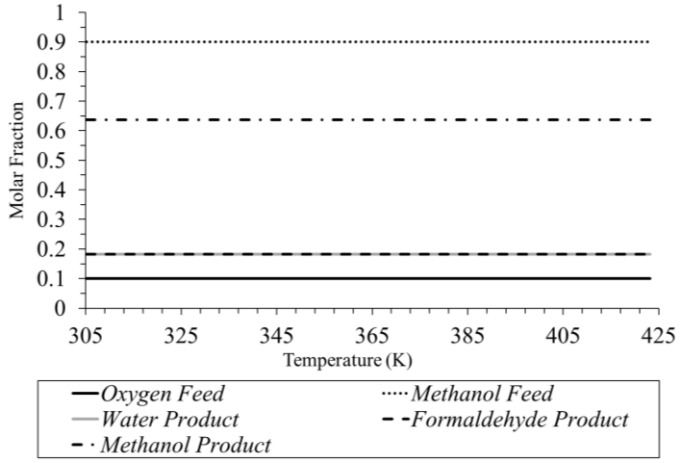

Figure II. 16. Feed and Equilibrium Compositions for Reactive Sound Speed of *10/90* Feed.

II.4.6. Sound Speed in Low-Pressure NG Pyrolysis

Lean NG or CH_4 pyrolysis produces olefins and acetylene at high temperatures, low pressures and short reaction times. Such process belongs to GTL category. Eqs. (II.55a) and (II.55b) show the relevant chemical reactions for a 100% CH_4 NG, both reducing the reactive molar mass (M_M). Moreover, both are non-spontaneous at 25ºC with $\Delta\overline{G}^o >> 0$, but are very endothermic, respectively with $\Delta\overline{H}^o = +202.2\ kJ/mol$ and $\Delta\overline{H}^o = +376.6\ kJ/mol$. Therefore, very high *T* can turn both into spontaneous reactions, displacing equilibrium towards the RHS of Eqs. (II.55a) and (II.55b).

$$2\ CH_4(g) = C_2H_4(g) + 2\ H_2(g) \quad \text{(II.55a)}$$

$$2\ CH_4(g) = C_2H_2(g) + 3\ H_2(g) \quad \text{(II.55b)}$$

Fig. II.17 depicts non-reactive and reactive *c*'s for a feed of CH_4 at *P=0.1333 bar* (*100 mmHg*) from *775 K* to *1375 K*. The non-reactive and reactive profiles, containing 60 points each, were respectively calculated with PEC-UOE and REC-UOE (CPU times: *1.2s* and *900s*) assuming ideal gas behavior. Non-reactive and reactive sound speeds have similar values below *950 K*, but become increasingly different as the equilibrium conversion evolves at higher *T*. As *T* increases, the equilibrium M_M decreases, increasing the ideal gas *c* by Eq. (II.51), so that at *1375 K* the reactive *c* is *≈33%* greater than the non-reactive analogue. Fig. II.18 depicts the temperature profiles of equilibrium mol fractions when calculating the reactive *c*. As *T* increases composition changes appreciably via chemical equilibrium.

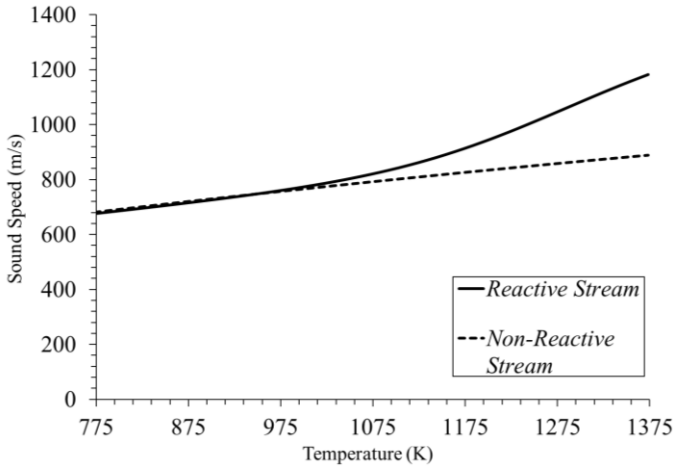

Figure II. 17. Reactive and Non-Reactive Sound Speeds for Low-Pressure CH_4 Pyrolysis.

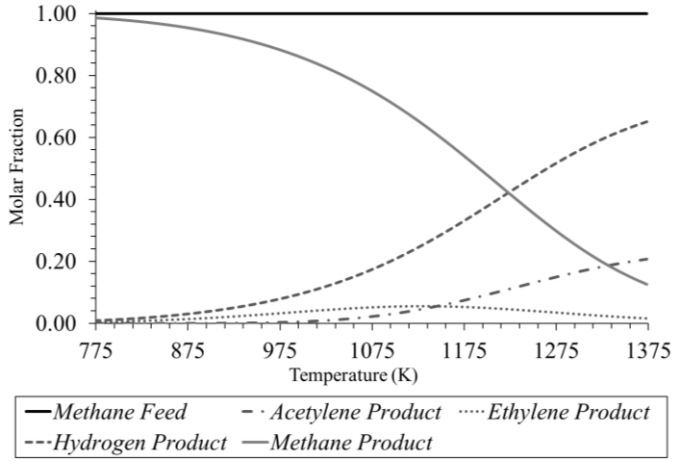

Figure II. 18. Feed and Equilibrium Compositions for Reactive Sound Speed of CH_4 Pyrolysis.

II.5. Conclusions

This work presents a theoretical framework for handling the thermodynamic sound speed for general multiphase and multi-reactive equilibrium streams. Sound speed *c* is approached as a property of Equilibrium Closed Systems (ECS). The ECS point-of-view is convenient because Thermodynamics does not depend on the real internal nature of closed systems, provided they are ECS's. The number of phases, the number of relevant chemical reactions, and even the existence of molecules or atoms, are of no importance provided there is true equilibrium. In this regard, the entire ECS internal complexity is overridden by using its only two state coordinates (*T*, *P*). This allowed us to develop a generalization of the sound speed formula for such complex streams by establishing a correspondence between an ECS and a plug-flow fluid element of a steady-state, 1D, horizontal, adiabatic, multiphase, multi-reactive, equilibrium compressible flow. The formula reduces to the classical *c* for non-reactive single-phase.

This work also approached the asymptotic behavior of *c* on the two sides of the critical neighborhood of a pure fluid by using Landau Model for phase transitions. It was proved that *c* does not exhibit critical point $\pm\infty$ singularities, only an ordinary discontinuity is present. This investigation was instigated by the critical point 2nd order transitions of $\overline{C}_P, \Xi_T, \Xi_P$ with lambda-shape $\pm\infty$ critical divergences. $\overline{C}_P, \Xi_T, \Xi_P$ (or $\hat{C}_P, \Xi_T, \Xi_P$) are used in the proposed ECS *c* formula, but despite their critical point $\pm\infty$ singularities, *c* is not singular. Such curious fact results from the mathematical mechanisms acting in the thermodynamic ECS *c* formula. A

useful consequence of this, is that the critical *c* can be calculated by a supercritical, single-phase, path (T-$T_c \rightarrow 0^+$), with constant P=P_c and $\underline{Z}$, towards the fluid critical point (T_c,P_c).

Calculation of multiphase and/or multi-reactive *c* was implemented via sound speed Unit Operation Extensions for HYSYS 8.8, namely, PEC-UOE for multiphase equilibrium streams and REC-UOE for multiphase multi-reactive equilibrium streams. These UOEs can run with any HYSYS thermodynamic package. PEC-UOE is much faster because it only uses the fast multiphase *Flash*(*P*,*T*) HYSYS built-in tool, while REC-UOE has to create temporary PFDs to run HGR. Calculations compared well with multiphase *c* from the literature. Calculations of multiphase *c* in NG processing were addressed in Prudhoe Bay NG examples and in SS processing of NG for WDPA+HCDPA. The multi-reactive multiphase *c* was demonstrated in SRs for lean NG pyrolysis (GTL) and two-phase methanol oxidation to formaldehyde. Reactive calculations show that, depending on *T*, *P* and conversion, differences to the correct reactive value of *c* may occur, if a reactive stream has its *c* calculated via non-reactive formulae merely substituting the stream composition in any point of a real chemical reactor.

Author Information

Corresponding Author

*Tel.: +55-21-3938-7535. E-mail: jlm@eq.ufrj.br.

Notes

Authors declare no competing financial interest.

Acknowledgement

Authors acknowledge financial support from PETROBRAS S.A. and CNPq-Brazil.

Supplementary Materials (Appendix D)

Limit Conditions of Multiphase, Multi-Reactive Compressible Steady-State 1D Isentropic Plug-Flow with Variable Flow Section with Equations (D.1) to (D.31). This information is available free of charge via the Internet.

Abbreviations

1D, 2D, 3D: One, Two and Three-Dimensional; BIP Binary Interaction Parameter; C3+ Propane and Heavier Alkanes; CPU Central Processing Unit; DLL Dynamic-Link Library; ECS

Equilibrium Closed System; EOS Equation of State; GTL Gas-to-Liquids; HC Hydrocarbon; HCDP Hydrocarbon Dew Point; HCDPA Hydrocarbon Dew Point Adjustment; HGR HYSYS Gibbs Reactor; LHS Left-Hand Side; LM Landau Model; MMsm^3/d 10^6 Standard m^3 per Day; NG Natural Gas; NGL Natural Gas Liquids; PFD Process Flow Diagram; PR Peng-Robinson; PVT Pressure, Volume & Temperature; RGB Red, Green & Blue True-color Pixel; RHS Right-Hand Side; SI International System of Units; SR Supersonic Reactor; SCF Supercritical Fluid; SS Supersonic Separator; UOE Unit Operation Extension; VB Visual Basic; VLE Vapor-Liquid Equilibrium; VLLE Vapor-Liquid-Liquid Equilibrium; WDP Water Dew Point; WDPA Water Dew Point Adjustment.

Nomenclature

$A(x)$: *Flow section at axial position x (m^2)*
$\overline{A}(T,v)$: *Molar Helmoltz free energy of pure fluid (J/mol)*
$A_i(T)$: *Temperature dependent terms of LM free energy*
A_{ij} : *Coefficients for temperature influence on LM free energy terms*
c : *Sound speed of multiphase multi-reactive fluid (m/s)*
$\overline{C}_P \equiv \left(\frac{\partial \overline{H}}{\partial T}\right)_{P,\underline{Z}}$: *Molar heat capacity at const. P, $\underline{Z}$ of multiphase fluid (J/K.mol)*
$\overline{C}_V \equiv \left(\frac{\partial \overline{U}}{\partial T}\right)_{\overline{V},\underline{Z}}$: *Molar heat capacity at const. $\overline{V}$, $\underline{Z}$ of multiphase fluid (J/K.mol)*
$\hat{C}_P \equiv \left(\frac{\partial \hat{H}}{\partial T}\right)_{P,\underline{Z}}$: *ECS heat capacity at const. P, $\underline{Z}$ per mass unit (J/K.kg)*
D : *Internal diameter (m)*
$\hat{G}$: *ECS Gibbs free energy per mass unit (J/kg)*
$\overline{H}$: *Molar enthalpy of multiphase fluid (J/mol)*
$\hat{H}$: *ECS enthalpy per mass unit (J/kg)*
$\underline{\underline{J}}$: *Jacobian matrix of multiphase equilibrium equations*
L : *SS total length (m)*
L_C : *SS converging section length (m)*
L_D : *SS diverging section length (m)*
$Ma = v/c$: *Mach Number*
Ma^{Shock} : *Mach Number just before condensate withdrawal and normal shock*
M_M : *Molar mass of multiphase fluid (kg/mol)*
nc : *Number of components*
P : *Pressure (Pa or bar)*
q : *Mass flow rate of multiphase multi-reactive stream (kg/s)*
$\overline{S}$: *Molar entropy of multiphase fluid (J/K.mol)*

$\hat{S}$: *ECS entropy per mass unit (J/K.kg)*
T : *Absolute temperature (K)*
$\overline{U}$: *Molar internal energy of multiphase fluid (J/mol)*
v : *Axial velocity of non-segregated multiphase flow (m/s)*
$v, \overline{V}$: *Molar volume in LM (m^3/mol)*
$\hat{V}$: *ECS volume per mass unit (m^3/kg)*
x : *Flow axial position (m)*
$\underline{Z}$: *Species total mol fractions vector (nc x 1) in ECS preparation*

Greek Symbols

α : *SS converging section half angle (deg)*
β : *SS diverging section half angle (deg) (Sec. II.4), mol vapor fraction (Sec. II.2)*
δT, δP : *Positive perturbations for numerical derivatives in Sec. II.3 (K, Pa)*
$\Delta \equiv (v_V - v_L)/2v_c$: *Dimensionless difference of vapor and liquid molar volumes*
ρ : *ECS density or multiphase fluid density (kg/m³)*
$\gamma = \overline{C}_P / \overline{C}_V$: *Ratio of molar heat capacities of multiphase fluid*
Γ : *Wall horizontal reaction per length unit (N/m)*
μ : *Chemical potential of pure fluid (J/mol)*
$\underline{\Omega}$: *Multiphase equilibrium constraints*
Ψ : *Scalar property of multiphase fluid*
$\Sigma \equiv (v_V + v_L)/2v_c$: *Dimensionless sum of vapor and liquid molar volumes*
$\underline{\theta}$: *Vector of multiphase equilibrium variables*
$\Xi_P \equiv \left(\frac{\partial \rho}{\partial P}\right)_{T,\underline{Z}}$: *ECS derivative of ρ with P at const. T, $\underline{Z}$ (kg/Pa.m^3)*
$\Xi_T \equiv \left(\frac{\partial \rho}{\partial T}\right)_{P,\underline{Z}}$: *ECS derivative of ρ with T at const. P, $\underline{Z}$ (kg/K.m^3)*

Subscripts

c : *Critical point*
C : *SS converging section*
D : *SS diverging section*
I : *SS inlet*
k : *Species index*
L : *Liquid phase*
O : *SS outlet*
SAT : *Saturated*
T : *SS throat*
V : *Vapor phase*

Superscripts

$'$: *Ideal gas property*
$Shock$: *Just before condensate withdrawal and normal shock*
$*$: *Sonic (choked) condition on steady-state 1D isentropic plug-flow*
VLE : *Vapor-Liquid Equilibrium*

References

Arinelli, L.O., Trotta, T.A.F., Teixeira, A.M., de Medeiros, J.L., Araújo, O.Q.F., 2017, Offshore Processing of CO2 Rich Natural Gas with Supersonic Separator versus Conventional Routes, J. of Natural Gas Science & Engineering. Under Submission.

Bedard, R.L., Naunheimer, C., Gavin P. Towler, G.P., 2014. Methane Conversion Apparatus and Process Using a Supersonic Flow Reactor. US Patent 2014/0058160A1

Cao, X., Yang, W., 2015. The dehydration performance evaluation of a new supersonic swirling separator. J. Nat. Gas Sci. Eng. 1–10. doi:10.1016/j.jngse.2015.10.029

Castier, M., 2011. Fluid Phase Equilibria Thermodynamic speed of sound in multiphase systems. Fluid Phase Equilib. 306, 204–211. doi:10.1016/j.fluid.2011.04.002

Cheng, A.T.Y. 2000. Process for Accelerating Fast Reactions Using High-Intensity Plug-Flow Tubular Reactors. Patent EP0995489 A2

Crowl, D. A., Louvar, J. F., 2002, Chemical Process Safety: Fundamentals with Applications, 2nd Ed., Prentice Hall, USA.

Ehinmowoa, A.B., Orodub O.D., Anaweb, P.A.L, Ogunleyec, O.O., 2016. Attenuating severe slug flow at large valve opening for increased oil production without feedback control signal. J. of Pet. Sci. & Eng., Volume 146, 1130–1141.

Fox, R.W., McDonald, A.T., Pritchard, P.J., 2004. Introduction to Fluid Mechanics, 6th Ed., John Wiley & Sons Inc., USA.

Hammer, M., Wahl, P.E., Anantharaman, R., Berstad, D., Lervåg, K.Y., 2014. CO2 Capture from Off-shore Gas Turbines Using Supersonic Gas Separation. Energy Procedia 63, 243–252. doi:10.1016/j.egypro.2014.11.026

Landau, L.D., 1969. On the Theory of Phase Transitions. Translated from Landau L.D. "Collected Papers" (Nauka, Moscow, 1969),V. 1, pp. 234–252.

Leung, J.C., Grolmes, M.A., 1987. The discharge of two-phase flashing flow in a horizontal duct, AIChE J., V. 33, 3, pp. 524–527. doi: 10.1002/aic.690330323

Libby, P.A., 1962, Theoretical Analysis of Turbulent Mixing of Reactive Gases With Application to Supersonic Combustion of Hydrogen, ARS J., V. 32, 3 pp. 388-396. http://dx.doi.org/10.2514/8.6033

Machado, P.B., Monteiro, J.G.M., Medeiros, J.L., Epsom, H.D., Araujo, O.Q.F., 2012. Supersonic separation in onshore natural gas dew point plant. J. Nat. Gas Sci. Eng. 6, 43–49. doi:10.1016/j.jngse.2012.03.001

Mcmurtrey, L.J., 1964. Nuclear Powered Water Jet Engine. US Patent US 3151596 A.

Nichita, D.V., Khalid, P., Broseta, D., 2010. Calculation of isentropic compressibility and sound velocity in two-phase fluids. Fluid Phase Equilibria 291 (1), 95e102.

Nichita, D.V., Broseta, D., Leibovici, C.F., 2007. Reservoir fluid applications of a pseudo-component delumping new analytical procedure J. Pet. Sci. Eng. 59, 59–72.

OGJ, 2014. Petrobras signs LOI to charter FPSO for Libra field. Oil Gas J.

Powers, J.M. and Paolucci, S., 2005. Accurate Spatial Resolution Estimates for Reactive Supersonic Flow with Detailed Chemistry. AIAA Journal, V. 43, 5, pp. 1088-1099. http://dx.doi.org/10.2514/1.11641

Raniere, F.D., Schuman, M.D., 1988. Method of Controlling Pyrolysis Temperature. US Patent 4,724,272.

Romm, L. and Somorjai, G.A., 2002. High-Temperature Short-Contact-Time Supersonic Nozzle Chemistry of Light Aliphatic Hydrocarbons. Topics in Catalysis V. 20, 1–4, pp. 53-63

Schinkelshoek, P., Epsom, H.D., 2008. Supersonic gas conditioning - Commercialisation of Twister Technology, in: GPA Annual Convention Proceedings. Grapevine, Texas, USA, pp. 739–745.

Secchi, R., Innocenti, G., Fiaschi, D., 2016. Supersonic Swirling Separator for natural gas heavy fractions extraction: 1D model with real gas EOS for preliminary design. J. Nat. Gas Sci. Eng. 34, 197–215. doi:10.1016/j.jngse.2016.06.061

Shandor, M., Stone, A.R., Walker, R.E., 1963. Secondary Gas Injection in a Conical Rocket Nozzle. AIAA J., V. 1, 2, pp. 334-338. http://dx.doi.org/10.2514/3.1533

Turner, J., 2009. F-18 Hornet High-Speed (Transonic) Flyby. https://www.youtube.com/watch?v=-mr9tam_c9g. Accessed 01/08/2017.

Wilkinson, J., 2012. Wilk4: Breaking the Sound Barrier (and Vapor Cones around Jets). http://www.wilk4.com/misc/soundbreak.htm. Retrieved 2012-10-31.

Wood, A.B., 1930. A Textbook of Sound: Being an Account of the Physics of Vibrations with Special Reference to Recent Theoretical and Technical Developments. The Macmillan Company, New York.

Yang, Y., Wen, C., Wang, S., Feng, Y., 2014. Numerical simulation of real gas flows in natural gas supersonic separation processing. J. Nat. Gas Sci. Eng. 21, 829–836. doi:10.1016/j.jngse.2014.10.010

CHAPTER III - OFFSHORE PROCESSING OF CO_2 RICH NATURAL GAS WITH SUPERSONIC SEPARATOR VERSUS CONVENTIONAL ROUTES

This paper was published in Journal of Natural Gas Science and Engineering, 46, 199-221, 2017. doi: 10.1016/j.jngse.2017.07.010 (Appendix T.9).

Offshore Processing of CO_2 Rich Natural Gas with Supersonic Separator versus Conventional Routes

Lara de Oliveira Arinelli, Thiago Affonso F. Trotta[1], Alexandre Mendonça Teixeira[2], José Luiz de Medeiros[3] and Ofélia de Queiroz F. Araújo[4]*

Escola de Química, Federal University of Rio de Janeiro, 21941-972, Rio de Janeiro, RJ, Brazil

**Corresponding Author – lara.arinelli@gmail.com*

[1]thiagotrotta@yahoo.com.br [2]alexandremtxr@gmail.com [3]jlm@eq.ufrj.br [4]ofelia@eq.ufrj.br

Abstract

The supersonic separator (SS) was investigated for treating humid natural gas with *44%mol* CO_2 in offshore rigs and compared to the conventional Water Dew Point Adjustment (WDPA) via TEG Absorption, Hydrocarbon Dew Point Adjustment (HCDPA) via Joule-Thomson Expansion (JTE) and CO_2 removal via Membrane Permeation (MP). SS was tested as a single-step operation for WDPA+HCDPA. To simulate SS and MP, two Unit Operation Extensions (UOE) were developed for simulator HYSYS 8.8 (AspenTech). MP-UOE uses an empirical approach calibrated with operation data, whereas SS-UOE is entirely funded on thermodynamics, not demanding calibration. MP-UOE and SS-UOE use the thermodynamic infrastructure of HYSYS: property packages and several proved multiphase flash algorithms. MP-UOE and SS-UOE performed accordingly the expected characteristics of the respective operations and were critical to accomplish this analysis as SS and MP are not available in simulators. In terms of final gas quality (WDP$\leq$*-45^{o}C @1.01 bar*, HCDP$\leq$*0^{o}C @45 bar*, *%CO_2 $\leq$15%mol*) the best process configuration was found to be a hybrid one: SS WDPA+HDPA and MP CO_2 removal, with low footprint and low power demand (*-6.9%*) relative to conventional 3-step way. If used for CO_2 removal, SS could abate CO_2 from *44%* to *21.85%mol*. Albeit less effective than MP, SS CO_2 removal is a noticeable option that produces fuel-gas for power generation with *%$CO_2$$\approx$20%* as required by new turbo-shafts. Moreover, CO_2 is withdrawn from SS as a pumpable liquid allowing a cut of *44%* in the power demanded for CO_2 separation and injection as EOR agent.

Keywords

Natural Gas Conditioning; Supersonic Separator; Membrane Permeation; CO_2 Removal; Unit Operation Extension

III.1. Introduction

Deepwater natural gas (NG) pipelines face problems created by H_2O, CO_2 and heavy hydrocarbons (HC). Although raw NG has low water content (*<0.5%*), it must be reduced (*<100 ppm*) to prevent gas hydrates under high pressure (*P*) and low temperatures (*T*). Under high CO_2 content (*>40%*) CO_2 abatement is necessary, at least in part, to avoid occupying pipeline capacity with inert. Besides, CO_2 must be withdrawn from NG for injection as enhanced oil recovery (EOR) fluid. Heavy HCs (C3+) should be removed to lower NG dew point for processing. These issues mean costs to treat CO_2 rich NG via Water Dew Point Adjustment (WDPA), Hydrocarbon Dew Point Adjustment (HCDPA) and CO_2 removal.

NG conditioning ascribes liquid segregation operations for WDPA and HCDPA, while CO_2 removal occurs via Membrane Permeation (MP). The objective of conditioning humid CO_2 rich NG is to deprive it from its liquid ([L]) and low supercritical fluid ([SCF]) fractions, delivering a saleable lean NG, while the C3+ in [L] is sold as NGL, and [SCF] is injected for EOR. With MP CO_2 removal, NG conditioning begins with WDPA, following HCDPA to collect C3+ as NGL. Common WDPA and HCDPA in offshore rigs are, respectively, TEG Absorption and Joule-Thomson Expansion (JTE) (GPSA, 2004).

With CO_2 rich NG (*$\%CO_2 \geq 40\%$*) HCDPA should be NGL selective. But JTE rarely is, besides being a power wasting HCDPA. JTE expands from *70-90 bar* to a still high *$P \approx 50$ bar* at *$T \approx 5^oC$*. This precipitates NGL with huge CO_2 condensation as JTE (*T,P*) path intersects with [SCF] condensation window. Consequently, NGL is lost because the [SCF] rich JTE fluid is pumped to EOR.

A better option is a HCDPA "passing" at low *P* and colder *T*, selectively ejecting [L] with low [SCF] content, and then "recovering" to high discharge *P*, releasing lean NG at high *P*. This selective HCDPA can be executed in Supersonic Separators (SS), which accomplishes both tasks, WDPA+HCDPA, with better power allocation than JTE. SS collects [L] at lower (*P*,*T*) than JTE, but recovers pressure, releasing lean NG at a higher *P* than JTE; i.e. SS demands less power for same HCDPA. Besides, SS condensate is more NGL selective: It has less [SCF] and more [L] by combining low (*P*,*T*).

SS produces WDPA+HCDPA by expanding raw NG to supersonic velocities, dropping (*T*,*P*) with milliseconds of residence time. Intense freezing and centrifugal [L] removal force WDPA+HCDPA guaranteeing lean NG specification.

SS comprises static swirling device, Laval nozzle, cyclonic separator and final diffuser. The Laval nozzle comprises converging, throat and diverging sections. The diffuser is a continuation of the Laval diverging section after the separator for collecting [L] formed in the Laval. The flow accelerates from subsonic to $Ma=1$ at the throat and then becomes supersonic ($Ma>1$) in the diverging section reducing (*T*,*P*). Due to high rate of conversion of enthalpy to kinetic energy, water and C3+ change to low enthalpy [L] mist, centrifugally collected by separating vanes. Given SS capacity, design comprehends sizing Laval nozzle, diffuser and vanes. A too large or too small sizing of vanes, degrade performance with loss of lean gas in the former and insufficient WDPA+HCDPA in the latter. Similarly, if vanes are prematurely or post-maturely positioned on SS axis excessive gas losses and insufficient WDPA+HCDPA result in both cases. The positioning of vanes relates to an idiosyncrasy of supersonic flow: towards a higher discharge pressure supersonic flow configures a metastable condition which aggravates as *Ma* increases above 1. Thus, assuming adiabatic flow, there is an analogous subsonic flow with same mass, momentum and energy flow rates, but hotter and with greater entropy flow rate, which is globally stable by the 2nd Law of Thermodynamics and is accessible via an irreversible, adiabatic, sudden collapse of supersonic flow at a specific location in the diverging section: the normal shock front.

As any metastable collapse, the shock is easily provoked by irreversibilities (e.g. friction) so that as the flow accelerates beyond $Ma=1$ the shock is gradually more prone to occur. Supersonic flow is unlikely to exist much above $Ma \approx 2$ in SS for NG processing with high pressure recovery as it progressively loses stability against a progressively higher discharge pressure. Entropy is adiabatically created as the fluid crosses normal shock and such creation rate increases with shock irreversibility, which, by its turn, increases with Ma^{Shock}, reducing backpressure. This affects the positioning of vanes: If condensate is not collected before shock, it re-vaporizes into exiting gas, destroying separation. Downstream the shock, the flow reaches the diffuser as subsonic and decelerates recovering some pressure.

SS for NG WDPA+HCDP suggests its investigation as a single-step conditioning of humid CO_2 rich NG versus conventional alternatives. Additionally, SS CO_2 removal has been only incipiently reported and the proof of concept of SS for WDPA+HCDPA and CO_2 abatement of humid CO_2 rich NG was never reported. To undertake this investigation, Sec. III.2 approaches the theoretical background: Sound speed, SS modeling, MP and SS CO_2 removal and CO_2 freeze-out. Sec. III.3 discloses MP and SS models as Unit Operation Extensions (UOE) – MP-UOE and SS-UOE – to be inserted in HYSYS 8.8 process flow diagrams (PFD). Sec. III.4 assesses MP-UOE and SS-UOE PFDs for conditioning water saturated CO_2 rich NG with results in Sec. III.5. Sec. III.6 discusses adiabatic expansion-compression efficiencies in SS-UOE. Sec. III.7 addresses conclusions.

III.2. Theoretical Background

Subsidiary subjects are addressed to apply SS for conditioning CO_2 rich NG. The main item is SS modeling itself, a resource not available in process simulators. These topics are discussed at the light shed by the literature.

III.2.1. Multiphase Sound Speed

SS modeling demands the speed of sound (c) as a property of single-phase and multiphase streams. Calculation of c is necessary to obtain Ma at any point of SS as $Ma=v/c$ where v is stream velocity. The literature discusses c of multiphase streams with constant total composition (CTC). Wood (1930) presented an approximate method composing c of pure component phases to obtain gas-liquid c. Secchi et al. (2016) approached gas-liquid c extending Wood's method with c of each multicomponent phase via GERG-EOS. Nichita et al. (2010) proposed a thermodynamic method for c of VLE streams using numerical derivatives of VLE analogs of isothermal compressibility, isobaric expansivity, isobaric heat capacity and density, solving CTC VLEs by a flash routine. A limitation of this method is its exclusive VLE formulation, while in SS vapor-liquid-water equilibrium (VLWE) is common. Castier (2011) presented a thermodynamic approach to multiphase c under constraints of volume, entropy and CTC using property derivatives via computing algebra.

These works have, rigorously or approximately, approached c for CTC multiphase streams. But, as a 2nd order thermodynamic property, the concept of c can be extended to the uppermost

general scenario of multiphase and multi-reactive equilibrium streams like any 1st or 2nd order thermodynamic property can. This was done in a parallel work of de Medeiros et al. (2017) by making a correspondence between a fluid element of a steady-state multiphase multi-reactive equilibrium plug-flow stream and an Equilibrium Closed System (ECS). The ECS thermodynamic state, given preparation conditions ($\underline{Z}$), is not in general CTC, but has constant mass and only two independent state variables (e.g. *T*,*P*). These authors also showed how to implement *c* for multiphase equilibrium streams and for multiphase multi-reactive equilibrium streams in the context of simulators, by creating two UOEs for HYSYS 8.8 to calculate *c*: (i) PEC-UOE for CTC phase equilibrium *c*; and (ii) REC-UOE for multiphase and multi-reactive equilibrium *c*. Several examples of utilization were provided, including multiphase multi-reactive *c*, critical point transition *c* and profiles of VLWE *c* along SS with humid CO_2 rich NG.

For SS modeling in the present work, *c* of single-phase or multiphase VLWE streams is determined via PEC-UOE. PEC-UOE uses molar basis and ECS formula Eq. (III.1a) for calculating *c* of multiphase fluid at (*T*,*P*,$\underline{Z}$), where $\underline{Z}$ is the vector of CTC fractions. The multiphase ECS 2nd order properties in Eq. (III.1a), namely, Ξ_T, Ξ_P and $\overline{C}_P$, are calculated at (*T*,*P*,$\underline{Z}$) via numerical central-point derivatives of multiphase ECS properties ρ and $\overline{H}$ by calling HYSYS *Flash*(*P*,*T*) in Eqs. (III.1b), (III.1c) and (III.1d). HYSYS *Flash*(*P*,*T*) is not a unit operation, therefore it can be called for a stream in the current PFD from a UOE without requiring to open a new PFD. This makes the calculation of *c* very fast. Five calls to *Flash*(*P*,*T*) are executed in Eqs. (III.1b), (III.1c) and (III.1d): one at (*T*,*P*,$\underline{Z}$) for the ECS $\rho(T,P,\underline{Z})$, $\overline{H}(T,P,\underline{Z})$, $M_M(T,P,\underline{Z})$; two calls at ($T\pm\delta T$,*P*,$\underline{Z}$) for the ECS $\rho(T\pm\delta T,P,\underline{Z})$, $\overline{H}(T\pm\delta T,P,\underline{Z})$; and two at (*T*,$P\pm\delta P$,$\underline{Z}$) for the ECS $\rho(T,P\pm\delta P,\underline{Z})$, $\overline{H}(T,P\pm\delta P,\underline{Z})$.

$$c=\frac{1}{\sqrt{\Xi_P-(M_M T/\rho^2)(\Xi_T^2/\overline{C}_P)}} \tag{III.1a}$$

$$\Xi_P(T,P,\underline{Z})=\frac{\rho(T,P+\delta P,\underline{Z})-\rho(T,P-\delta P,\underline{Z})}{2.\delta P} \tag{III.1b}$$

$$\Xi_T(T,P,\underline{Z})=\frac{\rho(T+\delta T,P,\underline{Z})-\rho(T-\delta T,P,\underline{Z})}{2.\delta T} \tag{III.1c}$$

$$\overline{C}_P(T,P,\underline{Z}) = \frac{\overline{H}(T+\delta T,P,\underline{Z}) - \overline{H}(T-\delta T,P,\underline{Z})}{2.\delta T} \tag{III.1d}$$

III.2.2. Further Aspects of Multiphase Sound Speed

It is worth noting that the thermodynamic *c* can be written according to several analogues that are transparent in the ECS analysis of de Medeiros et al. (2017). These analogues are valid for multiphase *c* as well as for multiphase multi-reactive *c*. For multiphase *c*, without chemical reactions, ECS is CTC with constant molar mass (M_M), therefore calculating *c* with mol basis is practical. For multiphase multi-reactive *c*, mass is the unique ECS invariant, thus *c* is expressed in mass basis. In SS context, *c* of multiphase VLWE streams is calculated in mol basis via equivalent ECS formulae Eqs. (III.1a), (III.1e), (III.1f) and (III.1g), where $\overline{C}_V$ is related to $\overline{C}_P$ via ECS formula Eq. (III.1h). The ideal gas $c'(T,\underline{Z})$ – $'$ marks ideal gas – derives from Eq. (III.1g) via ideal gas EOS in Eq. (III.1i).

$$c = \frac{1}{\sqrt{\left(\frac{\partial \rho}{\partial P}\right)_{\bar{S},\underline{Z}}}} \tag{III.1e}$$

$$c = \frac{1}{\sqrt{\Xi_T \left(\frac{\partial T}{\partial P}\right)_{\bar{S},\underline{Z}} + \Xi_P}} \tag{III.1f}$$

$$c = \sqrt{(\overline{C}_P / \overline{C}_V)/\Xi_P} \tag{III.1g}$$

$$\overline{C}_P - \overline{C}_V = (M_M T/\rho^2)\Xi_T^2/\Xi_P \tag{III.1h}$$

$$\Xi_P' = \frac{M_M}{R.T}\ ,\ \frac{\overline{C}_P'(T)}{\overline{C}_V'(T)} = \gamma'(T) \Rightarrow c'(T,\underline{Z}) = \sqrt{\frac{\gamma' RT}{M_M}} = \sqrt{\frac{\gamma' P}{\rho'}} \tag{III.1i}$$

The sound speed in Eq. (III.1a) is controlled by ECS properties $\rho(T,P,\underline{Z})$ and $\Xi_P(T,P,\underline{Z})$, with $\Xi_P(T,P,\underline{Z})$ dominating inside the square root. $\rho(T,P,\underline{Z})$ and $\Xi_P(T,P,\underline{Z})$ influence *c*

similarly: c decreases as ECS becomes denser and/or more isothermally compressible. Therefore, c can be very low in liquid water with suspended air bubbles (i.e. high density and compressibility). As a real (T,P,$\underline{Z}$) gas has greater $\rho(T,P,\underline{Z})$, $\overline{C}_P(T,P,\underline{Z})$, $\Xi_P(T,P,\underline{Z})$ than (T,P,$\underline{Z}$) ideal gas ($\overline{C}'_P$ and Ξ'_P independent of P), $c'(T,\underline{Z})$ is greater than real gas c (Eq. (III.1j)).

$$\left.\begin{array}{c}\rho(T,P,\underline{Z}) > \rho'(T,P,\underline{Z}) \\ \Xi_P(T,P,\underline{Z}) > \Xi'_P(T,\underline{Z}),\ \overline{C}_P(T,P,\underline{Z}) > \overline{C}'_P(T,\underline{Z})\end{array}\right\} \xrightarrow{Eq.(1a)} c'(T,\underline{Z}) \geq c(T,P,\underline{Z}) \qquad \text{(III.1j)}$$

III.2.3. SS Modeling for NG Conditioning

The literature on SS for NG processing can be discussed according to four classes of studies: (i) experimental setups; (ii) CFD approaches; (iii) thermodynamic approaches; and (iv) experimental-CFD approaches. Experiments are not considered here. CFD approaches erect frameworks within commercial CFD software to describe SS process. Several CFD works adopt a short-cut thermodynamic modeling as ideal gas or EOS only describing single-phase PVT behavior, without phase-change effects. To avoid any risk of phase-change in the supersonic path, a high supercritical working fluid is usually chosen – e.g. dry CH_4. Or even with a real humid NG, simply do not check condensation, proceeding the simulation of single-phase supersonic flow on (T,P) domains where single-phase is unrealistic. Unrealistic CFD SS solutions can be detected via rigorous calculation of the corresponding $\Delta\overline{S}$ in plane P x T (with phase-split allowed): unrealistic SS profiles adiabatically destroy entropy, which is forbidden by the 2nd Law. The underlying reason is that current CFD software cannot handle correct phase behavior and phase-change effects observed in SS with raw NG, neither can calculate rigorous multiphase sound speed, which is necessary to access Ma of mists. Arguable exceptions are CFD SS works modeling condensation (e.g. Cao and Yang, 2015a, 2015b) from binary gas with a single condensable (e.g. water), but which are, at least so far, also prisoners of approach limitations: empirical nucleation-condensation theory, single condensable, low pressure, Raoult's Law VLE with pure liquid, constant heats of condensation and heat capacities, and unrealistic single-phase sound speed of mists.

Nevertheless, it is necessary to cite CFD SS papers mainly because several important SS aerodynamic design aspects – e.g. swirling motion impellers, flow-vanes interaction, mist

collector, etc – do really need CFD, the precise and exclusive manner to address them. But, it is necessary to emphasize that present CFD approaches cannot give decisive insights in engineering of SS NG conditioning, if correct multicomponent multiphase-change is not in scene. In other words, NG SS modeling demands multiphase equilibrium thermodynamics under ($P,\bar{S}$) and/or ($P,\bar{H}$) and/or (P,T) constraints on a 1D continuum.

Karimi and Abdi (2009) investigated SS for high-pressure NG dehydration using a thermodynamic SS modeling combining MATLAB and HYSYS, but which was not disclosed. Probably they used a limited SS model that cannot handle phase-changes, but can represent supercritical 1D compressible flow correctly with PR-EOS, including normal shock. Model was tested with pure supercritical CH_4 expanding from (*18.5°C, 92.5 bar*) to a backpressure of *70 bar* under isentropic (excepting shock) and non-isentropic (with ordinary friction) flow conditions, comparing with CFD calculations also ignoring phase-change. Their SS model was used with a water saturated NG (*95% CH_4*) without phase-change. They concluded that the normal shock should occur close to SS throat for better pressure recovery, which is evident because SS separation is a consequence of cooling resulting from conversion of enthalpy into kinetic energy, a fact only relevant at supersonic *Ma*. SS irreversibility is mainly associated with shock intensity, so that the greater the *Ma* at normal shock (Ma^{Shock}), the greater the throat-shock distance, the greater the supersonic cooling, the greater the rate of entropy creation across shock and the lower the pressure recovery due to higher shock irreversibility. Similarly, it is not surprising that the degree of cooling and potential of water removal both decrease as Ma^{Shock} decreases, while pressure recovery increases.

Wen et al. (2012) analyzed an alternative NG liquefaction SS process with CFD calculations. Indeed, they did not model phase-change, but merely plotted the (*P,T*) SS path – for single-phase flow via CFD – onto the *P x T* NG phase envelope generated with HYSYS, concluding that would exist a potential for 100% NG liquefaction. The truth is that their (*P,T*) SS path is meaningless and wrong: a rigorous $\Delta\bar{S}$ calculation with their SS path reveals huge adiabatic destruction of entropy ($\Delta\bar{S} << 0$) because temperature cannot fall as reported by them, i.e. real SS condensation would promptly block such extreme cooling. Another shortcoming in Wen et al. (2012) are some “hump-like” anomalies in their *P, T, Ma* profiles across shock as also

noticed elsewhere (Castier, 2014). Wen et al. (2012) results are fully scrutinized and compared in Appendix H with the present thermodynamic SS modeling.

Shooshtari and Shahsavand (2013) modeled droplet growth and condensation in SS binary flow validated with low pressure literature data. These authors did not use CFD. SS was modeled as single-phase compressible flow with first order virial EOS (Virial-1) even with high inlet pressures of *90 bar* in NG cases (inlet $T=300\ K$, $F=15.89\ MMsm^3/d$). Sound speed was calculated for single-phase gas with an "analogue" of the ideal gas formula Eq. (III.1i) replacing ρ' by Virial-1 density. Another questionable point is that there is no shock modeling, neither preoccupation with shock or pressure recovery issues, consequently *Ma* reached very high unrealistic values such as $Ma\approx 2.5$ with extremely low temperatures ($\approx 150\ K$) and backpressures ($\approx 8\ bar$).

Yang et al. (2014) investigated SS effects using CFD for "real" and ideal gases without considering phase-change and swirling motion. CFD simulations were conducted for ideal gas and non-condensable "real gas" under same SS geometry, feed conditions ($T_{FEED}=15^oC$, $P_{FEED}=200\ bar$) and backpressure $\approx 145\ bar$. By a "real gas" it is understood the use of PR-EOS with CTC NG without condensation; i.e. fluid experiences supersonic flow in a permanent single-phase CTC condition of *95.938%* CH_4, *3%* C_2H_6, *1%* C_3H_8 and *0.062%* H_2O. With *620 ppm* H_2O, this fluid has a not too cold WDP curve, and its HCDP curve has critical point at (-72.4^oC, *53.2 bar*) and cricondentherm at (-67^oC, *45 bar*) via PR-EOS. Therefore, such WDP and HCDP curves are likely to be crossed by this (P,T) SS path, which reached (-84^oC, *40 bar*) at maximum *Ma* with PR-EOS. Consequently, the importance of this work in the context of SS NG conditioning is, from the outset, questionable. Firstly, it does not contemplate SS phase-change, a keystone for WDPA/HCDPA. Secondly, part of CFD results, especially in supersonic regime, corresponds to unstable single-phase gas without condensation; i.e. they are wrong: real T with condensation is higher. Thirdly, c was calculated for single-phase gas or ideal gas exclusively, ignoring the correct multiphase analogue. Even so, authors claim that supersonic flow properties calculated for ideal gas diverged significantly from "real gas": normal shock was located upstream relatively to ideal gas counterpart; maximum *Ma* and minimum T were $\approx 10\%$ above and $\approx 15^oC$ less than ideal gas counterparts. These results are not surprising given the inequalities in Eq. (III.1j) added to $\overline{H}(T,P,\underline{Z}) < \overline{H}'(T,P,\underline{Z})$. That is, as a real gas has lower

c and $\overline{H}$ than analogous ideal gas, for same change of kinetic energy (i.e. same velocity *v*), both ideal and real gases exhibit same $\overline{H}$ drop, but the "real gas" cooling at supersonic low pressure is greater due to a JTE-like contribution inexistent in ideal gas. Similarly, with a lower *c* by Eq. (III.1j) for same *v*, the maximum "real gas" *Ma* is higher than the analogous ideal counterpart, and its shock location – where *Ma* attains Ma^{Shock} – should also be upstream the ideal counterpart.

Secchi et al. (2016) used two sub-models to simulate swirling SS. The first is a thermodynamic 1D axial SS model conserving energy and entropy. Authors integrated two software: EES for solving equations and NIST REFPROP for thermodynamic properties and phase equilibrium with GERG-2008 EOS (Rowland et al., 2016). Despite being considered the best EOS for pure fluids and mixtures, GERG-2008 is limited to 21 components. Therefore, to improve model performance, NG compositions were simplified as component lumps with similar critical temperatures. Two-phase *c* was based on Wood (1930). The second sub-model describes centrifugal separation of droplets from gas considering tangential and axial velocities of droplets both equal to the gas axial velocity, disregarding gas radial motion and nucleation. Secchi et al. (2016) approach presents some issues: Firstly, it is not practical as it demands complex software integration, probably with poor final computing performance. Secondly, the use of GERG-2008 EOS, despite its high local precision, is hampered by its heavy numerical calibration of its numerous sets of single and binary parameters, entailing that only a few species are available for NG applications. Thirdly, GERG-2008 rather heavy numerical complexity forces cumbersome component lumping implying loss of accuracy in thermodynamic properties, HCDP, energy/entropy balances and phase equilibrium. Fourthly, their method for estimating multiphase *c* is based on the old theory of Wood (1930), a non-thermodynamic method limited to gas-liquid streams; besides, authors do not explain how to calculate *c* for three-phase VLWE in SS NG conditioning. Fifthly, their SS simulation scheme was not demonstrated for water saturated NG and probably cannot handle such feeds.

Castier (2014) proposed thermodynamic SS model with phase equilibrium and *c* calculated by his multiphase sound speed method (Castier, 2011). In his SS model, normal shock is located to obtain the backpressure for specific nozzle geometry. SS model was tested with PR-EOS, but any EOS is acceptable. Results were obtained for two NG compositions from the literature.

Despite his rigorous formulation, Castier (2014) did not address humid NG. All examples use NG feeds exempt of water; i.e. his method was only tested for HCDPA in NG conditioning. Water introduces extra palpable difficulties, like handling WDP curves, VLWE, third aqueous phase in SS flow affecting *c*, and high enthalpy effects of water condensation shortening the available cooling affecting temperature profile, i.e. other things constant, water saturated feeds imply higher pre-shock temperatures. Moreover, Castier's model (2014) is CTC as it neglects condensate withdrawn from the flow. Recently, Castier (2016) included condensate withdrawal in his model, investigating collecting points in the diverging section before normal shock. This model was tested using NG composition from Machado et al. (2012), again excluding water. Neglecting a third aqueous phase limited his results.

Compared to JTE HCDPA, SS reaches lower temperatures for same pressure drop or requires less compression for same minimum temperature: SS HCDPA demands *≈15%* less compression power than JTE (Alfyorov et al., 2005) and has better NGL recovery due to selective C3+ condensation (Schinkelshoek and Epsom, 2008). Machado et al. (2012) performed a technical-economic comparison of SS with conventional conditioning of water-saturated NG using UniSim Design with a SS plug-in from Twister BV. SS superiority resulted from dismissal of previous WDPA, essential as anti-hydrate in JTE.

III.2.4. CO_2 Removal from CO_2 Rich NG with Membrane Permeation (MP)

CO_2 removal is relevant for conditioning CO_2 rich NG, as in E&P of Brazilian Pre-Salt reserves (Araújo et al., 2016). MP with cellulose acetate membrane (CAM) is a tested technology for CO_2 removal on offshore rigs. Compared to other options MP is simpler to operate in Pre-Salt FPSOs (Honeywell, 2012). However, the discovery of Libra Field in 2010 brought a new challenge for CO_2 removal: it is the largest Pre-Salt reservoir so far with $\%CO_2 \geq 40\%$ and gas/oil ratio of *≈600 sm³/m³*, entailing a gas processing of $\approx 12 MMsm^3/d$ for *120000 bbl/d* of oil capacity FPSOs. Albeit successfully applied in Pre-Salt for $\%CO_2 \leq 20\%$, MP can handle higher $\%CO_2$ services.

III.2.5. SS CO_2 Removal

Few studies applied SS for CO_2 removal from high $\%CO_2$ NG. SS is designed to develop deep falls of (*T,P*) into the VLE envelope forcing CO_2 precipitation. The feed must have previous

WDPA and HCDPA to rule out water and C3+ condensations that hamper the cooling. Samawe et al. (2014) created a SS prototype for CO_2 removal, but $\%CO_2$ reduced from *70%* to only *67%*. Imaev et al. (2014) coupled SS to cryogenic distillation to remove CO_2 from *70%* CO_2 NG. Despite reducing $\%CO_2$ to *13%*, the column executes the separation effort, SS being a coadjutant expanding distillate vapor and refluxing condensate. Hammer et al. (2014) investigated SS CO_2 removal from dry *3%* CO_2 exhausts using a SS thermodynamic model describing solid-vapor equilibrium (SVE) CO_2 freeze-out.

SS CO_2 removal from CO_2 rich NG has an issue: CO_2 freeze-out; i.e. solid-vapor-liquid equilibrium (SVLE), solid-liquid equilibrium (SLE) or SVE as consequence of cooling to temperatures below the CO_2 triple-point (TP) temperature (T_{TP}=*-58°C*). Freeze-out is problematic in deep CO_2 withdrawal (e.g. $\%CO_2$>*40%*), as dry ice can plug SS. Thus, in big removal services, SS should be designed to precipitate liquid CO_2 preferably, i.e. with not too cold temperatures. Freeze-out is avoided for a CTC feed, by determining its freeze-out borders (FOBs) on plane *P x T* and maneuvering SS path to avoid them (Hlavinka, 2006).

Determination of Pure Solid CO_2 Freeze-out Borders (FOBs) on Plane *P x T*. Duhem's Theorem variables are *T*, *P*, phase mol fractions η^V, η^L, η^S and liquid and vapor component mol fractions $\underline{X}$, $\underline{Y}$. Three multiphase flashes are addressed to identify freeze-out borders (FOB), all specifying incipient solid CO_2 (η^S=*0*): (i) SVLE (FOB from VLE); (ii) SLE (FOB from liquid); and (iii) SVE (FOB from vapor). The fluid is a known CTC ($\underline{Z}$). The grand freeze-out border (GFOB) is the union of three FOBs: SVLE FOB, SLE FOB and SVE FOB. Fugacity of pure solid CO_2 ($f_{CO2}^S(T,P)$) is modeled by Poynting correcting the saturated solid fugacity of CO_2 using temperature correlations of Trusler (2011) for saturated solid CO_2 properties: if $T \leq T_{TP}$, SVE properties $P_{CO2}^{SVE}(T)$, $\rho_{CO2}^{S,SVE}(T)$ are used; otherwise ($T > T_{TP}$) SLE properties $P_{CO2}^{SLE}(T)$, $\rho_{CO2}^{S,SLE}(T)$ are used. Fugacity coefficients of SVE pure vapor ($\phi_{CO2}^{V,SVE}(T, P_{CO2}^{SVE}(T))$) and SLE pure liquid ($\phi_{CO2}^{L,SLE}(T, P_{CO2}^{SLE}(T))$) are predicted by PR-EOS with pure CO_2.

To exemplify, let a binary CO_2 rich NG with known CTC Z_{CH4}, Z_{CO2}. This system was approached with numerical strategies detailed in Appendix E. Let CTC *50%* CO_2+*50%* CH_4 (*50/50*) and CTC *90%* CO_2+*10%* CH_4 (*90/10*) with *P x T* planes in Figs. III.1 and III.2, where L, V, SLE, SVE, VLE identify 2D CTC loci. VLE envelope has usual shape with critical point.

Pure CO_2 1D VLE, SVE, SLE boundaries are drawn for comparison in light-cyan with triple-point TP (black) and critical point (cyan). GFOB is the union of SLE FOB (black), SVLE FOB (magenta solid) and SVE FOB (green). At any (*P*,*T*) on the left of GFOB the CTC is split in two or three phases where one is dry ice. VLE envelope is not valid on the left of GFBO. The "horseshoe" 2D SVE is delimited by SVLE FOB, $SVLE^2$ and SVE FOB, while the grand SVLE is the magenta "7" shape union of SVLE FOB (solid), $SVLE^2$ (dashed) and $SVLE^3$ (dotted). $SVLE^2$ is a physical SVLE border between SLE and SVE, but it is not a FOB as it is dominated by GFOB. $SVLE^2$ continues through low *T* and *P* towards CH_4 TP (T_{TP}=*-182.5°C*, P_{TP}=*0.117 bar*). $SVLE^3$ is connected to CO_2 TP and is non-physical for both CTCs. The grand "7" SVLE is exactly the same for CTCs *50/50* and *90/10*. Inside VLE, solid precipitates on the left of SVLE FOB, i.e. below SVLE temperatures of *≈-60°C* and *P<25 bar* in Fig. III.2, and SVLE temperatures from *≈-60°C* at *10 bar* to *≈-70°C* at *≈48 bar* in Fig. III.1. As SS paths drift within VLE, SS designs for *50/50* and *90/10* must not touch the SVLE FOBs. As a last remark on Figs. III.1 and III.2, as CO_2 content increases from *50/50* to *90/10*, SLE FOB and SVE FOB deforms towards SLE and SVE of pure CO_2, while VLE and SVLE FOB contracts towards CO_2 VLE and CO_2 TP.

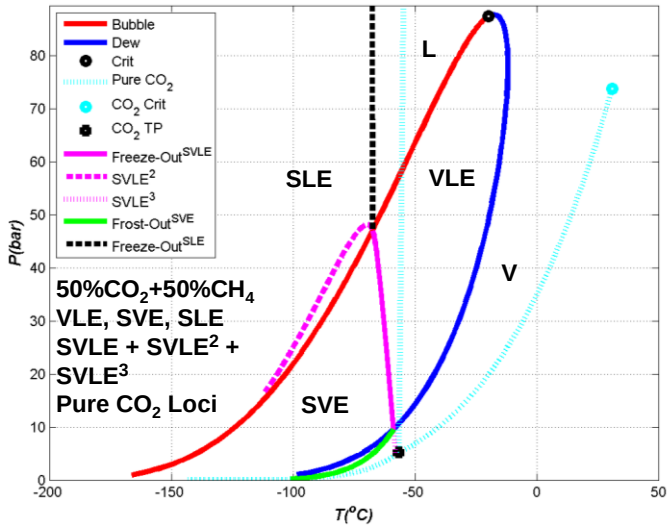

Figure III. 1. *50%CO_2+50%CH_4*: SLE, SVE, VLE 2D Domains. Grand Freeze-Out Border = SLE-L (*black dashed*)+SVLE (*magenta solid*)+SVE-V (*green*).

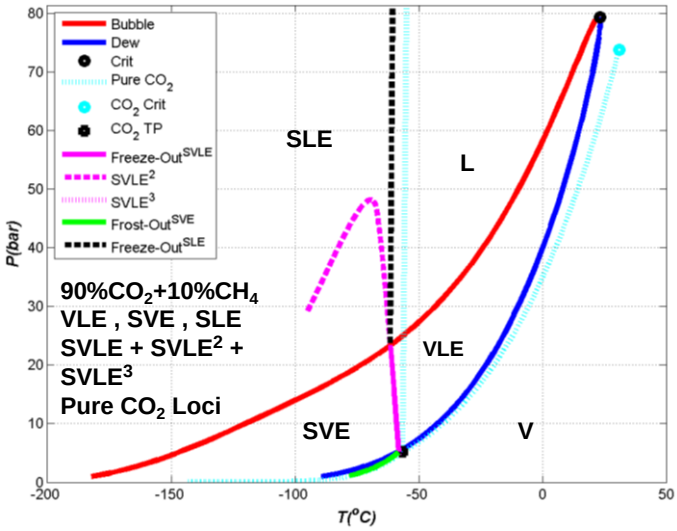

Figure III. 2. *90%CO_2+10%CH_4*: SLE, SVE, VLE 2D Domains. Grand Freeze-Out Border = SLE-L (*black dashed*)+SVLE (*magenta solid*)+SVE-V (*green*).

III.3. HYSYS Unit Operation Extensions for NG Conditioning

MP and SS units for conditioning humid CO_2 rich NG do not exist in HYSYS 8.8. Thus, simulation of PFDs with such units requires development of Unit Operation Extensions (UOE). MP-UOE and SS-UOE were developed as external DLLs to simulate MP and SS in steady-state HYSYS 8.8 PFDs. They are loaded by HYSYS user interface as customized operations directly into the HYSYS palette. MP-UOE and SS-UOE have their own property window to be consulted during PFD edition as both UOEs have design and operation parameters to be specified.

III.3.1. Steady-State MP Extension: MP-UOE

MP-UOE simulates steady-state MP via a short-cut method with calibrated permeances. MP-UOE input data comprehends: feed data, MP area, retentate and permeate pressures. User also selects the contact (countercurrent or parallel) and membrane type – hollow fiber (HF) or spiral-wound (SW). Table III.1 shows species permeances defined in MP-UOE, changeable via property window. Permeances were sought by adhering MP-UOE onto real MP data of Pre-Salt FPSOs assuming SW with countercurrent contact. Permeances of H_2S and H_2O were not adjusted; they were estimated as equal to the CO_2 value as they are known to be high for skin-dense CAM, but can be greater. C3+ permeances are very small and were estimated from C_2H_6 permeance losing *90%* of magnitude per additional C atom. Permeation of C5+ species is

negligible. Exiting temperatures of retentate and permeate are calculated with the specified final difference of temperature between retentate and permeate (ΔT_{VL}, default $\Delta T_{VL}=3^oC$). The numerical approach used in MP-UOE is detailed in Appendix F. MP-UOE is used in this work to simulate CO_2 removal from NG.

Table III. 1. MP-UOE Permeances.

Component	*Permeance (Π_k) (MMsm³/d.m².bar)*
CO_2	2.77E-06
CH_4	3.07E-07
C_2H_6	9.57E-09
H_2S	2.77E-06
H_2O	2.77E-06
N_2	3.07E-07
C_3H_8	9.57E-10
iC_4H_{10}	9.57E-11
C_4H_{10}	9.57E-11
C5+	9.57E-12

III.3.2. Steady-State SS Extension: SS-UOE

SS-UOE finishes the design of a SS and simulates it at steady-state within HYSYS environment. SS is modeled as a converging-diverging nozzle with linear profiles of diameters in Fig. III.3, which defines all SS geometric parameters. SS-UOE is a simulation and design tool. Only part of the sizing data – inlet and outlet diameters D_I, D_O, and angles of converging and diverging sections α, β – are entered by the user. SS-UOE finishes the SS design for supersonic performance and finds the product streams: lean gas and the ejected two-phase L+W condensate. The rectilinear diameter profiles are not optimal, but are sufficient for engineering purposes. Naturally, there are other sources of inaccuracy in this model, namely: limitations of EOS and phase behavior; hydrodynamics issues (turbulence, friction and boundary layer); zero kinetic energy of swirling motion of gas and condensate, etc. Certainly the linear diameter profiles are not the most important of them. Anyways, the kind of spatial dependence of SS diameter is not crucial in this model. Any $D(x)$ relationship can be used without affecting the proposed algorithm.

The SS design comprehends the sizing of the Laval nozzle and the length of the diffuser after normal shock in Fig. III.3. The Laval nozzle ends at the separation section just before the normal shock. The diffuser is a continuation of the diverging section of the Laval, so that the length of

the SS diverging section (L_D) comprehends the supersonic section of the Laval and the diffuser. SS-UOE uses HYSYS multiphase resources for calculating multiphase equilibrium properties $\overline{H}(T,P,\underline{Z})$, $\overline{S}(T,P,\underline{Z})$, $\overline{C}_P(T,P,\underline{Z})$, $\rho(T,P,\underline{Z})$, $\Xi_P(T,P,\underline{Z})$, $\Xi_T(T,P,\underline{Z})$, where $\underline{Z}$ is the vector of total mol fractions of multiphase stream. To do this, HYSYS multiphase flashes – *Flash*(P,T,$\underline{Z}$), *Flash*(P,$\overline{H}$,$\underline{Z}$), *Flash*(P,$\overline{S}$,$\underline{Z}$) – are used. By multiphase it is understood a VLWE conjunction: gas phase with HC liquid and aqueous super-cooled liquid. For feeds with high CO_2 content a CO_2 liquid phase may replace the HC liquid.

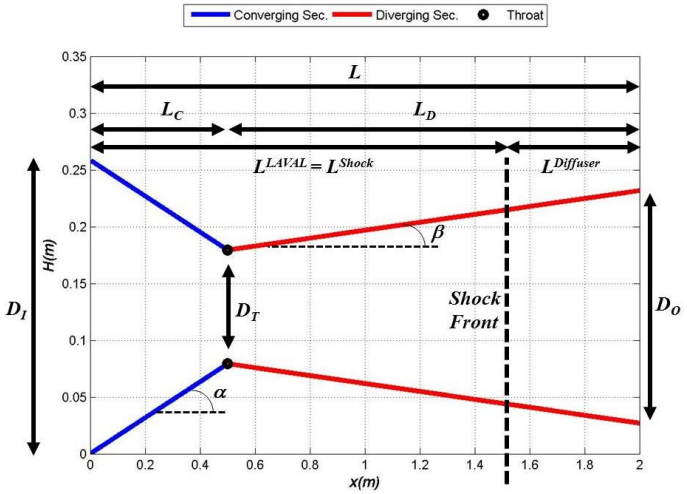

Figure III. 3. SS Geometric Parameters for SS-UOE [D_I, D_O, α, β Defined by User].

Parallel SS nozzles can be installed in the PFD dividing a gas feed equally among parallel SS-UOE, but this degrades CPU performance. A better strategy is to install only one SS-UOE receiving its proportional share of the gas feed and then use HYSYS spreadsheet to recompose the final lean gas and condensate as SS battery products.

Gas hydrates in the SS separation section are not issues, as the short SS residence time of milliseconds is not sufficient for nucleation of hydrates given its slow kinetics (Twister BV, 2010). However, the L+W condensate ejected by the SS separation section can form gas hydrates outside the SS in downstream processing. Therefore, L+W condensates are directed to a LTX separator in Fig. III.4. LTX produces a top slip gas and bottom L+W liquid at $\approx 20^oC$ preventing hydrates. The low flow rate slip gas carrying some water is added to the lean gas SS product as the resulting water content will be still within WDPA range. At the top of LTX there

is direct contact between cold L+W condensate and warm vapor ascending from LTX bottom, resulting a low flow rate slip gas. The PFD implementation of LTX adopts two cascaded flashes in Fig. III.4: bottom *Flash*(*P,T*) double-connected to top *Flash*($P,\overline{H}$), which imposes direct adiabatic contact of L+W condensate and warm bottom vapor. This is a small Cavett Problem, a bench-mark test for simulators decades ago (Cavett, 1963), which is easily solved by HYSYS.

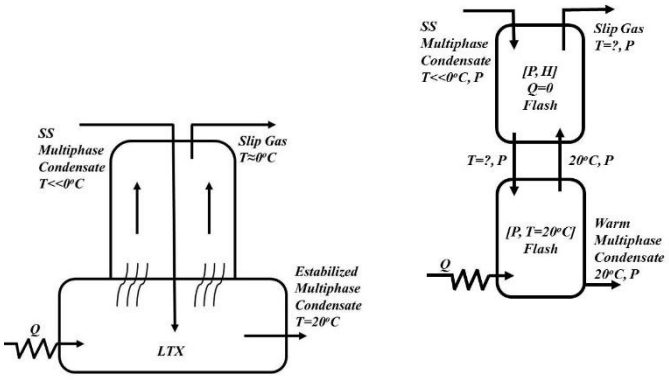

Figure III. 4. LTX as Cascaded (P,T) & ($P,\overline{H}$) Flashes.

III.3.2.1. SS-UOE Assumptions [SS1] to [SS10]

[SS1] Kinetic energy of swirling motion of gas and condensates is zero. Flow is 1D axial plug-flow with linear diameter profiles *D(x) – x* is SS axial position. **[SS2]** Solid ice (or dry ice), is not represented in ordinary EOS (e.g. PR-EOS) that can only handle segregated water as super-cooled liquid. Despite this limitation, the enthalpy error involved is of low relative magnitude: super-cooling enthalpy of liquid water at *-40°C ≈ -3 kJ/mol* counterpointing the low enthalpy of freezing *≈ -6 kJ/mol* plus sub-cooling enthalpy of ice to *-40°C ≈ -1.3kJ/mol*. This error of *≈ +4.3 kJ/mol* is small relatively to the high condensation enthalpy of water (*≈ -41 kJ/mol*) plus other sensible heat effects (*≈ -3 kJ/mol*); i.e., concerning the water heat effects, super-cooling entails *10%* less enthalpy change than the necessary to form ice at same conditions. But, given the extremely short SS residence time, one cannot rule out the exclusive formation of super-cooled water without ice. Thus, collected water is modeled as a super-cooled liquid in phase equilibrium with vapor and liquid HC. **[SS3]** SS-UOE is thermodynamically rigorous, excepting the mentioned ice-handling handicap. The bulk accuracy depends only on the

suitability of the thermodynamic package being used. PR-EOS is used in this work, but any EOS in HYSYS palette can be selected. **[SS4]** Input data: gas entering conditions F_E, T_E, P_E, $\underline{Z}_E$ – flow rate (mol/s), temperature (K), pressure (bar) and component mol fractions –, adiabatic efficiencies of expansion ($\eta^{EXP}\%$) and compression ($\eta^{CMP}\%$) steps; Mach Number just before normal shock and condensate withdrawal (Ma^{Shock}); and Laval nozzle parameters (Fig. III.3) D_I , D_O , α , β. SS design is finished for each simulation by calculating lengths L_C , L_D and throat diameter D_T so that $Ma^{Throat}=1$. Some works (Secchi et al., 2016), specify the SS discharge pressure (backpressure), but it is equivalent to choose Ma^{Shock} as the backpressure has a direct relationship with it, given feed and geometry; i.e. Ma^{Shock} can be varied to match the backpressure of interest. It seems natural to choose Ma^{Shock} as the main source of SS irreversibility is determined by it. Moreover, Ma^{Shock} is meaningful as the backpressure is usually greater than the minimal supersonic pressure in SS operation; i.e. a normal shock is required. **[SS5]** Phase separation is to be held in SS just before normal shock. There is conservation of mass flow rate, overall energy flow rate ($(\overline{H}+\overline{K}).q/M_M$) and entropy flow rate (if $\eta^{EXP}\%=100\%$) until phase separation. After condensate separation, the updated mass, momentum and overall energy flow rates are conserved through the normal shock. From this point on, until the SS discharge, mass flow rate, overall energy flow rate and entropy flow rate (if $\eta^{CMP}\%=100\%$) are conserved. **[SS6]** The pressure of ejected multiphase condensate is updated at SS exit to the discharge pressure of the final gas as a stagnant fluid via a *Flash*($P,\overline{H}$) specified with the discharge pressure and molar enthalpy of stagnation. **[SS7]** Adiabatic expansion and compression in SS flow path (excluding phase separation and normal shock) are considered as isentropic, but the user can associate adiabatic efficiencies to expansion ($\eta^{EXP}\%$) and compression ($\eta^{CMP}\%$) steps: appropriate corrections in the multiphase equilibrium, temperature and velocity calculations are implemented by the algorithm (Sec. III.6). Anyways, the main SS source of irreversibility occurs when the normal shock is crossed, as rigorously calculated in the algorithm. As reported elsewhere (GPSA, 2004), SS overall adiabatic efficiency is $\approx 90\%$, nearly corresponding to isentropic expansions/compressions, with the remaining $\approx 10\%$ loss of efficiency credited to normal shock irreversibility. **[SS8]** To represent the fluid path and profiles (*P(x), T(x), v(x), c(x), Ma(x),* etc), isentropic *Flash(* $P,\overline{S}$ *)* are executed ($\eta^{EXP}\%=100\%$) along the expansion path, decreasing pressure by small steps until the

normal shock location. After the normal shock, again isentropic *Flash*($P,\bar{S}$) are performed ($\eta^{CMP}\%=100\%$) along the compression path increasing pressure by small steps until $x=L$. When $\eta^{EXP}\%<100\%$ and/or $\eta^{CMP}\%<100\%$ appropriate corrections are applied (Sec. III.6). Phase separation is executed by a *Flash*(P,T) with P^{Shock} ,T^{Shock} at $Ma=Ma^{Shock}$ just before normal shock. **[SS9]** The normal shock is located at $Ma=Ma^{Shock}$. Normally SS flow path does not attain $Ma^{Shock} > 2$ due to high backpressures and increasing meta-stability of supersonic flow as *Ma* increases. Thus, when SS flow attains the specified Ma^{Shock}, L+W condensate is collected and the shock transition of *T*, *P*, *v*, *Ma* is executed with the remaining gas by solving material, momentum and energy balances on both shock sides. Following implication applies: $Ma^{Shock}\uparrow \Rightarrow T^{Shock}\downarrow$, $P^{Shock}\downarrow$, *L+W condensate*$\uparrow$, *backpressure*$\downarrow$, *overall SS adiabatic efficiency*$\downarrow$, *process power consumption*$\uparrow$. Thus, Ma^{Shock} is chosen according to the targeted backpressure and/or power consumption. **[S10]** At each SS point the sound speed *c* is calculated for multiphase VLWE flow at ($T,P,\underline{Z}$) with PEC-UOE (Sec. III.2.1).

III.3.2.2. SS-UOE Algorithm

Molar basis and strict SI units are used with symbols in the Nomenclature. All 1st and 2nd order thermodynamic properties are multiphase VLWE properties, excepting after the normal shock. HYSYS flashes automatically converge to single-phase equilibrium for unfeasible multiphase states. Algorithm assumes $\eta^{EXP}\%=\eta^{CMP}\%=100\%$; Sec. III.6 discusses $\eta^{EXP}\%<100\%$ and/or $\eta^{CMP}\%<100\%$. Throat diameter D_T is calculated to have $Ma=1$ at D_T. Tolerances: $\delta_M \approx 10^{-3}$ (Mach), $\delta_L \approx 10^{-3}$m (Length). Algorithm comprises eight phases which are detailed in Appendix G, namely: [P1] Input Data; [P2] Subsonic Expansion; [P3] SS Geometry; [P4] Supersonic Expansion; [P5] Pre-Shock Separation; [P6] Normal Shock; [P7] Subsonic Compression; [P8] Finishing Procedures.

III.3.2.3. Preliminary Results of NG Processing with SS-UOE

Two SS-UOE demonstrations are preliminarily addressed with SS-UOE and PEC-UOE within HYSYS 8.8 using PR-EOS with BIPs from HYSYS library.

Example 1: DRY-NG-1. SS-UOE operates with $\approx 2MMsm^3/d$ of DRY-NG-1, a dehydrated NG with high $\%CO_2$. LTX is not necessary as the feed is anhydrous. Table III.2 presents data of

feed and products lean NG and condensate. A single SS is used with $Ma^{Shock}=2$, isentropic flow ($\eta^{EXP}\%=\eta^{CMP}\%=100\%$) and nozzle parameters $D_I=0.12m$, $D_O=0.09m$, $\alpha=15^o$, $\beta=2.75^o$. This is an oversized design because Ma^{Shock} is too high. Consequently pre-shock temperature is too low ($T^{Shock}=-52.39^oC$) condensing *14.59%* of feed, with high SCF content (low SCF selectivity). Another consequence of a high Ma^{Shock} is a pressure recovery of only *48.2%*. The remaining geometric parameters (Fig. III.3) were designed by SS-UOE: $D_T=0.0397m$, $L_C=0.1498m$, $L_D=0.5243m$, $L=0.6741m$, $L^{Shock}=0.3478m$, $L^{Diff}=0.2993m$. Fig. III.5 shows SS geometry with throat position $L_C=0.1498m$. Profiles of vapor fraction, *P*, *T* and *Ma* follow respectively in Figs. III.6, III.7, III.8 and III.9, agreeing with the expected. As gas accelerates, *T* and *P* decrease and *Ma* increases until $x=L^{Shock}$, where the shock signature is seen: discontinuities recovering part of the initial (*T*,*P*) and turning the flow into subsonic. Fig. III.6 depicts the fall of vapor fraction towards its minimum of *85.41%* at pre-shock, where the $HC+CO_2$ condensate is withdrawn. Shock transition is then executed with the remaining lean gas, still in supersonic flow. After shock, gas velocity and *Ma* decrease through the diffuser with *T* and *P* increasing until SS outlet. Figs. III.7, III.8 and III.9 also exhibit the respective spatial gradient singularities at throat ($Ma \to 1^-$), namely $\frac{dT}{dx}=-\infty$, $\frac{dP}{dx}=-\infty$, $\frac{dMa}{dx}=+\infty$. These limit gradients are SS "signatures" which only occur at the throat under regular SS operation as rigorously proved for multiphase multi-reactive supersonic flow in de Medeiros et al. (2017, Supporting Information). Fig. III.10 shows the plane *P x T* with VLE envelopes of feed and lean gas and SS path superimposed with two branches: (i) expansion from superheated vapor (*40°C, 90 bar*), penetrating deeply into the feed envelope until *14.59%* of condensation (*-52.39°C, 11.75 bar*); and (ii) recompression, entirely on superheated vapor, starting with the rectilinear shock-jump back to (*22.8°C, 34.6 bar*), followed by diffuser recompression until (*39.13°C, 43.34 bar*). There is no freeze-out of dry-ice at the pre-shock point (*-52.39°C, 11.75 bar*) in SS path.

Table III. 2. Streams: SS Example Dry-NG-1.

Item	*RawNG*	*Condensate*	*LeanNG*
%CO_2	*44.741*	*48.35*	*44.13*
%CH_4	*41.667*	*7.01*	*47.58*
%C_2H_6	*6.94*	*10.70*	*6.30*
%C_3H_8	*3.97*	*17.23*	*1.71*
%i-C_4H_{10}	*0.992*	*5.85*	*0.16*
%C_4H_{10}	*0.992*	*6.21*	*0.10*
%i-C_5H_{12}	*0.496*	*3.31*	*0.02*
%C_5H_{12}	*0.198*	*1.34*	*0.00*
mol/s	*1000*	*145.88*	*854.12*
T(^{o}C)	*40*	*-52.39$^{*\#+}$*	*39.13*
P(bar)	*90*	*11.75$^{*\#+}$*	*43.34*

**As extracted* $^{\#}$*No freeze-out* $^{+}$*At stagnation: -53.14^{o}C, 43.34 bar*

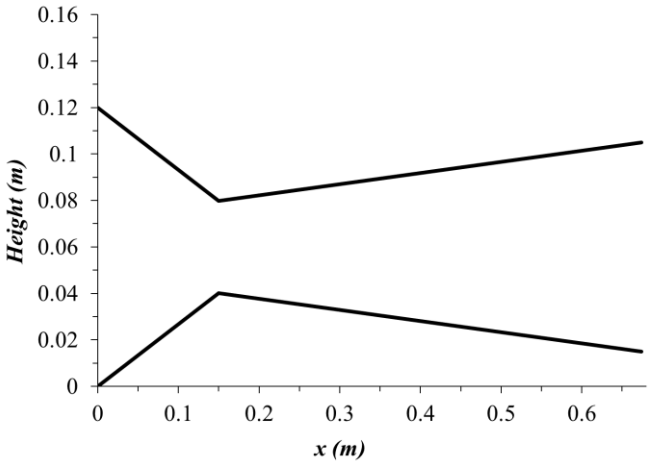

Figure III. 5. DRY-NG-1: SS Rectilinear Diameter Profiles.

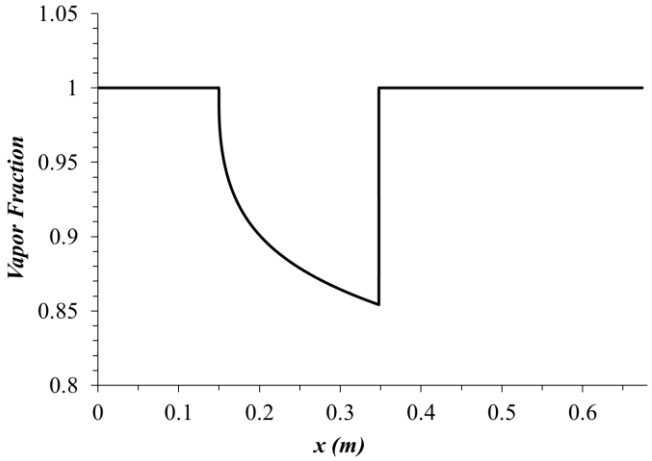

Figure III. 6. DRY-NG-1: Vapor Fraction versus SS Axial Position with Condensate Withdrawal before Shock.

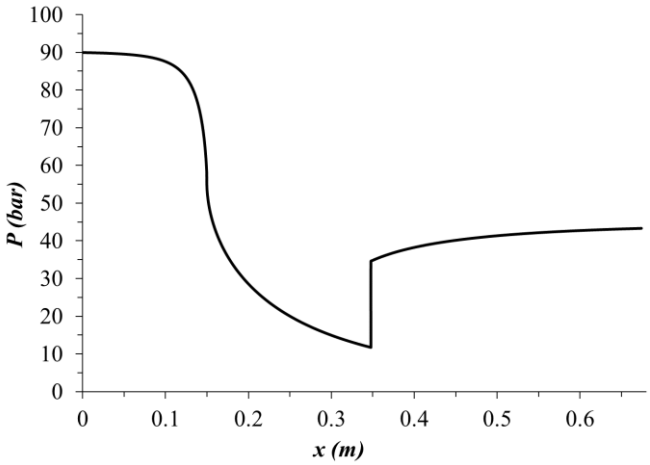

Figure III. 7. DRY-NG-1: SS Pressure Profile.

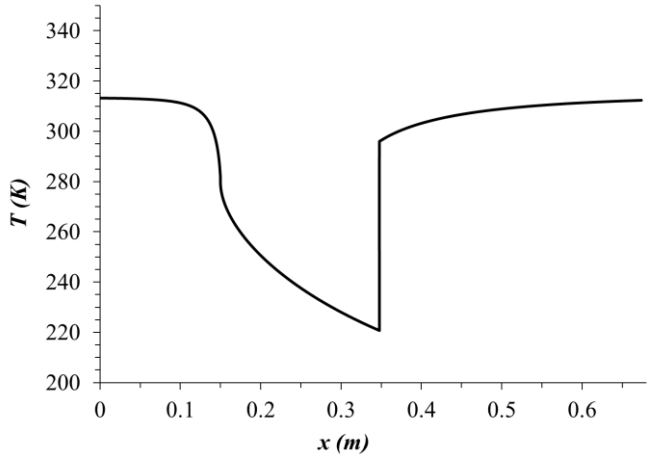

Figure III. 8. DRY-NG-1: SS Temperature Profile.

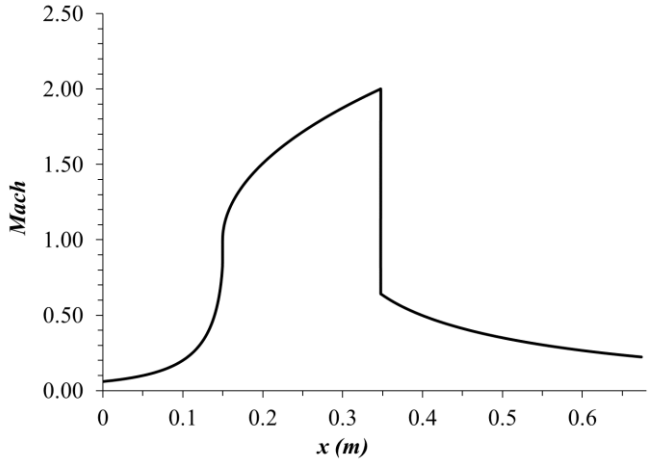

Figure III. 9. DRY-NG-1: SS Mach Number Profile.

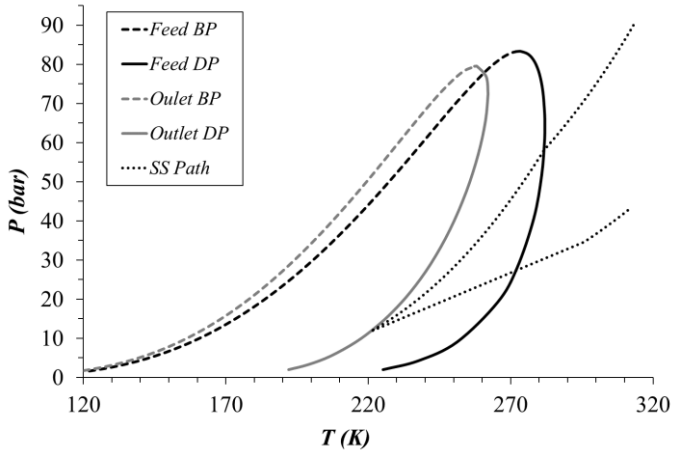

Figure III. 10. DRY-NG-1 *P x T* Plane: (i) Feed VLE Envelope (larger); (ii) Lean Gas VLE Envelope (slenderer); (iii) SS Path.

Example 2: NG liquefaction study from Wen et al. (2012). These authors simulated a geometrically defined SS nozzle with dry NG using CFD commercial software. Apparently they were led to a wrong conclusion that 100% NG liquefaction is possible with this process. It is not. The CFD treatment of Wen et al. (2012) simulated the SS path without phase change, attaining an unrealistic too cold temperature in the pre-shock, leading to the wrong liquefaction conclusion. A 2nd Law analysis of their results shows that their SS path has a strongly negative $\Delta\bar{S}$ from feed to the pre-shock zone, which configures an unfeasible solution since SS operates adiabatically. The case is solved with SS-UOE and HYSYS 8.8 for comparison in Appendix H.

III.4. Process Alternatives for Conditioning Humid CO_2 Rich NG

Alternatives are compared in terms of power consumption and following goal-attainments: NG with WDP $\leq$ *-45°C (1.01 bar)*, HCDP $\leq$ *0°C (45 bar)* and $\%CO_2 \leq 15\%$, sufficient for transportation to finish CO_2 removal elsewhere and power generation; low $\%CO_2$ NGL; and EOR fluid with $\%CO_2 \geq 75\%$.

III.4.1. PFD Assumptions [F1] to [F12]

[F1] Simulation: HYSYS 8.8 with MP-UOE and SS-UOE as MP and SS units. **[F2]** Thermodynamic models: PR-EOS (HYSYS) in general; HYSYS Glycol Package in TEG WDPA. **[F3]** Thermal approach: *5°C*. **[F4]** Tropical sea: Secondary cooling-water (CW) circuit at *30°C*, cooled by seawater at *25°C*. **[F5]** EOR fluid: At *250 bar*. **[F6]** TEG WDPA: *60 bar*

absorption, *1 bar* stripping. **[F7]** MP CO_2 removal: Countercurrent SW single-stage; feed at (*42 bar*, *50°C*); permeate at *4 bar*; retentate head loss of *1 bar*. **[F8]** SS WDPA+HCDPA: 06 SS's with LTX for L+W condensate; $Ma^{Shock}=1.5$, $\eta^{EXP}\%=\eta^{CMP}\%=100\%$, $D_I=0.0762$ *m*, $D_O=0.048$ *m*, $\alpha=15^o$, $\beta=2.75^o$. **[F9]** SS CO_2 removal: 06 SS's, no LTX, $Ma^{Shock}=1.6$, $\eta^{EXP}\%=\eta^{CMP}\%=100\%$, $D_I=0.0762$ *m*, $D_O=0.048$ *m*, $\alpha=15^o$, $\beta=2.75^o$. **[F10]** Water saturated NG feed (referred as *Saturated Gas*): *5.134 MMsm³/d* leaving oil-gas-water (OGW) separator (*25 bar*, *40°C*) with *0.36%* H_2O, *43.84%* CO_2, *49.82%* CH_4, *2.99%* C_2H_6, *1.99%* C_3H_8, *0.30%* iC_4H_{10}, *0.20%* C_4H_{10}, *0.20%* iC_5H_{12}, *0.10%* C_5H_{12}, *0.10%* C_6H_{14}, *0.05%* C_7H_{16}, *0.03%* C_8H_{18}, *0.01%* C_9H_{20}, *0.01%* $C_{10}H_{22}$. **[F11]** Compressors: *75%* adiabatically efficient. **[F12]** Intercoolers: Gas at *35°C*, CW at *30°C*, head loss of *0.5 bar*.

III.4.2. Processing Alternatives: Cases 1, 2, 3 and 3x

Only block PFDs are shown; HYSYS PFDs are available in Supplementary Materials (Appendix J). Cases 1, 2, 3 and 3x, are built combining two PFDs from PFDs A, B, C, D and E.

PFD A (Fig. III.11) applies TEG Absorption WDPA and JTE HCDPA. *Saturated Gas* is compressed and feeds the absorber with lean TEG on top. Rich TEG leaves the absorber to atmospheric stripping for TEG regeneration. Hot lean TEG is cooled with rich TEG and pumped to absorption after make-up. Dry NG goes to HCDPA via JTE C3+ removal.

PFD B (Fig. III.12) executes MP CO_2 removal from lean NG heated with pressurized hot water (PHW). MP retentate is the final NG. The CO_2 rich permeate at *4 bar* goes to 3-stage intercooled compression, leaving sufficiently dense at *35°C* to be pumped to EOR. An *ADJUST* HYSYS block sets MP area to produce *15%* CO_2 retentate.

PFD C (Fig. III.13) is alternative to PFD A with 6 SS's for WDPA+HCDPA and LTX for L+W condensate. SS feed is compressed to a lower pressure relatively to the feed of PFD A. As the *Saturated Gas* is water saturated, so is the SS feed in PFD C; i.e. it is on its WDP curve.

PFD D (Fig. III.14) is alternative to PFD B using 6 SS's to remove CO_2 from gas already with WDPA+HCDPA, therefore LTX is absent. As CO_2 removal is a hard SS service, PFDs D/E use $Ma^{Shock}=1.6$ to avoid freeze-out at pre-shock, as SS path would cross SVLE freeze-out border

at $Ma^{Shock} \approx 1.65$. SS feed requires additional compression and refrigeration to (*84 bar, -20°C*). CO_2 rich condensate at (*-60.11°C, 34.59 bar*) is pumped as EOR fluid in PFD D.

PFD E (Fig. III.15) is alternative to PFD D where SS feed is cooled with CO_2 condensate at (*-60.11°C, 34.59 bar*) instead of refrigeration, thus sparing power. SS operates as before, since SS feed and design are the same in PFDs D/E. After cooling the feed, the condensate is partially vapor, so it is split to be dispatched to EOR: liquid is pumped, and vapor goes to 3-stage compression.

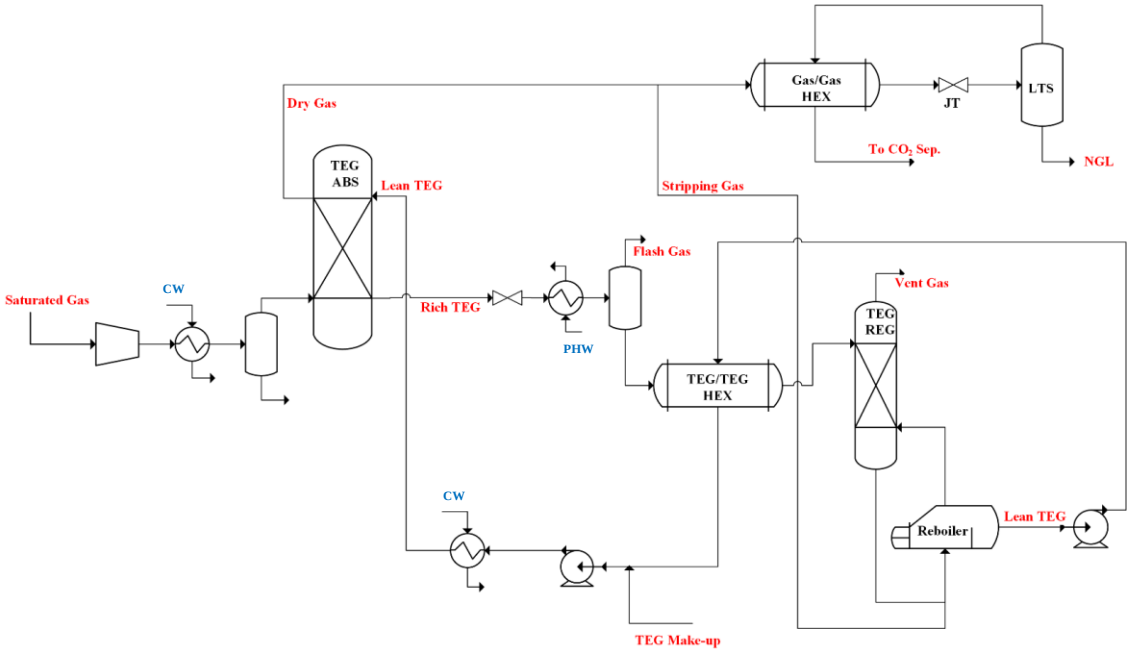

Figure III. 11. PFD A: TEG WDPA & JTE HCDPA.

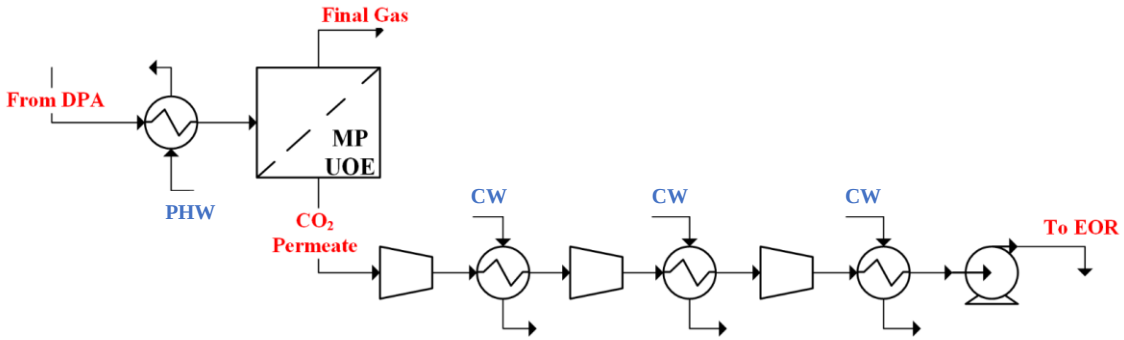

Figure III. 12. PFD B: MP CO_2 Removal & Compression to EOR.

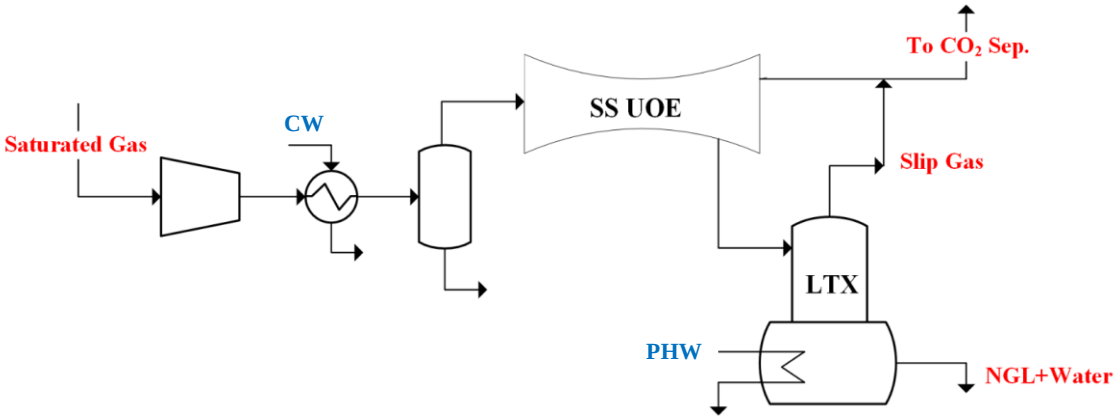

Figure III. 13. PFD C: SS WDPA+HCDPA with LTX.

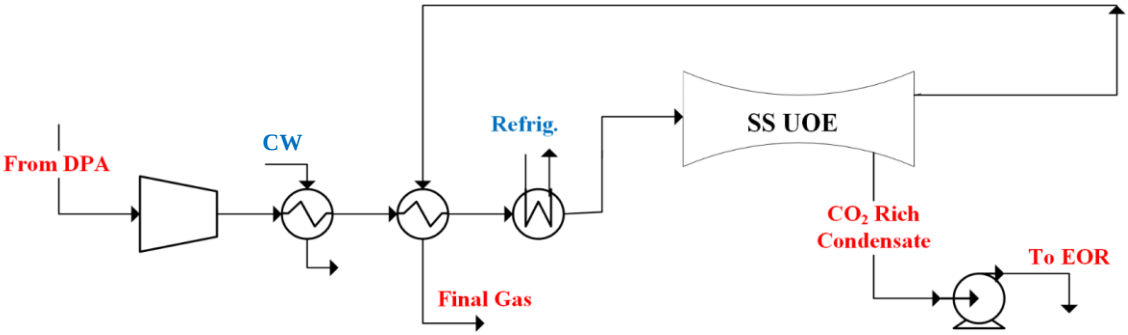

Figure III. 14. PFD D: SS CO_2 Removal. Refrigerated SS Feed and Cold Condensate Pumped to EOR.

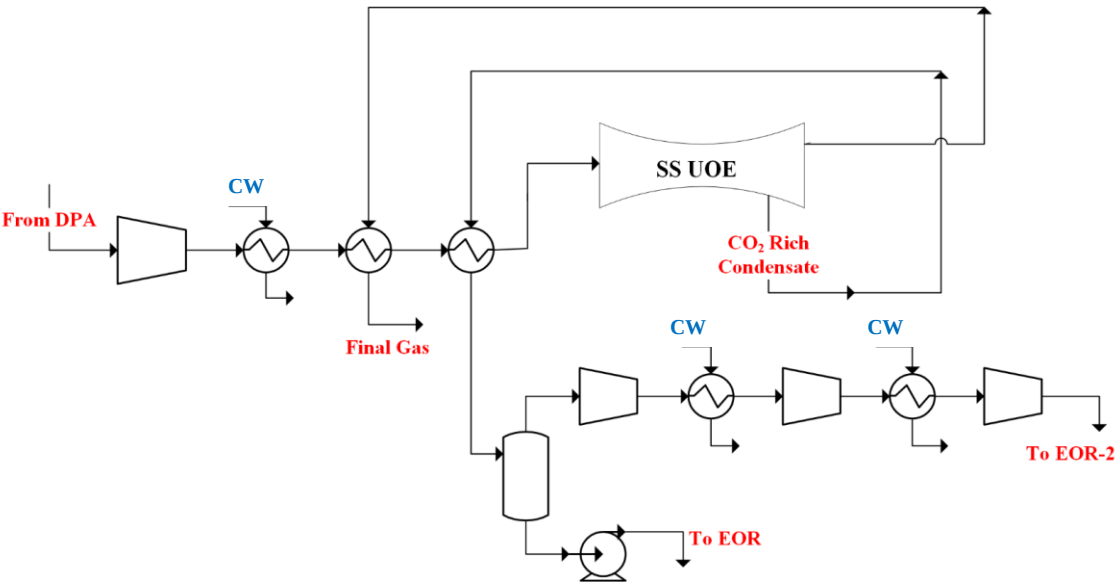

Figure III. 15. PFD E: SS CO_2 Removal. SS Feed Cooled by Condensate.

Conventional Case 1 connects PFDs A and B. Case 2 executes SS WDPA+HCDPA and MP CO_2 removal with PFDs C and B. Case 3 executes SS CO_2 removal with PFDs A and D. Case 3x is a variant with PFDs A and E. *Saturated Gas* is compressed and cooled with CW to meet the specific higher pressure of PFDs A or C, therefore changing gas composition regarding condensation in knock-out vessels. Similarly, feeds of PFDs B, D and E suffer changes before processing. Table III.3 presents the specific feeds of PFDs A, B, C, D and E.

Table III. 3. Feeds* of PFDs A, B, C, D, E vs Cases.

PFDs [Cases]	*A [1,3,3x]*	*B [1]*	*B [2]*	*C [2]*	*D, E [3,3x]*
P(bar)	*60.00*	*42.00*	*40.83*	*50.00*	*84.00*
T(°C)	*35.00*	*50.00*	*50.00*	*35.00*	*-20.00*
MMsm³/d	*5.12*	*5.09*	*5.05*	*5.12*	*5.09*
%CO_2	*43.93*	*44.02*	*44.17*	*43.92*	*44.02*
%CH_4	*49.92*	*50.17*	*50.56*	*49.91*	*50.17*
%C_2H_6	*3.00*	*3.00*	*2.98*	*2.99*	*3.00*
%C_3H_8	*2.00*	*1.97*	*1.83*	*2.00*	*1.97*
%iC_4H_{10}	*0.30*	*0.29*	*0.22*	*0.30*	*0.29*
%nC_4H_{10}	*0.20*	*0.19*	*0.13*	*0.20*	*0.19*
%iC_5H_{12}	*0.20*	*0.18*	*0.07*	*0.20*	*0.18*
%nC_5H_{12}	*0.10*	*0.09*	*0.03*	*0.10*	*0.09*
%C_6H_{14}	*0.10*	*0.07*	*0.01*	*0.10*	*0.07*
%C_7H_{16}	*0.05*	*0.02*	*0.00*	*0.05*	*0.02*
%C_8H_{18}	*0.03*	*0.01*	*0.00*	*0.03*	*0.01*
%C_9H_{20}	*0.01*	*0.00*	*0.00*	*0.01*	*0.00*
%$C_{10}H_{22}$	*0.01*	*0.00*	*0.00*	*0.01*	*0.00*
ppm H_2O	*1652.8⁺*	*29.9*	*18.4*	*1784.1⁺*	*29.9*

**After last knock-out or exchanger before processing* *⁺ At WDP*

III.5. Results and Discussion

Goal-Attainment Analysis. Table III.4 presents final NG, EOR fluid and NGL from all cases. NG productions of Cases 1 and 2 are similar, while Cases 3-3x produce *8.3%* more. The final NG pressure of Cases 3-3x is lower than Cases 1-2, a consequence of SS low pressure recovery of *41.18%* in PFDs D/E, whose lowest *P* and *T* at pre-shock, before separation ($Ma^{Shock}=1.6$), were *21.95 bar, -60.07°C.* Concerning CO_2 removal, MP Cases 1-2 gave better results: *%CO_2* was reduced from *≈44%* to *15%* with a single MP stage of *9305 m²* (Case 1) and *9588 m²* (Case

2). SS in Cases 3-3x, despite not reaching *15%* CO_2 in the final NG to avoid the freeze-out barrier, had a not bad performance: more than *70%* of CO_2 was abated (Table III.5) reducing its content from *44%* to *21.85%*, a promising result, taking into account the high *%CO_2* feed and the hard conditions of SS service. These figures, without comparison in the literature, quantify the SS potential as an alternative for CO_2 removal from CO_2 rich NG, with due attention to the freeze-out borders. On the other hand, at the light of present results, MP confirms its favoritism for offshore CO_2 removal from *44%* CO_2 NG.

Comparing Cases 1 and 2, SS produced a better NG via PFD C, with less C3+ and higher *%CH_4*. In addition, Case 2 demanded less compression power (*P^{Feed}=50 bar*, Table III.3) and less equipment than PFD A WDPA+HCDPA of Case 1. Comparing Cases 1 and 3-3x, all with PFD A for WDPA+HCDPA, it is clear that SS CO_2 removal via PFDs D/E produces a final NG with better *%CH_4* and less *%C2+* than PFD B with MP, despite the former higher *%CO_2* already recognized. SS WDPA+HCDPA in PFD C, already proved in the literature, is confirmed here by Case 2 results. SS WDP in Case 2 is better than TEG WDP in Cases 1 and 3-3x: *-60.1^oC @1.01 bar* versus *-45.8^oC @1.01 bar*, respectively. For HCDPA, results are even better: SS HCDP attains *-19.5^oC @45 bar* while JTE HCDP is *-2.8^oC @45 bar* in Cases 1 and 3-3x.

Comparing EOR fluids, the low pressure permeates from Cases 1-2 with *≈78%* CO_2 are similar, both from MP CO_2 removal. On the other hand, SS condensate in Cases 3-3x is a high pressure liquid, directly pumped to EOR in Case 3 requiring low power consumption. Despite its slightly lower flow rate, SS condensate in Cases 3-3x has *75.59%* CO_2 and *≈10%* C2+, both positive EOR factors. CH_4 losses in EOR fluid of Cases 3-3x are also lower than those from MP (Cases 1-2). Regarding NGLs, Cases 1 and 3-3x produce the same NGL with *34.14%* CO_2 as they use PFD A for WDPA+HCDPA, whereas Case 2 applies SS in PFD C for WDPA+HCDPA, giving NGL with less CO_2 (*27.33%*). Discounting the *12.01%* of water, NGL flow rate from PFD C is *≈205%* higher thanks to high capture of C_2H_6 and C3+, an economic advantage due to their values as petrochemical and LPG feedstocks.

Table III. 4. Final NG, EOR Fluid and NGL: Cases 1, 2, 3/3x.

	Final NG			*EOR Fluid*			*NGL*	
Item	***Case 1***	***Case 2***	***Case 3/3x***	***Case 1***	***Case 2***	***Case 3/3x***	***Case 1/3/3x***	***Case 2***
T(°C)	*38.59*	*38.78*	*25.00*	*35.59*$^{+}$	*35.78*$^{+}$	*-60.11**	*-2.55*$^{\#}$	*20.00*$^{\&\$}$
P(bar)	*41.00*	*39.83*	*34.09*	*4.00*$^{+}$	*4.00*$^{+}$	*34.59**	*43.00*$^{\#}$	*41.33*$^{\&\$}$
MMsm^3/d	*2.76*	*2.71*	*2.99*	*2.33*$^{+}$	*2.34*$^{+}$	*2.10**	*0.02169*$^{\#}$	*0.0754*$^{\&\$}$
%CO_2	*15.00*	*14.94*	*21.85*	*78.35*	*78.14*	*75.59*	*34.14*	*27.33*
%CH_4	*74.33*	*75.29*	*75.22*	*21.60*	*21.81*	*14.51*	*13.90*	*6.61*
%C_2H_6	*5.49*	*5.51*	*2.35*	*0.05*	*0.05*	*3.92*	*4.05*	*3.90*
%C_3H_8	*3.64*	*3.41*	*0.54*	*0.00*	*0.00*	*4.02*	*8.50*	*12.98*
%i-C_4H_{10}	*0.53*	*0.42*	*0.03*	*0.00*	*0.00*	*0.66*	*2.85*	*5.30*
%C_4H_{10}	*0.35*	*0.24*	*0.01*	*0.00*	*0.00*	*0.44*	*2.61*	*4.94*
%i-C_5H_{12}	*0.33*	*0.13*	*0.00*	*0.00*	*0.00*	*0.42*	*5.51*	*8.84*
%C_5H_{12}	*0.16*	*0.05*	*0.00*	*0.00*	*0.00*	*0.20*	*3.54*	*5.04*
%C_6H_{14}	*0.12*	*0.01*	*0.00*	*0.00*	*0.00*	*0.16*	*7.92*	*6.32*
%C_7H_{16}	*0.04*	*0.00*	*0.00*	*0.00*	*0.00*	*0.05*	*6.89*	*3.34*
%C_8H_{18}	*0.01*	*0.00*	*0.00*	*0.00*	*0.00*	*0.01*	*5.63*	*2.03*
%C_9H_{20}	*0.00*	*0.00*	*0.00*	*0.00*	*0.00*	*0.00*	*2.15*	*0.68*
%$C_{10}H_{22}$	*0.00*	*0.00*	*0.00*	*0.00*	*0.00*	*0.00*	*2.27*	*0.68*
ppm H_2O	*10.17*	*6.22*	*0.04*	*53.14*	*32.54*	*72.29*	*100.0*	*120062*$^{\&\$}$

$^{+}$*MP permeate* **SS stagnant condensate* $^{\#}$*From JTE* $^{\&}$*From LTX* $^{\$}$*Two-phase L+W*

Table III.5 presents SS designs of PFDs C (Case 2) and D/E (Cases 3-3x). Despite the same converging/diverging angles, same inlet/outlet diameters, same battery sizes and similar feed flow rates (Table III.3) and Ma^{Shock}, the resulting designs are different with very distinct pressure recoveries: SS in Case 2 operates at ease with excellent recovery of *82.66%*, while in Cases 3-3x SS is under stress recovering only *41.18%* of pressure. This difference is consequence of the distinct nature of both SS services concerning the withdrawal fraction of condensate: SS in Case 2 collects *1.47%* of condensate and abates only *0.98%* of CO_2, while in Cases 3-3x *41.26%* of the feed is withdrawn as condensate carrying *70.85%* of the fed CO_2. Fig. III.16 depicts the SS path of Case 2 on plane *P x T* with feed and final NG VLE envelopes. The SS path starts at the WDP curve of the water saturated SS feed in PFD C. This means water condensing from the outset, while HC precipitation only starts when SS path crosses the feed HCDP curve. The 1st branch of SS path ends at $Ma^{Shock}=1.5$, $P_{BS}=15.05$ *bar*, $T_{BS}=-38.28^oC$ (Table III.5), where the condensate is withdrawn, causing a fall of *Ma* to $Ma_{BS}=1.4378$. This supersonic condition triggers the 2nd branch of SS path as the gas crosses the shock front, seen

in Fig. III.16 as a rectilinear jump back to (*288.4 K, 33.0 bar*), followed by monotonous recompression and heating, with different inclination, through the diffuser.

Fig. III.17 depicts SS path on plane *P x T* for Cases 3-3x with the respective VLE envelopes of feed and final NG. SS path penetrates the envelope at the bubble locus near the critical point. As flow evolves, *T* and *P* fall, *Ma* and vapor fraction increase and gas $\%CO_2$ decreases (Fig. III.18). Fig. III.18 reports influence of Ma^{Shock} on vapor fraction, gas $\%CO_2$ and *Ma* after withdrawal (Ma_{BS}) for $Ma^{Shock} \geq 1.1$. A SS skirmish encountered the SVLE freeze-out border at $Ma^{Shock}=1.65$, $T=-62.51^oC$, $P=19.8$ *bar*, i.e., SS designs with $Ma^{Shock} \geq 1.65$ face dry ice precipitation at pre-shock as in Fig. III.18. To avoid freeze-out, SS design in PFDs D/E was defined with the 1st branch of SS path ending at $Ma^{Shock}=1.6$, $P_{BS}=21.95$ *bar*, $T_{BS}=-60.07^oC$, where the copious condensate (*41.26%* of feed) is withdrawn without solids, causing a fall of *Ma* to $Ma_{BS}=0.9111$ (under constant flow section) also in Fig. III.18. As this subsonic condition cannot provoke shock, the flow goes directly to the diffuser recompression, i.e. the small 2nd branch of SS path in Fig. III.17.

Table III. 5. SS Designs and Performances: Cases 2, 3/3x.

Specified Items	***Case 2***	***Case 3/3x***	***Calculated by SS-UOE***	***Case 2***	***Case 3/3x***
No.of SS	*6*	*6*	$D_T(m)$	*0.0355*	*0.0224*
$D_I(m)$	*0.0762*	*0.0762*	$L_C(m)$	*0.0906*	*0.1196*
$D_O(m)$	*0.048*	*0.048*	$L_D(m)$	*0.1349*	*0.2751*
$\alpha(^o)$	*15*	*15*	$L(m)$	*0.2255*	*0.3947*
$\beta(^o)$	*2.75*	*2.75*	$L^{Shock}(m)$	*0.1262*	*0.1803*
Ma^{Shock}	*1.5*	*1.6*	$L^{Diff}(m)$	*0.0993*	*0.2144*
$\eta^{EXP}\%$	*100*	*100*	$P_{BS}(bar)$	*15.05*	*21.95*
$\eta^{CMP}\%$	*100*	*100*	$T_{BS}(^oC)$	*-38.28*	*-60.07*
$P^{Feed}(bar)$	*50*	*84.0*	Ma_{BS}	*1.4378*[*]	*0.9111*[*+]
$T^{Feed}(^oC)$	*35*	*-20.04*	$P^{Discharge}(bar)$	*41.33*	*34.59*
$MMsm^3/d$	*5.12*	*5.09*	$T^{Discharge}(^oC)$	*31.57*	*-31.85*
$\%C3^{+Feed}$	*3%*	*2.82%*	*%Condensate*	*1.47%*	*41.26%*
$ppmH_2O^{Feed}$	*1784.1*	*29.9*	$REC\%CO_2$	*0.92%*	*70.85%*
$\%CO_2{}^{Feed}$	*44.17%*	*44.02%*	*%P Recovery*	*82.66%*	*41.18%*

[*] *After condensate withdrawal* [+] *Normal shock does not occur*

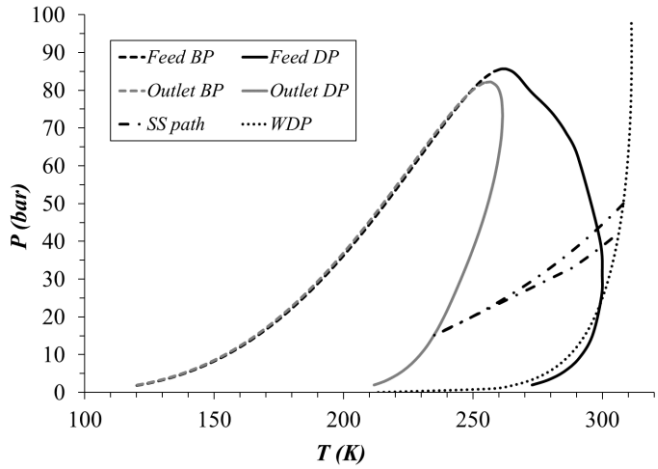

Figure III. 16. Plane *P x T* for SS Path in Case 2 with Humid NG: (i) Feed VLE Envelope; (ii) Feed WDP Curve; (iii) SS Path; (iv) Final NG VLE Envelope.

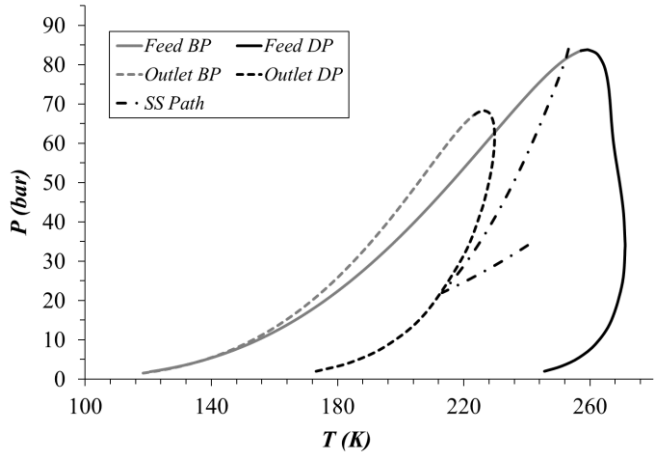

Figure III. 17. Plane *P x T* for SS Path in Cases 3-3x: (i) Feed VLE Envelope; (ii) SS Path; (iii) Final NG VLE Envelope.

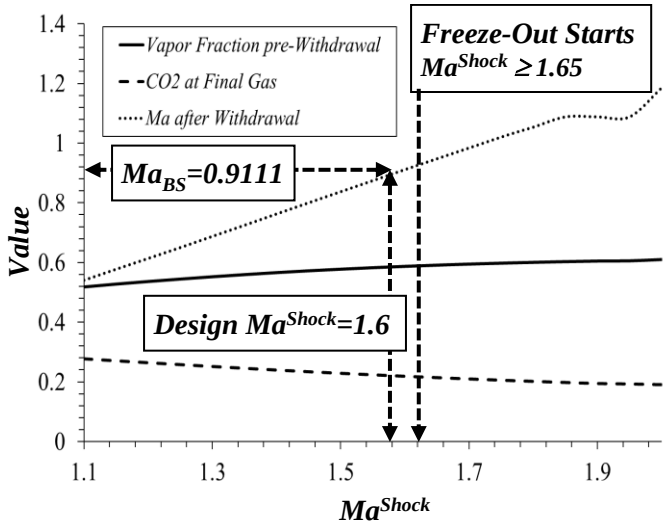

Figure III. 18. Influence of Ma^{Shock} in SS Operation for Cases 3-3x: (i) Vapor Fraction pre-Withdrawal; (ii) Final $\%CO_2$; (iii) Ma after Withdrawal (Ma_{BS}); (iv) Operation Point $Ma^{Shock}=1.6$ & $Ma_{BS}=0.9111$.

Power Demands. Power to drive pumps and compressors was evaluated for all cases, including requirements of a CO_2 refrigeration cycle to cool SS feed in Case 3, inexistent in Case 3x. Fig. III.19 depicts power demands. Relatively to Case 1, Case 2 demands *6.9%* less power due to lower SS feed pressure in PFD C, while Case 3 demands *22.1%* less power, a consequence of direct pumping of high pressure SS condensate to EOR, whereas Case 1 prescribes expensive 3-stage compression from *4 bar* to *250 bar* for same finality. Case 3x avoids refrigeration, demanding *10.3%* less power than Case 3 and 30.2*%* less than Case 1.

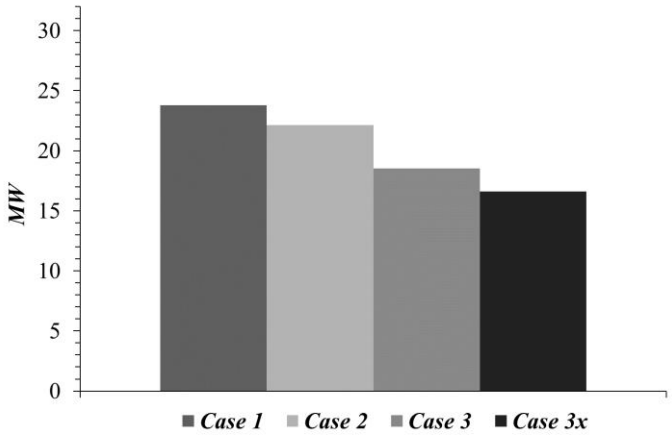

Figure III. 19. Power Demands: Cases 1, 2, 3 and 3x.

III.6. SS performance with adiabatic efficiencies

In order to take into account friction and other SS irreversibilities (excepting normal shock), SS-UOE allows to define adiabatic efficiencies for expansion ($\eta^{EXP}\%$) and compression ($\eta^{CMP}\%$) steps to correct the SS isentropic paths, doubling, consequently, the flash calls and CPU time. When operating with $\eta^{EXP}\%<100\%$ and/or $\eta^{CMP}\%<100\%$, the SS algorithm in Sec. III.3.2.2 (and Appendix G) is altered as follows. In each isentropic expansion step $Flash\,(P^{(n)},\bar{S}_E,\underline{Z}_E)$ or each isentropic compression step $Flash\,(P^{(n)},\bar{S}_{AS},\underline{Z}_{AS})$, the isentropic changes of molar enthalpy ($\Delta\bar{H}^{ISEN}$) and molar kinetic energy ($\Delta\bar{K}^{ISEN}$) are calculated as before. The following calculations are added: (i) adiabatic efficiencies correct the changes of kinetic energy for expansion step ($\Delta\bar{K}=\Delta\bar{K}^{ISEN}*\eta^{EXP}\%/100$) or for compression step ($\Delta\bar{K}=\Delta\bar{K}^{ISEN}*100/\eta^{CMP}\%$), giving the correct enthalpy change ($\Delta\bar{H}=-\Delta\bar{K}$) and final enthalpy of the step ($\bar{H}^{(n)}=\bar{H}^{(n-1)}+\Delta\bar{H}$); (ii) apply $Flash\,(P^{(n)},\bar{H}^{(n)},\underline{Z}_E)$ for expansion step or $Flash\,(P^{(n)},\bar{H}^{(n)},\underline{Z}_{AS})$ for compression step to calculate thermodynamic multiphase flow properties at the end of step.

To evaluate SS sensitivity with adiabatic efficiencies, SS operation with DRY-NG-1 (Sec. III.3.2.3) is revisited with same feed, design parameters, condensate removal and $Ma^{Shock}=2$, under three levels of adiabatic efficiencies: $\eta^{EXP}\%=\eta^{CMP}\%=\{80\%, 90\%, 100\%\}$. Figs. III.20, III.21 and III.22 depict profiles *P*, *T*, *Ma* for $\eta^{EXP}\%=\eta^{CMP}\%=\{80\%, 90\%, 100\%\}$, indicating that the normal shock moves downstream according to the loss of efficiency as the expansion path has to be longer to attain the same $Ma^{Shock}=2$ and to give decreasing pressure recoveries (backpressures). All cases have the same feed flow rate, same SS nozzle and, therefore, same throat position where $Ma=1$, which defines the SS flow capacity. The differences among the cases have to do only with backpressure and shock location. Lower efficiencies also reduce minimum (*P*,*T*) in the expansion path promoting a cooler pre-shock and slightly more condensation, but progressively with lower pressure recoveries as Ma^{Shock} is fixed: For $\eta^{EXP}\%=\eta^{CMP}\%=\{80\%, 90\%, 100\%\}$ pressure recoveries were, respectively, *27.7%*, *38.3%* and *48.2%*.

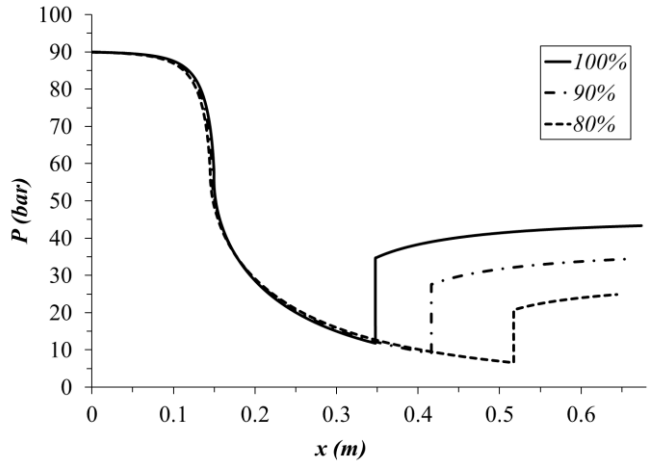

Figure III. 20. SS Pressure Profiles: $\eta^{EXP}\%=\eta^{CMP}\%=\{80\%,90\%,100\%\}$ ($Ma^{Shock}=2$).

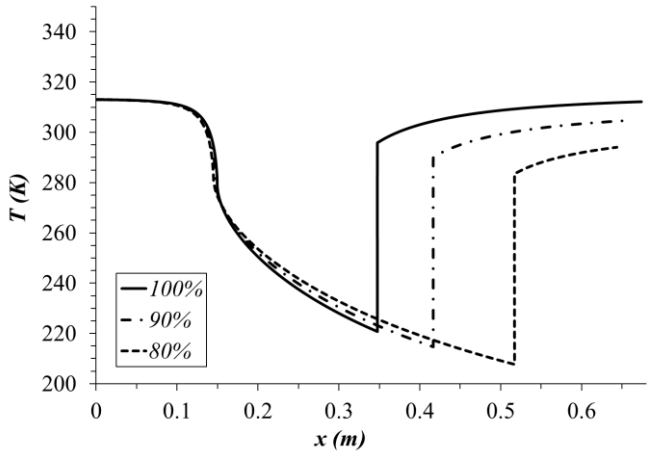

Figure III. 21. SS Temperature Profiles: $\eta^{EXP}\%=\eta^{CMP}\%=\{80\%,90\%,100\%\}$ ($Ma^{Shock}=2$).

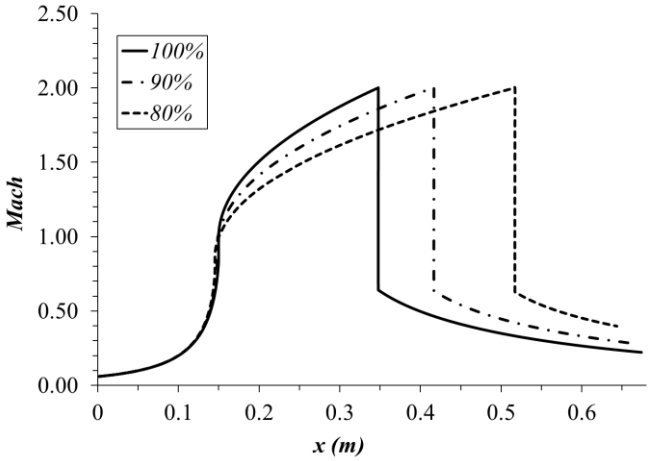

Figure III. 22. SS Mach Profiles: $\eta^{EXP}\%=\eta^{CMP}\%=\{80\%, 90\%, 100\%\}$ ($Ma^{Shock}=2$).

Karimi and Abdi (2009) simulated SS, under frictionless and frictional conditions, expanding 300 kg/s of CH_4 from (*18.5°C, 92.5 bar*) to a common backpressure of *70 bar*. The frictionless SS is reported to develop normal shock downstream the frictional counterpart, which is in total concordance with present results for different efficiencies. To make this explicit, DRY-NG-1 feed is expanded in the previous SS nozzle for $\eta^{EXP}\%=\eta^{CMP}\%=\{80\%, 90\%, 100\%\}$ with a common backpressure of *43.34 bar*, which was obtained in Table III.2 for isentropic SS expansions/compressions ($\eta^{EXP}\%=\eta^{CMP}\%=100\%$). Now, different Ma^{Shock}*'s* and reversed shock locations result for different efficiencies as shown in Fig. III.23 for the respective pressure profiles. Under fixed backpressure of *43.34 bar* the most efficient SS develops the latest shock at $Ma^{Shock}=2$ with coldest pre-shock at *T=221 K*, while the least efficient SS has the most precocious shock at $Ma^{Shock}=1.69$ with hottest pre-shock at *T=228 K* and the intermediate efficient SS has a shock at $Ma^{Shock}=1.84$ with pre-shock at *T=224 K*, so that all cases can match the common backpressure. This clearly evidences that SS performance is hampered – both in terms of degree of cooling at fixed backpressure or in terms of pressure recovery at fixed Ma^{Shock} – as its expansions/compressions become less adiabatically efficient.

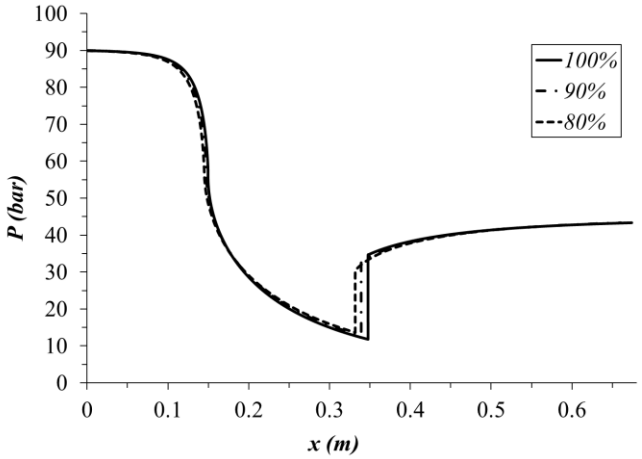

Figure III. 23. SS Pressure Profiles: $\eta^{EXP}\%=\eta^{CMP}\%=\{80\%, 90\%, 100\%\}$ with Backpressure=43.34 bar.

Fig. III.24 superimposes the corresponding SS (*P,T*) paths in Figs. III.20 and III.21 (with $Ma^{Shock}=2$) for $\eta^{EXP}\%=\eta^{CMP}\%=\{80\%, 90\%, 100\%\}$ on a plane *P x T* with feed and gas product VLE envelopes. DRY-NG-1 (*Point 1*) expands penetrating the feed VLE envelope at *Points 2*. The (*P,T*) paths change inclination now, until just before the normal shocks ($Ma^{Shock}=2$) at *Points 3* where condensates are collected. *Points 3* lie on the respective HCDP curves of the

slender VLE envelopes belonging to the vapors after the respective liquid withdrawals. After condensates removal, the respective normal shocks are executed with different rectilinear (*P*,*T*) jumps back to superheated gases at *Points 4*, spreading out with different (*P*,*T*) recoveries due to different efficiencies. From *Points 4* to *Points 5*, compression and heating (*P*,*T*) paths are less inclined, representing (*P*,*T*) recoveries through the diffuser. It is clear that lower efficiencies (at fixed Ma^{Shock}) achieve slightly lower HCDPs, but entail considerably lower pressure recoveries. Fig. III.25 3D renders the same *P x T* plane with a 3rd efficiency axis generating a 3D vista of the described behavior, where the foil is a cylindrical representation of the feed VLE envelope.

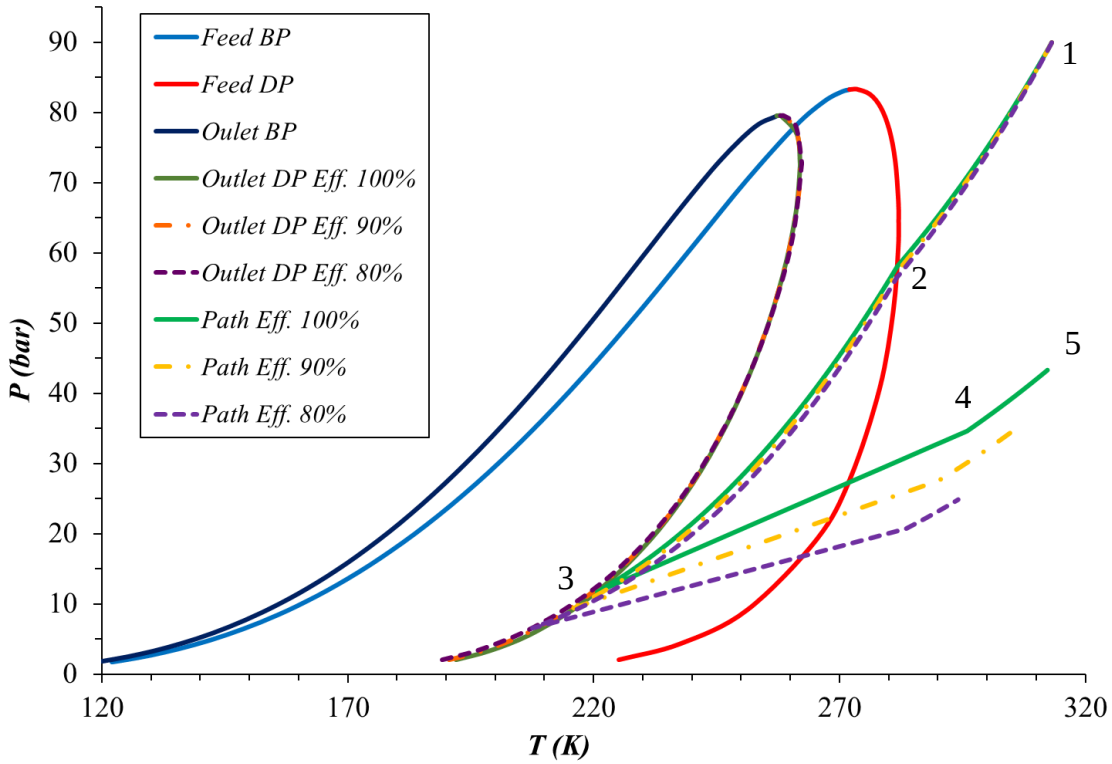

Figure III. 24. Plane *P x T* with Feed and Final Gases VLE Envelopes and SS Paths for $\eta^{EXP}\%=\eta^{CMP}\%=\{80\%, 90\%, 100\%\}$.

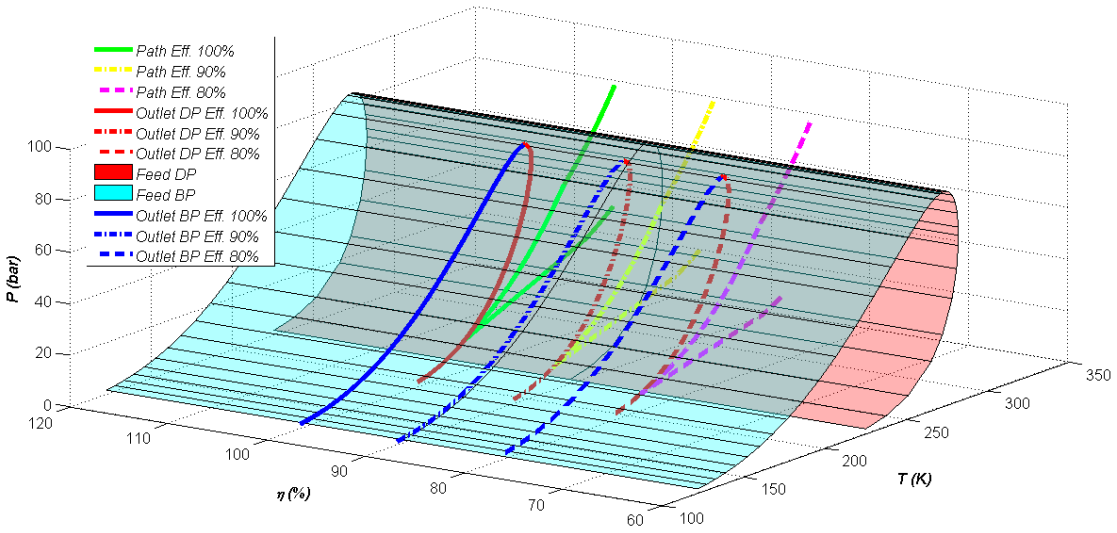

Figure III. 25. Plane *P x T* with 3rd Axis *η(%)*: (i) Feed (Foil) VLE Envelope; (ii) Final Gases VLE Envelopes and SS Paths for $\eta(\%)=\eta^{EXP}\%=\eta^{CMP}\%=\{80\%, 90\%, 100\%\}$.

III.7. Conclusions

Unit operation HYSYS extensions, SS-UOE and MP-UOE, were developed to simulate MP and SS units in steady state HYSYS PFDs. MP-UOE uses a short-cut MP model based on log-mean of differences of species partial pressures and permeances calibrated with real MP operation data. SS-UOE, on the other hand, is a pure phenomenological SS model comprising rigorous thermodynamic and phase equilibrium calculations along the SS flow path. SS-UOE can operate with water saturated NG with high CO_2 contents, correctly handling L+W condensate removal and normal shock transition (if present), essential steps for correct SS representation in NG context. SS-UOE uses the thermodynamic sound speed of multiphase VLWE compressible flow rigorously calculated by means of another HYSYS extension, PEC-UOE, developed in a parallel work (de Medeiros et al., 2017). Besides the feed stream, SS-UOE demands specification of inlet-outlet SS diameters, converging-diverging angles, expansion-compression adiabatic efficiencies and Mach Number just before normal shock and separation, Ma^{Shock}. The VLWE separation, the remaining SS geometric parameters and the backpressure, temperature, flow rate and composition of the final gas and L+W condensate are calculated in sequence. MP-UOE and SS-UOE performances are in total accordance with the expected behavior reported in the available literature. Several examples of SS-UOE with CO_2 rich NG were presented. As shown in this work, a pertinent measure in this subject is to check

if the SS path crosses the SVLE freeze-out border inside the VLE envelope. In this case, Ma^{Shock} has to be reduced, shortening the VLE SS path, otherwise copious solid dry ice can plug a conventional SS nozzle.

In the practical terrain, four processes were assessed for offshore conditioning of water saturated *44%* CO_2 NG. Conventional Case 1 comprises TEG WDPA, JTE HCDPA and MP CO_2 removal. Alternative Cases 2, 3, 3x apply SS for WDPA+HCDPA or SS for CO_2 removal. All HYSYS PFDs were simulated with SS-UOE and MP-UOE. In Case 2, SS was successfully used for WDPA+HCDPA of water saturated *44%* CO_2 NG with *6.9%* less power consumption than Case 1, thanks to a lower SS feed pressure, demanding less compression power. SS operated at ease in Case 2 using $Ma^{Shock}=1.5$ to condense *1.47%* of feed with an excellent *82.66%* coefficient of pressure recovery and producing a better quality lean NG with less equipment and footprint than Case 1.

Cases 1 and 2 with MP abated *81.5%* of the original CO_2 giving a *15%* CO_2 final NG using only a single-stage SW MP. On the other hand, in Cases 3-3x, SS removed *70.85%* of the original CO_2 giving a final gas with *21.85%* CO_2. In Cases 3-3x, SS could not make further progress in terms of CO_2 capture beyond *21.85%* CO_2 due to the SVLE freeze-out border encountered for $Ma^{Shock}\geq1.65$ with this feed. Nonetheless, Cases 3-3x prove the SS potential for partial abatement of CO_2 producing semi-decarbonated NG usable as fuel for power generation. Moreover, SS successful application for partial CO_2 removal from a *44%* CO_2 NG has never been reported before. Despite using a refrigeration cycle in SS feed, Case 3 demands *22.1%* less power than Case 1, mainly due to pumping SS condensate as EOR fluid in place of 3-stage compression in Case 1 for same finality. Case 3x, a variant of Case 3 without refrigeration, cooled SS feed with the (*-60.11°C, 34.59 bar*) SS condensate, demanding 10.3*%* less power.

Acknowledgements

Authors acknowledge financial support from Petrobras S.A. and CNPq-Brazil.

Supplementary Materials (Appendix J)

Supplementary data related to this article can be found in the online version.

Abbreviations

1D, 2D, 3D One, Two and Three-Dimensional; BIP Binary Interaction Parameter; C2+ Ethane and C3+; C3+ Propane and Heavier Alkanes; CAM Cellulose Acetate Membrane; CFD Computational Fluid Dynamics; CPU Central Processing Unit; CTC Constant Total Composition; CW Cooling Water; DLL Dynamic-Link Library; E&P Exploration & Production; ECS Equilibrium Closed System; EOR Enhanced Oil Recovery; EOS Equation of State; FOB Freeze-Out Border, FPSO Floating, Production, Storage & Offloading; GFOB Grand Freeze-Out Border; HC Hydrocarbon; HCDP Hydrocarbon Dew Point; HCDPA Hydrocarbon Dew Point Adjustment; HF Hollow-Fiber; JTE Joule-Thomson Expansion; L+W Condensate with HCs + Water; LNG Liquefied NG; LPG Liquefied Petroleum Gas; LTX Low-Temperature Separator; MMsm^3/d 10^6 standard m^3 per day; MP Membrane Permeation; NG Natural Gas; NGL Natural Gas Liquids; NRM Newton-Raphson Method; OGW Oil-Gas-Water. PFD Process Flow Diagram; PHW Pressurized Hot Water; PR Peng-Robinson; PVT Pressure, Volume & Temperature; SI International System of Units; SCF Supercritical Fluid; SS Supersonic Separator; SLE Solid-Liquid Equilibrium; SVE Solid-Vapor Equilibrium; SVLE Solid-Vapor-Liquid Equilibrium; SW Spiral-Wound; TEG Triethylene Glycol; TP Triple Point; UOE Unit Operation Extension, VB Visual Basic; VLE Vapor-Liquid Equilibrium; VLWE Vapor-Liquid-Water Equilibrium; WDP Water Dew Point; WDPA Water Dew Point Adjustment.

Nomenclature

A_{MP} : *MP area (m²)*

$c(T,P,\underline{Z})$: *Sound speed of multiphase fluid at (T, P, $\underline{Z}$) (m/s)*

$\overline{C}_P \equiv \left(\frac{\partial \overline{H}}{\partial T}\right)_{P,\underline{Z}}$: *Molar heat capacity at const. P, $\underline{Z}$ of multiphase fluid (J/K.mol)*

D : *Internal diameter (m)*

D_I, D_T, D_O : *SS inlet/throat/outlet internal diameters (m)*

$\overline{E}$: *Total molar energy of multiphase fluid (J/mol)*

$f_{CO2}^{S}(T,P)$: *Fugacity of pure solid CO_2*

F : *Molar flow rate of multiphase fluid (mol/s)*

$\overline{H}$: *Molar enthalpy of multiphase fluid (J/mol)*

$\overline{K}$: *Molar kinetic energy of multi-phase fluid (J/mol)*

L : *MP permeate molar flow rate (mol/s)*

L, L_C, L_D : *SS lengths: total/converging/diverging sections (m)*

L^{LAVAL} : *Laval nozzle length (m)*

L^{Shock} : *SS axial position just before normal shock (=L^{LAVAL}) (m)*

$Ma=v/c$: *Mach Number*
Ma^{Shock} : *Ma just before normal shock and before condensate withdrawal*
M_M : *Molar mass of multiphase fluid (kg/mol)*
nc : *Number of components*
N_k : *Species k permeation rate (MMsm^3/d)*
P : *Pressure (Pa in SS, bar in MP)*
P_L^{out}, P_V^{out} : *MP permeate/retentate pressures (bar)*
P_V^{in} : *MP gas feed pressure (bar)*
ΔP_k^{LN} : *MP log mean difference of partial pressures of species k (bar)*
q : *Mass flow rate of multiphase fluid (kg/s)*
$REC\%CO_2$: *Percent recovery of CO_2 in SS condensate*
$\overline{S}$: *Molar entropy of multiphase fluid (J/K.mol)*
T : *Temperature (K)*
T_L, T_V : *Temperatures of permeate/retentate (K)*
v : *Axial velocity of non-segregated multiphase fluid (m/s)*
v_V, v_{L+W} : *Axial velocities of segregated vapor and L+W two-phase liquid (m/s)*
V : *MP molar flow rate of retentate (mol/s)*
x : *SS axial position (m)*
$\underline{X}$: *Vector (nc x 1) of liquid phase mol fractions*
Y_k^{in}, Y_k^{out} X_k^{out} : *Species k mol fraction in feed/retentate/permeate MP streams*
$\underline{Y}$: *Vector (nc x 1) of vapor phase mol fractions*
$\underline{Z}$: *Vector (nc x 1) of total multiphase-fluid mol fractions*

Greek Symbols

α, β : *SS converging/diverging half angles (deg)*
δ_P, δ_M, δ_D : *Pressure step (Pa), Mach tolerance and spatial tolerance (m)*
Π_k : *MP permeance of species k (MMSm^3/d.m^2.bar)*
η : *Phase split mol fraction*
$\eta^{EXP}\%, \eta^{CMP}\%$: *SS expansion/compression adiabatic efficiencies (%)*
$\hat{\phi}_k, \phi_k$: *Fugacity coefficients of species k*
ρ : *Multiphase fluid density (kg/m^3)*
$\Xi_P \equiv \left(\frac{\partial \rho}{\partial P}\right)_{T,\underline{Z}}$: *Derivative of ρ with P at const. T, $\underline{Z}$ for multiphase fluid (kg/Pa.m^3)*
$\Xi_T \equiv \left(\frac{\partial \rho}{\partial T}\right)_{P,\underline{Z}}$: *Derivative of ρ with T at const. P, $\underline{Z}$ for multiphase fluid (kg/K.m^3)*

Subscripts

AS : *Just after normal shock*
BS : *Just before normal shock and after condensate withdrawal*
C, D : *Converging, Diverging sections*
E : *Entrance*
I, O, T : *SS inlet, outlet, throat*
k : *Species index*
L : *SS HC liquid at L^{Shock} or Permeate MP product*

$L+W$	*: Two-phase HC+Water condensate*
TP	*: Triple point*
V	*: SS vapor phase at L^{Shock} or Retentate MP product*
W	*: SS aqueous liquid at L^{Shock}*

Superscripts

$'$	*: Ideal gas property*
in, out	*: Inlet, outlet*
$LAVAL$	*: Laval nozzle*
$Shock$	*: Just before normal shock and condensate withdrawal*
$Throat$	*: SS Throat*
V, L, S	*: Vapor, liquid, solid*

References

Alfyorov, V., Bagirov, L., Dmitriev, L., Feygin, V., Imaev, S., Lacey, J., 2005. Supersonic nozzle efficiently separates natural gas components. Oil Gas J. 103, 53–58.

Araújo, O.Q.F., Reis, A.C., de Medeiros, J.L., do Nascimento, J.F., Grava, W.M., Musse, A.P.S., 2016. Comparative analysis of separation technologies for processing carbon dioxide rich natural gas in ultra-deepwater oil fields. Journal of Cleaner Production, (2016), http://dx.doi.org/10.1016/j.jclepro.2016.06.073.

Cao, X., Yang, W., 2015. The dehydration performance evaluation of a new supersonic swirling separator. J. Nat. Gas Sci. Eng. 27, 1667–1676. doi:10.1016/j.jngse.2015.10.029.

Cao, X., Yang, W., 2015. Numerical simulation of binary-gas condensation characteristics in supersonic nozzles. J. Nat. Gas Sci. Eng. 25, 197–206. doi:10.1016/j.jngse.2015.05.005.

Castier, M., 2016. Effect of side streams on supersonic gas separations. J. Nat. Gas Sci. Eng. 35, 299-308. doi: 10.1016/j.jngse.2016.08.065

Castier, M., 2014. Modeling and simulation of supersonic gas separations. J. Nat. Gas Sci. Eng. 18, 304–311. doi:10.1016/j.jngse.2014.03.014

Castier, M., 2011. Fluid Phase Equilibria Thermodynamic speed of sound in multiphase systems. Fluid Phase Equilib. 306, 204–211. doi:10.1016/j.fluid.2011.04.002

Cavett, R.H., 1963. Application of Numerical Methods to the Convergence of Simulated Processes Involving Recycle Loops, Am. Petrol. Inst., 43, 57

de Medeiros, J.L., Arinelli, L.O., Araújo, O.Q.F., 2017. Speed of sound of multiphase and multi-reactive equilibrium streams: a numerical approach for natural gas applications. J. Nat. Gas Sci. Eng. Under Submission.

GPSA (Gas Processors Suppliers Association), 2004. Engineering Data Book, 12th Ed. Gas Processors Suppliers Association, Tulsa.

Hammer, M., Wahl, P.E., Anantharaman, R., Berstad, D., Lervåg, K.Y., 2014. CO2 Capture from Off-shore Gas Turbines Using Supersonic Gas Separation. Energy Procedia 63, 243–252. doi:10.1016/j.egypro.2014.11.026

Hlavinka, M.W., Hernandez, V.N., McCartney, D., 2006. Proper Interpretation of Freezing and Hydrate Prediction Results from Process Simulation, Bryan Research & Engineering Inc..

Honeywell, 2012. Honeywell UOP technology is used to clean natural gas on FPSO vessels. Membr. Technol. 2012, 5. doi:10.1016/S0958-2118(12)70011-3

Imaev, S.Z., Bagirov, L.A., Borisov, V.E., Voytenkov, E. V, Engineering, E., 2014. New Low Temperature Process of CO2 Recovery from Natural Gases, in: SPE Asia Pacific Oil & Gas Conference and Exhibition. Society of Petroleum Engineers, Adelaide, Australia, 14–16.

Karimi, A., Abdi, M.A., 2009. Selective dehydration of high-pressure natural gas using supersonic nozzles. Chem. Eng. Process. Process Intensif. 48, 560–568. doi:10.1016/j.cep.2008.09.002

Machado, P.B., Monteiro, J.G.M., Medeiros, J.L., Epsom, H.D., Araujo, O.Q.F., 2012. Supersonic separation in onshore natural gas dew point plant. J. Nat. Gas Sci. Eng. 6, 43–49. doi:10.1016/j.jngse.2012.03.001

Nichita, D.V., Khalid, P., Broseta, D., 2010. Calculation of isentropic compressibility

and sound velocity in two-phase fluids. Fluid Phase Equilibria 291 (1), 95-102. doi:10.1016/j.fluid.2009.12.022

Rowland, D., Hughesb, T.J., Mayb, E.F., 2016. Extending the GERG-2008 equation of state: Improved departure function and interaction parameters for (methane + butane). J. of Chem. Thermodynamics, 97, 206–213.

Samawe, R.A., Rostani, K., Jalil, A.M., Esa, M., Othman, N., 2014. Concept proofing of supersonic nozzle separator for CO2 separation from natural gas using a flow loop, in: Offshore Technology Conference Asia. Offshore Technology Conference, Kuala Lumpur, Malaysia, 2373–2376.

Schinkelshoek, P., Epsom, H.D., 2008. Supersonic gas conditioning - Commercialisation of Twister Technology, in: GPA Annual Convention Proceedings. Grapevine, Texas, USA, pp. 739–745.

Secchi, R., Innocenti, G., Fiaschi, D., 2016. Supersonic Swirling Separator for natural gas heavy fractions extraction: 1D model with real gas EOS for preliminary design. J. Nat. Gas Sci. Eng. 34, 197–215. doi:10.1016/j.jngse.2016.06.061

Shooshtari, R.S.H., Shahsavand, A., 2013. Reliable prediction of condensation rates for purification of natural gas via supersonic separators. Sep. Purif. Technol. 116, 458–470. doi:10.1016/j.seppur.2013.06.009

Trusler, J. P. M., 2011. Equation of State for Solid Phase I of Carbon Dioxide Valid for

Temperatures up to 800 K and Pressures up to 12 GPa. J. Phys. Chem. Ref. Data, Vol. 40, No. 4, (2011).

Twister BV, 2010. Twister Supersonic Separator [WWW Document]. Prod. Serv. URL http://twisterbv.com/products-services/twister-supersonic-separator/ (accessed 1.1.15).

Wen, C., Cao, X., Yang, Y., Li, W., 2012. An unconventional supersonic liquefied technology for natural gas. Energy Education Science and Technology Part A: Energy Science and Research, 30(1), 651-660.

Wood, A.B., 1930. A Textbook of Sound: Being an Account of the Physics of Vibrations with Special Reference to Recent Theoretical and Technical Developments. The Macmillan Company, New York.

Yang, Y., Wen, C., Wang, S., Feng, Y., 2014. Numerical simulation of real gas flows in natural gas supersonic separation processing. J. Nat. Gas Sci. Eng. 21, 829–836. doi:10.1016/j.jngse.2014.10.010

CHAPTER IV - SUPERSONIC SEPARATOR FOR CLEANER OFFSHORE PROCESSING OF NATURAL GAS WITH HIGH CARBON DIOXIDE CONTENT: ENVIRONMENTAL AND ECONOMIC ASSESSMENTS

This paper was published in Journal of Cleaner Production, 233, 510-521, 2019 (doi: 10.1016/j.jclepro.2019.06.115) (Appendix T.27)

Supersonic Separator for Cleaner Offshore Processing of Natural Gas with High Carbon Dioxide Content: Environmental and Economic Assessments

*Lara de Oliveira Arinelli[a1], Alexandre Mendonça Teixeira[a2], José Luiz de Medeiros[*a] and Ofélia de Queiroz F. Araújo[a3]*
[a] Escola de Química, Federal University of Rio de Janeiro, Rio de Janeiro, RJ, Brazil

[*]Corresponding author: jlm@eq.ufrj.br
[1]lara.arinelli@gmail.com, [2]alexandremtxr@gmail.com, [3]ofelia@eq.ufrj.br

Abstract

Supersonic separators offer a cleaner offshore processing of natural gas with carbon dioxide content from deep-water oil-gas fields. Conventional offshore gas processing comprises water dew-point adjustment via glycol-absorption, hydrocarbon dew-point adjustment via Joule-Thomson expansion, and carbon dioxide removal via membrane-permeation. Alternative processing contemplates the use of supersonic separators for adjusting gas dew-points followed by carbon dioxide capture via membrane-permeation (so-called SS-MP scheme); or for adjusting gas dew-points and also accomplishing carbon dioxide abatement (so-called SS-SS scheme). The conventional process is environmentally and economically compared with SS-MP and SS-SS for application in offshore rigs treating raw gas (44%mol carbon dioxide) to produce exportable fuel-gas (≈20%mol carbon dioxide), while dispatching carbon dioxide rich fluid (≈75%mol carbon dioxide) for enhanced oil recovery in the oil-gas field. Results show that SS-MP requires 7.8% less power than the conventional process. Moreover, implementing SS-SS deepens the advantage against the conventional operation because SS-SS produces carbon dioxide rich fluid at high-pressure, requiring much less compression power for enhanced oil recovery than the low-pressure permeate from membrane-permeation. SS-SS has lowest carbon emission (-28.3%), lowest power consumption (-21.3%) and best economic performance: lowest manufacturing cost and lowest compressor investment. Thus, SS-SS is the overall best and cleanest solution, with highest 20 years net value (+860 MMUSD) and lowest environmental impact.

Keywords

CO_2-Rich Natural Gas Processing; Supersonic Separator; CO_2 Capture; Membrane Permeation; Environmental Assessment; Economic Assessment.

IV.1. Introduction

The pressing and harmful consequences of continued carbon emissions on the planet are undeniable, even if the depth of gravity is not completely clear. All possible routes for diminishing the impacts have its own criticisms; however, short/medium term solutions must be sought to start the healing process, while also investing in long-term solutions for future's sake (Montgomery, 2017).

Even though the sustainable future bends to renewable sources, it still faces challenges such as intermittency, location, transmission and costs issues, especially in emerging economies (Stram, 2016). There is also an industry move aiming at replacing conventional carbon-fired technologies by more efficient new ones with reduced carbon-fingerprint, as seen in the substitution of low H/C ratio fossil-fuels (oil, coal) by natural gas (NG), which has higher H/C and lower carbon emission rate per power produced. Therefore, NG is an easy bet for medium-term power solutions. However, over 10% of NG proven reserves contain 15-80%mol CO_2 (Burgers et al., 2011), which imposes challenges, requiring new NG exploration-and-production technologies.

Raw NG processing comprises operations usually applied in the following order (Kidnay and Parrish, 2006): (i) H_2S removal; (ii) water dew-point adjustment (WDPA) via dehydration; (iii) hydrocarbon dew-point adjustment (HCDPA) via propane and heavier hydrocarbons ($C3^+$) removal; and (iv) CO_2 removal. Considering a CO_2-rich raw NG with low H_2S content, gas processing comprises steps (ii) to (iv).

Conventional NG dehydration in offshore rigs comprises molecular-sieve adsorption and triethylene-glycol (TEG) absorption (Netusil and Ditl, 2011). The latter is the most common because it is rather simple to operate, with ordinary performance sufficient for NG treating purposes, while the former can reduce NG water down to 1 ppm, but at expenses of higher complexity, investment and costs. For instance, these authors report that the heat consumption of TEG absorption is ≈50% of the counterpart of molecular-sieve adsorption.

As observed by AlNouss et al. (2018), the simplest HCDPA alternative is Joule-Thomson expansion (JTE) comprising heat exchanger, isenthalpic valve, and vessel for natural gas liquids (NGL) extraction. These authors economically/environmentally assessed more complex

HCDPA systems considering six turbo-expander configurations for lower power consumption and CO_2 emissions, not surprisingly identifying an economic-environmental trade-off.

In offshore rigs, conventional CO_2 capture from NG is mostly done via chemical-absorption, membrane-permeation (MP) and physical-absorption (Araújo et al., 2017). Using multi-criterial analysis, these authors considered these alternatives and their hybrids for offshore processing of NG with 10%/30%/50%mol CO_2, assuming heating utility available as pressurized-hot-water (PHW) from waste-heat recovery units (WHRU) of power generation turboshafts. PHW favors chemical-absorption, which was concluded as the best alternative in a hybrid with MP, seconded by MP alone. As shown in Araújo et al. (2017), CO_2 removal is not only important to meet NG specifications; it is an asset of carbon capture and storage through CO_2 injection in oil fields for enhanced oil recovery (EOR). In this context, Reis et al. (2017) optimized MP with time-varying CO_2 content for minimum area subjected to bulk CO_2 removal and EOR constraints admitting a final polishing chemical-absorption. Later, Reis et al. (2018) evaluated the design of NG offshore processing oriented by lifetime parameters, considering CO_2 capture via the hybrid MP/chemical-absorption.

Larger NG reserves with high CO_2 content are located in SE-Asia, NW-Australia, Central-USA and SE-Brazil (Burgers et al., 2011). In SE-Brazil, the Pre-Salt offshore basins have associated gas with high CO_2 content, tying oil production to CO_2-rich NG processing. Some Pre-Salt fields have impressive CO_2 content: Jupiter field, with a large gas cap (79%mol CO_2) above oil (55%mol CO_2); and Libra field, with 4-15*10^9 bbl of oil, gas/oil ratio ≈500 Sm^3/m^3 and %CO_2 ≥40%mol (Gaffney, Cline & Associates, 2010). In the USA, LaBarge gas field produces 65%mol CO_2 gas to Riley Ridge facility, which exports CO_2 to EOR operators (Burgers et al., 2011).

IV.1.1. NG Processing with Supersonic Separators: State-of-the-Art

Supersonic separator (SS) is a recent NG treating technology applied mainly for simultaneous WDPA+HCDPA, extracting water-C3+ condensate. SS is a compact device (Fig. IV.1) with a converging-diverging Laval nozzle and stationary vanes at the inlet to induce swirling onto the axial flow. The Laval is followed by a liquid-collector and the ending diffuser. In the Laval the fluid expands accelerating to supersonic speeds accompanied by great temperature drop

liquefying condensable species. The flow is described by the Mach Number, $Ma=v/c$, where v is the axial flow velocity, and c represents the (multiphase) sound speed property. Flow starts subsonic ($Ma<1$) in the Laval converging section, becomes sonic ($Ma=1$) at the throat, and supersonic ($Ma>1$) in the Laval diverging section. Liquids formed in the Laval are centrifugally caught through lateral exits in the liquid-collector.

Supersonic flow is metastable with decreasing stability through the Laval diverging section, as the difference of SS outlet pressure to the supersonic pressure increases. Therefore, at some point, an irreversible normal shock adiabatic transition occurs, suddenly turning the supersonic flow into subsonic with higher entropy, pressure and temperature, while conserving mass, momentum and energy flow rates. For successful SS operation, the Laval condensate must be collected upstream the shock; otherwise the separation is lost re-vaporizing across the shock. After shock, the resulting subsonic flow decelerates through the ending diffuser, recovering (T,P) until SS exit. Fig. IV.1 illustrates SS axial velocity profile via color shading.

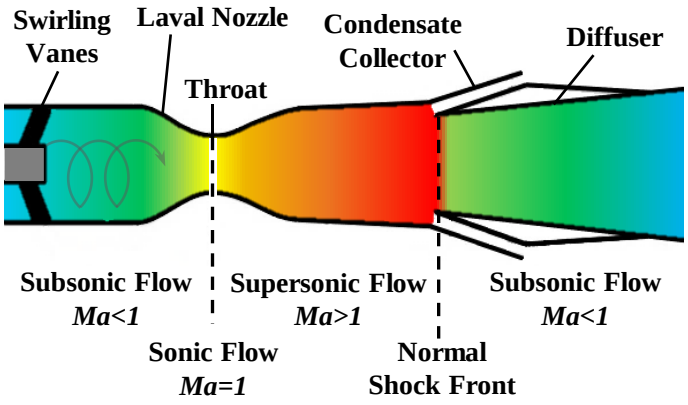

Figure IV. 1. SS sketch with axial velocity profile in color shading.

The SS shock is an irreversible transition, which always occurs if supersonic flow is attained and persists after condensate withdrawal. So, even for isentropic SS expansion/compression steps, it is impossible to recover the inlet pressure, resulting that P^{Outlet} is always lower than P^{Inlet}. SS head-loss increases, and the minimum achieved temperature decreases, with the increase of the maximum attained supersonic Ma, referred as Ma^{Shock} (Ma just before shock and condensate withdrawal). Then, condensate removal takes place promoting a fall of Ma at constant flow section to a lower supersonic Ma, referred as Ma_{BS} (Ma just before shock and *after* condensate withdrawal).

Two main research lines dictate current SS literature: the thermodynamic SS approach emblematically described in de Medeiros et al. (2019) and the computational fluid dynamic (CFD) frameworks used by Wen et al. (2012) and posteriorly, with a similar nozzle, by Yang et al.(2014). Arinelli et al. (2017) pointed out that CFD studies with condensing feeds cannot implement multicomponent vapor-liquid equilibrium (VLE), vapor-liquid-water equilibrium (VLWE), and multiphase sound speed on SS flow path. On the other hand, thermodynamic models rigorously address VLE, VLWE and multiphase *c*, despite the unlikelihood of full attainment of thermodynamic equilibrium during milliseconds of SS residence time. Nonetheless, thermodynamic approaches are more adequate than CFD for SS processing of raw NG feeds, since SS is represented in the thermodynamic limit, always obeying the Second Law of Thermodynamics. Meanwhile, CFD for SS with raw NG invariably achieves too cold pre-shock temperatures, adiabatically destroying entropy and violating the 2nd Law.

SS has been investigated for HCDPA of raw NG by Machado et al., 2012. Castier (2014) simulated the case of Machado et al. (2012) using a thermodynamic SS model. Arinelli et al. (2017) studied SS for WDPA+HCDPA of raw NG and Teixeira et al. (2018) explored an innovative process using SS to recover thermodynamic hydrate inhibitors from raw NG, simultaneously diminishing inhibitor losses and executing gas WDPA+HCDPA. Teixeira et al. (2019) showed that SS-methanol-recovery entails an economic leverage that affords a post-capture plant abating 43% of emitted CO_2; i.e., such SS processing is a cleaner gas production compared to the conventional counterpart. Brigagão et al. (2019) studied a new SS-based air pre-purification process, reducing the expensive adsorption load via SS air pre-dehydration.

Several studies addressed SS for CO_2 capture from CO_2-rich NG. As CO_2 condensation demands a much lower temperature, NG should be previously treated for WDPA+HCDPA avoiding water-C3+ condensation. Another issue is CO_2 freeze-out, which must be monitored to prevent SS plugging. In this regard, SS flow path must not cross the solid-vapor-liquid equilibrium (SVLE) CO_2 freeze-out boundary. This is achieved by stipulating a maximum Ma^{Shock} to keep temperature above the freeze-out point (de Medeiros et al., 2019). Sun et al. (2017) developed a SS CFD framework predicting CO_2 condensation from a high-pressure CH_4-CO_2 feed via nucleation and droplet-growth model. Despite attaining CO_2 capture from a CH_4-CO_2 stream with SS using CFD, this work has issues: (i) only feeds with CO_2 and an

"artificially" incondensable species (e.g., CH_4) can be treated by this two-fluid approach; (ii) consequently, only CO_2 condensation is contemplated, while reality prescribes non-negligible CH_4 condensation dissolved in liquid CO_2; (iii) VLE is constructed exclusively for CO_2 adopting Raoult's Law for dew-point calculation ignoring high-pressure, low-temperature and CH_4 condensation; (iv) the vapor-pressure formula ignores the inexorability of CO_2 triple-point (T_{TP}=*-56.6°C*, P_{TP}=*5.18 bar*) and predicts pure liquid CO_2 VLE for $T<T_{TP}$ and $P<P_{TP}$; (v) the sound speed property of a two-phase VLE CH_4-CO_2 stream is calculated using the ideal gas sound speed formula empirically corrected by inserting a gas-phase compressibility factor in the numerator under the square root (a wrong short-cut, which additionally ignores the liquid phase); and (vi) CO_2 freeze-out issues were ignored; for example, simulated temperature profiles attained very low values like -83°C and -93°C, well below freeze-out temperatures that range from -70°C to -60°C at such conditions (all below the T_{TP}, the freeze-out point of pure CO_2 VLE).

Arinelli et al. (2017) developed a thermodynamic SS model with rigorous multiphase compressible supersonic flow and created the unit operation extension SS-UOE for SS design/simulation in HYSYS environment. In SS-UOE the multiphase sound speed property *c* is calculated by another extension, PEC-UOE, from de Medeiros et al. (2017), considering all possible phase equilibria (single-phase gas, two-phase VLE or three-phase VLWE). SS-UOE was applied with CO_2-rich NG (44%mol CO_2) separately for WDPA+HCDPA and CO_2 abatement and compared to conventional technologies. For WDPA+HCDPA with SS, Arinelli et al. (2017) also modeled the LTX vessel for receiving SS cold condensates avoiding gas-hydrates. Results point SS as the best WDPA+HCDPA alternative, achieving better lean NG and lower power consumption. Single-stage MP attained the best CO_2 abatement with 15%mol CO_2 in the final NG, while SS CO_2 removal only attained 21.85%mol CO_2, barred by freeze-out issues. However, SS CO_2 removal produced a high-pressure CO_2-rich EOR fluid requiring 30% less power for injection.

IV.1.2. The Present Work

Machado et al. (2012) was the first work economically evaluating SS-based HCDPA of raw NG, yet with negligible water and CO_2 contents. Later, considering CO_2-rich NG in offshore rigs, Arinelli et al. (2017) technically investigated SS for WDPA+HCDPA complemented by

MP for CO_2 removal – the SS-MP alternative – and also showed that SS can abate CO_2 from 44%mol to ≈22%mol for a feed previously treated with conventional WDPA+HCDPA. However, Arinelli et al. (2017) left untouched a possible third configuration for treating CO_2-rich NG with 44%mol CO_2 in offshore rigs; namely, two consecutive SS units (SS-SS alternative), the 1st SS unit for WDPA+HCDPA and the 2nd SS unit for CO_2 removal. To inventory the gains of SS-SS and SS-MP relatively to conventional CO_2-rich NG processing, full economic and environmental assessments are necessary, a subject still lacking in SS literature.

Using the CO_2-rich NG of Arinelli et al. (2017), the objective of this work is to conduct a full analysis, inexistent in SS literature, comprising technical, economic and carbon-emission assessments of SS-MP, SS-SS and conventional gas processing alternatives in offshore rigs. It shows that SS implementation can bring economic and environmental benefits giving rise to a new, cleaner and more lucrative NG production chain from raw CO_2-rich NG.

IV.2. Methods

Methods for implementation of simulation of processes and SS units are discussed in the following sub-sections.

IV.2.1. SS Modeling for NG processing

SS-UOE from Arinelli et al. (2017), PEC-UOE from de Medeiros et al. (2017) and MP-UOE from Arinelli et al. (2017) are used in this work for SS and MP simulations with HYSYS. MP-UOE simulates a MP stage using log-mean partial-pressure differences and component permeances calibrated with field data, offering options of counter-current/parallel contacts and hollow-fiber/spiral-wound membranes. SS-UOE, MP-UOE and PEC-UOE run with any equation-of-state available in HYSYS. SS-UOE designs SS matching sonic throat flow and executing supersonic expansion, condensate withdrawal, shock transition and diffuser compression. *Ma* calculation is guaranteed by correct determination of multiphase sound speed (*c*) with PEC-UOE. SS-UOE designs SS with linear diameter profiles (Fig. IV.2), but any diameter profile (with/without cylindrical sections) can be used. SS-UOE specifications comprise: (i) feed data at stagnation conditions (*T*, *P*, flow rate, composition) retrieved from HYSYS flowsheet; (ii) number of parallel SS's; (iii) SS inlet/outlet diameters (D_I,D_O); (iv) SS

converging/diverging angles (α,β); (v) adiabatic expansion/compression efficiencies (η^{EXP}%,η^{CMP}%); and (vi) Ma^{Shock}. SS-UOE calculates (Fig. IV.2) throat diameter (D_T), converging/diverging lengths (L_C, L_D), SS head-loss, and exports lean gas and condensate product streams to HYSYS flowsheet at stagnation. SS-UOE was validated in Brigagão et al. (2019) and in de Medeiros et al. (2019); the latter discusses CO_2-rich NG processing, SS thermodynamics, multiphase sound speed, CO_2 freeze-out, and SS applications and comparisons with conventional processing.

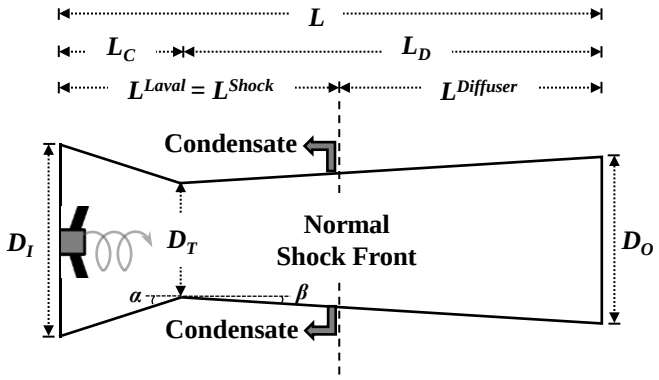

Figure IV. 2. SS geometric parameters for linear diameter profiles.

IV.2.2. Process Assumptions and Economic Parameters

Three CO_2-rich NG processing alternatives are considered: (i) Case 1, the conventional CO_2-rich NG processing comprising TEG absorption WDPA, JTE HCDPA and MP CO_2 removal; (ii) Case 2, the SS-MP alternative prescribing SS for WDPA+HCDPA and MP for CO_2 removal; and (iii) Case 3, the SS-SS alternative with 1st SS unit for WDPA+HCDPA and 2nd SS unit for CO_2 removal. The feed consists of 12 MMsm³/d of water-saturated NG with ≈44%mol CO_2, obtained after water/gas/oil separation on an offshore rig. Treated NG product should have ≈20%mol CO_2 to be eligible as fuel-gas (FG) for power generation at the rig and at other facilities. The CO_2-rich stream (%CO_2 ≥75%) extracted from NG is compressed and injected as EOR-Fluid. Table IV.1 lists feed data and other assumptions for process simulation and design, while Table IV.2 depicts economic assumptions for process evaluation. Simulation and design parameters were selected within the common operational range of equipment in NG processing (Kidnay and Parrish, 2006).

Power and utilities consumptions, and stream data are obtained via HYSYS simulation. CO_2 emissions are calculated from fuel-gas demand, equipment sized, and economic evaluation is accomplished via module costing technique (Turton et al., 2009), with economic relationships in the Supplementary Materials (Appendix K). Fixed capital investment (*FCI*, MMUSD), cost of manufacturing (*COM*, MMUSD/y), revenues (*REV*, MMUSD/y), cost of raw materials (*CRM*, MMUSD/y), gross annualized profit (*GAP*, MMUSD/y), depreciation (*DEPR*, MMUSD/y), annualized profit (*AP*, MMUSD/y), and net present value (*NPV*, MMUSD) for 20 years of operation are obtained for each alternative. Finally, the results of SS-MP, SS-SS and conventional process are discussed contemplating technical, environmental and economic aspects.

Table IV. 1. Assumptions: process simulation and design.

Item	*Subject*	*Description*
{A1}	*Process Modeling*	*Simulation: HYSYS 8.8;* *Thermodynamic Package: HYSYS PR-EOS; Glycol Package (TEG Unit);* *Pure-Water: HYSYS Steam-Table;* *MP: MP-UOE (Arinelli et al., 2017);* *SS: SS-UOE (Arinelli et al., 2017);* *Phase-Equilibrium c (Sound Speed): PEC-UOE (de Medeiros et al., 2017).*
{A2}	*Raw NG*	*$F=12\ MMSm^3/d$; $T=40^oC$; $P=25$ bar;* *%mol: CO_2=43.8%, CH_4=49.8%, C_2H_6=2.99%, C_3H_8=1.99%, C_4H_{10}=0.3%, C_5H_{12}=0.2%, C_6H_{14}=0.2%, C_7H_{16}=0.1%,C_8H_{18}=0.1%, C_9H_{20}=0.05%, $C_{10}H_{22}$=0.03%,H_2O=0.3623% (3623 ppm-mol).*
{A3}	*Conventional WDPA, HCDPA*	*Lean TEG=98.5%w/w; $P^{Absorber}=65$ bar; $P^{Regenerator}=1$ bar;* *TEG Flow Rate: Sufficient for Dry NG with $H_2O \leq 50$ ppm-mol;* *TEG Make-up: TEG losses from absorption and regeneration;* *JTE: ΔP^{JTE} for HCDP $\leq 0°C$@45 bar.*
{A4}	*MP*	*Single-Stage, Counter-Current, Spiral-Wound; $\Delta P^{Retentate}=1$ bar; $P^{Permeate}=4$ bar.*
{A5}	*SS*	*1st SS Unit (WDPA+HCDPA): $D_I=0.15$ m, $D_O=0.12$ m, $\alpha=12.67^o$, $\beta=2.66^o$, $\eta^{EXP}=\eta^{CMP}=100\%$, $Ma^{Shock}=1.344$;* *2nd SS Unit (CO_2 Removal): $D_I=0.15$ m, $D_O=0.12$ m, $\alpha=12.67^o$, $\beta=2.66^o$, $\eta^{EXP}=\eta^{CMP}=100\%$, $Ma^{Shock}=1.586$;*
{A6}	*Exported NG*	*$P=200$ bar; $CH_4 \geq 70\%$mol; $CO_2 \leq 20\%$mol; $H_2O \leq 50$ppm-mol.*
{A7}	*EOR-Fluid*	*$P=450$ bar; $CO_2 \geq 75\%$mol; $H_2O \leq 150$ppm-mol.*
{A8}	*NGL*	*Recycled to water-gas-oil separator upstream the gas processing (not in the scope).*
{A9}	*Heat Exchangers*	*$\Delta P^{SHELL}=0.5$ bar; $\Delta P^{TUBES}=0.5$ bar; $\Delta T^{APPROACH}=5^oC$;* *Intercoolers: $T^{GAS}=35°C$.*
{A10}	*Compressors, Pumps*	*Adiabatic efficiency: $\eta=75\%$;* *Driver: Electric.*
{A11}	*Vessels*	*$P^{DESIGN}=1.15*P^{OPERATION}$ (rounded up to 10 multiple)*
{A12}	*Hot Utility*	*PHW: $T \in [210°C,100^oC]$; $P=20$ bar.*
{A13}	*Cold Utility*	*CW: $T \in [30°C,55°C]$; $P=4$ bar.*
{A14}	*Gas-Turbines*	*FG: $CO_2 \leq 20\%$mol;* *FG Power-Ratio=161.4 $MW/MMSm^3d$ (Araújo et al., 2017);* *Number of 28MW Gas-Turbines: Ceil(Total Power/28 MW)+1.*
{A15}	*WHRUs*	*PHW Load:$75MW^{PHW}/100MW^{Power}$ (Araújo et al., 2017).*

Table IV. 2. Economic assumptions.

Item	*Subject*	*Description*
{E1}	*FCI (USD) Onshore Conditions*	*$FCI=FCI^{REF}*(Capacity÷Capacity^{REF})^{0.6}$ (Turton et al., 2009);* *$FCI^{SS}=FCI^{SS\text{-}REF}*(MMSm^3/d÷6)^{0.6}$, $FCI^{SS\text{-}REF}$@6MMSm³/d (Machado et al., 2012);* *$FCI^{LTX}=FCI^{LTX\text{-}REF}*(MMSm^3/d÷6)^{0.6}$, $FCI^{LTX\text{-}REF}$@6MMSm³/d (Machado et al., 2012);* *$FCI^{MP}=(500USD/m^2)*Area^{MP}(m^2)$ (Merkel et al., 2012);* *$FCI^{TEG}=1.2*(Volume^{Vessels}+0.16*Volume^{Columns})*(3000USD/m^3)$.*
{E2}	*FCI (USD) Offhore Conditions*	*$FCI^{OFFSHORE}=2.2*FCI^{ONSHORE}$.*
{E3}	*COM (USD/y)*	*CUT=FG(MMBTU/y)*(3.2USD/MMBTU).* *Costless Thermal Utilities CW, PHW;* *$CRM^{TEG}=TEG^{MAKE\text{-}UP}(m^3/y)*(3000USD/m^3)$;* *$CRM^{MP}=0.2*(200USD/y/m^2)*Area^{MP}(m^2)$ (Merkel et al., 2012);* *Taxation of Carbon Emitted: 65 USD/ton (Nguyen et al., 2016).*
{E4}	*REV (USD/y)*	*FG + NG Exportation: 3.2 USD/MMBTU.* *EOR-Fluid: 60 USD/ton (1 bbl^{OIL}/$ton^{EOR\text{-}FLUID}$) (McCoy, 2008).* *Oil: 60 USD/bbl.*
{E5}	*Economic Parameters*	*Horizon=20 years (invariant feed and conditions);* *Construction: 3 years, with 20%/30%/50% investment allocation;* *Annual Interest Rate: i=10%; Income Tax Rate: ITR=34%;* *DEPR (USD/y)=10%FCI (USD);* *Operation=8000 h/y; Working-Capital (USD)=5%FCI (USD);* *CEPCI=550.3 (Sept, 2015).*

IV.2.3. CO_2-Rich NG Processing Alternatives: Cases 1, 2 and 3

In the conventional process Case 1 (Fig. IV.3a) the water-saturated gas feed is first compressed to *P=65 bar* and then admitted at *$T=35^oC$* at the bottom of the absorber column with TEG in counter-current flow. The bottom rich solvent follows to the regeneration column at atmospheric pressure and *$T=140^oC$*, with stripping dry NG injected into the reboiler. The dry NG leaving the top of the absorber is cooled and expanded in the JTE unit to *P=48 bar* reaching *$T=0^oC$*, where the NGL is separated and recycled to the upstream three-phase oil/gas/water primary separator (not shown). Lean NG is heated to *$T=50^oC$* – to keep *$T>T^{HCDP}$* during permeation – and sent to MP unit for CO_2 removal. The low-pressure CO_2-rich MP permeate passes through a three-stage intercooled compressor train and an EOR pump becoming the EOR-Fluid at *P=450 bar*. The high-pressure MP retentate is the final treated NG. A part of it is segregated as FG for power production in the rig; the rest is compressed to *P=200 bar* for exportation.

SS-MP Case 2 (Fig. IV.3b) derives from Case 1 via substitution of TEG absorption and JTE by SS for WDPA+HCDPA. The water-saturated raw NG is compressed to *P=50 bar* and feeds 1st SS unit. The two-phase water-C3+ condensate from SS goes to the anti-hydrate LTX separator, whose bottom is kept at $T=20^oC$ to prevent downstream gas-hydrates. A small slip-gas stream leaves the top of LTX after direct-contact with cold water-C3+ condensate. The slip-gas (if any) joins the lean gas from SS, while the water-C3+ LTX bottoms ($T=20^oC$) are recycled to the upstream oil/gas/water separator (not shown). SS lean NG is heated to $T=50^oC$ and feeds the same block of Case 1 responsible by MP CO_2 capture, MP permeate compression, FG segregation from MP retentate and final NG compression for exportation.

SS-SS Case 3 (Fig. IV.3c) derives from Case 2 through replacement of MP by 2nd SS unit for CO_2 capture, while 1st SS unit for WDPA+HCDPA is the same of Case 2. The lean NG from 1st SS unit is compressed to *P=80 bar* and refrigerated to $T=-21.1^oC$ to allow CO_2 condensation in 2nd SS unit. The 2nd SS unit products – cold decarbonated NG ($T=-26.82^oC$, *P=36.57 bar*) and CO_2-rich condensate ($T=-46.73^oC$, *P=36.57 bar*) in Table IV.3 – provide refrigeration for the SS inlet. FG is segregated from SS decarbonated gas and the rest is compressed for exportation as final NG. The SS CO_2-rich condensate is partially vaporized after cooling down the SS feed. Thus, it is flashed, and the effluent vapor and liquid parts are respectively compressed and pumped to be united as liquids at the suction of the EOR pump.

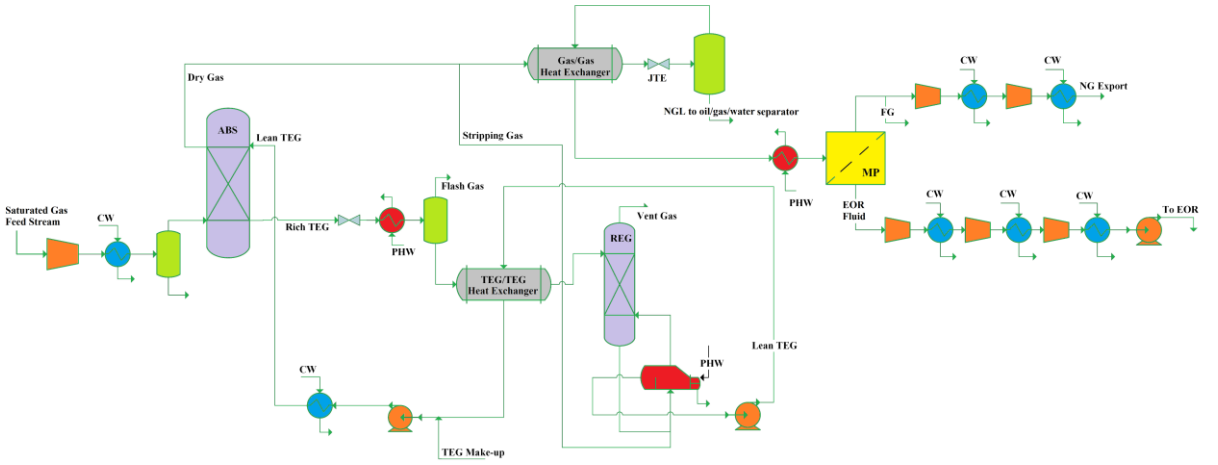

a)

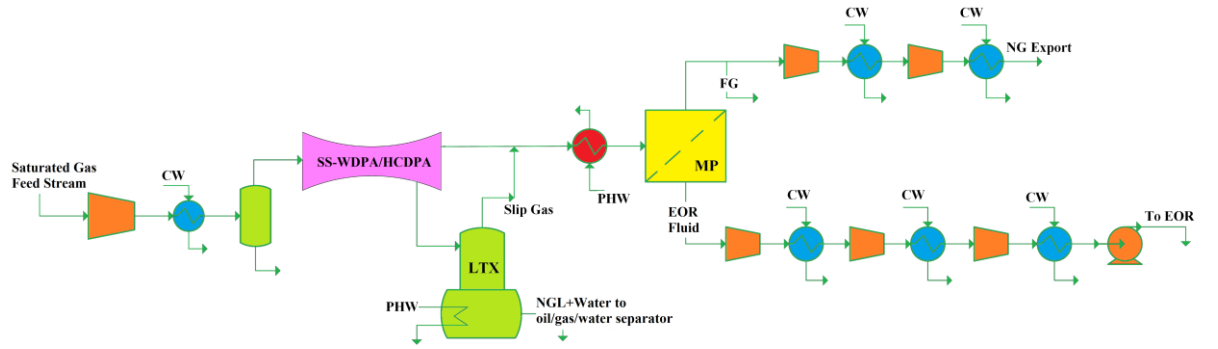

b)

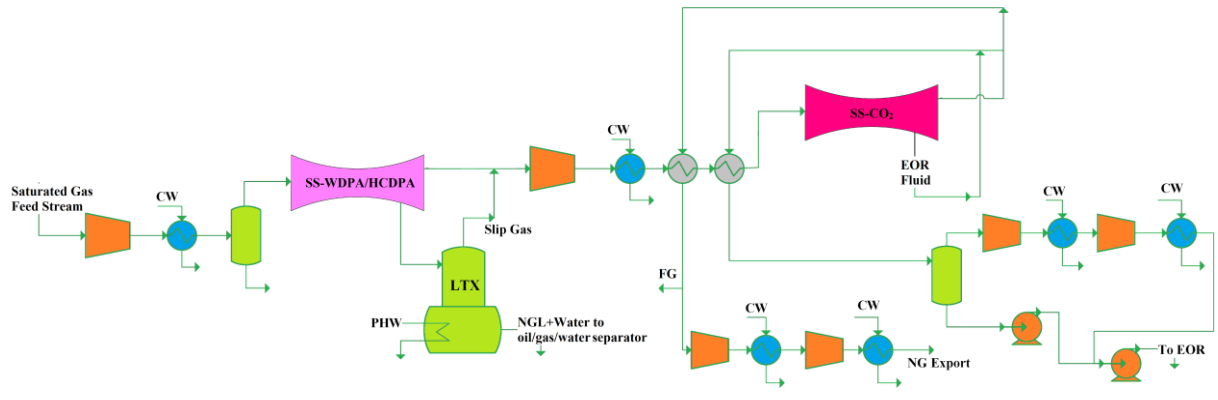

c)

Figure IV. 3. Process alternatives: a) Case 1 TEG absorption, JTE and MP; b) Case 2 SS-MP; and c) Case 3 SS-SS.

IV.3. Results and Discussion

Table IV.3 shows specifications and simulation results for 1st SS unit (WDPA+HCDPA) and 2nd SS unit (CO_2 removal), both with same design specifications, except for $Ma^{Shock}=1.344$ and $Ma^{Shock}=1.586$, respectively. $Ma^{Shock}=1.344$ in 1st SS unit gives less than 50 ppm-mol H_2O in dry NG (Assumption *{A6}*, Table IV.1) and an excellent pressure recovery of 95%. In 2nd SS unit, Ma^{Shock} is limited to $Ma^{Shock}=1.586$ to avoid crossing the SVLE CO_2 freeze-out boundary, resulting a final NG with ≈22%mol CO_2 and 46% of pressure recovery. Despite the similar specifications, the feeds of 1st and 2nd SS units are very distinct, leading to rather different SS results. The 2nd SS unit produces condensate with ≈80%mol CO_2 prescribing longer SS nozzles with smaller throat, higher pressures and lower temperatures than the 1st SS unit for WDPA+HCDPA, which produces water-C3+ two-phase condensate. The condensed fraction of 2nd SS unit (≈40%mol) is substantially larger than the counterpart of 1st SS unit (≈1%mol). This explains the high CO_2 recovery of 2nd SS unit and also its lower pressure recovery, since a large parcel of the SS flow is deviated as condensate. The great liquid withdrawal of 2nd SS unit promotes *Ma* reduction at constant flow section to $Ma_{BS}=0.94$, implying absence of shock transition.

In Table IV.3, different (*T*,*P*) states are observed for 1st and 2nd SS units. Since HYSYS process streams are meant to be quasi-stagnated fluids at the given flow rates (i.e., with negligible molar kinetic energy, $\bar{K} \approx 0$), when the feed material accesses a SS nozzle inlet it is not stagnated anymore, and a new (*T*,*P*) state (possibly multiphase) has to be calculated using two equations accounting for conservation of molar entropy ($\bar{S}$) and conservation of molar total flow energy ($\bar{H}+\bar{K}$) subject to the SS inlet section area (i.e., assuming adiabatic reversible transition from the stagnated flowsheet state to SS inlet). Therefore, (T^{Feed},P^{Feed}) refers to the stagnated feed in HYSYS flowsheet with properties $\bar{S}^{Feed}$, $\bar{K}^{Feed} \approx 0$, $\bar{H}^{Feed}$; while (T^{Inlet},P^{Inlet}) refers to SS inlet satisfying $\bar{K}(T^{Inlet},P^{Inlet})+\bar{H}(T^{Inlet},P^{Inlet})=\bar{H}^{Feed}+\bar{K}^{Feed}$ and $\bar{S}(T^{Inlet},P^{Inlet})=\bar{S}^{Feed}$. This procedure connects two states of a stream through a reversible adiabatic transition for calculating (*T*,*P*) of one of them conserving $\bar{K}+\bar{H}$ and $\bar{S}$. It is henceforth denominated KHS-bridge. KHS-bridges represent reversible and adiabatic expansion/compression transitions along a continuous transformation of flow section area subject to constant flow rate and

composition (the entire Laval expansion and ending diffuser compression are also KHS-bridges when $\eta^{EXP}\%=\eta^{CMP}\%=100\%$). Analogously, there is a KHS-bridge connecting the SS outlet state (T^{Outlet},P^{Outlet}) to the stagnated gas product state ($T^{GasProduct}$, $P^{GasProduct}$) in HYSYS flowsheet. Additionally, (T^{Laval},P^{Laval},Ma^{Shock}) refers to the multiphase-equilibrium fluid state at the Laval end before condensate withdrawal, where $Ma=Ma^{Shock}$. In this context, (T_{BS},P_{BS},Ma_{BS}) refers to the single-phase vapor state just after such condensate withdrawal, where $Ma=Ma_{BS}$. The state (T_{BS},P_{BS},Ma_{BS}) corresponds to the reversible adiabatic expansion at constant flow section of the vapor phase at Laval end while condensate is removed. Hence, it is connected via a KHS-bridge at constant flow section to the vapor flow only (i.e., not counting the condensate) at (T^{Laval},P^{Laval},Ma^{Shock}). Ma_{BS} determines whether the shock transition occurs ($Ma_{BS}>1$) or not ($Ma_{BS}\leq 1$). Finally, the stagnated liquid product state ($T^{LiqProduct}$,$P^{LiqProduct}$) is calculated via an irreversible stagnation at gas product pressure conserving only $\bar{H}+\bar{K}$ of the condensate at (T^{Laval},P^{Laval},Ma^{Shock}); i.e., friction stagnates the supersonic liquid at Laval end in order to attain $P^{LiqProduct}=P^{GasProduct}$ at LTX inlet, a transition accompanied by some creation of entropy.

Table IV. 3. Specifications and design of 1st SS unit (Cases 2 and 3) and 2nd SS unit (Case 3).

Specified Items	*SS WDPA HCDPA*	*SS CO_2 Removal*	*Calculated by SS-UOE*	*SS WDPA HCDPA*	*SS CO_2 Removal*
No.of SS	*3*	*3*	*$D_T(m)$*	*0.0772*	*0.0503*
$D_I(m)$	*0.15*	*0.15*	*$L_C(m)$*	*0.1619*	*0.2218*
$D_O(m)$	*0.12*	*0.12*	*$L_D(m)$*	*0.4606*	*0.7507*
$\alpha(^o)$	*12.67*	*12.67*	*L(m)*	*0.6225*	*0.9725*
$\beta(^o)$	*2.66*	*2.66*	*$L^{Shock}=L^{Laval}(m)$*	*0.2*	*0.3466*
Ma^{Shock}	*1.344*	*1.586*	*$L^{Diff}(m)$*	*0.4226*	*0.6259*
$\eta^{EXP}\%$	*100*	*100*	*$P^{Laval}(bar)$*	*18.43*	*21.46*
$\eta^{CMP}\%$	*100*	*100*	*$T^{Laval}(^oC)$*	*-27.96*	*-60.11*
$P^{Feed}(bar)$	*50.0*	*80.0*	*$P_{BS}(bar)$*	*18.39*	*24.88*
$T^{Feed}(^oC)$	*35.00*	*-21.10*	*$T_{BS}(^oC)$*	*-28.11*	*-51.30*
Feed $MMsm^3/d$	*12.02*	*11.90*	*Ma_{BS}*	*1.304**	*0.787*+*
Feed $\%C3^+$	*2.99%*	*2.51%*	*$P^{Outlet}(bar)$*	*45.42*	*36.04*
Feed $ppmH_2O$	*1784*	*43.02*	*$T^{Outlet}(^oC)$*	*34.63*	*-27.80*
Feed $\%CO_2$	*43.92%*	*44.14%*	*$P^{GasProduct}(bar)$*	*47.48*	*36.57*
$P^{Inlet}(bar)$	*49.23*	*79.86*	*$T^{GasProduct}(^oC)$*	*37.95*	*-26.82*
$T^{Inlet}(^oC)$	*33.91*	*-21.16*	*$P^{LiqProduct}(bar)$*	*47.48*	*36.57*
			$T^{LiqProduct}(^oC)$	*1.00*	*-46.73*
			%P Recovery	*94.96%*	*45.71%*
			%Condensate	*1.02%#*	*39.81%$*
			REC%H_2O	*97.61%*	*99.93%*
			REC%$C3^+$	*17.03%*	*85.14%*
			REC%CO_2	*0.54%*	*69.70%*

**After condensate withdrawal. #Total Condensate (60%molHC +17%molH_2O +23%molCO_2).*
+No normal shock.
$Total Condensate (23%molHC +0%molH_2O +77%molCO_2)

IV.3.1. Graphical Results for 1st SS Unit: Cases 2 and 3

Fig. IV.4 depicts operation of a nozzle of 1st SS unit (WDPA+HCDPA). Several SS axial profiles are depicted versus axial coordinate *x(m)*. Fig. IV.4a shows SS silhouette and molar vapor-fraction profiles. The fluid at SS inlet is almost 100%mol vapor since minuscule condensation occurs through the first KHS-bridge to the SS inlet. Vapor-fraction achieves its minimum 98.98%mol at *x=0.2 m* (at $Ma=Ma^{Shock}$) where liquids are collected and only gas remains until the SS exit. Fig. IV.4b depicts *P(bar)* and *Ma* profiles, while *T(K)* and *c(m/s)* profiles follow in Fig. IV.4c. All profiles exhibit the expected SS signatures – throat $\pm\infty$ spatial

gradient singularities – as discussed in de Medeiros et al. (2017; 2019) when $\left(\frac{dA}{dx}\right)^{Throat} \neq 0$, a geometric characteristic of SS nozzles in Figs. IV.1 and IV.2.

Fig. IV.4d shows SS %mol condensations and Fig. IV.4f depicts SS flow path on plane *PxT*, including feed WDP curve, and feed and product VLE envelopes. As SS flow path starts at the feed WDP, water starts condensing at SS inlet, corroborated in Fig. IV.4d, while $C3^+$ condenses later. Fig. IV.4c shows a sudden small fall of sound speed from *c=296 m/s* to *c=294 m/s* at *x=0.13 m*. This is a fingerprint of C3+ initiating condensation (Fig. IV.4d), as SS path crosses the feed HCDP (Fig. IV.4f). The maximum *Ma* achieved is $Ma^{Shock}=1.344$ at $x=L^{Laval}=0.2$ *m*, where ($T^{Laval}=-27.96^oC$, $P^{Laval}=18.43$ *bar*). After condensate withdrawal, *Ma* falls to $Ma=Ma_{BS}=1.304$ where ($T=T_{BS}=-28.11^oC$, $P=P_{BS}=18.39$ *bar*). This is theoretically the best point for shock transition, which occurs turning the flow into subsonic with *Ma=0.78*, $T=10.73^oC$ and *P=32.65 bar*, represented by vertical paths in Figs. IV.4a/IV.4b/IV.4c. In Fig. IV.4f the shock corresponds to the rectilinear jump back to higher (*T,P*) from the point where SS expansion path ends touching the lean gas HCDP curve. Fig. IV.4f also traces the CO_2 SVLE freeze-out boundary, which is much colder than the condensate withdrawal point, as water-C3+ condensation blocks deeper temperature drops. Fig. IV.4e shows the influence of Ma^{Shock} on Ma_{BS}, on the minimum molar vapor-fraction before withdrawal, and on lean gas *%mol* CO_2. It unveils that Ma_{BS} rises with Ma^{Shock}, while Ma^{Shock} has low influence on the minimum vapor-fraction and final %mol CO_2 in 1st SS unit. Fig. IV.4e also reports the necessary $Ma^{Shock}=1.85$ for freeze-out; i.e., where SS path hits the freeze-out boundary in Fig. IV.4f. As 1st SS unit is designed with $Ma^{Shock}=1.344$, there is no risk of dry-ice precipitation. After shock transition, lean gas flows sub-sonically through the ending diffuser, recovering (*T,P*) until ($T^{Outlet}=34.63^oC$, $P^{Outlet}=45.42$ *bar*). The final KHS-bridge delivers the stagnated lean gas to the flowsheet at ($T^{GasProduct}=37.95^oC$, $P^{GasProduct}=47.48$ *bar*).

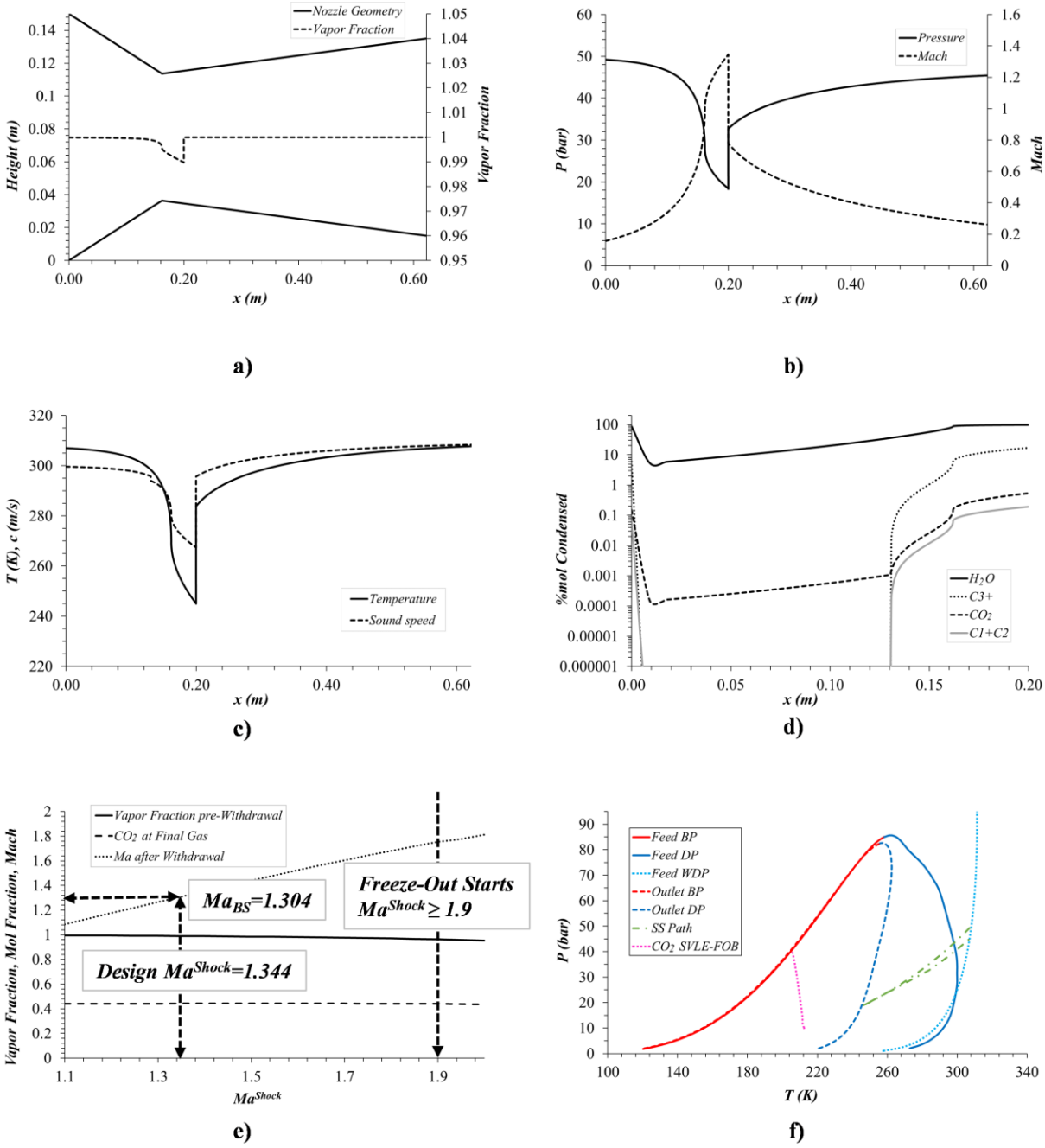

Figure IV. 4. Results for 1st SS unit (WDPA+HCDPA): a) SS silhouette and vapor-fraction vs *x(m)*; b) *P(bar)* and *Ma* vs *x(m)*; c) *T(K)* and *c(m/s)* vs *x(m)*; d) %mol condensed C1+C2, C3+, CO_2 and H_2O vs *x(m)*; e) Ma_{BS}, pre-shock vapor-fraction and lean gas CO_2 content vs Ma^{Shock} with CO_2 freeze-out limit; f) plane *PxT* with SS path, feed WDP locus, feed VLE envelope, feed SVLE freeze-out border and lean gas VLE envelope (slenderer).

IV.3.2. Graphical Results for 2st SS Unit: Case 3

Fig. IV.5 is the analogue of Fig. IV.4 for 2nd SS unit (CO_2 removal), with same SS profiles versus axial coordinate *x(m)*. Fig. IV.5a shows SS silhouette and molar vapor-fraction profiles. After the first KHS-bridge, the fluid at SS inlet is 72%mol liquid. Almost all water (traces), 81%mol of $C3^+$, 65%mol of CO_2 and 30%mol of C1+C2 condensed (Fig. IV.5d). Vapor-fraction increases from 28%mol until 60%mol at *x=0.35 m*, where liquids are collected. Through SS expansion C1+C2 components re-vaporize from the condensate; only 13%mol are left as liquid. Meanwhile, the recoveries of CO_2, $C3^+$ and water attain 70%, 85%mol and almost 100%, respectively (Table IV.3, Fig. IV.5d). Fig. IV.5b depicts *P(bar)* and *Ma* profiles, while Fig. IV.5c traces *T(K)* and *c(m/s)* profiles. Analogously to 1st SS unit, all profiles of 2nd SS unit exhibit SS signatures (throat $\pm\infty$ spatial gradient singularities). However, here the sound speed signature is positive, $(dc/dx)^{Throat} = +\infty$, the opposite of what happens in 1st SS unit. This behavior is explained in de Medeiros et al. (2019): when multiphase compressible flow is dominated by gas, *c* signature is negative because $(\partial c/\partial T)_{P,\underline{Z}} > 0$, $(\partial c/\partial P)_{T,\underline{Z}} < 0$, $|(\partial c/\partial T)_{P,\underline{Z}}| >> |(\partial c/\partial P)_{T,\underline{Z}}|$, while for liquid-dominated and highly compressible flow (the case of 2nd SS unit) the signature is positive because $(\partial c/\partial T)_{P,\underline{Z}} < 0$, $(\partial c/\partial P)_{T,\underline{Z}} > 0$, $|(\partial c/\partial T)_{P,\underline{Z}}| > |(\partial c/\partial P)_{T,\underline{Z}}|$. Fig. IV.5c shows *c* profile initiating at *c=118 m/s*, a low value characteristic of dense fluids with high isothermal compressibility $\Xi_P = \left(\frac{\partial \rho}{\partial P}\right)_{T,\underline{Z}}$. Along SS flow path, *c* reaches a minimum *c=92 m/s* at $x \approx 0.15$ *m* and then increases slowly, passing the throat at *x=0.2218 m* with $(dc/dx)^{Throat} = +\infty$. At the Laval end $x = L^{Laval} = 0.3466$ *m*, there is a sudden rise of *c* accompanying the withdrawal of ≈40%mol of liquid, turning the fluid into a gas ($T = T_{BS} = -51.3^oC$, $P = P_{BS} = 24.88$ *bar*) with *c=293 m/s*. At this point, $Ma = Ma_{BS} = 0.787$, so the flow is subsonic and there is no shock transition. From this point onwards, (*T,P*) and *c* increase slowly through the diffuser.

Fig. IV.5f depicts SS flow path on plane *PxT*, with feed and product VLE envelopes. After the first KHS-bridge, the fluid at SS inlet is two-phase, 28%mol vapor, discreetly inside the feed VLE envelope just beneath the bubble-point locus. The maximum *Ma* achieved is $Ma^{Shock} = 1.586$, where $T = T^{Laval} = -60.11^oC$ and $P = P^{Laval} = 21.46$ *bar*. At this point, SS flow path touches the decarbonated gas HCDP curve (Fig. IV.5f), just above the CO_2 SVLE freeze-out

border. After condensate withdrawal, $Ma_{BS}=0.787$, $T_{BS}=-51.3^{o}C$ and $P_{BS}=24.88\ bar$. Thus, there is no shock transition; the fluid just flows through the diffuser to the outlet, drawn in Fig. IV.5f as the last monotonous branch in SS path to ($T^{Outlet}=-27.80^{o}C$, $P^{Outlet}=36.04\ bar$).

Fig. IV.5e is analogue to Fig. IV.4e, depicting Ma^{Shock} influence on Ma_{BS}, on molar vapor-fraction at Laval end, and on CO_2 content of decarbonated final gas. The CO_2 freeze-out boundary is located in 2nd SS unit at $Ma^{Shock}=1.6$, representing risks of dry-ice, if crossed. Hence, the design choses $Ma^{Shock}=1.586$, stopping SS expansion a little bit from entering dry-ice zone, limiting CO_2 content of decarbonated gas to 22%mol and losing 13%mol of all C1+C2 to the condensate. Fig. IV.5e also shows that the withdrawal of high proportion of condensate turns Ma_{BS} into subsonic (indeed, a little deeper expansion would keep Ma_{BS} supersonic) and much lower than Ma^{Shock}, impacting negatively on SS pressure recovery.

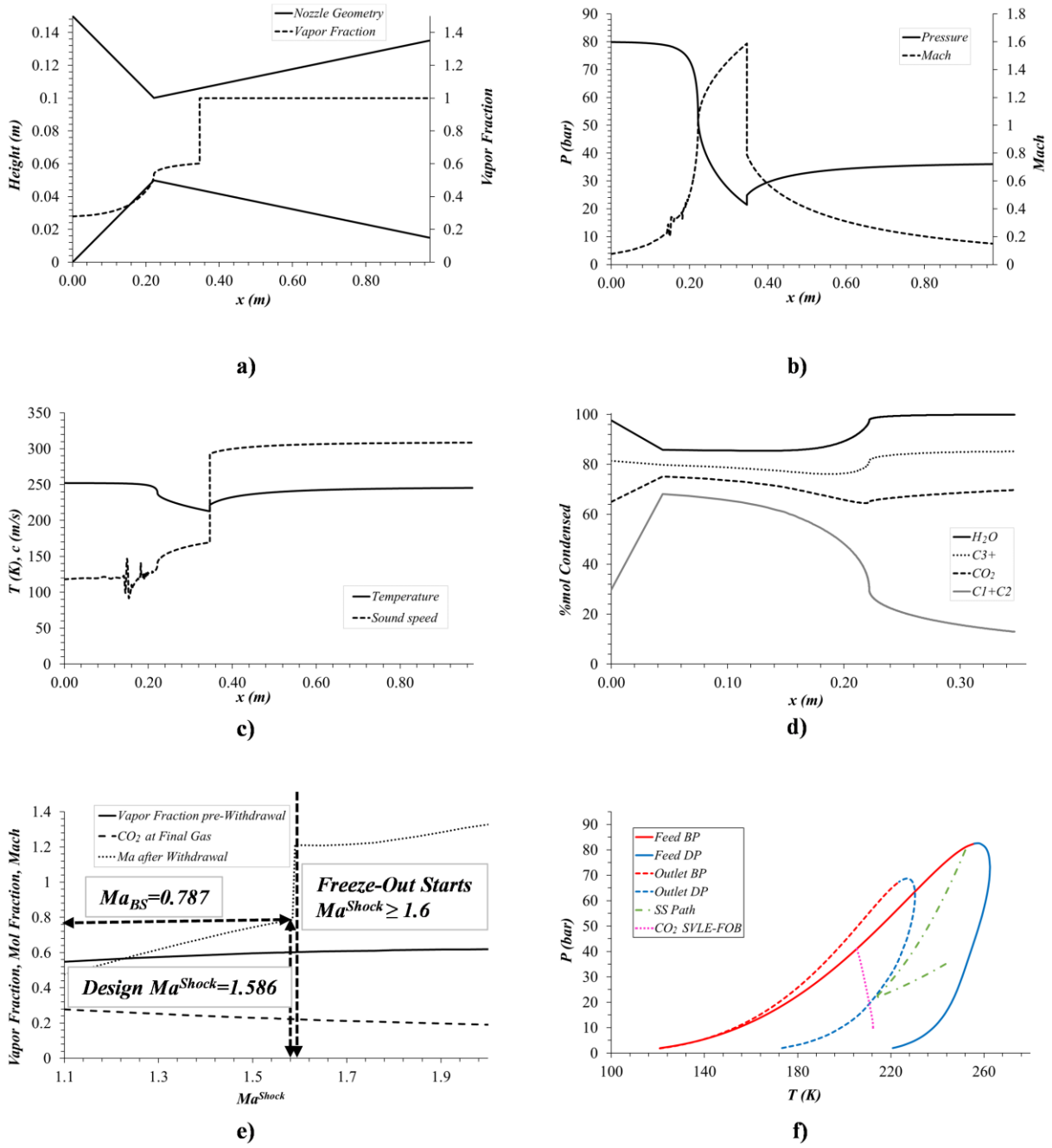

Figure IV. 5. Results of 2nd SS unit (CO_2 removal): a) SS silhouette and vapor-fraction vs *x(m)*; b) *P(bar)* and *Ma* vs *x(m)*; c) *T(K)* and *c(m/s)* vs *x(m)*; d) %mol condensed C1+C2, C3+, CO_2 and H_2O vs *x(m)*; e) Ma_{BS}, Laval end vapor-fraction and final gas CO_2 content vs Ma^{Shock} with CO_2 freeze-out limit; f) plane *PxT* with SS path, feed VLE envelope, feed SVLE freeze-out border and lean gas VLE envelope (slenderer).

IV.3.3. Technical, Environmental and Economic Analyses of Processing Alternatives

Table IV.4 exhibits final NG and EOR-Fluid results before compression for export and injection, respectively. Comparing the final NG of Cases 1 and 2 – with different WDPA+HCDPA and same MP CO_2 removal – 1st SS unit of Case 2 attains a higher C3+ extraction for same dehydration level (≈20ppm-mol H_2O), expressed in Table IV.4 as lower $C3^+$ content in final NG. In Case 3, with two consecutive SS units, this effect is more prominent, since there are additional traces of water-$C3^+$ condensation along with CO_2 in 2nd SS unit, attaining even lower $C2^+$ and water contents in final NG. In this case, water-C3+ contents in EOR-Fluid are slightly higher relatively to Cases 1 and 2; but insufficient to create injection issues. The CO_2 removal in Case 3 is limited due to CO_2 freeze-out proximity attained in 2nd SS unit, giving a final NG with 22%mol CO_2. Albeit being a little higher than the final CO_2 content in Cases 1 and 2 (20%mol), the final NG from 2nd SS unit implies great CO_2 capture of 69.70% (Table IV.3).

Table IV. 4. Final NG and EOR-Fluid before compression (*%mol* compositions).

Stream	***Final NG***			***EOR-Fluid***		
Case	***1***	***2***	***3***	***1***	***2***	***3***
T(°C)	*38.6*	*38.4*	*25.0*	*35.6*	*35.4*	*-3.0*
P(bar)	*46.0*	*46.0*	*36.1*	*4.0*	*4.0*	*36.1*
MMSm³/d	*6.50*	*6.42*	*6.59*	*4.68*	*4.73*	*4.74*
%CO_2	*20.1*	*19.9*	*22.2*	*81.0*	*80.8*	*77.3*
%CH_4	*70.3*	*71.0*	*74.7*	*19.0*	*19.1*	*13.5*
%C_2H_6	*4.91*	*4.94*	*2.45*	*0.04*	*0.04*	*3.81*
%C_3H_8	*3.25*	*3.17*	*0.57*	*0.00*	*0.00*	*3.94*
%C_4H_{10}	*0.48*	*0.43*	*0.03*	*0.00*	*0.00*	*0.60*
%C_5H_{12}	*0.32*	*0.27*	*0.01*	*0.00*	*0.00*	*0.38*
%C_6H_{14}	*0.30*	*0.19*	*0.00*	*0.00*	*0.00*	*0.28*
%C_7H_{16}	*0.15*	*0.08*	*0.00*	*0.00*	*0.00*	*0.12*
%C_8H_{18}	*0.12*	*0.03*	*0.00*	*0.00*	*0.00*	*0.04*
%C_9H_{20}	*0.04*	*0.00*	*0.00*	*0.00*	*0.00*	*0.01*
%$C_{10}H_{22}$	*0.01*	*0.00*	*0.00*	*0.00*	*0.00*	*0.00*
ppm-mol H_2O	*19.7*	*19.4*	*0.05*	*79.2*	*78.8*	*108.0*
ppm-mol TEG	*1.06*	-	-	*0.00*	-	-

Table IV.5 shows results of power consumption, utilities and carbon emissions, while Fig. IV.6 illustrates equipment power demand. An important aspect in Fig. IV.6 is the 29.1% reduction of feed compressor power in Cases 2 and 3 regarding Case 1. This is a consequence of replacing

TEG+JTE by 1st SS unit, which accomplishes the same dehydration with better C3+ extraction for lower feed pressure. Table IV.4 shows that power consumption is reduced by 7.8% in Case 2 regarding Case 1. Another remarkable result is the reduction of 77% of EOR-Fluid compression power obtained by Case 3 regarding Case 2, thanks to using 2nd SS unit in place of MP. The underlying reason is that Case 3 collects the EOR-Fluid from 2nd SS unit at high pressure (Table IV.3), hence requiring less compression power for EOR than the low-pressure MP permeate from Cases 1 and 2. Therefore, despite the poor pressure recovery of 2nd SS unit due to high condensation, the leverage of ejecting a high-pressure EOR-Fluid is more significant. Regarding the entire plant, Case 3 demands less 21.3% power than Case 1. Even considering the addition of a new feed compressor for 2nd SS unit, and slightly higher power in EOR pump and NG export compressors, the 2nd SS unit responds for 62.6% of reduction of total power consumption of Case 3 regarding Case 1, where 1st SS unit (WDPA+HCDPA) responds for the other 37.4%. Consequently, Case 3 presents the lowest carbon emissions rate, attaining 28.3% less than Case 1. Case 3 also presents the lowest utilities consumption (Table IV.5), making the whole SS-SS solution a cleaner CO_2-rich gas processing alternative relatively to conventional technologies.

Table IV. 5. Power consumption, utilities and CO_2 emissions.

Case	***1 Conventional***	***2 SS-MP***	***3 SS-SS***
Compressor Power (MW)	*64.5*	*59.0*	*48.5*
Pump Power (MW)	*5.99*	*6.01*	*6.98*
Total Power (MW)	*70.5*	*65.0*	*55.5*
CO_2 Emissions (t/d)	*934*	*864*	*669*
PHW Heat Load (MW)	*9.45*	*3.53*	*2.38*
CW Flow Rate (kg/h)	*0.28*	*0.25*	*0.22*

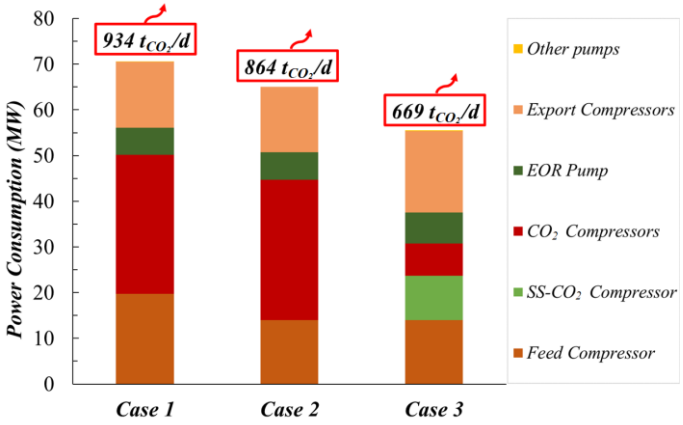

Figure IV. 6. Equipment power demand and CO_2 emissions: Cases 1, 2 and 3 (SS-CO2 ≡ 2nd SS unit).

Table IV.6 summarizes economic results. Figs. IV.7 and IV.8 illustrate equipment *FCI* and *NPV* versus year, respectively. Despite the higher investment of 1st SS unit and LTX relatively to TEG+JTE units, Case 2 shows that reducing compressor *FCI* for WDPA+HCDPA in 1st SS unit is worthwhile. In Case 3, the investments of 2nd SS unit, compressors and gas-turbines (power generation) are even lower, due to its lower compressor service and power demand.

Case 3 (SS-SS) also presents 14% less total *FCI* and 21.5% less *COM*, the latter a consequence of lower *FCI* and *CUT* (FG consumption). On the other hand, Case 3 revenue is inferior. In light of economic assumptions in Table IV.2 and simulation data from Table IV.4, there are two aspects explaining the revenue difference between Cases 3 and 2: (i) Case 3 EOR-Fluid flow rate is higher than Case 2 counterpart, giving incremental revenue relative to Case 2 of +5.6 MMUSD; and (ii) Case 3 FG plus export NG flow rate is lower and with inferior low heating value than Case 2, giving incremental revenue of -27.1 MMUSD. Hence, Case 3 has 21.5 MMUSD/y less revenue than Case 2.

Additionally, Case 2 has slightly less revenue than Case 1, which is explained by the lower NG flow rate after 1st SS unit (WDPA+HCDPA) due to its more efficient C3+ removal. Normally, such greater C3+ recovery would be rewarded by means of a higher oil production as C3+ is recycled to the primary oil-gas-water separator. But oil accountability is not in the present scope.

Despite these comparative revenue shortcomings, *FCI* and *COM* gains of Case 3 (SS-SS alternative) are solid, overcoming its revenue inferiority and leading to highest *NPV* of 860 MMUSD after 20 years of operation. Case 2 (SS-MP alternative) achieves only a slightly higher *NPV* than Case 1; however, the lower power consumption and CO_2 emissions of Case 2 justify the replacement of conventional WDPA+HCDPA by 1st SS unit.

Table IV.6. Economic results: Cases 1, 2 and 3.

Economic Results	*Case 1*	*Case 2*	*Case 3*
FCI (MMUSD)	*453.8*	*449.2*	*390.3*
COM (MMUSD/y)	*134.9*	*130.8*	*105.9*
REV (MMUSD/y)	*392.7*	*388.3*	*366.8*
CUT (MMUSD/y)	*24.42*	*24.07*	*16.35*
GAP (MMUSD/y)	*257.8*	*257.5*	*260.9*
AP (MMUSD/y)	*185.6*	*185.2*	*185.5*
20 years NPV (MMUSD)	*807.1*	*808.5*	*859.6*

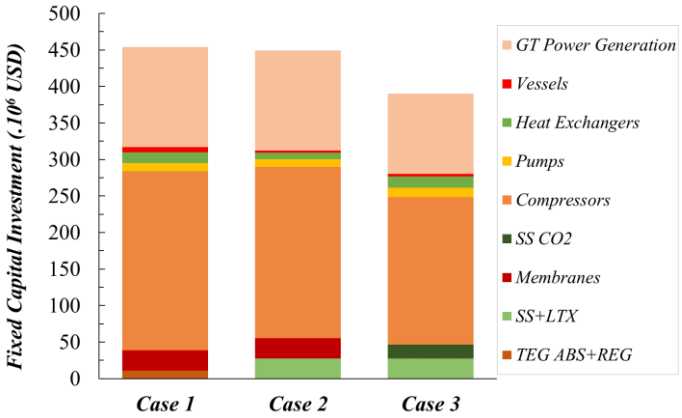

Figure IV. 7. Equipment *FCI*: Cases 1, 2 and 3 (GT≡Gas-Turbines; SS CO_2 ≡ 2nd SS unit; SS+LTX ≡1st SS unit & LTX; TEG ABS+REG ≡TEG Absorption & Regeneration).

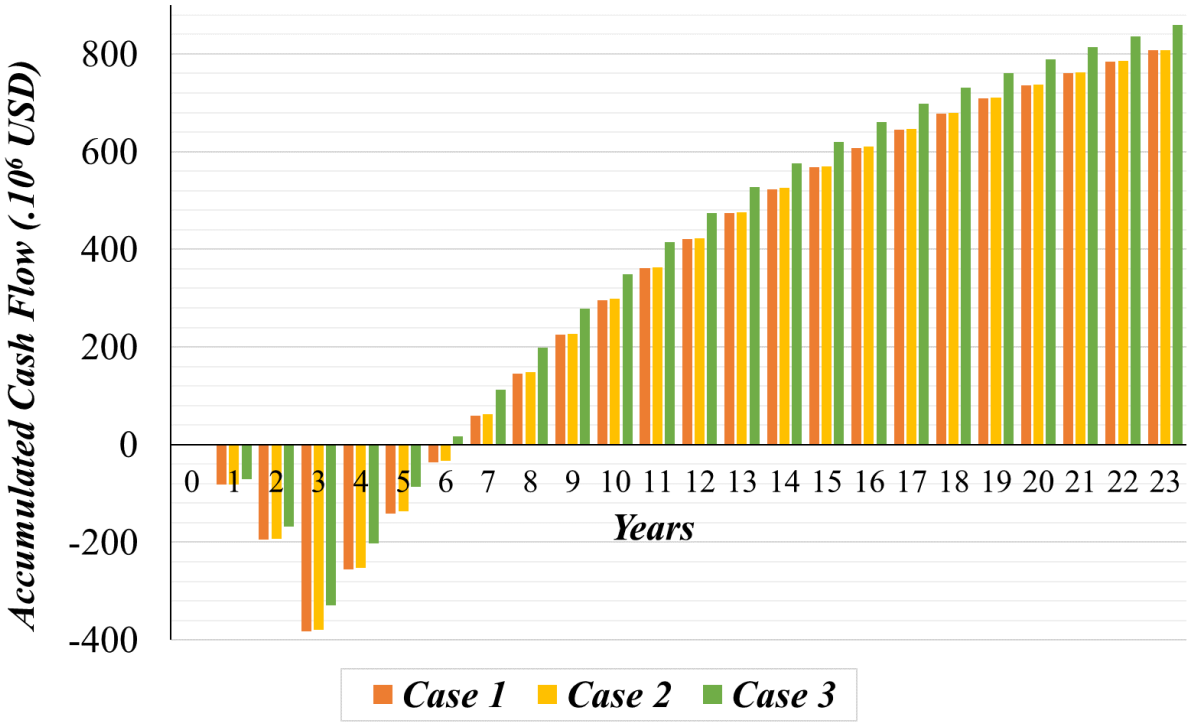

Figure IV. 8. *NPV* (MMUSD) versus year: Cases 1, 2 and 3.

IV.4. Conclusions

Three alternatives for CO_2-rich NG processing in offshore rigs are created to evaluate the economic and environmental advantages of implementing 1st SS unit for WDPA+HCDPA and 2nd SS unit for CO_2 removal; namely: (i) Case 1 – Conventional TEG absorption and JTE, followed by MP CO_2 removal; (ii) Case 2 – SS-MP; and (iii) Case 3 – SS-SS. Results show that for the same dehydration service, 1st SS unit extracts more C3+ than conventional TEG absorption and JTE, also requiring lower feed pressure, and thus lower feed compression power. The replacement of conventional WDPA+HCDPA by 1st SS unit in Case 2 cuts 7.8% of power consumption, avoiding ≈70 t/d of CO_2 emission. It also has economic implications, reducing *COM* and compressors *FCI* (despite higher SS *FCI*), obtaining a slightly higher *NPV* after 20 years of operation than Case 1. Only the environmental gain under similar economic response, justify replacing conventional WDPA+HCDPA by 1st SS unit.

Concerning CO_2 removal, despite the higher pressure and lower temperature of SS inlet in 2nd SS unit of Case 3, the EOR-Fluid produced is at high-pressure and low-temperature, providing feed refrigeration and reduced power demand for its compression to the injection pump suction.

On the other hand, the rather simple MP CO_2 removal produces a low-pressure CO_2 permeate requiring high compression power. Therefore, the power required for CO_2 separation/injection and NG exportation is 18.6% lower if 2nd SS unit is used instead of MP.

Thus, considering the whole SS-SS Case 3 solution, there is a reduction of 21.3% in total power consumption compared to conventional technologies, consequently decreasing CO_2 emissions in 264.7 t/d (-28.3%). Double SS implementation in Case 3 also impacts economic results, reducing plant *FCI* by 14%, *COM* by 21.5% regarding conventional Case 1, and achieving *NPV* of 860 MMUSD after 20 years of operation, 6.5% higher than Case 1.

After the complete analysis contemplating power demand, CO_2 emissions and economic results, it is clear that the new proposed process with two consecutive SS units (Case 3) can fully treat raw CO_2-rich NG and is the best and cleanest overall solution. A future extension of this work would contemplate SS modeling for CO_2 capture from CO_2-rich NG violating the freeze-out border; that is, including dry-ice collection and SVLE calculations in a completely new conceivable SS unit operation.

Supplementary Materials (Appendix K)

Economic relationships are found in the Supplementary Materials available online.

Acknowledgements

Authors acknowledge financial support from PETROBRAS S.A. (grant 0050.0096933.15.9). JL de Medeiros and OQF Araújo also acknowledge financial support from CNPq-Brazil (grant 311076/2017-3).

Abbreviations

C3+ Propane and Heavier Alkanes; CFD Computational Fluid Dynamics; CW Cooling-Water; EOR Enhanced Oil Recovery; FG Fuel-Gas; GT Gas-Turbine; HCDP Hydrocarbon Dew-Point; HCDPA Hydrocarbon Dew-Point Adjustment; JTE Joule-Thomson Expansion; LTX Anti-Hydrate Separator; MMSm^3/d Millions of Standard m^3 per day; MP Membrane-Permeation; NG Natural Gas; NGL Natural Gas Liquids; PHW Pressurized-Hot-Water; PR-EOS Peng-Robinson Equation-of-State; SS Supersonic Separator; SVLE Solid-Vapor-Liquid Equilibrium; TEG Triethylene Glycol; UOE Unit Operation Extension; USD US Dollars; VLE Vapor-Liquid

Equilibrium; VLWE Vapor-Liquid-Water Equilibrium; WDP Water Dew-Point; WDPA Water Dew-Point Adjustment; WHRU Waste-Heat Recovery Unit.

Nomenclature

A	*: Flow-section area (m²)*
AP	*: Annual profit (USD/y)*
$c(P,T,\underline{Z})$	*: Multiphase sound speed property (m/s)*
COM, CRM, CUT	*: Annual cost of manufacturing, raw materials and utilities (USD/y)*
D_I, D_O, D_T	*: SS inlet/outlet/throat internal diameters (m)*
$DEPR$	*: Depreciation (USD/y)*
FCI, GAP	*: Fixed capital investment (USD), gross annual profit (USD/y)*
$\bar{H}, \bar{K}$	*: Multiphase molar enthalpy, molar kinetic energy (J/mol)*
L_C, L_D	*: SS converging/diverging lengths (m)*
Ma, Ma^{Shock}	*: Mach Number, Ma before shock and condensate withdrawal*
N, NPV, REV	*: Horizon (years), net present value (USD), revenues (USD/y)*
P	*: Pressure (bar)*
$\bar{S}$	*: Multiphase molar entropy (J/mol/K)*
T	*: Temperature (K)*
v	*: Multiphase axial flow velocity (m/s)*
x	*: SS axial position (m)*
$\underline{Z}$	*: Vector of species mol fractions*
Greek Symbols	
α, β	*: SS converging/diverging wall angles (deg)*
$\eta^{EXP}\%, \eta^{CMP}\%$	*: SS expansion/compression adiabatic efficiencies (%)*
ρ	*: Density of multiphase fluid (kg/m^3)*
$\Xi_P = \left(\frac{\partial \rho}{\partial P}\right)_{T,\underline{Z}}$	*: Multiphase isothermal compressibility (kg/m^3.Pa)*
Subscripts	
TP	*: Triple-point*
BS	*: Just before shock and after condensate withdrawal*

References

AlNouss, A., Ibrahim, M., Al-Sobhi S.A., Potential energy savings and greenhouse gases (GHGs) emissions reduction strategy for natural gas liquid (NGL) recovery: Process simulation and economic evaluation, J. of Clean. Prod., 194, 525-539, 2018. https://doi.org/10.1016/j.jclepro.2018.05.107

Araújo, O.Q.F., Reis, A.C., de Medeiros, J.L., Nascimento, J.F., Grava, W.M., Musse, A.P.S., Comparative analysis of separation technologies for processing carbon dioxide rich natural gas in ultra-deepwater oil fields, J. of Clean. Prod., 155, 12-22, 2017. https://doi.org/10.1016/j.jclepro.2016.06.073

Arinelli, L.O., Trotta, T.A.F., Teixeira, A.M., de Medeiros, J.L., Araújo, O.Q.F., Offshore Processing of CO2 Rich Natural Gas with Supersonic Separator versus Conventional Routes, J. of Nat. Gas Sci. and Eng., 46, 199-221, 2017. http://dx.doi.org/10.1016/j.jngse.2017.07.010

Brigagão, G.V., Arinelli, L.O., de Medeiros, J.L., Araújo, O.Q.F., A new concept of air pre-purification unit for cryogenic separation: Lowpressure supersonic separator coupled to finishing adsorption, Sep. and Purif. Technol., 215, 173-189, 2019. https://doi.org/10.1016/j.seppur.2019.01.015

Burgers, W.F.J., Northrop, P.S., Kheshgi, H.S., Valencia, J.A., Worldwide Development Potential for Sour Gas, Energy Procedia, 4, 2178-2184, 2011. http://dx.doi.org/10.1016/j.egypro.2011.02.104

Castier, M., Modeling and simulation of supersonic gas separations, J. Nat. Gas Sci. Eng., 18, 304–311, 2014. https://doi.org/10.1016/j.jngse.2014.03.014

de Medeiros, J.L., Arinelli, L.O., Araújo, O.Q.F., Speed of Sound of Multiphase and Multi-Reactive Equilibrium Streams: A Numerical Approach for Natural Gas Applications, J. of Nat. Gas Sci. and Eng., 46, 222-241, 2017. http://dx.doi.org/10.1016/j.jngse.2017.08.006

de Medeiros, J.L., Arinelli, L.O., Teixeira, A.M., Araújo, O.Q.F., Offshore Processing of CO2-Rich Natural Gas with Supersonic Separator: Multiphase Sound Speed, CO2 Freeze-Out and HYSYS Implementation, 1st ed., Springer International Publishing, Springer Nature Switzerland AG, 2019. http://dx.doi.org/10.1007/978-3-030-04006-2. ISBN:978-3-030-04006-2(e-Book)/978-3-030-04005-5(Hardcover).

Gaffney, Cline & Associates, Review and Evaluation of Ten Selected Discoveries and Prospects in the Pre-Salt Play of the Deepwater Santos Basin, Brazil, CG/JW/RLG/C1820.00/GCABA.1914, “Agência Nacional do Petróleo, Gás Natural & Bicombustíveis” (ANP), Brazil, 2010.

Kidnay, A.J., Parrish, W., Fundamentals of natural gas processing, Mechanical Engineering Series, 1st ed., Taylor & Francis Group, Boca Raton, USA, 2006. ISBN:978-0-8493-3406-1.

Machado, P.B., Monteiro, J.G.M., de Medeiros, J.L., Epsom, H.D., Araújo, O.Q.F., Supersonic separation in onshore natural gas dew point plant, J. of Nat. Gas Sci. and Eng., 6, 43–9, 2012. https://doi.org/10.1016/j.jngse.2012.03.001

McCoy, S.T., The Economics of CO2 Transport by Pipeline and Storage in Saline Aquifers and Oil Reservoirs, Ph.D. Thesis, Carnegie Mellon University, USA, 2008.

Merkel, T.C., Zhou, M., Baker, R.W., Carbon dioxide capture with membranes at an IGCC power plant, J. of Memb. Sci., 389, 441-450, 2012. https://doi.org/10.1016/j.memsci.2011.11.012

Montgomery, H., Preventing the progression of climate change: one drug or polypill?, Biofuel Research Journal, 13, 536, 2017. http://dx.doi.org/10.18331/BRJ2017.4.1.2

Netusil, M., Ditl, P., Comparison of three methods for natural gas dehydration, J. of Nat. Gas Chem., 20, 471-476, 2011. http://dx.doi.org/10.1016/S1003-9953(10)60218-6

Nguyen, T.V., Tock, L., Breuhaus, P., Maréchal, F., Elmegaard, B., CO2-mitigation options for the offshore oil and gas sector, Applied Energy, 161, 673-694, 2016. http://dx.doi.org/10.1016/j.apenergy.2015.09.08

Reis, A.C., de Medeiros, J.L., Nunes, G.C., Araújo, O.Q.F., Lifetime oriented design of natural gas offshore processing for cleaner production and sustainability: High carbon dioxide content, J. of Clean. Prod., 200, 269-281, 2018. https://doi.org/10.1016/j.jclepro.2018.07.271

Reis, A.C., de Medeiros, J.L., Nunes, G.C., Araújo, O.Q.F., Upgrading of natural gas ultra-rich in carbon dioxide: Optimal arrangement of membrane skids and polishing with chemical absorption, J. of Clean. Prod., 165, 1013-1024, 2017. http://dx.doi.org/10.1016/j.jclepro.2017.07.198

Stram, B.N., Key challenges to expanding renewable energy, Energy Policy, 96, 728-734, 2016. http://dx.doi.org/10.1016/j.enpol.2016.05.034

Sun, W., Cao, X., Yang, W., Jin, X., Numerical simulation of CO2 condensation process from CH4-CO2 binary gas mixture in supersonic nozzles, Sep. and Purif. Technol., 188, 238-249, 2017. http://dx.doi.org/10.1016/j.seppur.2017.07.023

Teixeira, A.M., Arinelli, L.O., de Medeiros, J.L., Araújo, O.Q.F., Recovery of thermodynamic hydrate inhibitors methanol, ethanol and MEG with supersonic separators in offshore natural gas processing, J. of Nat. Gas Sci. and Eng., 52, 166-186, 2018. https://doi.org/10.1016/j.jngse.2018.01.038

Teixeira, A.M., Arinelli, L.O., de Medeiros, J.L., Araújo, O.Q.F., Economic leverage affords post-combustion capture of 43% of carbon emissions: Supersonic separators for methanol hydrate inhibitor recovery from raw natural gas and CO2 drying, J. of Env. Manag., 236, 534-550, 2019. https://doi.org/10.1016/j.jenvman.2019.02.008

Turton, R., Bailie, R.C., Whiting, W.B., Shaeiwitz, J. A., Analysis, Synthesis, and Design of Chemical Processes, 3rd ed, Prentice Hall Int., USA, 2009.

Wen C., Cao X., Yang Y., Li W., Numerical simulation of natural gas flows in diffusers for supersonic separators. Energy, 37, 195-200, 2012. http://dx.doi.org/10.1016/j.energy.2011.11.047

Yang Y., Wen C., Wang S., Feng Y., Theoretical and numerical analysis on pressure recovery of supersonic separators for natural gas dehydration, Applied Energy, 132, 248-253, 2014. http://dx.doi.org/10.1016/j.apenergy.2014.07.018

CHAPTER V - CARBON CAPTURE AND HIGH-CAPACITY SUPERCRITICAL FLUID PROCESSING WITH SUPERSONIC SEPARATOR: NATURAL GAS WITH ULTRA-HIGH CO_2 CONTENT

This paper was published in Journal of Natural Gas Science and Engineering, 66, 265-283. doi: 10.1016/j.jngse.2019.04.004 (Appendix T.26).

Carbon Capture and High-Capacity Supercritical Fluid Processing with Supersonic Separator: Natural Gas with Ultra-High CO_2 Content

Lara de Oliveira Arinelli[1], José Luiz de Medeiros[1], Darley Carrijo de Melo[2], Alexandre Mendonça Teixeira[1],George Victor Brigagão[1], Fabio Menezes Passarelli[2], Wilson Mantovani Grava[2], Ofélia de Queiroz .F. Araújo[1]*

[1] Escola de Química, Federal University of Rio de Janeiro, CT, E, Ilha do Fundão, Rio de Janeiro, RJ, Brazil.
[2] CENPES, PETROBRAS S.A., Ilha do Fundão, Rio de Janeiro, RJ, 21941-970, Brazil.

*jlm@eq.ufrj.br

Abstract

Some deep-water offshore fields produce oil with high gas/oil ratios and ultra-high %CO_2 (*>60%mol*) with the onus of processing low-grade gas simultaneously handling huge CO_2 dispatch goals. Thus, processing solutions are needed to make feasible such high-capacity gas rigs hundreds of kilometers offshore. Feasibility relies on the choices for CO_2 capture and adjustment of water and hydrocarbon dew-points of such high flow rate gas. This problem was approached adopting supersonic separators for dew-point adjustments and for CO_2 capture on a floating-hub processing *50 MMsm³/d* of CO_2 ultra-rich gas, reinjecting *96%* of treated CO_2-rich gas for enhanced oil recovery, while reserving *4%* as fuel-gas after CO_2 abatement to *20%mol* for power production. Process alternatives were assessed in terms of power demand and profitability comparing supersonic separator with membrane-permeation for CO_2 removal. Results show that 1st supersonic separator for dew-point adjustments of raw gas recycling condensate to the oil-gas-water separator and 2nd supersonic separator for CO_2 removal avoiding CO_2 freeze-out, give optimum net present value and minimum CO_2 emissions. On one hand, these facts are consequences of less compressor investment as 2nd supersonic separator ejects pressurized CO_2 condensate requiring *5%* less compression power for enhanced oil recovery relatively to the power required by the low-pressure CO_2-rich permeate from the membrane-permeation alternative. On the other hand, the best net value of supersonic separator alternative also reflects its highest revenues derived from recycling condensate from 1st supersonic separator entailing *18%* higher oil production.

Key Words: Supersonic Separator; Supercritical Fluid Processing; Ultra-High CO_2 Content; Natural Gas Conditioning; CO_2 Removal; CO_2 Freeze-Out

V.1. Introduction

The processing of raw natural gas (NG) to fuel-gas comprises well-known operations normally in the following order: (i) H_2S removal; (ii) water dew-point adjustment (WDPA) via dehydration; (iii) hydrocarbon dew-point adjustment (HCDPA) via hydrocarbon removal (i.e., propane and heavier or C3+); and (iv) CO_2 removal. Over 10% of world NG reserves contain *15-80%mol* CO_2 classified as medium (*15-30%mol*), rich (*30-60%mol*) and ultra-rich (*>60%mol*) CO_2 NG (Burgers et al., 2011). CO_2 removal is not only important to reach specifications, but also to reduce CO_2 emissions with economic benefits if CO_2 is injected in oil fields for enhanced oil recovery (EOR) (Araújo and De Medeiros, 2017). EOR is economically positive as shown by tests of CO_2 injection and depletion for heavy oil recovery after cold production with oil-sands in Canada (Shokri and Babadagli, 2017). In non-associated NG fields, CO_2 can be pipeline-dispatched to EOR, or can be stored in depleted fields or aquifers (Indonesia, Norway) (Burgers et al., 2011). Some examples of huge NG reserves with high CO_2 contents are: Brazil offshore fields with high gas-oil ratio (*GOR*) such as Libra ($Oil \approx 15*10^9$ *bbl*, $GOR \approx 500$ *sm³/m³*, $CO_2 \approx 45\%mol$); US LaBarge gas field ($CO_2 \approx 65\%mol$) and E-Natuna SE-Asia offshore gas field ($Gas \approx 1.3*10^{12}$ *sm³*, $CO_2 \approx 71\%mol$).

V.1.1. CO_2 Removal from CO_2-rich NG

Chemical-Absorption, Physical-Absorption, Membrane-Permeation, Gas-Liquid Membrane Contactor and Cryogenic-Distillation can remove CO_2 from CO_2-rich NG. Chemical-Absorption uses high-pressure chemical solvent absorption – aqueous MEA/MDEA – and low-pressure solvent regeneration releasing CO_2 top product, both steps modeled with reactive vapor-liquid equilibrium (VLE) (De Medeiros et al., 2013a). Chemical absorption solvents have high H_2O/amine molar ratio from 6 to 15 and absorb CO_2 via reversible, exothermic, ionizing reactions (De Medeiros et al., 2013a) as shown in Eq. (V.1) for MDEA (unitary amine/CO_2 ratio), preceded by formation of aqueous CO_2 in VLE at given fugacity ($\hat{f}_{CO2}$).

$$HOC_2H_4\text{-}NCH_3\text{-}C_2H_4OH + CO_2(aq) + H_2O \leftrightarrow HOC_2H_4\text{-}NH^+CH_3\text{-}C_2H_4OH + HCO_3^- \quad \text{(V.1)}$$

Chemical-Absorption accepts low to high CO_2 fugacity with high CO_2/CH_4 selectivity, implying low CH_4 losses to CO_2 product, but with issues such as high capture-ratio (*10-18*

$kg^{Solvent}/kg^{CO2}$) entailing high solvent circulation, high heat-ratio regeneration (*2-4* MJ/kg^{CO2}) and low-pressure stripped CO_2 requiring compression for EOR. In the context of new Chemical-Absorption solvents, Zhang et al. (2018) pointed out that amino-acid salts solutions show high-efficient CO_2 absorption in comparison with amines; however, there is still a need for novel amino-acid salts capable to improve CO_2 desorption and solvent regeneration performance, in addition to thermodynamically-based models to describe CO_2 absorbed in such mixtures (Zhang et al., 2018). In this regard, Li and Zhang (2018) proposed a prediction model based on generalized machine learning representation for CO_2 solubility data in order to overcome the drawbacks of conventional methods (e.g., Equation-of-State). This method captures the non-linear relationship between conditions and CO_2 solubility, allowing to understand the intrinsic trends of CO_2 solubility. Physical-Absorption has better capture-ratio (*1-10* $kg^{Solvent}/kg^{CO2}$) at high $\hat{f}_{CO2}$, but with poor CO_2/CH_4 selectivity and high CH_4 losses in CO_2 product at low-pressure. Membrane-Permeation splits CO_2/CH_4 through skin-dense hollow-fiber or spiral-wound membranes, with low footprint, modularity and flexibility to feed $\%CO_2$ as advantages, while disadvantages are inverse selectivity-capacity relationship, low-pressure CO_2 permeate and CH_4 losses for high $\%CO_2$ feeds (Araújo et al., 2017). Araújo et al. (2017) compared Chemical-Absorption, Physical-Absorption and Membrane-Permeation for *10-50%mol* CO_2 NG offshore processing, electing hybrid Membrane-Permeation/Chemical-Absorption as best alternative, assuming Pressurized-Hot-Water (PHW) available from Waste Heat Recovery Units (WHRU) of turboshafts. Nguyen et al. (2016) also appraised WHRU for thermally efficient Chemical-Absorption using PHW for solvent regeneration. The Gas-Liquid Membrane Contactor is a shell with non-selective hollow-fibers inside, where CO_2-rich NG is fed in shell side with chemical solvent flowing through hollow-fibers or vice-versa, both schemes accepting co-current/counter-current contacts (de Medeiros et al., 2013b; Kang et al., 2017). Gas-liquid Contactors with aqueous MEA/MDEA were modeled for high-pressure *10%mol* CO_2 NG with rigorous reactive VLE (e.g., Eq. (V.1)), thermal and compressible two-phase flow effects via one-dimensional (1D) framework, proving its feasibility for offshore rigs (de Medeiros et al., 2013b). Other authors confirmed contactor feasibility for treating *45-70%mol* CO_2 NG (Kang et al., 2017). Cryogenic-Distillation splits CH_4-CO_2 at low-temperature and high-pressure, with the leverage of liquid CO_2 product ready for EOR pumping. Cryogenic-Distillation was compared with Chemical-Absorption for *5-65%mol* CO_2

NG, being superior above *10%mol* CO_2 as liquid CO_2 demands less EOR power than low-pressure CO_2 from Chemical-Absorption (Langé et al., 2015). Dual-pressure Cryogenic-Distillation was also shown to have best exergy efficiency for *40%mol* CO_2 NG producing *50 ppm* CO_2 NG for liquefaction (Baccanelli et al., 2016).

V.1.2. Supersonic Separator for CO_2 Removal and NG Conditioning

Supersonic separator (SS) is a new operation for raw NG conditioning. It expands raw NG through a converging-diverging nozzle – Laval nozzle – to supersonic flow creating deep *T* falls causing condensation of propane and heavier hydrocarbons (C3+) and water, which are separated from gas by centrifugal swirl (Schinkelshoek and Epsom, 2008). Fig. V.1 sketches SS with linear diameter profiles assuming 1D axial fluid motion as dominant. A critical SS modeling aspect is the correct evaluation of sound speed (*c*) to calculate Mach Number (*Ma*) along the flow (Arinelli et al., 2017). As an equilibrium single-phase or multiphase thermodynamic property, *c* is highly affected by changes of density (ρ) and isothermal compressibility ($\Xi_P \equiv \left(\frac{\partial \rho}{\partial P}\right)_{T,\underline{Z}}$) of the multiphase fluid: both influence *c* inversely; i.e., as ρ or Ξ_P increases, *c* decreases (de Medeiros et al., 2017). Thus, *c* suddenly falls when gas initiates condensation of a single liquid C3+ or water, or of two immiscible liquids water-C3+. In SS modeling *c* is calculated either for vapor flow or for two-phase (vapor-C3+, vapor-water) flow or yet for three-phase flow (vapor-water-C3+). Multiphase compressible SS flow is described by *Ma*: (i) flow is subsonic in the converging section ($Ma<1$); (ii) sonic at the throat ($Ma=1$); (iii) supersonic in the diverging section ($Ma>1$) until the normal shock, which should be preceded by condensate collectors; and (iv) post-shock subsonic flow of lean gas through the diverging diffuser (Arinelli et al., 2017). A SS idiosyncrasy is the meta-stability of supersonic flow against higher discharge pressure, P^{out}, relatively to the supersonic *P*, so that the supersonic flow gradually loses stability as P^{out}-*P* increases positively, eventually leading to normal shock. This sudden irreversible transition turns supersonic flow into subsonic, increasing entropy, *P*, *T* subjected to mass, energy and momentum conservation (Arinelli et al., 2017). Thus, the water-C3+ condensate must be collected upstream the shock, otherwise it re-vaporizes destroying separation. In Fig. V.1, the Laval is the converging-diverging nozzle upstream the shock, while the diffuser is the downstream diverging prolongation, where lean NG subsonic

flow continuously decelerates gaining P and T until the discharge at P^{out}. The shock irreversibility impedes the final gas to recover its feed pressure P^{in}; i.e., non-negligible head-loss P^{in}-P^{out} occurs according to shock intensity: the higher the supersonic Ma at pre-shock (Ma^{Shock}), the higher P^{in}-P^{out}.

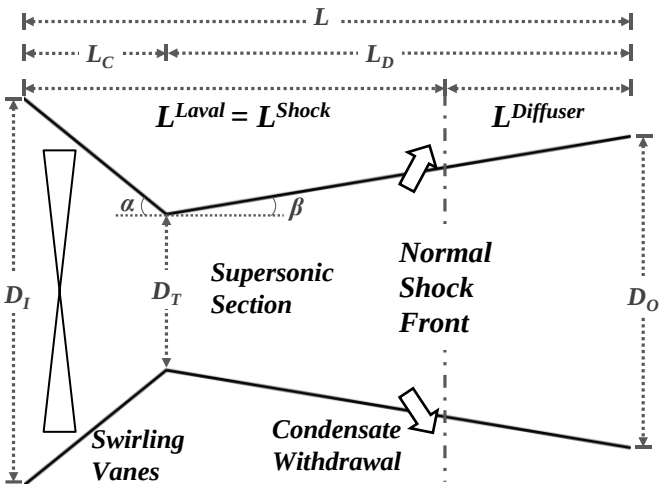

Figure V. 1. SS sketch with linear diameter profiles.

Since SS introduction twenty years ago (Schinkelshoek and Epsom, 2008; Machado et al., 2012), analytical SS research has evolved via thermodynamic approaches (Arinelli et al., 2017; De Medeiros et al., 2017; Castier, 2016; Secchi et al., 2016; Teixeira et al., 2018) and computational fluid dynamic (CFD) approaches (Wen et al., 2012; Yang et al., 2014; Shooshtari and Shahsavand, 2017). As pointed out elsewhere (Arinelli et al., 2017), despite easily implemented and with great presence in SS literature, CFD SS studies are incomplete as CFD still cannot handle complex phase-behavior and phase-change, neither the multiphase sound speed (c), all essential SS features with condensing feeds (e.g., raw NG). Thermodynamic SS approaches, on the other hand, handle phase transitions and multiphase c but impose thermodynamic equilibrium, a condition not fully manifested in SS lapse of few milliseconds. Nevertheless, SS thermodynamic approaches are more valuable for condensing feeds as they represent SS limiting behavior satisfying the 2nd Law of Thermodynamics. Meanwhile, ordinary CFD SS approaches with condensing feeds openly violate the 2nd Law as CFD leads to unrealistic too cold pre-shock temperatures translated as adiabatic destruction of entropy, a prohibited circumstance (Arinelli et al., 2017). Sec. V.2.1 addresses this and other controversial aspects of CFD SS modeling with raw NG. Since an extensive review on CFD SS simulation

for raw NG, including assessment of CFD flaws, was provided in Arinelli et al. (2017), there is no point in doing the same here, excepting considering recent emblematic SS-CFD specimens (Wen et al., 2012; Yang et al., 2014; Shooshtari and Shahsavand, 2017) which are questioned in Secs. V.1.3 and V.2.1 counterpointed by the present rigorous thermodynamic SS modeling.

SS was thermodynamically modeled for NG WDPA+HCDPA by Arinelli et al. (2017) with rigorous multiphase compressible supersonic flow and multiphase sound speed by de Medeiros et al. (2017), both considering all possibilities, single-phase vapor, two-phase (vapor-C3+ or vapor-water) or three-phase (vapor-water-C3+) equilibrium. A remarkable difference of (Arinelli et al., 2017; De Medeiros et al., 2017) to other thermodynamic SS studies with NG (Castier, 2016; Secchi et al., 2016) is that the latter only contemplated HCDPA for dehydrated NG feeds, circumventing three-phase vapor-liquid-water equilibrium (VLWE) on SS flow path with raw NG as fully done in Arinelli et al. (2017). Arinelli et al. (2017) additionally modeled the LTX which operates with SS when executing WDPA+HCDPA of raw NG; i.e., SS should discharge cold water-C3+ condensate into the heated LTX vessel to avoid gas-hydrates. Arinelli et al. (2017) also applied SS for CO_2 abatement from CO_2-rich NG, provided NG was previously treated for WDPA+HCDPA for exclusive CO_2 condensation under deep T fall. In this case, CO_2 freeze-out is a concern that must be avoided to prevent plugging; i.e., SS flow path must not cross the CO_2 freeze-out border by admitting a maximum Ma to keep $T>T^{Freeze-Out}$. That is, the appropriate solid-vapor-liquid equilibrium (SVLE) CO_2 freeze-out boundary must be pre-located for correct design of SS CO_2 removal. Arinelli et al. (2017) compared SS to treat *44%mol* CO_2 raw NG for WDPA+HCDPA and CO_2 removal versus conventional ways: glycol-absorption WDPA; Joule-Thomson expansion HCDPA; and membrane-permeation CO_2 removal. Results elected SS as best WDPA+HCDPA alternative, achieving better lean NG with less power consumption. Regarding CO_2 removal, membrane-permeation gave best separation achieving *15%mol* CO_2 in single-stage, while SS achieved only *21.85%mol* CO_2 – barred by freeze-out avoidance – but producing high-pressure CO_2-rich liquid, requiring *30%* less EOR power.

To simulate membrane-permeation and SS units, both not offered in HYSYS simulator, Arinelli et al. (2017) and de Medeiros et al. (2017) developed HYSYS Unit Operation Extensions (UOE): (i) MP-UOE a membrane-permeation model with estimated permeances from field data

(Arinelli et al., 2017); (ii) PEC-UOE for rigorous determination of phase-equilibrium *c* for *Ma* calculation on SS flow path (De Medeiros et al., 2017); and (iii) SS-UOE a rigorous thermodynamic model for SS multiphase flow, multiphase *c*, condensate separation and shock transition, which designs SS forcing $Ma^{Throat}=1$ with specifications (Fig. V.1) feed data, inlet-outlet diameters (D_I,D_O), converging-diverging wall angles (α,β), expansion-compression adiabatic efficiencies ($\eta^{EXP}\%,\eta^{CMP}\%$) and maximum pre-shock *Ma*, Ma^{Shock} (Arinelli et al., 2017). SS-UOE and PEC-UOE are rigorous tools running with any HYSYS thermodynamic package – e.g., Peng-Robinson Equation-of-State (PR-EOS) or Cubic-Plus-Association Equation-of-State (CPA-EOS) – rendering multiphase SS profiles with correct SS throat signatures (Appendix L). SS-UOE retrieves feed parameters from HYSYS flowsheet and installs SS products into it. SS-UOE designs SS obtaining L_C, L_D, L^{Shock}, $L^{Diffuser}$ and throat diameter D_T (Fig. V.1), calculating outlet gas, water-C3+ condensate and SS head-loss.

V.1.3. Present Work

SS for condensate segregation from high-pressure feeds is evolving beyond ordinary WDPA+HCDPA and CO_2 removal NG applications. Recently, Teixeira et al. (2018) presented an "out-of-the-box" SS recovery of hydroxylated thermodynamic hydrate inhibitors – methanol, ethanol and ethylene-glycol – from high-pressure raw NG contacted with inhibitors in flowlines, obtaining remarkable results. Treating such raw NG in SS with small water injection, allows to recover inhibitors as water-inhibitor condensate, besides collecting saleable C3+ and producing NG with WDPA+HCDPA grades. Such results were only possible because SS was modeled with supersonic three-phase flow of gas, liquid C3+ and water-inhibitor phase, simultaneously with three-phase equilibrium *c* property, solved with CPA-EOS appropriate for associative water-hydroxylated systems (Folas et al., 2005; Karakatsani and Kontogeorgis, 2013). SS results of (Teixeira et al., 2018) also come from HYSYS simulation using SS-UOE and PEC-UOE.

Here, such successful SS applications thermodynamically solved with SS-UOE and PEC-UOE (Arinelli et al., 2017; de Medeiros et al., 2017; Teixeira et al., 2018) were deepened in the innovative large-scale offshore processing of CO_2 ultra-rich raw NG exclusively using SS operations. The scenario is a floating-hub processing *≈120,000 bbl/d* of oil and *≈50 MMsm³/d* of *≈68%mol* CO_2 raw NG. About *4%* of raw NG is slipped to produce *≈1 MMsm³/d* of *≈20%mol*

CO_2 Fuel-Gas for power generation, while the rest is processed for injection as *≈71%mol* CO_2 EOR-Fluid with *≤ 250 ppmH_2O*, after enriched with CO_2 withdrawn from Fuel-Gas. For a compact flowsheet, suited to giant flow rates at remote locations, design should privilege modular reliable units and avoid cumbersome ones like glycol/adsorption dehydrations and CO_2 capture options in Sec. V.1.1, which entail prohibitive footprints, costs and make-up issues. Thus, two SS units were devised to execute WDPA+HCDPA and CO_2 capture from CO_2 ultra-rich raw NG. The literature of raw NG treatment never considered similar conditions, neither such high CO_2 content vis-à-vis CO_2 freeze-out issues.

V.1.3.1. Originality Aspects

The literature presents recent SS studies with raw NG, but, excepting (Arinelli et al., 2017; de Medeiros et al., 2017; Teixeira et al., 2018), all bear modeling deficiencies. For example, Wen et al. (2012) and Yang et al. (2014) simulated SS with raw NG. The former compared diffusers regarding pressure recovery, while the latter studied impacts of expansion ratios and pre-shock *Ma* on pressure recovery. Despite apparently different, these works share two basilar points: use raw NG with condensable C3+ and water; and model SS flow path with CFD commercial software. The consequence of such choices is evidently some error in SS profiles as CFD cannot generate phase-change along the SS supersonic flow, an inherent characteristic of raw NG. Other limitations found in these and other CFD works are: (i) did not calculate the correct sound speed (*c*) property for multiphase streams, a critical factor in SS with raw NG; (ii) ignoring phase-change in SS path leads to too cold and wrong pre-shock *T* profile; and (iii) *P*, *T*, *Ma* profiles across normal shock show inclined linear trends (i.e., no shock discontinuities) and improper oscillating numerical anomalies just upstream and downstream the front. Therefore, rigorous thermodynamic frameworks are needed for simulating SS with raw NG. As shown in Sec. V.2.1, the truth is that CFD is insufficient for engineering and design of SS with raw NG. Recently, Shooshtari and Shahsavand (2017) investigated SS with raw NG for better pressure recovery given the degree of water removal via condensation-nucleation theory and droplet growth. This work also explored a limited SS model as it presents a single-phase compressible flow model with PR-EOS, which is used only for calculating gas density and isothermal compressibility, and not for full phase-equilibrium and multiphase *c*; i.e., the phase-equilibrium on SS flow path and multiphase *c* property were not taken rigorously. Additionally, there are

other limitations: (i) normal shock via ideal gas with constant $\bar{C}_P / \bar{C}_V$ ratio; (ii) high-pressure water VLE via Raoult's Law; (iii) sound speed via ideal gas again with constant $\bar{C}_P / \bar{C}_V$; and (iv) the framework can handle only a single condensable species and was tested only with binary feeds such as CH_4/H_2O – always under constant heat capacity and vaporization enthalpy.

Therefore, excluding (Arinelli et al., 2017; de Medeiros et al., 2017; Teixeira et al., 2018), there are no works systematically taking into account rigorous multicomponent multiphase-equilibrium in SS flow path for processing raw NG feeds. Moreover, there are no works addressing high-capacity supercritical fluid processing using SS for CO_2 capture fully respecting the CO_2 freeze-out boundaries. The present work fills these literature gaps. It analyzes high-capacity CO_2-rich NG processing employing only SS units rigorously modeled with multiphase supersonic flow path and multiphase *c* rendered by HYSYS 8.8 with SS-UOE/PEC-UOE and observing CO_2 freeze-out limits. Processes have SS and membrane-permeation units solved with SS-UOE, PEC-UOE and MP-UOE (Arinelli et al., 2017; de Medeiros et al., 2017). Due to space limitations, models for SS, MP, LTX and multiphase *c* are not discussed here and can be found in (Arinelli et al., 2017; de Medeiros et al., 2017), but SS-UOE is validated with literature data (Yang et al., 2014) in Appendix L. Additionally, to demonstrate the capabilities of our methods, SS was double-simulated with both PR-EOS and CPA-EOS, the latter in Appendix N. Moreover, SS flow paths were traced on thermodynamic diagrams – PxT, $Tx\bar{S}$ – with bubble and dew loci displaying transitions and 2nd Law compliance. Finally, the high-capacity gas-hub is suited for oil production with high *GOR* processing CO_2 ultra-rich NG in remote offshore fields accounting for CO_2 sequestration goals. Such conjunction of subjects, methods and results never appeared before in the literature.

V.2. Methods

Energy and economic performances of a large-scale gas-oil floating-hub were analyzed assuming SS gas processing whenever possible. The hub extracts *≈37°API* oil (*≈1.2*10^5 bbl/d*) and processes *≈50 MMsm³/d* of *≈68%mol* CO_2 raw NG. Such gas-hub is centrally positioned on a remote oil-gas offshore field receiving high-pressure raw NG with ultra-high CO_2 content from nearby floating rigs that are deprived of gas processing facilities. So the gas-hub is the only ship with high topside investment (heavy compressors) for processing such impressive

flow rate of CO_2 ultra-rich raw NG and exporting high-pressure EOR-Fluid for injection in several wells throughout the field. The gas-hub also has its own oil-gas-water production which is mixed with the gas flow from other ships. This scheme is devised to lower costs of satellite rigs, which did not install heavy compressors and only have oil/water processing facilities, besides an oil-water-gas separator and small-scale fuel-gas plant for power generation. Such scenario is plausible for remote offshore fields producing oil with high gas-oil ratio and ultra-high $\%CO_2$, but without tiebacks to the coast.

Process begins with oil-gas-water separation centralized in the high-pressure (*120 bar*) separator (HPS). HPS-Gas processing comprises: (i) expansion to processing pressure; (ii) 1st SS unit for WDPA+HCDPA producing Dry-Gas and water-C3+ condensate; (iii) slippage of *≈4%* Dry-Gas to CO_2 removal producing *≈20%mol* CO_2 Fuel-Gas; and (iv) compression of Dry-Gas enriched with captured CO_2 for EOR. WDPA+HCDPA are done via 1st SS unit, obligating HPS-Gas expansion as SS has issues with *≈68%mol* CO_2 above *85 bar* due to high compressibility and density that damp *c* (De Medeiros et al., 2017), entailing flow not rapid enough for cooling.

Process alternatives address three structural decisions: (i) recycle (RC option) or no recycle (NR option) of water-C3+ condensate from 1st SS unit to HPS; (ii) expansion upstream 1st SS unit via Joule-Thomson-Expansion (JT option) or via Turbo-Expander (TX option); and (iii) CO_2 removal for Fuel-Gas production via 2nd SS unit (SS option) or via Membrane-Permeation (MP option). In TX option, HPS-Gas is pre-heated to $T=350^oC$ to generate power. Out of eight combinations, only four are relevant: [RC+JT+SS] (Base-Case), [RC+TX+SS], [NR+JT+SS] and [RC+JT+MP].

V.2.1. Modeling of Supersonic Separator with Raw NG

SS for raw NG conditioning is modeled in the literature via two trends: CFD and thermodynamic approaches. From the outset both are incomplete. CFD cannot handle thermodynamic issues such as multicomponent phase-change, multiphase sound speed (*c*) and raw NG phase-behavior. Conversely, thermodynamic approaches rely on equilibrium to access thermodynamic states, an idealistic assumption vis-à-vis difficulties of attaining true equilibrium on SS flow with milliseconds of lapse. Nevertheless, thermodynamic approaches

are more significant as they aim at operational limits obeying the 2nd Law of Thermodynamics besides mass, momentum and energy conservation. Several chemical engineering operations are also modeled in the thermodynamic limit despite its distance to real operation – e.g., staged-distillation and staged-absorption – and designed with empirical tolerances over equilibrium-based solutions. In this work SS is simulated via a rigorous multiphase thermodynamic approach in HYSYS 8.8 with SS-UOE and PEC-UOE, the former a complete SS model for multiphase compressible flow, multiphase *c*, condensate separation and normal shock transition (Arinelli et al., 2017); while the latter rigorously calculates the phase-equilibrium *c* (De Medeiros et al., 2017). Thermodynamic SS modeling is more significant for conceptual design of raw NG conditioning than current CFD counterparts.

Several points can be raised against indiscriminate use of CFD in SS with raw NG. It is not hard to identify such shortcomings, which recurrently distort CFD results for SS with raw NG. The most visible of them emerges from ignoring raw NG phase-behavior: CFD generates very super-cooled pre-shock gas solutions which are unfeasible vis-à-vis the 2nd Law for adiabatic transitions with phase-equilibrium allowed; i.e., entropy is destroyed adiabatically on CFD expansion path. For brevity, consider only the recent work Yang et al. (2014) which CFD modeled SS for following raw NG (*%mol*): *500000 Nm^3/d, P=100 bar, T=26.85°C, CH_4=91.36%, C_2H_6=3.63%, C_3H_8=1.44%, iC_4H_{10}=0.26%, nC_4H_{10}=0.46%, iC_5H_{12}=0.17%, nC_5H_{12}=0.16%, CO_2=0.45%, N_2=2.04%, H_2O=0.03%*. For this feed – holding water-C3+ condensable – authors prescribed a SS with inlet, throat and outlet diameters of *100 mm*, *17.4 mm* and *60 mm*, respectively; and converging, diverging and diffuser lengths of *186.6 mm*, *202.4 mm* and *300.3 mm*, respectively. SS was simulated for different area-expansion ratios ($r_c \equiv A^{Diverging}/A^{Throat}$) with normal shock always at Laval end (*x=389 mm*). Table V.1 shows their pre-shock states versus r_c, with entropy changes relative to SS feed via PR-EOS under thermodynamic equilibrium. Table V.1 proves that Yang et al. (2014) pre-shock states are forbidden by the 2nd Law, as fluid is unrealistically too cold for entropy conservation; i.e. entropy is destroyed adiabatically violating the 2nd Law. Thus CFD generates optimistic cooling and cannot address multiphase split; hence, subsequent results (pressure recovery ratios) are inaccurate for SS with raw NG. Appendix L discusses SS profiles and validates our SS framework against literature data.

Table V. 1. 2nd Law test of SS results of Yang et al. (2014) for several expansion ratios (r_c) with respective equilibrium entropy changes relative to raw NG feed.

Condition	*T (K)*	*P (bar)*	$\bar{S}$ * *(J/mol.K)*	$\Delta\bar{S}$ # *(J/mol.K)*	*Vapor Fraction&*	*Hydrocarbon Liquid Fraction&*	*Free Water Fraction&*
Feed	*300*	*100*	*143.123*	*0*	*1*	*0*	*0*
rc=1.118	*239.574*	*42.958*	*142.408*	*-0.7145*	*0.99178*	*0.00793*	*0.00029*
rc=1.513	*213.191*	*27.817*	*141.253*	*-1.8697*	*0.96899*	*0.03071*	*0.00030*
rc=2.131	*191.489*	*19.014*	*139.583*	*-3.5396*	*0.94394*	*0.05576*	*0.00030*

**Equilibrium entropy calculated by HYSYS with PR-EOS. #Entropy changes relative to feed.*
&Vapor mol fractions assuming phase-equilibrium allowed at given condition.

V.2.2. Process and Simulation Assumptions

Table V.2 lists assumptions for NG processing with high CO_2 content.

Table V. 2. Process simulation assumptions: offshore processing of NG with high %CO_2.

Code	*Topic or Unit*	*Description*
{F1}	*Simulation*	*HYSYS 8.8 with MP-UOE for membrane-permeation, SS-UOE for 1st and 2nd SS units, and PEC-UOE for phase-equilibrium c.*
{F2}	*Thermodynamic model*	*PR-EOS; 1st SS unit was also solved with CPA-EOS (Appendix N).*
{F3}	*Thermal approach*	*$\Delta T^{Approach}=10^oC$ (exception {F6}).*
{F4}	*Thermal utility loops for heating/cooling under heat recovery with specific T ranges*	*CW: Cooling-Water, P=4 bar, $T\in[35^oC,45^oC]$; WW: Warm-Water, P=4 bar, $T\in[35^oC,80^oC]$; HW: Hot-Water, P=4 bar, $T\in[35^oC,110^oC]$; PHW: Pressurized-Hot-Water, P=22 bar, $T\in[110^oC,210^oC]$; TF: Thermal-Fluid, P=4 bar, $T\in[220^oC,380^oC]$.*
{F5}	*Heat source*	*WHRUs fed with exhausts from electric turboshafts and gas-turbines drivers, producing PHW (210^oC) or TF (380^oC), assuming 75MW-heat per 100MW-power (Teixeira et al., 2016).*
{F6}	*CO_2 refrigeration-cycle for SS CO_2 removal*	*$T^{Evaporator}=-25^oC$; $T^{Condenser}=0^oC$; $\Delta T^{Approach}=5^oC$.*
{F7}	*EOR-Fluid*	*P=450 bar*
{F8}	*1st SS unit WDPA+HCDPA*	*12 SS's, LTX for water-C3+ condensate, $\eta^{EXP}\%=\eta^{CMP}\%=100\%$, $D_I=100mm$, $D_O=80mm$, $\alpha=12.67^o$, $\beta=2.66^o$, $P^{in}=80.5$ bar, $T^{in}\approx45^oC$, $Ma^{Shock}=1.52$.*
{F9}	*2nd SS unit CO_2 removal*	*Single SS, no LTX, $\eta^{EXP}\%=\eta^{CMP}\%=100\%$, $D_I=120mm$, $D_O=90mm$, $\alpha=15^o$, $\beta=2.5^o$, $P^{in}=84$ bar, $T^{in}\approx-22^oC$, $Ma^{Shock}=1.59$.*
{F10}	*Membrane-Permeation CO_2 removal*	*Counter-current spiral-wound single-stage, $P^{Feed}\approx43$ bar, $T^{Feed}=62^oC$, $P^{Permeate}=8$ bar, $P^{Retentate}\approx42$ bar, partial-pressure limit $PP_{CO2}\in[0,30bar]$.*
{F11}	*Oil-gas-water process feed*	*F=156250 kmol/h, P=120 bar, $T=16^oC$; %mol: H_2O=40.7%, CO_2=39.7%, N_2=0.154%, CH_4=14.6%, C_2H_6=1.36%, C_3H_8=0.747%, iC_4H_{10}=0.130%, C_4H_{10}=0.291%, iC_5H_{12}=0.094%, C_5H_{12}=0.142%, C_6H_{14}=0.148%, C_7H_{16}=0.208%, C_8H_{18}=0.231%, C_9H_{20}=0.184%, $C_{10}H_{22}$=0.148%, $C_{11}H_{24}$=0.125%, $C_{12}H_{26}$=0.107%, $C_{13}H_{28}$=0.113%, $C_{14}H_{30}$=0.101%, $C_{15}H_{32}$=0.077%, $C_{16}H_{34}$=0.053%, $C_{17}H_{36}$=0.047%, $C_{18}H_{38}$=0.047%, $C_{19}H_{40}$=0.042%, C20+=0.433% (hypothetical, 409 kg/kmol, 905 kg/m³@25^oC).*
{F12}	*Compressors and TX adiabatic efficiency*	*$\eta=75\%$*
{F13}	*Intercoolers using CW/WW/HW*	*$T^{Outlet-Gas}=45^oC$, $\Delta P^{Gas}=0.5$bar, $T^{Inlet-CW}=T^{Inlet-WW}=T^{Inlet-HW}=35^oC$.*
{F14}	*Electric-Driver (ED)*	*$Power^{ED}\in[0,13MW]$.*
{F15}	*Gas-Turbine Driver(GT)*	*$Power^{GT}\in[13MW,28MW]$.*

V.2.3. Energy Inputs, Thermal Utilities, Heat Sinks

Energy enters processes through compressor/pump shaft-power and heat recovered in WHRUs at *75 MW-heat* per *100 MW-power* (Teixeira et al., 2016). WHRU exhausts at $T \approx 600^oC$ heat up two hot utilities: PHW ($P=22\ bar$, $T \in [110^oC,210^oC]$) and TF ($P=4\ bar$, $T \in [220^oC,380^oC]$). All processes use PHW; while TF is only used in process [RC+TX+SS] to superheat HPS-Gas to $T=350^oC$. Energy leaves processes in product streams and as sink heat-effects: (i) ATM-Sink: exhaust to atmosphere; (ii) SW-Sink: plate-exchanger cooled by seawater (SW) at $T=25^oC$, returning to sea at $T=35^oC$. To reduce heat intake, three water loops – CW, WW, HW – recover heat when they cool streams down to $T=45^oC$, becoming hot utilities at different T ($T^{CW} \in [35^oC,45^oC]$, $T^{WW} \in [35^oC,80^oC]$, $T^{HW} \in [35^oC,110^oC]$). CW, WW and HW discharge heat to SW-Sink becoming 35^oC cold utilities.

V.2.4. CO_2 Refrigeration-Cycle

The 2nd SS unit for CO_2 removal (Sec. V.3.5) uses a CO_2 refrigeration-cycle for partial CO_2 condensation at $T=-20^oC$ from $\approx 68\%mol\ CO_2$ Dry-Gas reducing $\%CO_2$ of SS feed to $\approx 45\%mol$. It boils liquid CO_2 at $T=-25^oC$ and condenses CO_2 vapor at $T=0^oC$ in a coil on LTX cooled by water-C3+ condensate ($T=-17^oC$) from 1st SS unit.

V.2.5. Process Evaluation

Process net present value (*NPV,USD*) follows (Turton et al., 2009) with Fixed Capital Investment (*FCI,USD*) from equipment sizes. Revenues (*REV,USD/y*) comprise: Fuel-Gas for power production; incremental oil above lowest oil production at *45 USD/bbl*; and EOR-Fluid. EOR yield of pure CO_2 for Texas-US mature fields is $0.6\text{-}2.6\ bbl/t^{CO2}$ (McCoy, 2008). Here, oil field is young and EOR-Fluid ($\approx 71\%molCO_2$) has higher yield. Thus, $1\ bbl/t^{CO2}$ is conservatively chosen giving EOR-Fluid at *45 USD/t*. Investment and costs of membrane units were estimated with data from Merkel et al. (2012). Appendix M details formulas and assumptions.

V.3. Sub-Flowsheet Description

Oil-gas processing has five sections: (i) Oil-Gas-Water Separation; (ii) Gas Expansion; (iii) Gas Dehydration; (iv) Fuel-Gas Preparation; and (v) EOR Compression-Pumping. 2nd and 4th sections have one variant each giving seven sub-flowsheets: Plants A to G.

Two conventions are adopted: (i) thermal utilities CW/WW/HW/PHW/TF are identified *only at the hotter state in exchangers* – cooling utilities at outlets, heating utilities at inlets; (ii) compressor-block (Fig. V.2) unites compressor-stage, intercooler, knock-out vessel and driver – ED $\in$*[0,13MW]*, GT $\in$*[13MW,28MW]* or turbo-expander (TX) – and indicates the created hot utility (CW/WW/HW) depending on gas temperature.

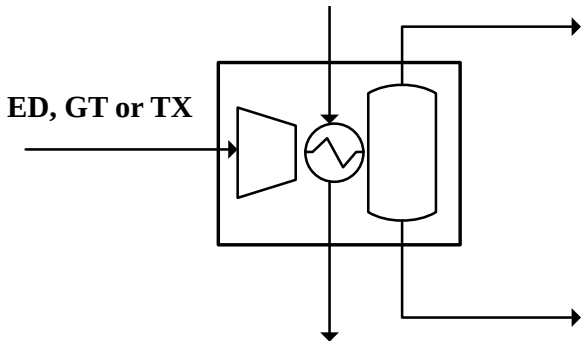

Figure V. 2. Compressor-block: compressor, driver, intercooler, hot utility and vessel.

V.3.1. Plant A – Oil-Gas-Water Separation

Plant A (Fig. V.3) splits oil-gas-water with three separators: High-Pressure Separator (HPS) (*P=120 bar*, *T=30^{o}C*) splitting oil/gas/water; Medium-Pressure Separator (MPS) (*P=20 bar*, *T=90^{o}C*) and Low-Pressure Separator (LPS) (*P=1.8 bar*, *T≈90^{o}C*) both splitting oil/gas. The multiphase feed (*P=120.5 bar*, *T=16^{o}C*) is heated to *T=30^{o}C* to avoid hydrates and feeds the HPS, where water is collected, HPS-Gas is dispatched to gas processing and HPS-Oil goes to heating to *T=90^{o}C* and expansion to *P=20 bar*, producing MPS-Gas. MPS-Oil expands to *P=1.8 bar* producing LPS-Gas. LPS-Gas and MPS-Gas are compressed to *P=80 bar* in the vapor recompression unit (VRU) with four stages and follow to gas processing. Stabilized oil is cooled down with HPS-Oil.

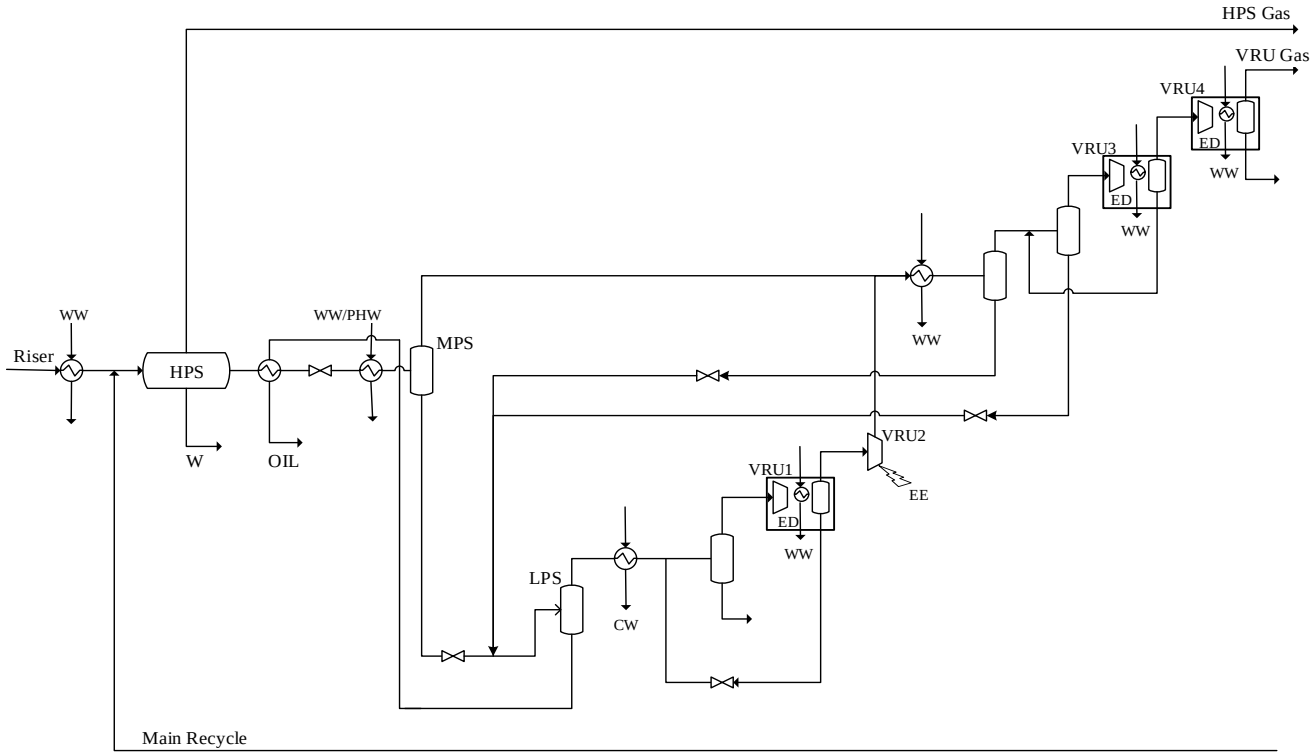

Figure V. 3. Plant A: Oil-Gas-Water separation (EE≡electric-energy).

V.3.2. Plant B – HPS-Gas Joule-Thomson Expansion

HPS-Gas is expanded to *80 bar* for SS operation. Fig. V.4 shows its JT-Expansion after pre-heating ($T=65.5^oC$) to avoid hydrates. Expanded HPS-Gas is united with VRU-Gas.

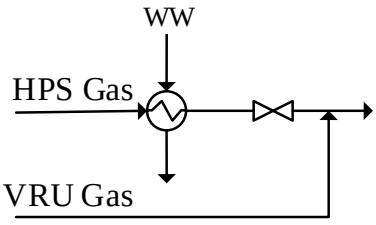

Figure V. 4. Plant B: HPS-Gas JT-Expansion (VRU≡Vapor-Recovery-Unit).

V.3.3. Plant C – HPS-Gas Expansion via Turbo-Expander (TX)

HPS-Gas expansion to *P=80 bar* is also done via Plant C (Fig. V.5), a power-producing alternative to Plant B. As TX power is nearly proportional to inlet absolute temperature, HPS-Gas is pre-heated to $T=350^oC$ via serial heating by HW, PHW and TF, while the still hot

(*T≈323ºC*) expanded HPS-Gas is cooled down to *T=45ºC* by cold utilities (*T=35ºC*) producing hot utilities PHW and HW.

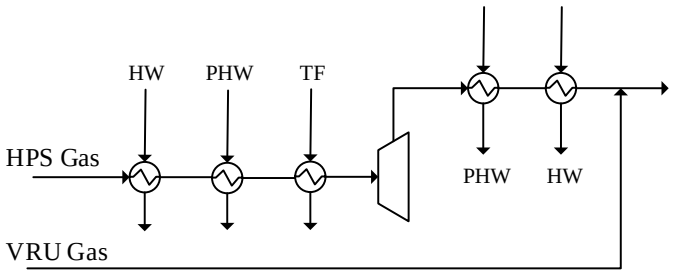

Figure V. 5: HPS-Gas expansion in turbo-expander (TX).

V.3.4. Plant D – 1st SS Unit for WDPA+HCDPA

Fig. V.6 sketches Plant D for WDPA+HCDPA of raw NG from Plants B/C. The 1st SS unit prescribes a LTX to collect water-C3+ condensate from SS's. LTX is heated to keep bottoms warm (*≈20ºC*) avoiding hydrates, releasing a top Slip-Gas after direct contact with cold water-C3+ condensate. The 1st SS unit is fed with gas (*P=80 bar, T=45ºC*) from Plants B/C after a pre-flash. The 1st SS unit has 12 SS's to treat its huge gas feed, promoting WDPA (from *≈2700 ppm* to *≈100 ppm* water) and HCDPA (*-17ºC@54bar*). SS's operate with a not too high *Ma* at pre-shock ($Ma^{Shock}=1.52$), but there is a high water-C3+ condensed fraction of *≈9.3%mol*. This lowers *Ma* after condensate ejection leading to normal shock at lower supersonic *Ma* ($Ma_{BS}=1.31$) and, consequently, to a final Lean-Gas at $P^{Discharge}\approx 54$ *bar* with pressure recovery of *66.76%* (Sec. V.5). Lean-Gas from SS's (*P≈54 bar, T≈38ºC*) incorporates the Slip-Gas from LTX creating the Dry-Gas (DHG) which feeds the DHG-Header. In alternatives with Plant E (Fig. V.7), a CO_2 refrigeration-cycle is installed to absorb heat at *T=-25ºC* cooling down Dry-Gas (*≈68%mol* CO_2) to *T=-20ºC*, partially condensing CO_2 such that the SS feed in Plant E has *≈45%mol* CO_2. This refrigeration-cycle has a high coefficient of performance (*≈8*) as it rejects heat at only *T=0ºC*. Therefore the LTX heat demand (Fig. V.6) offers an opportune cold sink to the refrigeration-cycle condenser on LTX top. This sink is the cold water-C3+ condensate from SS (*T≈-17ºC*). The pre-flash and LTX liquids are recycled to Plant A in alternatives with RC option, while in the only alternative without recycle, LTX liquids pass through a Liquid/Liquid Separator (LLS), to split water, and the humid C3+ liquid is sent with pre-flash liquid to EOR pump in Plant G.

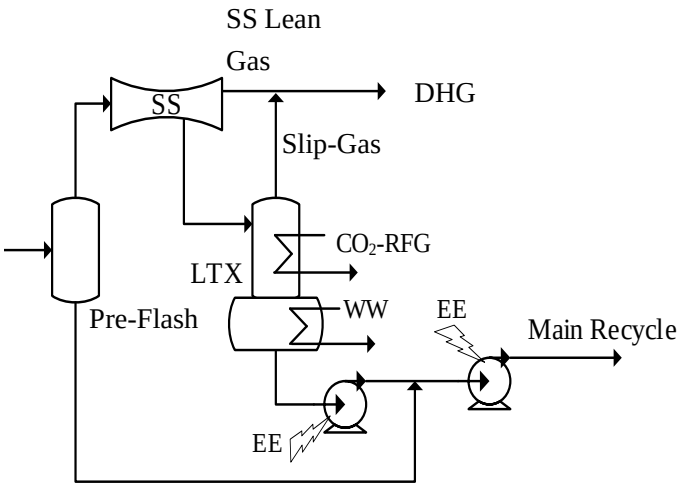

Figure V. 6. Plant D: 1st SS unit for WDPA+HCDPA (DHG≡Dry-Gas; EE≡Electricity).

V.3.5. Plant E – 2nd SS Unit for CO_2 Removal and Fuel-Gas Production

About *≈4%* of Dry-Gas (*≈68%mol* CO_2) from Plant D is slipped to produce Fuel-Gas (*≈20%mol* CO_2) for shaft-power in electric turboshafts and GT drivers. As proved in Arinelli et al. (2017), it is possible to abate $\%CO_2$ to *≈20%mol* via SS, provided SS feed has *P≈84 bar*, *T≈-22°C* and less than *≈45%mol* CO_2. Plant E, 2nd SS unit, in Fig. V.7 is conceived for such SS CO_2 removal using Arinelli et al. (2017) scheme. Firstly, the slipped Dry-Gas (*P≈54 bar*, *T≈38°C*) is cooled down to *-20°C* via cold recovery exchangers and CO_2 refrigeration-cycle absorbing heat at *T=-25°C*. At *P≈50 bar* and *T=-20°C*, CO_2 condenses from Dry-Gas reducing $\%CO_2$ from *≈68%mol* to *≈45%mol*. The collected CO_2-rich liquid is expanded to *P=10 bar* – above the triple-point pressure (*5.2 bar*) to avoid dry-ice – creating a two-phase cold stream (*T≈-40°C*) to pre-cool slipped Dry-Gas reducing refrigeration load. After heated at *P=10 bar*, this CO_2-rich stream becomes vapor (GFLS), being compressed (*P≈54 bar*) and returning to DHG-Header. The pre-decarbonated slipped Dry-Gas *(≈45%mol* CO_2, *P≈50 bar*) is compressed, pre-cooled with CW and cooled with SS outlet-gas (*P≈36 bar, T≈-28°C*) and CO_2-rich SS condensate (*P≈36 bar, T≈-61°C*), becoming ready as SS feed (*P=84 bar, T=-22°C*) to lose more CO_2 exiting as Fuel-Gas (*≈20%mol* CO_2). The 2nd SS unit operates with a limited pre-shock *Ma* ($Ma^{Shock}=1.6$) to avoid crossing the SVLE CO_2 freeze-out border inside the feed VLE envelope, which would create dry-ice (Arinelli et al., 2017). This explains why the 2nd SS unit can only reduce $\%CO_2$ to *≈20%mol*. Moreover, a high condensed fraction (*≈37.1%mol*) is ejected as cold liquid (*T≈-*

61°C) with *≈85%mol* CO_2, lowering *Ma* after ejection to a subsonic value ($Ma_{BS}=0.9651$), implying absence of normal shock in 2nd SS unit and hampering gas recompression. Consequently, 2nd SS unit discharges gas at $P^{Discharge}=36.58$ *bar* (*T≈-28°C*) with pressure-recovery of *43.55%*. After cooling the SS feed, the SS condensate (*85%mol* CO_2) is two-phase. It is flashed (*P≈36.1 bar*) separating liquid (LCO2) directed to EOR-pump, and gas (GCO2) compressed and returned to DHG-Header (*P≈54 bar, T≈38°C*), creating MC-Gas to the Main Compressor (Plant G).

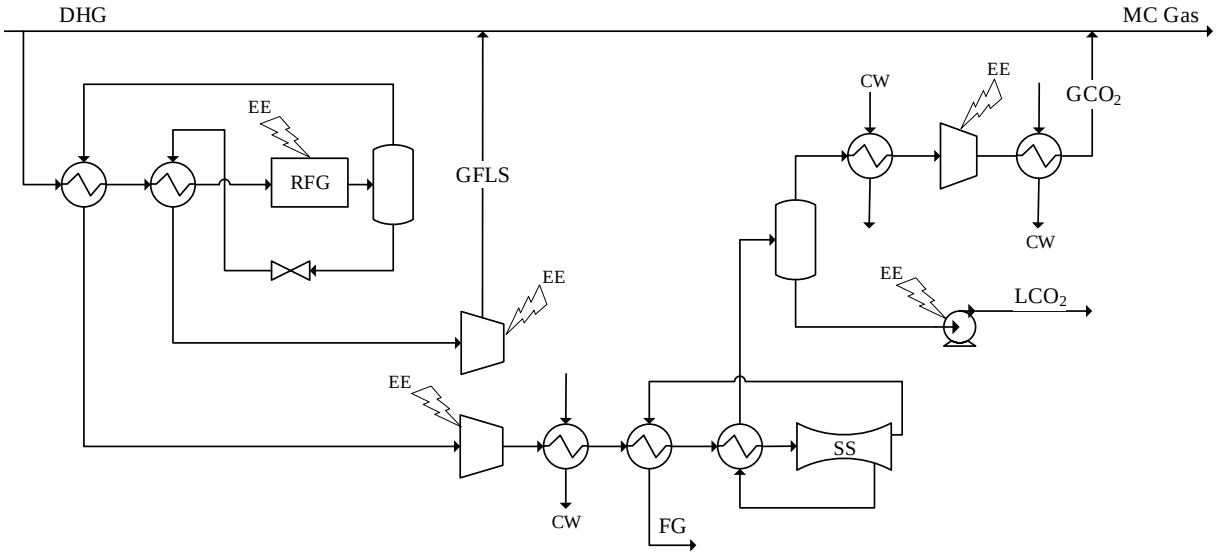

Figure V. 7. Plant E: 2nd SS unit for CO_2 removal (FG≡Fuel-Gas; DHG≡Dry-Gas).

V.3.6. Plant F – Membrane-Permeation CO_2 Removal for Fuel-Gas Production

Membrane-Permeation CO_2 capture (Fig. V.8) is classical in offshore rigs (Araújo et al., 2017). It is alternative to Plant E and is fed with *≈4%* of Dry-Gas (*≈68%mol* CO_2, *P≈54 bar, T≈38°C*). Dry-Gas expands to *P≈44.5 bar* ($PP_{CO2}\in[0,30bar]$) and is heated (*T=62°C*) to feed Membrane-Permeation. The retentate is Fuel-Gas (*≈20%mol* CO_2) and the permeate is CO_2-rich gas (*P=8 bar*), which is double-compressed returning to DHG-Header (*P≈54 bar, T≈38°C*), creating MC-Gas to Main-Compressor (Plant G).

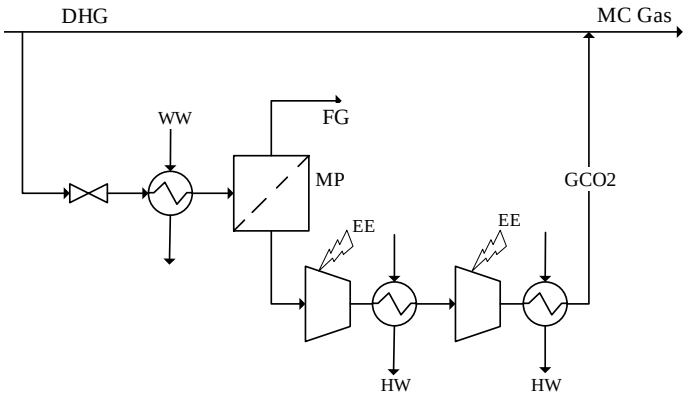

Figure V. 8. Plant F: Membrane-Permeation CO_2 removal (FG≡Fuel-Gas; DHG≡Dry-Gas).

V.3.7. Plant G – Main-Compressor and EOR-Pump

The critical unit of Plant G (Fig. V.9) is the Main-Compressor, fed by MC-Gas (Dry-Gas and CO_2-rich gas from Plants E/F). Main-Compressor has four shafts (one shaft shown in Fig. V.9) spinning two centrifugal stages each, accompanied by a 5^{th} spare shaft with two wheels. It compresses *≈43 MMsm^3/d* from *P≈54 bar* to *P=240 bar*. As each shaft-power exceeds electric-driver capacity (ED$\in$*[0,13MW]*), all shafts adopt gas-turbine drivers (GT$\in$*[13MW,28MW]*). In alternatives with Plant C, TX drives one of the four shafts, but as TX exceeds the requirements of two wheels, an electric generator is also on TX shaft to absorb the excess. TX has no spare driver; if it collapses, TX shaft is replaced by the 5^{th} spare GT-driven shaft and Plant C is replaced by the simpler Plant B with JT-Expansion. At *T=45^{o}C* Main-Compressor effluent is a liquid exiting the last knock-out vessel. It is mixed with CO_2-rich liquids (LCO2/LIQ) and compressed by electric-driven EOR-Pump to *P=450 bar* without after-cooling.

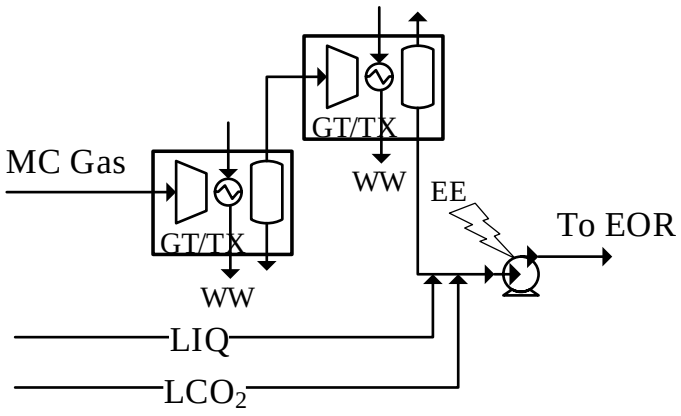

Figure V. 9. Plant G: Main-Compressor and EOR-Pump (EE≡Electricity; MC-Gas≡Main-Compressor-Gas).

V.4. Gas-Hub Processing Alternatives

Four alternatives were assembled in Fig. V.10 where blocks A, B, C, D, E, F and G correspond to Plants A to G discussed in Sec. V.3. The four alternatives were created choosing: (i) Plant B (JT-Expansion) or Plant C (TX) for expanding HPS-Gas; (ii) Plant E (SS) or Plant F (Membrane-Permeation) for CO_2 capture producing Fuel-Gas; and (iii) recycling (RC) or not recycling (NR) SS condensate from Plant D to Plant A. The Base-Case selects Plants A, B, D, E, G, with recycle. It is denominated [RC+JT+SS] (Fig. V.10a) with thermal utilities CW/WW/HW/PHW produced or allocated, where applicable.

The 1st variant replaces Plant B by Plant C (TX) converting heat into power. It is denominated [RC+TX+SS] (Fig. V.10b). The gain is less power consumption, despite greater complexity. Economic analysis unveils overall gain/loss.

The 2nd variant dismisses the water-C3+ condensate recycle from Plant D to A, pumping this liquid, after water separation, to EOR. It is denominated [NR+JT+SS] (Fig. V.10c). Water is segregated in separator LLS, so that only C3+ (LIQ) goes to EOR. Eliminating recycle is positive to Plants A, B and D by lowering process load, reducing equipment and power consumption. However, not recycling condensate is negative to oil production, the economically interesting factor. Economic analysis unveils whether reducing investment and costs of Plants A, B and D compensates lower revenues.

The 3rd variant replaces SS CO_2 removal (Plant E) by Membrane-Permeation CO_2 removal (Plant F). It is denominated [RC+JT+MP] (Fig. V.10d). Plant F is simpler than Plant E, however, the low-pressure CO_2-rich permeate requires compressors, while the CO_2-rich effluents from Plant E are at high-pressure and partially liquefied. Again, economic analysis reveals the best long-term option.

a)

b)

c)

d)

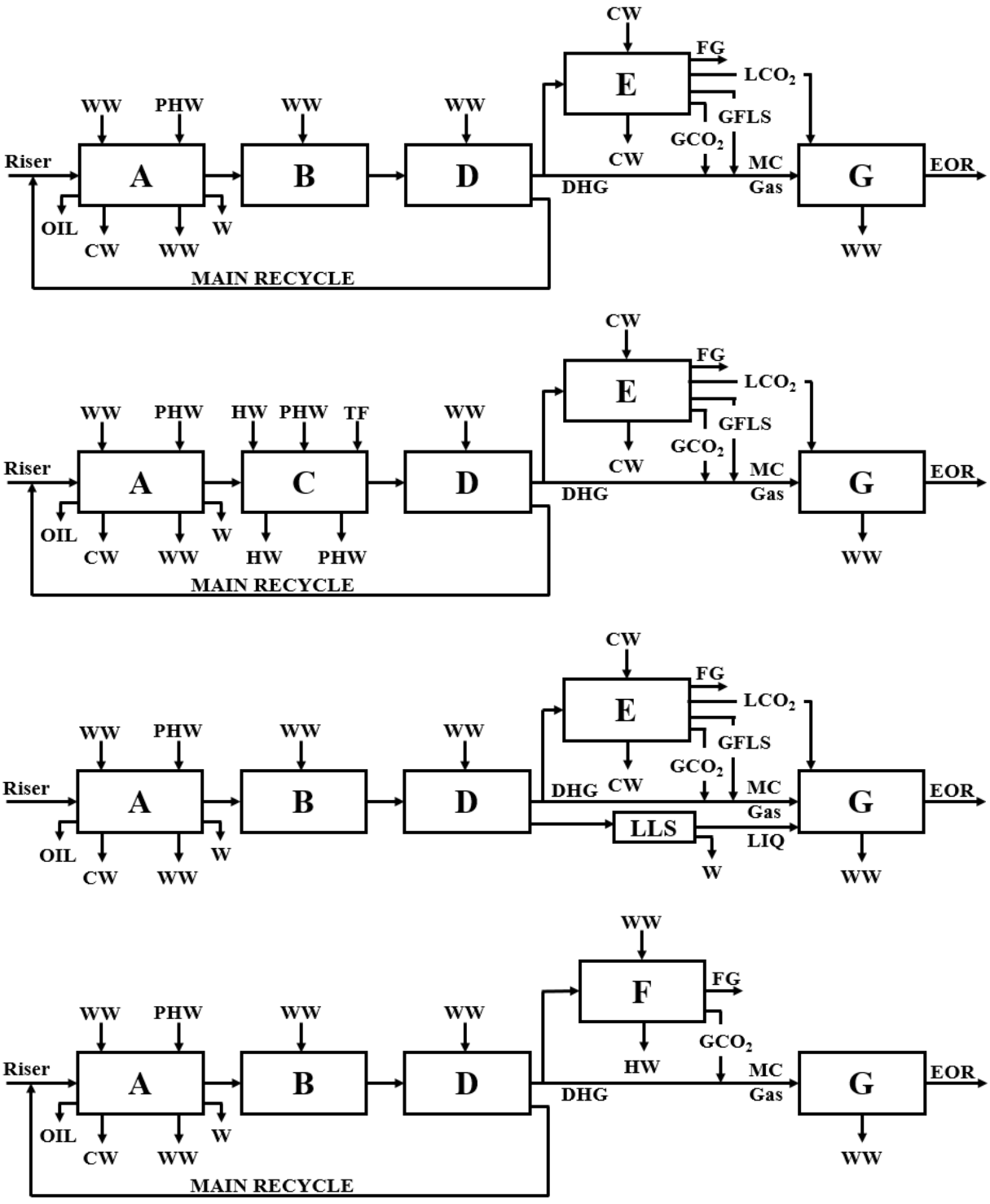

Figure V. 10. Gas-Hub processing alternatives: a)[RC+JT+SS](Base-Case), b)[RC+TX+SS], c)[NR+JT+SS], d)[RC+JT+MP] (FG≡Fuel-Gas; DHG≡Dehydrated-Gas; CW≡Cooling-Water; WW≡Warm-Water; HW≡Hot-Water; PHW≡Pressurized-Hot-Water; TF≡Thermal-Fluid; MC-Gas≡Main-Compressor-Gas).

V.5. Results

Base-Case [RC+JT+SS] and three alternatives – [RC+TX+SS], [NR+JT+SS], [RC+JT+MP] – were simulated with the respective HYSYS flowsheets in Figs. O.1, O.2, O.3 and O.4 (Supplementary Materials – Appendix O). Detailed numerical and graphical results – Table V.3 of process streams, Table V.4 of SS designs and results, Fig. V.11 of SS profiles of 1st SS unit (HCDPA+WDPA), Fig. V.12 of SS profiles of 2nd SS unit (CO_2 removal) and Fig. V.13 with SS paths of 1st SS and 2nd SS units on plane $T\,x\,\overline{S}$ – are presented only for the Base-Case [RC+JT+SS]. Table V.3 analogues for alternatives are found in Supplement (Appendix P) – Table P.1 ([RC+TX+SS]), Table P.2 ([NR+JT+SS]) and Table P.3 ([RC+JT+MP]). Table V.4 analogues for alternatives are found in Supplement (Appendix Q) – Table Q.1 ([RC+TX+SS]), Table Q.2 ([NR+JT+SS]), and Table Q.3 ([RC+JT+MP]). Fig. V.11 analogues for alternatives are found in Supplement (Appendix R) – Fig. R.1 ([RC+TX+SS]), Fig. R.2 ([NR+JT+SS]) and Fig. R.3 ([RC+JT+MP]). At last, Fig. V.12 analogues for alternatives are found in Supplement (Appendix S) – Fig. S.1 ([RC+TX+SS]) and Fig. S.2 ([NR+JT+SS]) only, as [RC+JT+MP] does not have 2nd SS unit. Supplements are in the Supplementary Materials (Appendix O to Appendix S). Their objects are analogues of the ones analyzed in Sec. V.5.1 and are not commented. However, there is an exception in Figs. S.2a and S.2d, whose vapor-fraction profiles in 2nd SS unit of [NR+JT+SS] start with *100%* at SS inlet, radically distinct from analogous Figs. V.12a, V.12d, S.1a and S.1d of [RC+JT+SS] and [RC+TX+SS]. This occurs because SS flow paths of Figs. V.12 and S.1 start in the critical neighborhood on the bubble curve (*0%* vapor), while in Fig. S.2 it starts also in the critical neighborhood, but on the dew curve (*100%* vapor). These SS inlet states are proximate and thermodynamically similar, though with nominally distinct vapor-fractions.

V.5.1. Base-Case [RC+JT+SS]

Base-Case has a 1st SS unit for HCDPA+WDPA producing Dry-Gas. It is followed by a 2nd SS unit for removing CO_2 from Dry-Gas producing Fuel-Gas. [RC+JT+SS] produces *≈123000 bbl/d* of *37.91°API* oil from the riser feed, both in Table V.3. Several other streams are shown: EOR-Fluid and Fuel-Gas – whose flow rate matches power demand – and the feed, gas and condensates of 1st and 2nd SS units.

The 1st SS unit produces Dry-Gas reducing water from saturation to *95.90 ppm* and *C3+* from *4.83%mol* to *2.15%mol*. The SS two-phase water-C3+ condensate goes to LTX. Since there is no Slip-Gas from LTX, the LTX bottoms have the same composition of SS water-C3+ cold condensate (Table V.3). The 2nd SS unit removes CO_2 from Dry-Gas as a CO_2-rich condensate (*≈85%mol* CO_2) producing Fuel-Gas (*≈22%mol* CO_2) for power generation in turboshafts and gas-turbines. EOR-Fluid represents the union of Dry-Gas and CO_2-rich streams from 2nd SS unit, with matched specifications (*≈71%mol* CO_2*, 98.39 ppm* H_2O). Table V.4 shows SS design and results obtained by SS-UOE for 1st and 2nd SS units. Raw NG demands a large 1st SS unit for WDPA/HCDPA with 12 SS's, while 2nd SS unit has only a single SS without LTX, as its feed is a small slip-stream from Dry-Gas. Feed composition of 2nd SS unit differs from Dry-Gas, thanks to partial condensation of CO_2 in Plant E, reducing *%* CO_2 from *≈68%mol* to *≈45%mol* in SS feed, allowing 2nd SS unit to produce *≈22%mol* Fuel-Gas without CO_2 freeze-out.

Table V. 3. Gas-hub streams for CO_2 ultra-rich NG: Base-Case [RC+JT+SS].

System	***HPS***				***Oil***	***VRU***	***SS WDPA+HCDPA***				***SS CO_2 Removal***				***Main Compressor***		***EOR***
Stream	*Riser*	*Main Recycle*	*HPS Water*	*HPS Gas*	*Final Oil*	*VRU Gas*	*Feed*	*Gas SS*	*L+W SS*	*L+W LTX*	*Feed*	*FG*	*GCO2*	*LCO2*	*DHG*	*MC Gas*	*Final Fluid*
T(°C)	*30.0*	*36.4*	*32.5*	*32.5*	*42.5*	*45.0*	*46.3*	*37.7*	*-17.0*	*20.0*	*-22.0*	*35.0*	*45.0*	*16.3*	*37.7*	*38.0*	*80.2*
P(bar)	*120.0*	*120.0*	*120.0*	*120.0*	*1.30*	*80.50*	*80.50*	*53.74*	*53.74*	*53.74*	*84.00*	*36.08*	*53.74*	*240.0*	*53.74*	*53.74*	*450.0*
MMsm^3/d	*90.15*	*8.31*	*36.76*	*52.24*	*2.00*	*7.44*	*56.68*	*51.39*	*5.29*	*5.29*	*2.07*	*1.30*	*0.63*	*0.14*	*42.71*	*49.96*	*50.09*
%Vapor	*53.20*	*0.00*	*0.00*	*100*	*0.00*	*100*	*100*	*100*	*0.00*	*0.00*	*23.31*	*100*	*100*	*0.00*	*100*	*100*	*0.00*
%CO_2	*39.72*	*54.39*	*0.13*	*67.31*	*0.64*	*68.51*	*68.52*	*69.57*	*58.39*	*58.39*	*45.34*	*21.85*	*83.50*	*92.90*	*69.57*	*70.74*	*70.80*
%CH_4	*14.59*	*6.91*	*0.00*	*23.55*	*0.05*	*19.12*	*23.70*	*25.60*	*5.20*	*5.20*	*51.02*	*74.73*	*12.59*	*2.62*	*25.60*	*24.38*	*24.32*
%C_2H_6	*1.36*	*2.76*	*0.00*	*2.34*	*0.09*	*3.15*	*2.43*	*2.39*	*2.85*	*2.85*	*2.18*	*2.06*	*2.52*	*1.74*	*2.39*	*2.40*	*2.40*
%C_3H_8	*0.75*	*4.81*	*0.00*	*1.62*	*0.46*	*2.89*	*1.69*	*1.29*	*5.55*	*5.55*	*0.59*	*0.25*	*1.04*	*1.67*	*1.29*	*1.32*	*1.32*
%i-C_4H_{10}	*0.13*	*1.97*	*0.00*	*0.41*	*0.37*	*0.80*	*0.41*	*0.21*	*2.32*	*2.32*	*0.06*	*0.01*	*0.10*	*0.29*	*0.21*	*0.22*	*0.22*
%C_4H_{10}	*0.29*	*6.04*	*0.00*	*1.08*	*1.64*	*2.25*	*1.06*	*0.44*	*7.07*	*7.07*	*0.09*	*0.01*	*0.14*	*0.57*	*0.44*	*0.46*	*0.46*
%i-C_5H_{12}	*0.09*	*3.25*	*0.00*	*0.47*	*1.88*	*0.91*	*0.42*	*0.09*	*3.60*	*3.60*	*0.01*	*0.00*	*0.01*	*0.09*	*0.09*	*0.09*	*0.09*
%C_5H_{12}	*0.14*	*5.09*	*0.00*	*0.72*	*3.71*	*1.32*	*0.60*	*0.10*	*5.47*	*5.47*	*0.01*	*0.00*	*0.01*	*0.08*	*0.10*	*0.10*	*0.10*
%C_6H_{14}	*0.15*	*3.67*	*0.00*	*0.53*	*5.80*	*0.51*	*0.32*	*0.02*	*3.28*	*3.28*	*0.00*	*0.00*	*0.00*	*0.01*	*0.02*	*0.02*	*0.02*
%C_7H_{16}	*0.21*	*2.41*	*0.00*	*0.37*	*8.81*	*0.09*	*0.16*	*0.00*	*1.65*	*1.65*	*0.00*	*0.00*	*0.00*	*0.00*	*0.00*	*0.00*	*0.00*
%C_8H_{18}	*0.23*	*2.12*	*0.00*	*0.33*	*10.10*	*0.02*	*0.10*	*0.00*	*1.03*	*1.03*	*0.00*	*0.00*	*0.00*	*0.00*	*0.00*	*0.00*	*0.00*
%C_9H_{20}	*0.18*	*1.38*	*0.00*	*0.22*	*8.18*	*0.00*	*0.04*	*0.00*	*0.44*	*0.44*	*0.00*	*0.00*	*0.00*	*0.00*	*0.00*	*0.00*	*0.00*
%$C_{10}H_{22}$	*0.16*	*0.97*	*0.00*	*0.15*	*7.35*	*0.00*	*0.02*	*0.00*	*0.20*	*0.20*	*0.00*	*0.00*	*0.00*	*0.00*	*0.00*	*0.00*	*0.00*
%$C_{11}H_{24}$	*0.11*	*0.65*	*0.00*	*0.10*	*4.90*	*0.00*	*0.01*	*0.00*	*0.08*	*0.08*	*0.00*	*0.00*	*0.00*	*0.00*	*0.00*	*0.00*	*0.00*
%$C_{12}H_{26}$	*0.13*	*0.53*	*0.00*	*0.08*	*5.93*	*0.00*	*0.00*	*0.00*	*0.04*	*0.04*	*0.00*	*0.00*	*0.00*	*0.00*	*0.00*	*0.00*	*0.00*
%$C_{13}H_{28}$	*0.09*	*0.35*	*0.00*	*0.06*	*3.96*	*0.00*	*0.00*	*0.00*	*0.02*	*0.02*	*0.00*	*0.00*	*0.00*	*0.00*	*0.00*	*0.00*	*0.00*
%$C_{14}H_{30}$	*0.12*	*0.28*	*0.00*	*0.04*	*5.21*	*0.00*	*0.00*	*0.00*	*0.01*	*0.01*	*0.00*	*0.00*	*0.00*	*0.00*	*0.00*	*0.00*	*0.00*
%$C_{15}H_{32}$	*0.07*	*0.17*	*0.00*	*0.03*	*3.13*	*0.00*	*0.00*	*0.00*	*0.00*	*0.00*	*0.00*	*0.00*	*0.00*	*0.00*	*0.00*	*0.00*	*0.00*
%$C_{16}H_{34}$	*0.05*	*0.11*	*0.00*	*0.02*	*2.08*	*0.00*	*0.00*	*0.00*	*0.00*	*0.00*	*0.00*	*0.00*	*0.00*	*0.00*	*0.00*	*0.00*	*0.00*
%$C_{17}H_{36}$	*0.07*	*0.09*	*0.00*	*0.01*	*3.25*	*0.00*	*0.00*	*0.00*	*0.00*	*0.00*	*0.00*	*0.00*	*0.00*	*0.00*	*0.00*	*0.00*	*0.00*
%$C_{18}H_{38}$	*0.04*	*0.05*	*0.00*	*0.01*	*1.95*	*0.00*	*0.00*	*0.00*	*0.00*	*0.00*	*0.00*	*0.00*	*0.00*	*0.00*	*0.00*	*0.00*	*0.00*
%$C_{19}H_{40}$	*0.03*	*0.12*	*0.00*	*0.02*	*1.30*	*0.00*	*0.00*	*0.00*	*0.00*	*0.00*	*0.00*	*0.00*	*0.00*	*0.00*	*0.00*	*0.00*	*0.00*
%C_{20+}	*0.43*	*0.01*	*0.00*	*0.00*	*19.21*	*0.00*	*0.00*	*0.00*	*0.00*	*0.00*	*0.00*	*0.00*	*0.00*	*0.00*	*0.00*	*0.00*	*0.00*
%N_2	*0.15*	*0.03*	*0.00*	*0.25*	*0.00*	*0.12*	*0.25*	*0.27*	*0.02*	*0.02*	*0.71*	*1.09*	*0.07*	*0.01*	*0.27*	*0.25*	*0.25*
ppm H_2S	*29.65*	*81.91*	*0.00*	*51.57*	*4.21*	*85.63*	*55.08*	*51.61*	*88.83*	*88.83*	*28.56*	*12.57*	*52.34*	*70.94*	*51.61*	*52.57*	*52.52*
ppmH_2O		*18396*		*2584*	*18.93*	*2972*	*2666*	*95.90*	*27651*	*27651*	*7.93*	*0.06*	*6.58*	*88.66*	*95.90*	*98.41*	*98.39*
%H_2O	*40.70*	*1.84*	*99.87*			*0.297*	*0.267*		*2.765*	*2.765*							

L+W ≡ water-C3+; DHG≡Dehydrated Gas; FG≡Fuel-Gas; HPS≡High-Pressure Separator; MC-Gas≡Main-Compressor-Gas; VRU≡Vapor-Recovery-Unit

Table V. 4. SS design parameters and results of 1st (WDPA+HCDPA) and 2nd (CO_2 removal) SS units of Base-Case [RC+JT+SS].

Specified Items	***WDPA HCDPA***	***CO_2 Removal***	***Calculated by SS-UOE***	***WDPA HCDPA***	***CO_2 Removal***
No.of SS	*12*	*1*	$D_T(m)$	*0.0662*	*0.03573*
$D_I(m)$	*0.10*	*0.08*	$L_C(m)$	*0.0752*	*0.1573*
$D_O(m)$	*0.12*	*0.09*	$L_D(m)$	*0.1486*	*0.6219*
$\alpha(^o)$	*12.67*	*15*	$L(m)$	*0.2238*	*0.7792*
$\beta(^o)$	*2.66*	*2.5*	$L^{Shock}(m)$	*0.1596*	*0.2560*
Ma^{Shock}	*1.52*	*1.6*	$L^{Diff}(m)$	*0.0642*	*0.5232*
$\eta^{EXP}\%$	*100*	*100*	$P_{BS}(bar)$	*25.60*	*21.70*
$\eta^{CMP}\%$	*100*	*100*	$T_{BS}(^oC)$	*-16.78*	*-61.10*
$P^{Feed}(bar)$	*80.5*	*84.0*	Ma_{BS}	*1.3114**	*0.9651*$^{*+}$
$T^{Feed}(^oC)$	*45*	*-22*	$P^{Discharge}(bar)$	*53.74*	*36.58*
$MMsm^3/d$	*56.7*	*2.07*	$T^{Discharge}(^oC)$	*37.73*	*-28.55*
$\%C3^{+Feed}$	*4.83%*	*0.75%*	*%Condensate*	*9.33%*	*37.10%*
$ppmH_2O^{Feed}$	*2666*	*7.93*	$REC\%CO_2$	*7.95%*	*69.69%*
$\%CO_2^{Feed}$	*68.52%*	*45.34%*	*%P Recovery*	*66.76%*	*43.55%*

**After condensate withdrawal.* $^+$*No normal shock.*

V.5.1.1. 1st SS Unit

The 1st SS unit of [RC+JT+SS] executes HCDPA+WDPA in 12 SS's with sizes in Table V.4. SS's have throat diameter $D_T=66.2mm$ at $L_C=75.2mm$, maximum $Ma=Ma^{Shock}=1.52$ at $L^{Shock}=159.6mm$, *Ma* before-shock after condensate withdrawal $Ma_{BS}=1.3114$ and normal shock at $L^{Shock}=159.6mm$. SS's recover *66.76%* of pressure and condense *9.33%mol* of feed as water-C3+ condensate at $T_{BS}=-16.78^oC$, capturing *7.95%* of CO_2. Fig. V.11 depicts SS operation showing recognizable SS signatures. SS signatures – Eqs. (L.2)/(L.3), Appendix L – are rigorous graphical "fingerprints" of SS profiles which were proved (De Medeiros et al., 2017) for SS nozzles with $\frac{dA}{dx} \neq 0$ at the throat (e.g., Fig. V.1), where *A* and *x* are flow-section area and SS axial position. Fig. V.11a depicts SS axial profiles of nozzle walls and vapor-fraction. Fluid is *100%* vapor at inlet and *90.67%* vapor at pre-shock ($x=L^{Shock}=0.1596\ m$), where $Ma=Ma^{Shock}=1.52$. water-C3+ condensate is removed at this point decreasing *Ma* under constant (*T*,*P*) to $Ma=Ma_{BS}=1.3114$, when shock happens and vapor becomes superheated. Fig. V.11b depicts *P* and *Ma* axial profiles with SS signatures $dP/dx=-\infty$, $dMa/dx=+\infty$ at throat ($Ma\rightarrow 1^-$). Pre-shock ($Ma=Ma^{Shock}=1.52$) minimal pressure is $P=P_{BS}=25.6\ bar$ and

$P^{Discharge}=53.74\ bar$. water-C3+ removal does not affect (*T*,*P*), but decreases *Ma* from $Ma^{Shock}=1.52$ to $Ma_{BS}=1.3114$, which subsequently vertically falls at normal shock to $Ma_{AS}=0.8$.

Fig. V.11c depicts *T* and *c* axial profiles also with SS signatures $dT/dx=-\infty$, $dc/dx=-\infty$ at throat ($Ma\rightarrow 1^{-}$). Pre-shock ($Ma=Ma^{Shock}=1.52$) minimal temperature is $T=T_{BS}=-16.78^{o}C$ and $T^{Discharge}=37.73^{o}C$. Here two remarks are necessary. Firstly, SS signatures of Eq. (V.A.2), confirmed in Figs. V.11b/V.11c, are rigorous features of single-phase or multiphase equilibrium compressible flow through SS nozzles with $\left(\frac{dA}{dx}\right)^{Throat} \neq 0$ (De Medeiros et al., 2017). Secondly, the two small sudden falls of *c* (Fig. V.11c) at $x\approx 0^{+}m$ and $x\approx 0.03m$ demand explanation: Single-phase or multiphase equilibrium property *c* is inversely impacted by multiphase density and isothermal compressibility $\Xi_P=(\partial\rho/\partial P)_{T,\underline{Z}}$, and it is easy to see that both increase sharply at $x\approx 0^{+}m$ and $x\approx 0.03m$, in the first case due to liquid appearance as the HCDP is crossed at $x\approx 0^{+}m$ (Figs. V.11d/V.11f) and in the second case due to water condensation starting at $x\approx 0.03m$ (Figs. V.11d/V.11c/V.11f) as WDP is crossed. Just after the throat, *T* and *c* profiles fall monotonously until pre-shock at $x=0.1596m$, where water condensation is almost total. Fig. V.11d shows that *7.95%* of CO_2 and *≈10%* of hydrocarbons condensed, where only the nozzle length upstream the pre-shock is portrayed because condensate is collected at this point with $T_{BS}=-16.78^{o}C$.

Fig. V.11e reveals no risks of CO_2 freeze-out in 1st SS unit and depicts the influence of Ma^{Shock} on pre-withdrawal vapor-fraction, $\%CO_2$ in final gas and Ma_{BS}. It shows that 1st SS unit has no practical effect on final $\%CO_2$, but pre-withdrawal condensate can be boosted by increasing Ma^{Shock} and, due to high water-C3+ condensation, *Ma* after condensate withdrawal (Ma_{BS}) is lesser than Ma^{Shock} negatively impacting pressure recovery. The SVLE CO_2 freeze-out border is located deep inside the feed VLE *PxT* envelope (Fig. V.11f). Actually, the grand freeze-out border is the union of three freeze-out borders: (i) quasi-vertical Solid-Liquid-Equilibrium locus on the left outside the VLE envelope; (ii) highly inclined SVLE locus below $-60^{o}C$ within the VLE envelope; and (iii) Solid-Vapor-Equilibrium locus on the right outside the VLE envelope. Only the SVLE freeze-out border is located in Fig. V.11f (using HYSYS freeze-out tool) since it is the only potentially hit by SS path. SVLE is reached only for $T<-60^{o}C$ and has no chance

of collision with SS path in 1st SS unit, because it would require $Ma^{Shock} \geq 2.25$ (Fig. V.11e), which is out of question as SS design-point is $Ma^{Shock} = 1.52$. Fig. V.11f displays SS path on plane *PxT* traversing the feed VLE envelope, with the feed WDP curve also present. The slenderer VLE envelope belongs to Dry-Gas product and is touched by SS path at pre-shock – where water-C3+ condensate is collected just before normal shock. Fig. V.11f shows that as soon as raw NG enters SS inlet, C3+ starts condensing followed by water when WDP is crossed. Both condensations impede deep *T* falls annihilating the importance of CO_2 freeze-out as an issue of 1st SS unit. After condensate withdrawal, SS path exhibits a rectilinear (*P*,*T*) shock-jump (Fig. V.11f) back to superheated vapor. From this point on, the gas proceeds heating and recompressing along the ending diffuser, seen as linear small prolongation of the (*P*,*T*) shock-jump.

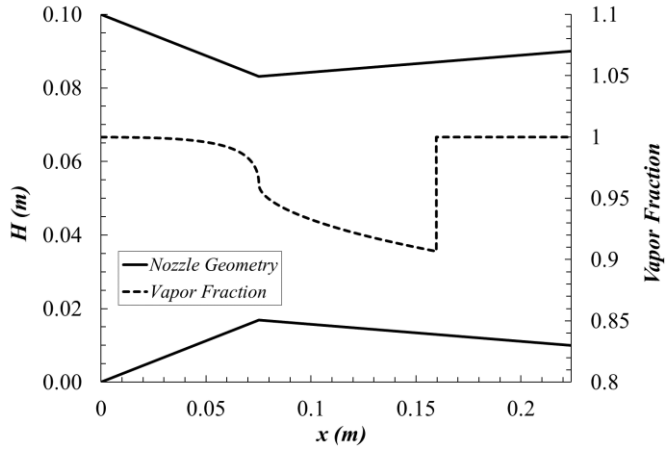

a)

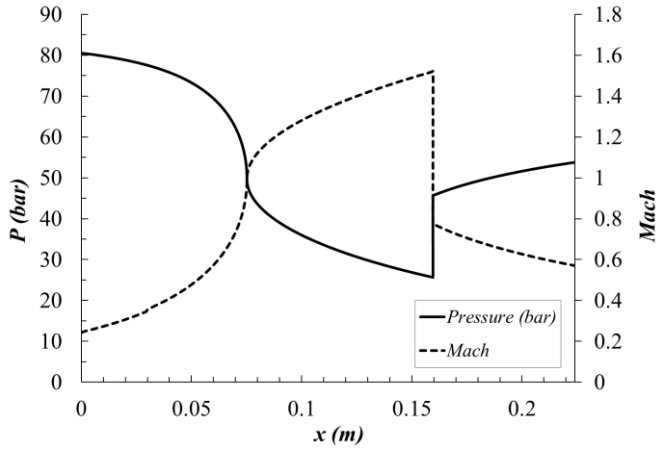

b)

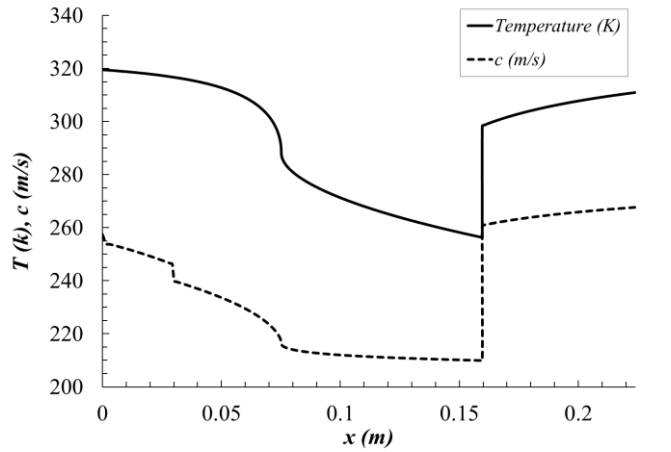

c)

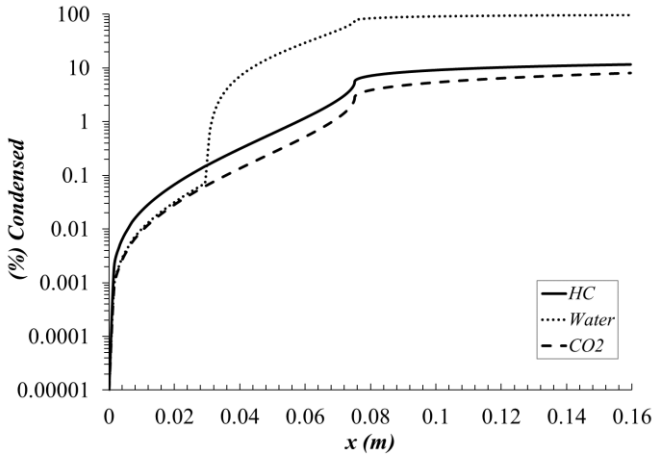

d)

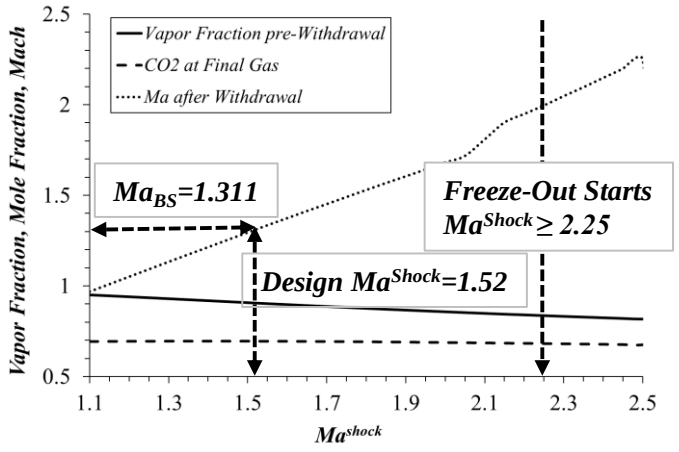

e)

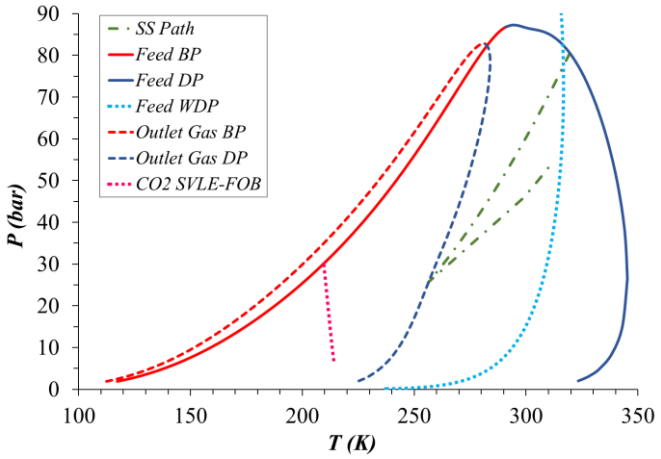

f)

Figure V. 11. 1st SS unit WDPA+HCDPA results for Base-Case [RC+JT+SS]: a) SS silhouette & vapor fraction vs *x(m)*; b) *P(bar)*, *Ma* vs *x(m)*; c) *T(K)*, *c(m/s)* vs *x(m)*; d) hydrocarbons, CO_2 & H_2O %Condensed vs *x(m)*; e) Ma_{BS} vs Ma^{Shock} & CO_2 freeze-out; f) plane *PxT*: feed WDP locus, feed VLE envelope, feed SVLE freeze-out border, Dry-Gas (slenderer) VLE envelope and SS path.

V.5.1.2. 2st SS Unit

The 2nd SS unit of [RC+JT+SS] has a single nozzle with sizes in Table V.4. SS has throat diameter $D_T=3.573\ cm$ at $L_C=15.73\ cm$, maximum $Ma=Ma^{Shock}=1.6$ at $L^{Shock}=0.2560m$, and *Ma* before shock after condensate withdrawal $Ma_{BS}=0.9651$ entailing no normal shock. SS recovers *43.55%* of pressure and condenses *37.1%mol* of feed (with *45.34%mol* CO_2) as a *≈85%mol* CO_2 liquid collected at $L^{Shock}=0.2560m$ with $T=T_{BS}=-61.10^oC$. The 2nd SS unit abates *69.69%* of the feed CO_2 in the condensate with good selectivity. Fig. V.12 shows that it operates differently from 1st SS unit. Fig. V.12a depicts SS silhouette and vapor-fraction versus *x(m)*, while Fig. V.12f traces SS path on plane *PxT* within the larger VLE envelope of the *45.34%mol* CO_2 feed (WDP curve is absent as SS feed is dehydrated). SS path ends expansion touching the slenderer VLE envelope of de-carbonated Fuel-Gas (*21.85%mol* CO_2) at $Ma=Ma^{Shock}=1.6$ and $T_{BS}=-61.10^oC$ (Figs. V.12b/V.12c). After huge withdrawal of *≈85%mol* CO_2 condensate, *Ma* falls to subsonic $Ma_{BS}=0.9651$ impeding normal shock occurrence. From this point on, the subsonic gas continually heats and recompresses through the ending diffuser, tracing an almost linear (*P,T*) compressing path (Fig. V.12f). The feed is admitted as a bubble-point, highly compressible, liquid ($T^{in}=-22^oC$, $P^{in}=84\ bar$) close to its critical point. The vapor-fraction in Figs. V.12a/V.12d is initially *≈20%mol* thanks to critical proximity, which squeezes VLE tie-lines to tiny segments with liquid and vapor virtually of same compositions (Figs. V.12d/V.12f). Fig. V.12a shows vapor-fraction increasing on SS path, corroborated by Fig. V.12d showing all condensed fractions decreasing – oppositely to 1st SS unit – as SS path descends the VLE envelope (Fig. V.12f) through an isentropic. The fluid has high density and high isothermal compressibility $\Xi_P=(\partial\rho/\partial P)_{T,\underline{Z}}$, imposing very low *c* in the beginning of SS converging section (Fig. V.12c/V.12a). Fig. V.12c shows *c*, already with low value, still decreasing towards a minimum of few dozens of *m/s* at $x\approx0.08m$ (Fig. V.12a), creating a local *Ma* peak (Fig. V.12b). Fig. V.12b depicts *P* and *Ma* profiles with SS signatures $dP/dx=-\infty$, $dMa/dx=+\infty$ at throat ($Ma\rightarrow1^-$), reaching pre-shock ($Ma=Ma^{Shock}=1.6$) minimal pressure of $P=P_{BS}=21.7\ bar$ and $P^{Discharge}=36.58\ bar$. As before, condensate removal does not affect (*T,P*), but reduces *Ma* from $Ma^{Shock}=1.6$ to $Ma_{BS}=0.9651$ undermining normal shock, such that $Ma_{AS}=Ma_{BS}=0.9651$. Fig. V.12c depicts *T* and *c* profiles with SS signatures $dT/dx=-\infty$, $dc/dx=+\infty$ at throat ($x=L_C=0.1573m$, $Ma\rightarrow1^-$), reaching pre-shock ($Ma=Ma^{Shock}=1.6$) minimum temperature of $T=T_{BS}=-61.10^oC$ and $T^{Discharge}=-28.55^oC$. Again, two remarks are necessary. Firstly, SS throat

signatures $dT/dx=-\infty$, $dP/dx=-\infty$, $dMa/dx=+\infty$ in Eq. (V.A.3), are confirmed here (Figs. V.12b/V.12c) as rigorous features of single-phase or multiphase equilibrium compressible flow through SS. The throat sound speed signature $dc/dx=+\infty$ happens with positive signal (Eq. (V.A.3)), opposite as it appears in 1st SS unit (Eq. (V.A.2)). The reason is that Eq. (V.A.2) is valid for a multiphase compressible gas-dominated flow – $(\partial c/\partial T)_{P,\underline{Z}}>0$, $(\partial c/\partial P)_{T,\underline{Z}}<0$, $|(\partial c/\partial T)_{P,\underline{Z}}| >> |(\partial c/\partial P)_{T,\underline{Z}}|$ – while here the situation is opposite as the throat flow is liquid-dominated (Fig. V.12a) and is highly compressible – $(\partial c/\partial T)_{P,\underline{Z}}<0$, $(\partial c/\partial P)_{T,\underline{Z}}>0$, $|(\partial c/\partial T)_{P,\underline{Z}}|>|(\partial c/\partial P)_{T,\underline{Z}}|$ – so that Eq. (V.A.3) prevails. Secondly, the large and sudden increase of c (Fig. V.12c) at pre-shock $x=L_C=0.1573m$ derives from sudden withdrawal of dense and highly compressible liquid at high proportion ($37.1\%mol$) at this location, leaving behind a low-pressure gas with a "regular" $c\approx 300\ m/s$. Just after condensate withdrawal, the flow is subsonic and no shock occurs, so that T, P and c rise slowly through the diffuser.

Fig. V.12e reveals a great risk of CO_2 freeze-out in 2st SS unit and also depicts the influence of Ma^{Shock} on pre-withdrawal vapor-fraction, $\%CO_2$ in final gas and Ma_{BS}. As Ma^{Shock} rises, $\%CO_2$ in Fuel-Gas discreetly falls, while the pre-withdrawal vapor-fraction is nearly constant at $\approx 60\%mol$. Fig. V.12d corroborates this, showing a continuously decreasing condensed fraction of hydrocarbons, while CO_2 condensed fraction slowly increases towards $\approx 70\%$ as Ma increases above 1. But Ma^{Shock} must be kept below 1.65, otherwise SS path intersects SVLE freeze-out border precipitating dry-ice and clogging SS. Hence, SS design-point was chosen as $Ma^{Shock}=1.6$ to stop SS path just above SVLE (Fig. V.12f), limiting CO_2 abatement to a final $\%CO_2=21.85\%mol$ in Fuel-Gas and conceding $\approx 10\%mol$ of hydrocarbon in condensate (Fig. V.12d). Fig. V.12e shows that the high condensation forces Ma after withdrawal (Ma_{BS}) to become subsonic and much lesser than Ma^{Shock}, impacting SS pressure recovery. In Fig. V.12f the SVLE traverses, quasi-vertically below -60^oC, the middle of the feed VLE envelope. From all freeze-out borders, only the SVLE is drawn as only it can be hit by SS path.

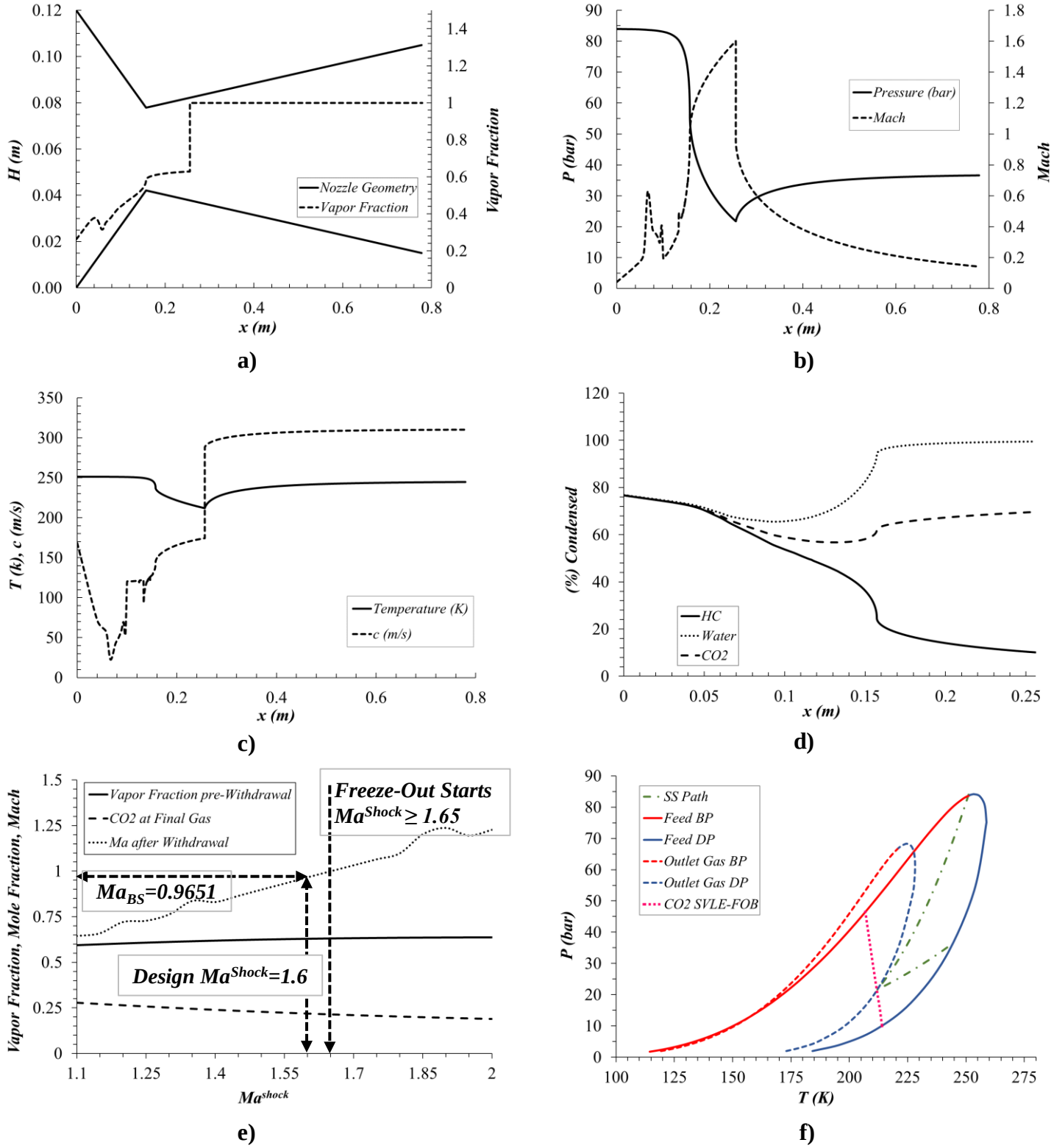

Figure V. 12. 2nd SS unit CO_2 removal results for Base-Case [RC+JT+SS]: a) SS walls, vapor-fraction *vs x(m)*; b) *P(bar), Ma vs x(m)*; c) *T(K), c(m/s) vs x(m)*; d) *hydrocarbons, CO_2 & H_2O %Condensed vs x(m)*; e) Ma_{BS} *vs* Ma^{Shock} & CO_2 freeze-out; f) plane *PxT*: feed VLE envelope, feed SVLE freeze-out border, Fuel-Gas (slenderer) VLE envelope and SS path.

V.5.1.3. SS Paths of 1st and 2nd SS Units on $T\,x\,\bar{S}$ Plane

It is enlightening to visualize SS paths of 1st and 2nd SS units on $T\,x\,\bar{S}$ diagram as it exposes 2nd Law aspects pertinent to SS transitions, particularly the indestructibility of entropy. Figs. V.13a/V.13b depict the SS path of 1st SS unit on $T\,x\,\bar{S}$, the latter a magnification of the former, while Figs. V.13c/V.13d do the same for 2nd SS unit, V.13d also magnifying V.13c. All transitions in Figs. V.13a/V.13b correspond to SS path in Figs. V.11a to V.11f, and all transitions in Figs. V.13c/V.13d to SS path in Figs. V.12a to V.12f. Figs. V.13a/V.13b include the WDP locus of raw NG feed and VLE envelopes of feed and Dry-Gas product, while Figs. V.13c/V.13d have VLE envelopes of feed and Fuel-Gas product, and feed SVLE freeze-out border.

In 1st SS unit (Figs. V.13a/V.13b) SS path initiates with the isentropic expansion A→B at feed HCDP, immediately crossing WDP where water starts condensing. At B, water-C3+ condensate is isothermally removed on B→C ending at Dry-Gas HCDP ($T=T_{BS}=-16.78^oC$). Molar entropy increases on B→C as low entropy liquids are withdrawn without changing (*T,P*) and vapor with higher $\bar{S}$. At C, shock occurs via the rectilinear jump C→D inclined to the right (Fig. V.13b) as the shock is a spontaneous adiabatic entropy-creating heating transition. At D, superheated Dry-Gas flows sub-sonically through the diffuser on isentropic D→E increasing (*T,P*) monotonously. Point E is outlet Dry-Gas.

The SS path of 2nd SS unit (Figs. V.13c/V.13d) starts with isentropic expansion A→B at the bubble-point near the critical point. On A→B (*T,P*) drop, forming hydrocarbon-rich vapor, leaving the liquid CO_2 richer. At B, liquid ($\approx 85\%mol$ CO_2) is withdrawn isothermally and SS path follows B→C towards the higher entropic HCDP vapor at $T=T_{BS}=-61.1^oC$. Point B lies little above the SVLE onto feed VLE envelope, entailing no dry-ice on A→B. This is not conflicting with SVLE apparently crossing B→C, but it doesn't, as SVLE belongs to the feed envelope, while B→C connects B on the feed envelope to C on the Fuel-Gas envelope. After withdrawal of liquid fraction (*37.1%mol*), *Ma* becomes subsonic, entailing no shock. Thus, from C gas flows sub-sonically in the diffuser raising (*T,P*) on isentropic C→D until Fuel-Gas outlet at D.

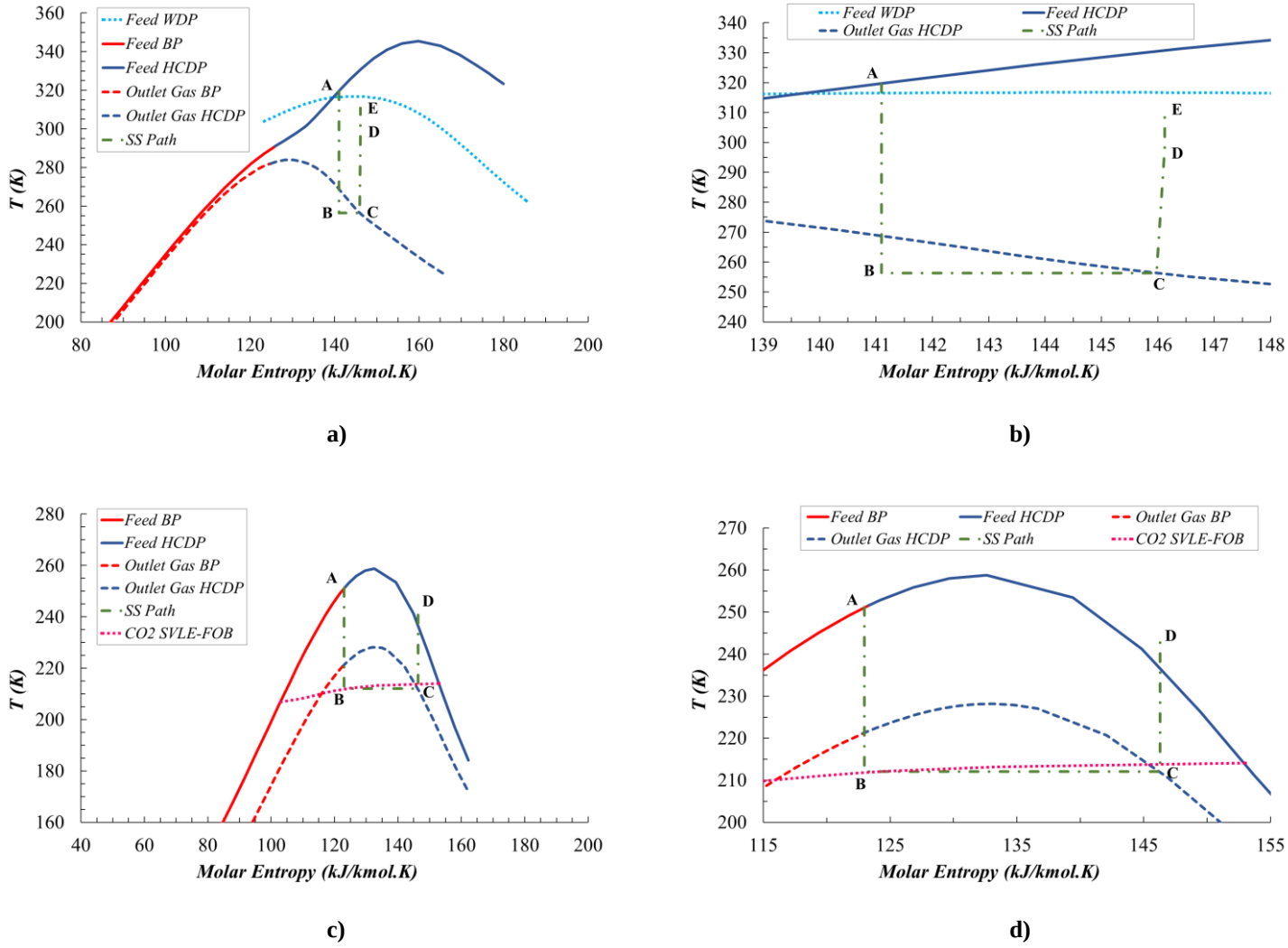

Figure V. 13. Base-Case SS paths on $T\,x\,\bar{S}$: (a) 1st SS unit SS path with feed WDP locus, feed and Dry-Gas VLE envelopes; (c) 2nd SS unit SS path with feed and Fuel-Gas VLE envelopes and feed SVLE; (b) and (d) are magnifications of (a) and (c) (FOB≡Freeze-Out Boundary; BP≡Bubble-Point).

V.5.1.4. 1st SS Unit with CPA-EOS

The 1st SS unit of Base-Case [RC+JT+SS] for WDPA+HCDPA of raw CO_2-rich NG was solved in Sec. V.5.1.1 with PR-EOS. To demonstrate further capabilities of unit operation extension SS-UOE for SS simulation, 1st SS unit was also simulated using the Cubic-Plus-Association EOS (CPA-EOS) (Folas et al., 2005; Karakatsani and Kontogeorgis, 2013) as thermodynamic model rendered by HYSYS. Appendix N shows these results. As CPA-EOS is suitable for multiphase systems with associating species (e.g., water), the 1st SS unit is appropriate for such demonstration. CPA-EOS in SS processing of CO_2-rich NG is inexistent in the literature,

excepting (Teixeira et al., 2018) which addressed capture of methanol/ethanol/MEG from raw NG using SS with water injection.

V.5.2. Performance of Gas-Hub Processing Alternatives

With flowsheet solutions – Table V.3 for Base-Case [RC+JT+SS] and Tables P.1, P.2 and P.3 (Supplementary Materials – Appendix P) for [RC+TX+SS], [NR+JT+SS] and [RC+JT+MP] – all four alternatives were assessed in Fig. V.14 in terms of oil production, EOR-Fluid $ppmH_2O$, power-consumption and Fixed Capital Investment (*FCI*). Fig. V.15 depicts the Net Present Value (*NPV*) of alternatives along 20 years of production (3 years construction), showing the Base-Case [RC+JT+SS] with best cash-flow and *NPV*. Base-Case [RC+JT+SS] power demand – supplied by turboshafts and gas-turbine drivers – was *167.2 MW* (Fig. V.14) demanding *1.3* $MMsm^3/d$ of ($\approx 22\%mol\ CO_2$) Fuel-Gas (Table V.5). Most demanding units are Main-Compressor and EOR-Pump, respectively accounting for *≈58.4%* and *≈26.1%* of total power consumption. [RC+JT+SS] has *FCI=919 MMUSD* (Fig. V.14), annualized profit *AP=+940 MMUSD/y* and *NPV=+5242 MMUSD* (Fig. V.15) after 20 operation-years.

Base-Case gave the best *NPV*, but there are other aspects to be considered in Table V.5, which summarizes $MMsm^3/d$ of key-streams of [RC+JT+SS], [RC+TX+SS], [NR+JT+SS] and [RC+JT+MP]. $MMsm^3/d$ of oil in Table V.5 does not follow the proportion of Fig. V.14a (*bbl/d*) due to different oil compositions.

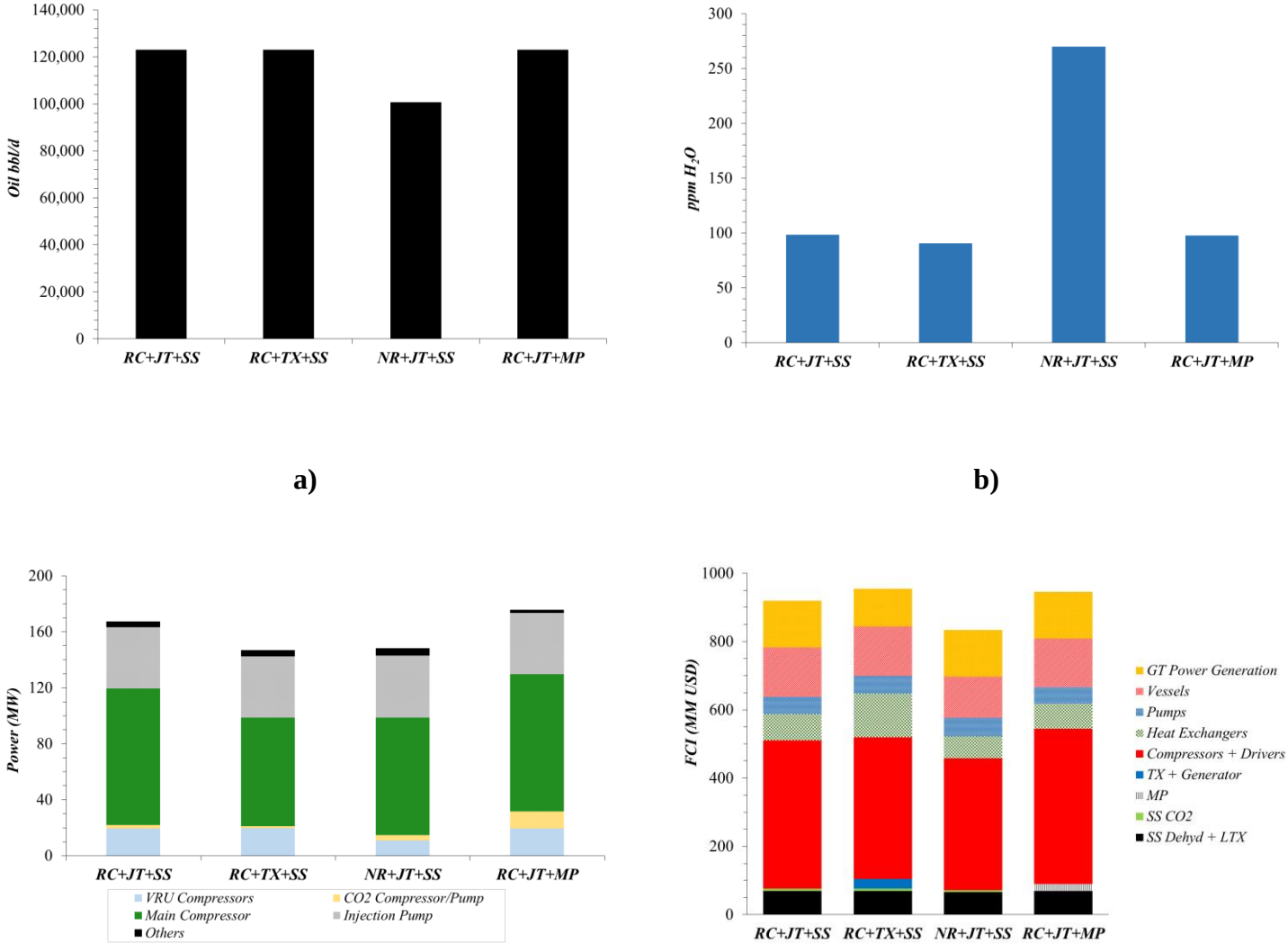

Figure V. 14. Gas-hub alternatives: (a) oil (bbl/d); (b) EOR-Fluid *ppmH_2O*; (c) power-consumption (MW); (d) *FCI* (MMUSD).

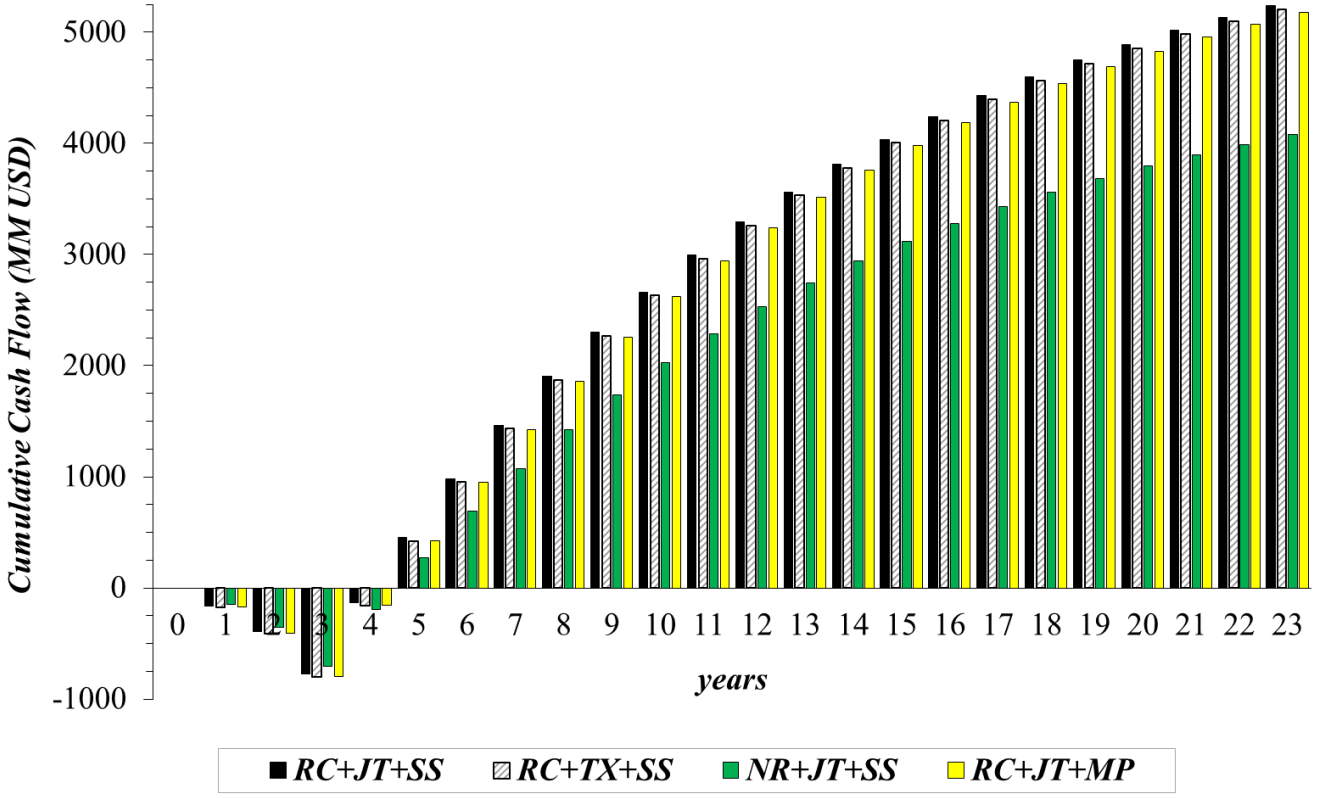

Figure V. 15. NPV (MMUSD) of gas-hub alternatives for 20 operation-years.

Table V. 5. Key-streams ($MMsm^3/d$) of alternatives (MP≡Membrane-Permeation).

$MMsm^3/d$	*[RC+JT+SS] Base-Case*	*[RC+TX+SS]*	*[NR+JT+SS]*	*[RC+JT+MP]*
Riser (including water)	*90.15*	*90.15*	*90.15*	*90.15*
EOR-Fluid	*50.09*[*1]	*50.19*[&1]	*50.51*[$1]	*50.05*[#1]
Fuel-Gas	*1.30*[*2]	*1.16*[&2]	*1.27*[$2]	*1.34*[#2]
Main Recycle	*8.31*	*8.99*	*----*	*8.31*
Water-C3+ Condensate (1st SS Unit)	*5.29*	*5.65*	*3.98*	*5.29*
HPS-Gas	*52.24*	*52.85*	*47.98*	*52.24*
Captured CO_2 (2nd SS or MP)	*0.65611*	*0.712599*	*0.67056*	*3.14384*
Captured CH_4 (2nd SS or MP)	*0.078585*	*0.079595*	*0.068*	*0.326096*
CO_2 Emissions (Fuel-Gas)	*1.31989*	*1.1834*	*1.284839*	*1.71024*
Oil	*2.0*	*2.0*	*1.43*	*2.0*

*[*1]70.8%CO_2 . [&1]70.68%CO_2 . [$1]70.14%$CO_2$. [#1]70.9%CO_2.[*2]21.85%CO_2, 74.73%C1, 2.06%C2, 0.25%C3, 0.02%C4.
[&2]22.08%CO_2, 74.47%C1, 2.12%C2, 0.25%C3, 0.02%C4. [$2]21.69%$CO_2$, 74.95%C1, 2.0%C2, 0.22%C3, 0.02%C4.
[#2]20.0%CO_2, 62.87%C1, 8.6%C2, 4.71%C3, 2.40%C4, 0.68%C5, 0.06%C6, 0.01%C7.

V.6. Discussion

Besides the technical discussion of 1st and 2nd SS units in Sec. V.5, here two other points are discussed: the technical-economic-environmental comparison of alternatives and the use of thermal utility loops recovering heat to match gas-hub heating requirements without resorting to combustion or electricity.

V.6.1. Technical-Economic-Environmental Comparison of Gas-Hub Alternatives

Comparisons of Base-Case [RC+JT+SS] and alternatives [RC+TX+SS], [NR+JT+SS] and [RC+JT+MP] are done as percent deviations relative to [RC+JT+SS], unless stated otherwise. Fig. V.14, Fig. V.15 and Table V.5 depict performance metrics for comparisons.

Despite presenting the lowest *FCI* (*-9.36%)* and the second lowest power demand (*-11.45%)*, the non-recycle alternative [NR+JT+SS] (Fig. V.10c) presents also lowest *bbl/d* of oil (*-18.33%)* and highest *ppmH_2O* in EOR-Fluid (*+174%)*, both results credited to not recycling water-C3+ condensate from 1st SS unit. Despite the LLS separation of water from water-C3+ condensate, the C3+ stream (LIQ) carries saturation water increasing *ppmH_2O* of EOR-Fluid raising the risk of downstream hydrates in EOR system. Albeit alternatives that recycle condensate from 1st SS unit – [RC+JT+SS], [RC+TX+SS], [RC+JT+MP] (Figs. V.10a/V.10b/V.10d) – have higher HPS-Gas flow rates than [NR+JT+SS] (*+8.9%* to *+10.15%* above [NR+JT+SS]), and consequently being penalized with larger equipment and extra compression power, recycling 1st SS unit condensate dramatically rises oil production, an important revenue. Therefore, the power-consumption and *FCI* benefits by eliminating recycle in [NR+JT+SS] are insignificant in face of its lowest revenues, leading to worst *NPV* and cash-flows (Fig. V.15). On the other hand, the three recycle alternatives have similar oil productions and *ppmH_2O* in EOR-Fluid, with different power-consumption, *FCI*, Fuel-Gas flow rate and CO_2 emissions.

Considering the three recycle alternatives, despite [RC+TX+SS] has the least power-consumption by using TX (*-19.16%),* it has (Fig. V.14) the highest *FCI* (*+3.76%*). Fig. V.14d shows that *FCI* reduction of compressor drivers in [RC+TX+SS] is overshadowed by greater exchangers *FCI* added to TX *FCI*. *FCI* of exchangers of [RC+TX+SS] is higher because larger exchangers are needed to heat up the huge HPS-Gas (*T=350^oC*) to extract TX power efficiently;

and again to cool down the still hot expanded gas recovering heat to PHW/HW. Thus, in spite of its attempt to produce power expanding HPS-Gas from *120 bar* to *80.5 bar*, the truth is that [RC+TX+SS] paid the price of immobilizing capital, being outperformed by the pragmatic [RC+JT+SS], which neglected power reclamation from HPS-Gas expansion. Thus [RC+TX+SS] achieved the second best *NPV* in Fig. V.15. Nevertheless, as shown in Fig. V.14 and Table V.5, [RC+TX+SS] has minimal power-consumption and, consequently, minimal Fuel-Gas and CO_2 emissions. In other words, [RC+TX+SS], which seconded Base-Case by narrow *NPV* margin (Fig. V.15), achieved best environmental performance with *10.34%* less CO_2 emissions.

However, one could suggest using TX without the massive exchangers for pre-heating and after-cooling the TX fluid (Fig. V.5). Certainly this solution would save *≈45 MMUSD* of *FCI* for such exchangers (Fig. V.14d, 2nd bar), but since the power produced in adiabatic expanders is nearly proportional to the inlet absolute temperature, the TX power would only reach *≈13.7 MW*, while with the pre-heating/after-cooling scheme (Fig. V.5) TX power is greater than *≈28 MW*, enabling the TX shaft to neatly replace one of the four modularized Gas-Turbine shafts driving the giant Main-Compressor (Sec. V.3.7, Plant G), hence keeping invariant the *FCI* of drivers. Using TX without the pre-heating/after-cooling scheme, the *FCI* of drivers would be greater creating an intermediate solution between [RC+JT+SS] and [RC+TX+SS] in terms of *FCI* and *NPV* (in Fig. V.15 the cash-flow bars of such cold TX solution would be squeezed between the bars of [RC+JT+SS] and [RC+TX+SS]), as well as in terms of consumption of gas-fired power and CO_2 emissions (Table V.5). Even though, this would not change the facts that [RC+JT+SS] is the best process on economic grounds by a narrow margin and that [RC+TX+SS] is the best in terms of consumption of gas-fired power and CO_2 emissions by a wide margin. In a plausible scenario of carbon taxation, [RC+TX+SS] would also become the economically best.

Considering Membrane-Permeation instead of SS to capture CO_2, Fig. V.14 shows that the conventional [RC+JT+MP] has highest power-consumption (*+4.99%*) and high *FCI* (*+2.81%*), explained by its greater dependence on centrifugal machines to compress its low-pressure CO_2-rich permeate. Thus, [RC+JT+SS] and [RC+TX+SS], both with less power-consumption and

less compressor *FCI* – thanks to SS CO_2 removal – outperformed [RC+JT+MP] in terms of *NPV*.

Discrimination of alternatives is straightforward from *NPV* perspective (Fig. V.15). Base-Case [RC+JT+SS] presents highest cash-flows and *NPV=5242 MMUSD*, being the best alternative for this scenario. Despite the lowest *FCI* and 2nd lowest power-consumption, [NR+JT+SS] has lowest cash-flows and *NPV=4076 MMUSD*. The lowest power-consumption of [RC+TX+SS] did not compensate its highest *FCI*, which besides implying negatively worst cash-flows in the construction years, indirectly increase *COM* in Eq. (M.3a), reducing cash-flows and giving *NPV=5207 MMUSD*. Therefore, from the economic standpoint of [RC+JT+SS], there is scarce justification to replace JT-Expansion by TX. However, from the perspective of CO_2 emissions [RC+TX+SS] is better than [RC+JT+SS]. Thus, the choice between [RC+JT+SS] and [RC+TX+SS] must be done with care. Finally, alternative [RC+JT+MP] with conventional Membrane-Permeation CO_2 capture has highest compressor *FCI* and highest power-consumption, both caused by highest compression power due to CO_2-rich permeate compressors, leading to second worst cash-flows and *NPV=5181 MMUSD*.

V.6.2. Heat Recovery via Thermal Utility Loops

Alternatives of gas-hub processing of CO_2-rich raw NG adopt a new heat recovery strategy with five utility loops – Cooling-Water (CW), Warm-Water (WW), Hot-Water (HW), Pressurized-Hot-Water (PHW) and Thermal-Fluid (TF) – absorbing heat at distinct thermal levels and supplying heating at several temperatures, while usual rigs have only two circuits: CW and PHW or TF. These five loops avoid extra heating costs and additional carbon emissions by cascading heat from the energy intakes – heat-recovery from WHRUs and shaft-power – towards the SW-Sink; while ATM-Sink disposes combustion heat not entering the process. Fig. V.16 depicts the cascading heat-flow through all processes and performances of CW/WW/HW/PHW/TF, unveiling that the heat-recoveries of WHRUs and intercoolers are sufficient to supply heat demand. Fig. V.16 offers two types of data: (i) energy intakes: WHRUs (dashed-box) and shaft-power; (ii) CW/WW/HW/PHW/TF heat-loads as pie-diagrams: gray-sector as the heat absorbed allocated to heating; and white-sector as the heat absorbed discharged to SW-Sink. Using heat-recovery loops avoids heating/cooling costs despite the huge heating/cooling services. In Fig. V.16 the fraction of WHRUs heat-recovery conveyed to

process corresponds only to the megawatts to PHW/TF in dashed-boxes; the rest goes to ATM-Sink. Fig. V.16 reports differences between energy intakes (shaft-power plus WHRUs heat-recovery) and SW-Sink heat-effects, which mainly corresponds to enthalpy conveyed by the massive EOR-Fluid streams from EOR-Pump at *T=80.2ºC* (Table V.3).

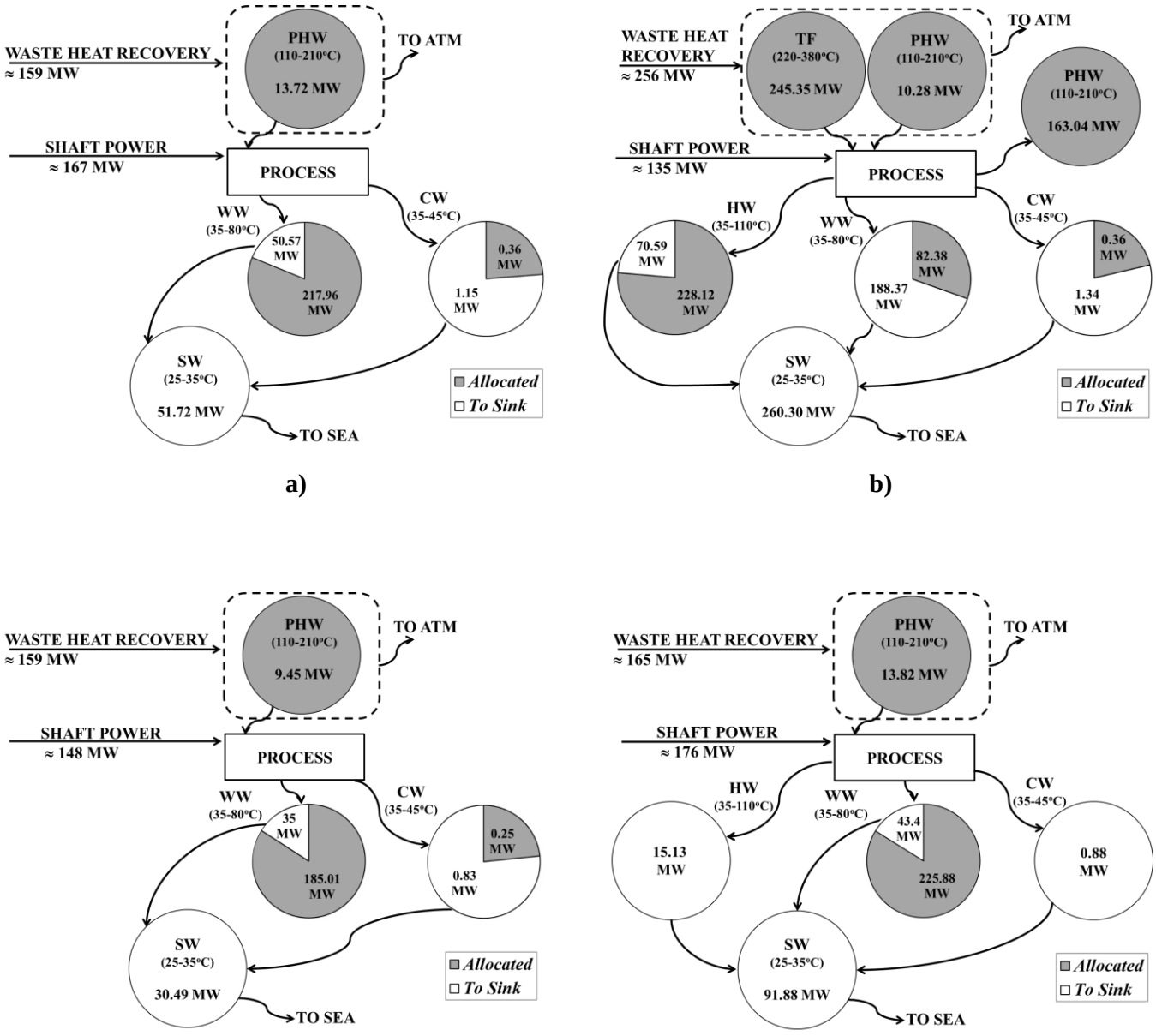

Figure V. 16. Energy inputs (WHRUs+shaft-power), utilities (CW/WW/HW/PHW/TF) and sinks (SW/ATM): (a)[RC+JT+SS]; (b)[RC+TX+SS]; (c)[NR+JT+SS]; (d)[RC+JT+MP].

V.7. Conclusions

Offshore processing alternatives were investigated for large-scale conditioning of CO_2-rich raw NG based on supersonic separators (SS). Gas-hub promotes EOR by injecting almost all processed supercritical fluid enriched with CO_2 captured from raw NG to produce Fuel-Gas (*≈20%mol CO_2*) for power sufficiency. Processes contemplate oil/gas/water separation, gas expansion, 1st SS unit for WDPA+HCDPA, 2nd SS unit and Membrane-Permeation removing CO_2 for Fuel-Gas production and EOR compression. Gas-hub treats *≈56MMsm³/d* of *≈68%mol CO_2* raw NG with 1st SS unit for WDPA+HCDPA. Alternatives differ in three ways: (i) recycling or not recycling condensate from 1st SS unit; (ii) expansion of HPS-Gas by JT or TX to SS working pressure; and (iii) 2nd SS unit or Membrane-Permeation for CO_2 removal. Cases were compared via technical results, power-consumptions, profitability and CO_2 emissions.

For simulation of 1st and 2nd SS units and Membrane-Permeation, HYSYS UOEs previously developed – SS-UOE (Arinelli et al., 2017), MP-UOE (Arinelli et al., 2017), PEC-UOE (De Medeiros et al., 2017) – were used directly integrated to HYSYS flowsheets facilitating obtaining results and designs. The SS applications with CO_2-rich raw NG – for WDPA/HCDPA and CO_2 abatement – directly integrated to simulation process flowsheets as done here, configure novelties to the current literature.

Results show that recycling condensate from 1st SS unit – despite causing higher gas circulation rate and equipment sizes – increases oil revenues raising *NPV* and lowering *ppmH_2O* in EOR-Fluid. Conversely, there is no room for decisions that increase investment without favoring oil extraction – e.g., replacing JT-Expansion by turbo-expander (TX) to reclaim power – except if environmental factors come into consideration. Here, the pragmatic Base-Case [RC+JT+SS] achieved best *NPV*, while the power-saving TX solution [RC+TX+SS] implied highest *FCI* from expensive exchangers added with TX, entailing higher costs without revenues increase; i.e. lower cash-flow and *NPV*. Nevertheless, [RC+TX+SS] attained second best profitability by a narrow margin and lowest Fuel-Gas consumption and CO_2 emissions, being environmentally the best scheme. Thus, the choice between [RC+JT+SS] and [RC+TX+SS] implies considering economic and environmental aspects. In case of carbon taxation, for example, it is probable that [RC+TX+SS] would also become economically the best option. Regarding CO_2 capture, the 2nd SS unit for CO_2 removal outperformed Membrane-Permeation, despite requiring cryogenic-

integration and CO_2 refrigeration. The 2nd SS unit entails lower *FCI* and lesser power-consumption than Membrane-Permeation, both explained by the extra compression burden of low-pressure CO_2-rich permeate.

Supplementary Materials (Appendices L to S)

HYSYS Flowsheets and Supplements are found in the Supplementary Materials available online.

Acknowledgements

Authors acknowledge research grant from PETROBRAS S.A. (0050.0096933.15.9). JL de Medeiros and OQF Araújo acknowledge research grants from CNPq-Brazil (311076/2017-3).

Abbreviations

C3+ Propane and Heavier; CFD Computational Fluid Dynamics; CPA-EOS Cubic-Plus-Association EOS; CW Cooling-Water; ED Electric-Driver; EOR Enhanced Oil Recovery; EOS Equation-of-State; GT Gas-Turbine; HCDP Hydrocarbon Dew-Point; HCDPA Hydrocarbon Dew-Point Adjustment; HPS High-Pressure Separator; HW Hot-Water; JT Joule-Thomson; LLS Liquid-Liquid Separator; LTX Low-Temperature Condensate Catcher; MMsm^3/d Millions of standard m^3 per day; NG Natural Gas; PHW Pressurized-Hot-Water; PR-EOS Peng-Robinson EOS; SS Supersonic Separator; SVLE Solid-Vapor-Liquid Equilibrium; SW Seawater; TF Thermal-Fluid; TX Turbo-Expander; USD US Dollar; UOE Unit Operation Extension; VLE Vapor-Liquid Equilibrium; VLWE Vapor-Liquid-Water Equilibrium; WDP Water Dew-Point; WDPA Water Dew-Point Adjustment; WHRU Waste-Heat Recovery Unit; WW Warm-Water.

Nomenclature

$A(x)$	*: SS flow section area (m^2) dependent of x*
$c(T,P,\underline{Z})$	*: Sound speed of multiphase fluid at (T, P, $\underline{Z}$) (m/s)*
D_I, D_T, D_O	*: Inlet, throat and outlet SS diameters (m)*
$\hat{f}_{CO2}$	*: CO_2 fugacity (bar)*
GOR	*: Gas-Oil Ratio (sm^3/m^3)*
L, L_C, L_D	*: Total, converging and diverging SS lengths (m)*
L^{LAVAL}, L^{Shock}	*: Laval nozzle length and SS axial position at normal shock ($L^{Shock}=L^{LAVAL}$) (m)*
$Ma=v/c$	*: Mach Number*
Ma^{Shock}	*: Ma just before normal shock and condensate withdrawal*
nc	*: Number of components*

P, PP_{CO2} : Absolute pressure (bar),CO_2 partial pressure (bar)
r_c , $REC\%CO_2$: SS area expansion ratio and SS % CO_2 recovery
T : Absolute temperature (K)
v, x : Axial velocity of multiphase fluid (m/s) and SS axial position (m
$\underline{Z}$: Vector (nc x 1) of total species mol fractions in multiphase fluid
Economy Terms
AP, GAP, REV : Annual profit, gross profit and revenues (USD/y)
CUT, COM : Annual utility and manufacturing costs (USD/y)
FCI, ITR, NPV : Fixed capital investment (USD), income tax rate (%),net present value (USD)
Greek Terms
α, β : SS converging and diverging angles (deg) with linear diameter profiles
β : Mole vapor fraction
$\eta^{EXP}\%, \eta^{CMP}\%$: SS expansion and compression adiabatic efficiencies (%)
ρ : Multiphase fluid density (kg/m³)
$\Xi_P \equiv \left(\frac{\partial \rho}{\partial P}\right)_{T,\underline{Z}}$: *Derivative of ρ with P at const. T, $\underline{Z}$ for multiphase fluid (kg/Pa.m^3)*
Subscripts
AS, BS : Just after shock and just before shock after condensate withdrawal
C, D, I, O, T : Converging, diverging, inlet, outlet, throat
L, V, W : Liquid hydrocarbon, vapor and liquid water at L^{Shock}
Superscripts
in, out ,LAVAL : Inlet, outlet, and Laval nozzle
Diffuser, Diff : Diffuser
Discharge, Feed : SS discharge, SS feed
Shock : Just before normal shock and before condensate withdrawal
Throat, V, L, S : Throat, vapor, liquid, solid

References

Araújo, O.Q.F., de Medeiros, J.L., Carbon capture and storage technologies: present scenario and drivers of innovation. Current Opinion in Chemical Engineering 2017, 17, 22–34, doi 10.1016/j.coche.2017.05.004

Araújo, O.Q.F., Reis, A.C., de Medeiros, J.L., Nascimento, J.F., Grava, W.M., Musse, A.P.S., Comparative analysis of separation technologies for processing carbon dioxide rich natural gas in ultra-deepwater oil fields. J. of Clean. Production 2017, 155, 12-22, doi 10.1016/j.jclepro.2016.06.073

Arinelli, L.O., Trotta, T.A.F., Teixeira, A.M., de Medeiros, J.L., Araújo, O.Q.F., Offshore Processing of CO2 Rich Natural Gas with Supersonic Separator versus Conventional Routes. J. of Nat. Gas Sci. and Eng. 2017, 46, 199-221, doi 10.1016/j.jngse.2017.07.010

Baccanelli, M., Langé, S., Rocco, M.V., Pellegrini, L.A., Colombo, E., Low temperature techniques for natural gas purification and LNG production: An energy and exergy analysis. Applied Energy 2016, 180, 546-559, doi 10.1016/j.apenergy.2016.07.119

Burgers, W.F.J, Northrop, P.S., Kheshgi, H.S., Valencia, J.A., Worldwide Development Potential for Sour Gas. Energy Procedia 2011, 4, 2178-2184, doi 10.1016/j.egypro.2011.02.104

Castier, M., Effect of side streams on supersonic gas separations. J. of Nat. Gas Sci. and Eng. 2016, 35, 299-308, doi 10.1016/j.jngse.2016.08.065

de Medeiros, J.L., Barbosa, L.C., Araújo, O.Q.F., Equilibrium Approach for CO2 and H2S Absorption with Aqueous Solutions of Alkanolamines: Theory and Parameter Estimation. Ind.Eng.Chem.Res. 2013a, 52, 9203−9226, doi 10.1021/ie302558b

de Medeiros, J.L., Nakao, A., Grava, W.M., Nascimento, J.F., Araújo, O.Q.F., Simulation of an Offshore Natural Gas Purification Process for CO2 Removal with Gas−Liquid Contactors Employing Aqueous Solutions of Ethanolamines. Ind.Eng.Chem.Res. 2013b, 52, 7074−7089, doi 10.1021/ie302507n

de Medeiros, J.L., Arinelli, L.O., Araújo, O.Q.F., Speed of Sound of Multiphase and Multi-Reactive Equilibrium Streams: A Numerical Approach for Natural Gas Applications. J. of Nat. Gas Sci. and Eng. 2017, 46, 222-241, doi 10.1016/j.jngse.2017.08.006

Folas, G.K., Gabrielsen, J., Michelsen, M.L., Stenby, E.H., Kontogeorgis, G.M., Application of the Cubic-Plus-Association (CPA) Equation-of-State to Cross-Associating Systems. Ind.Eng.Chem.Res. 2005, 44, 3823−3833.

Kang, G., Chan, Z.P., Saleh, S.B.M., Cao, Y., Removal of high concentration CO2 from natural gas using highpressure membrane contactors. Int. J. of Greenh. Gas Control 2017, 60, 1-9, doi 10.1016/j.ijggc.2017.03.003

Karakatsani, E.K., Kontogeorgis, G.M., Thermodynamic Modeling of Natural Gas Systems Containing Water. Ind.Eng.Chem.Res. 2013, 52, 3499−3513, doi 10.1021/ie302916h.

Langé, S., Pellegrini, L.A., Vergani, P., Savio, M., Energy and Economic Analysis of a New Low-Temperature Distillation Process for the Upgrading of High-CO2 Content Natural Gas Streams. Ind.Eng.Chem.Res. 2015, 54(40), 9770-9782, doi 10.1021/acs.iecr.5b02211

Li, H. and Zhang, Z., Mining the intrinsic trends of CO2 solubility in blended solutions. Journal of CO2 utilization 2018, 26, 496-502, doi 10.1016/j.jcou.2018.06.008

Machado, P.B., Monteiro, J.G.M., de Medeiros, J.L., Epsom, H.D., Araujo, O.Q.F., Supersonic separation in onshore natural gas dew-point plant. J. of Nat. Gas Sci. and Eng. 2012, 6, 43–9, doi 10.1016/j.jngse.2012.03.001

McCoy, S.T., The Economics of CO2 Transport by Pipeline and Storage in Saline Aquifers and Oil Reservoirs. PhD Thesis, Carnegie Mellon University, USA, 2008.

Merkel, T.C., Zhou, M., Baker, R.W., Carbon dioxide capture with membranes at an IGCC power plant. J. of Memb. Sci. 2012, 389, 441-450, doi 10.1016/j.memsci.2011.11.012

Nguyen, T.V., Tock, L., Breuhaus, P., Maréchal, F., Elmegaard, B., CO2-mitigation options for the offshore oil and gas sector. Applied Energy 2016, 161, 673-694, doi 10.1016/j.apenergy.2015.09.088

Schinkelshoek, P., Epsom, H.D., Supersonic gas conditioning - Commercialization of Twister Technology. GPA 87th Annual Conv. Proc., Texas, USA, March 2008, 739–745

Secchi, R., Innocenti, G., Fiaschi, D., Supersonic Swirling Separator for natural gas heavy fractions extraction: 1D model with real gas EOS for preliminary design. J. Nat. Gas Sci. and Eng. 2016, 34, 197–215. doi:10.1016/j.jngse.2016.06.061

Shokri, A.R., Babadagli, T., Feasibility assessment of heavy-oil recovery by CO2 injection after cold production with sands: Lab-to-field scale modeling considering nonequilibrium foamy oil behavior. Applied Energy 2017, 205, 615-625, doi 10.1016/j.apenergy.2017.08.029

Shooshtari, S.H.R., Shahsavand, A., Maximization of energy recovery inside supersonic separator in the presence of condensation and normal shock wave. Energy 2017, 120, 153-163, doi 10.1016/j.energy.2016.12.060

Teixeira, A.M., Arinelli, L.O., de Medeiros, J.L., Araújo, O.Q.F., Exergy Analysis of monoethylene glycol recovery processes for hydrate inhibition in offshore natural gas fields. J. of Nat. Gas Sci. and Eng. 2016, 35, 798-813, doi 10.1016/j.jngse.2016.09.017.

Teixeira, A.M., Arinelli, L.O., de Medeiros, J.L., Araújo, O.Q.F., Recovery of thermodynamic hydrate inhibitors methanol, ethanol and MEG with supersonic separators in offshore natural gas processing. J. Nat. Gas Sci. and Eng. 2018, 52, 166-186. doi:10.1016/j.jngse.2018.01.038

Turton, R., Bailie, R.C., Whiting, W.B., Shaeiwitz, J.A., Analysis, Synthesis, and Design of Chemical Processes. 3rd ed. New Jersey: Prentice Hall Int. 2009

Wen, C., Cao, X., Yang, Y., Li, W., Numerical simulation of natural gas flows in diffusers for supersonic separators. Energy 2012, 37, 195-200, doi 10.1016/j.energy.2011.11.047

Yang, Y., Wen, C., Wang, S., Feng, Y., Theoretical and numerical analysis on pressure recovery of supersonic separators for natural gas dehydration. Applied Energy 2014, 132, 248-253, doi 10.1016/j.apenergy.2014.07.018

Zhang, Z., Li, Y., Zhang, W., Wang, J, Soltanian, M.R., Olabi, A.G., Effectiveness of amino acid salt solutions in capturing CO2: A review. Renewable and Sustainable Energy Reviews 2018, 98, 179-188, doi 10.1016/j.rser.2018.09.019

CHAPTER VI – FURTHER PUBLICATIONS WITH SUPERSONIC SEPARATORS AND MEMBRANE PERMEATION

This Chapter gathers other published works where MP-UOE and SS-UOE were used for simulations of new SS applications and for further assessments on CO_2-rich natural gas processing.

VI.1. Recovery of thermodynamic hydrate inhibitors methanol, ethanol and MEG with supersonic separators in offshore natural gas processing

This work was published in Journal of Natural Gas Science and Engineering, 52, 166-186, 2018. doi: https://doi.org/10.1016/j.jngse.2018.01.038 (Appendix T.16).

To avoid hydrate formation in subsea pipelines from oil and gas reservoirs to the processing rigs, the injection of thermodynamic hydrate inhibitors (THIs) in well-heads is commonly used. However, there is a non-negligible loss of THIs carried with the gas phase after the three-phase high-pressure separation (HPS) in the platform, entailing costs related to THI make-up, storage and transport, mainly for more volatile THIs such as methanol and ethanol. Therefore, Teixeira et al. (2018) proposed an innovative process adopting SS to recover THI from the HPS gas phase offshore, simultaneously treating NG in terms of dewpoints: SS-THI-Recovery. The results obtained with this process consolidated a pending patent in Brazilian Patent and Trademark Office (Teixeira et al., 2017).

Two process configurations were approached in this paper, one for methanol or ethanol as THI, and another for MEG as THI (Figs. VI.1 and VI.2, respectively). To enhance THI recovery from the gas phase using SS, a small amount of liquid water was injected in SS feed, at a 3:1 ratio of moles of water per THI mol. The condensate stream leaving the SS+LTX unit contemplates two liquid phases: one rich in C3+, and an aqueous phase with THI. This condensate stream is sent to a high-pressure liquid-liquid separator (LLS), with more injection of water (at 4:1 ratio of water moles per THI mol) to enhance separation of the water+THI phase. The process configurations differ for the water+THI phase after the LLS: for methanol or ethanol (Fig. VI.1), a small atmospheric distillation column is employed in order to recover pure water in the bottom to use for water injections in the SS-THI-Recovery process. With

MEG as THI (Fig. VI.2), the atmospheric distillation column is dismissed, since fresh water is naturally recovered in columns for THI recovery from the HPS aqueous phase.

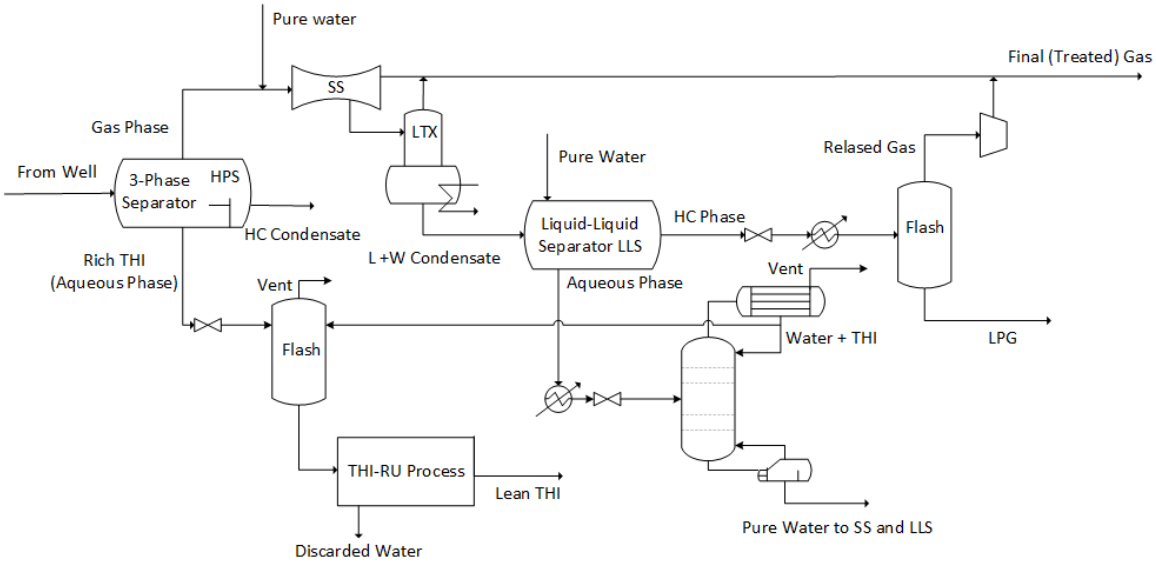

Figure VI. 1. SS-THI-Recovery PFD for ethanol or methanol as THI (Teixeira et al., 2018).

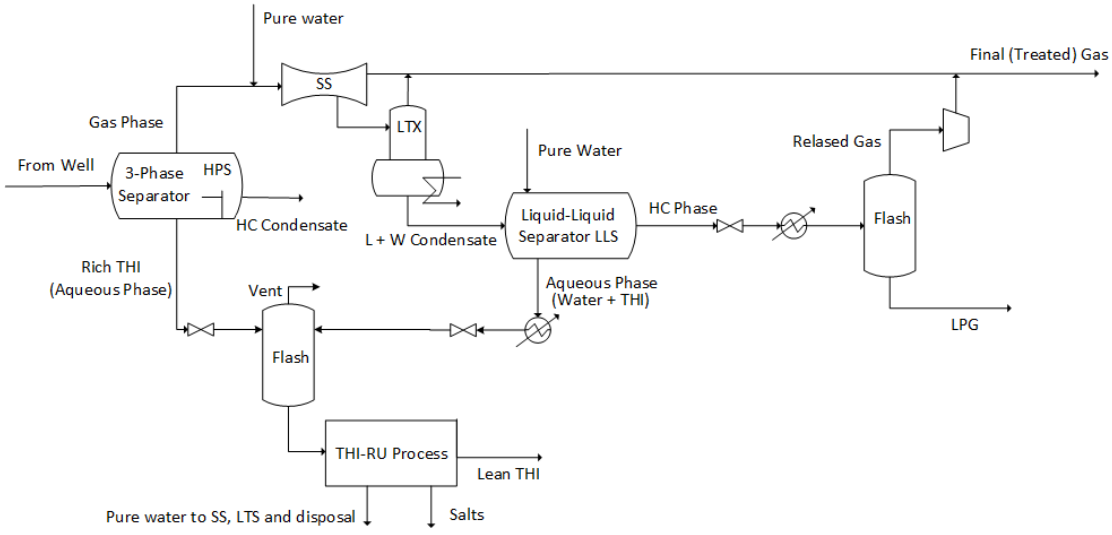

Figure VI. 2. SS-THI-Recovery PFD for MEG as THI (Teixeira et al., 2018).

For simulation of process configurations, SS-UOE unit was employed in HYSYS PFDs with CPA-EOS. SS geometry and performance for the methanol case are depicted in Fig. VI.3. The SS signatures at the throat are present in all profiles derived from the fact that the flow area section gradient is nonzero (Fig. VI.3a). Fig. VI.3f shows that SS fluid enters the device with

molar vapor fraction already below 100% due to the water injection in SS feed. This behavior agrees with Fig. VI.3g, where almost 90% of water condensed in SS inlet. Therefore, the SS-THI-Recovery process is based on maintaining a permanent aqueous phase through SS to continuously extract THI from the gas phase and from the HC liquid phase. The water injection upstream the SS unit guarantees it by admitting this small excess of liquid water. Fig. VI.3h illustrates the plane *P x T* with feed HCDP and WDP curves, lean gas HCDP curve, and SS flow path. The SS path starts with expansion of the two-phase humid vapor – below feed WDP curve – entering the feed VLE envelope until the suddenly linear shock-jump, recompressing to superheated vapor, followed by final smooth recompression and heating through the diffuser.

Fig. VI.4 shows the results of THI loss for processes with and without SS-THI-Recovery. Despite the reduction of 99% on MEG loss, the amount of this THI carried with gas phase is rather small, representing only 0.02% of loss. On the other hand, for the more volatile THIs, the amount of THI that would be lost with the gas phase is considerable: 26% of methanol and 17% for ethanol. With SS-THI-Recovery, methanol and ethanol losses are reduced by 92% and 79% to only 2.3% and 3.6%, respectively.

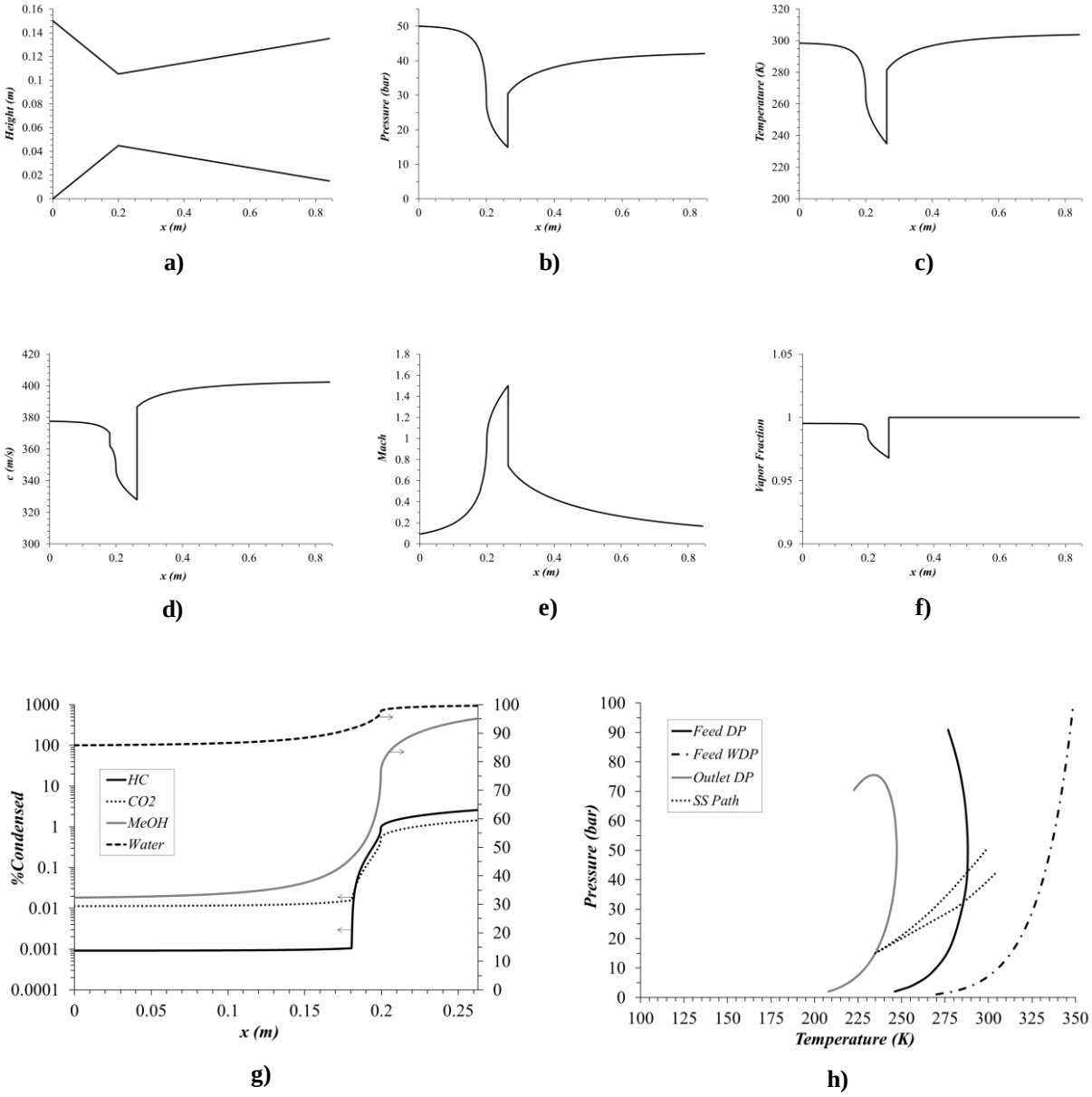

Figure VI. 3. SS Profiles for SS-THI-Recovery with Methanol: (a) Flow Section; (b) *P*; (c) *T*; (d) Sound Speed *c*; (e) *Ma*; (f) Mol Vapor Fraction; (g) %Condensed HCs, CO_2, H_2O, THI; (h) Plane *T x P* with SS Path, HCDP and WDP Curves of SS Feed and HCDP Curve of Lean Gas (Teixeira et al., 2018).

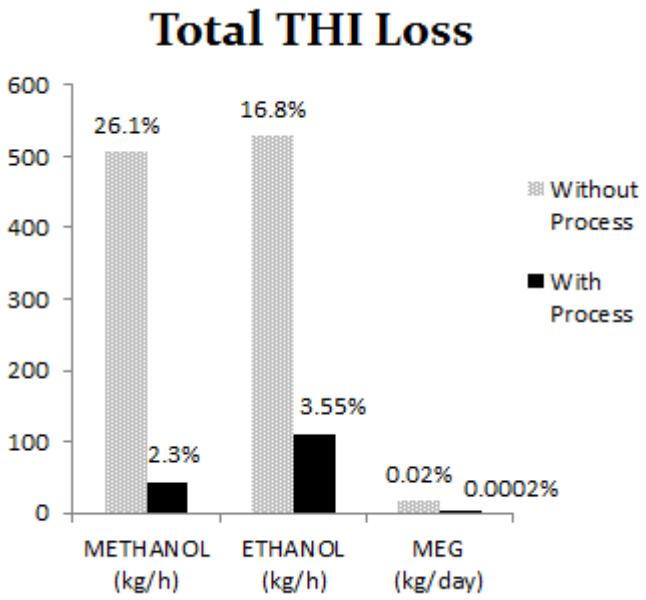

Figure VI. 4. Total THI Losses with/without SS-THI-Recovery Process (Teixeira et al., 2018).

The assessment of SS-THI-Recovery shows that it is a simple process, with low footprint and easy implementation, even for less volatile THIs such as MEG. High recoveries were obtained for all THIs simulated, entailing an important reduction of costs related to THI make-up, storage and transport.

VI.2. Economic leverage affords post-combustion capture of 43% of carbon emissions: Supersonic separators for methanol hydrate inhibitor recovery from raw natural gas and CO_2 drying

This work was published in Journal of Environmental Management, 236, 534-550, 2019. doi: https://doi.org/10.1016/j.jenvman.2019.02.008 (Appendix T.25).

In this paper, the offshore SS-THI-Recovery process is further investigated for the use of methanol as THI (SS-MeOH-Recovery), contemplating a full technical, economic and environmental analysis. In this case, the economic leverage of SS-MeOH-Recovery process is used to afford a post-combustion CO_2 capture plant, reducing 43% of carbon emissions. The SS-MeOH-Recovery PFD is the same as in Fig. VI.1 from Teixeira et al. (2018) for methanol as THI. In this work, it is expanded to also include the post-combustion capture (PCC) plant of

chemical absorption with aqueous MEA. The captured CO_2 is subsequently dehydrated with SS and compressed for exportation to EOR as high pressure liquid, as shown in Fig. VI.5.

For SS simulations, SS-UOE module was employed with CPA-EOS. Fig. VI.6 shows the SS geometry and performance results for the innovative application of CO_2 dehydration. Pressure, temperature, sound speed and *Ma* profiles all show $\pm\infty$ spatial gradient singularities at the throat corresponding to the SS signatures. SS fluid enters the device with 100% of vapor phase, as shown in Fig. VI.6a, and condensation of water starts near the throat, rapidly achieving almost 100% (Fig. VI.6d). Fig. VI.6e depicts SS flow path in plane *P x T* with feed CO_2 WDP, dew-point and bubble-point loci, and dry CO_2 dew-point and bubble-point loci. Both feed and dry CO_2 VLE envelopes are extremely thin and practically coincident. The SS flow path starts above the WDP curve, crossing it when water starts condensing along with a small quantity of CO_2, possibly dissolved in water (from Fig. VI.6d). The SS path attains maximum specified *Ma* and minimum temperature, touching the dew-point locus of dry CO_2. After water condensate removal, normal shock occurs, causing a sudden rectilinear recompression and heating to superheated vapor flow. Then, dry CO_2 goes through the ending diffuser, with smooth recompression and heating.

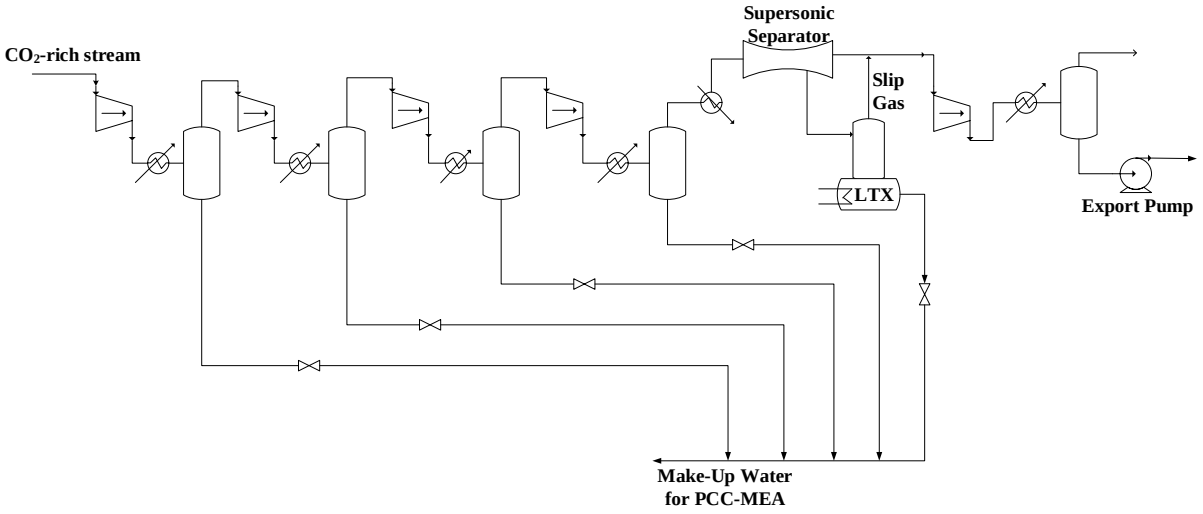

Figure VI. 5. Compression and dehydration unit for CO_2 product to EOR (Teixeira et al., 2019).

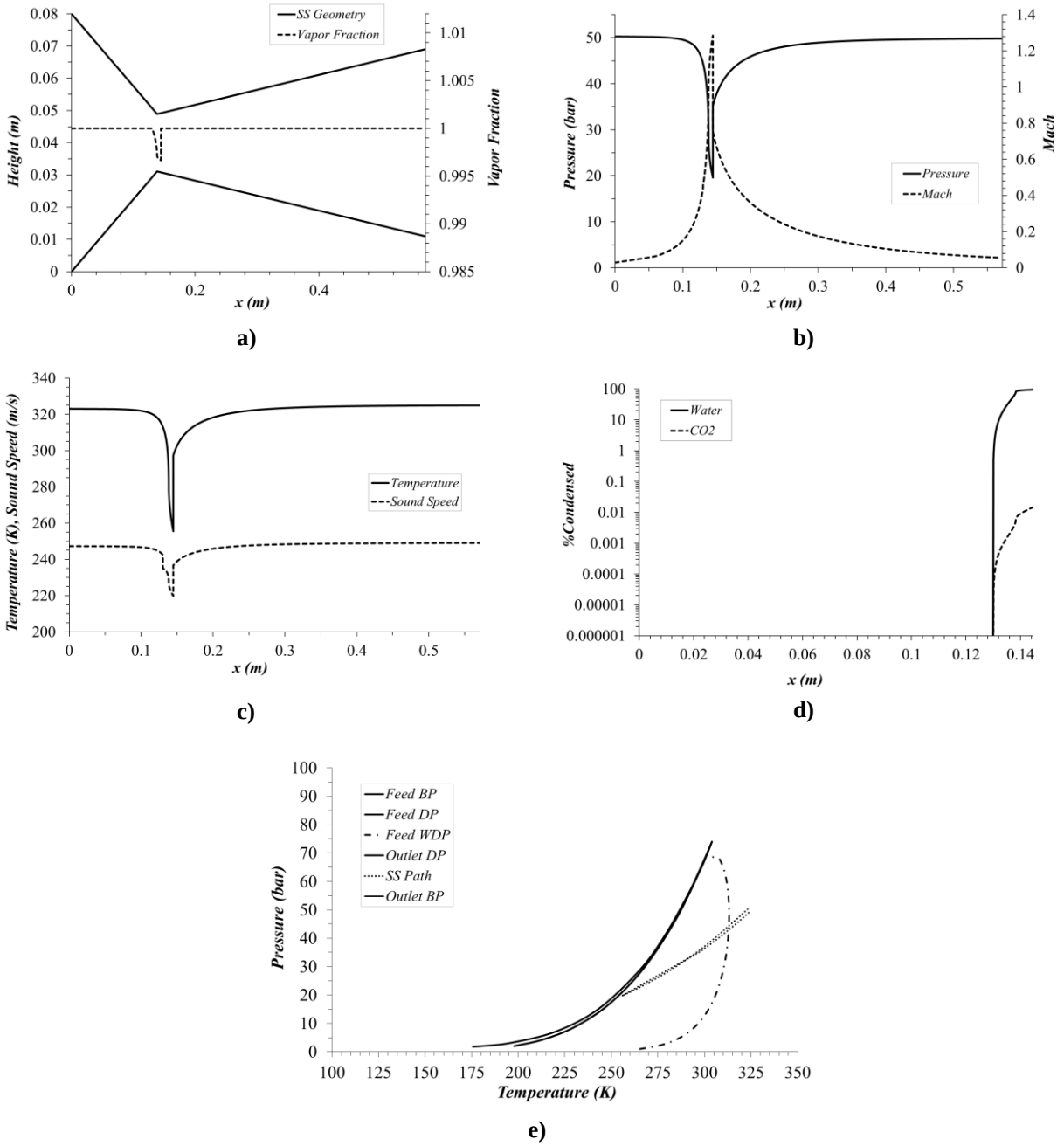

Figure VI. 6. SS axial profiles for CO_2 dehydration: (a) SS walls and mol vapor-fraction vs *x*; (b) *P* and *Ma* vs *x*; (c) *T* and *c* vs *x*; (d) %condensed CO_2 and H_2O vs *x*; (e) plane *P x T* with SS path, dew-point, bubble-point and WDP loci of CO_2 feed and dry CO_2 (Teixeira et al., 2019).

The proposed SS-MeOH-Recovery process with PCC was compared with a conventional NG processing configuration without carbon capture and with MeOH loss to the exported gas. Despite the much higher investment with the use of SS and the addition of a PCC plant, the new process achieved a higher net present value after 20 years of operation, as shown in Fig. VI.7. This is only possible due to higher revenue from greater C3+ produced by SS when compared to conventional JT expansion, and revenue from CO_2 captured with PCC, which also abated a significant percentage of carbon emissions. A sensitivity analysis on the crude oil price was also conducted, as depicted in Fig. VI.8, entailing that the SS-MeOH-Recovery process outperforms the conventional gas processing in terms of net present values for oil prices above 55 MMUSD.

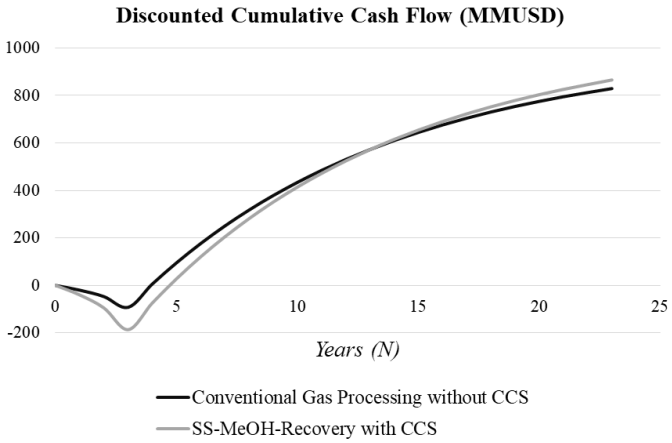

Figure VI. 7. Profiles of net present value (NPV) of process alternatives (Teixeira et al., 2019).

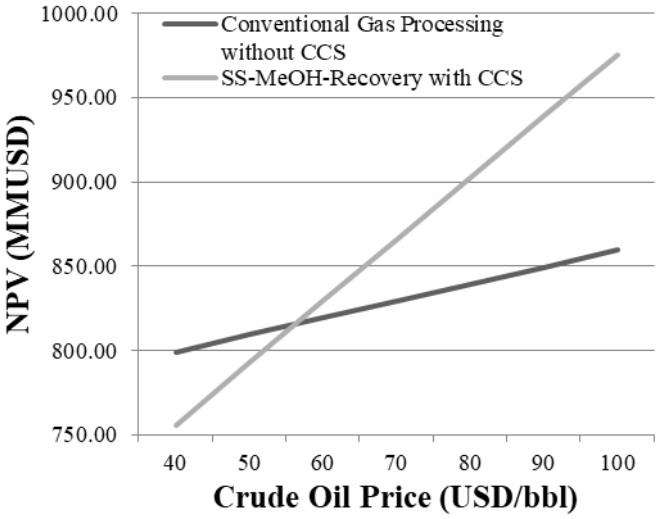

Figure VI. 8. Influence of oil price on NPV (Teixeira et al., 2019).

Therefore, SS-MeOH-Recovery proposed in this work, in conjunction with a PCC plant with capacity to reduce CO_2 emissions by 43%, followed by SS CO_2 dehydration, is superior on both economic and environmental grounds when compared to conventional NG processing. It is an economically feasible process, which provides cleaner NG production with adequate CO_2 management.

VI.3. A new concept of air pre-purification unit for cryogenic separation: Low-pressure supersonic separator coupled to finishing adsorption

This work was published in Separation and Purification Technology, 215, 173-189, 2019. doi: https://doi.org/10.1016/j.seppur.2019.01.015 (Appendix T.23).

For production of oxygen via cryogenic process, air fed to the Cold-Box must pass first through a pre-purification unit (PPU) to remove water, CO_2 and other impurities. The conventional PPU comprises compression, cooling, and temperature-swing adsorption (TSA) over an activated alumina (AA) bed followed by a molecular sieve (MS) bed respectively for dehydration, and CO_2 and HCs removal (FULL-TSA process), supplying treated air to the Cold-Box at 3.1 bar. TSA operation involves periodic bed regeneration combining heating with depressurization, using heated N_2 from Cold-Box. As purging water from AA bed is harder than purging CO_2+HCs from MS bed, TSA requires N_2 above 120°C for complete desorption.

This work proposes a new PPU alternative adopting a supersonic separator (SS) upstream to TSA to execute a pre-dehydration step in order to diminish TSA service and costs (SS-TSA, Fig. VI.9). SS is designed to abate ≈98.5% of the water load from pre-cooled 10°C raw air (≈3886 ppmH2O), reducing TSA service to less than 500 ppm of contaminants, where CO_2 is the main load (≈370 ppm). Thus, the AA bed is dismissible, and only a MS bed can be used, approximately ≈15% larger than its size in FULL-TSA, for same cycle-time and with lower heat consumption for bed regeneration. In SS-TSA, MS operates with reduced adsorption load, as well as smaller vessels and less adsorbent inventory. It requires less adsorbent replacement costs, due to lower thermo-mechanical stress from less frequent switches, increasing bed lifetime. Besides, temperature of N_2 for bed regeneration is reduced to 80ºC due to lower H_2O content and weaker water interaction with MS than with AA. An alternative of SS-TSA process

with heat integration (SS-TSA-HI) is also approached to improve the process by dismissing the use of low-pressure steam to heat the N_2 for bed regeneration.

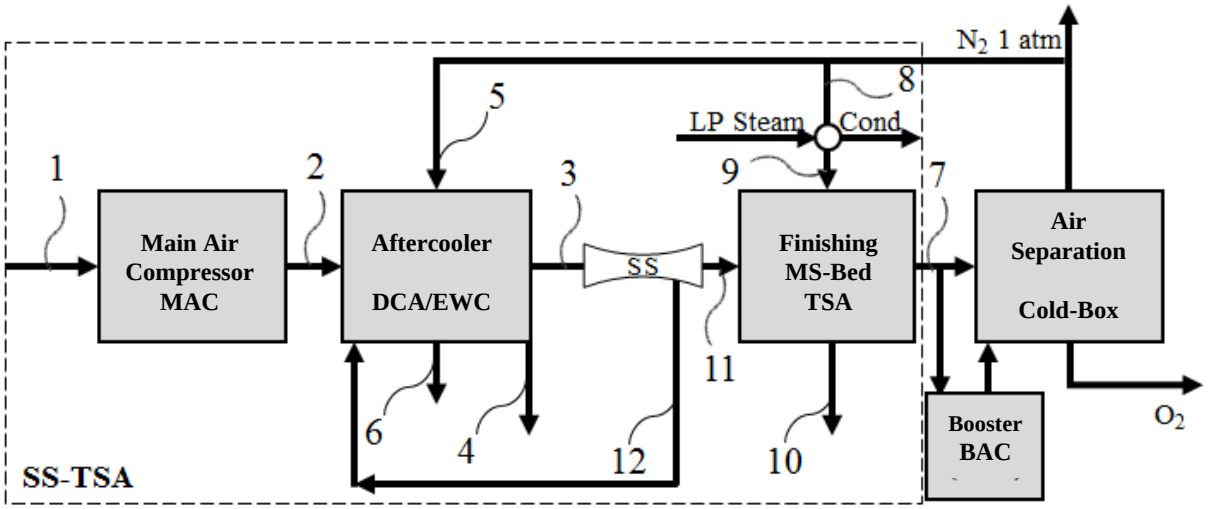

Figure VI. 9. SS-TSA PPU for purified air supply to Cold-Box (Brigagão et al., 2019).

SS-UOE was used in this work for simulation of SS-TSA and SS-TSA-HI alternatives in HYSYS with PR-EOS. SS operation is depicted in Fig. VI.10, with the presence of SS signatures ($\pm\infty$ spatial gradient singularities at the throat) for nonzero flow area section gradient (Fig. VI.10a). For air purification, a low-pressure SS is used (P^{Feed}=*3.23 bar*), differently to high-pressure NG applications. Therefore, in this case, SS device has higher dimensions when compared to typical NG SS for similar molar flow rates, with inlet diameter of 87 cm, as depicted in Fig. VI.10a. Ma^{Shock} was specified as 1.2, leading to a high pressure recovery of 96.54% (Fig. VI.10b), and capturing 98.56% of water (Fig. VI.10d) as supercooled liquid at -48ºC. Fig. VI.10f displays the SS path on plane $P \times T$ with WDP curves of the SS air feed for several water contents: saturated feed (3886 ppmH_2O), SS outlet dry air (56.4 ppmH_2O) and intermediate dehydration levels (1000 ppmH_2O and 300 ppmH_2O). Figs. VI.10f and VI.10.d show that condensation starts immediately after entering SS, since the feed stream is saturated, with most intense condensation near and after the throat. SS path starts with a smooth descending expansion arc towards the lowest *(T,P)* on the 56.4 ppmH_2O WDP locus, where liquid is collected. Normal shock occurs, depicted by a rectilinear jump back to higher *(T,P)* condition, followed by sub-sonic path through the ending diffuser, regaining more temperature and pressure towards SS outlet.

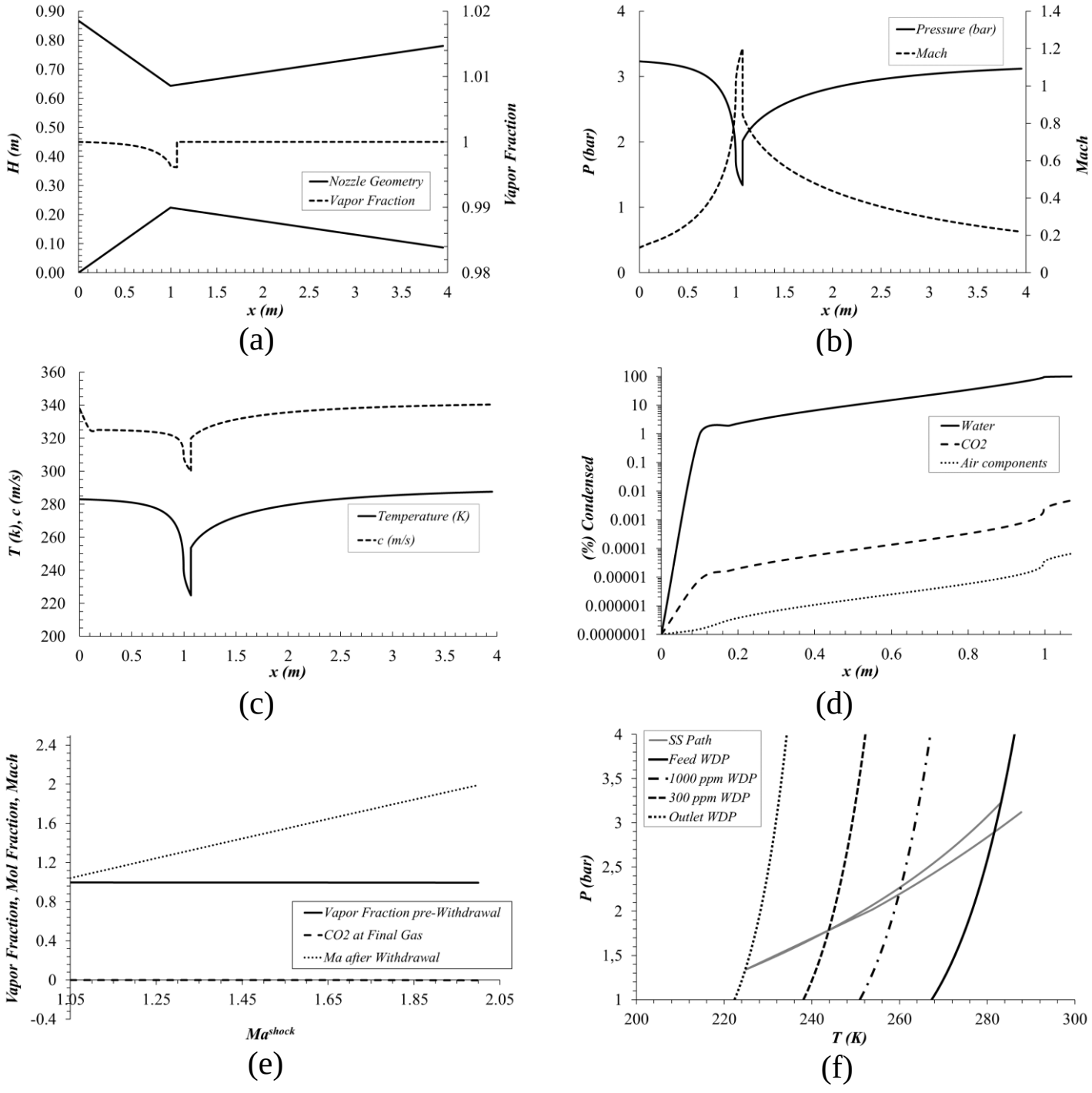

Figure VI. 10. SS air drying: (a) SS diameter & mol vapor fraction vs x; (b) P, Ma vs x; (c) T, c vs x; (d) %Condensed H_2O, CO_2 & air species vs x; (e) pre-shock values (mol vapor fraction, CO_2 mol fraction, Ma_{BS}) vs Ma^{Shock}; (f) SS path on plane $P \times T$ and WDP loci (3886 ppmH2O fed air, 56.4 ppmH2O dry air, 300 ppmH2O air, 1000 ppmH2O air) (Brigagão et al., 2019).

The conventional FULL-TSA process exhibits higher FCI and COM when compared with SS-TSA and SS-TSA-HI. Fig. VI.11 illustrates NPV profiles of FULL-TSA, SS-TSA and SS-TSA-HI for a horizon of 30 years. SS-TSA-HI surpasses SS-TSA in profitability after 6 years of operation, which means that the payback of the FCI increment in SS-TSA-HI occurs at that point. Furthermore, despite not included in the economic analysis, another comparative advantage of SS-TSA and SS-TSA-HI is the availability of dry N_2 for commercialization, due to lower flow rate of regeneration nitrogen.

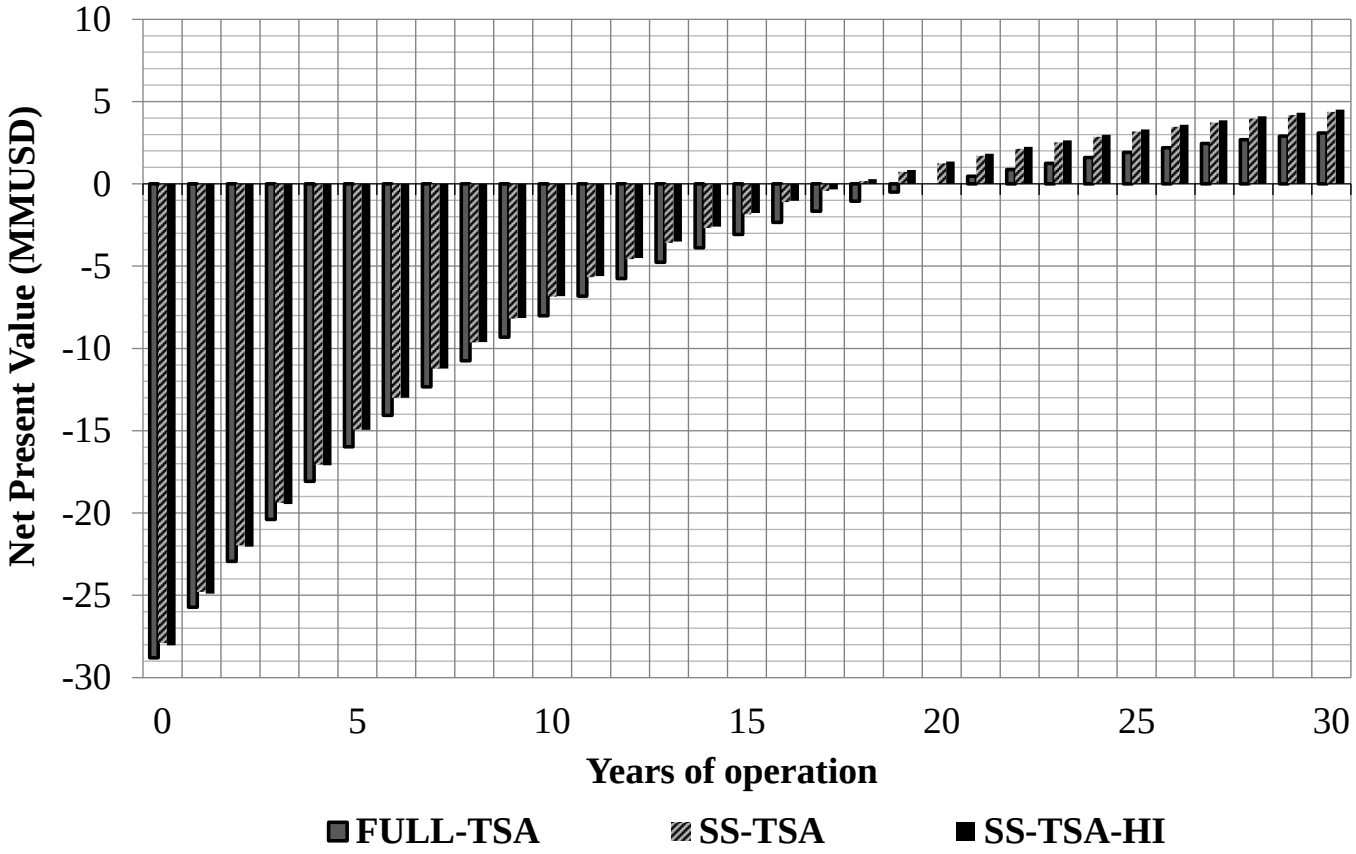

Figure VI. 11. *NPV* of FULL-TSA, SS-TSA and SS-TSA-HI (purified air at *5.28 USD/kNm³*) (Brigagão et al., 2019).

VI.4. Supersonic separator for cleaner offshore processing of supercritical fluid with ultra-high carbon dioxide content: Economic and environmental evaluation

This work was published in Journal of Cleaner Production, Vol. 234, p. 1385-1398, 2019 (doi: 10.1016/j.jclepro.2019.06.304) (Appendix T.28).

In this paper, the offshore processing of high-pressure supercritical fluid at high flow rate with 68%mol CO_2 of Chapter V is revisited. The SS-SS gas hub with condensate recycle and JT valve ([RC+JT+SS], Chapter V) is compared with a conventional process comprising a molecular sieve (MS) for dehydration, JT expansion for C3+ removal and MP for CO_2 capture ([MS-JT-MP]). The large-scale floating plant is designed to produce 100000 bbl/d of 34.3ºAPI oil, 36318m³/d of water and to process about 50 $MMSm^3/d$ of raw supercritical NG with 68%mol CO_2. The multiphase riser fluid enters the topside high-pressure oil-gas-water separator (HPS) at 120 bar. The gas phase from HPS is sent to WDPA+HCDPA, and a small fraction of the treated fluid is slipped to decarbonation, producing fuel-gas (FG) with 20%mol CO_2. The captured CO_2 joins the remaining treated gas for compression and pumping to EOR.

Differently from SS-SS alternative, where a depressurization of HPS gas to 80 bar is required for SS operation outside the supercritical neighborhood, in [MS-JT-MP], dehydration is carried out at 120 bar, in 12 high-pressure MS vessels. Then, about 5 MMSm³/d of the dry fluid is sent to JT expansion to 55 bar, producing ≈2 MMSm³/d of C3+ condensate, which is recycled to HPS to enhance oil production, and ≈3 MMSm³/d of lean dry fluid, that follows to decarbonation in MP. The permeated CO_2 is compressed and mixed with the remaining 49 MMSm³/d of dry fluid, following to compression and pumping for EOR.

MS-JT-MP and SS-SS alternatives are compared in terms of oil production, ppmH_2O in EOR fluid, power demand, CO_2 emissions, FCI and NPV – Figs. VI.12 and VI.13. The power demand of SS-SS (Fig. VI.12c) is 167.2 MW, while MS-JT-MP requires only 105 MW. This is a consequence of supercritical fluid depressurization to 80 bar to feed the 1st SS unit, while MS works at high-pressure (120 bar); hence there is only one stage for main compression to EOR in MS-JT-MP, while SS-SS alternative requires two. Therefore, MS-JT-MP produces lower flow rate of FG for power generation, emitting 1.195 $MMSm^3/d$ of CO_2, while SS-SS emits 1.32 $MMSm^3/d$ (Fig. VI.12d). On the other hand, Fig. VI.12a shows that SS-SS has greater oil

production, a consequence of its higher recycle of water-C3+ condensate from 1st SS unit (5.29 $MMSm^3/d$, 58.4%mol CO_2) against the MS-JT-MP highly-carbonated condensate from JT unit (2.03 $MMSm^3/d$, 78.3%mol CO_2). This recycle impacts oil production, because the heavier species from 1st SS or JT accumulate in HPS, enlarging the respective oil effluents. Therefore, Fig. VI.12a entails that SS is a greater C3+ catcher than JT, while Fig. VI.12b unveils the MS unit as greater water remover than the 1st SS unit. However, the ≈100ppm H_2O left by 1st SS unit in the EOR fluid does not imply any operational issue, whereas the 1ppm of H_2O left by MS inflicts a high cost of FCI due to the 12 expensive MS vessels, as shown in Fig. VI.12e, where MS is the greater share of MS-JT-MP FCI. Fig. VI.12f reports MS-JT-MP with greater CH_4 capture into the EOR fluid, a consequence of the poor CO_2/CH_4 selectivity of MP compared to the 2nd SS unit, which preserves most of CH_4 in the FG. After 20 years of operation, the gas processing plant with SS-SS would have 33% higher NPV than with conventional MS-JT-MP process (Fig. VI.13).

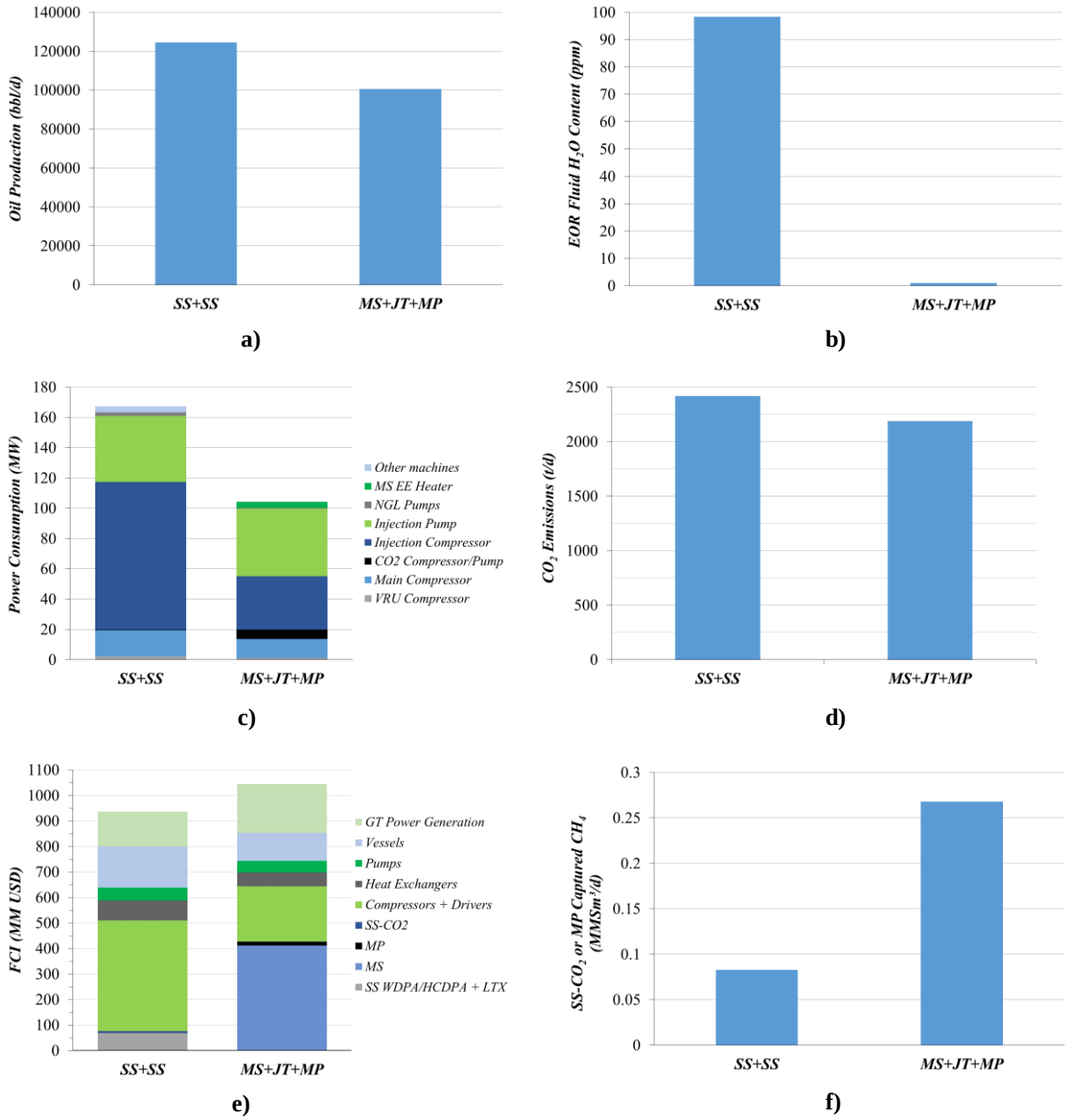

Figure VI. 12. SS-SS versus MS-JT-MP: (a) oil production; (b) EOR-Fluid ppmH_2O; (c) power consumption; (d) CO_2 emissions; (e) *FCI*; (f) CH_4 into EOR-Fluid (De Melo et al., 2019).

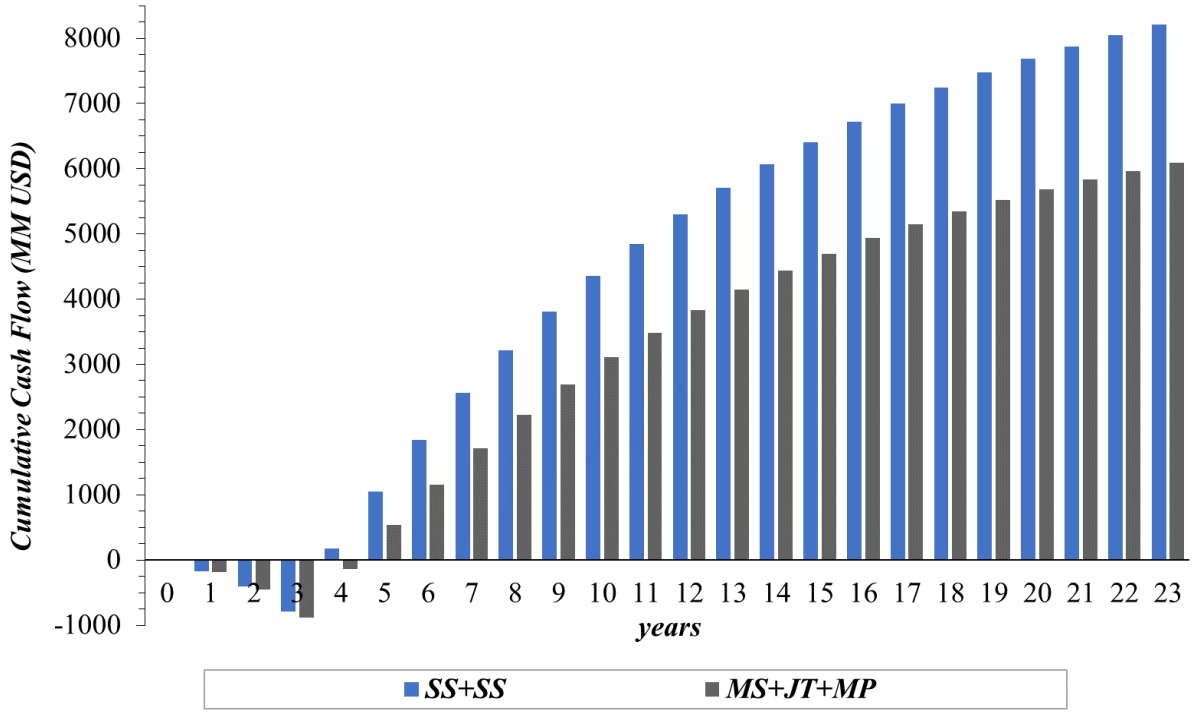

Figure VI. 13. Net present value (20 years of operation) (De Melo et al., 2019).

SS-SS has ≈10% lesser investment costs, due to the outstanding FCI of MS units in MS-JT-MP for this size of service, and 33% higher NPV after 20 years of operation, accounting for the inferior FCI of SS-SS as well as its much greater oil production due to higher recycle of C3+ condensate from 1st SS unit to HPS. Regarding CO_2 capture, the 2nd SS unit is comparatively better than MP: despite its higher complexity, heat integration and use of refrigeration, the 2nd SS unit has lower FCI relatively to MP when CO_2 compression steps are accounted for. Therefore, the best alternative on economic grounds is the SS-SS process. Nevertheless, this alternative produces ≈9.5% more CO_2 emissions than the conventional MS-JT-MP. However, SS-SS can also be environmentally superior to the conventional process if its economic leverage is used to afford a post-combustion capture plant to abate emissions above such 9.5% excess. In other words, the richer SS-SS solution can afford its self-cleaning by installing a post-combustion plant to remove its excessive emissions relative to the conventional MS-JT-MP process, such as in Teixeira et al., 2019.

VI.5. Automatized Monte-Carlo analysis of offshore processing of CO_2-rich natural gas: Conventional versus supersonic separator routes

This work was published in Journal of Natural Gas Science and Engineering, 69, 102943, 2019. doi: https://doi.org/10.1016/j.jngse.2019.102943 (Appendix T.29).

Offshore oil and gas production with high $\%CO_2$ and gas/oil ratio requires first-of-a-kind designs, creating design uncertainties besides the offshore operation uncertainties. Therefore, the design of offshore units under influence of stochastic factors is recommended to avoid oversized designs or underachieved specifications, implying economic and/or environmental losses. This paper proposes a novel CAE tool, MCAnalysis (Fig. VI.14), which is a VB.NET/XML interoperability framework between HYSYS and MATLAB to generate automatized Monte-Carlo analysis based on collecting process responses after submitting process flowsheet to samples of stochastic input variables with known PDF. Based on success probability, the engineer can evaluate if the design is approved or if further changes are required to raise such probability.

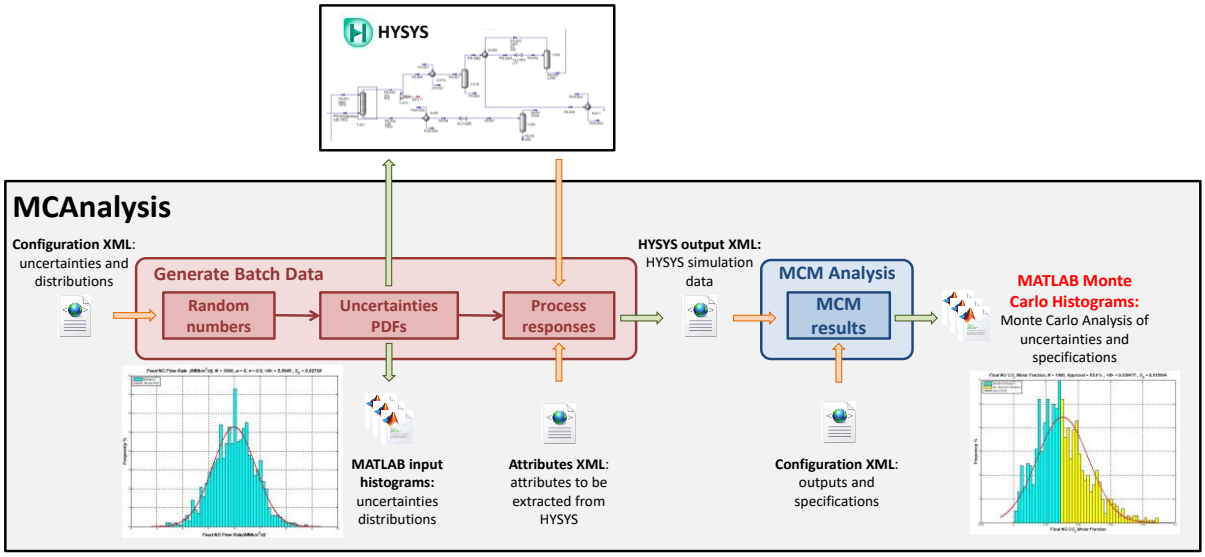

Figure VI. 14. *MCAnalysis* modular architecture (Gonzaga et al., 2019).

Offshore processing of CO_2-rich NG via conventional process comprising TEG absorption, JT expansion and MP, and via SS+MP alternative were submitted to Monte-Carlo analysis considering non-deterministic feed variables: [U1] NG flow rate; [U2] NG %mol of CO_2; and [U3] GOR (Table VI.1). Monte-Carlo analysis was based on the statistical behavior of chosen

output variables [S_1] to [S_{10}] (Table VI.2) with minimum and maximum threshold values for commercial specification and/or attainment of process constraints. SS-UOE and MP-UOE were used for simulation of process alternatives in HYSYS flowsheet with PR-EOS. Processes were initially sized considering average values of the three stochastic input variables. Subsequently, the 1st Monte-Carlo round was executed and both original designs of the conventional and SS routes were considered insufficient as three out of ten output variables – NG y_{CO2}, $HCDP^{NG}$, $P^{EOR\text{-}Delivery}$ – did not attain at least *75%* of approved samples in both routes.

The process alternatives were then re-designed with appropriate increases of MP area, EOR well diameter, Ma^{Shock} of SS, and decrease of inlet temperature of JT unit (by increasing the heat exchanger area). A 2nd round of Monte-Carlo analysis then approved both debottlenecked designs based on at least *75%* of samples accomplishing specifications for all output variables. This demonstration illustrates the importance of Monte-Carlo analysis for testing and correcting designs of offshore CO_2-rich NG processing under uncertainties. In all instances of both routes, Monte-Carlo analysis also unveiled several process responses not following normal pattern and changes of stochastic behaviors of some responses after the re-design, indicating highly non-linear causality relationships for these responses (for example, $HCDP^{NG}$).

Table VI. 1. Parameters for normal *PDF*s of input variables (feed variables) (Gonzaga et al., 2019).

Input Variable	Description	Mean (μ)	St. Deviation (σ)	*99.99%* probability interval
[U_1]	*Dry CO_2-rich NG flow rate*	*6.0 $MMsm^3/d$*	*0.9 $MMsm^3/d$*	*$U_1 \in [2.4MMsm^3/d, 9.6MMsm^3/d]$*
[U_2]	*Dry CO_2-rich NG CO_2 molar fraction*	*0.45*	*0.03*	*$U_2 \in [0.33, 0.57]$*
[U_3]	*Multiphase feed GOR*	*450 sm^3/m^3*	*30 sm^3/m^3*	*$U_3 \in [330sm^3/m^3, 570sm^3/m^3]$*

Table VI. 2. Selected process responses for Monte-Carlo analysis and their specifications (*DP≡Dew-Point, y≡molar fraction in NG product*).

Output Variable	*Description*	*Specification*	*Comment*
$[S_1]$	*NG CO_2 content: $S_1=y_{CO2}$*	$y_{CO2} \leq 0.03$	*NG sales spec.*
$[S_2]$	*NG CH_4 content: $S_2=y_{CH4}$*	$y_{CH4} \geq 0.85$	*NG sales spec.*
$[S_3]$	*NG water DP: $S_3=WDP^{NG}$*	$WDP^{NG} \leq -45°C@1atm$	*NG pipeline spec.*
$[S_4]$	*NG hydrocarbon DP: $S_4=HCDP^{NG}$*	$HCDP^{NG} \leq 0°C@45bar$	*NG sales spec.*
$[S_5]$	*NG onshore delivery pressure: $S_5=P^{NG\text{-}Delivery}$*	$P^{NG\text{-}Delivery} \geq 70$ bar	*NG pipeline spec.*
$[S_6]$	*EOR-Fluid Water DP: $S_6=WDP^{EOR\text{-}Fluid}$*	$WDP^{EOR\text{-}Fluid} \leq -45°C@1atm$	*EOR pipeline spec.*
$[S_7]$	*Reservoir delivery pressure: $S_7=P^{EOR\text{-}Delivery}$*	$P^{EOR\text{-}Delivery} \geq 650$ bar	*EOR pipeline spec.*
$[S_8]$	*MP-Feed hydrocarbon DP: $S_8=HCDP^{MP\text{-}Feed}$*	$HCDP^{MP\text{-}Feed} \leq -10°C@45bar$	*MP constraint**
$[S_9]$	*MP CO_2 partial-pressure: $S_9=PPCO2^{MP\text{-}Feed}$*	$PPCO2^{MP\text{-}Feed} \leq 30$ bar	*MP constraint**
$[S_{10}]$	*Plant power-consumption: S_{10}=Power*	$Power \leq 84$ MW	*Power constraint#*

**To avoid membrane damage (Shahid and Nijmeijer, 2014). #Plant powered by 3x28MW gas-fired turboshafts (Araújo et al., 2017).*

The Monte-Carlo assessments of conventional and SS based process designs showed that the latter presented less sensitivity of the stochastic behavior of responses regarding debottlenecking. In other words, SS route was re-designed with tighter margins of debottlenecking to achieve all specifications in at least *75%* of the sampled cases. This means that the SS alternative has a greater resilience or elasticity, which translates a simpler, more straightforward and safer process. Moreover, SS-Route consistently showed lower power consumption and compressor investment, requiring, in average, *15%* less power and extracting water-C3+ condensate for HCDPA more selectively in terms of CO_2 (i.e. *≈23%mol* CO_2 versus *≈61%mol* in conventional counterpart). Therefore, the SS based process is statistically better on economic and environmental grounds.

Abbreviations

AA Activated Alumina; C3+ Propane and Heavier; COM Cost of Manufacture; CPA-EOS Cubic-Plus-Association; DP Dew Point; EOS; EOR Enhanced Oil Recovery; EOS Equation-of-State; FCI Fixed Capital Investment; GOR Gar to Oil Ratio; HCDP Hydrocarbon Dew-Point; HCDPA Hydrocarbon Dew-Point Adjustment; HPS High-Pressure Separator; JT Joule-Thomson; LLS Liquid-Liquid Separator; $MMsm^3/d$ Millions of standard m^3 per day; MP Membrane Permeation; MS Molecular Sieve; NG Natural Gas; NPV Net Present Value; PCC Post-Combustion Capture; PPU Pre-Purification Unit; PR-EOS Peng-Robinson EOS; SS

Supersonic Separator; TEG Triethylene Glycol; THI Thermodynamic Hydrate Inhibitor; TSA Temperature Swing Adsorption; UOE Unit Operation Extension; WDP Water Dew-Point; WDPA Water Dew-Point Adjustment.

References

Brigagão, G. V.; Arinelli, L. O.; de Medeiros, J. L.; Araújo, O. Q. F. A new concept of air pre-purification unit for cryogenic separation: low-pressure supersonic separator coupled to finishing adsorption. Separation and Purification Technology, 215, p. 173-189, 2019a. doi: https://doi.org/10.1016/j.seppur.2019.01.015

Gonzaga, C. S. B.; Arinelli, L. O.; de Medeiros, J. L.; Araújo, O. Q. F. Automatized Monte-Carlo analysis of offshore processing of CO_2-rich natural gas: Conventional versus supersonic separator routes. Journal of Natural Gas Science and Engineering, 69, 102943, 2019. doi: https://doi.org/10.1016/j.jngse.2019.102943

De Melo, D. C.; Arinelli, L. O.; de Medeiros, J. L.; Teixeira, A. M.; Brigagão, G. V.; Passarelli, F.; Grava, W. M.; Araújo, O. Q. F. Supersonic separator for cleaner offshore processing of supercritical fluid with ultra-high carbon dioxide content: economic and environmental evaluation. Journal of Cleaner Production, 234, p. 1385-1398, 2019. doi: https://doi.org/10.1016/j.jclepro.2019.06.304

Teixeira, A. M.; Arinelli, L. O.; de Medeiros, J. L.; Araújo, O. Q. F. Recovery of thermodynamic hydrate inhibitors methanol, ethanol and MEG with supersonic separators in offshore natural gas processing. Journal of Natural Gas Science and Engineering, 52, 166-186, 2018. doi: 10.1016/j.jngse.2018.01.038

Teixeira, A. M.; Arinelli, L. O.; de Medeiros, J. L.; Araújo, O. Q. F. Economic leverage affords post-combustion capture of 43% of carbon emissions: Supersonic separators for methanol hydrate inhibitor recovery from raw natural gas and CO_2 drying. Journal of Environmental Management, 236, 534-550, 2019a. doi: 10.1016/j.jngse.2018.01.038

CHAPTER VII - MEMBRANE-PERMEATION MODELING FOR CARBON CAPTURE FROM CO_2-RICH NATURAL GAS

This Chapter presents further developments of MP-UOE that are object of submissions in 2019.

VII.1. Introduction

CO_2 removal from natural gas (NG) using membrane permeation (MP) technology is becoming gradually more common in the context of large-scale NG processing and purification systems. This is especially true, among several other applications, in connection to offshore rigs that treat high flow rates of CO_2-rich raw NG streams (from *20%mol* to *45%mol* CO_2), producing exportation gas in the retentate (from *3%mol* to *5%mol* CO_2) and, in the permeate, CO_2-rich product streams (from *70%mol* to *80%mol* CO_2) for enhanced oil recovery (EOR) destinations (Ebner and Ritter, 2009; Arinelli et al., 2019b). Ho et al. (2006) and Bernardo et al. (2009) present complete surveys on gas processing applications of membrane permeation technology.

Regarding decarbonation of CO_2-rich NG, it is worthwhile to notice that chemical absorption of CO_2 with aqueous monoethanolamine (MEA) and aqueous methyl-diethanolamine (MDEA) are very mature technologies considered as benchmark options for such service (de Medeiros et al., 2013). Nevertheless, MP with polymeric skin-dense membranes is growing fast and it is being much more used than aqueous-amine absorption for CO_2-rich NG decarbonation at high-pressure, such as in deep-water offshore platforms, where space and weight are major concerns and the modularity of MP units is an important advantage (Araújo and de Medeiros, 2017). Other advantages of MP over aqueous-amines for NG decarbonation services on offshore platforms comprise: (i) MP is a simpler process solution; (ii) MP units are smaller and lighter systems; (iii) MP is a cleaner solution with no chemical additives; (iv) MP has low fire or explosion hazards; (v) MP can execute simultaneous removal of CO_2, H_2S and H_2O; (vi) MP has less maintenance, lower capital and operational costs; and (vii) MP can treat NG at well-heads. On the other hand, some major comparative disadvantages of MP to aqueous-amines absorption are: (i) decreasing selectivity for increasing CO_2 partial pressure; (ii) inferior economic competitiveness at higher scales; (iii) decreasing membrane stability and resilience for increasing (T,P); (iv) degradation issues and limited lifetime of membranes; (v) MP technology is not sufficiently mature according to industrial standards (Araújo et al., 2017).

Fig. VII.1 presents the types of membrane-permeation modules and the most used ones – spiral-wound membrane (SWM) and hollow-fiber membrane (HFM) – for CO_2 removal from NG in offshore platforms.

Several MP process configurations for CO_2-rich NG decarbonation are possible, with the aim of meeting product CO_2 content, while maximizing methane recovery and minimizing costs. Compared to the multi-stage configurations, the single stage MP is distinguished by its small weight and footprint, which are both crucial for offshore applications. However, methane losses in the single stage process – and thus the associated loss in revenues – could be significant to the extent that it is not economically feasible for operating companies (Hao et al., 2008). The two-stage configurations reduce the methane loss in the process, yet at the cost of increased footprints, weight, and costs associated to higher number of equipment and power demand for recycle purposes (Echt, 2017). Some of the possible process configurations of MP units with one and two stages are shown in Fig. VII.2 (Hoorfar et al., 2018).

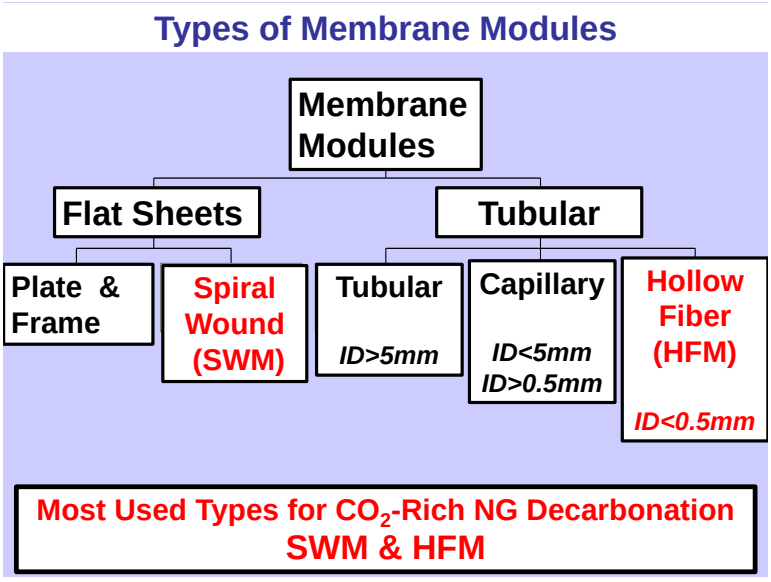

Figure VII. 1. Types of MP modules versus CO_2-rich NG decarbonation.

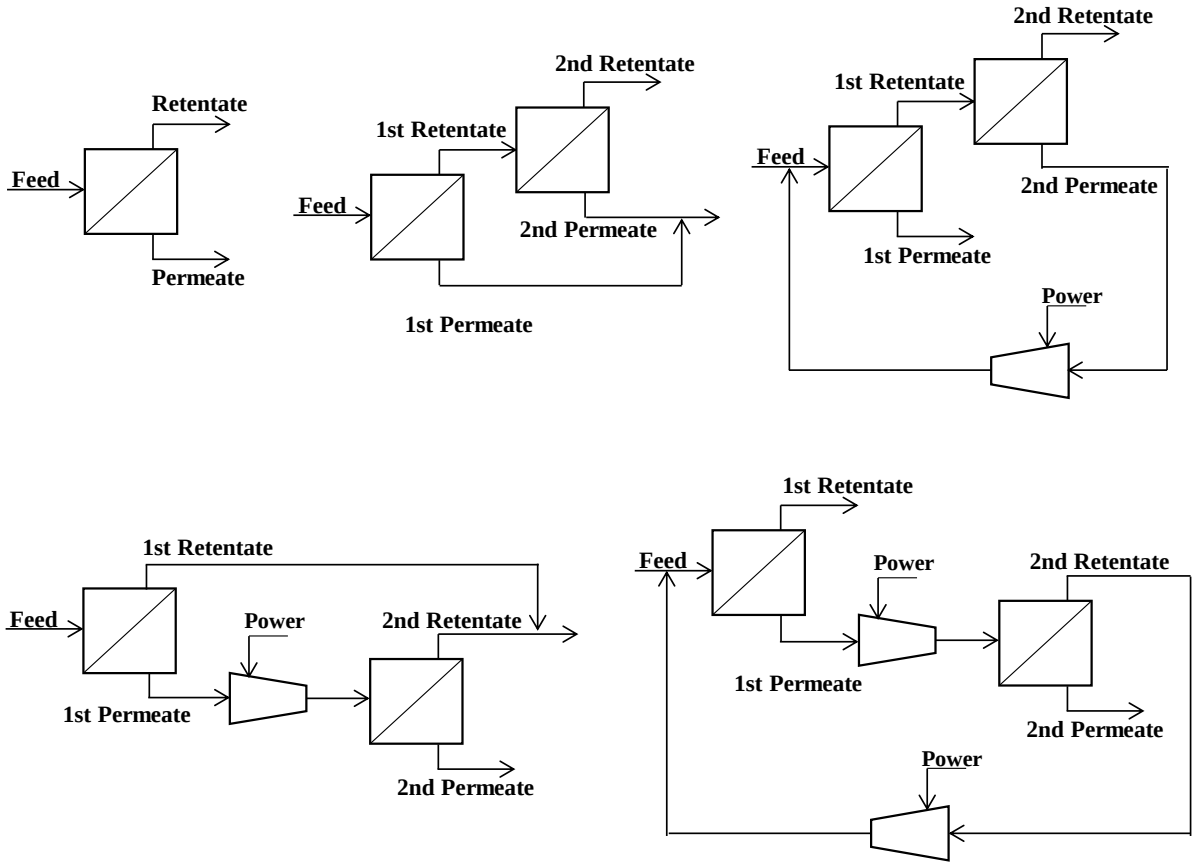

Figure VII. 2. Process configurations of MP units for NG decarbonation.

NG purification is probably the largest worldwide application of gas separation. Membrane permeation has a few percent of this market but exhibits a great potential of expansion, only considering eight or nine polymeric materials that respond for 90% of applications, where cellulose-acetate membranes (CAM) and polyimide membranes are the most used for decarbonation of CO_2-rich NG under SWM as well as HFM modules. Table VII.1 lists some manufacturers of commercial CAM membranes for CO_2 removal from NG. Published studies have approached hundreds of new polymer materials for MP applications in the last years. Nonetheless, the harder obstacle to approve new materials for commercial MP applications has to do with membrane resiliency regarding real processing conditions and membrane capability to maintain its characteristics (e.g., selectivity and capacity) through reasonable operation times.

Table VII. 1. Manufacturers of cellulose-acetate membranes for NG processing.

Manufacturer	*Membrane Type*	*Element Orientation*	*Element L x D*	*Element Installation*	*Gas Contact*
UOP	*SWM**	*Horizontal*	*1m x 0.2m*	*Tandem Elements in Tubes*	*Cross-Flow*
NATCO Schlumberger	*HFM**	*Vertical*	*2m x 0.4m Several*	*Single Element*	*Cross-Flow Parallel-Flow*
Air Liquid	*HFM*	*Vertical Horizontal*	*Several*	*Single Element*	*Cross-Flow Parallel-Flow*

**SWM = Spiral-Wound Membrane; HFM = Hollow-Fiber Membrane*

VII.2. Software for Simulation of MP Units in Natural Gas Processing

Currently, there are no commercial computational tools available for rigorous design and simulation of general membrane permeation units. When existent, such type of software is normally developed for local and restricted *ad hoc* finalities of MP developers, MP manufacturers and certain MP users. On the other hand, oil and gas companies, which operate large-capacity processing plants of CO_2-rich NG at offshore sites, are experiencing a crucial dependence on such category of simulation and design tools.

These MP modeling tools are necessary, for example, to revamp operating MP units in order to accommodate – in a new processing flowsheet – new raw NG flow rates, CO_2 contents and new CO_2 separation targets. Accurate MP models are also necessary for daily supervision of operating MP plants, particularly regarding loss prevention and safety because membrane cartridges can burst with certain frequency during the lifetime of MP units for high-pressure NG processing (Bernardo et al., 2009).

However, since MP units have a large number of specific parameters – geometric aspects (diameters, lengths, thicknesses), material bulk properties (density, heat capacity, operational limits), external and internal heat transfer coefficients (trans-membrane and trans-shell), permeate/retentate contact configurations (parallel flows, countercurrent flows, crossed flows), permeate/retentate locations relative to the membrane (inside/outside), permeate/retentate head-loss parameters, species permeances, etc – the development of a truly rigorous steady-state MP simulator is a hard task, not counting the thermodynamic aspects of non-isothermal, non-

isobaric, composition-changing permeate/retentate compressible flows and the geometrical/mathematical issues characteristic of one-dimensional (1D) or two-dimensional (2D) frameworks.

Moreover, several material/structural parameters of MP units for high-pressure NG processing are not constant and expressively change with service time (Baker, 2004). Some changing parameters are evidently related to the degradations that the membrane material experiences through its lifetime; namely, CO_2/CH_4 selectivity, chemical stability, structural resiliency and mechanical stability. Such properties are known to change drastically with time in high-pressure NG processing, always towards performance deterioration, eventually culminating with bursts due to loss of structural stability or irreversible swelling and plasticization due to excessive intake of CO_2 and H_2S into the membrane body (Bernardo et al., 2009; Ebner and Ritter, 2009).

Nevertheless, a variety of MP models have been investigated in literature, considering certain simplifications to facilitate the calculations of membrane modeling, such as constant permeances, lumped models (Arinelli et al., 2017), isothermal operation (Lock et al., 2015), uniform axial flows (Chu et al., 2019), negligible pressure drops in feed and permeate sides (Xu et al., 2019), etc. Concerning CO_2-rich NG processing in offshore platforms, membrane permeation is one of many steps of gas purification. Therefore, for simulation and assessments of such complex processes comprising MP, specific membrane models must be developed to be inserted in the simulator process flow diagrams (PFDs). In the case of HYSYS professional software simulation, these customizable modules are called unit operation extensions (UOEs).

Lock et al. (2015) developed a mathematical model to characterize multicomponent CO_2 capture from NG, adapting hollow fiber membrane modules for radial crossflow, countercurrent flow, and co-current flow. The operation within the HFM module is considered isothermal, thus only mass balances are solved. The model consists of an algorithm coupling the succession of states method with Newton bisection solution, and it was later incorporated within HYSYS as an UOE. The model accuracy has been validated with experimental results available in literature. A case study of CO_2 removal from NG was also approached to compare the performance of different flow configurations based on their separation efficiency and process economics. The results show that ideally the countercurrent configuration presents a slightly higher separation performance in comparison to the radial crossflow, both being superior to the

co-current configuration. However, the most effective flow configuration in terms of separation performance is not always the most economical. Under circumstances of high separation services, it may engender extra membrane area, auxiliary equipment with power consumption and methane loss that increase the NG processing cost. Hence, a tradeoff must be determined among these parameters to choose the optimal flow configuration for efficient CO_2 capture under different operating conditions.

Hoorfar et al. (2018) developed a guide to find the cost optimum MP process configuration for NG decarbonation. The MP model is based on the solution-diffusion mechanism through mass transfer equation coupled with equations for mass balance across the membrane and local area mass balances. The driving force is the component partial pressure difference. The authors do not mention energy balances across the membrane, nor if it is considered an isothermal operation, yet this is probably the case, such as in Lock et al. (2015). The algorithm is solved by the series solution method, which is efficient for boundary value problems. This model was developed as an UOE (MemCal) for HYSYS, with the possibility of choosing between HFM/SWM, and countercurrent/co-current flow. It was validated with literature experimental data. The study was conducted for a binary CO_2/CH_4 gas with CO_2 concentrations ranging from 5% to 40% v/v, reducing it to 2% v/v via a variety of MP configurations. The crude gas pressure ranges from 30–90 barg, and permeate pressure is fixed at 1 barg. The two-stage configuration with recycle of retentate exhibited the lowest cost among all other – one stage, two stage and even three stage configurations – for most of the evaluated scenarios. The control of permeation area distribution between MP stages was proven to be a critical factor in optimizing MP cost. Costs of multi-stage units are not much sensitive to variations in the gas price, differently to single stage units, for which the cost is very sensitive. Crude gas capacity has an insignificant impact on MP costs, while the increase of feed pressure has a notable positive effect.

Arinelli et al. (2017) also developed a steady-state MP unit for simulation in HYSYS: MP-UOE. The model consists of a lumped short-cut method that makes an analogy with shell and tube heat exchangers, where the driving force of MP is the log mean of species partial pressure differences in membrane extremities. Overall mass balance and component mass balance equations complete the permeation model. MP-UOE component permeances were calibrated with real data from offshore platforms with CAM decarbonating CO_2-rich NG, therefore,

despite being a short-cut method, it reproduces with good agreement real NG separation results. On the other hand, permeances were adjusted as constant average values, thus independent of temperature and CO_2 fugacity (the main permeating component), which is a simplification of the real operation. After permeation calculations, energy balance around MP module finishes MP-UOE algorithm, considering a default value for the difference between product temperatures. The extension admits both HFM and SWM types, for countercurrent or parallel flows. MP-UOE was used in a variety of CO_2-rich NG decarbonating studies of the authors, with different processing scenarios and configurations (Araújo et al., 2017; Arinelli et al., 2017; Arinelli et al., 2019a; de Melo et al., 2019; Gonzaga et al., 2019).

In this work, MP-UOE is further developed with improvements regarding the energy balance, which is now defined locally for each stream inside MP, generating two new model categories: (i) Lumped MP models for parallel and counter-current permeate/retentate flows using average driving-forces and lumped balances (MPx-UOE); and (ii) 1D-Distributed MP models for parallel permeate/retentate flows using distributed driving-forces and distributed balances (MPd-UOE).

VII.3. Membrane Permeation Unit Operation Extensions: MPx-UOE and MPd-UOE

VII.3.1. Premises

UOEs were developed with Visual Basic (VB) programming language, generating DLLs to be installed in HYSYS. They are loaded in HYSYS as customized operations, and after installation, their icons appear on the HYSYS operations palette. MPx-UOE and MPd-UOE have their own property window to set specifications such as design parameters and operational conditions. The property windows were designed in View Editor, a software available in the Aspentech HYSYS package.

MPx-UOE and MPd-UOE both simulate steady-state MP units using a short-cut method to calculate the species *k* transmembrane molar fluxes, N_k *(MMSm^3/m^2.d)*, that needs calibration of permeances. The model draws an analogy between membrane units and shell and tube heat exchangers, where retentate would flow in the shell, and permeate, in the tube. The permeation driving force is the log mean difference of partial pressures of species *k*, ΔP_k^{LN} (bar). The difference between the two units is that MPx-UOE is a lumped model that considers the

membrane unit as one block with one feed and two products, thus the short-cut method is applied for this block and the fluids paths through the membrane are not assessed.

Differently from MPx-UOE, MPd-UOE is a distributed model; i.e., profiles of dependent variables are obtained throughout the MP unit. MPd-UOE divides the membrane unit into smaller membrane cells of same permeation area, consecutively applying the MP algorithm for each element. The outlet condition of first MP cell is calculated based on the specified inlet condition and will be the inlet condition of the subsequent cell, and from then on until it completes the entire membrane unit. Therefore, if the number of MP elements is high enough, the fluids paths can be attained. The short-cut method error decreases for more distributed simulations, as the number of elements increases and the size of permeation cells decreases, thus calculations are more accurate.

Permeation area A_{MP} *(m²)*, retentate and permeate pressures P_V^{out}, P_L^{out} *(bar)*, and membrane type – HFM or SWM, as depicted in Fig. VII.1 – must be selected by user in both MPx-UOE and MPd-UOE property windows. The extensions automatically retrieve feed data – molar composition $\underline{Y}^{in}$, molar flow rate V^{in} (*MMSm³/d*), temperature T_V^{in} (*K*), pressure (*bar*) P_V^{in}, and molar enthalpy $\bar{H}_V^{in}$ – from the material stream connected to the unit operation. For MPx-UOE, the user must also select the contact type – counter-current contact (CC) or parallel contact (PC) – while for MPd-UOE, only parallel contact type is admitted. Transmembrane molar fluxes (N_k) are considered positive in the direction retentate $\rightarrow$ permeate. In MPd-UOE, the permeate head-loss is fixed as 0.1 bar and equally distributed through the permeation elements.

Permeances Π_k of main species involved in CO_2 separation from NG are defined in the MP models for both HFM and SWM, as shown in Table VII.2, yet can be set otherwise in the UOE property window. Table VII.2 values were calibrated in part with real MP separation data of Pre-Salt offshore NG processing with CAM. Permeances of H_2S and H_2O were estimated as equal to the CO_2 value, since they are known to be high for skin-dense CAM, showing good adherence when compared to the real data. N_2 permeance was estimated as similar to the CH_4 value. C3+ permeances are small, so they were estimated from the C_2H_6 value with reduction of *90%* per additional C atom. Permeation of C5+ species is negligible with CAM. Such as in

Arinelli et al. (2017), despite being calibrated with real operation data, the permeances were adjusted as constant average values, independent of temperature and CO_2 fugacity.

Table VII. 2. Permeances in MPx-UOE and MPd-UOE.

Component	***Permeance HF (Π_k) (MMSm³/d.m².bar)***	***Permeance SW (Π_k) (MMSm³/d.m².bar)***
CO_2	*2.77E-6*	*1.95E-5*
CH_4	*2.77E-7*	*2.16E-6*
C_2H_6	*9.57E-9*	*6.75E-8*
H_2S	*2.77E-6*	*1.95E-5*
H_2O	*2.77E-6*	*1.95E-5*
N_2	*3.07E-7*	*2.16E-6*
C_3H_8	*9.57E-10*	*6.75E-9*
iC_4H_{10}	*9.57E-11*	*6.75E-10*
C_4H_{10}	*9.57E-11*	*6.75E-10*
C5+	*9.57E-12*	*6.75E-11*

Retentate and permeate temperatures, T_V^{out}, T_L^{out} *(K)*, are calculated via energy balance equations for both streams, considering the partial molar enthalpies of species permeating from retentate to permeate ($N_k A_{MP} < \bar{H}_k >$), and external and internal heat exchanges. Considering the shell and tube analogy of the short-cut method, the external heat transfer in MP is between retentate and the vicinity, while the internal heat transfer is between retentate and permeate streams. The external temperature T_E is defined as 25ºC in the MP models but can be set otherwise in the UOE property window. Overall heat transfer coefficients for internal and external heat exchanges are defined as 5 *W/m².K* and 2 *W/m².K*, respectively.

For determination of log mean of temperature differences in membrane extremities for internal heat transfer calculation, temperature of permeate at the beginning of permeation is needed. Since it is unknown, the parameter ΔT_F was created, where $\Delta T_F = T_V^{out} - T_L^{in}$ for counter-current contact type, and $\Delta T_F = T_V^{in} - T_L^{in}$ for parallel contact type. ΔT_F has a default value of 3ºC in the extensions yet can be changed by the user in the UOE property window. In MPd-UOE, ΔT_F specification is only valid for the first membrane element; it can be calculated for the next elements as $\Delta T_F = T_V^{in} - T_L^{in}$, where the inlet streams are the outlet streams of the previous element. In Sec. VII.4.4, a sensitivity analysis is conducted to assess the impact of ΔT_F specification for both MPx-UOE and MPd-UOE.

For the distributed model, as the number of elements increases, the area of each membrane element decreases, and the log-means used in the short-cut method approximate to the respective arithmetic means. Therefore, in MPd-UOE it was considered that for a number of elements equal or higher than 10, the log means are replaced by arithmetic means.

VII.3.2 Lumped Model Algorithm: MPx-UOE

The algorithm for MPx-UOE model comprises five steps, which are described below: [S1] Input data; [S2] Parameters for energy balance; [S3] Initial values for NRM; [S4] Lumped permeation and energy balance calculations; [S5] Returning product data to simulation.

[S1] Input data: Feed temperature, pressure, molar flow, composition, and enthalpy are rescued from feed stream in HYSYS PFD in Eq. (VII.1a). Permeation area, product pressures, and contact type are defined by the user in the UOE property window – Eq. (VII.1b). Default values for species *k* permeances are depicted in Table VII.2, yet the user can specify otherwise in the UOE property window, as depicted in Eq. (VII.1c).

$$T_V^{in}, P_V^{in}, V^{in}, \underline{Y}^{in}, \bar{H}_V^{in} \ \textit{from simulation environment} \tag{VII.1a}$$

$$A_{MP}, P_V^{out}, P_L^{out}, \textit{Contact defined by user} \tag{VII.1b}$$

$$\Pi_k \ \textit{default from Table } 3.1 \textit{ or defined by user} \tag{VII.1c}$$

[S2] Parameters for energy balance: ΔT_F and external temperature (T_E) both have default value specified in MPx-UOE – Eqs. (VII.2a) and (VII.2b), respectively – however the user can set other values in UOE property window. Internal and external overall heat transfer coefficients (U_I and U_E) are defined in Eqs. (VII.2c) and (VII.2d), respectively. The internal area for heat transfer is equal to the defined permeation area via Eq. (VII.2e). Eq. (VII.2f) shows the relation between the external and internal areas for heat transfer.

$$\Delta T_F = 3\ ^oC\ (\textit{default})\ \textit{or defined by user} \tag{VII.2a}$$

$$T_E = 25\ ^oC\ (\textit{default})\ \textit{or defined by user} \tag{VII.2b}$$

$$U_I = 5\ W/m^2.K \tag{VII.2c}$$

$$U_E = 2\ W / m^2.K \qquad \text{(VII.2d)}$$

$$A_I = A_{MP} \qquad \text{(VII.2e)}$$

$$A_E = A_I / 276 \qquad \text{(VII.2f)}$$

[S3] Initial values for NRM: Eqs. (VII.3a) to (VII.3j) set initial values of species trans-membrane molar fluxes. Initial values of retentate and permeate temperatures are defined respectively by Eqs. (VII.3k) and (VII.3m) if contact is CC, or by Eqs. (VII.3n) and (VII.3o) if contact is PC.

$$N_{CO_2} = 0.5 * V_{CO_2}^{in} / A_{MP} \qquad \text{(VII.3a)}$$

$$N_{CH_4} = 0.075 * V_{CH_4}^{in} / A_{MP} \qquad \text{(VII.3b)}$$

$$N_{C_2H_6} = 0.01 * V_{C_2H_6}^{in} / A_{MP} \qquad \text{(VII.3c)}$$

$$N_{C_3H_8} = 0.005 * V_{C_3H_8}^{in} / A_{MP} \qquad \text{(VII.3d)}$$

$$N_{i-C_4H_{10}} = 0.0015 * V_{i-C_4H_{10}}^{in} / A_{MP} \qquad \text{(VII.3e)}$$

$$N_{n-C_4H_{10}} = 0.0015 * V_{n-C_4H_{10}}^{in} / A_{MP} \qquad \text{(VII.3f)}$$

$$N_{H_2O} = 0.5 * V_{H_2O}^{in} / A_{MP} \qquad \text{(VII.3g)}$$

$$N_{H_2S} = 0.5 * V_{H_2S}^{in} / A_{MP} \qquad \text{(VII.3h)}$$

$$N_{N_2} = 0.075 * V_{N_2}^{in} / A_{MP} \qquad \text{(VII.3i)}$$

$$N_{k \neq CO_2, CH_4, C_2H_6, C_3H_8, iC_4H_{10}, nC_4H_{10}, H_2O, H_2S, N_2} = 0.0001 * V_k^{in} / A_{MP} \qquad (k = 1...nc) \qquad \text{(VII.3j)}$$

If Contact=Counter-Current Then

$$T_V^{out} = T_V^{in} - 10 \qquad \text{(VII.3k)}$$

$$T_L^{out} = T_V^{in} - 5 \qquad \text{(VII.3m)}$$

Elseif Contact=Parallel Then

$$T_V^{out^{(0)}} = T_V^{in^{(0)}} - 5 \qquad \text{(VII.3n)}$$

$$T_L^{out^{(0)}} = T_V^{in^{(0)}} - 15 \qquad \text{(VII.3o)}$$

End if

[S4] Lumped permeation and energy balance calculations: The Newton-Raphson method (NRM) is applied for the target equations described in Eqs. (VII.4a) to (VII.4c), which represent the transmembrane molar fluxes of species *k*, and the energy balance equations for retentate and permeate streams, respectively. The driving force in Eq. (VII.4a) is the log mean of partial pressure differences of species *k* (ΔP_k^{LN}), which varies accordingly to the contact type: if CC, it is defined by Eq. (VII.4d); if PC, by Eq. (VII.4f); where $P_V^{in}Y_k^{in}$, $P_V^{out}Y_k^{out}$, $P_L^{out}X_k^{out}$ represent the partial pressures of species *k* in feed, retentate and permeate, respectively. The same methodology applies to the log mean of temperature differences for internal heat transfer (ΔT_I^{LN}): if contact is counter-current, Eq. (VII.4e) is applied; if it is parallel, Eq. (VII.4g) is selected. Eqs. (VII.4h) and (VII.4i) represent the log mean of temperature differences between the retentate and the external area, and the log mean of partial molar enthalpies of species *k* in retentate stream, respectively. Eqs. (VII.4j) to (VII.4p) are applied to calculate the molar flow rates and molar compositions of retentate and permeate streams ($V^{out}, L^{out}, \underline{Y}^{out}, \underline{X}^{out}$ respectively). The molar enthalpies of retentate and permeate streams ($\bar{H}_V^{out}$ and $\bar{H}_L^{out}$) are obtained via $flash(T_V^{out}, P_V^{out}, \underline{Y}^{out})$ and $flash(T_L^{out}, P_L^{out}, \underline{X}^{out})$, respectively. In summary, the MPx-UOE model comprises a system of *7nc+6* non-linear equations Eqs. (VII.4a) to (VII.4p), to be numerically solved by NRM for *7nc+6* variables $N_k, \Delta P_k^{LN}, T_V^{out}, T_L^{out}, \Delta T_I^{LN}, \Delta T_E^{LN}$, $< \bar{H}_k >, L_k^{out}, L^{out}, X_k^{out}, V_k^{out}, V^{out}, Y_k^{out}$.

Target Equations:

$$N_k - \Pi_k \Delta P_k^{LN} = 0 \qquad (k = 1...nc) \qquad \text{(VII.4a)}$$

$$V^{out}\bar{H}_V^{out} - V^{in}\bar{H}_V^{in} - U_E A_E \Delta T_E^{LN} + U_I A_I \Delta T_I^{LN} + \sum_{k=1}^{nc} N_k A_I < \bar{H}_k > = 0 \qquad \text{(VII.4b)}$$

$$L^{out}\bar{H}_L^{out} - U_I A_I \Delta T_I^{LN} - \sum_{k=1}^{nc} N_k A_I < \bar{H}_k > = 0 \qquad \text{(VII.4c)}$$

Auxiliary Equations:

If Contact=Counter-Current Then

$$\Delta P_k^{LN} = \left(\frac{\left(P_V^{in} Y_k^{in} - P_L^{out} X_k^{out}\right) - \left(P_V^{out} Y_k^{out}\right)}{\ln\left(\frac{P_V^{in} Y_k^{in} - P_L^{out} X_k^{out}}{P_V^{out} Y_k^{out}} \right)} \right) \qquad (k = 1...nc) \qquad \text{(VII.4d)}$$

$$\Delta T_I^{LN} = \left[\frac{\Delta T_F - T_V^{in} + T_L^{out}}{\ln\left(\frac{\Delta T_F}{T_V^{in} - T_L^{out}} \right)} \right] \qquad \text{(VII.4e)}$$

Elseif Contact=Parallel Then

$$\Delta P_k^{LN} = \left(\frac{\left(P_V^{in} Y_k^{in}\right) - \left(P_V^{out} Y_k^{out} - P_L^{out} X_k^{out}\right)}{\ln\left(\frac{P_V^{in} Y_k^{in}}{P_V^{out} Y_k^{out} - P_L^{out} X_k^{out}} \right)} \right) \qquad (k = 1...nc) \qquad \text{(VII.4f)}$$

$$\Delta T_I^{LN} = \left[\frac{\Delta T_F - T_V^{out} + T_L^{out}}{\ln\left(\frac{\Delta T_F}{T_V^{out} - T_L^{out}} \right)} \right] \qquad \text{(VII.4g)}$$

End if

$$\Delta T_E^{LN} = \left[\frac{T_V^{in} - T_V^{out}}{\ln\left(\frac{T_E - T_V^{out}}{T_E - T_V^{in}} \right)} \right] \qquad \text{(VII.4h)}$$

$$< \bar{H}_k >= \frac{\bar{H}_{V_k}^{out} - \bar{H}_{V_k}^{in}}{\ln\left(\frac{\bar{H}_{V_k}^{out}}{\bar{H}_{V_k}^{in}} \right)} \qquad (k = 1...nc) \qquad \text{(VII.4i)}$$

$$L_k^{out} = N_k A_{MP} \qquad (k = 1...nc) \tag{VII.4j}$$

$$L^{out} = \sum_k^{nc} L_k^{out} \tag{VII.4k}$$

$$X_k^{out} = \frac{L_k^{out}}{L^{out}} \qquad (k = 1...nc) \tag{VII.4m}$$

$$V_k^{out} = V^{in} Y_k^{in} - N_k A_{MP} \qquad (k = 1...nc) \tag{VII.4n}$$

$$V^{out} = \sum_k^{nc} V_k^{out} \tag{VII.4o}$$

$$Y_k^{out} = \frac{V_k^{out}}{V^{out}} \qquad (k = 1...nc) \tag{VII.4p}$$

[S5] Returning product data to simulation: Data of retentate and permeate streams are pasted onto the product streams of MPx-UOE in HYSYS PFD via Eqs. (VII.5a) and (VII.5b).

Retentate Stream: $T_V^{out}, P_V^{out}, V^{out}, \underline{Y}^{out}$ (VII.5a)

Permeate Stream: $T_L^{out}, P_L^{out}, L^{out}, \underline{X}^{out}$ (VII.5b)

VII.3.3. Distributed Model Algorithm: MPd-UOE

The algorithm for MPd-UOE model comprises six steps, which are described below: [S1] Input data; [S2] Adjusting input parameters for first permeation element; [S3] Parameters for energy balance; [S4] Initial values for first permeation element NRM; [S5] Distributed permeation and energy balance calculations loop; [S6] Returning product data to simulation.

[S1] Input data: Feed temperature, pressure, molar flow, composition, and enthalpy are rescued from feed stream in HYSYS PFD in Eq. (VII.6a). Total permeation area, product pressures, and contact type are defined by the user in the UOE property window – Eq. (VII.6b). Note that differently from MPx-UOE, the contact type is not a specification, since the MPd-UOE model is valid only for parallel MP. Default values for species *k* permeances are depicted

in Table VII.2, yet the user can specify otherwise in the UOE property window, as depicted in Eq. (VII.6c).

$$T_V^{in}, P_V^{in}, V^{in}, \underline{Y}^{in}, \bar{H}_V^{in} \ \textit{from simulation environment} \tag{VII.6a}$$

$$A_{MP}, P_V^{out}, P_L^{out}, n\_elements \ \textit{defined by user} \tag{VII.6b}$$

$$\Pi_k \ \textit{default from Table 3.1 or defined by user} \tag{VII.6c}$$

[S2] Adjusting input parameters for first permeation element: Feed conditions are set as main inlet parameters for the first permeation element in Eq. (VII.7a). Since there is no second inlet stream in the MP module, the molar flow and composition for the first element are set to zero in Eq. (VII.7b). Head-loss in retentate stream is linearly distributed through the permeation elements, so for the first element, the outlet retentate pressure is set by Eq. (VII.7c). For the permeate stream, the final outlet pressure was specified in Eq. (VII.6b), yet there is no inlet permeate stream, so the head-loss is selected and fixed as 0.1 bar, and linearly distributed through the permeation elements; thus, the outlet permeate pressure for the first element is given by Eq. (VII.7d). Permeation elements are equally distributed in the total permeation area also defined in Eq. (VII.6b), so for each element, the permeation area is a fraction of the total specification, as shown in Eq. (VII.7e).

$$T_V^{in^{(0)}} = T_V^{in}, P_V^{in^{(0)}} = P_V^{in}, V^{in^{(0)}} = V^{in}, \underline{Y}^{in^{(0)}} = \underline{Y}^{in}, \bar{H}_V^{in^{(0)}} = \bar{H}_V^{in} \tag{VII.7a}$$

$$L^{in^{(0)}} = 0, \underline{X}^{in^{(0)}} = \underline{0} \tag{VII.7b}$$

$$P_V^{out^{(0)}} = P_V^{in} - (P_V^{in} - P_V^{out}) / n\_elements \tag{VII.7c}$$

$$P_L^{out^{(0)}} = P_L^{out} + (0.1 / n\_elements) * (n\_elements - 1) \tag{VII.7d}$$

$$A_{MP} = A_{MP} / n\_elements \tag{VII.7e}$$

[S3] Parameters for energy balance: $\Delta T_F^{(0)}$ and external temperature (T_E) both have default values specified in MPd-UOE – Eqs. (VII.8a) and (VII.8b), respectively – however the user can set other values in UOE property window. Note that differently from MPx-UOE algorithm, in MPd-UOE the ΔT_F specification is set as the value for the first permeation element only (

$\Delta T_F^{(0)}$), since it is calculated for the next elements in step [S5]. Internal and external overall heat transfer coefficients (U_I and U_E) are defined in Eqs. (VII.8c) and (VII.8d), respectively. The internal area for heat transfer is equal to the permeation area of each element, via Eq. (VII.8e). Eq. (VII.8f) shows the relation between the external and internal areas for heat transfer.

$$\Delta T_F^{(0)} = 3\ ^oC\ (default)\ or\ defined\ by\ user \quad \text{(VII.8a)}$$

$$T_E = 25\ ^oC\ (default)\ or\ defined\ by\ user \quad \text{(VII.8b)}$$

$$U_I = 5\ W/m^2.K \quad \text{(VII.8c)}$$

$$U_E = 2\ W/m^2.K \quad \text{(VII.8d)}$$

$$A_I = A_{MP} \quad \text{(VII.8e)}$$

$$A_E = A_I / 276 \quad \text{(VII.8f)}$$

[S4] Initial values for first permeation element NRM: Eqs. (VII.9a) to (VII.9j) set initial values of species transmembrane molar fluxes for the first permeation area, which depend on the number of membrane elements chosen by the user; the more distributed, the lower the permeation area for each element, yet the higher the number of elements, which is quadratic, so the lower is the permeation flux. Eqs. (VII.9k) and (VII.9m) respectively define initial values of retentate and permeate temperatures for the first permeation area.

$$N_{CO_2}^{(0)} = 0.5 * V_{CO_2}^{in\ (0)} / (A_{MP} * n\_elements^2) \quad \text{(VII.9a)}$$

$$N_{CH_4}^{(0)} = 0.075 * V_{CH_4}^{in\ (0)} / (A_{MP} * n\_elements^2) \quad \text{(VII.9b)}$$

$$N_{C_2H_6}^{(0)} = 0.01 * V_{C_2H_6}^{in\ (0)} / (A_{MP} * n\_elements^2) \quad \text{(VII.9c)}$$

$$N_{C_3H_8}^{(0)} = 0.005 * V_{C_3H_8}^{in\ (0)} / (A_{MP} * n\_elements^2) \quad \text{(VII.9d)}$$

$$N_{i-C_4H_{10}}^{(0)} = 0.0015 * V_{i-C_4H_{10}}^{in\ (0)} / (A_{MP} * n\_elements^2) \quad \text{(VII.9e)}$$

$$N_{n-C_4H_{10}}^{(0)} = 0.0015 * V_{n-C_4H_{10}}^{in\ (0)} / (A_{MP} * n\_elements^2) \quad \text{(VII.9f)}$$

$$N_{H_2O}^{(0)} = 0.5 * V_{H_2O}^{in\ (0)} / (A_{MP} * n\_elements^2) \quad \text{(VII.9g)}$$

$$N_{H_2S}{}^{(0)} = 0.5 * V_{H_2S}^{in}{}^{(0)} / (A_{MP} * n\_elements^2) \quad \text{(VII.9h)}$$

$$N_{N_2}{}^{(0)} = 0.075 * V_{N_2}^{in(0)} / (A_{MP} * n\_elements^2) \quad \text{(VII.9i)}$$

$$N_{k\neq CO_2,CH_4,C_2H_6,C_3H_8,iC_4H_{10},nC_4H_{10},H_2O,H_2S,N_2}{}^{(0)} = 10^{-4} * V_k^{in^{(0)}} \div (A_{MP} * n\_elements^2) \ (k = 1...nc) \quad \text{(VII.9j)}$$

$$T_V^{out^{(0)}} = T_V^{in^{(0)}} - 5 \quad \text{(VII.9k)}$$

$$T_L^{out^{(0)}} = T_V^{in^{(0)}} - 15 \quad \text{(VII.9m)}$$

[S5] Distributed permeation and energy balance calculations loop: The distributed model comprises *n_elements* loops, starting from index *m=0* until *(n_elements-1)*. The NRM is applied for the target equations of the current MP element, described in Eqs. (VII.10a) to (VII.10c), which represent the transmembrane molar fluxes of species *k*, and the energy balance equations for retentate and permeate streams, respectively. As the number of elements selected by the user increases, the area of each membrane element decreases, and the log mean approximates to the arithmetic mean. Therefore, the log means of MPx-UOE algorithm ($\Delta P_k^{LN}, \Delta T_I^{LN}, \Delta T_E^{LN}, < \bar{H}_k >$) are valid in MPd-UOE for *n_elements<10*; for higher values, they are replaced by the respective arithmetic means. This procedure is described by Eqs. (VII.10d) to (VII.10k). Eqs. (VII.10m) to (VII.10r) are applied to calculate the molar flow rates and molar compositions of outlet streams of the current element ($V^{out^{(m)}}, L^{out^{(m)}}, \underline{Y}^{out^{(m)}}, \underline{X}^{out^{(m)}}$). The respective molar enthalpies ($\bar{H}_V^{out^{(m)}}$ and $\bar{H}_L^{out^{(m)}}$) are obtained via $flash(T_V^{out^{(m)}}, P_V^{out^{(m)}}, \underline{Y}^{out^{(m)}})$ and $flash(T_L^{out^{(m)}}, P_L^{out^{(m)}}, \underline{X}^{out^{(m)}})$. The model comprises a system of *7nc+6* non-linear equations Eqs. (VII.10a) to (VII.10r), to be numerically solved by NRM for *7nc+6* variables $N_k^{(m)}, \Delta P_k^{LN}, T_V^{out^{(m)}}, T_L^{out^{(m)}}, \Delta T_I^{LN}, \Delta T_E^{LN}, < \bar{H}_k >, L_k^{out^{(m)}}, L^{out^{(m)}}, X_k^{out^{(m)}}, V_k^{out^{(m)}}, V^{out^{(m)}}, Y_k^{out^{(m)}}$ for each MP element. After finding the NRM solution for the current element, Eqs. (VII.10s) to (VII.10y) are applied to set parameters and initial values for the next element as follows: (i) retentate and permeate streams from current element respectively become main and second feed of the next element – Eqs. (VII.10s) to (VII.10u); (ii) ΔT_F of the next element is calculated as

the difference between the temperatures of the two feed streams – Eq. (VII.10v); and (iii) initial values for NRM of the next element are set for $N_k, T_V^{out}, T_L^{out}$ variables – Eqs. (VII.10x) to (VII.10y). Then, the algorithm loops again for the next *m* MP element.

For m=0 to (n_ elements – 1)

----------*NRM Block Begins*----------

Target Equations:

$$N_k^{(m)} - \Pi_k \Delta P_k^{LN} = 0 \qquad (k = 1...nc) \tag{VII.10a}$$

$$V^{out^{(m)}} \bar{H}_V^{out^{(m)}} - V^{in^{(m)}} \bar{H}_V^{in^{(m)}} - U_E A_E \Delta T_E^{LN} + U_I A_I \Delta T_I^{LN} + \sum_{k=1}^{nc} N_k^{(m)} A_I < \bar{H}_k > = 0 \tag{VII.10b}$$

$$L^{out^{(m)}} \bar{H}_L^{out^{(m)}} - L^{in^{(m)}} \bar{H}_L^{in^{(m)}} - U_I A_I \Delta T_I^{LN} - \sum_{k=1}^{nc} N_k^{(m)} A_I < \bar{H}_k > = 0 \tag{VII.10c}$$

Auxiliary Equations:

If $n\_elements \geq 10$ *then*

$$\Delta P_k^{LN} \approx \Delta P_k^{Arith.} = \left(\frac{\left(P_V^{in^{(m)}} Y_k^{in^{(m)}} \right) + \left(P_V^{out^{(m)}} Y_k^{out^{(m)}} - P_L^{out^{(m)}} X_k^{out^{(m)}} \right)}{2} \right) \qquad (k = 1...nc) \tag{VII.10d}$$

$$\Delta T_I^{LN} \approx \Delta T_I^{Arith.} = \left[\frac{\Delta T_F^{(m)} + (T_V^{out^{(m)}} - T_L^{out^{(m)}})}{2} \right] \tag{VII.10e}$$

$$\Delta T_E^{LN} \approx \Delta T_E^{Arith.} = \left[\frac{(T_E - T_V^{in^{(m)}}) + (T_E - T_V^{out^{(m)}})}{2} \right] \tag{VII.10f}$$

$$< \bar{H}_k >= \frac{\bar{H}_{V_k}^{out^{(m)}} + \bar{H}_{V_k}^{in^{(m)}}}{2} \qquad (k = 1...nc) \tag{VII.10g}$$

Else

$$\Delta P_k^{\,LN} = \left(\frac{\left(P_V^{in^{(m)}} Y_k^{in^{(m)}}\right) - \left(P_V^{out^{(m)}} Y_k^{out^{(m)}} - P_L^{out^{(m)}} X_k^{out^{(m)}}\right)}{\ln\left(\frac{P_V^{in^{(m)}} Y_k^{in^{(m)}}}{P_V^{out^{(m)}} Y_k^{out^{(m)}} - P_L^{out^{(m)}} X_k^{out^{(m)}}} \right)} \right) \qquad (k = 1...nc) \qquad \text{(VII.10h)}$$

$$\Delta T_I^{\,LN} = \left[\frac{\Delta T_F^{\,(m)} - T_V^{out^{(m)}} + T_L^{out^{(m)}}}{\ln\left(\frac{\Delta T_F^{\,(m)}}{T_V^{out^{(m)}} - T_L^{out^{(m)}}} \right)} \right] \qquad \text{(VII.10i)}$$

$$\Delta T_E^{\,LN} = \left[\frac{T_V^{in^{(m)}} - T_V^{out^{(m)}}}{\ln\left(\frac{T_E - T_V^{out^{(m)}}}{T_E - T_V^{in^{(m)}}} \right)} \right] \qquad \text{(VII.10j)}$$

$$< \bar{H}_k >= \frac{\bar{H}_{V_k}^{out^{(m)}} - \bar{H}_{V_k}^{in^{(m)}}}{\ln\left(\frac{\bar{H}_{V_k}^{out^{(m)}}}{\bar{H}_{V_k}^{in^{(m)}}} \right)} \qquad (k = 1...nc) \qquad \text{(VII.10k)}$$

End if

$$L_k^{out^{(m)}} = L^{in^{(m)}} X_k^{in^{(m)}} + N_k^{\,(m)} A_{MP} \qquad (k = 1...nc) \qquad \text{(VII.10m)}$$

$$L^{out^{(m)}} = \sum_k^{nc} L_k^{out^{(m)}} \qquad \text{(VII.10n)}$$

$$X_k^{\,out^{(m)}} = \frac{L_k^{out^{(m)}}}{L^{out^{(m)}}} \qquad (k = 1...nc) \qquad \text{(VII.10o)}$$

$$V_k^{out^{(m)}} = V^{in^{(m)}} Y_k^{in^{(m)}} - N_k^{\,(m)} A_{MP} \qquad (k = 1...nc) \qquad \text{(VII.10p)}$$

$$V^{out^{(m)}} = \sum_k^{nc} V_k^{out^{(m)}} \qquad \text{(VII.10q)}$$

$$Y_k^{out^{(m)}} = \frac{V_k^{out^{(m)}}}{V^{out^{(m)}}} \qquad (k = 1...nc) \qquad \text{(VII.10r)}$$

----------*NRM Block Ends*----------

Adjusting parameters and initial values for next element:

If $m < (n\_elements - 1)$ *Then*

$$V^{in^{(m+1)}} = V^{out^{(m)}}, L^{in^{(m+1)}} = L^{out^{(m)}}, P_V^{\ in^{(m+1)}} = P_V^{\ out^{(m)}}, P_L^{\ in^{(m+1)}} = P_L^{\ out^{(m)}} \qquad \text{(VII.10s)}$$

$$T_V^{\ in^{(m+1)}} = T_V^{\ out^{(m)}}, T_L^{\ in^{(m+1)}} = T_L^{\ out^{(m)}}, \bar{H}_V^{\ in^{(m+1)}} = \bar{H}_V^{\ out^{(m)}}, \bar{H}_L^{\ in^{(m+1)}} = \bar{H}_L^{\ out^{(m)}} \qquad \text{(VII.10t)}$$

$$Y_k^{\ in^{(m+1)}} = Y_k^{\ out^{(m)}}, X_k^{\ in^{(m+1)}} = X_k^{\ out^{(m)}} \qquad (k = 1...nc) \qquad \text{(VII.10u)}$$

$$\Delta T_F^{\ (m+1)} = T_V^{in^{(m+1)}} - T_L^{in^{(m+1)}} \qquad \text{(VII.10v)}$$

$$N_k^{\ (m+1)} = 0.3 * L_k^{in^{(m+1)}} / (m+1) \qquad (k = 1...nc) \qquad \text{(VII.10w)}$$

$$T_V^{\ out^{(m+1)}} = T_V^{in^{(m+1)}} - (5 / n\_elements) * (m+2) \qquad \text{(VII.10x)}$$

$$T_L^{\ out^{(m+1)}} = T_V^{out^{(m+1)}} - 10 \qquad \text{(VII.10y)}$$

End if

Next m

[S6] Returning product data to simulation: Data of retentate and permeate streams of the final permeation element are pasted onto the product streams of MPd-UOE in the HYSYS PFD via Eqs. (VII.11a) and (VII.11b).

Retentate Stream: $T_V^{out}, P_V^{out}, V^{out}, \underline{Y}^{out}$ (VII.11a)

Permeate Stream: $T_L^{out}, P_L^{out}, L^{out}, \underline{X}^{out}$ (VII.11b)

VII.4. Models Performance for CO_2-Rich Natural Gas Processing

VII.4.1. Premises

MPx-UOE and MPd-UOE were applied to simulate CO_2 removal from a hypothetical CO_2-rich NG after water dew-point adjustment (WDPA) and hydrocarbon dew-point adjustment (HCDPA) on offshore platforms. Table VII.3 shows the NG feed conditions used in all simulations. MP cases were simulated in HYSYS v8.8 with PR-EOS, which is indicated as thermodynamic modeling of NG processing operations. All optional parameters of MPx-UOE and MPd-UOE were used as default values, except for ΔT_F regarding the sensitivity analysis in Sec. VII.4.4. Retentate pressure was set according to a fixed head-loss of *1 bar* per MP stage. Permeate pressure was chosen as *4 bar* in all simulations. Both counter-current and parallel contact types were evaluated for MPx-UOE. Permeation areas defined for each stage configuration in Sec. VII.4.2 are maintained for the next sections simulations. Head-loss of heat exchangers was fixed at *0.5 bar*. Cooling-water (CW) was used in compressors intercoolers, reducing gas temperature to *45ºC*. Pressurized-hot-water (PHW) produced in gas turbines waste heat recovery units in the platform was used as heating utility.

Table VII. 3. Feed conditions of CO_2-rich natural gas.

Parameter	*Value*
Vapor Fraction	*1.00*
Temperature (ºC)	*62.00*
Pressure (bar)	*45.00*
Molar Flow (MMSm³/d)	*12.00*
%CO_2	*45.23*
%CH_4	*42.22*
%C_2H_6	*6.03*
%C_3H_8	*4.02*
%i-C_4H_{10}	*0.50*
%n-C_4H_{10}	*1.01*
%i-C_5H_{12}	*0.26*
%n-C_5H_{12}	*0.19*
%n-C_6H_{14}	*0.24*
%n-C_7H_{16}	*0.03*
%n-C_8H_{18}	*0.01*
%N_2	*0.26*
ppmH_2O	*1.00*

VII.4.2. Stage Configuration: MPx-UOE

Different process configurations can be used in MP modules to capture CO_2 from NG as shown in Fig. VII.2. Three configurations were selected for evaluation with MPx-UOE: (i) one single MP stage (Fig. VII.3a); (ii) two serial MP stages (Fig. VII.3b); and (iii) one MP stage followed by a second stage for the first permeate stream with recycle of second retentate to the first stage (Fig. VII.3c). To compare the three possibilities, MPx-UOE was used with CC contact, HFM, and default values of parameters described in Sec. VII.3.1. For two serial stage configuration, the permeation area of the second stage was set as half of the area set for the first stage. Moreover, a heater was added between the two stages to avoid condensation in the second stage, which would happen otherwise for this contact type – temperature drop in retentate stream is higher for CC than for PC. For the two-stage configuration with recycle, the permeation area of the second stage was set as 1/3 of the area set for the first stage.

Product streams results for each configuration are depicted in Table VII.4. Comparing both two-stage configuration, the recycled scheme produces a final retentate stream richer in methane (73%mol versus 67%mol) and with higher molar flow rate (≈ +28%) than the serial configuration. Consequently, the final permeate of the recycled configuration is richer in CO_2 (91%mol versus 74%mol) and has lower molar flow rate (≈ -19%) than the serial counterpart. The one stage configuration has the worst results: there is condensation inside the membrane unit (retentate stream is 1% condensed) and it produces retentate with lowest methane content and permeate with lowest CO_2 content (66%mol and 73%mol, respectively), though close to the two serial stages results.

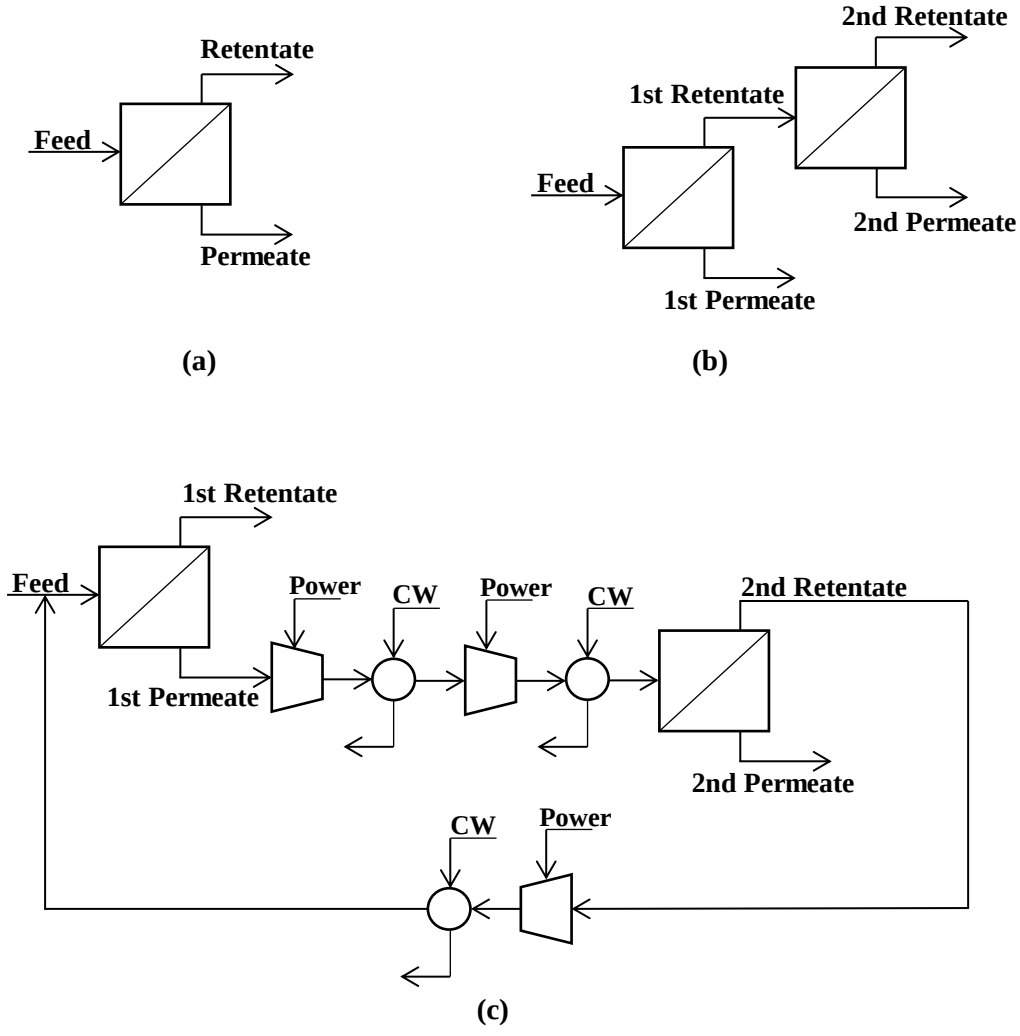

Figure VII. 3. Membrane process configurations: (a) one single stage; (b) two serial stages; (c) two stages with recycle of 2nd retentate.

Table VII. 4. Product streams results for counter-current MPx-UOE process configurations.

Parameter	*2 Serial Stages*		*2 Recycled Stages*		*1 Stage*	
	Retentate	*Permeate*	*Retentate*	*Permeate*	*Retentate*	*Permeate*
Vapor Fraction	*1.00*	*1.00*	*1.00*	*1.00*	*0.99*	*1.00*
Temperature (ºC)	*58.14*	*54.60*	*38.60*	*48.43*	*39.77*	*54.57*
Pressure (bar)	*42.50*	*4.00*	*44.00*	*4.00*	*43.00*	*4.00*
Molar Flow (MMSm³/d)	*4.87*	*7.13*	*6.22*	*5.78*	*4.75*	*7.25*
%CO_2	*3.00*	*74.08*	*3.00*	*90.72*	*3.00*	*72.89*
%CH_4	*66.59*	*25.57*	*72.87*	*9.21*	*65.85*	*26.74*
%C_2H_6	*14.63*	*0.16*	*11.63*	*0.00*	*14.97*	*0.18*
%C_3H_8	*9.89*	*0.01*	*7.76*	*0.00*	*10.14*	*0.01*
%i-C_4H_{10}	*1.24*	*0.00*	*0.97*	*0.00*	*1.27*	*0.00*
%n-C_4H_{10}	*2.48*	*0.00*	*1.94*	*0.00*	*2.54*	*0.00*
%i-C_5H_{12}	*0.63*	*0.00*	*0.50*	*0.00*	*0.65*	*0.00*
%n-C_5H_{12}	*0.47*	*0.00*	*0.37*	*0.00*	*0.48*	*0.00*
%n-C_6H_{14}	*0.59*	*0.00*	*0.47*	*0.00*	*0.61*	*0.00*
%n-C_7H_{16}	*0.06*	*0.00*	*0.05*	*0.00*	*0.07*	*0.00*
%n-C_8H_{18}	*0.02*	*0.00*	*0.01*	*0.00*	*0.02*	*0.00*
%N_2	*0.39*	*0.17*	*0.44*	*0.07*	*0.39*	*0.18*
ppmH_2O	*0.07*	*1.64*	*0.07*	*2.01*	*0.07*	*1.61*

Total permeation area, methane loss, CO_2 capture and power demand of all configurations are displayed in Fig. VII.4, including a fourth case comprising two parallel contact serial stages (with no inter-stage heater, since condensation is absent) for comparison of contact types. Methane loss is the lowest for the two recycled stages configuration (*10.5%* against *38.3%, 36.0%* and *37.5%* for one CC stage, two serial CC stages and two serial PC stages, respectively), as a result of methane recovery from the first permeate stream in the second MP stage, producing final retentate and permeate with better quality, as discussed in Table VII.4. However, this result comes with a price: there is a power consumption of almost *40 MW* for compression of first permeate to the second MP stage and for recycle of second retentate to the first MP stage, absent in all other cases. Moreover, total permeation area is the highest of all (*508800 m²* against *308000 m², 270450 m²* and *284550 m²* for one CC stage, two serial CC stages and two serial PC stages, respectively). The other three configurations show similar results in Fig. VII.4, with two counter-current serial stages being slightly best, followed by the parallel counterpart. CO_2 capture is approximately *97%* on molar basis for all cases. It is important to remember that permeances are independent of CO_2 fugacity, and since the

composition in each stage differs considerably, the permeation area set for each stage is super or sub dimensioned.

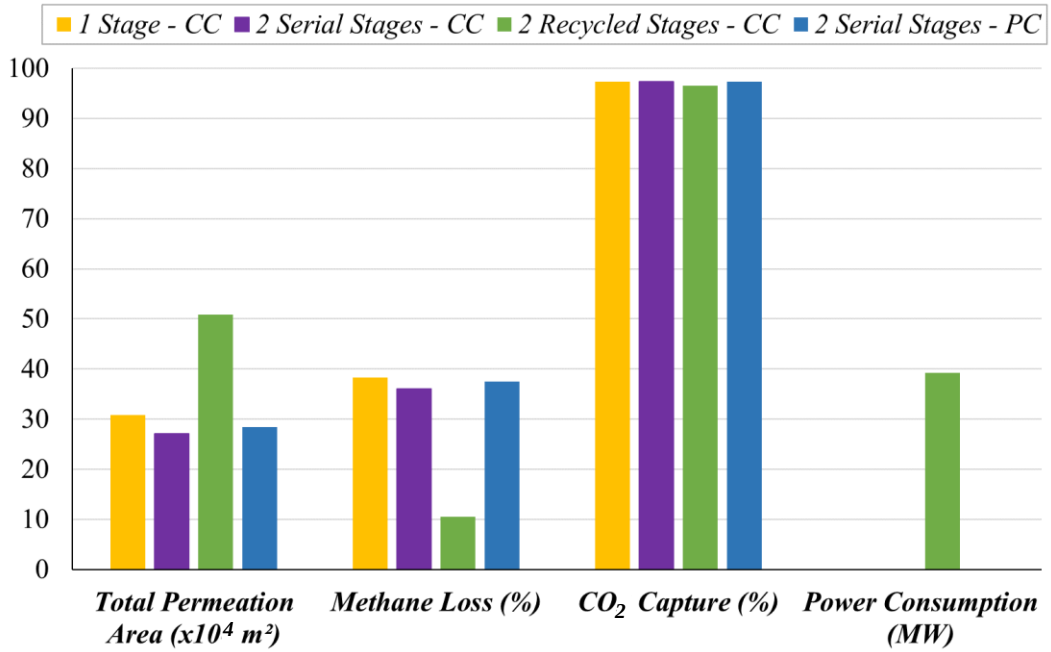

Figure VII. 4. Total permeation area, methane loss, CO_2 capture and power consumption of process configurations for counter-current and parallel MPx-UOE.

VII.4.3. Profiles: MPd-UOE

To evaluate the performance of the distributed model MPd-UOE, the two serial parallel stages configuration was simulated with 100 permeation elements in the first stage (*189700 m²*), and 50 permeation elements in the second stage (*94850 m²*). Figs. VII.5 to VII.8 display pressure, temperature, molar flow rate and molar composition profiles for retentate and permeate streams along both MP stages. Pressure profiles in Fig. VII.5 show linear head-loss through membrane stages – 1 bar for retentate and *0.1 bar* for permeate, per stage – as described in Sec. VII.3.3. Temperature profiles in Fig. VII.6 are both smoothly decreasing, with the exception of a small deviation of about *1.5ºC* in the beginning of each stage. This oscillation is a result of the $\Delta T_F = T_V^{in} - T_L^{in}$ specification with default value of *3ºC* in the first permeation element of each parallel stage, since the temperature of the permeate stream in MP inlet is unknown. The effects of this parameter in MPd-UOE results are discussed in Sec. VII.4.4.

Molar flow rates and compositions in Figs. VII.7 and VII.8 also display smooth profiles, with a deviation in permeate in the stage change due to the withdrawal of the first permeate stream. Fig. VII.8 shows that CO_2 and H_2O contents decrease in the retentate stream while hydrocarbons contents increase, due to the higher permeation fluxes of the first two through the membrane. In the permeate stream, CO_2 and H_2O contents are higher at the beginning of each stage, as a result of high inlet driving force, with both contents decreasing slightly through the membrane, as the driving force is reduced, and the other components permeate. Fig. VII.9 shows the driving force of CO_2 decreasing through the membrane due to permeation. The CO_2 driving force for a case with one single parallel stage (simulated with 150 elements in MPd-UOE) is also shown in Fig. VII.9. For PC type, one could think that separating the permeation in two stages would make no difference. However, since a permeate stream is withdrawn in the first stage, there is a sudden increase of CO_2 driving force at the beginning of the second stage, enhancing the overall MP operation.

In MPd-UOE, the simplification of constant component permeances impacts the profiles of temperature, molar flow, and compositions through the membrane unit (Figs. VII.6 to VII.8). The permeance of CO_2, for example, would be higher in the beginning, where the partial pressure in retentate is higher, decreasing with the permeation of CO_2 along the unit. Therefore, the profiles would be more incisive in the beginning of permeation, smoothing towards the end. This simplification could be easily overcome by implementing permeances dependent of temperature and CO_2 fugacity in MPd-UOE model, updating the values for each permeation element. However, the real operation data used for calibration of permeances in MPx-UOE and MPd-UOE is not enough for this purpose. Thus, other literature or experimental data could be implemented for the adjustment of equations to correct the component permeances according to the temperature and CO_2 fugacity.

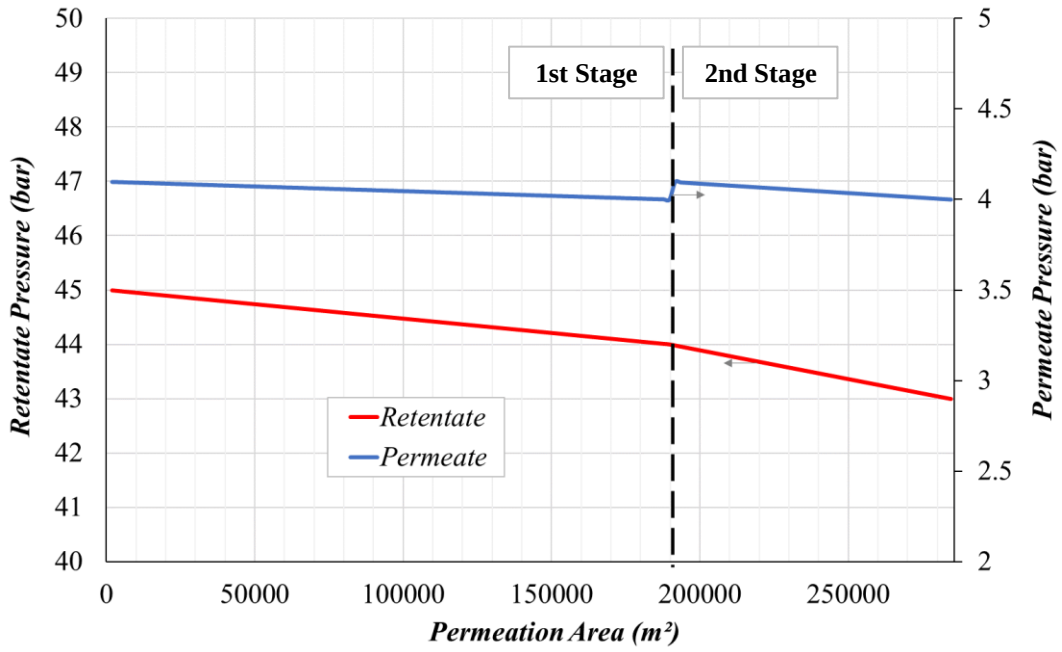

Figure VII. 5. Retentate and permeate pressure profiles through MPd-UOE for two serial stages with parallel contact.

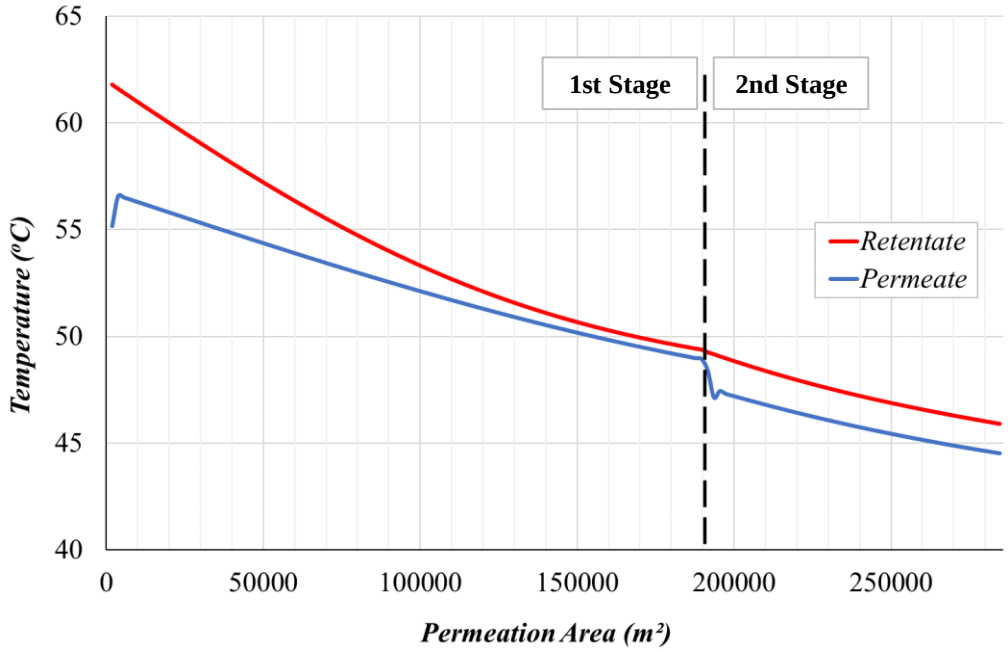

Figure VII. 6. Retentate and permeate temperature profiles through MPd-UOE for two serial stages with parallel contact.

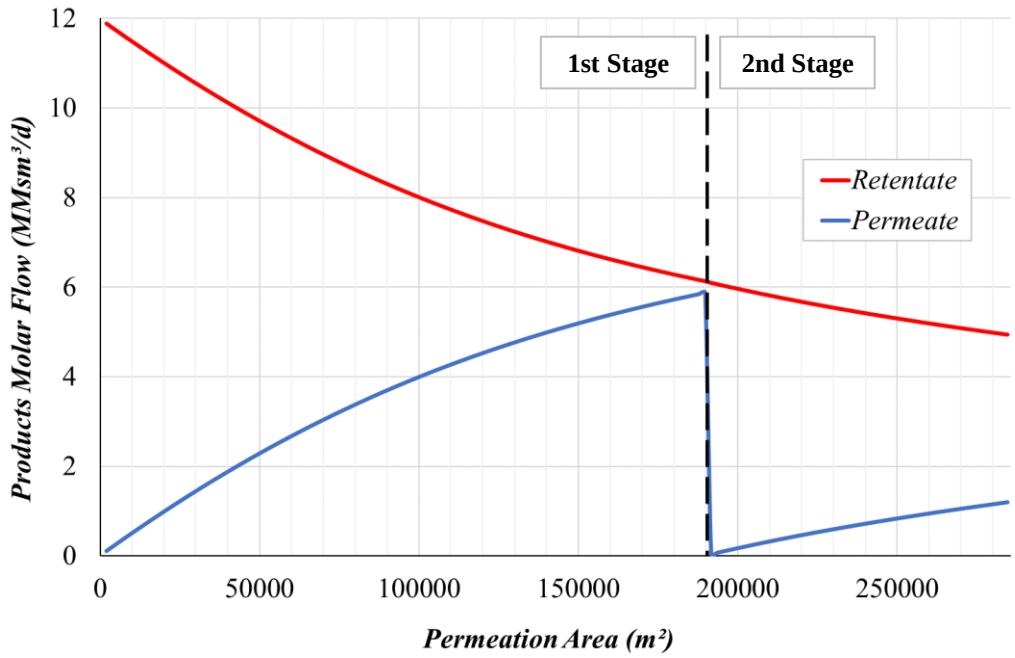

Figure VII. 7. Retentate and permeate molar flow rate profiles through MPd-UOE for two serial stages with parallel contact.

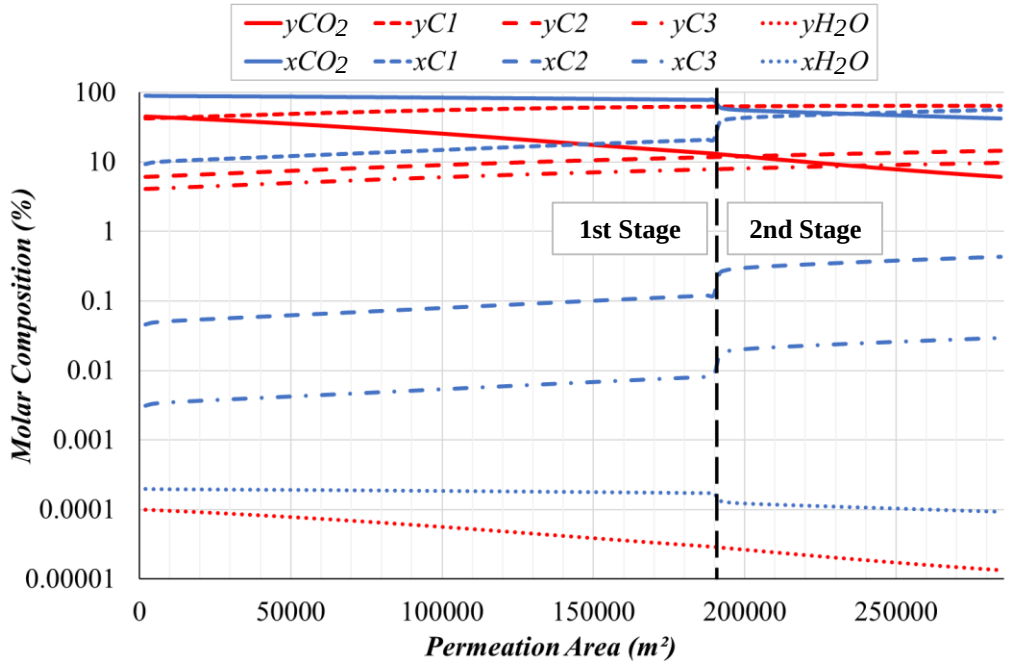

Figure VII. 8. Retentate and permeate main component molar compositions through MPd-UOE for two serial stages with parallel contact.

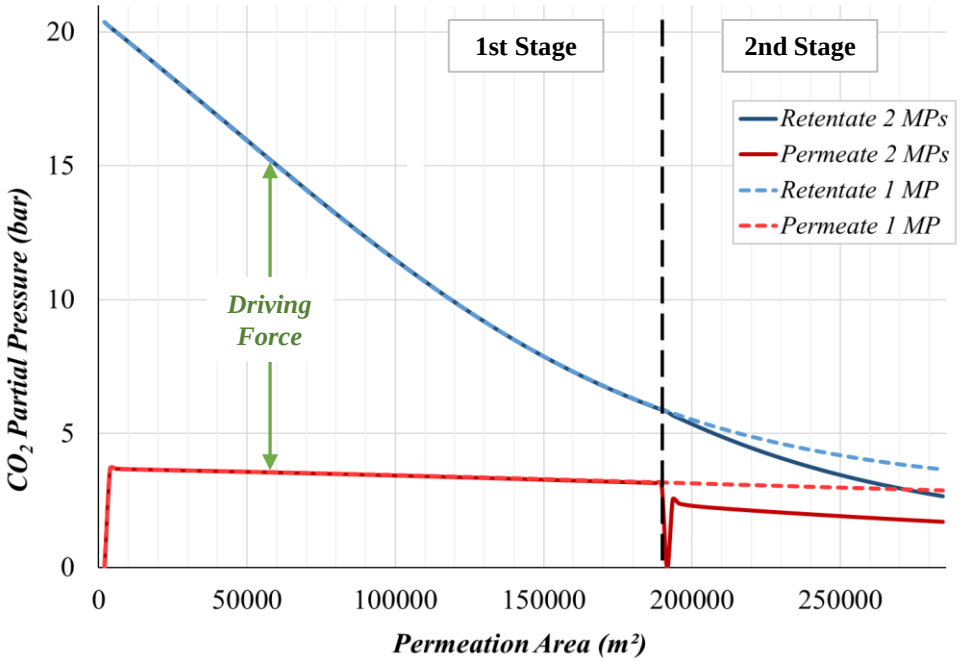

Figure VII. 9. CO_2 partial pressure in retentate and permeate through MPd-UOE for two serial stages and one single stage, with parallel contact.

VII.4.4. Sensitivity Analysis: MPx-UOE and MPd-UOE

In this section, three sensitivity analyses are conducted: (i) on the ΔT_F specification for MPx-UOE; (ii) on the number of permeation elements for MPd-UOE; and (iii) on the ΔT_F specification for MPd-UOE. For the sake of simplicity, MP configuration for all sensitivity analyses were conducted in one single stage MP: for CC MPx-UOE, the configuration chosen is one single stage from Sec. VII.4.2, with *308000 m²* of permeation area; in the case of PC, both MPx-UOE and MPd-UOE adopted one single stage from Sec. VII.4.3, with *284550 m²* of permeation area.

Fig. VII.10 displays the results obtained for product temperatures with both CC and PC MPx-UOE, varying ΔT_F specification from *0.02ºC* to *20ºC*. The first notable characteristic is the opposite behavior between contact types: for parallel MP the product temperatures converge for higher ΔT_F values, with retentate temperature above permeate temperature; while for counter-current MP, product temperatures diverge for higher ΔT_F values, always with higher permeate temperature than the retentate counterpart. Moreover, the amplitude of product

temperatures difference is notably higher for CC MP, achieving $\approx 25^{o}C$ of temperature difference for the highest ΔT_F analyzed, while for PC, the highest temperature difference is only $\approx 7^{o}C$, for the lowest ΔT_F analyzed. Therefore, the ΔT_F specification clearly impacts more the counter-current MP operation. The default value for this variable in the MP models is $3^{o}C$, which gives good average results for both contact types.

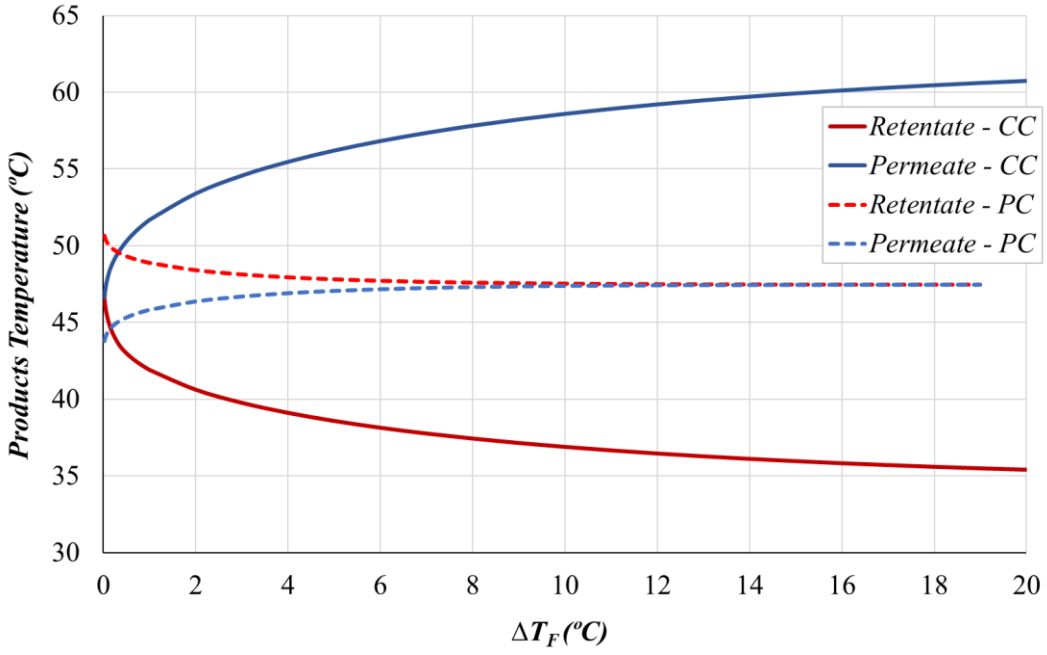

Figure VII. 10. Retentate and permeate temperatures in MPx-UOE versus ΔT_F specification for one single counter-current stage and one single parallel stage.

Figs. VII.11 and VII.12 show, respectively, product molar flow rates, and product CO_2 and methane molar compositions, versus the number of permeation elements selected for MPd-UOE (with default $\Delta T_F = 3^{o}C$). The outcome is that the distributed MP model rapidly converges to constant values for products results as the number of permeation elements increases, with less than *1%* of variation in all output variables for *n_elements≥5*. The first conclusion is that the short-cut method adopted in the MP models presents great performance even for few permeation elements, or just one – as in MPx-UOE – with low variations against the more rigorous distributed simulations. For one permeation element only, the average deviation was *0.7%* for all analyzed parameters (products molar flow rates, molar compositions and temperatures), with highest oscillation value of *6.3%* for CO_2 content in the retentate (which

in absolute values represent only 0.01 on CO_2 molar fraction). On the other hand, the consideration of constant component permeances also contributes to this reduced variation between MPx-UOE and MPd-UOE results. If the permeance values were corrected according to the temperature and component compositions along the membrane, the deviation of the lumped model results to the distributed more rigorous model results would be more expressive, since in the latter the correction would be applied to each membrane element. Another important conclusion obtained with Figs. VII.11 and VII.12 is that the approximation of log means by arithmetic means in MPd-UOE algorithm (Sec. VII.3.3) for *n_elements≥10* was smooth, since results converge to practically constant values for *n_elements≥5*, before the change of means calculation. Therefore, a great suggestion to achieve accurate results with easy convergence in MPd-UOE, is to use *n_elements=10*, since calculations and derivatives are simpler with arithmetic means, and higher number of elements is excessive, with no important gains in model accuracy.

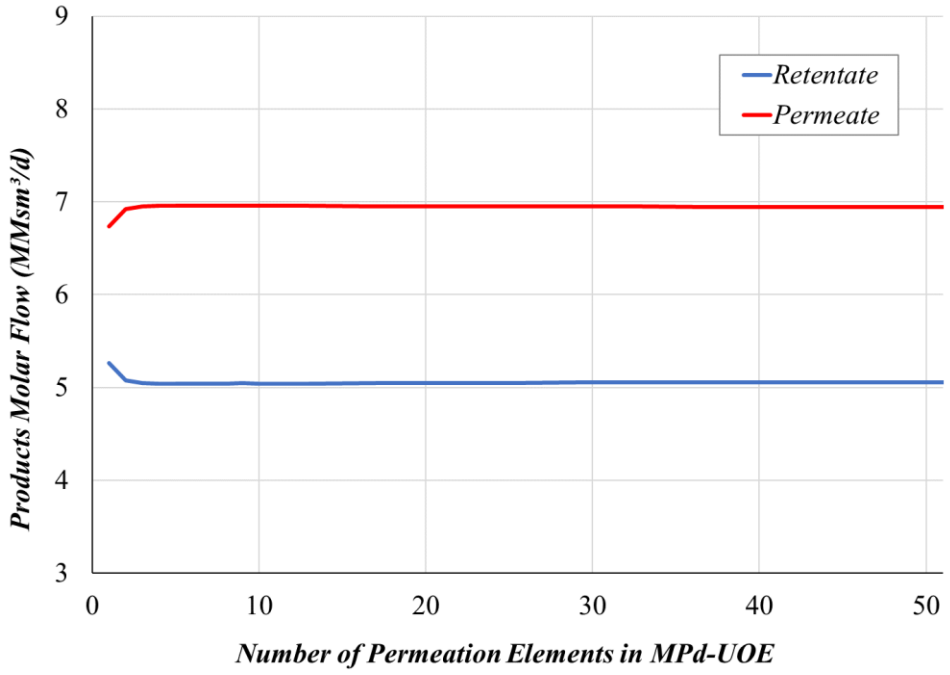

Figure VII. 11. Retentate and permeate molar flow rates in MPd-UOE versus the number of permeation elements selected for one single parallel stage.

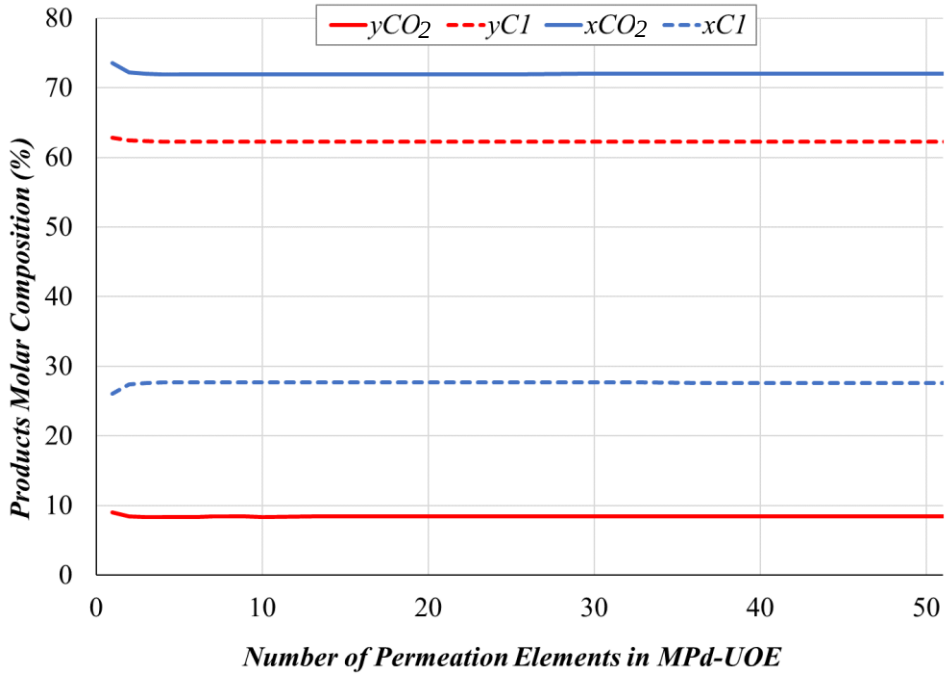

Figure VII. 12. Retentate and permeate main molar compositions in MPd-UOE versus the number of permeation elements selected for one single parallel stage.

Fig. VII.13 displays product temperature profiles versus the number of permeation elements selected for MPd-UOE with $\Delta T_F = \{0.1^o C, 3^o C, 10^o C\}$. The temperature profiles show the same behavior discussed for Figs. VII.11 and VII.12 of rapid convergence to constant values as the number of elements increases. As discussed in MPx-UOE sensitivity analysis, the value selected for ΔT_F clearly impacts the non-distributed model (*n_elements=1*). Since MPd-UOE only admits parallel contact type, products temperature variations are mainly for lower ΔT_F values, as already observed in MPx-UOE model for PC MP. The higher oscillation observed in MPd-UOE was 5% for both product temperatures, for $\Delta T_F = 0.1^o C$ and *n_elements=1*. For the other ΔT_F values, this oscillation was reduced to only ≈1%. However, as the number of permeation elements increases, the influence of this specification becomes meaningless: for *n_elements≥3*, the final product temperature oscillations reduce to less than *0.1%* for all ΔT_F.

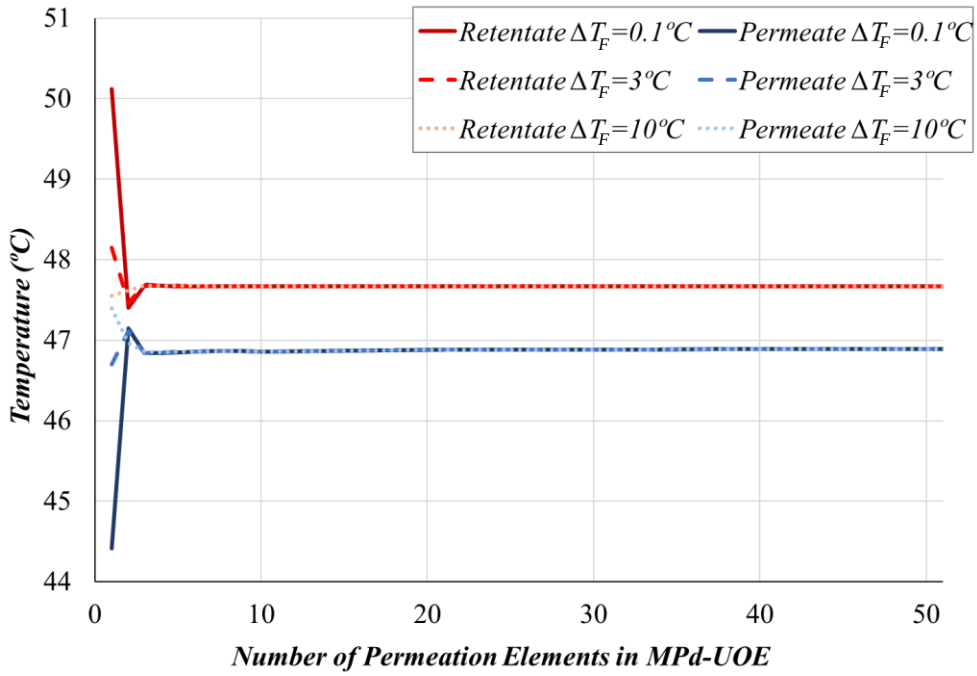

Figure VII. 13. Retentate and permeate final temperatures in MPd-UOE versus the number of permeation elements selected for one single parallel stage with $\Delta T_F = \{0.1^o C, 3^o C, 10^o C\}$.

VII.5. Concluding Remarks

MP-UOE model developed for HYSYS in a previous work was expanded to include local energy balances for each stream inside MP, thus calculating products temperatures with more precision, and originating a new version of the lumped model extension: MPx-UOE. A distributed MP model was also developed, MPd-UOE, dividing the MP unit into smaller MP cells and applying MPx-UOE methodology for each cell consecutively, thus reproducing stream profiles inside the membrane. The MP models were calibrated using real NG processing operation data for CO_2 removal from CO_2-rich NG in offshore oil-and-gas fields in Brazil.

Both extensions were evaluated for CO_2-rich NG decarbonation simulations in HYSYS with PR-EOS. Different MP process configurations were investigated with MPx-UOE, concluding that the two-stage scheme with recycle of retentate led to minimum methane loss, yet at the cost of power consumption for compression and higher permeation area, as already stated otherwise in MP literature. MPd-UOE successfully represented smooth profiles of temperature, pressure, molar flow rates, and compositions through the membrane unit. Comparisons between both extensions indicate that the lumped model obtained results in good agreement with the distributed more accurate model results, with small deviations. MPx-UOE and MPd-UOE

models can be improved with the admission permeance equations dependent of retentate temperature and CO_2 fugacity, in order to mimic membrane plasticization effects caused by high CO_2 fugacity.

Acknowledgments

Authors acknowledge financial support from Petrobras S.A. (0050.0096933.15.9). J.L. de Medeiros and O.Q.F. Araújo also acknowledge financial support from CNPq-Brazil (311076/2017-3).

Abbreviations

1D One-Dimensional; 2D Two-Dimensional; CAM Cellulose-Acetate Membrane; CC Counter-current Contact; CW Cooling-Water; DLL Dynamic-Link Library; EOR Enhanced Oil Recovery; EOS Equation of State; HCDPA Hydrocarbons Dew-Point Adjustment; HFM Hollow-Fiber Membrane; MMSm^3/d Millions of Standard m^3/d; MP Membrane-Permeation; NG Natural Gas; NRM Newton-Raphson Method; PC Parallel Contact; PHW Pressurized-Hot-Water; PFD Process Flow Diagram; PR-EOS Peng-Robinson Equation-of-State; SWM Spiral-Wound Membrane; UOE Unit Operation Extension, VB Visual Basic; WDPA Water Dew-Point Adjustment.

Nomenclature

A_{MP}	*: MP area (m²)*
A_I, A_E	*: Internal and external MP heat exchange areas (m²)*
$\overline{H}$	*: Molar enthalpy of multiphase or single-phase fluid (J/mol, kJ/mol)*
$\bar{H}_k$	*: Partial molar enthalpy of k^{th} species (J/mol, kJ/mol)*
L	*: Permeate molar flow rate (mol/s, MMNm^3/d, MMSm^3/d)*
nc	*: Number of components (species)*
N_k	*: Species k permeation rate (mol/s, MMNm^3/d, MMSm^3/d)*
P, P_V, P_L	*: Pressure, retentate pressure and permeate pressure (Pa, bar)*
P_V^{out}, P_L^{out}	*: MP retentate/permeate outlet pressures (bar)*
P_V^{in}, P_L^{in}	*: MP retentate/permeate inlet pressures (bar)*
ΔP_k^{LN}	*: MP log mean difference of partial pressures of species k (bar)*
T	*: Temperature (K, ^oC)*
T_L, T_V	*: Temperatures of permeate/retentate (K, ^oC)*
T_V^{out}, T_L^{out}	*: MP retentate/permeate outlet temperatures (K, ^oC)*
T_V^{in}, T_L^{in}	*: MP retentate/permeate inlet temperatures (K, ^oC)*
ΔT_F	*: MP Temperature difference at the initial condition of permeate flow (^oC)*
$\Delta T_I^{LN}, \Delta T_E^{LN}$	*: MP log-mean temperature difference for internal/external heat transfers (^oC)*
U_I, U_E	*: MP internal and external heat transfer coefficients (W/m².K)*
V	*: Molar flow rate of retentate (mol/s, MMNm^3/d, MMSm^3/d)*

$\underline{X}$: *Vector (nc x 1) of permeate (or liquid phase) mol fractions*

$Y_k^{in}, Y_k^{out}, X_k^{out}$: *Species k mol fraction in retentate/permeate inlet/outlet MP streams*

$\underline{Y}$: *Vector (nc x 1) of retentate (or vapor phase) mol fractions*

$\underline{Z}$: *Vector (nc x 1) of total mol fractions of multiphase or single-phase fluid*

Greek Symbols

Π_k : *Permeance of species k (mol/s.m².bar, MMNm^3/d.m².bar, MMSm^3/d.m².bar)*

Subscripts

k : *Species index*

L : *Liquid phase or permeate*

V : *Vapor phase or retentate*

Superscripts

in, out : *Inlet, outlet*

V, L : *Vapor, liquid or retentate, permeate*

References

Araújo, O. Q. F.; de Medeiros, J. L. Carbon capture and storage technologies: present scenario and drivers of innovation, Current Opinion in Chemical Engineering, 17, 22-34, August 2017. doi: 10.1016/j.coche.2017.05.004.

Araújo, O. Q. F.; Reis, A. C.; de Medeiros, J. L.; Nascimento, J.F.; Grava, W.M.; Musse, A. P. S. Comparative analysis of separation technologies for processing carbon dioxide rich natural gas in ultra-deepwater oil fields, Journal of Cleaner Production, 155, 12-22, 2017. doi 10.1016/j.jclepro.2016.06.073

Arinelli, L. O.; Trotta, T. A. F.; Teixeira, A. M.; de Medeiros, J. L.; Araújo, O. Q. F. Offshore processing of CO_2 rich natural gas with supersonic separator versus conventional routes, Journal of Natural Gas Science and Engineering, 46, 199-221, 2017. doi: 10.1016/j.jngse.2017.07.010.

Arinelli, L. O.; Teixeira, A. M.; de Medeiros, J. L.; Araújo, O. Q. F. Supersonic separator for cleaner offshore processing of natural gas with high carbon dioxide content: Environmental and economic assessments, Journal of Cleaner Production, 233, 510-521, 2019. doi: 10.1016/j.jclepro.2019.06.115.

Arinelli, L. O.; de Medeiros, J. L.; de Melo, D. C.; Teixeira, A. M.; Brigagão, G. V.; Passarelli, F. M.; Grava, W. M.; Araújo, O. Q. F. Carbon capture and high-capacity supercritical fluid processing with supersonic separator: Natural gas with ultra-high CO_2 content, Journal of Natural Gas Science and Engineering, 66, 265–283, 2019. doi: 10.1016/j.jngse.2019.04.004.

Baker, R., Membrane Technology and Applications, 2nd Ed, John Wiley & Sons, England, 2004.

Bernardo, P.; Drioli, E.; Golemme, G. Membrane Gas Separation: A Review/State of the Art. Industrial & Engineering Chemistry Research, 48, 4638–4663, 2009.

Chu, Y.; Lindbråthen, A.; Lei, L.; He, X.; Hillestad, M. Mathematical modeling and process parametric study of CO_2 removal from natural gas by hollowfiber membranes, Chemical Engineering Research and Design, 148, 45-55, 2019. doi: 10.1016/j.cherd.2019.05.054

de Medeiros, J. L.; Barbosa, L. C.; Araújo, O. Q. F. Equilibrium Approach for CO_2 and H_2S Absorption with Aqueous Solutions of Alkanolamines: Theory and Parameter Estimation, Industrial & Engineering Chemistry Research, 52, 9203−9226, 2013. doi: 10.1021/ie302558b

de Melo, D. C.; Arinelli, L. O.; de Medeiros, J. L.; Teixeira, A. M.; Brigagão, G. V.; Passarelli, F. M.; Grava, W. M.; Araújo, O. Q. F. Supersonic separator for cleaner offshore processing of supercritical fluid with ultra-high carbon dioxide content: Economic and environmental evaluation, Journal of Cleaner Production, 234, 1385-1398, 2019. doi: 10.1016/j.jclepro.2019.06.304.

Ebner, A. D.; Ritter, J. A. State-of-the-art Adsorption and Membrane Separation Processes for Carbon Dioxide Production from Carbon Dioxide Emitting Industries, Separation Science and Technology, 44, 1273, 2009.

Echt, W. Hybrid Systems: Combining Technologies Leads to More Efficient Gas Conditioning, UOP LLC, 2017. Available at: https://www.uop.com/?document=hybrid-systems-for-more-efficient-gas-conditioning&download=1

Gonzaga, C. S. B.; Arinelli, L. O.; de Medeiros, J. L.; Araújo, O. Q. F. Automatized Monte-Carlo analysis of offshore processing of CO2-rich natural gas: Conventional versus supersonic separator routes, Journal of Natural Gas Science and Engineering, 69, 102943, 2019. doi: 10.1016/j.jngse.2019.102943.

Hao, J.; Rice, P.; Stern, S. A. Upgrading low-quality natural gas with H_2S- and CO_2-selective polymer membranes, Journal of Membrane Science, 320, 108–122, 2008. doi: 10.1016/j.memsci.2008.03.040

Ho, M. T.; Allinson, G.; Wiley, D.E. Comparison of CO_2 separation options for geo-sequestration: are membranes competitive?, Desalination, 192, 288-295, 2006.

Hoorfar, M.; Alcheikhhamdon, Y.; Chen, B. A novel tool for the modeling, simulation and costing of membrane based gas separation processes using Aspen HYSYS: Optimization of the CO_2/CH_4 separation process, Computers and Chemical Engineering, 117, 11-24, 2018. doi: 10.1016/j.compchemeng.2018.05.013

Lock, S. S. M.; Lau, K. K.; Ahmad, F.; Shariff, A. M. Modeling, simulation and economic analysis of CO_2 capture from natural gas using cocurrent, countercurrent and radial crossflow hollow fiber membrane, International Journal of Greenhouse Gas Control, 36, 114–134, 2015. doi: 10.1016/j.ijggc.2015.02.014

Xu, J.; Wang, Z.; Qiao, Z.; Wu, H.; Dong, S.; Zhao, S.; Wang, J. Post-combustion CO_2 capture with membrane process: Practical membrane performance and appropriate pressure, Journal of Membrane Science, 581, 195-213, 2019. doi: 10.1016/j.memsci.2019.03.052

CHAPTER VIII – CONCLUDING REMARKS

Unit operation extensions, SS-UOE and MP-UOE, were developed to simulate MP and SS units in steady state HYSYS PFDs. MP-UOE is composed by a lumped short-cut method of permeation, including mass and energy balances around MP, and calibrated with real MP process data. SS modelling in SS-UOE is purely phenomenological, based on rigorous thermodynamic and phase equilibrium calculations via equation of state. SS-UOE can operate with water saturated NG with high CO_2 contents, correctly handling two-phase condensate removal and normal shock transition (if present), essential steps for correct SS representation in NG context.

SS-UOE uses the thermodynamic sound speed of multiphase VLWE compressible flow rigorously calculated by means of another HYSYS extension, PEC-UOE. Multiphase multi-reactive sound speed was also implemented as HYSYS extension, REC-UOE. PEC-UOE and REC-UOE performances were assessed via several simulations, comparing well with multiphase sound speed from literature. Reactive calculations show that, depending on temperature, pressure, and conversion, differences to the correct reactive value of sound speed may occur if a reactive stream has its sound speed calculated via nonreactive formulae, merely substituting the stream composition in any point of a real chemical reactor.

MP-UOE and SS-UOE were used in various simulations of CO_2-rich (and ultra-rich) offshore NG processing. MP was applied for CO_2 removal from NG in order to produce fuel-gas for power generation, while SS was implemented for different steps of NG processing: (i) for water and hydrocarbon dew-points adjustment; and (ii) for CO_2 removal. Comparisons between SS operation and conventional technologies (including MP) for NG processing were conducted to investigate the advantages of supersonic separation.

The main conclusions derived for SS in dew-points adjustment are:

- SS requires lower feed pressure when compared to TEG+JT process for the same dehydration service, diminishing power consumption and associated CO_2 emissions. Besides, C3+ removal is more effective in SS, producing a greater condensate volume with higher selectivity for C3+ over CO_2. It also has economic implications, reducing

COM and compressors FCI (despite higher SS FCI), and obtaining a slightly higher NPV after 20 years of operation. Even under similar economic responses, the environmental gain justifies replacing the conventional dew-point adjustments process by SS unit;

- Still in comparison with conventional TEG+JT process, SS presents greater resilience or elasticity, which translates as a simpler, more straightforward and safer process;
- When compared to conventional MS+JT process for high-pressure high-capacity NG processing, SS presents lower investment costs, due to the outstanding FCI of MS units for this size of service;
- There is greater oil production due to the excellent recycle of C3+ condensate from SS unit to the primary oil-gas-water separator, contributing to higher oil revenues when compared with JT.

Concerning SS for CO_2 removal, the major conclusions are:

- It is fundamental to check if the SS path crosses the SVLE CO_2 freeze-out border inside the feed VLE envelope, in order to avoid formation of abundant solid dry ice that can plug a conventional SS nozzle;
- Despite the higher pressure and lower temperature of SS inlet, the produced EOR fluid is at high-pressure and low temperature, providing feed refrigeration and reduced power demand for its compression to injection. On the other hand, the rather simple MP operation produces a low-pressure CO_2 permeate requiring high compression power, and consequently higher COM and FCI spent on the huge CO_2 compression train.

After the thorough analysis contemplating power demand, CO_2 emissions and economic results, for both CO_2-rich (45%mol) and CO_2 ultra-rich (68%mol) offshore NG processing, it is clear that the SS based process with two consecutive SS units presents the best, most lucrative and cleanest overall solution.

Furthermore, MP-UOE model was expanded to include local energy balances for each stream inside MP, thus calculating product temperatures with more precision, and originating a new version of the lumped model extension: MPx-UOE. A distributed MP model was also

developed, MPd-UOE, dividing the MP unit into smaller MP cells and applying MPx-UOE methodology for each cell consecutively, thus reproducing stream profiles inside MP. The new extensions were evaluated for CO_2-rich NG decarbonation simulations in HYSYS and are object of future publications in 2019. Besides, the MP models can be improved with the admission of permeance equations dependent of retentate temperature and CO_2 fugacity.

SS-UOE was also applied for innovative applications other than NG conditioning:

- For THI recovery from NG in offshore processing platforms with water injection into the raw NG SS feed, reducing costs related to THI transport, make-up and storage. SS-THI-Recovery process is simple, with low footprint and easy implementation. It was demonstrated that for methanol as THI, the SS based process attained sufficient economic leverage to afford a post-combustion capture plant, while maintaining economic superiority relative to the conventional gas processing;
- For CO_2 dehydration, with excellent pressure recovery, thus producing high pressure dry CO_2 ready for compression and injection for EOR;
- For air dehydration in pre-purification units for oxygen production, where SS handles most of the dehydration service, thus considerably reducing the adsorption unit in terms of energy consumption and costs.

The content of this Thesis is of great importance to the oil and gas industry, especially in the area of E&P and offshore NG processing. The development of tools for simulating new steady state unit operations opens the horizon of process engineering for alternative technologies. Besides all the published material, clearly stating the value of this research, future submissions and developments are expected. MP-UOE and SS-UOE have already suffered improvements that will culminate in new modelling publications. Moreover, CO_2-rich and ultra-rich NG processing must be further investigated for different operating conditions and goals – such as reducing CO_2 content in lean NG to 3%mol specification – aiming the minimization of carbon emissions and maximization of economic return. Other innovative applications of SS in separation processes will also be researched, determining the technical and economic feasibility of the new alternatives.

APPENDIX A - COMPLETE DIFFERENTIALS OF ECS DENSITY AND ECS ENTHALPY PER UNIT OF MASS ON PLANE (*T,P*)

To obtain the complete differentials of density and specific enthalpy of the ECS on plane (*T,P*) fundamental relationships are written for ECS properties enthalpy and Gibbs free energy per unit of mass under constant $\underline{Z}$ in Eqs. (A.1) and (A.2). From Eq. (A.2) results the ECS Maxwell relationship Eq. (A.3). Other ECS formulae are Eqs. (A.4), (A.5), the former from the definition of ECS isobaric heat capacity and the latter by dividing Eq. (A.1) by *dT* at constant *P*.

$$d\hat{H} = Td\hat{S} + \hat{V}dP \qquad \text{(const. } \underline{Z}\text{)} \tag{A.1}$$

$$d\hat{G} = -\hat{S}dT + \hat{V}dP \qquad \text{(const. } \underline{Z}\text{)} \tag{A.2}$$

$$\left(\frac{\partial \hat{S}}{\partial P}\right)_{T,\underline{Z}} = -\left(\frac{\partial \hat{V}}{\partial T}\right)_{P,\underline{Z}} = \frac{1}{\rho^2}\left(\frac{\partial \rho}{\partial T}\right)_{P,\underline{Z}} = \frac{\Xi_T}{\rho^2} \tag{A.3}$$

$$\left(\frac{\partial \hat{H}}{\partial T}\right)_{P,\underline{Z}} = \hat{C}_P \tag{A.4}$$

$$\left(\frac{\partial \hat{S}}{\partial T}\right)_{P,\underline{Z}} = \frac{\hat{C}_P}{T} \tag{A.5}$$

On an isothermal transformation, Eq. (A.1) is divided by *dP* giving Eq. (A.6) after using Eq. (A.3). The ECS changes state only on a path of equilibrium states. On such path, the changes of density and specific enthalpy of the ECS are described on plane (*T,P*) by Eqs. (A.7) and (A.8) – i.e. Eqs. (32) and (33) in Sec. II.2.2 – after using Eqs. (A.4) and (A.6).

$$\left(\frac{\partial \hat{H}}{\partial P}\right)_{T,\underline{Z}} = \hat{V} - T\left(\frac{\partial \hat{V}}{\partial T}\right)_{P,\underline{Z}} \Rightarrow \left(\frac{\partial \hat{H}}{\partial P}\right)_{T,\underline{Z}} = \frac{1}{\rho}\left(1 + \frac{T.\Xi_T}{\rho}\right) \tag{A.6}$$

$$d\rho = \Xi_T.dT + \Xi_P.dP \qquad , \ \Xi_P = \left(\frac{\partial \rho}{\partial P}\right)_{T,\underline{Z}} \quad , \qquad \Xi_T = \left(\frac{\partial \rho}{\partial T}\right)_{P,\underline{Z}} \tag{A.7}$$

$$d\hat{H} = \hat{C}_P.dT + \left(\frac{\partial \hat{H}}{\partial P}\right)_{T,\underline{Z}} dP \ \Rightarrow \ d\hat{H} = \hat{C}_P.dT + \frac{1}{\rho}\left(1 + \frac{T.\Xi_T}{\rho}\right).dP \tag{A.8}$$

APPENDIX B - ASYMPTOTIC BEHAVIOR OF THE SOUND SPEED IN THE SUBCRITICAL VLE DOME OF PURE FLUID VIA LANDAU MODEL (LM).

With $T<T_c$ near the critical point of the pure fluid at (T_c,v_c), the molar Helmholtz free energy $\overline{A}(T,v)$ can be expressed as a 4th order polynomial of (v-v_c) with coefficients as linear functions of (T-T_c) as in Eqs. (B.1). The 4th order in molar volume v is the minimal order to access criticality with stability. The independent terms A_{20} and A_{30} of $A_2(T)$ and $A_3(T)$ are zero, and the independent term A_{40} of $A_4(T)$ is positive ($A_{40}>0$) in order to satisfy the pure fluid critical conditions in Eq. (B.1d) jointly with the stability of the critical phase. Additionally, A_{21} has to be positive to ensure mechanical stability of the non-critical fluid. Eqs. (B.2) and (B.3) give the equilibrium pressure (P) and chemical potential (μ) of the fluid. The isobaric and isothermal differential coefficients of density, Ξ_T and Ξ_P, and the molar entropy follow in Eqs. (B.4a), (B.4b) and (B.4c). It is seen (Eqs. (B.2), (B.4b)) that the divergence $\Xi_P \to +\infty$ at (T_c , v_c) occurs naturally with $A_{21}>0$. On the other hand, Ξ_T must diverge as $\Xi_T \to -\infty$ at (T_c , v_c), i.e. it is also necessary that $A_{11}<0$ via Eqs. (B.2) and (B.4a). Critical values are obtained by substituting (T_c , v_c) as done in Eq. (B.4d).

$$\overline{A} = A_0(T) + A_1(T)(v - v_c) + A_2(T)(v - v_c)^2 + A_3(T)(v - v_c)^3 + A_4(T)(v - v_c)^4 \quad \text{(B.1a)}$$

$$A_0(T) = A_{00} + A_{01}(T - T_c),\ A_1(T) = A_{10} + A_{11}(T - T_c),\ A_2(T) = A_{21}(T - T_c) \quad \text{(B.1b)}$$

$$A_3(T) = A_{31}(T - T_c),\ A_4(T) = A_{40} + A_{41}(T - T_c),\ A_{40} > 0, A_{21} > 0, A_{11} < 0 \quad \text{(B.1c)}$$

$$\left(\frac{\partial^2 \overline{A}}{\partial v^2}\right)_T = \left(\frac{\partial^3 \overline{A}}{\partial v^3}\right)_T = 0\ ,\ \left(\frac{\partial^4 \overline{A}}{\partial v^4}\right)_T > 0\ \ (T = T_c, v = v_c) \quad \text{(B.1d)}$$

$$P = -\left(\frac{\partial \overline{A}}{\partial v}\right)_T = -A_1(T) - 2A_2(T)(v - v_c) - 3A_3(T)(v - v_c)^2 - 4A_4(T)(v - v_c)^3 \quad \text{(B.2)}$$

$$\mu = \overline{A} + Pv = A_0(T) - A_1(T).v_c - A_2(T).(v^2 - v_c^2) - A_3(T)(2v + v_c)(v - v_c)^2 - A_4(T)(3v + v_c)(v - v_c)^3 \quad \text{(B.3)}$$

$$\Xi_T = \left(\frac{\partial \rho}{\partial T}\right)_P = \frac{M_M}{v^2} \cdot \frac{(\partial P / \partial T)_v}{(\partial P / \partial v)_T} \tag{B.4a}$$

$$\Xi_P = \left(\frac{\partial \rho}{\partial P}\right)_T = \frac{M_M}{v^2} \cdot \frac{-1}{(\partial P / \partial v)_T} \tag{B.4b}$$

$$\bar{S} = -\left(\frac{\partial \bar{A}}{\partial T}\right)_v = -A_{01} - A_{11}(v - v_c) - A_{21}(v - v_c)^2 - A_{31}(v - v_c)^3 - A_{41}(v - v_c)^4 \tag{B.4c}$$

$$\bar{A}_c = A_{00} \ , \bar{S}_c = -A_{01} \ , \ \rho_c = M_M / v_c \ \ , \ \ P_c = -A_{10} \qquad (A_{10} < 0) \tag{B.4d}$$

The coexistence of liquid (v_L) and vapor (v_V) at T < Tc imposes the VLE constraints Eqs. (B.5).

$$\mu(T, v_V) - \mu(T, v_L) = 0 \tag{B.5a}$$

$$P(T, v_v) - P(T, v_L) = 0 \tag{B.5b}$$

Firstly, Eqs. (B.2) and (B.3) are substituted on both terms of Eqs. (B.5a) and (B.5b). Then, dividing Eq. (B.5a) by (v_V-v_L).(v_V+v_L) and Eq. (B.5b) by (v_V-v_L), the forms in Eqs (B.6a) and (B.6b) are respectively obtained.

$$-A_2(T) - A_3(T)\left(v_V + v_L - 3v_c + \frac{v_V^2 + v_L^2}{v_V + v_L}\right) - 3A_4(T)\left(v_V^2 + v_L^2 + 2v_c^2 - \left(\frac{8}{3}v_c\right)\frac{v_V^2 + v_V v_L + v_L^2}{v_V + v_L}\right) = 0 \tag{B.6a}$$

$$2A_2(T) + 3A_3(T)(v_V + v_L - 2v_c) + 4A_4(T)((v_V + v_L - 2v_c)^2 - (v_V - v_c)(v_L - v_c)) = 0 \tag{B.6b}$$

With dimensionless variables $\Delta \equiv (v_V - v_L)/2v_c$ and $\Sigma \equiv (v_V + v_L)/2v_c$, Eqs. (B.6a) and (B.6b) are re-written as Eqs. (B.7a) and (B.7b), respectively.

$$A_2(T) + 3v_c A_3(T)\left(\Sigma - 1 + \frac{\Delta^2}{3\Sigma}\right) + 6v_c^2 A_4(T)\left((\Sigma - 1)^2 + \Delta^2 - \frac{2\Delta^2}{3\Sigma}\right) = 0 \tag{B.7a}$$

$$A_2(T) + 3v_c A_3(T)(\Sigma - 1) + 6v_c^2 A_4(T)\left((\Sigma - 1)^2 + \Delta^2 / 3\right) = 0 \tag{B.7b}$$

Eq. (B.8) results by subtraction of Eq. (B.7b) from (B.7a). It is solved for Σ in Eq. (B.9) as $\Delta^2 > 0$. Inserting Σ from Eq. (B.9) into Eq. (B.7b), Δ^2 is isolated in Eq. (B.10).

$$\Delta^2.\left(4v_c^2 A_4(T) - (4v_c^2 A_4(T) - v_c A_3(T))/\Sigma\right) = 0 \tag{B.8}$$

$$\Sigma = 1 - \frac{A_3(T)}{4v_c A_4(T)} \tag{B.9}$$

$$\Delta^2 = \frac{1}{2v_c^2 A_4(T)}\left(\frac{3}{8}.\frac{A_3(T)^2}{A_4(T)} - A_2(T)\right) \tag{B.10}$$

As $T - T_c \approx 0^-$, Eqs. (B.1b) and (B.1c) imply $A_3(T)^2 << A_2(T)$, with $A_2(T)>0$, $A_4(T)>0$. Therefore, the first term in the parentheses of Eq. (B.10) can be asymptotically neglected relatively to the second, giving Eq. (B.11), where $A_2(T)$ was replaced by $A_{21}(T-T_c)$ via Eq. (B.1b). Again, as $T - T_c \approx 0^-$, $A_4(T)$ can be replaced by A_{40}, leading to the classical asymptotic result in Eq. (B.12a) for the difference of molar volumes of phases as the critical point is approached. Another classical landmark is recovered in Eq. (B.9): As $T - T_c \approx 0^-$, $A_4(T)$ can be replaced by A_{40}, and $A_3(T)/4v_cA_{40}$ becomes much smaller than *1*, leading asymptotically to Eq. (B.12b), the Rectilinear Diameter Law. Eqs. (B.12a) and (B.12b) are classical pure fluid results that establish the coherency of our LM formalism. Solving Eqs. (B.12a) and (B.12b), the molar liquid and vapor saturated volumes result in Eqs. (B.12c) and (B.12d).

$$\Delta^2 = \frac{A_{21}(T_c - T)}{2v_c^2 A_4(T)} \tag{B.11}$$

$$\Delta = \frac{v_V - v_L}{2v_c} = (A_{21}/(2v_c^2 A_{40}))^{1/2}.(T_c - T)^{1/2} \quad , \quad T - T_c \to 0^- \tag{B.12a}$$

$$\Sigma = \frac{v_V + v_L}{2v_c} = 1 \quad , \quad T - T_c \to 0^- \tag{B.12b}$$

$$v_V(T) = v_c + \sqrt{A_{21}/2A_{40}}.(T_c - T)^{1/2} \quad , \quad T - T_c \to 0^- \tag{B.12c}$$

$$v_L(T) = v_c - \sqrt{A_{21}/2A_{40}}.(T_c - T)^{1/2} \quad , \quad T - T_c \to 0^- \tag{B.12d}$$

The vapor pressure is obtained via Eqs. (B.13a) or (B.13b) substituting $v = v_V(T)$ or $v = v_{:L}(T)$ in Eq. (B.2). There is a small difference between Eqs. (B.13a) and (B.13b) (asymptotically vanishing to zero) due to truncation when creating Eq. (B.12b) from (B.9), so that P^{SAT} is better given by averaging Eqs. (B.13a) and (B.13b). The molar entropy of saturated phases $\bar{S}_V(T), \bar{S}_L(T)$ follows from Eq. (B.4c) inserting $v = v_V(T)$ or $v = v_{:L}(T)$. Molar vaporization changes of volume and entropy follow in Eqs. (B.13c) and (B.13d), leading to the Clausius–Clapeyron formula in Eq. (B.13e), whereas Eq. (B.13f) gives temperature derivatives on the VLE locus. Eq. (B.13g) and (B.13h) give, respectively, the vapor fraction (β) and the density (ρ) of a VLE conjunction with total molar entropy $\bar{S}$. Differentiating β with T under VLE and constant $\bar{S}$ as in Eq. (B.13i), we are in position to write the isentropic derivative of the two-phase density with pressure in Eq. (B.13j), where the Clausius-Clapeyron coefficient is seen in the last term. The two-phase LM sound speed is written in Eq. (B.13m) via an analogue of Eq. (49) with Eq. (B.13j).

$$P^{SAT}(T) = -A_1(T) - 2A_2(T)(v_V(T) - v_c) - 3A_3(T)(v_V(T) - v_c)^2 - 4A_4(T)(v_V(T) - v_c)^3 \tag{B.13a}$$

$$P^{SAT}(T) = -A_1(T) - 2A_2(T)(v_L(T) - v_c) - 3A_3(T)(v_L(T) - v_c)^2 - 4A_4(T)(v_L(T) - v_c)^3 \tag{B.13b}$$

$$\Delta v(T) = v_V(T) - v_L(T) \tag{B.13c}$$

$$\Delta\bar{S}(T) = \bar{S}_V(T) - \bar{S}_L(T) \Rightarrow \Delta\bar{S} = -(A_{11} + A_{31}\Delta v^2/4).\Delta v \tag{B.13d}$$

$$(dT/dP)^{SAT} = \Delta v/\Delta\bar{S} \Rightarrow (dT/dP)^{SAT} = -(A_{11} + A_{31}\Delta v^2/4)^{-1} \tag{B.13e}$$

$$v_{LT} = dv_L/dT,\ \Delta v_T = d\Delta v/dT,\ \bar{S}_{LT} = d\bar{S}_L/dT,\ \Delta\bar{S}_T = d\Delta\bar{S}/dT \tag{B.13f}$$

$$\beta(T,\bar{S}) = (\bar{S} - \bar{S}_L(T))/\Delta\bar{S}(T) = (v - v_L(T))/\Delta v(T) \tag{B.13g}$$

$$\rho(T,\bar{S}) = M_M/(v_L(T) + \beta(T,\bar{S}).\Delta v(T)) \tag{B.13h}$$

$$\left(\frac{\partial\beta}{\partial T}\right)_{\bar{S}} = -(\bar{S}_{LT} + \beta.\Delta\bar{S}_T)/\Delta\bar{S} \tag{B.13i}$$

$$\left(\frac{\partial \rho}{\partial P}\right)_{\bar{S}} = -\frac{\rho}{(v_L + \beta.\Delta v)}\left(v_{LT} + \beta.\Delta v_T + \Delta v.\left(\frac{\partial \beta}{\partial T}\right)_{\bar{S}}\right)\frac{\Delta v}{\Delta \bar{S}} \qquad \text{(B.13j)}$$

$$c_{T<Tc}^{VLE} = \frac{1}{\sqrt{\left(\frac{\partial \rho}{\partial P}\right)_{\bar{S}}}} \qquad \text{(B.13m)}$$

APPENDIX C - ASYMPTOTIC BEHAVIOR OF THE SOUND SPEED IN THE LOWER SUPERCRITICAL FLUID (SCF) DOMAIN OF PURE FLUID VIA LANDAU MODEL (LM).

With $T>T_c$ near the critical point of the pure fluid at (T_c,v_c), the molar Helmholtz free energy $\overline{A}(T,v)$ is used again, but now with 2nd order temperature dependent coefficients $A_0(T)$, $A_1(T)$, $A_2(T)$, $A_3(T)$, $A_4(T)$ in Eqs. (C.1). Such expedient is necessary to address heat capacities that involve 2nd order derivatives of $\overline{A}(T,v)$ with T. For the same reasons already explained in Appendix B, independent terms A_{20} and A_{30} in $A_2(T)$ and $A_3(T)$ are zero and $A_{21}>0$, $A_{11}<0$, $A_{40}>0$. The isochoric molar heat capacity is given by Eq. (C.2a). As $\overline{C}_V$ is a positive property, its critical value $\overline{C}_V(T_c,v_c)$ imposes $A_{02} < 0$. The isobaric molar heat capacity is left as in Eq. (C.2b) from Eq. (50e). $\overline{C}_P(T,v)$ can be also developed as in Eq. (C.2c) by using Eqs. (B.4a) and (B.4b). The final form $\overline{C}_P(T,v)$ is operated with Eqs. (C.2a), (C.2c) and (B.2).

$$A_0(T)=A_{00}+\sum_{k=1}^{2}A_{0k}(T-T_c)^k, A_1(T)=A_{10}+\sum_{k=1}^{2}A_{1k}(T-T_c)^k, A_{02}<0, A_{11}<0 \tag{C.1a}$$

$$A_2(T)=\sum_{k=1}^{2}A_{2k}(T-T_c)^k,\quad A_3(T)=\sum_{k=1}^{2}A_{3k}(T-T_c)^k\quad,\quad A_{21}>0 \tag{C.1b}$$

$$A_4(T)=A_{40}+\sum_{k=1}^{2}A_{4k}(T-T_c)^k\quad,\quad A_{40}>0 \tag{C.1c}$$

$$\overline{C}_V(T,v)=-T\left(\frac{\partial^2\overline{A}}{\partial T^2}\right)_v=-2T(A_{02}+A_{12}(v-v_c)+A_{22}(v-v_c)^2+A_{32}(v-v_c)^3+A_{42}(v-v_c)^4) \tag{C.2a}$$

$$\overline{C}_P=\overline{C}_V+(M_M T/\rho^2)\Xi_T^2/\Xi_P \tag{C.2b}$$

$$\overline{C}_P(T,v)=\overline{C}_V(T,v)-T\left(\frac{\partial P}{\partial T}\right)_v^2/\left(\frac{\partial P}{\partial v}\right)_T \tag{C.2c}$$

The expressions $\overline{C}_P(T,v), \Xi_T(T,v), \Xi_P(T,v)$ are obtained with Eqs. (C.2a), (C.2c), (B.2), (C.1a), (C.1b), (C.1c), (B.4a) and (B.4b). Applying them at $v=v_c$ and $T-T_c \approx 0^+$, one gets, respectively, Eqs. (C.3a), (C.3b) and (C.3c).

$$\overline{C}_P(T,v_c) = -2A_{02}T + \frac{T(A_{11}+2A_{12}(T-T_c))^2}{2(A_{21}+A_{22}(T-T_c))(T-T_c)} \tag{C.3a}$$

$$\Xi_T(T,v_c) = \left(\frac{M_M}{v_c^2}\right)\frac{A_{11}+2A_{12}(T-T_c)}{2(A_{21}+A_{22}(T-T_c))(T-T_c)} \tag{C.3b}$$

$$\Xi_P(T,v_c) = \left(\frac{M_M}{v_c^2}\right)\frac{1}{2(A_{21}+A_{22}(T-T_c))(T-T_c)} \tag{C.3c}$$

While $\overline{C}_V(T,v)$ is not singular as $T-T_c \to 0^+$, Eqs. (C.3a), (C.3b) and (C.3c) show that $\overline{C}_P(T,v)$ suffers a 2nd order phase transition (lambda transition) $\overline{C}_P(T_c,v_c) \to +\infty$ shared with the density derivatives $\Xi_T(T_c,v_c) \to -\infty$ $\Xi_P(T_c,v_c) \to +\infty$. To access the sound speed at $v=v_c$, $T-T_c \to 0^+$, Eq. (50d) is used with Eqs. (C.3a), (C.3b) and (C.3c) giving Eq. (C4). Eq. (C4) is simplified to Eq. (C.5a), leading in the limit $T-T_c \to 0^+$ to Eq. (C.5b), which plainly shows that the sound speed c does not have any singularity at the critical point from the SCF standpoint.

$$c(T,v_c) = \frac{(v_c/M_M^{1/2}).\sqrt{2(A_{21}+A_{22}(T-T_c))(T-T_c)}}{\sqrt{1-\dfrac{(A_{11}+2A_{12}(T-T_c))^2}{-2A_{02}(A_{21}+A_{22}(T-T_c))(T-T_c)+(A_{11}+2A_{12}(T-T_c))^2}}} \tag{C.4}$$

$$c(T,v_c) = \frac{v_c\sqrt{-2A_{02}(A_{21}+A_{22}(T-T_c))(T-T_c)+(A_{11}+2A_{12}(T-T_c))^2}}{M_M^{1/2}\sqrt{-A_{02}}} \tag{C.5a}$$

$$c(T_c^+,v_c) = (v_c/M_M^{1/2})\sqrt{-A_{11}^2/A_{02}} \quad , \; A_{02}<0 \; , \; A_{11}<0 \tag{C.5b}$$

APPENDIX D – Limit Conditions of Multiphase Multi-Reactive Compressible Steady-State 1D Isentropic Plug-Flow with Variable Flow Section

The present material is a necessary theoretical complement of the paper ***Speed of Sound of Multiphase and Multi-Reactive Equilibrium Streams: A Numerical Approach for Natural Gas Applications.***

As several parts of this paper are used as starting points in the present text, we prefer to briefly cite their location in the paper, instead of re-addressing or re-explaining the corresponding theoretical objects. Consequently the above paper is cited several times in the body of this complementary material. Therefore, on behalf of conciseness, it is referred here as Main Document, or, preferably, under the abbreviated form MDOC. The pertinent nomenclature and abbreviations used in the present text are all from MDOC. They are listed in the Abbreviations and Nomenclature Sections at the end of MDOC. Units are strictly SI.

Eqs. (II.42) and (II.43) below are recovered from Sec. II.2.3 of MDOC. These relationships respectively correspond to the momentum and energy balances of a steady-state 1D multiphase multi-reactive, horizontal, adiabatic, frictionless, equilibrium plug-flow with variable flow section. The steady-state obligates the mass flow rate q to be constant. Wall shear stress and gravity are not pertinent to this horizontal and frictionless scenario. The flow is evidently isentropic, compressible, 1D and at equilibrium at each point x along the flow path with variable flow section. The correspondence between a traveling multiphase multi-reactive fluid element of steady-state 1D isentropic plug-flow with variable flow section and an ECS (*Equilibrium Closed System*) has been applied at this point of MDOC, so that the only dependent variables on the flow path are (P,T), whereas the mol fractions preparation vector, $\underline{Z}$, is a known constant of the flow. The solely independent variable is the flow axial position x, with two dependent variables (P,T). All remaining properties are direct functions of x, like $A(x)$, or ECS thermodynamic properties that depend on $(T,P,\underline{Z})$, with $\underline{Z}$ constant.

$$\left(1-\left(\frac{q}{\rho A}\right)^2 \Xi_P\right)\frac{dP}{dx}-\left(\left(\frac{q}{\rho A}\right)^2 \Xi_T\right)\frac{dT}{dx}-\frac{q^2}{\rho A^3}\frac{dA}{dx}=0 \qquad \text{(II.42)}$$

$$\left(1-\left(\frac{q}{\rho A}\right)^2 \Xi_P+\frac{T\Xi_T}{\rho}\right)\frac{dP}{dx}+\left(\rho\hat{C}_P-\left(\frac{q}{\rho A}\right)^2 \Xi_T\right)\frac{dT}{dx}-\frac{q^2}{\rho A^3}\frac{dA}{dx}=0 \qquad \text{(II.43)}$$

Eqs. (II.42) and (II.43) are recast as Eqs. (D.1) and (D.2), where the flow section terms were moved to the respective RHS's. The flow section area is a function only of *x*, i.e. *A(x)*.

$$\left(1-\left(\frac{q}{\rho A}\right)^2 \Xi_P\right)\frac{dP}{dx}-\left(\left(\frac{q}{\rho A}\right)^2 \Xi_T\right)\frac{dT}{dx}=\frac{q^2}{\rho A^3}\frac{dA}{dx} \qquad \text{(D.1)}$$

$$\left(1-\left(\frac{q}{\rho A}\right)^2 \Xi_P+\frac{T\Xi_T}{\rho}\right)\frac{dP}{dx}+\left(\rho\hat{C}_P-\left(\frac{q}{\rho A}\right)^2 \Xi_T\right)\frac{dT}{dx}=\frac{q^2}{\rho A^3}\frac{dA}{dx} \qquad \text{(D.2)}$$

Keeping Eq. (D.1) and subtracting Eq. (D.1) from (D.2), a more compact set of state relationships is obtained for the steady-state 1D isentropic multiphase multi-reactive plug-flow with variable flow section as given in Eqs. (D.3) and (D.4).

$$\left(1-\left(\frac{q}{\rho A}\right)^2 \Xi_P\right)\frac{dP}{dx}-\left(\left(\frac{q}{\rho A}\right)^2 \Xi_T\right)\frac{dT}{dx}=\frac{q^2}{\rho A^3}\frac{dA}{dx} \qquad \text{(D.3)}$$

$$\left(\frac{T.\Xi_T}{\rho}\right)\left(\frac{dP}{dx}\right)+\rho.\hat{C}_P\left(\frac{dT}{dx}\right)=0 \qquad \text{(D.4)}$$

Dividing Eqs. (D.3) and (D.4) by $\frac{dT}{dx}$, the isentropic flow condition ($\hat{S}$ constant), at constant preparation $\underline{Z}$, authorizes us to write the ECS thermodynamic identity Eq. (D.5). This ECS identity allows to rewrite Eqs. (D.3) and (D.4) respectively under the forms of Eqs. (D.6) and (D.7).

$$\left(\frac{dP}{dx}\right)/\left(\frac{dT}{dx}\right)=\left(\frac{dP}{dT}\right)_{\hat{S},\underline{Z}}=\left(\frac{\partial P}{\partial T}\right)_{\hat{S},\underline{Z}} \qquad \text{(D.5)}$$

$$\left(1-\left(\frac{q}{\rho A}\right)^2 \Xi_P\right)\left(\frac{\partial P}{\partial T}\right)_{\hat{S},\underline{Z}}-\left(\frac{q}{\rho A}\right)^2 \Xi_T=\frac{q^2}{\rho A^3}\left(\frac{dA}{dx}/\frac{dT}{dx}\right) \qquad \text{(D.6)}$$

$$\left(\frac{T.\Xi_T}{\rho}\right)\left(\frac{\partial P}{\partial T}\right)_{\hat{S},\underline{Z}} + \rho.\hat{C}_P = 0 \tag{D.7}$$

Manipulating Eq. (D.6), one obtains Eq. (D.8) for the temperature profile of the 1D isentropic multiphase multi-reactive plug-flow with variable flow section. In the same way, with Eq. (D.5) and Eq. (D.8), one can write Eq. (D.9) for the pressure profile along the 1D isentropic multiphase multi-reactive plug-flow with variable flow section. Eqs. (D.8) and (D.9) express the state relationships that the dependent variables (*T*,*P*) have to satisfy for a given flow section area profile imposed by the function *A(x)* and its gradient *dA/dx*.

$$\frac{dT}{dx} = \frac{\left(\frac{q}{\rho A}\right)^2}{\left(\frac{\partial P}{\partial \theta}\right)_{\hat{S},\underline{Z}} - \left(\frac{q}{\rho A}\right)^2\left(\Xi_P\left(\frac{\partial P}{\partial T}\right)_{\hat{S},\underline{Z}} + \Xi_T\right)}\left(\frac{\rho}{A}\right)\frac{dA}{dx} \tag{D.8}$$

$$\frac{dP}{dx} = \frac{\left(\frac{q}{\rho A}\right)^2}{\left(\frac{\partial P}{\partial \theta}\right)_{\hat{S},\underline{Z}} - \left(\frac{q}{\rho A}\right)^2\left(\Xi_P\left(\frac{\partial P}{\partial T}\right)_{\hat{S},\underline{Z}} + \Xi_T\right)}\left(\frac{\rho}{A}\right)\left(\frac{\partial P}{\partial T}\right)_{\hat{S},\underline{Z}}\frac{dA}{dx} \tag{D.9}$$

Eqs. (D.8) and (D.9) can be rearranged in the forms shown in Eqs. (D.10) and (D.11).

$$\frac{dT}{dx} = \frac{\left(\frac{q}{\rho A}\right)^2}{\left(\frac{\left(\frac{\partial P}{\partial T}\right)_{\hat{S},\underline{Z}}}{\Xi_P\left(\frac{\partial P}{\partial T}\right)_{\hat{S},\underline{Z}} + \Xi_T}\right) - \left(\frac{q}{\rho A}\right)^2}\left(\frac{1}{\Xi_P\left(\frac{\partial P}{\partial T}\right)_{\hat{S},\underline{Z}} + \Xi_T}\right)\left(\frac{\rho}{A}\right)\frac{dA}{dx} \tag{D.10}$$

$$\frac{dP}{dx}=\frac{\left(\frac{q}{\rho A}\right)^2}{\left(\frac{\left(\frac{\partial P}{\partial T}\right)_{\hat{S},\underline{Z}}}{\Xi_P\left(\frac{\partial P}{\partial T}\right)_{\hat{S},\underline{Z}}+\Xi_T}\right)-\left(\frac{q}{\rho A}\right)^2}\left(\frac{\left(\frac{\partial P}{\partial T}\right)_{\hat{S},\underline{Z}}}{\Xi_P\left(\frac{\partial P}{\partial T}\right)_{\hat{S},\underline{Z}}+\Xi_T}\right)\left(\frac{\rho}{A}\right)\frac{dA}{dx} \tag{D.11}$$

The square of the multiphase multi-reactive equilibrium property, thermodynamic sound speed, from Eq. (II.53) of MDOC, is written in Eq. (D.12). The square of the multiphase multi-reactive Mach Number (*Ma*), also from Eq. (II.56g) of MDOC, follows in Eq. (D.13).

$$c^2=\left(\frac{q^*}{\rho.A}\right)^2=\frac{\left(\frac{\partial P}{\partial T}\right)_{\hat{S},\underline{Z}}}{\Xi_T+\Xi_P\left(\frac{\partial P}{\partial T}\right)_{\hat{S},\underline{Z}}} \tag{D.12}$$

$$Ma^2=\left(\frac{q}{\rho.A}\right)^2\div\frac{\left(\frac{\partial P}{\partial T}\right)_{\hat{S},\underline{Z}}}{\Xi_T+\Xi_P\left(\frac{\partial P}{\partial T}\right)_{\hat{S},\underline{Z}}} \qquad \left\{Ma=\frac{\frac{q}{\rho.A}}{c}\right. \tag{D.13}$$

With Eqs. (D.12) and (D.13), Eqs. (D.10) and (D.11) can be rearranged in the forms shown in Eqs. (D.14) and (D.15), now containing the multiphase multi-reactive Mach Number.

$$\frac{dT}{dx}=c^2\left(\frac{Ma^2}{1-Ma^2}\right)\left(\frac{1}{\left(\frac{\partial P}{\partial T}\right)_{\hat{S},\underline{Z}}}\right)\left(\frac{\rho}{A}\right)\frac{dA}{dx} \tag{D.14}$$

$$\frac{dP}{dx}=c^2\left(\frac{Ma^2}{1-Ma^2}\right)\left(\frac{\rho}{A}\right)\frac{dA}{dx} \tag{D.15}$$

The flow velocity (*v*) profile – as well as any thermodynamic property profile – can now be approached for the multiphase multi-reactive 1D isentropic flow with variable flow section by using the gradients of dependent variables in Eqs. (D.14), (D.15). The mass flow rate *q* and the

preparation composition vector $\underline{Z}$ are constant along the multiphase multi-reactive 1D isentropic flow with variable flow section. Therefore, Eq. (D.16) applies.

$$q = \rho.v.A(x) \equiv const. \Rightarrow 0 = v.A.\frac{d\rho}{dx} + \rho.A.\frac{dv}{dx} + v.\rho.\frac{dA}{dx} \qquad \{\underline{Z}\ const. \tag{D.16}$$

As the density, according to the ECS point-of-view, responds only to the flow dependent variables (*T, P*), the RHS of Eq. (D.16) can be modified to the form in Eq. (D.17). This comes also from Eq. (II.40) in MDOC, when the correspondence between a traveling fluid element and ECS was imposed.

$$0 = v.A.\left(\Xi_T \frac{dT}{dx} + \Xi_P \frac{dP}{dx}\right) + \rho.A.\frac{dv}{dx} + v.\rho\frac{dA}{dx} \qquad \{\underline{Z}\ const. \tag{D.17}$$

Relocating *dT/dx* from the parentheses term in Eq. (D.17), and using Eq. (D.5), one gets Eq. (D.18). Eq. (D.18), by its turn, is reduced to Eq. (D.19) by using Eq. (D.14) for *dT/dx*.

$$0 = v.A.\left(\Xi_T + \Xi_P\left(\frac{\partial P}{\partial T}\right)_{\hat{S},\underline{Z}}\right)\frac{dT}{dx} + \rho.A.\frac{dv}{dx} + v.\rho\frac{dA}{dx} \qquad \{\underline{Z}\ const. \tag{D.18}$$

$$0 = v.\rho\left\{1 + c^2\left(\frac{Ma^2}{1-Ma^2}\right)\left(\frac{\Xi_T + \Xi_P\left(\frac{\partial P}{\partial T}\right)_{\hat{S},\underline{Z}}}{\left(\frac{\partial P}{\partial T}\right)_{\hat{S},\underline{Z}}}\right)\right\}\frac{dA}{dx} + \rho.A\frac{dv}{dx} \tag{D.19}$$

With the square of the sound speed in Eq. (D.12), Eq. (D.19) gives the differential relationship Eq. (D.20) to the flow velocity (*v*) profile.

$$\frac{1}{v}\frac{dv}{dx} = -\left(\frac{1}{1-Ma^2}\right)\frac{1}{A}\frac{dA}{dx} \tag{D.20}$$

Therefore, the basic differential relationships that must be satisfied by the *T, P ,v* profiles along the multiphase multi-reactive 1D isentropic plug-flow with variable flow section can be written as in Eqs. (D.21), (D.22) and (D.23), all them parametrized in terms of *Ma*.

$$\frac{dT}{dx} = c^2\left(\frac{Ma^2}{1-Ma^2}\right)\left(\frac{1}{\left(\frac{\partial P}{\partial T}\right)_{\hat{S},\underline{Z}}}\right)\left(\frac{\rho}{A}\right)\frac{dA}{dx} \tag{D.21}$$

$$\frac{dP}{dx} = c^2\left(\frac{Ma^2}{1-Ma^2}\right)\left(\frac{\rho}{A}\right)\frac{dA}{dx} \tag{D.22}$$

$$\frac{1}{v}\frac{dv}{dx} = -\left(\frac{1}{1-Ma^2}\right)\frac{1}{A}\frac{dA}{dx} \tag{D.23}$$

At this point it is pertinent to make some reflections about Eqs. (D.21), (D.22) and (D.23). These formulae are absolutely rigorous to any fluid in multiphase multi-reactive isentropic 1D plug-flow with variable flow section. The thermodynamic properties c, ρ and $\left(\frac{\partial P}{\partial T}\right)_{\hat{S},\underline{Z}}$ are ECS properties valid for single-phase or multiphase, multi-reactive ECS. They are well-defined and finite along the multiphase multi-reactive isentropic 1D plug-flow with variable flow section, which is characterized by complete internal equilibrium at each point x. The same happens with $A(x)$ and dA/dx which express only geometric facts belonging to the pipe (or nozzle) with variable section area. Therefore, Eqs. (D.21), (D.22) and (D.23) imply that the gradients $\frac{dT}{dx}$, $\frac{dP}{dx}$, $\frac{dv}{dx}$, will pass by $\pm\infty$ singularities when $Ma \to 1^-$ and $Ma \to 1^+$ depending on the algebraic signal of $\frac{dA}{dx}$.

In summary, as consequence of Eqs. (D.21), (D.22) and (D.23), we have the limiting facts expressed by Eqs. (D.24) and (D.25) when $Ma \to 1$. Such limiting facts, despite being qualitative, are true "fingerprints" characteristic of the multiphase multi-reactive 1D isentropic plug-flow with variable flow section area. They are valid on any isentropic 1D flow, i.e. single-phase or multiphase, non-reactive or multi-reactive. The unique condition is true thermodynamic equilibrium along the flow path. Therefore, Eqs. (D.24) and (D.25) are a "graphical certification" of the reliability of the solutions presented in MDOC.

In other words, the (*T, P, v*) profiles, plotted against the axial position *x* on a variable flow section nozzle, must cross the sonic condition ($Ma \to 1^-$ or $Ma \to 1^+$) in the nozzle with gradients exhibiting $\pm\infty$ singularities as shown in Eqs. (D.24) and (D.25).

$$\frac{dA}{dx} < 0 \quad \Rightarrow \ell im_{Ma \to 1^-} \frac{dT}{dx} = -\infty \ , \ \ell im_{Ma \to 1^-} \frac{dP}{dx} = -\infty \ , \ \ell im_{Ma \to 1^-} \frac{dv}{dx} = +\infty \qquad \text{(D.24)}$$

(Converging Nozzle)

$$\frac{dA}{dx} > 0 \quad \Rightarrow \ell im_{Ma \to 1^+} \frac{d\theta}{dx} = -\infty \ , \ \ell im_{Ma \to 1^+} \frac{dP}{dx} = -\infty \ , \ \ell im_{Ma \to 1^+} \frac{dv}{dx} = +\infty \qquad \text{(D.25)}$$

(Diverging Nozzle)

Such singularities are perfectly seen in Figs. II.10 and II.11 of Sec. II.4.4 of MDOC at the throat position in the SS example, i.e. at the end of the converging section (*dA/dx <0)*, on the SS nozzle, as shown in Eq. (D.26). The results in Eqs. (D.24) and (D.25) are rigorous and general for any multiphase, multi-reactive isentropic 1D flow and are, therefore, present in the three-phase particular SS example in Sec. II.4.4 of MDOC. Nevertheless, this example has the following particularity: it is a three-phase flow dominated by the gas phase. This allow us to prove that similar singularities also occur for the gradients of the sound speed and Mach Number in Eq. (D.26), at least in this particular context of a multiphase, gas-dominated, flow. That is, Figs. II.10 and II.11 of MDOC and Eq. (D.26) clearly show the occurrence of the following singularities in Eq. (D.26), but the two last ones will be proved only for a multiphase, gas-dominated, flow.

$$Ma \to 1^+ \Rightarrow dT/dx \to -\infty, \ dP/dx \to -\infty, \ dc/dx \to -\infty, \ dMa/dx \to +\infty \qquad \text{(D.26)}$$

The $-\infty$ divergence of the gradient of *c* in the two-phase SS example in Sec. II.4.4 of MDOC, Fig. II.10, is explained as follows. Initially it is used the general ECS point-of-view at constant preparation vector $\underline{Z}$ which gives Eq. (D.27). Then, Eq. (D.27) is particularized to a multiphase, gas-dominated, flow, which allows to write Eq. (D.28), where it was used that, for multiphase fluids, dominated by the gas phase, *c* is an increasing function of *T* and a slowly decreasing function of *P*, i.e. $\left|\left(\frac{\partial c}{\partial T}\right)_{P,\underline{Z}}\right| >> \left|\left(\frac{\partial c}{\partial P}\right)_{T,\underline{Z}}\right|$ in SI units. Such characteristic of gases can be

graphically confirmed in MDOC, for example in the low pressure gas territory of Fig. II.3D, Sec. II.2.4.3, and the right side of Fig. II.5, Sec. II.4.1.

$$c^{ECS}(T(x),P(x),\underline{Z}) \xrightarrow{\underline{Z}\ constant} \left(\frac{dc}{dx}\right)^{ECS} = \left(\frac{\partial c}{\partial T}\right)^{ECS}_{P,\underline{Z}} \frac{dT}{dx} + \left(\frac{\partial c}{\partial P}\right)^{ECS}_{T,\underline{Z}} \frac{dP}{dx} \tag{D.27}$$

$$\left(\frac{dc}{dx}\right) = \left(\frac{\partial c}{\partial T}\right)_{P,\underline{Z}} \frac{dT}{dx} + \left(\frac{\partial c}{\partial P}\right)_{T,\underline{Z}} \frac{dP}{dx} \xrightarrow[\left(\frac{\partial c}{\partial T}\right)_{P,\underline{Z}}>0,\left(\frac{\partial c}{\partial P}\right)_{T,\underline{Z}}<0,\left|\left(\frac{\partial c}{\partial T}\right)_{P,\underline{Z}}\right|>>\left|\left(\frac{\partial c}{\partial P}\right)_{T,\underline{Z}}\right|}{Ma \to 1^- \Rightarrow \frac{dT}{dx} \to -\infty,\ \frac{dP}{dx} \to -\infty} \frac{dc}{dx} \to -\infty \tag{D.28}$$

On the other hand, the $-\infty$ divergence of the gradient of *c* and the $+\infty$ ECS divergence of the gradient of *v* in Eq. (D.24), explain – for multiphase, gas-dominated, flow – the $+\infty$ divergence of the gradient of *Ma* in Fig. II.11 of MDOC, Sec. II.4.4. We start with the relationship in Eq. (D.29) which is valid in the ECS point-of-view. This is perfectly general for any multiphase multi-reactive isentropic flow. Now, we apply the particular condition (D.28) which was proven for a multiphase, gas-dominated, flow in Eq. (D.30). This proves the $+\infty$ divergence of the gradient of *Ma* in Fig. II.11 of MDOC, Sec. II.4.4.

$$Ma^{ECS} = \frac{v^{ECS}(x)}{c^{ECS}(T(x),P(x),\underline{Z})} \Rightarrow \left(\frac{dMa}{dx}\right)^{ECS} = \left(\frac{Ma}{v}\right)\left(\frac{dv}{dx}\right)^{ECS} - \left(\frac{Ma}{c}\right)\left(\frac{dc}{dx}\right)^{ECS} \tag{D.29}$$

$$\frac{dMa}{dx} = \left(\frac{Ma}{v}\right)\frac{dv}{dx} - \left(\frac{Ma}{c}\right)\frac{dc}{dx} \xrightarrow{Ma \to 1^- \Rightarrow \frac{dv}{dx} \to +\infty,\ \frac{dc}{dx} \to -\infty} \frac{dMa}{dx} \to +\infty \tag{D.30}$$

Now we come back to the strict ECS point-of-view in order to finish our analysis on limit conditions of multiphase multi-reactive isentropic flow. Specifically, we return to Eqs. (D.21), (D.22), (D.23), (D.24) and (D.25).

When $Ma \neq 1$, the consequences of Eqs. (D.21), (D.22) and (D.23) for profiles (*T*, *P*, *v*) can be summarized in terms of the qualitative behaviors shown in Eq. (D.31) for converging and diverging nozzles with multiphase multi-reactive 1D isentropic flow. According to this, to produce intense cooling in a multiphase multi-reactive 1D isentropic flow through a SS or a SR (supersonic reactor), the design of the equipment must follow the geometry of a converging-diverging nozzle, so as to produce cooling both in the converging section ($dA/dx < 0$) as well as

in the diverging section ($dA/dx > 0$). According to this, through the converging-diverging nozzle there will be constant acceleration, constant cooling and constant expansion, naturally while the characteristics of the flow are maintained; i.e. while the flow sustains its isentropic pattern. Albeit the metastable supersonic flow can stand against small irreversibilities or small disturbances – like small levels of friction on the contact surfaces – it does not tolerate big irreversibilities or big disturbances. In this case, the pattern of acceleration, cooling and expansion with $Ma>1$ will be suddenly destroyed and the supersonic flow will suddenly turn into subsonic. An example of this sudden interruption of the supersonic flow is the occurrence of a normal shock front at $Ma>1$ on the diverging section of the converging-diverging nozzle. The normal shock produces abrupt discontinuities on the profiles of T, P, v, Ma, ρ. The normal shock occurs because the 1D multiphase multi-reactive isentropic flow is metastable for $Ma>1$ against a higher discharge pressure and this meta-stability worsens with the increase of Ma beyond 1 and with the decrease of P at pre-shock conditions.

The normal shock discontinuities imply sudden heating ($T\uparrow$) , sudden recompression of the fluid ($P\uparrow$), sudden increase of the fluid density ($\rho\uparrow$), with a sudden fall of the velocity to subsonic values ($v\downarrow$, $Ma\downarrow$). These behaviors are also seen in Figs. II.10 and II.11 of MDOC, Sec. II.4.4, at the normal shock location in the diverging section of the SS. The discontinuities at the multiphase multi-reactive normal shock front must be modeled imposing conservation of the basic flow properties: mass flow rate, momentum flow rate and the total flow rate of energy (enthalpy + kinetic). The fluid specific entropy is not conserved at the normal shock front. That is, as the flow is adiabatic and an irreversibility has occurred (i.e. there will be no spontaneous return to supersonic flow), by the 2nd Law of Thermodynamics the specific entropy of the fluid must exhibit a sharp increase across the shock front. Moreover, the greater the value of the supersonic Ma in the pre-shock condition, the greater the increase of specific entropy across the normal shock.

$$
Ma<1 \Rightarrow \begin{cases} \dfrac{dA}{dx}<0 \xrightarrow{\substack{Converging\\Nozzle}} \dfrac{dv}{dx}>0, \dfrac{dT}{dx}<0, \dfrac{dP}{dx}<0 \ \{ Acceleration, Cooling, Expansion \\ \dfrac{dA}{dx}>0 \xrightarrow{\substack{Diverging\\Nozzle}} \dfrac{dv}{dx}<0, \dfrac{dT}{dx}>0, \dfrac{dP}{dx}>0 \ \{ Deacceleration, Heating, Compression \end{cases}
$$

$$
Ma>1 \Rightarrow \begin{cases} \dfrac{dA}{dx}<0 \xrightarrow{\substack{Converging\\Nozzle}} \dfrac{dv}{dx}<0, \dfrac{dT}{dx}>0, \dfrac{dP}{dx}>0 \ \{ Deacceleration, Heating, Compression \\ \dfrac{dA}{dx}>0 \xrightarrow{\substack{Diverging\\Nozzle}} \dfrac{dv}{dx}>0, \dfrac{dT}{dx}<0, \dfrac{dP}{dx}<0 \ \{ Acceleration, Cooling, Expansion \end{cases}
$$

(D.31)

APPENDIX E - DETERMINATION OF FREEZE-OUT BORDERS (FOBS) IN CO_2-CH_4 SYSTEMS

Let a binary CO_2 rich NG with known CTC Z_{CH4}, Z_{CO2}. In the SVLE, SLE and SVE freeze-out border (FOB) blocks below, θ is an input parameter to sweep a 1D FOB in terms of *P* or *T*. The Grand Freeze-Out Border (GFOB) is the union of SVLE FOB, SLE FOB and SVE FOB. These FOBs were solved via Newton-Raphson Method (NRM) with analytical Jacobian and linear initialization as θ changes. PR-EOS ($k_{CO2\text{-}CH4}=0.1$) is used in liquid and vapor phases.

SVLE FOB: Eqs. (E.1) to (E.5) are solved for η^V, η^L, η^S, X_{CH4}, X_{CO2}, Y_{CH4}, Y_{CO2}, *T*, *P*.

$$P.Y_{CO2}.\hat{\phi}_{CO2}^{V} - f_{CO2}^{S}(T,P) = 0 \quad , \quad P.X_{CO2}.\hat{\phi}_{CO2}^{L} - f_{CO2}^{S}(T,P) = 0 \tag{E.1}$$

$$P.Y_{CH4}.\hat{\phi}_{CH4}^{V} - P.X_{CH4}.\hat{\phi}_{CH4}^{L} = 0 \tag{E.2}$$

$$\eta^V.Y_{CO2} + \eta^L.X_{CO2} + \eta^S - Z_{CO2} = 0 \quad , \quad \eta^V.Y_{CH4} + \eta^L.X_{CH4} - Z_{CH4} = 0 \tag{E.3}$$

$$Y_{CO2} + Y_{CH4} - 1 = 0 \quad , \quad X_{CO2} + X_{CH4} - 1 = 0 \tag{E.4}$$

$$\eta^S = 0 \quad , \quad (P-\theta)\,\big|\,(T-\theta) = 0 \tag{E.5}$$

SLE FOB: Eqs. (E.6) to (E.8) are solved for η^L, η^S, X_{CH4}, X_{CO2}, *T*, *P*.

$$P.X_{CO2}.\hat{\phi}_{CO2}^{L} - f_{CO2}^{S}(T,P) = 0 \quad , \quad X_{CO2} + X_{CH4} - 1 = 0 \tag{E.6}$$

$$\eta^L.X_{CO2} + \eta^S - Z_{CO2} = 0 \quad , \quad \eta^L.X_{CH4} - Z_{CH4} = 0 \tag{E.7}$$

$$\eta^S = 0 \quad , \quad (P-\theta)\,\big|\,(T-\theta) = 0 \tag{E.8}$$

SVE FOB: Eqs. (E.9) to (E.11) are solved for η^V, η^S, Y_{CH4}, Y_{CO2}, *T*, *P*.

$$P.Y_{CO2}.\hat{\phi}_{CO2}^{V} - f_{CO2}^{S}(T,P) = 0 \quad , \quad Y_{CO2} + Y_{CH4} - 1 = 0 \tag{E.9}$$

$$\eta^V.Y_{CO2} + \eta^S - Z_{CO2} = 0 \quad , \quad \eta^V.Y_{CH4} - Z_{CH4} = 0 \tag{E.10}$$

$$\eta^S = 0 \qquad , \quad (P-\theta)\,\big|\,(T-\theta) = 0 \tag{E.11}$$

The GFOB was successfully swept by specifying θ in Eqs. (E.5), (E.8) and (E.11). Some facts are related to the Phase Rule and CTC Duhem problems of CH_4-CO_2 systems. By the Phase Rule, SLE and SVE domains are 2D, while SLE FOB and SVE FOB are 1D as CTC Duhem problems with one of its two degrees of freedom specified as $\eta^S=0$. As CTC Duhem problems, SLE FOB and SVE FOB change with (Z_{CH4}, Z_{CO2}). The grand SVLE locus, on the other hand, is 1D on plane *P x T* by the Phase Rule, implying it is unique and independent of (Z_{CH4}, Z_{CO2}). Moreover, as a three-phase locus, it begins and ends at the TPs of CO_2 and CH_4. The grand SVLE is, therefore, an invariant curve on plane *P x T* connecting TPs of CO_2 and CH_4, but only parts of it "are seen" by a given CTC Z_{CH4}, Z_{CO2}. That is, the grand SVLE is invariant, but each CTC can use only portions of it, as the forbidden portions have non-physical split fractions (>1 and <0). The SVLE FOB is the physical part of the grand SVLE over VLE. The other physical part of the grand SVLE – the border between SLE and SVE – is not FOB as it is dominated by GFOB.

APPENDIX F - MODELING OF NG MEMBRANE PERMEATION (MP) UNITS IN MP-UOE

MP-UOE draws an analogy with a heat exchanger to calculate the permeation rate of species *k* (N_k) in Eq. (F.1), where Π_k is the permeance of species *k* (*MMsm*^{3}*/d.bar.m*^{2}), A_{MP} is the MP area (*m*^{2}) and ΔP_k^{LN} is the log mean difference of partial pressures (*bar*) of species *k* through MP unit. ΔP_k^{LN} follows the chosen contact: Eq. (F.2) is applied for countercurrent and Eq. (F.3) for parallel contact; where $P_V^{in}Y_k^{in}$, $P_V^{out}Y_k^{out}$, $P_L^{out}X_k^{out}$ respectively represent partial pressures (*bar*) of species *k* in the feed, retentate (*V*) and permeate (*L*). The algebraic system of MP-UOE includes also *nc* component balances for retentate – Eq. (F.4) – and *nc* balances for permeate – Eq. (F.5), with Eqs. (F.6) and (F.7) imposing retentate and permeate mol fractions normalizations. Trans-membrane transfer rates N_k (*MMsm*^{3}*/d*) are positive in the direction retentate $\rightarrow$ permeate. MP-UOE comprises *4nc+2* non-linear constraints Eqs. (F.1) to (F.7), numerically solved for *4nc+2* variables $N_k, \Delta P_k^{LN}, Y_k^{out}, X_k^{out}, L^{out}, V^{out}$ by Newton-Raphson Method (NRM). MP specifications comprise species permeances (Π_k , *MMsm*^{3}*/d.bar.m*^{2}), feed data – composition (Y_k^{in}), flow rate (V^{in} , *MMsm*^{3}*/d*), temperature (T_V^{in} , ^oC), pressure (P_V^{in} , *bar*) – retentate and permeate pressures (P_V^{out} , P_L^{out} , *bar*), area (A_{MP}, *m*^{2}) and ΔT_{VL} (^oC). After NRM convergence of Eqs. (F.1) to (F.7), the exiting retentate and permeate temperatures (T_V^{out} , T_L^{out}) are calculated by another NRM solving MP energy balance with ΔT_{VL} – Eqs. (F.8) and (F.9).

$$N_k = \Pi_k * A_{MP} * \Delta P_k^{LN} \qquad (k = 1...nc) \tag{F.1}$$

$$\Delta P_k^{LN} = \left(\frac{\left(P_V^{in}Y_k^{in} - P_L^{out}X_k^{out}\right) - \left(P_V^{out}Y_k^{out}\right)}{ln\left(\frac{P_V^{in}Y_k^{in} - P_L^{out}X_k^{out}}{P_V^{out}Y_k^{out}}\right)} \right) \qquad (k = 1...nc) \tag{F.2}$$

$$\Delta P_k^{LN} = \left(\frac{\left(P_V^{in} Y_k^{in}\right) - \left(P_V^{out} Y_k^{out} - P_L^{out} X_k^{out}\right)}{ln\left(\frac{P_V^{in} Y_k^{in}}{P_V^{out} Y_k^{out} - P_L^{out} X_k^{out}} \right)} \right) \qquad (k = 1...nc) \tag{F.3}$$

$$V^{in} Y_k^{in} - V^{out} Y_k^{out} - N_k = 0 \qquad (k = 1...nc) \tag{F.4}$$

$$L^{out} X_k^{out} - N_k = 0 \qquad (k = 1...nc) \tag{F.5}$$

$$\sum_k^{nc} Y_k^{out} - 1 = 0 \tag{F.6}$$

$$\sum_k^{nc} X_k^{out} - 1 = 0 \tag{F.7}$$

$$V^{out} * \overline{H}(T_V^{out}, P_V^{out}, \underline{Y}^{out}) + L^{out} * \overline{H}(T_L^{out}, P_L^{out}, \underline{X}^{out}) = V^{in} * \overline{H}(T_V^{in}, P_V^{in}, \underline{Y}^{in}) \tag{F.8}$$

$$T_V^{out} - T_L^{out} = \Delta T_{VL} \tag{F.9}$$

APPENDIX G - DESCRIPTION OF THE EIGHT PHASES OF SS-UOE ALGORITHM

[P1] Input Data. F_E, T_E, P_E and $\underline{Z}_E$ are rescued from SS feed in the PFD. D_I, D_O, α, β, Ma^{Shock} are entered via SS-UOE property window. Calculate M_{ME} and $q_E=F_E.M_{ME}$. Entry flow properties are calculated by Eqs. (G.1) to (G.4).

$$Flash\,(P_E, T_E, \underline{Z}_E) \xrightarrow{Multiphase\ Property} \overline{H}_E, \overline{S}_E, \rho_E \tag{G.1}$$

$$PEC-UOE\,(P_E, T_E, \underline{Z}_E) \xrightarrow{Multiphase\ c} c_E \tag{G.2}$$

$$v_E = 4q_E/(\pi.D_I^2.\rho_E)\ ,\ \overline{K}_E = M_{ME}.v_E^2/2 \tag{G.3}$$

$$\overline{E}_E = \overline{H}_E + \overline{K}_E\ \ ,\ Ma_E = v_E/c_E \tag{G.4}$$

[P2] Subsonic Expansion. Solved by successive small isentropic expansions (index *n*) from entry point until *Ma=1* in the converging section giving the throat diameter D_T. Expansion step δ_P ($\leq 10^4$ *Pa*) is manipulated. Eqs. (G.5) to (G.7) are initializations. Eqs. (G.8) to (G.14) are iterated.

$$n=0,\quad x^{(0)}=0,\ P^{(0)}=P_E\ ,\ T^{(0)}=T_E \tag{G.5}$$

$$D^{(0)}=D_I\ ,\ v^{(0)}=v_E\ ,\ \delta_P=10^4\,Pa \tag{G.6}$$

$$\overline{K}^{(0)}=\overline{K}_E\ ,\ \overline{H}^{(0)}=\overline{H}_E\ ,\ c^{(0)}=c_E\ ,\ Ma^{(0)}=Ma_E \tag{G.7}$$

---------- *Loop Begins* ----------

$$n \equiv n+1,\quad P^{(n)} \equiv P^{(n-1)} - \delta_P \tag{G.8}$$

$$Flash\,(P^{(n)}, \overline{S}_E, \underline{Z}_E) \xrightarrow{Multiphase\ Prop.} T^{(n)}, \overline{H}^{(n)}, \rho^{(n)} \tag{G.9}$$

$$PEC-UOE\,(P^{(n)}, T^{(n)}, \underline{Z}_E) \xrightarrow{Multiphase\ c} c^{(n)} \tag{G.10}$$

$$\overline{K}^{(n)} = \overline{E}_E - \overline{H}^{(n)},\ \ v^{(n)} = \sqrt{2.\overline{K}^{(n)}/M_{ME}} \tag{G.11}$$

$$Ma^{(n)} = v^{(n)}/c^{(n)}\ ,\ D^{(n)} = \sqrt{4q_E/(\pi.v^{(n)}.\rho^{(n)})} \tag{G.12}$$

$$if\ Ma^{(n)} < 1-\delta_M \rightarrow \text{Re}vise\ \delta_P\ with\ Ma^{(n)},\ Execute\ Eqs.(G.8)\ to\ (G.14) \tag{G.13}$$

$$if\ Ma^{(n)} > 1+\delta_M \rightarrow \text{Re}duce\ \delta_P,\ n \equiv n-1,\ Execute\ Eqs.(G.8)\ to\ (G.14) \tag{G.14}$$

---------- *Loop Ends* ----------

$$D_T = D^{(n)} \tag{G.15}$$

$$if\ 1-\delta_M \le Ma^{(n)} \le 1+\delta_M \longrightarrow Stop \tag{G.16}$$

[P3] SS Geometry. Eqs. (G.17) and (G.18) determinate SS lengths and axial locations of all diameters with D_T.

$$L_C = \frac{D_I - D_T}{2.\tan\alpha},\ L_D = \frac{D_O - D_T}{2.\tan\beta},\ L = L_C + L_D \tag{G.17}$$

$$For\ all\ D^{(k)}\ (k = 1 \rightarrow n)\ calculate\ x^{(k)} = L_C - \frac{D^{(k)} - D_T}{2.\tan\alpha} \tag{G.18}$$

[P4] Supersonic Expansion. Solved by successive small isentropic expansions (index *n*) from the throat location until $Ma=Ma^{Shock}$ in the diverging section. Expansion step δ_P ($\le 10^4\ Pa$) is manipulated. Eq. (G.19) is initialization. Eqs. (G.20) to (G.27) are iterated.

$$\delta_P = 10^4\ Pa \tag{G.19}$$

---------- *Loop Begins* ----------

$$n \equiv n+1, \quad P^{(n)} \equiv P^{(n-1)} - \delta_P \tag{G.20}$$

$$Flash\ (P^{(n)}, \overline{S}_E, \underline{Z}_E) \xrightarrow{Multiphase\ Prop.} T^{(n)}, \overline{H}^{(n)}, \rho^{(n)} \tag{G.21}$$

$$PEC-UOE\ (P^{(n)}, T^{(n)}, \underline{Z}_E) \xrightarrow{Multiphase\ c} c^{(n)} \tag{G.22}$$

$$\overline{K}^{(n)} = \overline{E}_E - \overline{H}^{(n)},\ \ v^{(n)} = \sqrt{2.\overline{K}^{(n)} / M_{ME}} \tag{G.23}$$

$$Ma^{(n)} = v^{(n)} / c^{(n)},\ D^{(n)} = \sqrt{4q_E / (\pi.v^{(n)}.\rho^{(n)})} \tag{G.24}$$

$$x^{(n)} = L_C + \frac{D^{(n)} - D_T}{2.\tan\beta} \tag{G.25}$$

$$if\ Ma^{(n)} < Ma^{Shock} - \delta_M \rightarrow \mathrm{Re}vise\ \delta_P\ with\ Ma^{(n)}, Execute\ Eqs.(G.20)\ to (G.27) \tag{G.26}$$

$$if\ Ma^{(n)} > Ma^{Shock} + \delta_M \rightarrow \mathrm{Re}duce\ \delta_P\ ,\ n \equiv n-1, Execute\ Eqs.(G.20)\ to\ (G.27) \tag{G.27}$$

---------- *Loop Ends* ----------

$$T^{Shock} = T^{(n)},\ P^{Shock} = P^{(n)} \tag{G.28}$$

$$L^{Shock} = x^{(n)},\ D^{Shock} = D^{(n)},\ v^{Shock} = v^{(n)} \tag{G.29}$$

$$if\ \ Ma^{Shock} - \delta_M \le Ma^{(n)} \le Ma^{Shock} + \delta_M \ \rightarrow Stop \tag{G.30}$$

[P5] Pre-Shock Separation. $Flash(P^{Shock},T^{Shock},\underline{Z}_E)$ is invoked at $x=L^{Shock}$ in Eq. (G.31). Liquid phases "L" and "W" are extracted forming the two-phase condensate "$L+W$". The vapor phase is kept as working fluid. The stagnation (T,P) of condensate $L+W$ will be adjusted later at the discharge pressure. Eqs. (G.32) and (G.33) give velocities of $L+W$ condensate and of vapor (v_{L+W}, v_V) after phase separation assuming constant flow section. Properties before shock are recovered from segregated vapor via Eq. (G.34) to (G.37). Eqs. (G.38) to (G.40) consolidate flow properties before shock.

$$Flash\,(P^{Shock},T^{Shock},\underline{Z}_E) \rightarrow \left\{ \begin{array}{c} F_V, \underline{Y}, \rho_V, \overline{H}_V, \overline{S}_V, M_{MV} \\ F_L, \underline{X}_L, \rho_L, \overline{H}_L, \overline{S}_L, M_{ML} \\ F_W, \underline{X}_W, \rho_W, \overline{H}_W, \overline{S}_W, M_{MW} \end{array} \right\} \tag{G.31}$$

$$v_V = \frac{(F_V.M_{MV}/\rho_V).v^{Shock}}{F_V.M_{MV}/\rho_V + F_L.M_{ML}/\rho_L + F_W.M_{MW}/\rho_W} \tag{G.32}$$

$$v_{L+W} = \frac{(F_L.M_{ML}/\rho_L + F_W.M_{MW}/\rho_W).v^{Shock}}{F_V.M_{MV}/\rho_V + F_L.M_{ML}/\rho_L + F_W.M_{MW}/\rho_W} \tag{G.33}$$

$$P_{BS} \equiv P^{Shock}\ ,\ T_{BS} \equiv T^{Shock}\ ,\ D_{BS} = D^{Shock} \tag{G.34}$$

$$M_{MBS} = M_{MV}\ ,\ \overline{H}_{BS} = \overline{H}_V\ ,\ \overline{S}_{BS} = \overline{S}_V \tag{G.35}$$

$$\underline{Z}_{BS} = \underline{Y}\ ,\ v_{BS} = v_V\ ,\ \rho_{BS} = \rho_V \tag{G.36}$$

$$F_{BS} = F_V\ ,\ q_{BS} = F_{BS}.M_{MBS} \tag{G.37}$$

$$PEC-UOE\ (P_{BS},T_{BS},\underline{Z}_{BS}) \xrightarrow{Multiphase\ c} c_{BS} \tag{G.38}$$

$$Ma_{BS} = v_{BS} / c_{BS} \tag{G.39}$$

$$\overline{K}_{BS} = M_{MBS}.v_{BS}^2 / 2 \ , \quad \overline{E}_{BS} = \overline{K}_{BS} + \overline{H}_{BS} \tag{G.40}$$

[P6] Normal Shock. If flow is supersonic after condensate withdrawal (checked by Eq. (G.41) with Ma_{BS}), normal shock is solved via mass, energy, momentum and mass balances – Eqs. (G.42), (G.43) and (G.45) – for temperature (T_{AS}), pressure (P_{AS}) and velocity (v_{AS}) after shock. An embedded *Flash*(P_{AS},T_{AS}) provides single (multi) phase properties $\overline{H}$, ρ after shock. v_{AS} is eliminated in terms of T_{AS} and P_{AS} by Eq. (G.45), resulting Eqs. (G.42) and (G.43) for T_{AS} and P_{AS}. NRM solves them numerically. Eqs. (G.46) to (G.51) calculate single-phase after shock flow properties (with/without an actual shock).

$$if \quad Ma_{BS} \le 1 \longrightarrow T_{AS} = T_{BS}\ ,\ P_{AS} = P_{BS}\ ,\ v_{AS} = v_{BS}\ ,\quad Go\ to\ Eq.(G.46) \tag{G.41}$$

---------- *NRM Block Begins* ----------

$$\overline{H}(T_{AS},P_{AS},\underline{Z}_{BS}) + M_{MBS}\frac{(v_{AS}(T_{AS},P_{AS}))^2}{2} - \overline{H}_{BS} - \overline{K}_{BS} = 0 \tag{G.42}$$

$$\rho(T_{AS},P_{AS},\underline{Z}_{BS}).(v_{AS}(T_{AS},P_{AS}))^2 + P_{AS} - \rho_{BS}v_{BS}^2 - P_{BS} = 0 \tag{G.43}$$

$$Flash\ (P_{AS},T_{AS},\underline{Z}_{BS}) \xrightarrow{Single/Multi\ Phase\ Property} \overline{H}(P_{AS},T_{AS},\underline{Z}_{BS}),\ \rho(P_{AS},T_{AS},\underline{Z}_{BS}) \tag{G.44}$$

$$v_{AS}(T_{AS},P_{AS}) = \frac{4q_{BS}}{\pi D_{BS}^2 \rho(T_{AS},P_{AS},\underline{Z}_{BS})} \tag{G.45}$$

---------- *NRM Block Ends* ----------

$$M_{MAS} = M_{MBS}\ ,\ \underline{Z}_{AS} = \underline{Z}_{BS}\ ,\ \rho_{AS} = \rho(T_{AS},P_{AS},\underline{Z}_{AS}) \tag{G.46}$$

$$\overline{H}_{AS} = \overline{H}(T_{AS},P_{AS},\underline{Z}_{AS})\ ,\ \overline{S}_{AS} = \overline{S}(T_{AS},P_{AS},\underline{Z}_{AS}) \tag{G.47}$$

$$PEC-UOE\ (P_{AS},T_{AS},\underline{Z}_{AS}) \xrightarrow{Single-Phase\ c} c_{AS} \tag{G.48}$$

$$q_{AS} = q_{BS}\,,\; F_{AS} = F_{BS}\;,\; D_{AS} = D_{BS}\;,\; v_{AS} = \frac{4q_{AS}}{\pi D_{AS}^2 \rho_{AS}} \tag{G.49}$$

$$\overline{K}_{AS} = M_{MAS}\frac{v_{AS}^2}{2}\;\;,\;\; \overline{E}_{AS} = \overline{H}_{AS} + \overline{K}_{AS} \tag{G.50}$$

$$Ma_{AS} = v_{AS} / c_{AS}\;\;\;,\;\;\; \Delta\overline{S}^{Shock} = \overline{S}_{AS} - \overline{S}_{BS} \tag{G.51}$$

[P7] Subsonic Compression. Diffuser subsonic compression is solved by successive small isentropic compressions (index *n*) from $x=L^{Shock}$ to $x=L$. Compression step δ_P ($\leq 10^4$ *Pa*) is manipulated. Eqs. (G.52) to (G.54) are initializations. Eqs. (G.55) to (G.62) are sequentially iterated.

$$n = n+1,\;\; x^{(n)} = L^{Shock},\;\; P^{(n)} = P_{AS}\,,\; T^{(n)} = T_{AS} \tag{G.52}$$

$$D^{(n)} = D_{AS}\;\;,\;\; v^{(n)} = v_{AS}\;\;,\;\; \delta_P = 10^4\,Pa \tag{G.53}$$

$$\overline{K}^{(n)} = \overline{K}_{AS}\,,\; \overline{H}^{(n)} = \overline{H}_{AS}\,,\; c^{(n)} = c_{AS}\,,\; Ma^{(n)} = Ma_{AS} \tag{G.54}$$

---------- *Loop Begins* ----------

$$n \equiv n+1,\quad P^{(n)} \equiv P^{(n-1)} + \delta_P \tag{G.55}$$

$$Flash\,(P^{(n)}, \overline{S}_{AS}, \underline{Z}_{AS}) \xrightarrow{Single-Phase\ Prop.} T^{(n)}, \overline{H}^{(n)}, \rho^{(n)} \tag{G.56}$$

$$PEC-UOE\,(P^{(n)}, T^{(n)}, \underline{Z}_{AS}) \xrightarrow{Single-Phase\ c} c^{(n)} \tag{G.57}$$

$$\overline{K}^{(n)} = \overline{E}_{AS} - \overline{H}^{(n)},\;\; v^{(n)} = \sqrt{2.\overline{K}^{(n)} / M_{MAS}} \tag{G.58}$$

$$Ma^{(n)} = v^{(n)} / c^{(n)},\; D^{(n)} = \sqrt{4q_{AS} / (\pi . v^{(n)} . \rho^{(n)})} \tag{G.59}$$

$$x^{(n)} = L_C + \frac{D^{(n)} - D_T}{2.\tan\beta} \tag{G.60}$$

$$if\;\; x^{(n)} < L - \delta_L \;\rightarrow\; \text{Re}vise\;\delta_P\; with\; x^{(n)}, Execute\; Eqs.(G.55)\; to\; (G.62) \tag{G.61}$$

$$if\;\; x^{(n)} > L + \delta_L \;\rightarrow\; \text{Re}duce\;\delta_P\,,\; n \equiv n-1,\; Execute\; Eqs.(G.55)\; to\; (G.62) \tag{G.62}$$

---------- *Loop Ends* ----------

$$P^{Discharge} = P^{(n)},\ T^{Discharge} = T^{(n)},\ \underline{Z}^{Discharge} = \underline{Z}_{AS}\ ,\ F^{Discharge} = F_{AS} \tag{G.63}$$

$$\overline{H}^{Discharge} = \overline{H}^{(n)}\ \ ,\ \ \overline{S}^{Discharge} = \overline{S}(P^{(n)}, T^{(n)}, \underline{Z}_{AS}) \tag{G.64}$$

$$v^{Discharge} = v^{(n)},\ Ma^{Discharge} = Ma^{(n)}\ ,\ \rho^{Discharge} = \rho^{(n)} \tag{G.65}$$

$$if\ \ L - \delta_L \le x^{(n)} \le L + \delta_L \ \longrightarrow Stop \tag{G.66}$$

[P8] Finishing Procedures. Eqs. (G.67) and (G.68) consolidate data of $L+W$ condensate from separation section. Eq. (G.69) adjusts its state to stagnation at $P^{Discharge}$. Data of discharge gas and stagnant condensate are pasted onto the product streams of SS-UOE in the PFD via Eqs. (G.70) and (G.71).

$$F_{L+W} = F_L + F_W\ \ ,\ \ P_{L+W} = P^{Discharge}\ \ ,\ \ \underline{Z}_{L+W} = \frac{F_L \underline{Z}_L + F_W \underline{Z}_W}{F_L + F_W} \tag{G.67}$$

$$\overline{H}_{L+W} = \left(\frac{F_L \overline{H}_L + F_W \overline{H}_W}{F_L + F_W} \right) + \left(\frac{F_L M_{ML} + F_W M_{MW}}{F_L + F_W} \right) \frac{v_{L+W}^2}{2} \tag{G.68}$$

$$Flash\ (P_{L+W}, \overline{H}_{L+W}, \underline{Z}_{L+W}) \xrightarrow{Multiphase\ Property} T_{L+W}, \rho_{L+W}, \overline{S}_{L+W} \tag{G.69}$$

$$L+W\ \ Condensate:\ \ F_{L+W},\ T_{L+W},\ P_{L+W},\ \underline{Z}_{L+W}\ ,\ \overline{H}_{L+W}\ ,\ \rho_{L+W}\ ,\ \overline{S}_{L+W} \tag{G.70}$$

$$Lean\ Gas:\ \ F^{Discharge},\ T^{Discharge},\ P^{Discharge},\ \underline{Z}^{Discharge},\ \overline{H}^{Discharge},\ \rho^{Discharge},\ \overline{S}^{Discharge} \tag{G.71}$$

APPENDIX H - SS-UOE WITH NG LIQUEFACTION STUDY OF WEN ET AL. (2012)

SS-UOE is compared with SS results from Wen et al. (2012) for a dry NG with *96.044%mol* CH_4, *2.98%mol* C_2H_6 and *0.976%mol* C_3H_8. These authors used CFD commercial software to simulate this feed in a geometrically defined SS nozzle in Table 1 of Wen et al. (2012), shown in Table D.1. Here, an initial constant diameter section with 0.12m of length was removed from the apparatus. Molar (F_E) or mass (q_E) entry feed flow rates were not informed, only $Ma^{Inlet} = 0.18 = 4q_E/(\pi.D_I^2.\rho^{Inlet})/c^{Inlet}$ is given, which is not conclusive as there is no information on how c^{Inlet} was calculated.

In Wen et al. (2012) the diameter *D(x)* of the converging section is described by Eq. (H.1) in terms of axial position *x*, where D_I, D_T and L_C are inlet and throat diameters and converging length. The diverging section adopts rectilinear diameters with diverging half-angle $\beta=2.33439^o$ in Eq. (H.2), where D_O and L_D are outlet diameter and total diverging length (i.e. Laval diverging length plus diffuser length) in Fig. III.3 and Table H.1. In order to force SS-UOE to use the same nozzle of Wen et al. (2012), SS-UOE algorithm (APPENDIX G) was modified as follows: (i) Eq. (G.17): L_C is now specified as $L_C=0.10956\ m$, with L_D and L still given by Eq. (G.17); (ii) Eq. (G.18): inversion of *D(x)* linear relationship for rectilinear diameters is replaced by numerical inversion of Eq. (H.1) via successive substitution in the iteration function in Eq. (H.3) to find $x^{(n)}$ for $D^{(n)}$. Molar feed flow rate F_E was adjusted to give *Ma=1* at the throat diameter of Wen et al. (2012) $D_T = 0.03671m$. These measures guarantee that the nozzle of Wen et al. (2012) is correctly being used by SS-UOE. By last, Wen et al. (2012) define SS backpressure as *70 bar*, thus Ma^{shock} is sought with SS-UOE to match this value. Preparatory results are shown in Table D.1.

$$\left(\frac{D_T}{D(x)}\right)^2 = 1 - \left(1 - \left(\frac{D_T}{D_I}\right)^2\right)\frac{\left\{1 - \left(\frac{x}{Lc}\right)^2\right\}^2}{\left\{1 + \frac{1}{3}\left(\frac{x}{Lc}\right)^2\right\}^3} \tag{H.1}$$

$$tan(\beta) = \frac{D_O - D_T}{2 * L_D} \Rightarrow \beta = 2.33439^o \tag{H.2}$$

$$\frac{x_{k+1}^{(n)}}{L_C} = \sqrt{1-\sqrt{\Omega}*\left\{1+\frac{\left(\frac{x_k^{(n)}}{L_C}\right)^2}{3}\right\}^{3/2}} \quad , \quad x_0^{(n)} = x^{(n-1)} \quad , \quad \Omega = \left(\frac{1-\left(\frac{D_T}{D^{(n)}}\right)^2}{1-\left(\frac{D_T}{D_I}\right)^2}\right) \tag{H.3}$$

Table H.1. SS Parameters of Wen et al. (2012) and Equivalent SS Parameters of SS-UOE.

*Item**	*Unit*	*Table 1**	*SS-UOE*	
		Value	*Symbol Fig. III.3*	*Value*
Inlet Diameter	*m*	*0.13*	D_I	*0.13*
Throat Diameter	*m*	*0.03671*	D_T	*0.03671*
Outlet Diameter	*m*	*0.13*	D_O	*0.13*
Converging Length	*m*	*0.10956*	L_C	*0.10956*
Diverging Length	*m*	*0.56481*	L_D	*1.14423*
Diffuser Length	*m*	*0.57942*		
Total Length[+]	*m*	*1.25379*[+]	L [#]	*1.25379*
Diverging Half-Angle	*o*	*2.33439*	β	*2.33439*
Feed P	*bar*	*138*	*N/A*	*138*
Feed T	*K*	*252*	*N/A*	*252*
Feed Flow Rate	*kmol/h* / *MMsm*^{3}*/d*	*?*	*N/A*	*9052.50*[&] / *5.223*[&]
Backpressure	*bar*	*70*	*N/A*	*70*[$]

[*] *Wen et al. (2012)* [+] *Discounted 0.12m of constant diameter section*

[#] L_C+L_D *with* L_D *as diverging plus diffuser lengths of Wen et al. (2012)*

[&] *For Ma=1 at throat with converging section of Wen et al. (2012)*

[$] Ma^{Shock} *is adjusted to match backpressure of 70 bar*

Results of Wen et al. (2012) were also compared by Castier (2014) and Secchi et al. (2016). However, these works neglected SS liquid withdrawal. As SS-UOE rigorously simulate SS with multiphase equilibrium, two withdrawal policies are followed here for full comparison: (A) SS-

UOE operates with habitual liquid withdrawal at pre-shock, i.e. only vapor phase undergoes shock transition; and (B) SS-UOE operates without withdrawal, i.e. two-phase supersonic fluid undergoes shock transition.

Fig. H.1 traces nozzle geometry used by SS-UOE in Policies (A) and (B). Figs. H.2 to H.6 depict *Ma*, *P*, *T*, vapor fraction and *c* profiles obtained by SS-UOE for both withdrawal policies, with sampled points retrieved from Figs. 4 to 6 of Wen et al. (2012), discounting the mentioned idle length of 0.12 m. Fig. H.7 projected (*P*,*T*) SS paths for both withdrawal policies onto *P x T* plane with feed and gas product VLE envelopes (without withdrawal, these envelopes are the same). In Figs. H.2 to H.4 the SS "signatures" – i.e. the spatial gradient $\pm\infty$ singularities of *Ma*, *P* and *T* profiles – are seen at throat location, also observed in Wen et al. (2012) results, despite a small discrepancy of throat positions. Throat position is exactly L_C (*0.10956 m*) in SS-UOE profiles, while in Wen et al. (2012) it seems slightly shifted downstream.

Just after the throat, a change in the SS-UOE *Ma* profile is perceived as a sudden *Ma* increase from *1.13* to *1.64* in Fig. H.2. This is explained in Figs. H.5 and H.7 as the point where both (*P*,*T*) SS paths touch the HCDP curve initiating condensation; i.e. vapor fraction starts to fall below 1. The beginning of condensation strongly affects *c*, which now becomes two-phase, decreasing suddenly from *296.53* to *203.59 m/s* in Fig. H.6 due to a sudden higher density coupled to high compressibility typical of gas-liquid systems. This fall of *c* suddenly increases *Ma* as calculated by SS-UOE. However, this behavior is not seen in Wen et al. (2012) results since phase-change is disregarded in CFD simulations. This constitutes one major difference between rigorous thermodynamic SS profiles obtained by SS-UOE and typical SS profiles from CFD simulations which ignore phase-changes completely. The absence of condensation in CFD results also triggers other differences relatively to SS-UOE results in Figs. H.2 to H.7 and Table H.2. Firstly, *T* profile of Wen et al. (2012) reaches colder pre-shock temperatures comparatively to SS-UOE thanks to zero release of condensation latent heat: $\approx$*20 K* and $\approx$*4 K* less with and without liquid withdrawal. This point was also noticed by Castier (2014) whose results recovered a similar behavior and similar vapor fraction of $\approx$*70%mol* at pre-shock. Secondly, the abnormally colder pre-shock points of Wen et al. (2012) leave the VLE envelope in Fig. H.7 through the bubble point curve, dragging the authors to the wrong conclusion that full liquefaction could be obtained for this NG with SS operation. The truth is revealed by SS-UOE,

which shows that only *≈24%mol* of this NG can be liquefied. Moreover, this condensate is a rather impure LNG (Table H.2) with *≈86%mol* CH_4, *≈10%mol* C_2H_6 and *≈4%mol* C_3H_8. Thirdly, the correct *Ma* obtained by SS-UOE along the diverging section is a little higher than the reported by Wen et al. (2012); i.e. to achieve backpressure of 70 bar, normal shock should be located upstream the normal shock of Wen et al. (2012) thanks to the rapid *Ma* increase predicted correctly by SS-UOE due to incoming condensation. Fourthly, SS modeling demands correct representation of the normal shock transition, which is accomplished by SS-UOE. On the other hand, Wen et al. (2012) results exhibit unexpected shock patterns such as slightly curved/inclined shock-jumps in Figs. 4 to 7 of Wen et al. (2012) instead of straight jumps. Also, there are notable "hump-like" anomalies in Wen et al. (2012) *T*, *P*, *Ma* profiles just after the normal shock as seen in their Figs. 4 to 6 (also noticed by Castier, 2014). These abnormalities are also apparent in Wen and al. (2012) points on the *P x T* plane of Fig. H.7, while the SS-UOE path across normal shock is a clear rectilinear (*P*,*T*) jump back to superheated vapor followed by a monotonous (*P*,*T*) increase with different inclination in the SS diffuser.

Regarding liquid extraction, it is clear in Figs. H.2 to H.6 that to obtain the same backpressure, the condensate withdrawal displaces shock location upstream in the nozzle as mass flow rate across shock is lower, with a lower pressure increase. Thus, shock happens upstream with a lower *Ma* just before shock (Ma_{BS}), at a more pressurized location (so that same backpressure is achieved). Note that neglecting condensate removal is nonsense, since SS purpose is phase-split as simulated by SS-UOE in Policy (A). Policy (B) without liquid withdrawal is executed only for comparison with third parties.

Table H.2 shows available literature results for comparison with SS-UOE: Wen et al. (2012), Castier (2014) and Secchi et al. (2016). Entropy values at feed, throat, pre-shock, after shock and outlet locations were obtained via HYSYS with PR-EOS using feed composition and (*T*,*P*) attained in each work. Entropy of a (*T*,*P*) state is determined after solving full phase equilibrium via HYSYS *Flash*(*P*,*T*).

Regarding the entropy change along the SS, it is clear that SS-UOE is isentropic except for phase separation and normal shock. Despite the slight falls of throat and before-shock entropy values of Castier (2014) and slight increases for Secchi et al. (2016), these small variations can be attributed to EOS divergences, so that nearly isentropic SS flows were generated in these

works. Counterpointing this, Wen et al. (2012) results clearly violate the 2nd Law of Thermodynamics, producing unquestionable adiabatic entropy destruction in their SS as the adiabatic variation of entropy from feed to pre-shock states is remarkably negative: $\Delta\bar{S}^{Pre-Shock} = \bar{S}^{Pre-Shock} - \bar{S}^{Feed} = -31.68\ kJ/kmol.K$. As the 2nd Law forbids this, their reported (*T*,*P*,*Ma*) profiles are unfeasible and wrong.

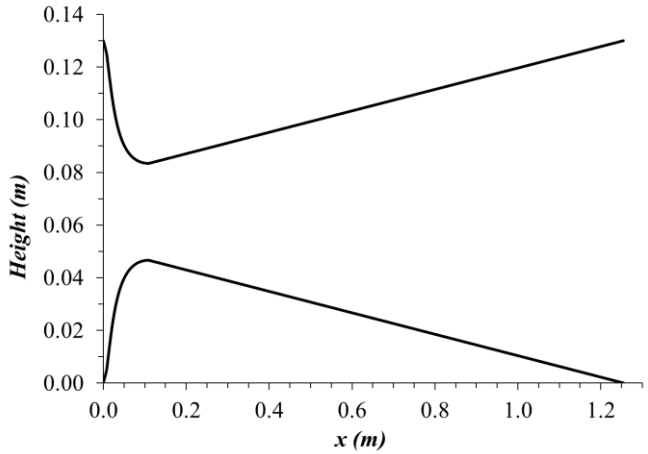

Figure H.1. Nozzle Diameter Profile for SS-UOE.

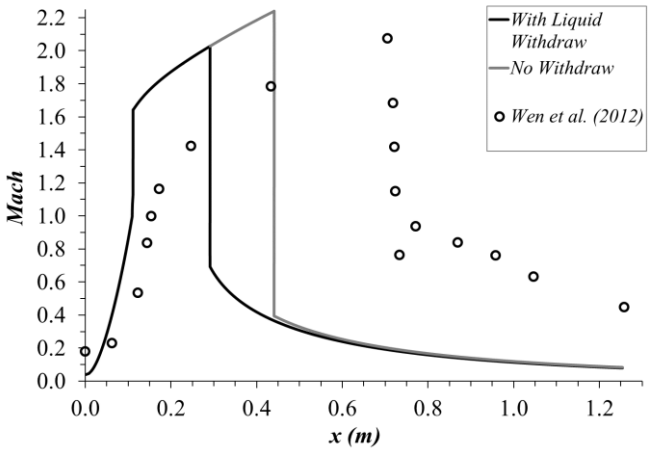

Figure H.2. SS-UOE *Ma* Profiles with and Without Liquid Withdrawal.

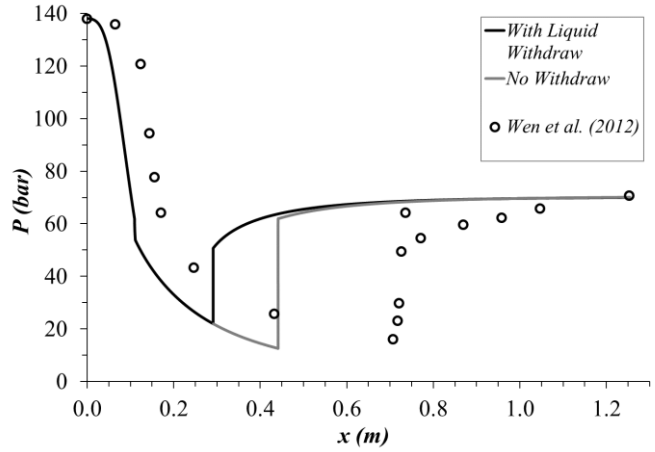

Figure H.3. SS-UOE Pressure Profiles with and Without Liquid Withdrawal.

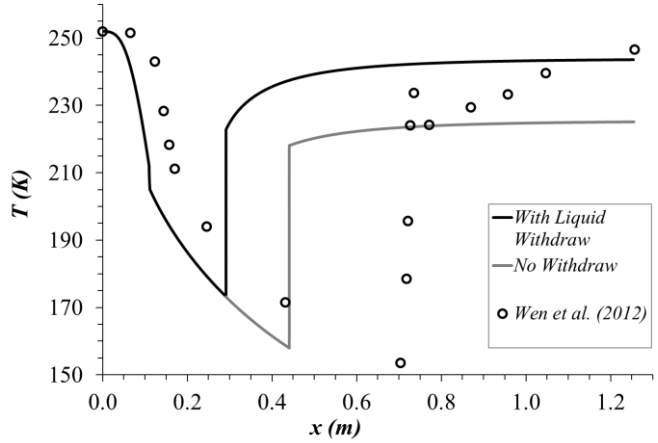

Figure H.4. SS-UOE Temperature Profiles with and Without Liquid Withdrawal.

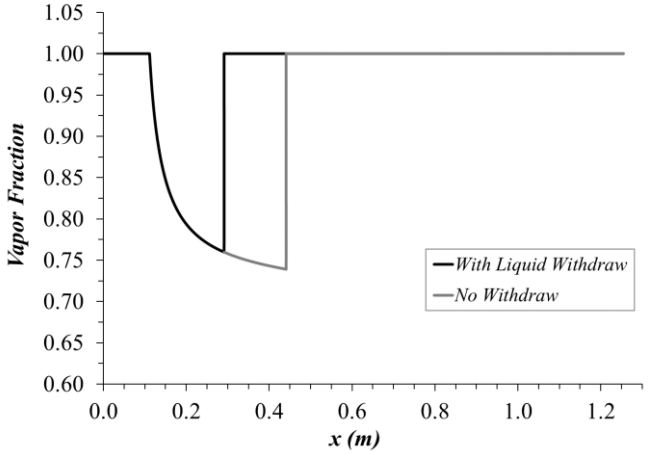

Figure H.5. SS-UOE Vapor Fraction Profiles with and Without Liquid Withdrawal (no points of Wen et al., (2012)).

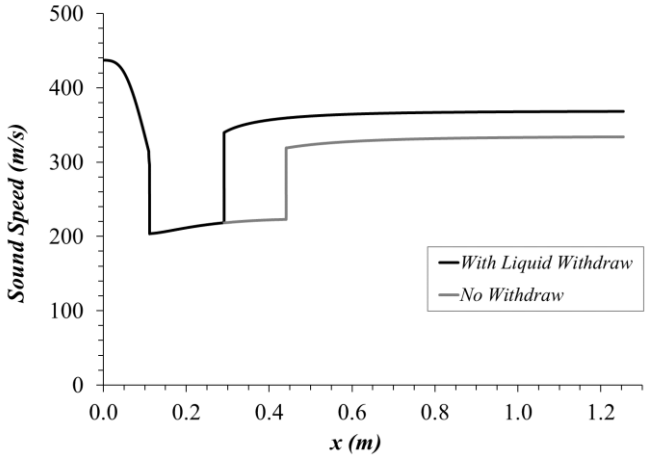

Figure H.6. SS-UOE Sound Speed Profiles with and Without Liquid Withdrawal.

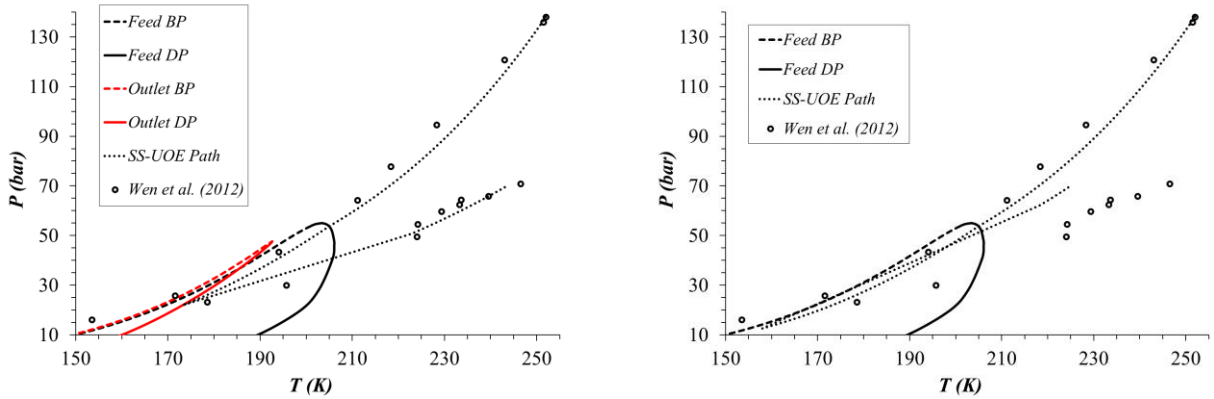

Figure H.7. *P x T* Plane with and Without Liquid Withdrawal: (i) Feed VLE Envelope (larger); (ii) Lean Gas VLE Envelope (red slenderer, only with Liquid Withdrawal); (iii) SS Path; (iv) Wen et al. (2012) Points.

Table H.2. Literature and SS-UOE Results for Wen et al. (2012) Study.

*Results**	*Wen et al. (2012)*	*Castier (2014)*	*Secchi et al. (2016)*	*SS-UOE Withdrawal Policy (A)*	*SS-UOE Withdrawal Policy (B)*
P_T *(bar)*	*77.68*	*60.15*	*68.00*	*61.70*	*61.70*
T_T *(K)*	*218.36*	*210.16*	*217.00*	*211.86*	*211.86*
c^{Throat} *(m/s)*	-	*326.57*	-	*314.45*	*314.45*
Ma^{Shock}	*2.074*	*2.286*	-	*2.029*	*2.241*
P^{min} *(bar)*	*16.12*	*12.40*	*6.30*	*21.90*	*12.55*
T^{min} *(K)*	*154.29*	*157.22*	*143.00*	*173.17*	*157.97*
ΔP^{Shock} *(bar)*	*48.25*	*51.60*	*35.30*	*28.74*	*49.34*
ΔT^{Shock} *(K)*	*80.15*	*62.78*	*60.00*	*49.63*	*60.11*
Backpressure (bar)	*70*	*70*	*70*	*70*	*70*
S^{Feed} *(kJ/kmol.K)*	*127.48*	*127.48*	*127.48*	*127.48*	*127.48*
S_T *(kJ/kmol.K)*	*124.86*	*127.16*	*127.67*	*127.48*	*127.48*
S_{BS} *(kJ/kmol.K)*	*95.80*	*125.78*	*130.01*	*127.48*	*127.48*
S_{AW} *(kJ/kmol.K)*	-	-	-	*135.48*	-
S_{AS} *(kJ/kmol.K)*	*135.39*	*130.72*	*133.58*	*135.87*	*130.70*
S^{Out} *(kJ/kmol.K)*	*137.10*	*132.16*	*133.77*	*135.87*	*130.70*
Condensate Product					
%mol CH_4	-	-	-	*86.07%*	-
%mol C_2H_6	-	-	-	*9.99%*	-
%mol C_3H_8	-	-	-	*3.94%*	-
T (K)	-	-	-	*173.77*	-
P (bar)	-	-	-	*69.9 bar*	-
kmol/h	-	-	-	*2173.95*	-
Gas Product					
%mol CH_4	-	-	-	*99.2%*	-
T (K)	-	-	-	*243.56*	-
P (bar)	-	-	-	*69.9 bar*	-
kmol/h	-	-	-	*6878.55*	-

* *BS, AS, AW just before/after shock, after withdrawal; Out gas outlet*

APPENDIX J - HYSYS PROCESS FLOWSHEETS FOR CASES 1, 2, 3 AND 3X

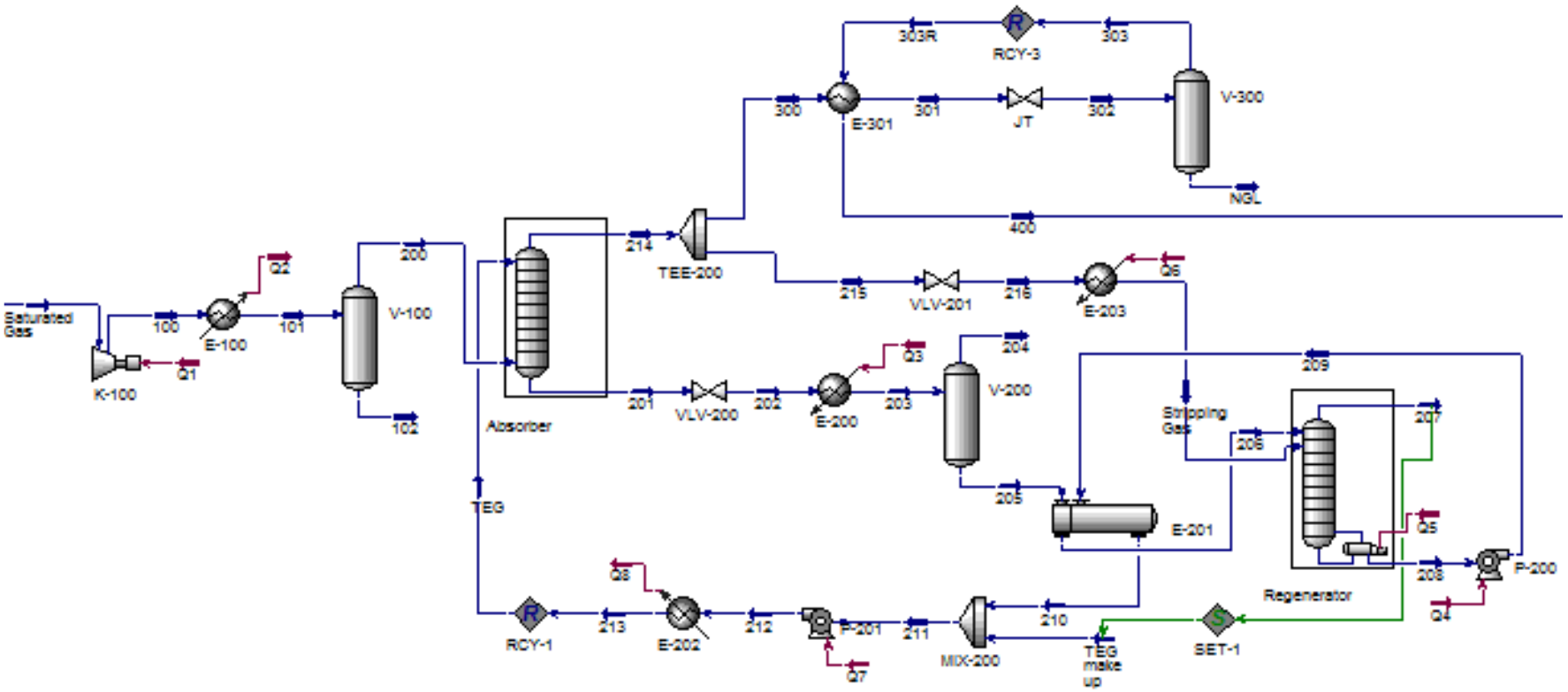

Figure J.1. HYSYS PFD A: TEG Dehydration and JT Expansion

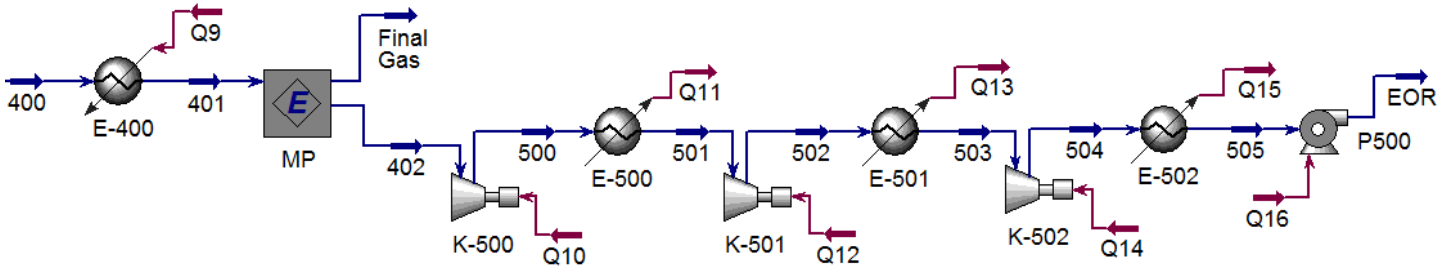

Figure J.2. HYSYS PFD B: Membrane Permeation for CO_2 Removal

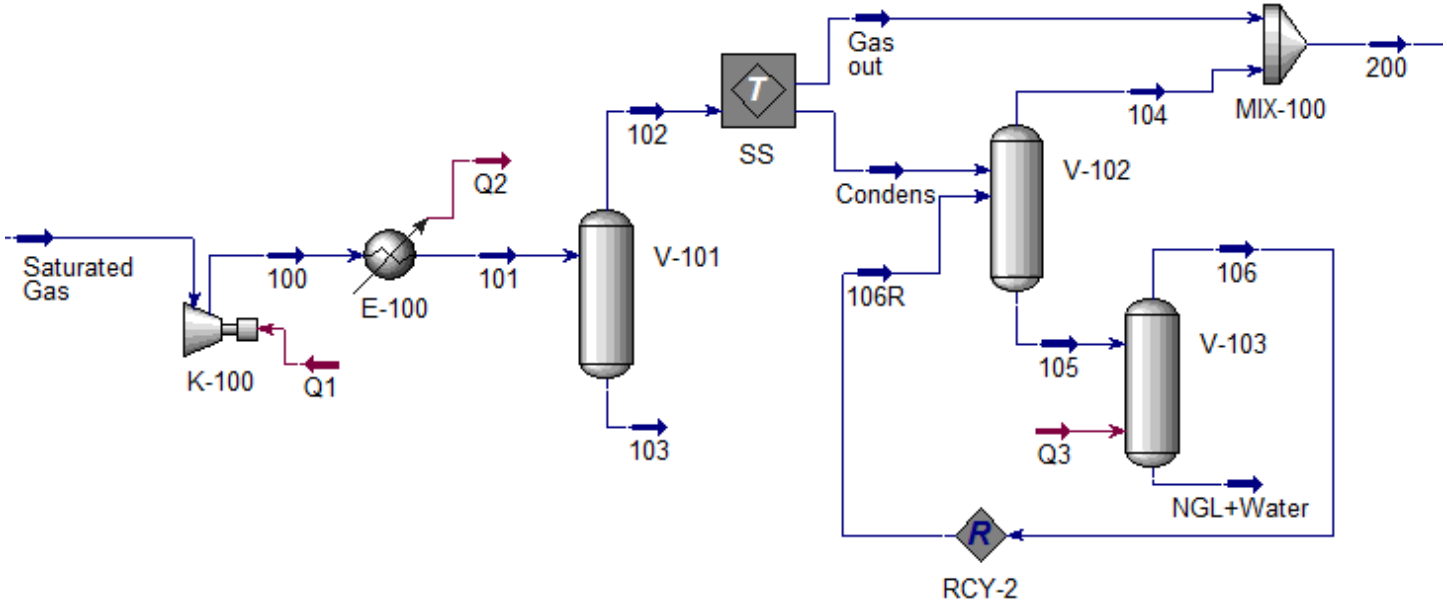

Figure J.3. HYSYS PFD C: Supersonic Separator for WDPA+HCDPA

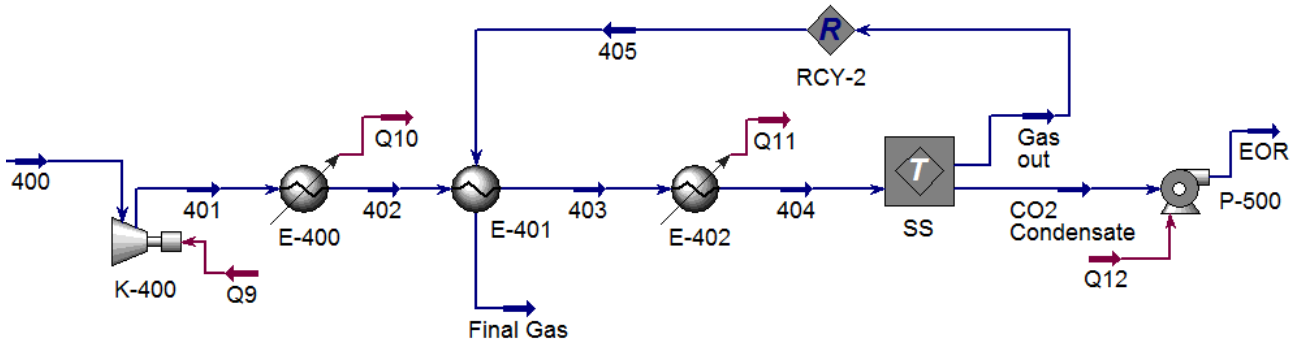

Figure J.4. HYSYS PFD D: Supersonic Separator for CO_2 Removal with SS Feed Refrigeration

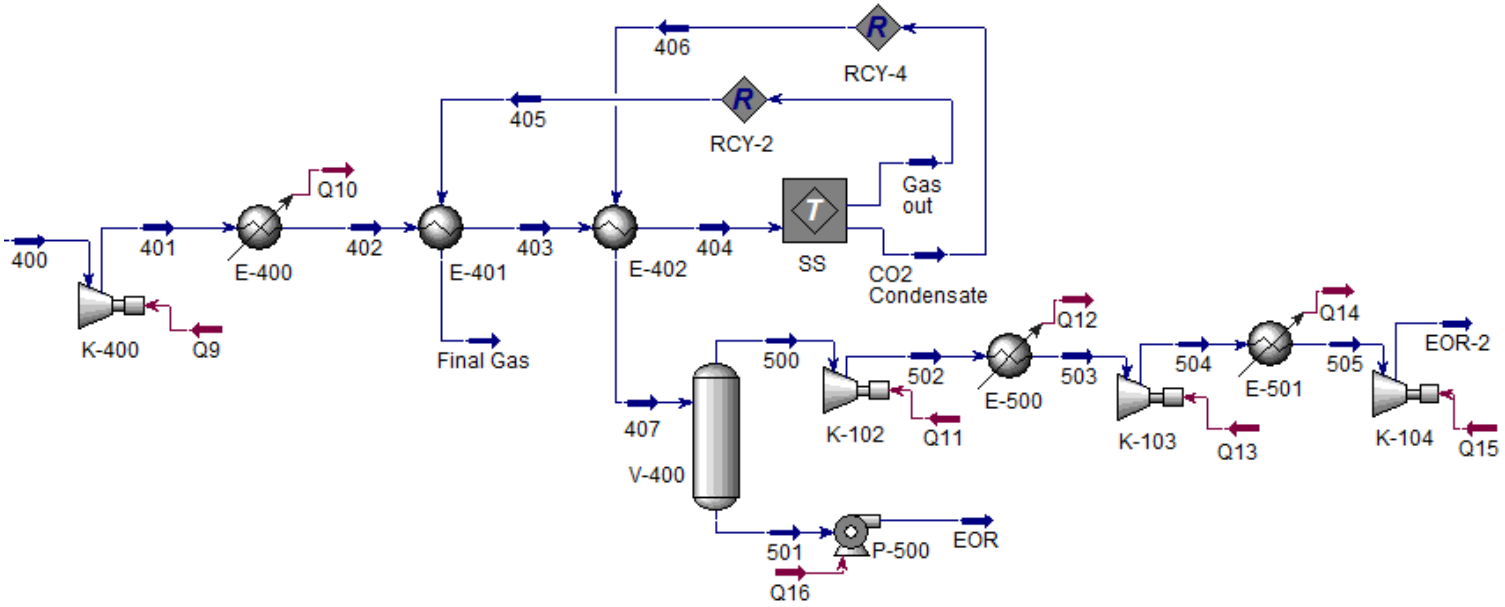

Figure J.5. HYSYS PFD E: Supersonic Separator for CO_2 Removal Cooling SS Feed with EOR Fluid

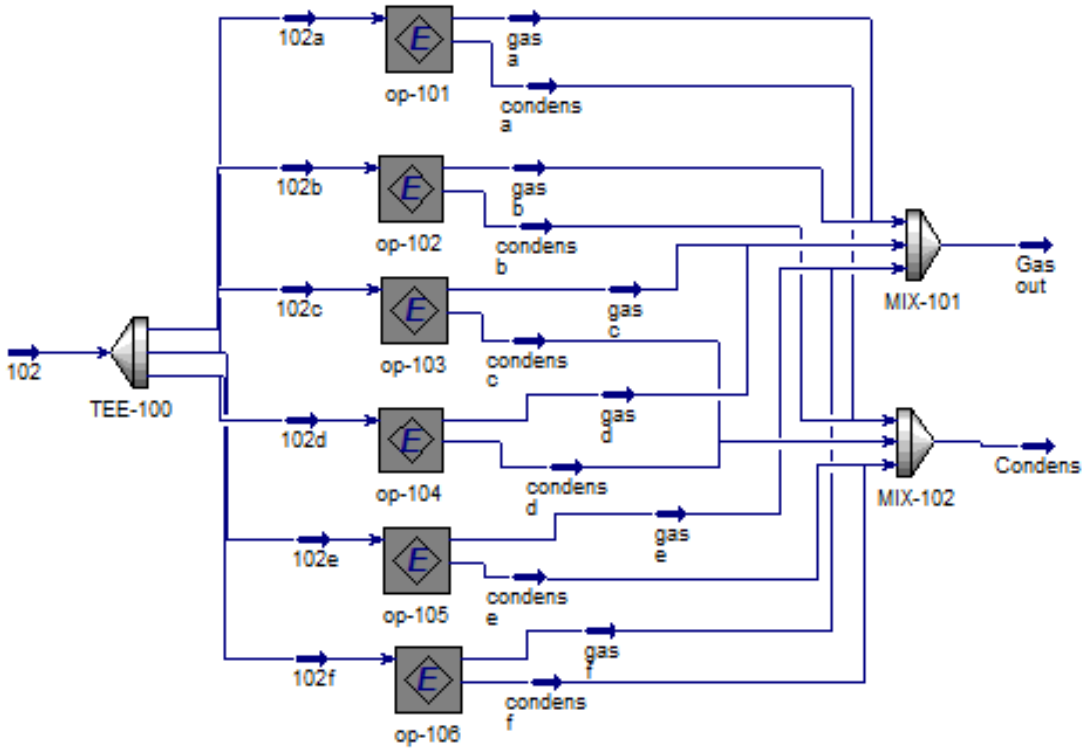

Figure J.6. PFD SS-UOE Sub-Flowsheet

APPENDIX K - RELATIONSHIPS FOR ECONOMIC ANALYSIS OF PROCESSES

The fixed capital investment (*FCI*, USD) is estimated via base bare module cost (C^0_{BM}) in a reference condition, corrected with design, pressure and material factors (F_{BM}) to give the bare module installed cost ($C_{BM}=C^0_{BM}*F_{BM}$). Contingency costs ($C_{CF}=C_{BM}*0.18$) and auxiliary facility costs are added to *FCI*, the former accounting for unexpected expenses and uncertainties, the latter regarding land purchase, off-sites and utility systems as *50%* of reference bare module costs. Thus, for onshore processes, *FCI* is obtained via Eq. (K.1), where N_{EQ} is the number of equipment items, and C^0_{BMi} is updated with Chemical Engineering Plant Cost Index of *550.3* (Sept-2015, Chem. Eng. Magazine 2016). When capacity limits of cost predictors are below the required capacities, costs are extrapolated with the *Six-Tenths Rule*, Eq. (K.2a), where *CF* is a capacity factor (power, area or flow rate). Since installation and indirect costs of offshore systems are higher than onshore counterparts, an empirical *2.2* factor is used in Eq. (K.2b). Annual cost of manufacturing (*COM*, USD/y) is estimated with Eq. (K.3a), where *COL*, *CRM*, *CUT*, *CWT* are, respectively, annual costs (USD/y) of labor, raw materials, utilities and waste treatment. Gross annual profit (*GAP*, USD/y), annual profit (*AP*, USD/y) and net present value (*NPV*, USD) follow in Eqs. (K.3b) to (K.3d), where *REV* (USD/y), *ITR* (%), *DEPR* (USD/y), *N* and *i* (%) refer to revenues, income tax rate (*ITR=34%*.), annual depreciation (*10% FCI*), horizon (*N=20*) and annual interest rate (*i=10%*), respectively.

$$FCI^{ONSHORE} = 1.18 * \sum_{i=1}^{N_{EQ}} C_{BM\,i} + 0.5 * \sum_{i=1}^{N_{EQ}} C^0{}_{BM\,i} \tag{K.1}$$

$$FCI^{ONSHORE} = FCI^{ONSHORE^{LIMIT}} * \left(CF / CF^{LIMIT}\right)^{6/10} \tag{K.2a}$$

$$FCI^{OFFSHORE} = 2.2 * FCI^{ONSHORE} \tag{K.2b}$$

$$COM = 0.18 * FCI^{OFFSHORE} + 2.73 * COL + 1.23 * (CRM + CUT + CWT) \tag{K.3a}$$

$$GAP = REV - COM \tag{K.3b}$$

$$AP = GAP - (ITR/100) * (GAP - DEPR) \quad (GAP > DEPR) \quad or \quad AP = GAP \tag{K.3c}$$

APPENDIX L - SS PROFILES AND SS-UOE VALIDATION

L.1. SS Signatures

Let *A(x)* and *x* be flow section area and axial position of converging-diverging nozzles. It can be proved (De Medeiros et al., 2017) that any compressible isentropic 1D flow through converging-diverging nozzles with $\left(\frac{dA}{dx}\right)^{Throat} \neq 0$ (e.g., Fig. 1), with either ideal gas or single-phase real gas or two-phase gas-liquid equilibrium or any multiphase equilibrium compressible fluid or even any multiphase and multi-reactive equilibrium (i.e. undertaking chemical-equilibrium reactions) compressible fluid must exhibit $\pm\infty$ spatial gradient singularities at throat sonic limit ($Ma^{Throat} \to 1^-$) in Eq. (L.1), where *v* is axial velocity, *c* is the thermodynamic sound speed and *Ma=v/c*. Eq. (L.1) is very general as the flow can be single-phase or multiphase and/or multi-reactive as well, being necessary and sufficient 1D compressible isentropic equilibrium flow with $\left(\frac{dA}{dx}\right)^{Throat} \neq 0$. It can also be shown that Eq. (L.1) implies Eqs. (L.2) or (L.3) whether the multiphase and/or multi-reactive 1D compressible isentropic flow is, respectively, *vapor-dominated* ($\beta <\approx 1.0$) or *liquid-dominated* ($\beta <\approx 0.5$), where β represents molar vapor-fraction (Eqs. (L.2) and (L.3) only differ in the *dc/dx* sign).

$$\frac{dT}{dx} = -\infty \quad , \quad \frac{dP}{dx} = -\infty \quad , \quad \frac{dv}{dx} = +\infty \qquad \left(Ma^{Throat} \to 1^- \, , \left(\frac{dA}{dx}\right)^{Throat} \neq 0\right) \tag{L.1}$$

$$\frac{dT}{dx} = -\infty \quad , \quad \frac{dP}{dx} = -\infty \quad , \quad \frac{dv}{dx} = +\infty \quad , \quad \frac{dc}{dx} = -\infty \quad , \quad \frac{dMa}{dx} = +\infty \qquad \left(Ma^{Throat} \to 1^- \, , \beta <\approx 1.0\right) \tag{L.2}$$

$$\frac{dT}{dx} = -\infty \quad , \quad \frac{dP}{dx} = -\infty \quad , \quad \frac{dv}{dx} = +\infty \quad , \quad \frac{dc}{dx} = +\infty \quad , \quad \frac{dMa}{dx} = +\infty \qquad \left(Ma^{Throat} \to 1^- \, , \beta <\approx 0.5\right) \tag{L.3}$$

These limit singular gradients are true SS "signatures" which only occur in regular SS operation under throat sonic limit ($Ma^{Throat} \to 1^-$) as rigorously proved in (De Medeiros et al., 2017) for 1D compressible isentropic SS flow with $\left(\frac{dA}{dx}\right)^{Throat} \neq 0$.

L.2. Inexistent SS Signatures at Throat Sonic Flow: SS-UOE Validation

SS profiles cannot exhibit SS "signatures" for SS nozzle with $\left(\frac{dA}{dx}\right)^{Throat} = 0$. This was the case when Yang et al. (2014) validated their SS CFD framework with the work of Arina (2004) involving a SS expanding *3.071 kmol/h* of dry synthetic air (O_2*=21%mol,* N_2*=79%mol*) from P^{Inlet}*=100 kPa,* T^{Inlet}*=14.85°C* to P^{Outlet}*=83.049 kPa*. This is a low-pressure SS without phase-change as air is dry and supercritical. Arina's SS nozzle (Fig. L.1a) has non-linear diameter profiles in Eqs. (L.4) satisfying $\left(\frac{dA}{dx}\right)^{Throat} = 0$, with inlet, throat and outlet diameters respectively of D_I*=17.84mm,* D_T*=11.28mm* and D_O*=13.82mm,* and converging, diverging and total lengths respectively of L_C*=50mm,* L_D*=50mm* and *L=100mm.*

$$D(mm) = \sqrt{400 * \left(2.5 + (Z - 1.5) * 3Z^2\right) / \pi} \quad , \quad Z = x / L_C \quad , \quad 0 \le x \le L_C \tag{L.4a}$$

$$D(mm) = \sqrt{400 * \left(3.5 - (6 - 4.5Z + Z^2) * Z\right) / \pi} \quad , \quad Z = x / L_C \quad , \quad L_C \le x \le L \tag{L.4b}$$

Yang et al. (2014) validated their CFD modeling by plotting SS pressure profile against Arina's data in their Fig. 2 with good concordance. Both profiles, as expected, did not have $dP/dx = -\infty$ singularity at sonic throat, a consequence of $\left(\frac{dA}{dx}\right)^{Throat} = 0$.

Analogously, the thermodynamic SS framework of the present work – i.e. Unit Operation Extension SS-UOE – can also be validated by Arina's data (Arina, 2004). Firstly, Arina's diameter profiles where installed in SS-UOE as depicted in Fig. L.1a in SI units (throat at $x = L_C = 0.05m$). Arina's SS was simulated by SS-UOE using PR-EOS with results in Figs. L.1b, L.1c and L.1d. Fig. L.1b depicts SS-UOE pressure profile against Arina's counterpart. As phase-change effects are ruled out, the concordance of pressure profiles is everywhere perfect, except at normal shock where Arina's CFD profile exhibits a discreet, but perceptible, inclined shock jump, which must be a vertical discontinuity as obtained by SS-UOE. On the other hand, Figs. L.1c and L.1d depict only SS-UOE profiles for *T* and *c* (Fig. L.1c) and *Ma* (Fig. L.1d), as there were no Arina's analogues.

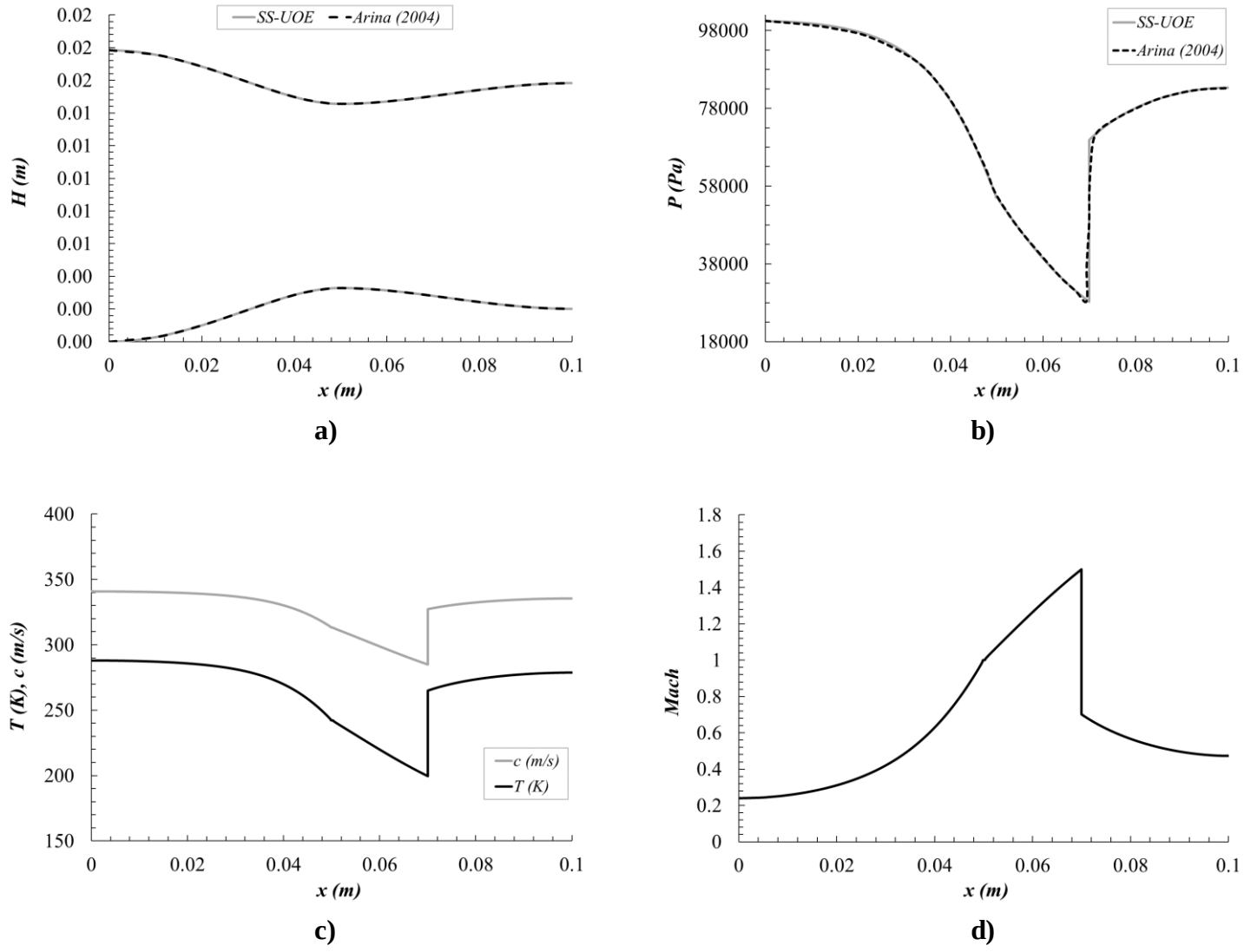

Figure L.1. SS with dry air: (a) silhouette *H(m)* of Arina's nozzle vs *x(m)*; (b) *P(Pa)* vs *x(m)* via SS-UOE and Arina's data; (c) SS-UOE *T(K)*, *c(m/s)* vs *x(m)*; (d) SS-UOE *Ma* vs *x(m)*

APPENDIX M - ECONOMIC ANALYSIS: RELATIONSHIPS AND ASSUMPTIONS

Fixed Capital Investment (*FCI,USD*) is estimated via base bare-module cost (C^0_{BM}) corrected with design/pressure/material factors (Turton et al., 2009) giving bare-module installed-cost ($C_{BM}=C^0_{BM}*F_D*F_P*F_M$). Contingency costs are added to *FCI* as $0.5*C^0_{BM}$. Thus, for onshore processes, *FCI* follows Eq. (M.1) for N_{EQ} equipment items with updated C^0_{BM} using *CEPCI=550.3,* Sept-2015 Chemical Engineering Plant Cost Index (Chem.Eng., Jan-2016).

$$FCI^{ONSHORE} = 1.18 * \sum_{i=1}^{N_{EQ}} C_{BM\,i} + 0.5 * \sum_{i=1}^{N_{EQ}} C^0{}_{BM\,i} \tag{M.1}$$

When required capacities exceed cost correlations capacity limits, costs were extrapolated via Eq. (M.2a), "*Six-Tenth Rule",* where *C* is capacity – power (machines), area (exchangers), flow rate (separators). Eq. (M.2b) adopts a *2.2* factor as offshore systems have costlier installation than onshore counterparts. Eq. (M.3a) estimates Cost of Manufacturing (*COM,USD/y*), where *COL*, *CRM*, *CUT*, *CWT* are, respectively, costs (*USD/y*) of labor, raw materials, utilities and waste treatment. Gross Annual Profit (*GAP,USD/y*), Annual Profit (*AP,USD/y*) and Net Present Value (*NPV,USD*) follow in Eqs. (M.3b) to (M.3d), where *REV(USD/y)*, *ITR(%)*, *DEPR(USD/y)*, *N(years)*, represent, respectively, revenues, income tax rate (*ITR=34%*), depreciation (*0.1*FCI*), horizon (*N=20*) and annual interest rate (*i=10%*). The remaining economic assumptions follow in Table M.1.

$$FCI^{ONSHORE} = FCI^{ONSHORE^{LIMIT}} * \left(C / C^{LIMIT} \right)^{6/10} \tag{M.2a}$$

$$FCI^{OFFSHORE} = 2.2 * FCI^{ONSHORE} \tag{M.2b}$$

$$COM = 0.18 * FCI^{OFFSHORE} + 2.73 * COL + 1.23 * (CRM + CUT + CWT) \tag{M.3a}$$

$$GAP = REV - COM \tag{M.3b}$$

$$AP = GAP - (ITR/100) * (GAP - DEPR) \quad (GAP > DEPR) \quad or \quad AP = GAP \tag{M.3c}$$

$$NPV = -\left(0.2 + 0.3 * q^{-1} + 0.5 * q^{-2}\right) FCI^{OFFSHORE} + AP \left\{ \sum_{k=3}^{N+3} q^{-k} \right\}, \; q \equiv (1 + i/100) \tag{M.3d}$$

Table M.1. Complementary economic assumptions for process evaluation.

Code	*Topic or Equipment*	*Description*
{E1}	*Vessels*	$P^{DESIGN}=1.15*P^{OPERATION}$
{E2}	*Spiral-wound membrane*	$FCI^{ONSHORE}(USD)=500*area(m^2)$; $CRM(USD/y)=40*area(m^2)$ *(Merkel et al., 2012).*
{E3}	*Turboshafts/GTs*	*28MW at 161.4MW/MMsm³/d* for *20%molCO_2 Fuel-Gas.*
{E4}	*Fuel-Gas flow rate*	$MMsm^3/d=POWER^{RIG}(MW)/161.4$; $POWER^{RIG}(MW)=1.1*POWER^{Gas\text{-}Plant}(MW)+28MW$.
{E5}	*Power-Plant* $FCI^{ONSHORE}$	*From number of 28MW turboshafts for electricity peak-demand plus one.*
{E6}	*SS* $FCI^{ONSHORE}$	*Eq. (M.2a) using* $FCI^{ONSHORE}$ *for 6MMsm³/d from Machado et al. (2012).*
{E7}	*Prices*	*Raw-NG=0; Oil=45USD/bbl*; *Fuel-Gas=3.2 USD/MMBTU; EOR-Fluid=45USD/t.*
{E8}	*Thermal utilities*	*Costless SW/CW/WW/HW/PHW/TF.*
{E9}	*CUT (USD/y)*	*Fuel-Gas*
{E10}	*Construction*	*Three years allocating 20%/30%/50% capital*
{E11}	*Operation*	*8000 h/y*

APPENDIX N - 1ST SS UNIT WITH CPA-EOS

SS-UOE also simulated 1st SS unit with CPA-EOS for WDPA+HCDPA. This is of significance as CPA-EOS is more accurate than PR-EOS for hydrocarbon-CO_2-water systems (Folas et al., 2005; Karakatsani and Kontogeorgis, 2013). Fig. N.1 depicts SS path on plane $T\,x\,\overline{S}$. Figs. N.1a/N.1b are similar to Figs. V.13a/V.13b, excepting the hotter feed WDP with CPA-EOS; i.e., there is, from the outset, liquid water at SS inlet (SS feed is two-phase) which did not represent special concern for successful SS-UOE simulation of 1st SS unit with CPA-EOS.

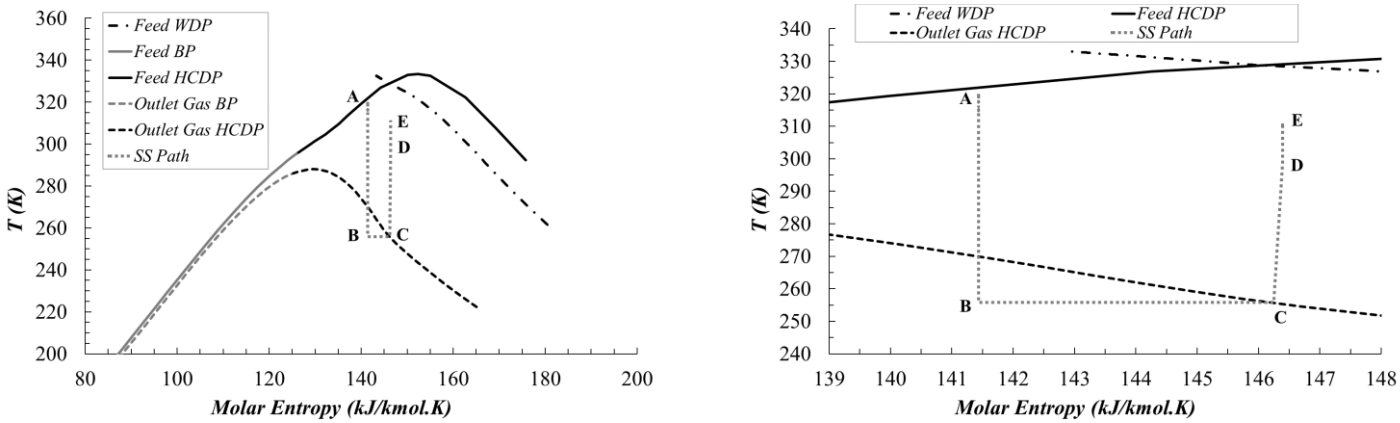

a) **b)**

Figure N.1. Plane $T\,x\,\overline{S}$ for 1st SS unit with CPA-EOS: (a) SS path with feed WDP locus, and feed and Dry-Gas VLE envelopes; (b) magnification of (a)

Fig. N.2 shows SS axial profiles and SS path on *PxT* plane with feed WDP locus and VLE envelopes of feed and Dry-Gas for 1st SS unit with CPA-EOS. SS design (lengths, throat diameter in Fig. N.2a), is similar to PR-EOS counterpart (Fig. V.11a). Main differences are vapor-fraction and condensation profiles (Figs. N.2a/N.2d) starting with *≈1/3* of water already condensed as CPA-EOS predicts hotter WDP. Other differences are in *c* profile: initial and minimal *c* from PR-EOS (Fig. V.11c) are *≈259 m/s* and *≈210 m/s*, given in Fig. N.2c as *≈242 m/s* and *≈218 m/s*. Also at *x=0.025m* (Fig. V.11c), the sudden *c* fall marks water starting condensation, a feature absent in Fig. N.2c as SS feed is already two-phase for CPA-EOS.

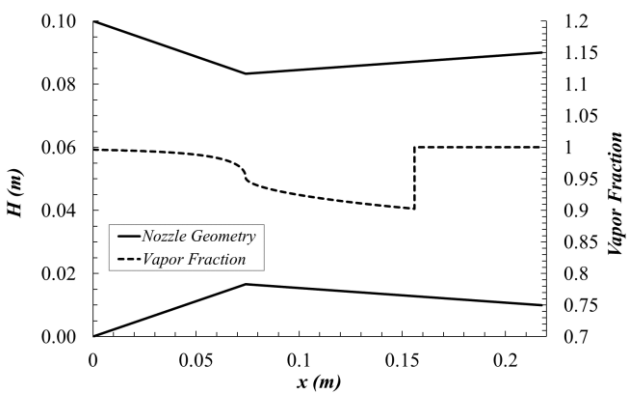

a)

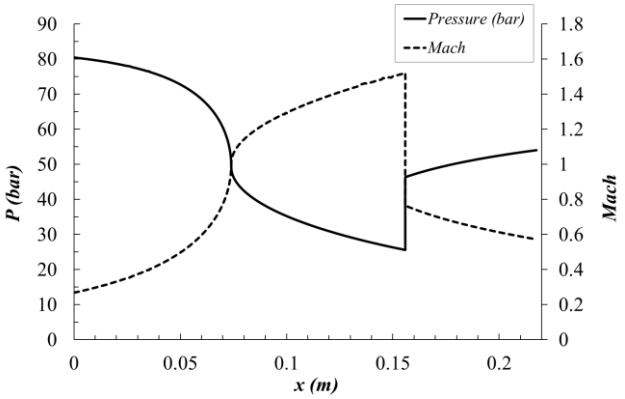

b)

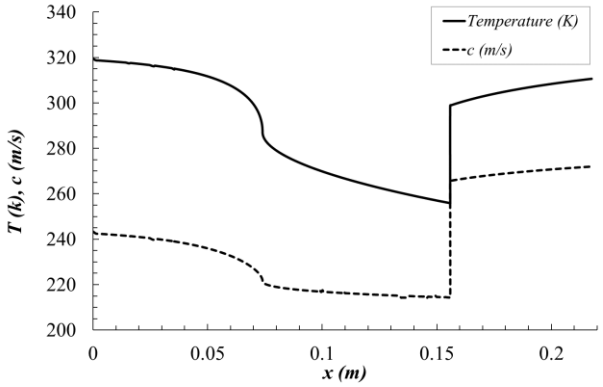

c)

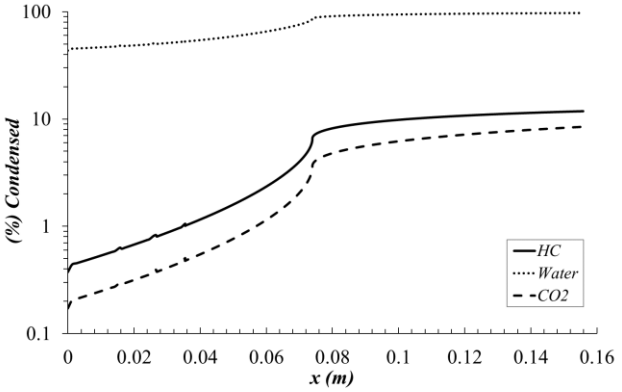

d)

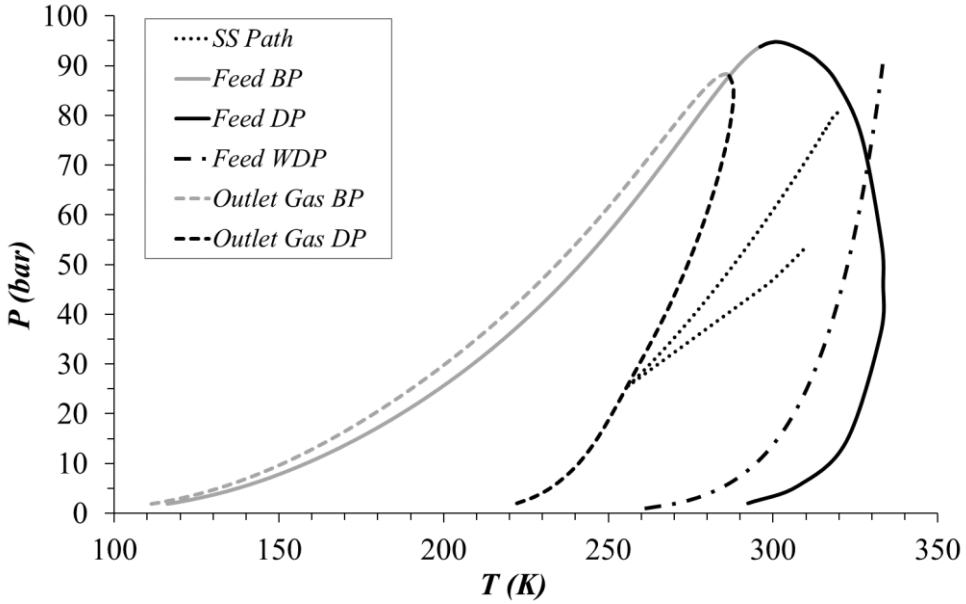

e)

Figure N.2. Base-Case 1st SS unit for WDPA/HCDPA with CPA-EOS: a) SS silhouette and vapor-fraction *vs x(m)*; b) *P(bar), Ma vs x(m)*; c) *T(K), c(m/s) vs x(m)*; d) *hydrocarbons, CO_2 & H_2O %Condensed vs x(m)*; e) plane *PxT*: feed WDP locus, VLE envelopes of feed and Dry-Gas (slenderer) and SS path.

APPENDIX O - HYSYS PFDS OF BASE-CASE [RC+JT+SS] AND ALTERNATIVES [RC+TX+SS], [NR+JT+SS], [RC+JT+MP] FOR PROCESSING HUMID CO2 ULTRA-RICH NG

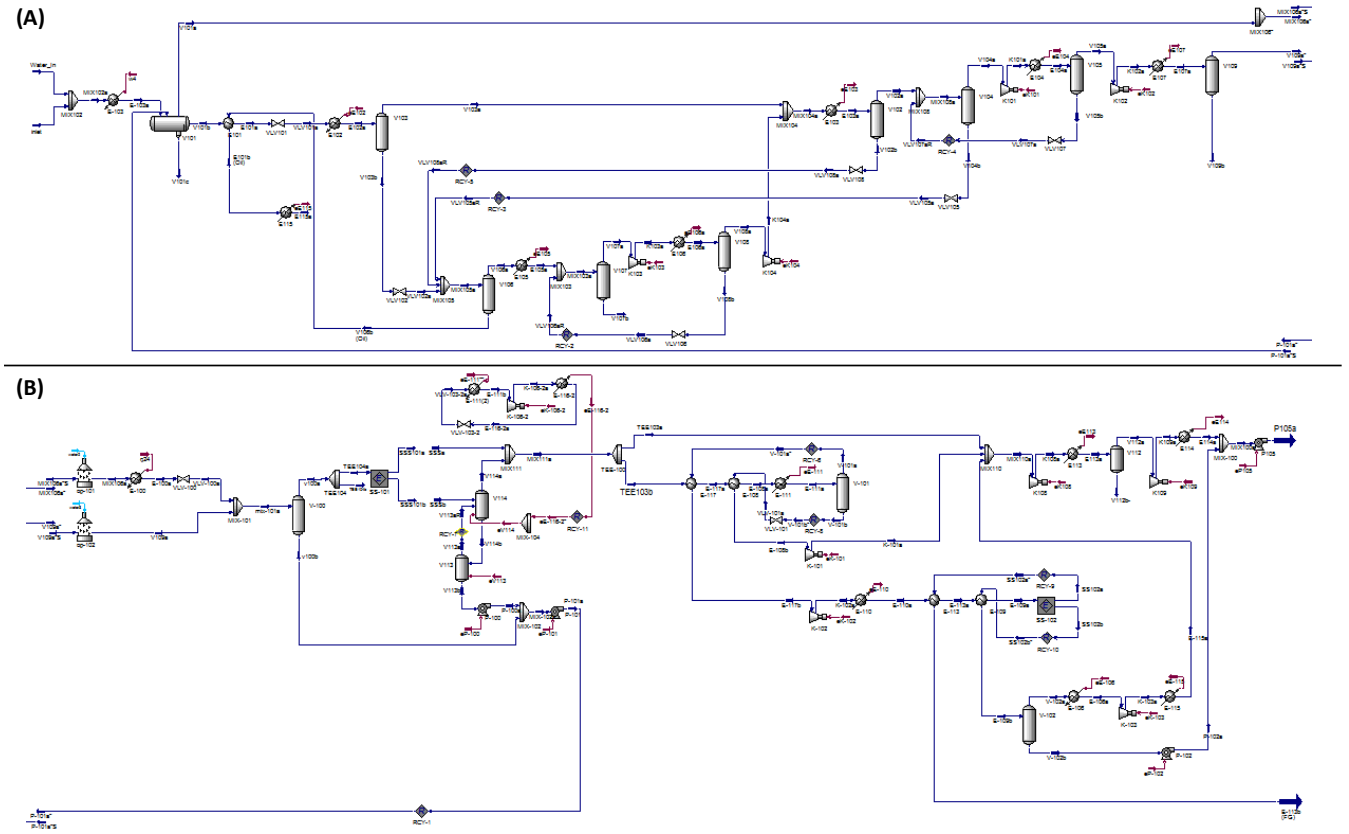

Figure O.1. HYSYS PFD for Base-Case Process [RC+JT+SS].

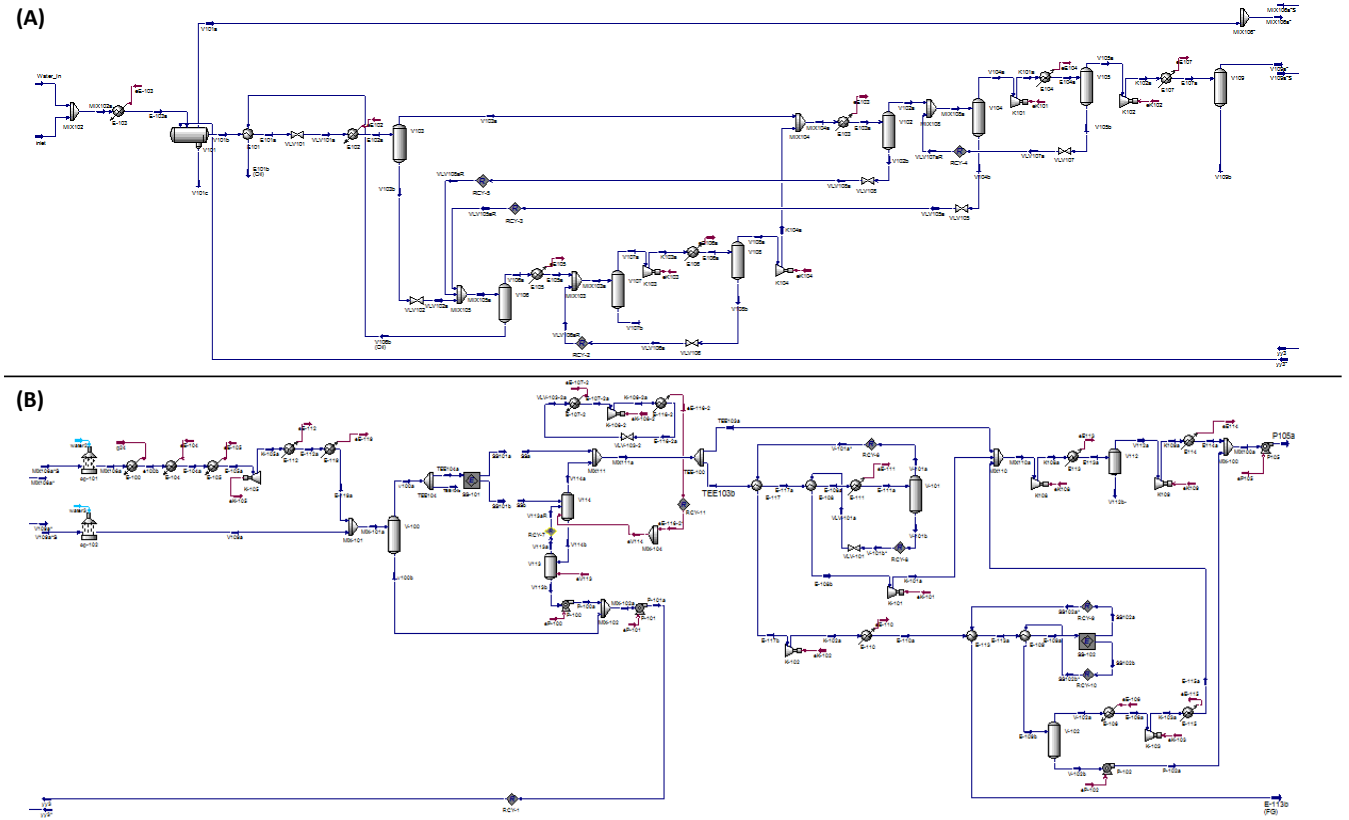

Figure O.2. HYSYS PFD for Process Alternative [RC+TX+SS].

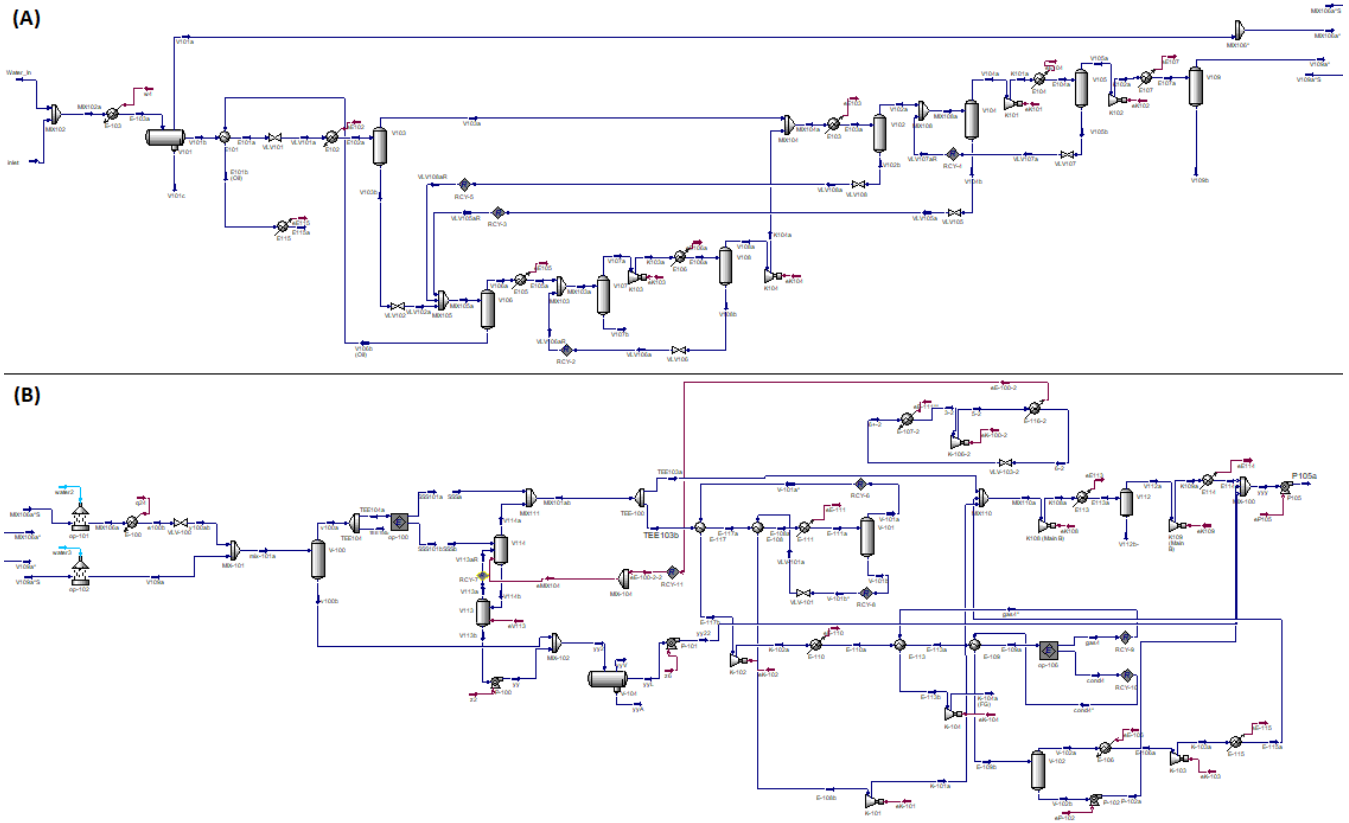

Figure O.3. HYSYS PFD for Process Alternative [NR+JT+SS].

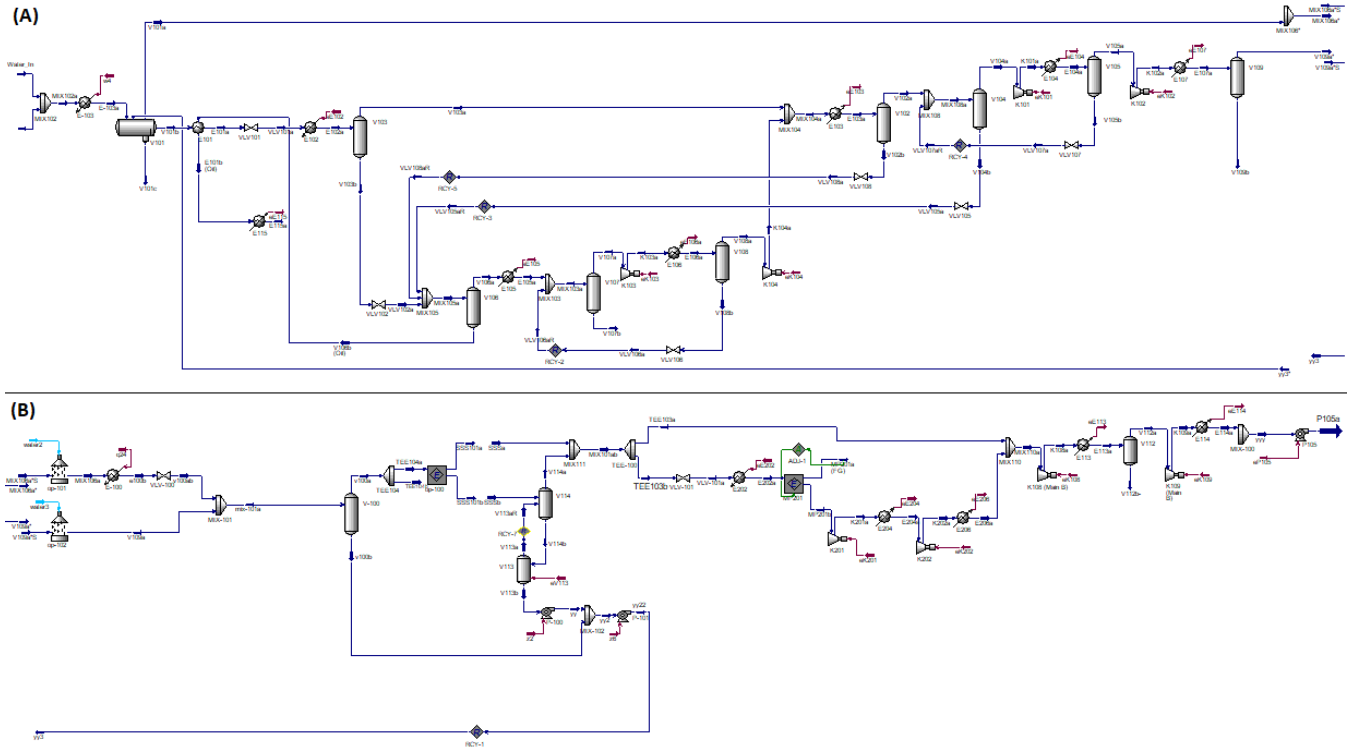

Figure O.4. HYSYS PFD for Process Alternative [RC+JT+MP].

APPENDIX P - ANALOGUES OF TABLE V.3 FOR CASES [RC+TX+SS], [NR+JT+SS], [RC+JT+MP]

Table P.1. Streams of gas-hub for CO_2 ultra-rich NG: Case [RC+TX+SS].

System	*HPS*				*Oil*	*VRU*	*SS WDPA+HCDPA*				*SS CO_2 Removal*				*Main Compressor*		*EOR*
Stream	***Riser***	***Main Recycle***	***HPS Water***	***HPS Gas***	***Final Oil***	***VRU Gas***	***Feed***	***Gas SS***	***L+W SS***	***L+W LTX***	***Feed***	***FG***	***GCO2***	***LCO2***	***DHG***	***MC Gas***	***Final Fluid***
T(°C)	*30.0*	*36.5*	*32.5*	*32.5*	*42.6*	*45.0*	*45.1*	*34.2*	*-18.1*	*20.0*	*-22.0*	*35.0*	*45.0*	*15.2*	*34.2*	*34.0*	*80.3*
P(bar)	*120.0*	*120.0*	*120.0*	*120.0*	*1.30*	*80.50*	*80.50*	*50.96*	*50.96*	*50.96*	*84.00*	*35.10*	*50.96*	*240.0*	*50.96*	*50.96*	*450.0*
MMsm³/d	*90.15*	*8.99*	*36.76*	*52.85*	*2.00*	*7.52*	*56.99*	*51.34*	*5.65*	*5.65*	*1.91*	*1.16*	*0.62*	*0.13*	*44.72*	*50.07*	*50.19*
%Vapor	*53.20*	*0.00*	*0.00*	*100*	*0.00*	*100*	*100*	*100*	*0.00*	*0.00*	*100*	*100*	*100*	*0.00*	*100*	*100*	*0.00*
%CO_2	*39.72*	*55.16*	*0.13*	*67.39*	*0.64*	*68.40*	*68.57*	*69.57*	*59.43*	*59.43*	*45.59*	*22.08*	*83.66*	*92.99*	*69.58*	*70.62*	*70.68*
%CH_4	*14.59*	*6.91*	*0.00*	*23.36*	*0.04*	*19.05*	*23.58*	*25.61*	*5.12*	*5.12*	*49.53*	*74.47*	*12.37*	*2.49*	*25.61*	*24.53*	*24.48*
%C_2H_6	*1.36*	*2.75*	*0.00*	*2.34*	*0.09*	*3.15*	*2.43*	*2.39*	*2.84*	*2.84*	*2.25*	*2.12*	*2.58*	*1.76*	*2.39*	*2.40*	*2.40*
%C_3H_8	*0.75*	*4.83*	*0.00*	*1.66*	*0.46*	*2.93*	*1.72*	*1.29*	*5.57*	*5.57*	*0.61*	*0.25*	*1.06*	*1.70*	*1.29*	*1.32*	*1.32*
%i-C_4H_{10}	*0.13*	*1.99*	*0.00*	*0.43*	*0.39*	*0.82*	*0.42*	*0.21*	*2.34*	*2.34*	*0.06*	*0.01*	*0.10*	*0.29*	*0.21*	*0.22*	*0.22*
%C_4H_{10}	*0.29*	*6.10*	*0.00*	*1.13*	*1.70*	*2.34*	*1.10*	*0.44*	*7.11*	*7.11*	*0.09*	*0.01*	*0.14*	*0.57*	*0.44*	*0.45*	*0.45*
%i-C_5H_{12}	*0.09*	*3.22*	*0.00*	*0.50*	*1.95*	*0.94*	*0.43*	*0.09*	*3.53*	*3.53*	*0.01*	*0.00*	*0.01*	*0.09*	*0.09*	*0.09*	*0.09*
%C_5H_{12}	*0.14*	*4.97*	*0.00*	*0.74*	*3.81*	*1.34*	*0.60*	*0.09*	*5.26*	*5.26*	*0.01*	*0.00*	*0.01*	*0.08*	*0.09*	*0.09*	*0.09*
%C_6H_{14}	*0.15*	*3.44*	*0.00*	*0.53*	*5.76*	*0.50*	*0.31*	*0.02*	*3.00*	*3.00*	*0.00*	*0.00*	*0.00*	*0.01*	*0.02*	*0.02*	*0.02*
%C_7H_{16}	*0.21*	*2.27*	*0.00*	*0.38*	*8.74*	*0.08*	*0.15*	*0.00*	*1.50*	*1.50*	*0.00*	*0.00*	*0.00*	*0.00*	*0.00*	*0.00*	*0.00*
%C_8H_{18}	*0.23*	*2.02*	*0.00*	*0.34*	*10.04*	*0.02*	*0.09*	*0.00*	*0.93*	*0.93*	*0.00*	*0.00*	*0.00*	*0.00*	*0.00*	*0.00*	*0.00*
%C_9H_{20}	*0.18*	*1.32*	*0.00*	*0.22*	*8.15*	*0.00*	*0.04*	*0.00*	*0.40*	*0.40*	*0.00*	*0.00*	*0.00*	*0.00*	*0.00*	*0.00*	*0.00*
%$C_{10}H_{22}$	*0.16*	*0.94*	*0.00*	*0.16*	*7.33*	*0.00*	*0.02*	*0.00*	*0.18*	*0.18*	*0.00*	*0.00*	*0.00*	*0.00*	*0.00*	*0.00*	*0.00*
%$C_{11}H_{24}$	*0.11*	*0.63*	*0.00*	*0.11*	*4.89*	*0.00*	*0.01*	*0.00*	*0.07*	*0.07*	*0.00*	*0.00*	*0.00*	*0.00*	*0.00*	*0.00*	*0.00*
%$C_{12}H_{26}$	*0.13*	*0.52*	*0.00*	*0.09*	*5.93*	*0.00*	*0.00*	*0.00*	*0.04*	*0.04*	*0.00*	*0.00*	*0.00*	*0.00*	*0.00*	*0.00*	*0.00*
%$C_{13}H_{28}$	*0.09*	*0.35*	*0.00*	*0.06*	*3.95*	*0.00*	*0.00*	*0.00*	*0.01*	*0.01*	*0.00*	*0.00*	*0.00*	*0.00*	*0.00*	*0.00*	*0.00*
%$C_{14}H_{30}$	*0.12*	*0.27*	*0.00*	*0.05*	*5.21*	*0.00*	*0.00*	*0.00*	*0.01*	*0.01*	*0.00*	*0.00*	*0.00*	*0.00*	*0.00*	*0.00*	*0.00*
%$C_{15}H_{32}$	*0.07*	*0.16*	*0.00*	*0.03*	*3.13*	*0.00*	*0.00*	*0.00*	*0.00*	*0.00*	*0.00*	*0.00*	*0.00*	*0.00*	*0.00*	*0.00*	*0.00*
%$C_{16}H_{34}$	*0.05*	*0.11*	*0.00*	*0.02*	*2.09*	*0.00*	*0.00*	*0.00*	*0.00*	*0.00*	*0.00*	*0.00*	*0.00*	*0.00*	*0.00*	*0.00*	*0.00*
%$C_{17}H_{36}$	*0.07*	*0.09*	*0.00*	*0.02*	*3.27*	*0.00*	*0.00*	*0.00*	*0.00*	*0.00*	*0.00*	*0.00*	*0.00*	*0.00*	*0.00*	*0.00*	*0.00*
%$C_{18}H_{38}$	*0.04*	*0.06*	*0.00*	*0.01*	*1.96*	*0.00*	*0.00*	*0.00*	*0.00*	*0.00*	*0.00*	*0.00*	*0.00*	*0.00*	*0.00*	*0.00*	*0.00*
%$C_{19}H_{40}$	*0.03*	*0.12*	*0.00*	*0.02*	*1.31*	*0.00*	*0.00*	*0.00*	*0.00*	*0.00*	*0.00*	*0.00*	*0.00*	*0.00*	*0.00*	*0.00*	*0.00*
%C_{20+}	*0.43*	*0.01*	*0.00*	*0.00*	*19.16*	*0.00*	*0.00*	*0.00*	*0.00*	*0.00*	*0.00*	*0.00*	*0.00*	*0.00*	*0.00*	*0.00*	*0.00*
%N_2	*0.15*	*0.03*	*0.00*	*0.25*	*0.00*	*0.12*	*0.25*	*0.27*	*0.02*	*0.02*	*0.66*	*1.05*	*0.06*	*0.01*	*0.27*	*0.25*	*0.25*
ppm H_2S	*29.65*	*82.48*	*0.00*	*51.99*	*4.19*	*85.75*	*55.35*	*51.59*	*89.53*	*89.53*	*29.54*	*12.70*	*52.86*	*71.32*	*52.44*	*52.47*	*52.49*
ppm H_2O				*2606*	*18.90*	*2974*	*2687*	*88.48*	*26295*	*26295*	*7.15*	*0.06*	*5.69*	*79.95*	*88.62*	*90.70*	*90.68*
%H_2O	*40.70*	*1.73*	*99.87*	*0.261*		*0.297*	*0.269*		*2.630*	*2.630*							

Table P.2. Streams of gas-hub for CO_2 ultra-rich NG: Case [NR+JT+SS].

System	*HPS*				*Oil*	*VRU*	*SS WDPA+HCDPA*				*SS CO_2 Removal*				*Main Compressor*		*EOR*
Stream	***Riser***	***Main Recycle***	***HPS Water***	***HPS Gas***	***Final Oil***	***VRU Gas***	***Feed***	***Gas SS***	***L+W SS***	***L+W LTX***	***Feed***	***FG***	***GCO2***	***LCO2***	***DHG***	***MC Gas***	***Final Fluid***
T(°C)	*30.0*	*N.A.*	*30.0*	*30.0*	*40.0*	*45.0*	*45.3*	*40.5*	*-20.1*	*20.0*	*-22.0*	*35*	*45.0*	*18.3*	*40.5*	*41.3*	*78.6*
P(bar)	*120.0*	*N.A.*	*120.0*	*120.0*	*1.30*	*80.50*	*80.50*	*59.33*	*59.33*	*59.33*	*84.00*	*37.90*	*59.33*	*240.0*	*59.33*	*59.33*	*450.0*
MMsm³/d	*90.15*	*N.A.*	*36.64*	*47.98*	*1.43*	*4.12*	*51.38*	*47.40*	*3.98*	*3.98*	*1.92*	*1.27*	*0.53*	*0.13*	*37.77*	*46.01*	*50.72*
%Vapor	*53.20*	*N.A.*	*0.00*	*100*	*0.00*	*100*	*100*	*100*	*0.00*	*0.00*	*100*	*100*	*100*	*0.00*	*100*	*100*	*0.00*
%CO_2	*39.72*	*N.A.*	*0.13*	*68.41*	*0.80*	*71.11*	*68.93*	*68.70*	*71.69*	*71.69*	*43.48*	*21.69*	*83.95*	*93.67*	*68.70*	*69.93*	*69.94*
%CH_4	*14.59*	*N.A.*	*0.00*	*25.74*	*0.06*	*19.54*	*25.46*	*27.15*	*5.36*	*5.36*	*53.10*	*74.95*	*12.53*	*2.70*	*27.15*	*25.90*	*24.06*
%C_2H_6	*1.36*	*N.A.*	*0.00*	*2.27*	*0.11*	*3.34*	*2.35*	*2.34*	*2.55*	*2.55*	*2.08*	*2.00*	*2.39*	*1.64*	*2.34*	*2.35*	*2.37*
%C_3H_8	*0.75*	*N.A.*	*0.00*	*1.18*	*0.42*	*2.50*	*1.26*	*1.04*	*3.87*	*3.87*	*0.48*	*0.22*	*0.89*	*1.36*	*1.04*	*1.06*	*1.31*
%i-C_4H_{10}	*0.13*	*N.A.*	*0.00*	*0.20*	*0.22*	*0.48*	*0.21*	*0.13*	*1.18*	*1.18*	*0.04*	*0.01*	*0.07*	*0.19*	*0.13*	*0.13*	*0.23*
%C_4H_{10}	*0.29*	*N.A.*	*0.00*	*0.42*	*0.79*	*1.15*	*0.46*	*0.24*	*3.13*	*3.13*	*0.05*	*0.01*	*0.09*	*0.33*	*0.24*	*0.24*	*0.49*
%i-C_5H_{12}	*0.09*	*N.A.*	*0.00*	*0.13*	*0.61*	*0.35*	*0.14*	*0.04*	*1.28*	*1.28*	*0.00*	*0.00*	*0.01*	*0.04*	*0.04*	*0.04*	*0.15*
%C_5H_{12}	*0.14*	*N.A.*	*0.00*	*0.19*	*1.15*	*0.51*	*0.19*	*0.04*	*1.99*	*1.99*	*0.00*	*0.00*	*0.01*	*0.04*	*0.04*	*0.04*	*0.22*
%C_6H_{14}	*0.15*	*N.A.*	*0.00*	*0.18*	*2.34*	*0.34*	*0.16*	*0.01*	*1.88*	*1.88*	*0.00*	*0.00*	*0.00*	*0.01*	*0.01*	*0.01*	*0.20*
%C_7H_{16}	*0.21*	*N.A.*	*0.00*	*0.18*	*6.14*	*0.18*	*0.13*	*0.00*	*1.67*	*1.67*	*0.00*	*0.00*	*0.00*	*0.00*	*0.00*	*0.00*	*0.19*
%C_8H_{18}	*0.23*	*N.A.*	*0.00*	*0.18*	*8.15*	*0.07*	*0.10*	*0.00*	*1.27*	*1.27*	*0.00*	*0.00*	*0.00*	*0.00*	*0.00*	*0.00*	*0.18*
%C_9H_{20}	*0.18*	*N.A.*	*0.00*	*0.12*	*7.38*	*0.01*	*0.05*	*0.00*	*0.63*	*0.63*	*0.00*	*0.00*	*0.00*	*0.00*	*0.00*	*0.00*	*0.12*
%$C_{10}H_{22}$	*0.16*	*N.A.*	*0.00*	*0.09*	*7.35*	*0.00*	*0.02*	*0.00*	*0.32*	*0.32*	*0.00*	*0.00*	*0.00*	*0.00*	*0.00*	*0.00*	*0.08*
%$C_{11}H_{24}$	*0.11*	*N.A.*	*0.00*	*0.06*	*4.90*	*0.00*	*0.01*	*0.00*	*0.14*	*0.14*	*0.00*	*0.00*	*0.00*	*0.00*	*0.00*	*0.00*	*0.06*
%$C_{12}H_{26}$	*0.13*	*N.A.*	*0.00*	*0.05*	*6.71*	*0.00*	*0.01*	*0.00*	*0.07*	*0.07*	*0.00*	*0.00*	*0.00*	*0.00*	*0.00*	*0.00*	*0.04*
%$C_{13}H_{28}$	*0.09*	*N.A.*	*0.00*	*0.03*	*4.47*	*0.00*	*0.00*	*0.00*	*0.03*	*0.03*	*0.00*	*0.00*	*0.00*	*0.00*	*0.00*	*0.00*	*0.03*
%$C_{14}H_{30}$	*0.12*	*N.A.*	*0.00*	*0.02*	*6.52*	*0.00*	*0.00*	*0.00*	*0.01*	*0.01*	*0.00*	*0.00*	*0.00*	*0.00*	*0.00*	*0.00*	*0.02*
%$C_{15}H_{32}$	*0.07*	*N.A.*	*0.00*	*0.01*	*3.91*	*0.00*	*0.00*	*0.00*	*0.00*	*0.00*	*0.00*	*0.00*	*0.00*	*0.00*	*0.00*	*0.00*	*0.01*
%$C_{16}H_{34}$	*0.05*	*N.A.*	*0.00*	*0.01*	*2.61*	*0.00*	*0.00*	*0.00*	*0.00*	*0.00*	*0.00*	*0.00*	*0.00*	*0.00*	*0.00*	*0.00*	*0.01*
%$C_{17}H_{36}$	*0.07*	*N.A.*	*0.00*	*0.01*	*4.09*	*0.00*	*0.00*	*0.00*	*0.00*	*0.00*	*0.00*	*0.00*	*0.00*	*0.00*	*0.00*	*0.00*	*0.01*
%$C_{18}H_{38}$	*0.04*	*N.A.*	*0.00*	*0.00*	*2.46*	*0.00*	*0.00*	*0.00*	*0.00*	*0.00*	*0.00*	*0.00*	*0.00*	*0.00*	*0.00*	*0.00*	*0.00*
%$C_{19}H_{40}$	*0.03*	*N.A.*	*0.00*	*0.01*	*1.64*	*0.00*	*0.00*	*0.00*	*0.00*	*0.00*	*0.00*	*0.00*	*0.00*	*0.00*	*0.00*	*0.00*	*0.01*
%C_{20+}	*0.43*	*N.A.*	*0.00*	*0.00*	*27.17*	*0.00*	*0.00*	*0.00*	*0.00*	*0.00*	*0.00*	*0.00*	*0.00*	*0.00*	*0.00*	*0.00*	*0.00*
%N_2	*0.15*	*N.A.*	*0.00*	*0.28*	*0.00*	*0.11*	*0.23*	*0.29*	*0.02*	*0.02*	*0.77*	*1.13*	*0.07*	*0.01*	*0.29*	*0.27*	*0.25*
ppm H_2S	*29.65*	*N.A.*	*0.00*	*47.43*	*5.25*	*91.62*	*50.71*	*47.73*	*86.23*	*86.23*	*26.08*	*12.04*	*50.07*	*67.05*	*47.73*	*48.66*	*52.00*
ppm H_2O		*N.A.*		*2241*	*18.06*	*2960*	*2308*	*71.75*	*28939*	*28939*	*6.37*	*0.05*	*5.53*	*73.38*	*71.75*	*73.72*	*269.76*
%H_2O	*40.70*	*N.A.*	*99.87*	*0.224*		*0.296*	*0.231*		*2.894*	*2.894*							

Table P.3. Streams of gas-hub for CO_2 ultra-rich NG: Case [RC+JT+MP].

System	*HPS*				*Oil*	*VRU*	*SS WDPA+HCDPA*				*MP CO_2 Removal*				*Main Compressor*		*EOR*
Stream	***Riser***	***Main Recycle***	***HPS Water***	***HPS Gas***	***Final Oil***	***VRU Gas***	***Feed***	***Gas SS***	***L+W SS***	***L+W LTX***	***Feed***	***FG***	***GCO2***	***LCO2***	***DHG***	***MC Gas***	***Final Fluid***
T(°C)	*30.0*	*36.4*	*32.5*	*32.5*	*42.5*	*45.0*	*46.3*	*37.7*	*-17.0*	*20.0*	*62.0*	*44.4*	*45.0*	*N.A.*	*37.7*	*38.2*	*80.5*
P(bar)	*120.0*	*120.0*	*120.0*	*120.0*	*1.30*	*80.50*	*80.50*	*53.74*	*53.74*	*53.74*	*43.13*	*42.13*	*53.74*	*N.A.*	*53.74*	*53.74*	*450.00*
MMsm³/d	*90.15*	*8.31*	*36.76*	*52.24*	*2.00*	*7.44*	*56.68*	*51.39*	*5.29*	*5.29*	*4.90*	*1.34*	*3.56*	*N.A.*	*46.49*	*50.05*	*50.05*
%Vapor	*53.20*	*0.00*	*0.00*	*100*	*0.00*	*100*	*100*	*100*	*0.00*	*0.00*	*100*	*100*	*100*	*N.A.*	*100*	*100*	*0.00*
%CO_2	*39.72*	*54.39*	*0.13*	*67.31*	*0.64*	*68.51*	*68.52*	*69.57*	*58.39*	*58.39*	*69.57*	*20.00*	*88.31*	*N.A.*	*69.57*	*70.90*	*70.90*
%CH_4	*14.59*	*6.91*	*0.00*	*23.55*	*0.05*	*19.12*	*23.70*	*25.60*	*5.20*	*5.20*	*25.60*	*62.87*	*11.50*	*N.A.*	*25.60*	*24.60*	*24.60*
%C_2H_6	*1.36*	*2.76*	*0.00*	*2.34*	*0.09*	*3.15*	*2.43*	*2.39*	*2.85*	*2.85*	*2.39*	*8.60*	*0.04*	*N.A.*	*2.39*	*2.22*	*2.22*
%C_3H_8	*0.75*	*4.81*	*0.00*	*1.62*	*0.46*	*2.89*	*1.69*	*1.29*	*5.55*	*5.55*	*1.29*	*4.71*	*0.00*	*N.A.*	*1.29*	*1.20*	*1.20*
%i-C_4H_{10}	*0.13*	*1.97*	*0.00*	*0.41*	*0.37*	*0.80*	*0.41*	*0.21*	*2.32*	*2.32*	*0.21*	*0.78*	*0.00*	*N.A.*	*0.21*	*0.20*	*0.20*
%C_4H_{10}	*0.29*	*6.04*	*0.00*	*1.08*	*1.64*	*2.25*	*1.06*	*0.44*	*7.07*	*7.07*	*0.44*	*1.62*	*0.00*	*N.A.*	*0.44*	*0.41*	*0.41*
%i-C_5H_{12}	*0.09*	*3.25*	*0.00*	*0.47*	*1.88*	*0.91*	*0.42*	*0.09*	*3.60*	*3.60*	*0.09*	*0.33*	*0.00*	*N.A.*	*0.09*	*0.08*	*0.08*
%C_5H_{12}	*0.14*	*5.09*	*0.00*	*0.72*	*3.71*	*1.32*	*0.60*	*0.10*	*5.47*	*5.47*	*0.10*	*0.35*	*0.00*	*N.A.*	*0.10*	*0.09*	*0.09*
%C_6H_{14}	*0.15*	*3.67*	*0.00*	*0.53*	*5.80*	*0.51*	*0.32*	*0.02*	*3.28*	*3.28*	*0.02*	*0.06*	*0.00*	*N.A.*	*0.02*	*0.02*	*0.02*
%C_7H_{16}	*0.21*	*2.41*	*0.00*	*0.37*	*8.81*	*0.09*	*0.16*	*0.00*	*1.65*	*1.65*	*0.00*	*0.01*	*0.00*	*N.A.*	*0.00*	*0.00*	*0.00*
%C_8H_{18}	*0.23*	*2.12*	*0.00*	*0.33*	*10.10*	*0.02*	*0.10*	*0.00*	*1.03*	*1.03*	*0.00*	*0.00*	*0.00*	*N.A.*	*0.00*	*0.00*	*0.00*
%C_9H_{20}	*0.18*	*1.38*	*0.00*	*0.22*	*8.18*	*0.00*	*0.04*	*0.00*	*0.44*	*0.44*	*0.00*	*0.00*	*0.00*	*N.A.*	*0.00*	*0.00*	*0.00*
%$C_{10}H_{22}$	*0.16*	*0.97*	*0.00*	*0.15*	*7.35*	*0.00*	*0.02*	*0.00*	*0.20*	*0.20*	*0.00*	*0.00*	*0.00*	*N.A.*	*0.00*	*0.00*	*0.00*
%$C_{11}H_{24}$	*0.11*	*0.65*	*0.00*	*0.10*	*4.90*	*0.00*	*0.01*	*0.00*	*0.08*	*0.08*	*0.00*	*0.00*	*0.00*	*N.A.*	*0.00*	*0.00*	*0.00*
%$C_{12}H_{26}$	*0.13*	*0.53*	*0.00*	*0.08*	*5.93*	*0.00*	*0.00*	*0.00*	*0.04*	*0.04*	*0.00*	*0.00*	*0.00*	*N.A.*	*0.00*	*0.00*	*0.00*
%$C_{13}H_{28}$	*0.09*	*0.35*	*0.00*	*0.06*	*3.96*	*0.00*	*0.00*	*0.00*	*0.02*	*0.02*	*0.00*	*0.00*	*0.00*	*N.A.*	*0.00*	*0.00*	*0.00*
%$C_{14}H_{30}$	*0.12*	*0.28*	*0.00*	*0.04*	*5.21*	*0.00*	*0.00*	*0.00*	*0.01*	*0.01*	*0.00*	*0.00*	*0.00*	*N.A.*	*0.00*	*0.00*	*0.00*
%$C_{15}H_{32}$	*0.07*	*0.17*	*0.00*	*0.03*	*3.13*	*0.00*	*0.00*	*0.00*	*0.00*	*0.00*	*0.00*	*0.00*	*0.00*	*N.A.*	*0.00*	*0.00*	*0.00*
%$C_{16}H_{34}$	*0.05*	*0.11*	*0.00*	*0.02*	*2.08*	*0.00*	*0.00*	*0.00*	*0.00*	*0.00*	*0.00*	*0.00*	*0.00*	*N.A.*	*0.00*	*0.00*	*0.00*
%$C_{17}H_{36}$	*0.07*	*0.09*	*0.00*	*0.01*	*3.25*	*0.00*	*0.00*	*0.00*	*0.00*	*0.00*	*0.00*	*0.00*	*0.00*	*N.A.*	*0.00*	*0.00*	*0.00*
%$C_{18}H_{38}$	*0.04*	*0.05*	*0.00*	*0.01*	*1.95*	*0.00*	*0.00*	*0.00*	*0.00*	*0.00*	*0.00*	*0.00*	*0.00*	*N.A.*	*0.00*	*0.00*	*0.00*
%$C_{19}H_{40}$	*0.03*	*0.12*	*0.00*	*0.02*	*1.30*	*0.00*	*0.00*	*0.00*	*0.00*	*0.00*	*0.00*	*0.00*	*0.00*	*N.A.*	*0.00*	*0.00*	*0.00*
%C_{20+}	*0.43*	*0.01*	*0.00*	*0.00*	*19.21*	*0.00*	*0.00*	*0.00*	*0.00*	*0.00*	*0.00*	*0.00*	*0.00*	*N.A.*	*0.00*	*0.00*	*0.00*
%N_2	*0.15*	*0.03*	*0.00*	*0.25*	*0.00*	*0.12*	*0.25*	*0.27*	*0.02*	*0.02*	*0.27*	*0.66*	*0.12*	*N.A.*	*0.27*	*0.26*	*0.26*
ppm H_2S	*29.65*	*81.91*	*0.00*	*51.57*	*4.21*	*85.63*	*55.08*	*51.61*	*88.83*	*88.83*	*51.61*	*14.84*	*65.52*	*N.A.*	*51.61*	*52.60*	*52.60*
ppm H_2O		*18396*		*2584*	*18.93*	*2972*	*2666*	*95.90*	*27651*	*27651*	*95.90*	*27.57*	*121.7*	*N.A.*	*95.90*	*97.74*	*97.74*
%H_2O	*40.70*	*1.84*	*99.87*			*0.297*	*0.267*		*2.765*	*2.765*				*N.A.*			

APPENDIX Q - ANALOGUES OF TABLE 4 FOR CASES [RC+TX+SS], [NR+JT+SS], [RC+JT+MP]

Table Q.1. SS design parameters and results of 1st (WDPA+HCDPA) and 2nd (CO_2 removal) SS units: Case [RC+TX+SS].

Specified Items	*WDPA HCDPA*	*CO_2 Capture*	*Calculated by SS-UOE*	*WDPA HCDPA*	*CO_2 Capture*
No.of SS	*12*	*1*	*$D_T(m)$*	*0.0666*	*0.03421*
$D_I(m)$	*0.10*	*0.08*	*$L_C(m)$*	*0.0744*	*0.1601*
$D_O(m)$	*0.12*	*0.09*	*$L_D(m)$*	*0.1445*	*0.6749*
$\alpha(^o)$	*12.67*	*15*	*$L(m)$*	*0.2188*	*0.8350*
$\beta(^o)$	*2.66*	*2.5*	*$L^{Shock}(m)$*	*0.1664*	*0.2570*
Ma^{Shock}	*1.52*	*1.6*	*$L^{Diff}(m)$*	*0.0524*	*0.5780*
$\eta^{EXP}\%$	*100*	*100*	*$P_{BS}(bar)$*	*24.95*	*21.60*
$\eta^{CMP}\%$	*100*	*100*	*$T_{BS}(^oC)$*	*-17.95*	*-60.92*
$P^{Feed}(bar)$	*80.5*	*84.0*	*Ma_{BS}*	*1.3055**	*0.9384*+*
$T^{Feed}(^oC)$	*45*	*-22*	*$P^{Discharge}(bar)$*	*50.96*	*35.60*
$MMsm^3/d$	*56.99*	*1.91*	*$T^{Discharge}(^oC)$*	*34.19*	*-29.85*
$\%C3^{+Feed}$	*4.90%*	*0.78%*	*%Condensate*	*9.91%*	*39.11%*
$ppmH_2O^{Feed}$	*2687*	*7.15*	*$REC\%CO_2$*	*8.59%*	*71.26%*
$\%CO_2^{Feed}$	*68.57%*	*46.78%*	*%P Recovery*	*63.31%*	*42.38%*

**After condensate withdrawal* +*Normal shock does not occur*

Table Q.2. SS design parameters and results of 1st (WDPA+HCDPA) and 2nd (CO_2 removal) SS units: Case [NR+JT+SS].

Specified Items	*WDPA HCDPA*	*CO_2 Capture*	*Calculated by SS-UOE*	*WDPA HCDPA*	*CO_2 Capture*
No.of SS	*12*	*1*	*$D_T(m)$*	*0.0627*	*0.0347*
$D_I(m)$	*0.10*	*0.08*	*$L_C(m)$*	*0.0830*	*0.1592*
$D_O(m)$	*0.12*	*0.09*	*$L_D(m)$*	*0.1867*	*0.6346*
$\alpha(^o)$	*12.67*	*15*	*$L(m)$*	*0.2697*	*0.7938*
$\beta(^o)$	*2.66*	*2.5*	*$L^{Shock}(m)$*	*0.1549*	*0.2517*
Ma^{Shock}	*1.52*	*1.6*	*$L^{Diff}(m)$*	*0.1148*	*0.5421*
$\eta^{EXP}\%$	*100*	*100*	*$P_{BS}(bar)$*	*26.15*	*21.80*
$\eta^{CMP}\%$	*100*	*100*	*$T_{BS}(^oC)$*	*-20.21*	*-61.28*
$P^{Feed}(bar)$	*80.5*	*84.0*	*Ma_{BS}*	*1.3217**	*1.0062**
$T^{Feed}(^oC)$	*45*	*-22*	*$P^{Discharge}(bar)$*	*59.33*	*38.40*
$MMsm^3/d$	*51.38*	*1.92*	*$T^{Discharge}(^oC)$*	*36.45*	*-25.79*
$\%C3^{+Feed}$	*2.75%*	*0.57%*	*%Condensate*	*7.75%*	*33.97%*
$ppmH_2O^{Feed}$	*2308*	*6.37*	*$REC\%CO_2$*	*8.06%*	*67.06%*
$\%CO_2^{Feed}$	*68.93%*	*43.48%*	*%P Recovery*	*73.71%*	*45.71%*

**After condensate withdrawal*

Table Q.3. SS design parameters and results of 1st (WDPA+HCDPA) SS unit: Case [RC+JT+MP] (No 2nd SS unit).

Specified Items	***WDPA HCDPA***	***CO_2 Capture***	***Calculated by SS-UOE***	***WDPA HCDPA***	***CO_2 Capture***
No.of SS	*12*	*-*	*D_T(m)*	*0.0662*	*-*
D_I(m)	*0.10*	*-*	*L_C(m)*	*0.0752*	*-*
D_O(m)	*0.12*	*-*	*L_D(m)*	*0.1486*	*-*
$\alpha(^o)$	*12.67*	*-*	*L(m)*	*0.2238*	*-*
$\beta(^o)$	*2.66*	*-*	*L^{Shock}(m)*	*0.1596*	*-*
Ma^{Shock}	*1.52*	*-*	*L^{Diff}(m)*	*0.0642*	*-*
η^{EXP}%	*100*	*-*	*P_{BS}(bar)*	*25.60*	*-*
η^{CMP}%	*100*	*-*	*$T_{BS}(^oC)$*	*-16.78*	*-*
P^{Feed}(bar)	*80.5*	*-*	*Ma_{BS}*	*1.3114**	*-*
$T^{Feed}(^oC)$	*45*	*-*	*$P^{Discharge}$(bar)*	*53.74*	*-*
MMsm^3/d	*56.7*	*-*	*$T^{Discharge}(^oC)$*	*37.73*	*-*
%$C3^{+Feed}$	*4.83%*	*-*	*%Condensate*	*9.33%*	*-*
ppmH_2O^{Feed}	*2666*	*-*	*REC%CO_2*	*7.95%*	*-*
%CO_2^{Feed}	*68.52%*	*-*	*%P Recovery*	*66.76%*	*-*

**After condensate withdrawal*

APPENDIX R - ANALOGUES OF FIGURE V.11 FOR CASES [RC+TX+SS], [NR+JT+SS], [RC+JT+MP]

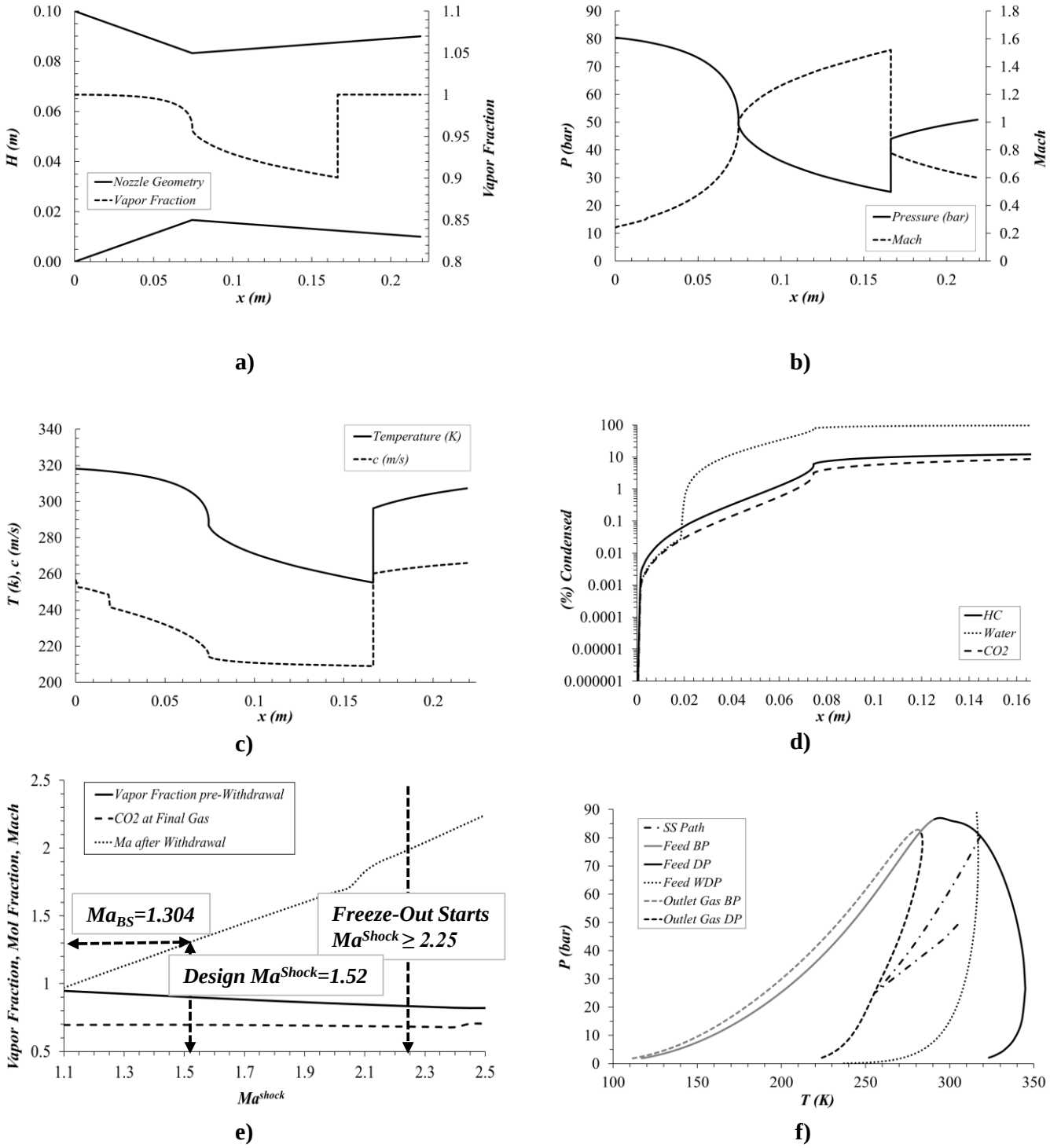

Figure R.1. SS WDPA/HCDPA results for [RC+TX+SS]: a) SS walls & vapor fraction *vs x(m)*; b) *P(bar), Ma vs x(m)*; c) *T(K), c(m/s) vs x(m)*; d) *hydrocarbons, CO_2 & H_2O %Condensed vs x(m)*; e) *Ma_{BS} vs Ma^{Shock}* & CO_2 Freeze-Out; f) plane *PxT*: feed WDP curve, feed VLE envelope, feed SVLE freeze-out border, Dehydrated-Gas product VLE envelope and SS path.

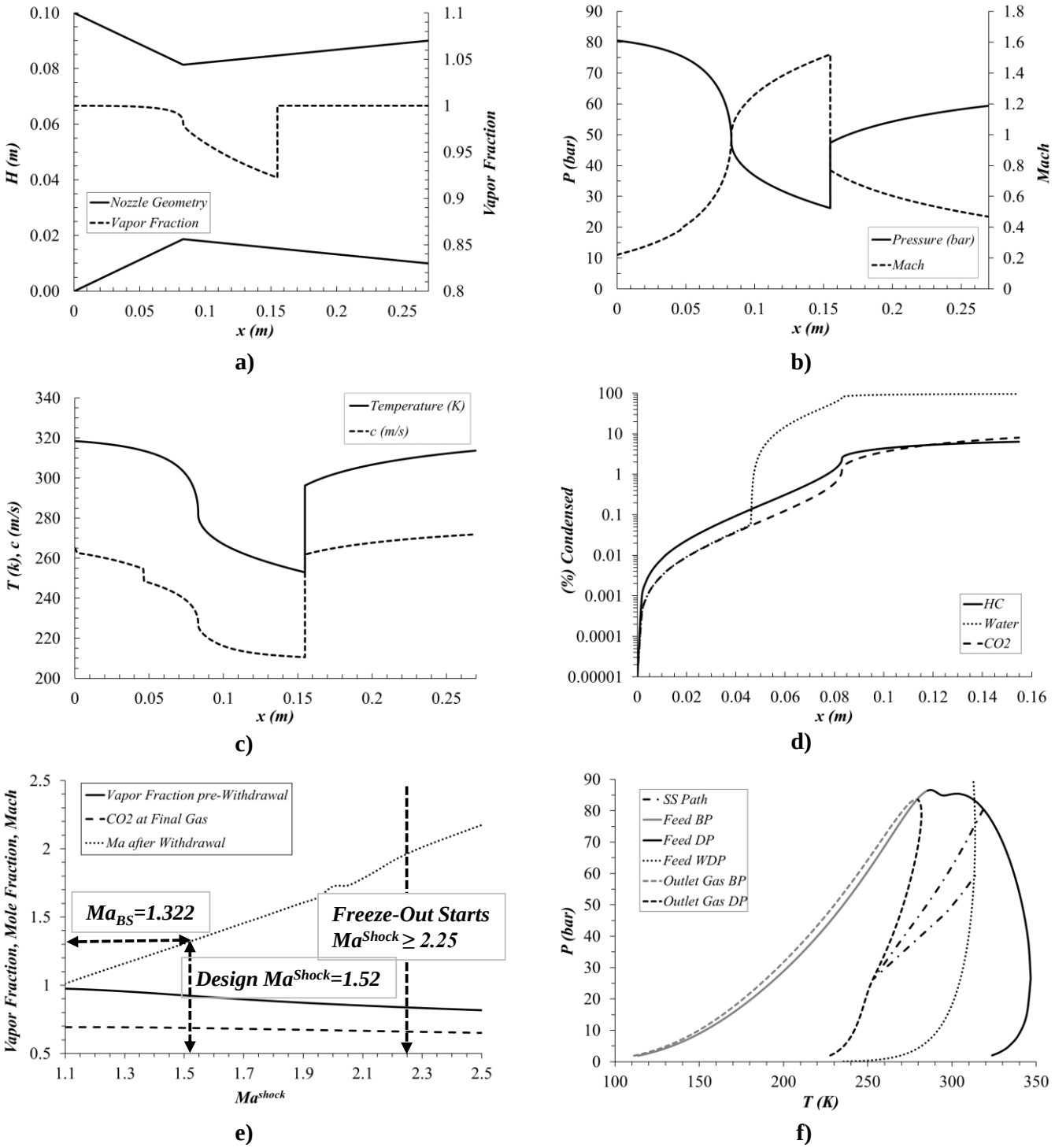

Figure R.2. SS WDPA/HCDPA results for [NR+JT+SS]: a) SS walls & vapor fraction *vs x(m)*; b) *P(bar), Ma vs x(m)*; c) *T(K), c(m/s) vs x(m)*; d) *hydrocarbons, CO_2 & H_2O %Condensed vs x(m)*; e) Ma_{BS} *vs* Ma^{Shock} & CO_2 Freeze-Out; f) plane *PxT*: feed WDP curve, feed VLE envelope, feed SVLE freeze-out border, Dehydrated-Gas product VLE envelope and SS path.

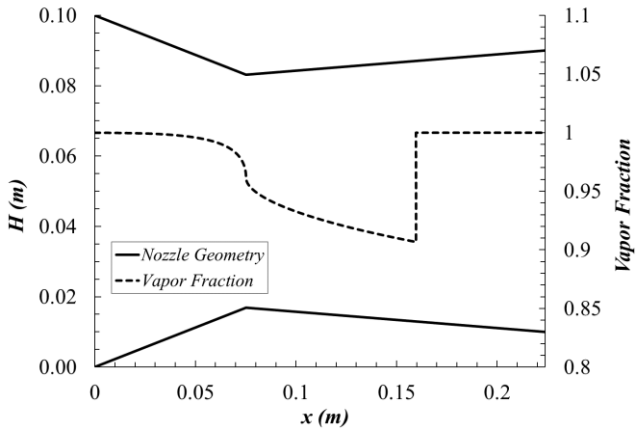

a)

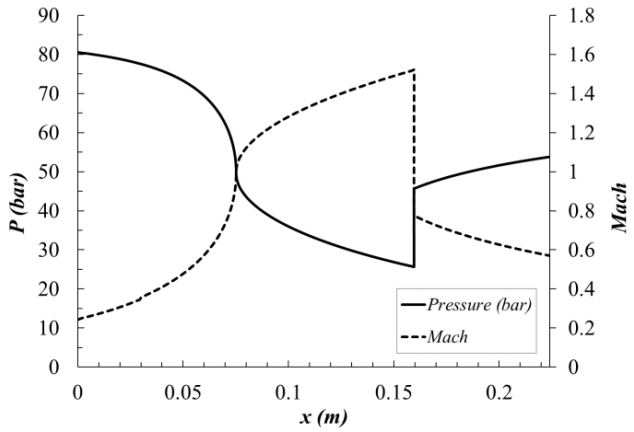

b)

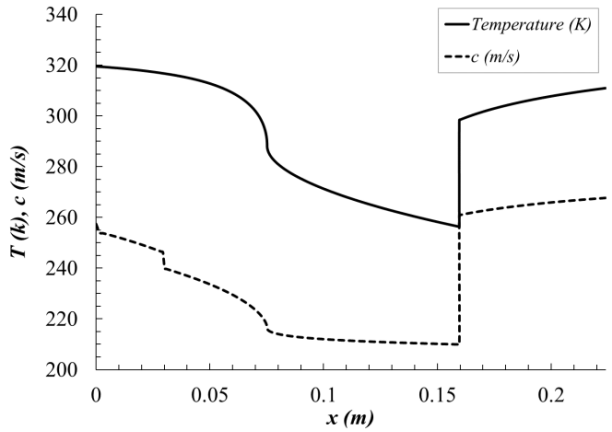

c)

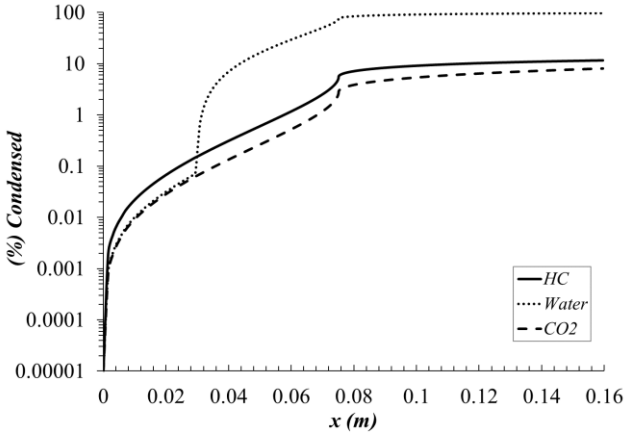

d)

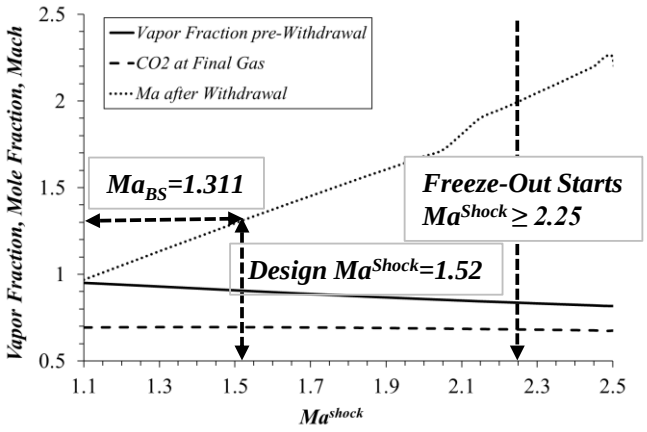

e)

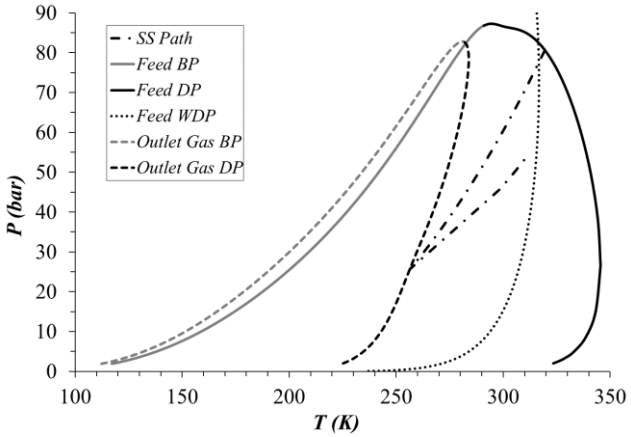

f)

Figure R.3. SS WDPA/HCDPA results for [RC+JT+MP]: a) SS walls & vapor fraction *vs x(m)*; b) *P(bar), Ma vs x(m)*; c) *T(K), c(m/s) vs x(m)*; d) *hydrocarbons, CO_2 & H_2O %Condensed vs x(m)*; e) Ma_{BS} *vs* Ma^{Shock} & CO_2 Freeze-Out; f) plane *PxT*: feed WDP curve, feed VLE envelope, feed SVLE freeze-out border, Dehydrated-Gas product VLE envelope and SS path.

APPENDIX S - ANALOGUES OF FIGURE V.12 FOR CASES [RC+TX+SS], [NR+JT+SS]

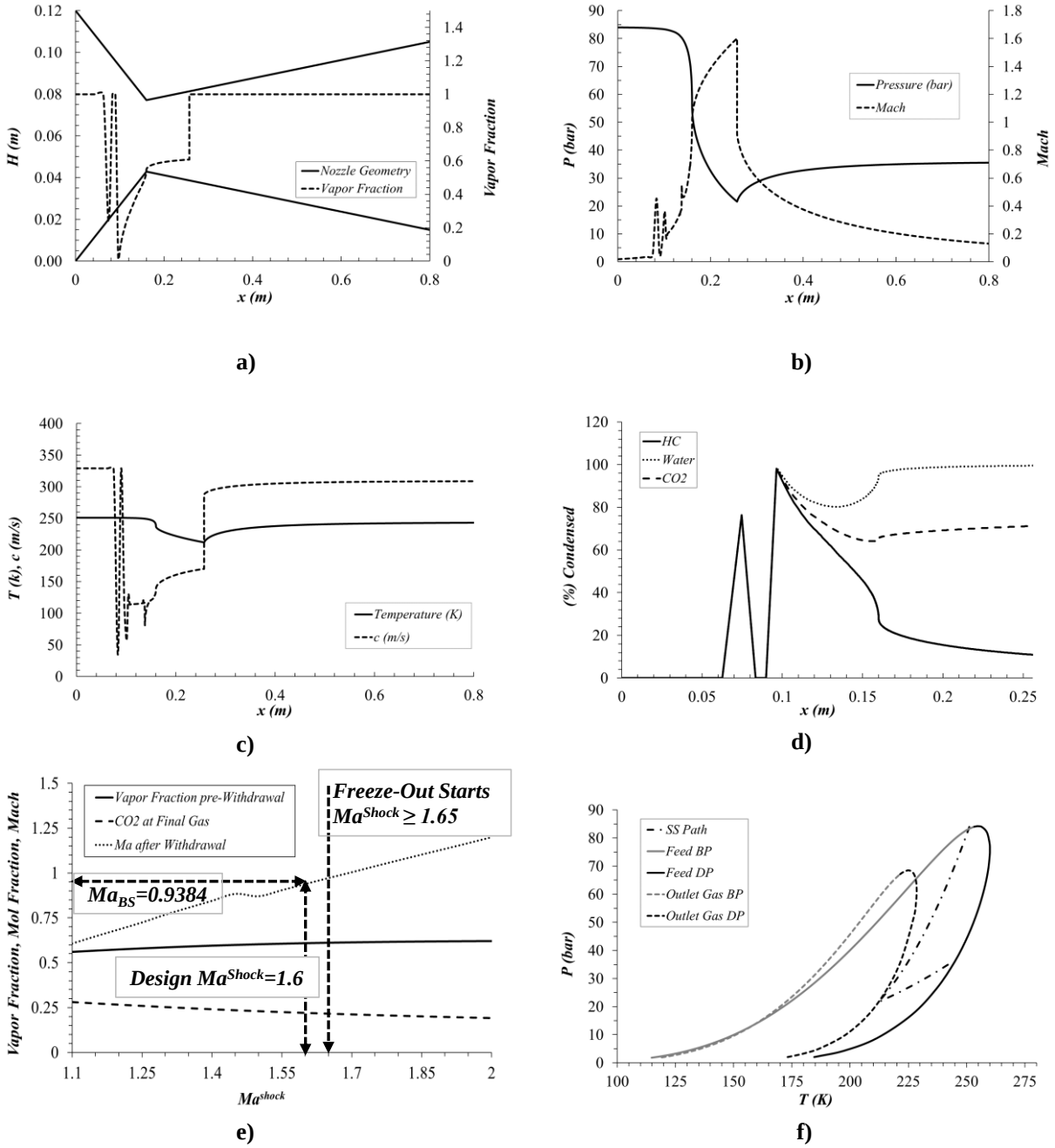

Figure S.1. SS CO_2 removal results for [RC+TX+SS]: a) SS walls & vapor fraction *vs x(m)*; b) *P(bar), Ma vs x(m)*; c) *T(K), c(m/s) vs x(m)*; d) *hydrocarbons, CO_2 & H_2O %Condensed vs x(m)*; e) Ma_{BS} *vs* Ma^{Shock} & CO_2 Freeze-Out; f) plane *PxT*: feed VLE envelope, feed SVLE freeze-out border, Fuel-Gas product VLE envelope and SS path.

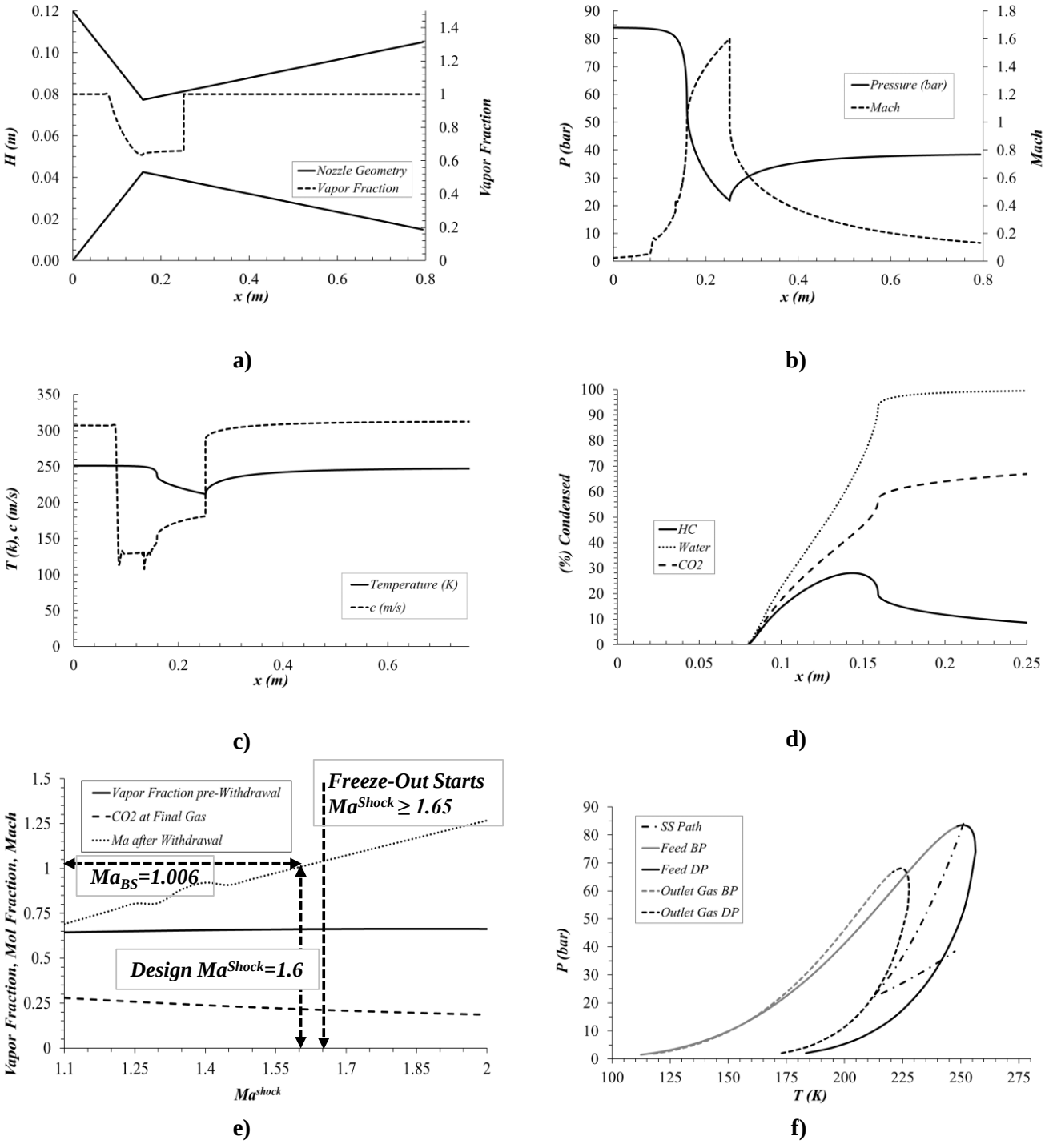

Figure S.2. SS CO_2 removal results for [NR+JT+SS]: a) SS walls & vapor fraction *vs x(m)*; b) *P(bar), Ma vs x(m)*; c) *T(K), c(m/s) vs x(m)*; d) *hydrocarbons, CO_2 & H_2O %Condensed vs x(m)*; e) Ma_{BS} *vs* Ma^{Shock} & CO_2 Freeze-Out; f) plane *PxT*: feed VLE envelope, feed SVLE freeze-out border, Fuel-Gas product VLE envelope and SS path.

APPENDIX T – PUBLICATIONS RESULTED FROM THIS THESIS RESEARCH

T.1. Dynamic Simulation and Analysis of Slug Flow Impact on Offshore Natural Gas Processing: TEG Dehydration, Joule-Thomson Expansion and Membrane Separation. Proceedings of 12th International Symposium on Process Systems Engineering and 25th European Symposium on Computer Aided Process Engineering, 2015. doi: https://doi.org/10.1016/B978-0-444-63577-8.50141-8

Krist V. Gernaey, Jakob K. Huusom and Rafiqul Gani (Eds.), 12th International Symposium on Process Systems Engineering and 25th European Symposium on Computer Aided Process Engineering.
31 May – 4 June 2015, Copenhagen, Denmark © 2015 Elsevier B.V. All rights reserved.

Dynamic Simulation and Analysis of Slug Flow Impact on Offshore Natural Gas Processing: TEG Dehydration, Joule-Thomson Expansion and Membrane Separation

Lara de O. Arinelli[a]*, Ofélia Q. F. Araújo[a], José Luiz de Medeiros[a]

[a]*Federal University of Rio de Janeiro, Av. Athos da Silveira Ramos, 149, Rio de Janeiro 21941-909, Brazil*
**lara.arinelli@gmail.com*

Abstract

Crude natural gas (NG) can contain a significant amount of contaminants that must be removed to guarantee safe transportation and sales specification. Water and hydrocarbon dew point (WDP and HCDP) adjustments are important for conditioning NG. In Brazil, Pre-Salt reservoirs have large amounts of NG with high CO_2 content, which also must be adjusted by a suitable operation like Membrane Permeation (MP). Furthermore, offshore processing requires reduced footprints, which minimize inventories and, consequently, intensify propagation of feed disturbances to downstream units. The dynamic scenario is inherently related to riser oscillations caused by slug flow, that may cause operational problems, losses and environmental and safety issues. Hence, the process control system must be sufficiently robust to ensure stability within such context. This work approaches the dynamical analysis of an offshore NG treating process for a typical Pre-Salt feed with the following operations: phase separation,

T.2. Performance Analysis and Comparison of Membrane Permeation versus Supersonic Separators for CO_2 Removal from a Plausible Natural gas of Libra Field, Brazil. Proceedings of Offshore Technology Conference Brazil (OTC Brazil), 2015.

OTC-26164-MS

Performance Analysis and Comparison of Membrane Permeation Versus Supersonic Separators for CO_2 Removal From a Plausible Natural Gas of Libra Field, Brazil

L. O. Arinelli, J. L. de Medeiros, and O. Q. Araújo, Federal University of Rio de Janeiro

Copyright 2015, Offshore Technology Conference

This paper was prepared for presentation at the Offshore Technology Conference Brasil held in Rio de Janeiro, Brazil, 27–29 October 2015.

This paper was selected for presentation by an OTC program committee following review of information contained in an abstract submitted by the author(s). Contents of the paper have not been reviewed by the Offshore Technology Conference and are subject to correction by the author(s). The material does not necessarily reflect any position of the Offshore Technology Conference, its officers, or members. Electronic reproduction, distribution, or storage of any part of this paper without the written consent of the Offshore Technology Conference is prohibited. Permission to reproduce in print is restricted to an abstract of not more than 300 words; illustrations may not be copied. The abstract must contain conspicuous acknowledgment of OTC copyright.

Abstract

Libra Field is a giant oil and gas offshore field situated in Santos Basin, at 200 km from southeastern Brazil coast, 2200 m water depth and 5 km crust depth. The product of Libra is a 27°API oil with a remarkable characteristic: an impressive gas/oil ratio of approximately 600 sm^3/m^3 with a CO_2 content over 40%mol. The extraction of this oil obligates the processing of such CO_2 rich gas, which must end with the reinjection of all CO_2 into the field for environmental reasons and to sustain oil production. The removal of CO_2 and adequate destination of specified gas with minimum footprint – due to space and weight constraints in offshore platforms – and energy consumption configure a central challenge in the Libra scenario. A strategy involves the separation of CO_2 from natural gas at the platform and the transportation of the processed gas to shore via pipelines. Four alternatives of topside gas conditioning are

T.3. Performance Analysis and Comparison of Membrane Permeation versus Supersonic Separators for CO_2 Removal from a Plausible Natural gas of Libra Field, Brazil. Proceedings of Rio Oil & Gas Expo and Conference, 2016.

RIO OIL & GAS 2016 EXPO AND CONFERENCE
24-27 de outubro de 2016
Riocentro | Rio de Janeiro - Brasil

IBP1169_16

INVESTIGATION OF TECHNICAL FEASIBILITY OF SUPERSONIC SEPARATION FOR CO2 REMOVAL FROM A PLAUSIBLE LIBRA FIELD NATURAL GAS

Lara de O. Arinelli[1], José Luiz de Medeiros [2], Ofélia Q. F. Araújo[3]

Copyright 2016, Brazilian Petroleum, Gas and Biofuels Institute - IBP
This Technical Paper was prepared for presentation at the ***Rio Oi & Gas Expo and Conference 2016***, held between October, 24-27, 2016, in Rio de Janeiro. This Technical Paper was selected for presentation by the Technical Committee of the event according to the information contained in the final paper submitted by the author(s). The organizers are not supposed to translate or correct the submitted papers. The material as it is presented, does not necessarily represent Brazilian Petroleum, Gas and Biofuels Institute' opinion, or that of its Members or Representatives. Authors consent to the publication of this Technical Paper in the ***Rio Oil & Gas Expo and Conference 2016 Proceedings.***

Abstract

This study addresses the application of supersonic separation (SS) for CO_2 removal from natural gas (NG). In this case, the gas stream should be previously treated with dehydration and hydrocarbon dew pointing processes. An extremely low temperature must be achieved inside the separator at specific range of pressure in order to promote significant condensation of CO_2 by entering the biphasic region of the phase envelope. Therefore, this paper assesses the best pressure and temperature conditions at the SS inlet for CO_2 separation through process simulation and sensitivity analysis. The proposed plant comprises dehydration by TEG absorption and dew point adjustment by JT expansion before the supersonic separation unit, all part of an offshore gas processing unit. The inlet NG stream is supposedly from Libra Field in Santos Basin (Brazil), presenting over 40%mol of CO_2. The destination of the CO_2 captured in the process is injection for enhanced oil recovery. The results show that low inlet temperature at the SS is essential for a significant CO_2 separation from NG. Moreover, the CO_2 stream obtained in this process is liquid, needing only pumping for reinjection and thus lower power than the CO_2 gas compressors required by other technologies. However, there is also a great energy penalty related to the refrigeration duty of the SS inlet, representing about 60% of the gas plant total power demand in the best CO_2 capture case. Besides, the lower CO_2 content observed in the final gas is still considerably high – 17%mol. Therefore, this study should be extended to a comparison with other technologies to better evaluate its benefits. Nonetheless, it indicates the possibility of CO_2 separation from NG by supersonic separation, under specific conditions.

T.4. Exergy Analysis of Monoethylene Glycol Recovery Processes for Hydrate Inhibition in Offshore Natural Gas Fields. Journal of Natural Gas Science and Engineering, 35, 798-813, 2016. doi: 10.1016/j.jngse.2016.09.017

Journal of Natural Gas Science and Engineering 52 (2018) 166–186

Contents lists available at ScienceDirect

Journal of Natural Gas Science and Engineering

journal homepage: www.elsevier.com/locate/jngse

Recovery of thermodynamic hydrate inhibitors methanol, ethanol and MEG with supersonic separators in offshore natural gas processing

Alexandre Mendonça Teixeira, Lara de Oliveira Arinelli, José Luiz de Medeiros*, Ofélia de Queiroz F. Araújo

Escola de Química, Federal University of Rio de Janeiro, Av. Horacio Macedo, 2030, Bl. E, 21949–900, Rio de Janeiro, RJ, Brazil

ARTICLE INFO

Keywords:
Thermodynamic hydrate inhibitor
THI recovery
Supersonic separator
Three-phase supersonic flow
Multiphase sound speed
HYSYS Unit Operation Extension

ABSTRACT

In offshore natural gas (NG) production, hydrate formation is a big concern that can impact the production and even stop NG flow. In this context, the injection of Thermodynamic Hydrate Inhibitors (THIs) in wellheads is widely employed in order to avoid these undesirable problems on subsea flowlines to gas processing rigs. However, in the main three-phase high-pressure separator in the gas rig, THI losses for gas phase are significant, particularly when the adopted THI is volatile like methanol and ethanol. This work discloses a new supersonic separator (SS) THI recovery process – SS-THI-Recovery – that treats the gas effluent from three-phase high-pressure separator achieving four simultaneous results: (i) gas water dew-point adjustment (WDPA); (ii) gas hydrocarbon dew-point adjustment (HCDPA); (iii) production of C3+ (propane and heavier) liquids as LPG; and (iv) recovery of almost all THI which would be lost in the gas otherwise. The proposition employs a supersonic separator (SS) battery followed by an anti-hydrates separator (LTX), a liquid-liquid THI extraction step and auxiliary THI distillation. SS-THI-Recovery was evaluated with HYSYS 8.8 simulator using methanol, ethanol and monoethylene glycol (MEG) as THIs. Supposing that the THI in the gas phase would be totally lost along with the exported gas otherwise, with SS-THI-Recovery the losses of methanol, ethanol and MEG were reduced by 91.9%, 79.3% and 99.2%, respectively, and such recovery factors could be further improved by increasing water flow rate in liquid-liquid THI extraction. Such high THI recovery entails reduction of THI costs with make-up, storage and transportation. Additionally, SS-THI-Recovery process is simple, with low footprint, and of easy implementation even for non-volatile THIs like MEG. Furthermore, the produced NG is ready for commercia-

T.5. HEPEC (Hysys Extension Phase Equilibrium Sound Speed). Registered software BR 512017000629-6, in 20/06/2017.

REPÚBLICA FEDERATIVA DO BRASIL
Ministério Da Indústria, Comércio Exterior e Serviços
Instituto Nacional da Propriedade Industrial
Diretoria de Patentes, Programas de Computador e Topografias de Circuitos Integrados

Certificado de Registro de Programas de Computador

Processo nº: BR 51 2017 000629-6

O Instituto Nacional da Propriedade Industrial expede o presente certificado de Registro de Programas de Computador, válido por 50 anos a partir de 1º de janeiro subsequente à data de Criação: 01 de março de 2017 , em conformidade com o parágrafo 2º , artigo 2º da Lei Nº 9.609, de 19 de Fevereiro de 1998.

Título: **HEPEC (HYSYS EXTENSION PHASE EQUILIBRIUM SOUND SPEED)**

Data de Criação: 01 de março de 2017

Titular(es): UNIVERSIDADE FEDERAL DO RIO DE JANEIRO (33.663.683/0001-16), Endereço: AV. PEDRO CALMON, 550 - PRÉDIO DA REITORIA, 2º ANDAR - ILHA DO FUNDÃO, RIO DE JANEIRO, RJ, 21941901

Autor(es): ALEXANDRE MENDONÇA TEIXEIRA (122.930.237-96)
/ GEORGE VICTOR BRIGAGÃO (140.346.427-85)
/ JOSÉ LUIZ DE MEDEIROS (495.399.577-53)
/ LARA DE OLIVEIRA ARINELLI (132.099.567-58)
/ OFÉLIA DE QUEIROZ FERNANDES ARAUJO (728.121.337-91)

Linguagem: ASPEN HYSYS VIEW, VISUAL BASIC 6.0

Campo de Aplicação: IN-02, IN-03

Tipo Programa: SM-01

Expedido em: 20 de junho de 2017

T.6. HEREC (Hysys Extension Reactive Equilibrium Sound Speed (C)). Registered software BR512017000628-8, in 20/06/2017.

REPÚBLICA FEDERATIVA DO BRASIL
Ministério Da Indústria, Comércio Exterior e Serviços
Instituto Nacional da Propriedade Industrial
Diretoria de Patentes, Programas de Computador e Topografias de Circuitos Integrados

Certificado de Registro de Programas de Computador

Processo nº: BR 51 2017 000628-8

O Instituto Nacional da Propriedade Industrial expede o presente certificado de Registro de Programas de Computador, válido por 50 anos a partir de 1º de janeiro subsequente à data de Criação: 01 de março de 2017 , em conformidade com o parágrafo 2º , artigo 2º da Lei Nº 9.609, de 19 de Fevereiro de 1998.

Título: **HEREC (HYSYS EXTENSION REACTIVE EQUILIBRIUM SOUND SPEED (C))**

Data de Criação: 01 de março de 2017

Titular(es): UNIVERSIDADE FEDERAL DO RIO DE JANEIRO (33.663.683/0001-16), Endereço: AV. PEDRO CALMON, 550 - PRÉDIO DA REITORIA, 2º ANDAR - ILHA DO FUNDÃO, RIO DE JANEIRO, RJ, 21941901

Autor(es): ALEXANDRE MENDONÇA TEIXEIRA (122.930.237-96)
/ GEORGE VICTOR BRIGAGÃO (140.346.427-85)
/ JOSÉ LUIZ DE MEDEIROS (495.399.577-53)
/ LARA DE OLIVEIRA ARINELLI (132.099.567-58)
/ OFÉLIA DE QUEIROZ FERNANDES ARAUJO (728.121.337-91)

Linguagem: ASPEN HYSYS VIEW, VISUAL BASIC 6.0

Campo de Aplicação: IN-02, IN-03

Tipo Programa: SM-01

Expedido em: 20 de junho de 2017

T.7. HESSO (Hysys Extension Supersonic Separator Operation). Registered software BR512017000627-0, in 20/06/2017.

REPÚBLICA FEDERATIVA DO BRASIL
Ministério Da Indústria, Comércio Exterior e Serviços
Instituto Nacional da Propriedade Industrial
Diretoria de Patentes, Programas de Computador e Topografias de Circuitos Integrados

Certificado de Registro de Programas de Computador

Processo nº: BR 51 2017 000627-0

O Instituto Nacional da Propriedade Industrial expede o presente certificado de Registro de Programas de Computador, válido por 50 anos a partir de 1º de janeiro subsequente à data de Criação: 01 de março de 2017 , em conformidade com o parágrafo 2º , artigo 2º da Lei Nº 9.609, de 19 de Fevereiro de 1998.

Título: **HESSO (HYSYS EXTENSION SUPERSONIC SEPARATOR OPERATION)**

Data de Criação: 01 de março de 2017

Titular(es): UNIVERSIDADE FEDERAL DO RIO DE JANEIRO (33.663.683/0001-16), Endereço: AV. PEDRO CALMON, 550 - PRÉDIO DA REITORIA, 2º ANDAR - ILHA DO FUNDÃO, RIO DE JANEIRO, RJ, 21941901

Autor(es): ALEXANDRE MENDONÇA TEIXEIRA (122.930.237-96)
/ GEORGE VICTOR BRIGAGÃO (140.346.427-85)
/ JOSÉ LUIZ DE MEDEIROS (495.399.577-53)
/ LARA DE OLIVEIRA ARINELLI (132.099.567-58)
/ OFÉLIA DE QUEIROZ FERNANDES ARAUJO (728.121.337-91)

Linguagem: ASPEN HYSYS VIEW, VISUAL BASIC 6.0

Campo de Aplicação: IN-02, IN-03

Tipo Programa: SM-01

Expedido em: 20 de junho de 2017

T.8. Speed of sound of multiphase and multi-reactive equilibrium streams: a numerical approach for natural gas applications. Journal of Natural Gas Science and Engineering, 46, p. 222-241, 2017. doi: 10.1016/j.jngse.2017.08.006

Journal of Natural Gas Science and Engineering 46 (2017) 222–241

Contents lists available at ScienceDirect

Journal of Natural Gas Science and Engineering

journal homepage: www.elsevier.com/locate/jngse

Speed of sound of multiphase and multi-reactive equilibrium streams: A numerical approach for natural gas applications

José Luiz de Medeiros*, Lara de Oliveira Arinelli, Ofélia de Queiroz F. Araújo

Escola de Química, Federal University of Rio de Janeiro, P.O. Box 68.594, 21941-972, Rio de Janeiro, RJ, Brazil

ARTICLE INFO

Article history:
Received 23 February 2017
Received in revised form
29 June 2017
Accepted 7 August 2017
Available online 12 August 2017

Keywords:
Thermodynamic sound speed
Multiphase sound speed
Multi-reactive sound speed
Supersonic separator
Landau model sound speed
Natural gas pyrolysis

ABSTRACT

A method is presented for calculating the thermodynamic sound speed of multiphase multi-reactive streams. A rigorous formula for the thermodynamic sound speed is developed via a steady-state, uni-dimensional, horizontal, adiabatic, frictionless, multiphase and multi-reactive equilibrium plug-flow. The main theoretical point is a correspondence between a multiphase multi-reactive plug-flow element and an Equilibrium Closed System (ECS), which has only two equilibrium state coordinates. Momentum and energy flow balances are processed via the ECS framework allowing the sound speed derivation for complex streams. The method uses ECS thermodynamic properties provided by multiphase *Flash*(*P,T*) of HYSYS 8.8 simulator. Unit Operation Extensions (UOE) are developed for calculating the multiphase multi-reactive sound speed by HYSYS. HYSYS solves the multiphase multi-reactive equilibria, including liquid water separation, to feed the ECS sound speed formula with required properties. The sound speed is also investigated in the critical neighborhood via the Landau Model approach to prove that it does not exhibit $\pm\infty$ singularities at the critical point, despite the critical lambda-shape $\pm\infty$ singularities of $\overline{C}_P$ and (*T,P*) derivatives of the density. Multiphase examples are solved by the sound speed UOEs for simultaneous adjustments of water and hydrocarbon dew points of natural gas with supersonic separator. Multi-reactive multiphase sound speeds are also predicted in supersonic reactors for natural gas pyrolysis (GTL) and for two-phase methanol oxidation to formaldehyde.

© 2017 Elsevier B.V. All rights reserved.

T.9. Offshore Processing of CO_2 Rich Natural Gas with Supersonic Separator versus Conventional Routes. Journal of Natural Gas Science and Engineering, 46, p. 199-221, 2017. http://dx.doi.org/10.1016/j.jngse.2017.07.010.

Journal of Natural Gas Science and Engineering 46 (2017) 199–221

Contents lists available at ScienceDirect

Journal of Natural Gas Science and Engineering

journal homepage: www.elsevier.com/locate/jngse

Offshore processing of CO_2 rich natural gas with supersonic separator versus conventional routes

Lara de Oliveira Arinelli*, Thiago Affonso F. Trotta, Alexandre Mendonça Teixeira, José Luiz de Medeiros, Ofélia de Queiroz F. Araújo

Escola de Química, Federal University of Rio de Janeiro, P.O. Box 68.594, 21941-972, Rio de Janeiro, RJ, Brazil

ARTICLE INFO

Article history:
Received 20 February 2017
Received in revised form
8 July 2017
Accepted 16 July 2017
Available online 12 August 2017

Keywords:
Natural gas conditioning
Supersonic separator
Membrane permeation
CO_2 removal
Unit operation extension

ABSTRACT

The supersonic separator (SS) was investigated for treating humid natural gas with *44%mol* CO_2 in offshore rigs and compared to the conventional Water Dew Point Adjustment (WDPA) via TEG Absorption, Hydrocarbon Dew Point Adjustment (HCDPA) via Joule-Thomson Expansion (JTE) and CO_2 removal via Membrane Permeation (MP). SS was tested as a single-step operation for WDPA + HCDPA. To simulate SS and MP, two Unit Operation Extensions (UOE) were developed for simulator HYSYS 8.8 (AspenTech). MP-UOE uses an empirical approach calibrated with operation data, whereas SS-UOE is entirely funded on thermodynamics, not demanding calibration. MP-UOE and SS-UOE use the thermodynamic infrastructure of HYSYS: property packages and several proved multiphase flash algorithms. MP-UOE and SS-UOE performed accordingly the expected characteristics of the respective operations and were critical to accomplish this analysis as SS and MP are not available in simulators. In terms of final gas quality (WDP $\leq$ *-45°C @1.01 bar*, HCDP $\leq$ *0°C @45 bar*, *%*CO_2 $\leq$ *15%mol*) the best process configuration was found to be a hybrid one: SS WDPA + HDPA and MP CO_2 removal, with low footprint and low power demand (*-6.9%*) relative to conventional 3-step way. If used for CO_2 removal, SS could abate CO_2 from *44%* to *21.85%mol*. Albeit less effective than MP, SS CO_2 removal is a noticeable option that produces fuel gas for power generation with *%*CO_2 $\approx$ *20%* as required by new turbo-shafts. Moreover, CO_2 is withdrawn from SS as a pumpable liquid allowing a cut of *44%* in the power demanded for CO_2 separation and injection as EOR agent.

© 2017 Elsevier B.V. All rights reserved.

T.10. Processo para Recuperar Inibidores Termodinâmicos de Hidratos de Cargas de Gás Natural Utilizando Separador Supersônico Simultaneamente Ajustando Ponto de Orvalho de Hidrocarbonetos e Ponto de Orvalho de Água do Gás Final. Brazilian Patent Application BR 102017015092-5, deposited in 13/07/2017.

República Federativa do Brasil
Ministério da Economia
Instituto Nacional da Propriedade Industrial

(21) BR 102017015092-5 A2

(22) Data do Depósito: 13/07/2017

(43) Data da Publicação Nacional: 29/01/2019

(54) Título: PROCESSO PARA RECUPERAR INIBIDORES TERMODINÂMICOS DE HIDRATOS DE GÁS DE CARGAS DE GÁS NATURAL UTILIZANDO SEPARADOR SUPERSÔNICO SIMULTANEAMENTE AJUSTANDO PONTO DE ORVALHO DE HIDROCARBONETOS E PONTO DE ORVALHO DE ÁGUA DO GÁS FINAL

(51) Int. Cl.: C10L 3/10.

(52) CPC: C10L 3/107; C10L 3/108; C10L 2290/08; C10L 2290/545.

(71) Depositante(es): UNIVERSIDADE FEDERAL DO RIO DE JANEIRO.

(72) Inventor(es): ALEXANDRE MENDONÇA TEIXEIRA; LARA DE OLIVEIRA ARINELLI; OFÉLIA DE QUEIROZ FERNANDES ARAÚJO.

(57) Resumo: A presente invenção define um novo processo para recuperar inibidores termodinâmicos de hidratos de gás (ITH) de cargas de gás natural utilizando separador supersônico, com injeção ou não de água líquida, de modo a extrair o ITH dos hidrocarbonetos pela formação de duas fases líquidas no condensado produzido no separador supersônico, simultaneamente ajustando o ponto de orvalho de hidrocarbonetos e o ponto de orvalho de água do gás final tratado pelo processo.

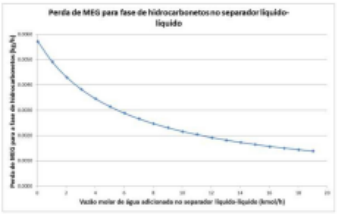

T.11. Purificação do ar para fracionamento criogênico com separador supersônico de baixa pressão. BR Patent Application 102017027727-5, deposited in 21/12/2017.

República Federativa do Brasil
Ministério da Economia
Instituto Nacional da Propriedade Industrial

(21) BR 102017027727-5 A2

(22) Data do Depósito: 21/12/2017

(43) Data da Publicação Nacional: 09/07/2019

(54) Título: PROCESSO DE PREPARO E PURIFICAÇÃO DO AR PARA FRACIONAMENTO CRIOGÊNICO UTILIZANDO SEPARADOR SUPERSÔNICO DE BAIXA PRESSÃO

(51) Int. Cl.: B01D 53/00; B01D 53/02; B01D 53/04; B01D 53/047.

(52) CPC: B01D 53/002; B01D 53/02; B01D 53/04; B01D 53/0454; B01D 53/047; (...).

(71) Depositante(es): UNIVERSIDADE FEDERAL DO RIO DE JANEIRO.

(72) Inventor(es): GEORGE VICTOR BRIGAGÃO; JOSÉ LUIZ DE MEDEIROS; LARA DE OLIVEIRA ARINELLI; OFÉLIA DE QUEIROZ FERNANDES ARAÚJO.

(57) Resumo: A presente invenção define um novo conceito de unidade PPU ? Air Preparation and Purification Unit ? para preparo e purificação de ar a ser fracionado criogenicamente na etapa seguinte conhecida como Cold-Box. O conceito PPU Alternativa aqui proposto utiliza separador supersônico (SS) em baixa pressão para remover 97,5% da água do ar, seguindo-se etapa de remoção de acabamento por adsorção (ERAA) ou tratamentos similares com meio sólido (por exemplo, adsorção química) para remoção de contaminantes CO2, N2O e hidrocarbonetos, além de traços residuais de H2O, adequando os níveis de contaminantes para posterior processamento na Cold-Box de uma planta criogênica de fracionamento de ar.

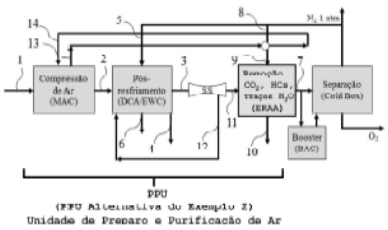

T.12. Monoethylene Glycol as Hydrate Inhibitor in Offshore Natural Gas Processing: From Fundamentals to Exergy Analysis. SpringerBriefs in Petroleum Geoscience & Engineering, SPRINGER, 2018. doi: 10.1007/978-3-319-66074-5 / ISBN: 978-3-319-66073-8

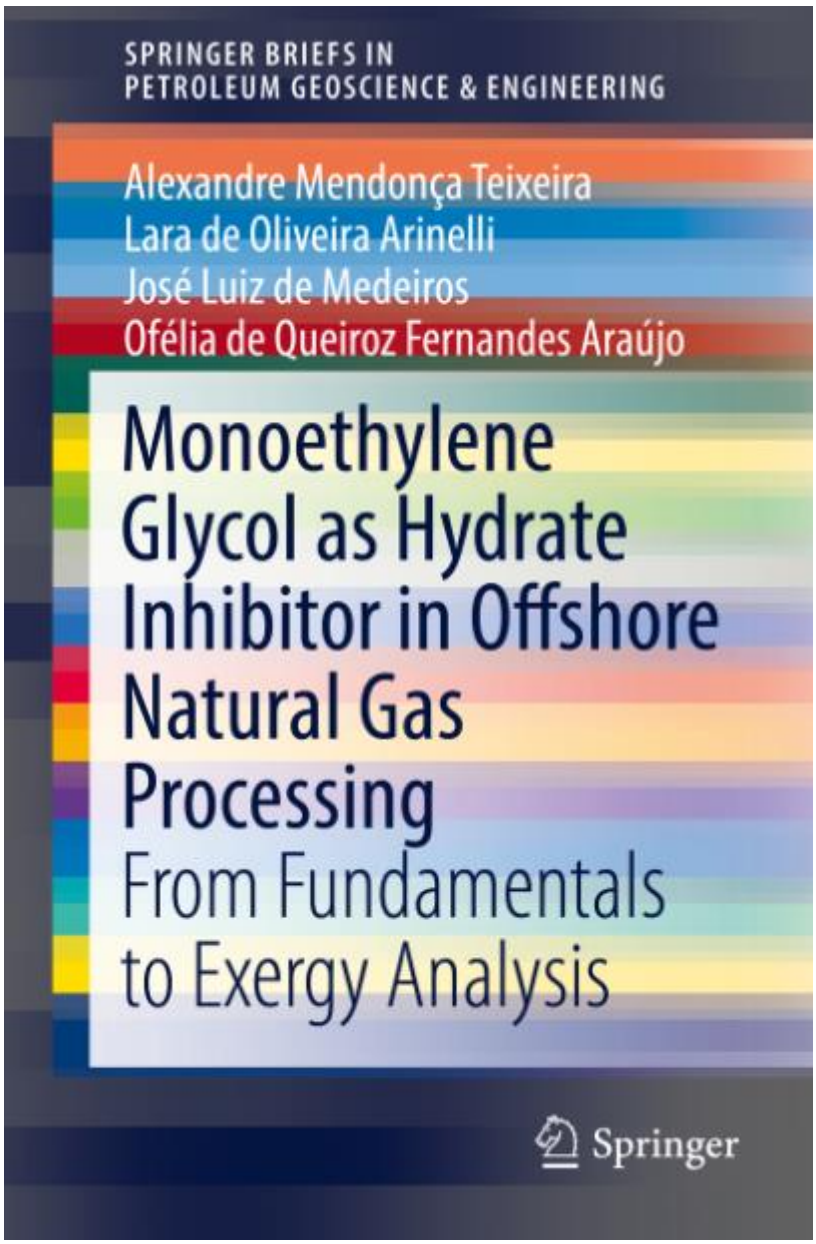

T.13. Technological alternatives for high CO_2 natural gas processing aiming offshore production of gas associated giant oil fields. 1st Latin-American Conference on Sustainable Development of Energy Water and Environment Systems (LA-SDEWES), 2018.

Conference on Sustainable Development of Energy, Water and Environment Systems, Rio de Janeiro 28.-31.1.2018

SDEWES.LA2018.0067

Technological Alternatives for High CO2 Natural Gas Processing Aiming Offshore Production of Gas Associated Giant Oil Fields

D. C. De Melo*[1], L. De O. Arinelli[2], A. M. Teixeira[2], G. Victor[2], F. M. Passarelli[1], J. Ferreira Do Nascimento[1], W. M. Grava[1], J.L. De Medeiros[3]

[1]PETROBRAS, Brazil; [2]Universidade Federal do Rio de Janeiro, Brazil; [3]Federal University of Rio de Janeiro, Brazil (*darley@petrobras.com.br)

Abstract

The population growth followed by economy activity intensification is the driver of a growing demand for energy, among its various forms, for oil and natural gas (NG). The importance of the energy sector for socio-economic development is undeniable. Today in the world one can not imagine a developed country that does not have adequate access to energy sources. In addition, it is notable that a country's energy matrix should be diversified and cleaned as much as possible, for strategic, environmental and supply security reasons. In the Americas, some countries such as Brazil, Canada, Colombia, the United States and Peru have growing and robust energy sectors with technological and operational practice advances. These innovations allow the production development, for example, of tight oil and shale gas in the United States, oil sands in Canada, and of ultra deepwater offshore hydrocarbon sources, with both oil and gas, in Brazil, located in a very promising area known as Pre-Salt.

The oil-associated gas produced contain water and in some cases, relatively high content of acid components, which may present problems to its final utilization, like hydrates build up and corrosion in flowlines. Therefore, offshore process units, with a desirable simpler scheme, have to be designed to process this gas. In this case, the main purposes of the process are to remove acid

T.14. AMPEC (Aspen Model of Phase Equilibrium Sound Speed (C)). Registered software BR512018001031-8, in 26/06/2018.

INSTITUTO NACIONAL DA PROPRIEDADE INDUSTRIAL

26/06/2018 870180054895 09:23

29409191710344696

Pedido de Registro de Programa de Computador - RPC - Pedido de Registro de Programas de Computador - RPC

Número do Processo: 512018001031-8

Dados do Titular

Titular 1 de 1

Nome ou Razão Social:	UNIVERSIDADE FEDERAL DO RIO DE JANEIRO
Tipo de Pessoa:	Pessoa Jurídica
CPF/CNPJ:	33663683000116
Nacionalidade:	Brasileira
Qualificação Jurídica:	Instituição de Ensino e Pesquisa
Endereço:	Av. Pedro Calmon, 550 - Cidada Universitária
Cidade:	Rio de Janeiro
Estado:	RJ
CEP:	21941901
País:	Brasil
Telefone:	(21)37331793
Fax:	
Email:	agenciadeinovacao@inovacao.ufrj.br

T.15. AMSSO (Aspen Model of Supersonic Separator Operation). Registered software BR512018001032-6.

INSTITUTO NACIONAL DA PROPRIEDADE INDUSTRIAL

26/06/2018 870180054908 09:59

29409191710344890

Pedido de Registro de Programa de Computador - RPC - Pedido de Registro de Programas de Computador - RPC

Número do Processo: 512018001032-6

Dados do Titular

Titular 1 de 1

Nome ou Razão Social:	UNIVERSIDADE FEDERAL DO RIO DE JANEIRO
Tipo de Pessoa:	Pessoa Jurídica
CPF/CNPJ:	33663683000116
Nacionalidade:	Brasileira
Qualificação Jurídica:	Instituição de Ensino e Pesquisa
Endereço:	Av. Pedro Calmon, 550 - Cidada Universitária
Cidade:	Rio de Janeiro
Estado:	RJ
CEP:	21941901
País:	Brasil
Telefone:	(21)37331793
Fax:	
Email:	agenciadeinovacao@inovacao.ufrj.br

T.16. Recovery of thermodynamic hydrate inhibitors methanol, ethanol and MEG with supersonic separators in offshore natural gas processing. Journal of Natural Gas Science and Engineering, Vol. 52, p. 166-186, 2018. doi: 10.1016/j.jngse.2018.01.038

Journal of Natural Gas Science and Engineering 52 (2018) 166–186

Contents lists available at ScienceDirect

Journal of Natural Gas Science and Engineering

journal homepage: www.elsevier.com/locate/jngse

Recovery of thermodynamic hydrate inhibitors methanol, ethanol and MEG with supersonic separators in offshore natural gas processing

Alexandre Mendonça Teixeira, Lara de Oliveira Arinelli, José Luiz de Medeiros*, Ofélia de Queiroz F. Araújo

Escola de Química, Federal University of Rio de Janeiro, Av. Horacio Macedo, 2030, Bl. E, 21949–900, Rio de Janeiro, RJ, Brazil

ARTICLE INFO

Keywords:
Thermodynamic hydrate inhibitor
THI recovery
Supersonic separator
Three-phase supersonic flow
Multiphase sound speed
HYSYS Unit Operation Extension

ABSTRACT

In offshore natural gas (NG) production, hydrate formation is a big concern that can impact the production and even stop NG flow. In this context, the injection of Thermodynamic Hydrate Inhibitors (THIs) in wellheads is widely employed in order to avoid these undesirable problems on subsea flowlines to gas processing rigs. However, in the main three-phase high-pressure separator in the gas rig, THI losses for gas phase are significant, particularly when the adopted THI is volatile like methanol and ethanol. This work discloses a new supersonic separator (SS) THI recovery process – SS-THI-Recovery – that treats the gas effluent from three-phase high-pressure separator achieving four simultaneous results: (i) gas water dew-point adjustment (WDPA); (ii) gas hydrocarbon dew-point adjustment (HCDPA); (iii) production of C3+ (propane and heavier) liquids as LPG; and (iv) recovery of almost all THI which would be lost in the gas otherwise. The proposition employs a supersonic separator (SS) battery followed by an anti-hydrates separator (LTX), a liquid-liquid THI extraction step and auxiliary THI distillation. SS-THI-Recovery was evaluated with HYSYS 8.8 simulator using methanol, ethanol and monoethylene glycol (MEG) as THIs. Supposing that the THI in the gas phase would be totally lost along with the exported gas otherwise, with SS-THI-Recovery the losses of methanol, ethanol and MEG were reduced by 91.9%, 79.3% and 99.2%, respectively, and such recovery factors could be further improved by increasing water flow rate in liquid-liquid THI extraction. Such high THI recovery entails reduction of THI costs with make-up, storage and transportation. Additionally, SS-THI-Recovery process is simple, with low footprint, and of easy implementation even for non-volatile THIs like MEG. Furthermore, the produced NG is ready for commercia-

T.17. CO_2 rich natural gas processing: technical, power consumption and emission comparisons of conventional and supersonic separator technologies. Proceedings of 4th Brazilian Congress on CO_2 in the Oil, Gas and Biofuels Industries, 2018.

IBP0086_18

CO_2 RICH NATURAL GAS PROCESSING: TECHNICAL, POWER CONSUMPTION AND EMISSION COMPARISONS OF CONVENTIONAL AND SUPERSONIC SEPARATOR TECHNOLOGIES

Lara O. Arinelli[1], Alexandre M. Teixeira [2], José L. de Medeiros[3], Ofélia O.Q. F. Araújo[4]

Copyright 2018, Brazilian Petroleum, Gas and Biofuels Institute - IBP
This Technical Paper was prepared for presentation at the ***4th Brazilian Congress on CO_2 in the Oil, Gas and Biofuels Industries***, held between June 28-29, 2018, in Rio de Janeiro. This Technical Paper was selected for presentation by the Technical Committee of the event according to the information contained in the final paper submitted by the author(s). The organizers are not supposed to translate or correct the submitted papers. The material as it is presented, does not necessarily represent Brazilian Petroleum, Gas and Biofuels Institute' opinion, or that of its Members or Representatives. Authors consent to the publication of this Technical Paper in the ***4th Brazilian Congress on CO_2 in the Oil, Gas and Biofuels Industries Proceedings.***

Abstract

Supersonic Separator (SS) is investigated via process simulation for treating CO_2 rich (>40%) natural gas (NG) in terms of water dew-point adjustment (WDPA), hydrocarbon dew-point adjustment (HCDPA) and CO_2 removal for Enhanced Oil Recovery (EOR). These applications are compared in terms of technical and energetic performances with conventional technologies, also comparing CO_2 emissions by power generation. The context is that of an offshore platform to treat NG with 45%mol of CO_2, producing a lean NG stream with maximum CO_2 composition of ≈20%mol, suitable for use as fuel gas, and a CO_2 rich stream that is compressed and injected for EOR. The conventional process comprises WDPA by chemical absorption in TEG, JT expansion for HCDPA and membrane permeation (MP) for CO_2 removal. The other alternatives use SS for WDPA/HCDPA, and MP or SS for CO_2 capture. Simulations are carried out in HYSYS 8.8, where MP and SS are modeled via Unit Operation Extensions (UOE) developed in a previous work: MP-UOE and SS-UOE. A full technical and energetic analysis is performed for comparison of the three cases. The results show that the replacement of conventional dehydration technology by SS decreases power demand by 8.5%, consequently reducing 69.66 t/d of CO_2 emitted to the atmosphere. The use of SS for CO_2 capture is also superior than MP, mainly due to the production of a high-pressure CO_2 stream, that requires much less power for EOR compression than the low-pressure permeate stream from MP. Therefore, the SS-SS Case presents the best results: lowest energetic demand (-23.9% than Conventional Case), directly impacting on CO_2 emissions, which are reduced by 2598 t/d (-27.82%).

T.18. Offshore natural gas conditioning and recovery of methanol as hydrate inhibitor with supersonic separators: increasing energy efficiency with lower CO_2 emissions. Proceedings of 4th Brazilian Congress on CO_2 in the Oil, Gas and Biofuels Industries, 2018.

IBP0087_18

OFFSHORE NATURAL GAS CONDITIONING AND RECOVERY OF METHANOL AS HYDRATE INHIBITOR WITH SUPERSONIC SEPARATORS: INCREASING ENERGY EFFICIENCY WITH LOWER CO_2 EMISSIONS

Alexandre M. Teixeira[1], Lara de O. Arinelli[2], José L. de Medeiros[3], Ofélia de Q. F. Araújo[4],

Copyright 2018, Brazilian Petroleum, Gas and Biofuels Institute - IBP
This Technical Paper was prepared for presentation at the ***4th Brazilian Congress on CO_2 in the Oil, Gas and Biofuels Industries***, held between June 28-29, 2018, in Rio de Janeiro. This Technical Paper was selected for presentation by the Technical Committee of the event according to the information contained in the final paper submitted by the author(s). The organizers are not supposed to translate or correct the submitted papers. The material as it is presented, does not necessarily represent Brazilian Petroleum, Gas and Biofuels Institute' opinion, or that of its Members or Representatives. Authors consent to the publication of this Technical Paper in the ***4th Brazilian Congress on CO_2 in the Oil, Gas and Biofuels Industries Proceedings.***

Abstract

The oil and gas industry represents one of the largest contributors to global emissions of carbon dioxide, as oil and gas platforms are highly energy intensive for processing and transportation of hydrocarbons. In offshore rigs CO_2 emissions mainly come from on-site gas-fired power generation for heat and electricity production. The accumulation of atmospheric CO_2 is one of the main causes of the planetary greenhouse effect, thus CO_2 emissions should be minimized. To achieve that, more energy efficient processes for natural gas conditioning are needed in order to minimize platform power consumption and thus lowering the associated generation of CO_2. In offshore platforms, the three-phase high-pressure separator (HPS) is fed with incoming raw natural gas (NG), where the HPS gas goes to NG conditioning for hydrocarbon dew point adjustment (HCDPA) and water dew point adjustment (WDPA) so as to make NG exportable, and the bottom aqueous phase, particularly where offshore natural gas fields require continuous hydrate inhibition, is sent to a THI recovery unit (THI-RU) for re-concentration of THI. In conventional plants, WDPA and HCDPA are done by glycol absorption and Joule-Thomson expansion respectively. Moreover, the HPS gas carries some THI such as methanol that is lost in the processing. This work analyses a new process – SS-THI-Recovery – where HPS gas feeds a supersonic separator (SS) with injected water and compares it to the conventional processing. As a result, SS ejects a cold two-phase condensate with almost all water, THI and C3+ hydrocarbons, discharging exportable NG with enough HCDPA and WDPA grades, while the condensate gives aqueous THI returned to the THI-RU and LPG with high commercial value. Thus, SS-THI-Recovery not only avoids THI losses as well as exports NG and LPG. Both conventional gas plant and SS-THI-Recovery alternative coupled to THI-RU were simulated in HYSYS 8.8

T.19. CO_2 emission and energy assessments of a novel pre-purification unit for cryogenic air separation using supersonic separator. Proceedings of 4th Brazilian Congress on CO_2 in the Oil, Gas and Biofuels Industries, 2018.

IBP0096_18

CO_2 EMISSION AND ENERGY ASSESSMENTS OF A NOVEL PRE-PURIFICATION UNIT FOR CRYOGENIC AIR SEPARATION USING SUPERSONIC SEPARATOR

George V. Brigagão[1], Lara de O. Arinelli[1], José L. de Medeiros[2], Ofélia Q. F. Araújo[3]

Copyright 2018, Brazilian Petroleum, Gas and Biofuels Institute - IBP
This Technical Paper was prepared for presentation at the ***4th Brazilian Congress on CO_2 in the Oil, Gas and Biofuels Industries***, held between June 28-29, 2018, in Rio de Janeiro. This Technical Paper was selected for presentation by the Technical Committee of the event according to the information contained in the final paper submitted by the author(s). The organizers are not supposed to translate or correct the submitted papers. The material as it is presented, does not necessarily represent Brazilian Petroleum, Gas and Biofuels Institute' opinion, or that of its Members or Representatives. Authors consent to the publication of this Technical Paper in the ***4th Brazilian Congress on CO_2 in the Oil, Gas and Biofuels Industries Proceedings.***

Abstract

Thermal power plants with oxy-combustion CO_2 capture are featured by large scale oxygen demand, where cryogenic air separation is most suitable. In such context, a Pre-Purification Unit (PPU) is required, prior to air fractionation, to remove hazardous air contaminants – H_2O, CO_2 and several trace-species – preventing ingress into the Cold Box. The conventional PPU – named FULL-TSA – remove those contaminants by means of Temperature Swing Adsorption (TSA), ordinarily using double-layered bed with activated alumina for adsorbing H_2O and zeolitic molecular sieve for adsorbing CO_2 and further trace-species, which implicates in relatively high demand of low-pressure steam for impurities desorption. A novel pre-purification concept (SS-TSA) embraces a Supersonic Separator (SS) performing the bulk of separation service, abating nearly 98.5% of H_2O, followed by a finishing single-bed molecular sieve (MS) TSA step, which is featured by its relatively small size, for removing CO_2 and remaining impurities. This work presents the energy analysis, as well as the related indirect CO_2 emissions, of such a novel concept (SS-TSA) comprising air compression, cooling, SS dehydration and finishing MS-TSA against the conventional method fully based in TSA purification (FULL-TSA). Process simulation in HYSYS 8.8 assisted technical evaluation and comparison of alternatives, which included the use of two Hysys Unit Operation Extensions – SS-UOE and PEC-UOE – for rigorous thermodynamic SS modeling with phase-equilibrium sound speed. SS was designed to impose only 1.4% of head loss, while shrinking TSA service to about 10% of FULL-TSA counterpart, also recovering super-cooled aqueous condensate that reduces water make-up and N_2 consumption for cooling. Changing from FULL-TSA to SS-TSA the average demand of low-pressure steam reduced from 1.37 to 0.16 MW. In terms of electricity demand the difference was

T.20. CO_2 Rich Natural Gas Offshore Processing with Supersonic Separator: CO_2 Capture, Energy and Economic Assessments. Proceedings of 13th Conference on Sustainable Development of Energy Water and Environment Systems (SDEWES), 2018.

Conference on Sustainable Development of Energy, Water and Environment Systems, Palermo, 30.9.-4.10.2018

Energy Systems Analysis

SDEWES2018.0134

CO2 Rich Natural Gas Offshore Processing with Supersonic Separator: CO2 Capture, Energy and Economic Assessments

L. De Oliveira Arinelli*, A. Teixeira, J.L. De Medeiros, O. Araujo

Federal University of Rio de Janeiro, Brazil (*lara.arinelli@gmail.com)

Abstract

Supersonic separation (SS) is an emerging technology for natural gas (NG) offshore processing. There are few works on correct SS thermodynamic modeling and simulation for CO_2 rich (>40%mol) NG conditioning steps such as Water Dew-Point Adjustment (WDPA), Hydrocarbon Dew-Point Adjustment (HCDPA) and CO_2 removal. In this work, SS is investigated via HYSYS 8.8 process simulation for WDPA, HCDPA and CO_2 removal for conditioning CO_2 rich raw NG. These applications are compared in terms of technical, energy and economic performances with conventional glycol absorption WDPA, Joule-Thomson Expansion HCDPA and Membrane Permeation (MP) CO_2 removal. The scenario corresponds to an offshore platform treating 45%mol CO_2 raw NG to produce lean NG with maximum %mol CO_2 of ≈20%mol suitable to gas-fired power generation and a CO_2 rich fluid that is compressed and injected for Enhanced Oil Recovery (EOR). Besides the conventional three-steps NG processing above-mentioned (so-called Case 1), two other processing alternatives are considered: (i) SS for WDPA/HCDPA and MP CO_2 removal (Case 2), and (ii) SS for WDPA/HCDPA and SS for CO_2 removal (Case 3). In HYSYS simulations MP and SS are modeled via Unit Operation Extensions MP-UOE and SS-UOE developed ad hoc in a previous work. Technical, energy and economic assessments are performed for comparison of Case 1, Case 2 and Case 3. Results show that replacing conventional WDPA+HCDPA by SS reduces power demand relatively to Case 1 by 7.8% while maintaining positive Net Present Value (NPV). Moreover, SS CO_2 removal also outperformed conventional MP CO_2 removal, mainly due to SS production of CO_2 rich EOR stream at high-pressure, entailing much less compression power for EOR than the low-pressure CO_2 rich MP permeate. Besides the environmental gain of lowest CO_2 emission, the lowest power consumption of SS-SS Case 3 (-20.5%) leads to best economic results: lowest cost of manufacturing and lowest compressor capital investment. Thus, Case 3 with two serial SS's for both WDPA/HCDPA and CO_2 removal is the overall best solution, with highest NPV after 20 years of operation (+860MMUSD).

T.21. Economic leverage of thermodynamic hydrate inhibitor recovery from raw natural gas with supersonic separator: post-combustion capture of 43% of CO_2 emissions preserving offshore gas plant profitability. Proceedings of 13th Conference on Sustainable Development of Energy Water and Environment Systems (SDEWES), 2018.

Conference on Sustainable Development of Energy, Water and Environment Systems, Palermo, 30.9.-4.10.2018

SDEWES2018.0107

Economic Leverage of Thermodynamic Hydrate Inhibitor Recovery from Raw Natural Gas with Supersonic Separator: Post-Combustion Capture of 43% of CO2 Emissions Preserving Offshore Gas Plant Profitability

A. Teixeira*, L. De Oliveira Arinelli, J.L. De Medeiros, O. Araujo

Federal University of Rio de Janeiro, Brazil (*alexandremtxr@gmail.com)

Abstract

Offshore oil and gas production is a major CO_2 emitter as gas processing is highly power intensive for conditioning and transporting natural gas (NG). In offshore rigs CO_2 emissions mainly come from gas-fired power generation. In order to make room for economically sustained post-combustion carbon capture, new more efficient NG processing is needed. Offshore NG fields requiring injection of thermodynamic hydrate inhibitor (THI) must have a THI recovery unit (THI-RU) for re-concentration of THI in the bottom water phase from the high-pressure separator (HPS) fed with incoming raw NG, while the HPS gas goes to NG conditioning for hydrocarbon dew point adjustment (HCDPA) and water dew point adjustment (WDPA) so as to make NG exportable. In conventional plants, WDPA and HCDPA are done by glycol absorption and Joule-Thomson expansion respectively. Moreover, the HPS gas carries some THI (e.g. methanol) that is lost in the processing. This work analyses a new process – SS-THI-Recovery – where HPS gas feeds a supersonic separator (SS) with injected water. As a result, SS ejects a cold two-phase condensate with almost all water, THI and C3+ hydrocarbons, discharging exportable NG with enough HCDPA and WDPA grades, while the condensate gives aqueous THI returned to the THI-RU and tradable LPG. Thus, SS-THI-Recovery not only avoids THI losses as well as exports NG and LPG, improving dramatically the gas plant profitability. It is shown that such leverage for methanol as THI can pay a post-combustion mono-ethanolamine (MEA) plant capturing about 43% of the gas plant CO_2 emissions, assuming 80MW of power generation. Both conventional gas plant and SS-THI-Recovery alternative (both coupled to respective THI-RUs and the latter also coupled to a post-combustion MEA plant) were simulated in HYSYS v8.8 with subsequent equipment design and economic analysis. Despite the higher capital investment of SS-THI-Recovery alternative, it has several advantages: (i) superior revenues due to higher production of better grade LPG; (ii) much lower THI make-up costs; and (iii) 43% lower carbon taxation costs. Even paying post-combustion costs, SS-THI-Recovery gave slightly higher net

T.22. Exergy analysis of a novel air pre-purification unit for cryogenic fractionation based on low-pressure supersonic separator combined with finishing adsorption step. Proceedings of 13th Conference on Sustainable Development of Energy Water and Environment Systems (SDEWES), 2018.

Conference on Sustainable Development of Energy, Water and Environment Systems, Palermo, 30.9.-4.10.2018

SDEWES2018.0068

Exergy Analysis of a Novel Air Pre-Purification Unit for Cryogenic Fractionation Based on Low-Pressure Supersonic Separator Combined with Finishing Adsorption Step

G. Brigagão*, L. De Oliveira Arinelli, J.L. De Medeiros, O. Araujo

Federal University of Rio de Janeiro, Brazil (*george.victor@poli.ufrj.br)

Abstract

Cryogenic air fractionation requires raw air compression and pre-purification, and the conventional process – FULL-TSA – uses Temperature-Swing-Adsorption (TSA) with large activated-alumina beds for removing H_2O and small molecular-sieve beds for CO_2 and trace-species. A novel alternative – SS-TSA – prescribes a Supersonic Separator (SS) abating 98.65% H_2O followed by molecular-sieve TSA for finishing purification. A new variant deriving from SS-TSA – SS-TSA-HI – uses compression heat to regenerate TSA beds. Exergy analysis of FULL-TSA, SS-TSA and SS-TSA-HI was executed to investigate thermodynamic performances also locating where improvements can better reduce utilities consumption. Air compression and cooling steps were unveiled as major exergy destructors, with SS-TSA-HI being slightly superior at this point due to lower temperature approach in intercoolers. Utilization of SS reduced exergy loss of pre-purification by 61% for savings on steam and nitrogen demand in TSA system. Overall exergy efficiencies of FULL-TSA, SS-TSA and SS-TSA-HI were found as 57.9%, 60.0%, and 60.3%, respectively.

T.23. A new concept of air pre-purification unit for cryogenic separation: low-pressure supersonic separator coupled to finishing adsorption. Separation and Purification Technology, 215, p. 173-189, 2019. doi: https://doi.org/10.1016/j.seppur.2019.01.015

Separation and Purification Technology 215 (2019) 173–189

Contents lists available at ScienceDirect

Separation and Purification Technology

journal homepage: www.elsevier.com/locate/seppur

A new concept of air pre-purification unit for cryogenic separation: Low-pressure supersonic separator coupled to finishing adsorption

George Victor Brigagão, Lara de Oliveira Arinelli, José Luiz de Medeiros*, Ofélia de Queiroz F. Araújo

Escola de Química, Federal University of Rio de Janeiro, CT, E, Ilha do Fundão, Rio de Janeiro, RJ 21941-909, Brazil

ARTICLE INFO

Keywords:
Air pre-purification
Air dehydration
Supersonic separator
Multiphase supersonic flow
Multiphase sound speed

ABSTRACT

In commercial cryogenic manufacturing of oxygen, air to the Cold-Box must pass through a Pre-Purification Unit (PPU) to remove water, CO_2 and other impurities. The conventional PPU – FULL-TSA – comprises compression, cooling pre-dehydration and temperature-swing adsorption (TSA) for dehydration and CO_2 removal, supplying treated air at *3.1 bar*. This work discloses a new PPU concept – SS-TSA – prescribing a supersonic separator (SS) upstream to TSA handling *98.5%* of dehydration, greatly lowering TSA costs. SS-TSA comprises compression, cooling pre-dehydration, SS dehydration and a smaller TSA for finishing dehydration and CO_2 removal. A SS-TSA variant – TSA-HI – additionally recovers compression heat lowering heating costs. SS-TSA, FULL-TSA and SS-SS-TSA-HI were analyzed. Flowsheets were simulated in HYSYS with full thermodynamic SS modeling via a new HYSYS Unit Operation Extension – SS-UOE – rigorously calculating the multiphase sound speed. SS was designed for only *3.5%* of head-loss, recovering *98.5%* of water as super-cooled liquid, lowering make-up and chilled-water costs, while shrinking the TSA service to 10% of the FULL-TSA counterpart. For commercial-scale PPU considering 20 years of operation at 10% interest rate, the purified *3.1 bar* air breakeven prices reached *5.28*, *5.19*, and *5.18 US$/kNm³*, respectively for FULL-TSA, SS-TSA and SS-TSA-HI, establishing superiority of SS alternatives over the conventional FULL-TSA.

T.24. Offshore Processing of CO_2-Rich Natural Gas with Supersonic Separator. Multiphase Sound Speed, CO_2 Freeze-Out and HYSYS Implementation. SPRINGER, 2019. doi: 10.1007/978-3-030-04006-2 / ISBN: 978-3-030-04005-5

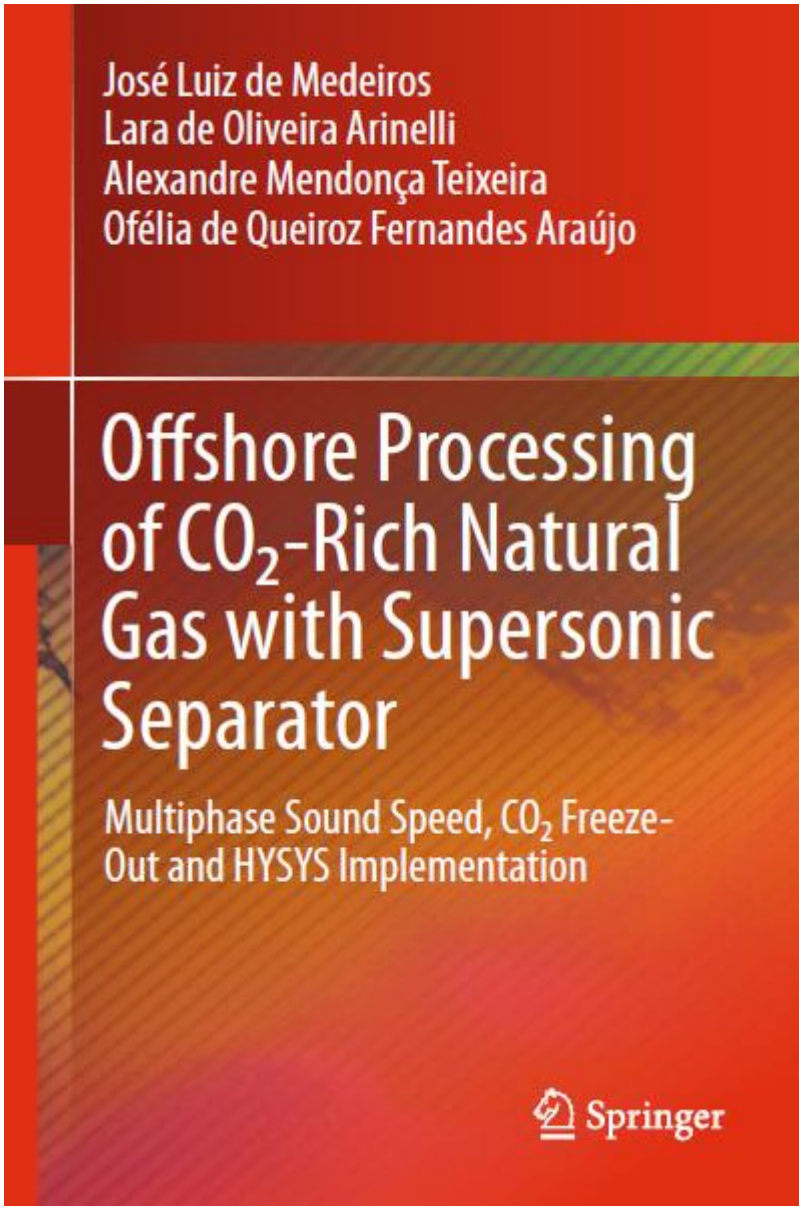

T.25. Economic Leverage Affords Post-Combustion Capture of 43% of Carbon Emissions: Supersonic Separators for Methanol Hydrate Inhibitor Recovery from Raw Natural Gas and CO_2 Drying. Journal of Environmental Management, Vol. 236, pp. 534-550, 2019. doi: 10.1016/j.jenvman.2019.02.008

Journal of Environmental Management 236 (2019) 534–550

Contents lists available at ScienceDirect

Journal of Environmental Management

journal homepage: www.elsevier.com/locate/jenvman

Research article

Economic leverage affords post-combustion capture of 43% of carbon emissions: Supersonic separators for methanol hydrate inhibitor recovery from raw natural gas and CO_2 drying

Alexandre Mendonça Teixeira, Lara de Oliveira Arinelli, José Luiz de Medeiros*, Ofélia de Queiroz F. Araújo

Escola de Química, Federal University of Rio de Janeiro, Av. Horacio Macedo, 2030, Bl. E, 21949–900, Rio de Janeiro, RJ, Brazil

ARTICLE INFO

Keywords:
Supersonic separator
Methanol hydrate inhibitor
CO_2 capture and storage
Post-combustion capture
Supersonic separator CO_2 drying

ABSTRACT

Offshore oil/gas productions are power intensive and CO_2 emitters from gas-fired power generation. This work investigates supersonic separator as a strategy for affording post-combustion capture backed up by cost reductions. Conventional offshore gas processing usually loses thermodynamic hydrate inhibitor methanol in processing and exported gas. This work analyses a supersonic separator variant gas processing simultaneously reducing methanol losses. Such process dramatically improves gas-plant profitability via cost-reduction of methanol make-up and power-consumption, simultaneously increasing revenues from liquefied-petroleum-gas by-product. This economic leverage affords post-combustion carbon capture, including subsequent CO_2 dehydration and compression for exportation of high-pressure liquid CO_2. This corresponds to abate 43% of CO_2 emissions boosting revenues via enhanced oil recovery. Moreover, CO_2 is dehydrated via another supersonic separator operating with minimum head-loss, minimizing compression costs. Despite its much higher investment, the new process with carbon capture presents higher net value (865.63 MMUSD) than the conventional processing without carbon capture (829.31 MMUSD), being economically feasible and more environmentally adequate with cleaner natural gas production and successful CO_2 management. The new process is superior in several scenarios and particularly favored by oil prices above 55 USD/bbl. Rising oil price from 40 to 100 USD/bbl, the new process net value rises 29%, whereas the conventional counterpart rises only 7.5%. In addition, as a plausible future scenario, CO_2 taxation favors the new process, which always has superior economic performance, even without CO_2 taxation. In summary, implementing supersonic separators in offshore natural gas processing aiming at anti-hydrate recovery and CO_2 dehydration for enhanced oil recovery creates economic leverage sustaining Carbon Capture & Storage without loss of competitiveness. This result, backed up by rigorous ther-

T.26. Carbon capture and high-capacity supercritical fluid processing with supersonic separator: Natural gas with ultra-high CO_2 content. Journal of Natural Gas Science and Engineering, Vol. 66, p. 265-283, 2019. doi: 10.1016/j.jngse.2019.04.004

Journal of Natural Gas Science and Engineering 66 (2019) 265–283

Contents lists available at ScienceDirect

Journal of Natural Gas Science and Engineering

journal homepage: www.elsevier.com/locate/jngse

Carbon capture and high-capacity supercritical fluid processing with supersonic separator: Natural gas with ultra-high CO_2 content

Lara de Oliveira Arinelli[a], José Luiz de Medeiros[a,*], Darley Carrijo de Melo[b], Alexandre Mendonça Teixeira[a], George Victor Brigagão[a], Fabio Menezes Passarelli[b], Wilson Mantovani Grava[b], Ofélia de Queiroz F. Araújo[a]

[a] Escola de Química, Federal University of Rio de Janeiro, CT, E, Ilha do Fundão, Rio de Janeiro, RJ, 21941-909, Brazil
[b] CENPES, PETROBRAS S.A., Ilha do Fundão, Rio de Janeiro, RJ, 21941-970, Brazil

ARTICLE INFO

Keywords:
Supersonic separator
Supercritical fluid processing
Ultra-high CO_2 content
Natural gas conditioning
CO_2 removal
CO_2 freeze-out

ABSTRACT

Some deep-water offshore fields produce oil with high gas/oil ratios and ultra-high %CO_2 (> *60%mol*) with the onus of processing low-grade gas simultaneously handling huge CO_2 dispatch goals. Thus, processing solutions are needed to make feasible such high-capacity gas rigs hundreds of kilometers offshore. Feasibility relies on the choices for CO_2 capture and adjustment of water and hydrocarbon dew-points of such high flow rate gas. This problem was approached adopting supersonic separators for dew-point adjustments and for CO_2 capture on a floating-hub processing 50 MMsm³/*d* of CO_2 ultra-rich gas, reinjecting *96%* of treated CO_2-rich gas for enhanced oil recovery, while reserving *4%* as fuel-gas after CO_2 abatement to *20%mol* for power production. Process alternatives were assessed in terms of power demand and profitability comparing supersonic separator with membrane-permeation for CO_2 removal. Results show that 1st supersonic separator for dew-point adjustments of raw gas recycling condensate to the oil-gas-water separator and 2nd supersonic separator for CO_2 removal avoiding CO_2 freeze-out, give optimum net present value and minimum CO_2 emissions. On one hand, these facts are consequences of less compressor investment as 2nd supersonic separator ejects pressurized CO_2 condensate requiring *5%* less compression power for enhanced oil recovery relatively to the power required by the low-pressure CO_2-rich permeate from the membrane-permeation alternative. On the other hand, the best net value of supersonic separator alternative also reflects its highest revenues derived from recycling condensate from 1st supersonic separator entailing *18%* higher oil production.

T.27. Supersonic separator for cleaner offshore processing of natural gas with high carbon dioxide content: Environmental and economic assessments. Journal of Cleaner Production, v. 233, p. 510-521, 2019. doi: https://doi.org/10.1016/j.jclepro.2019.06.115

Journal of Cleaner Production 233 (2019) 510–521

Contents lists available at ScienceDirect

Journal of Cleaner Production

journal homepage: www.elsevier.com/locate/jclepro

Supersonic separator for cleaner offshore processing of natural gas with high carbon dioxide content: Environmental and economic assessments

Lara de Oliveira Arinelli, Alexandre Mendonça Teixeira, José Luiz de Medeiros*, Ofélia de Queiroz F. Araújo

Escola de Química, Federal University of Rio de Janeiro, Rio de Janeiro, RJ, Brazil

ARTICLE INFO

Article history:
Received 23 February 2019
Received in revised form
13 May 2019
Accepted 11 June 2019
Available online 12 June 2019

Keywords:
CO_2-Rich natural gas processing
Supersonic separator
CO_2 capture
Membrane permeation
Environmental assessment
Economic assessment

ABSTRACT

Supersonic separators offer a cleaner offshore processing of natural gas with carbon dioxide content from deep-water oil-gas fields. Conventional offshore gas processing comprises water dew-point adjustment via glycol-absorption, hydrocarbon dew-point adjustment via Joule-Thomson expansion, and carbon dioxide removal via membrane-permeation. Alternative processing contemplates the use of supersonic separators for adjusting gas dew-points followed by carbon dioxide capture via membrane-permeation (so-called SS-MP scheme); or for adjusting gas dew-points and also accomplishing carbon dioxide abatement (so-called SS-SS scheme). The conventional process is environmentally and economically compared with SS-MP and SS-SS for application in offshore rigs treating raw gas (44%mol carbon dioxide) to produce exportable fuel-gas (≈20%mol carbon dioxide), while dispatching carbon dioxide rich fluid (≈75%mol carbon dioxide) for enhanced oil recovery in the oil-gas field. Results show that SS-MP requires 7.8% less power than the conventional process. Moreover, implementing SS-SS deepens the advantage against the conventional operation because SS-SS produces carbon dioxide rich fluid at high-pressure, requiring much less compression power for enhanced oil recovery than the low-pressure permeate from membrane-permeation. SS-SS has lowest carbon emission (−28.3%), lowest power consumption (−21.3%) and best economic performance: lowest manufacturing cost and lowest compressor investment. Thus, SS-SS is the overall best and cleanest solution, with highest 20 years net value (+860 MMUSD) and lowest environmental impact.

© 2019 Elsevier Ltd. All rights reserved.

T.28. Supersonic separator for cleaner offshore processing of supercritical fluid with ultra-high carbon dioxide content: economic and environmental evaluation. Journal of Cleaner Production, 234, p. 1385-1398, 2019. doi: https://doi.org/10.1016/j.jclepro.2019.06.304

Journal of Cleaner Production 234 (2019) 1385–1398

Contents lists available at ScienceDirect

Journal of Cleaner Production

journal homepage: www.elsevier.com/locate/jclepro

Supersonic separator for cleaner offshore processing of supercritical fluid with ultra-high carbon dioxide content: Economic and environmental evaluation

Darley C. de Melo [b], Lara de O. Arinelli [a], José Luiz de Medeiros [a, *], Alexandre M. Teixeira [a], George Victor Brigagão [a], Fabio M. Passarelli [b], Wilson M. Grava [b], Ofélia de Q.F. Araujo [a]

[a] Escola de Química, Federal University of Rio de Janeiro, CT, E, Ilha do Fundão, Rio de Janeiro, RJ, 21941-909, Brazil
[b] CENPES, PETROBRAS S.A., Ilha do Fundão, Rio de Janeiro, RJ, 21941-970, Brazil

ARTICLE INFO

Article history:
Received 2 March 2019
Received in revised form
29 May 2019
Accepted 27 June 2019
Available online 28 June 2019

Handling editor: Prof. Jiri Jaromir Klemeš

Keywords:
Natural gas
Supercritical fluid
CO_2
Supersonic separator
Offshore processing
Environmental analysis

ABSTRACT

Offshore gas processing presents challenges, especially when high flow rates, high-pressure and high carbon dioxide contents are involved. The present scenario comprehends offshore processing of high flow rate of high-pressure natural gas with 68%mol carbon dioxide, which results from oil production and behaves as a dense supercritical fluid. The processing goals with this fluid comprise: [A] water dew-point adjustment; [B] hydrocarbon dew-point adjustment; [C] decarbonation of a small part to 20%mol carbon dioxide fuel-gas for power production; and [D] compression/pumping of the remaining fluid enriched with carbon dioxide from decarbonation for enhanced oil recovery. For these tasks the industry considers traditional well established processes such as molecular-sieves adsorption for water dew-point adjustment, Joule-Thompson expansion for hydrocarbon dew-point adjustment and membrane-permeation for carbon dioxide removal. However, conventional technologies can become cumbersome in such awkward conditions. Thus, unconventional solutions are sought for reliability, lower equipment size/weight, and better power consumption, emissions and environmental sustainability. Recently, supersonic separators have been analyzed in proof-of-concept researches for natural gas processing. In this regard, this work quantitatively proves that goals [A],[B],[C] are achievable using only supersonic separators, attaining 33% higher net value, 40% greater oil production, 10% lower investment and economic leverage to reach lower carbon emission relatively to conventional counterparts.

© 2019 Elsevier Ltd. All rights reserved.

T.29. Automatized Monte-Carlo analysis of offshore processing of CO_2-rich natural gas: Conventional versus supersonic separator routes. Journal of Natural Gas Science and Engineering, 69, 102943, 2019. doi: https://doi.org/10.1016/j.jngse.2019.102943

Journal of Natural Gas Science and Engineering 69 (2019) 102943

Contents lists available at ScienceDirect

Journal of Natural Gas Science and Engineering

journal homepage: www.elsevier.com/locate/jngse

Automatized Monte-Carlo analysis of offshore processing of CO_2-rich natural gas: Conventional versus supersonic separator routes

Cristiane São Bento Gonzaga, Lara de Oliveira Arinelli, José Luiz de Medeiros*, Ofélia de Queiroz F. Araújo

Escola de Química, Federal University of Rio de Janeiro, CT, E, Ilha do Fundão, Rio de Janeiro, RJ, 21941-909, Brazil

ARTICLE INFO

Keywords:
CO_2-Rich natural gas conditioning
Supersonic separator
Membrane permeation
Monte-Carlo analysis
Computer-aided engineering
Interoperability

ABSTRACT

Offshore oil/gas production with high $\%CO_2$ and gas-to-oil ratio impose processing large volumes of CO_2-rich gas. This requires first-of-a-kind designs and creates design uncertainties besides offshore operation uncertainties. Therefore, the design of offshore units under influence of stochastic factors is recommended to avoid oversized worst-case designs or underachieved specifications implying economic/environmental losses. This work presents a novel Computer-Aided Engineering tool, *MCAnalysis*, a VB.NET/XML interoperability framework between HYSYS and MATLAB to statistically assess design performance via Monte-Carlo analysis. Designs of offshore processing of CO_2-rich gas via Conventional-Route and a novel Supersonic-Separator-Route were tested submitting stochastic populations of gas flow rate, $\%CO_2$ and gas-to-oil ratio. Supersonic-Separator-Route presented higher resilience to input overshoots and less necessity of design changes to accomplish specifications in at least 75% of sampled cases compared to Conventional-Route. Supersonic-Separator-Route also showed 15% less average power consumption and hydrocarbons dew-point adjustment with lower $\%CO_2$ in the condensate.

T.30. CO_2 Rich Natural Gas Processing: Technical, Power Consumption and Emission Comparisons of Conventional and Supersonic Technologies. Materials Science Forum, 965, p. 79-86, 2019. doi: 10.4028/www.scientific.net/MSF.965.79

Materials Science Forum
ISSN: 1662-9752, Vol. 965, pp 79-86
doi:10.4028/www.scientific.net/MSF.965.79
© 2019 Trans Tech Publications Ltd, Switzerland
Submitted: 2018-12-18
Revised: 2019-05-14
Accepted: 2019-05-14
Online: 2019-08-08

CO_2 Rich Natural Gas Processing: Technical, Power Consumption and Emission Comparisons of Conventional and Supersonic Technologies

Lara de Oliveira Arinelli[1,a*], Alexandre Mendonça Teixeira[1,b], José Luiz de Medeiros[1,c] and Ofélia de Queiroz Fernandes Araújo[1,d]

[1]Escola de Química, Federal University of Rio de Janeiro (UFRJ), Av. Athos da Silveira Ramos, 149, Centro de Tecnologia, Cidade Universitária, 21941-972, Rio de Janeiro, RJ, Brazil

[a]lara.arinelli@gmail.com, [b]alexandremtxr@gmail.com, [c]jlm@eq.ufrj.br, [d]ofelia@eq.ufrj.br

*corresponding author: lara.arinelli@gmail.com

Keywords: Rich CO_2 Natural Gas Processing, Supersonic Separator, CO_2 Capture, Membranes, Energy Analysis, CO_2 Emissions, Process Engineering, Enhanced Oil Recovery

Abstract. Supersonic separator is investigated via process simulation for treating CO_2 rich (>40%) natural gas in terms of dew-points adjustment and CO_2 removal for enhanced oil recovery. These applications are compared in terms of technical and energetic performances with conventional technologies, also comparing CO_2 emissions by power generation. The context is that of an offshore platform to treat raw gas with 45%mol of CO_2, producing a lean gas stream with maximum CO_2 composition of ≈20%mol, suitable for use as fuel gas, and a CO_2 rich stream that is compressed and injected to the oil and gas fields. The conventional process comprises dehydration by chemical absorption in TEG, Joule-Thomson expansion for C3+ removal, and membrane permeation for CO_2 capture. The other alternatives use supersonic separation for dew-points adjustment, and membranes or another supersonic separation unit for CO_2 capture. Simulations are carried out in HYSYS 8.8, where membranes and supersonic separation are modeled via unit operation extensions developed in a previous work: MP-UOE and SS-UOE. A full technical and power consumption analysis is performed for comparison of the three cases. The results show that the replacement of

T.31. Offshore Natural Gas Conditioning and Recovery of Methanol as Hydrate Inhibitor with Supersonic Separators: Increasing Energy Efficiency with Lower CO_2 Emissions. Materials Science Forum, Vol. 965, pp 97-105, 2019. doi: 10.4028/www.scientific.net/MSF.965.97

Materials Science Forum
ISSN: 1662-9752, Vol. 965, pp 97-105
doi:10.4028/www.scientific.net/MSF.965.97
© 2019 Trans Tech Publications Ltd, Switzerland
Submitted: 2018-12-19
Revised: 2019-05-14
Accepted: 2019-05-14
Online: 2019-08-08

Offshore Natural Gas Conditioning and Recovery of Methanol as Hydrate Inhibitor with Supersonic Separators: Increasing Energy Efficiency with Lower CO_2 Emissions

Alexandre Mendonça Teixeira[1,a*], Lara de Oliveira Arinelli[1,b], José Luiz de Medeiros[1,c] and Ofélia de Queiroz Fernandes Araújo[1,d]

[1]Escola de Química, Federal University of Rio de Janeiro (UFRJ), Av. Athos da Silveira Ramos, 149, Centro de Tecnologia, Cidade Universitária, 21941-972, Rio de Janeiro, RJ, Brazil

[a]alexandremtxr@gmail.com, [b]lara.arinelli@gmail.com, [c]jlm@eq.ufrj.br, [d]ofelia@eq.ufrj.br

* corresponding author: alexandremtxr@gmail.com

Keywords: supersonic separator; thermodynamic hydrate inhibitor; natural gas; CO2 emissions.

Abstract. The oil and gas industry represents an important contributor to CO_2 emissions as offshore platforms are power intensive for producing, processing and transporting hydrocarbons. In offshore rigs CO_2 emissions mainly come from on-site gas-fired power generation for heat and electricity production. The accumulation of atmospheric CO_2 is one of the main causes of the planetary greenhouse effect, thus CO_2 emissions should be minimized. To achieve that, more energy efficient processes for natural gas (NG) conditioning are needed in order to minimize platform power consumption and thus lowering the associated generation of CO_2. In addition, in offshore scenarios gas-hydrate obstructions are a major concern in flow assurance strategies, since thermodynamic conditions favoring hydrate formation are present, such as high pressure, low external temperature and gas contact with free water. To avoid hydrate issues, hydrate inhibition is carried out by the injection of a thermodynamic hydrate inhibitor (THI) in well-heads such that it flows along with production fluids, thus removing the thermodynamic conditions for hydrate formation and ensuring unimpeded flow. Therefore, the three-phase high-pressure separator (HPS) is fed with production fluids, where the HPS splits the feed into: (i) an upper gas phase, (ii) hydrocarbon condensate, and (iii) a bottom aqueous phase. The gas phase goes to NG conditioning for hydrocarbon dew point adjustment (HCDPA) and water dew point adjustment (WDPA) so as to make NG exportable. The hydrocarbon condensate (if present) is collected for stabilization and the bottom aqueous phase consisting of water, salts and THI is sent to a THI recovery unit (THI-RU) for THI re-concentration and reinjection. In conventional plants, WDPA and HCDPA are done by glycol absorption and Joule-Thomson expansion respectively. Moreover, the HPS gas carries some THI such as methanol

T.32. CO_2 emission and energy assessments of a novel pre-purification unit for cryogenic air separation using supersonic separator. Materials Science Forum, 965, p. 59–67, 2019. doi: 10.4028/www.scientific.net/MSF.965.59

Materials Science Forum
ISSN: 1662-9752, Vol. 965, pp 59-67
doi:10.4028/www.scientific.net/MSF.965.59
© 2019 Trans Tech Publications Ltd, Switzerland
Submitted: 2018-12-15
Accepted: 2019-04-26
Online: 2019-08-08

CO_2 Emission and Energy Assessments of a Novel Pre-Purification Unit for Cryogenic Air Separation Using Supersonic Separator

George Victor Brigagão[1,a*], Lara de Oliveira Arinelli[1,b], José Luiz de Medeiros[1,c*] and Ofélia de Queiroz Fernandes Araújo[1,d]

[1]Escola de Química, Federal University of Rio de Janeiro, CT, E, Ilha do Fundão, Rio de Janeiro, RJ, 21941-909, Brazil

[a]george.victor@poli.ufrj.br, [b]lara.arinelli@gmail.com, [c]jlm@eq.ufrj.br, [d]ofelia@eq.ufrj.br

*corresponding author: george.victor@poli.ufrj.br

Keywords: air pre-purification; air dehydration; supersonic separator; cryogenic air separation.

Abstract. Thermal power plants with oxy-combustion CO_2 capture are featured by large scale oxygen demand, where cryogenic air separation is most suitable. In such context, a Pre-Purification Unit (PPU) is required, prior to air fractionation, to remove hazardous air contaminants – H_2O, CO_2 and several trace-species – preventing ingress into the Cold Box. The conventional PPU – named FULL-TSA – remove those contaminants by means of Temperature Swing Adsorption (TSA), ordinarily using double-layered bed with activated alumina for adsorbing H_2O and zeolitic molecular sieve for adsorbing CO_2 and further trace-species, which implicates in relatively high demand of low-pressure steam for impurities desorption. A novel pre-purification concept (SS-TSA) embraces a Supersonic Separator (SS) performing the bulk of separation service, abating nearly 98.5% of H_2O, followed by a finishing single-bed molecular sieve (MS) TSA step, which is featured by its relatively small size, for removing CO_2 and remaining impurities. This work presents the energy analysis, as well as the related indirect CO_2 emissions, of such a novel concept (SS-TSA) comprising air compression, cooling, SS dehydration and finishing MS-TSA against the conventional method fully based in TSA purification (FULL-TSA). Process simulation in HYSYS

T.33. Honorable Mention for the presentation of the technical work "Investigation of Technical Feasibility of Supersonic Separation for CO_2 removal from a plausible Libra Field Natural Gas" in the 2016 Rio Oil & Gas Conference, IBP.

T.34. 2018 Plínio Catanhede Award for best technical work published by IBP in technology and innovation theme between 2016 and 2018 for the work "Investigation of Technical Feasibility of Supersonic Separation for CO_2 removal from a plausible Libra Field Natural Gas", presented in the 2016 Rio Oil & Gas Conference.

PRÊMIO PLÍNIO CANTANHEDE 2018

CERTIFICADO

O Instituto Brasileiro de Petróleo, Gás e Biocombustíveis, em conformidade com a decisão da Comissão Julgadora, confere a ***LARA DE OLIVEIRA ARINELLI*** *pela autoria do seu trabalho* ***INVESTIGATION OF TECHNICAL FEASIBILITY OF SUPERSONIC SEPARATION FOR CO2 REMOVAL FROM A PLAUSIBLE LIBRA FIELD NATURAL GAS*** *, que trouxe uma grande contribuição para a Indústria de Petróleo, Gás e Biocombustíveis.*

José Firmo
Presidente

Milton Costa Filho
Secretario Geral

RIO OIL & GAS

Promoção e Organização:
ibp

T.35. Best Paper Award in "Capture" theme for the work "CO_2 rich natural gas processing: technical, power consumption and emission comparisons of conventional and supersonic separator technologies" presented in the 2018 Brazilian Congress of CO_2 in the Industry of Oil, Gas and Biofuels, IBP.

ibp INSTITUTO BRASILEIRO DE PETRÓLEO, GÁS E BIOCOMBUSTÍVEIS | A casa da nossa indústria.

CERTIFICADO

O Comitê Técnico Científico, confere ao(s) autor(es) do trabalho IBP086_18 - **CO2 RICH NATURAL GAS PROCESSING: TECHNICAL, POWER CONSUMPTION AND EMISSION COMPARISONS OF CONVENTIONAL AND SUPERSONIC SEPARATOR TECHNOLOGIES**, **Lara de Oliveira Arinelli, Alexandre Mendonça Teixeira, José Luiz de Medeiros e Ofélia de Queiroz Fernandes Araújo**, o certificado de melhor trabalho apresentado no **4º Congresso Brasileiro de CO_2 na Indústria do Petróleo, Gás e Biocombustíveis**, no tema **Captura,** promovido pelo Instituto Brasileiro de Petróleo, Gás e Biocombustíveis - IBP.

Rio de Janeiro, 28 de Junho de 2018.

José Firmo
Presidente

Milton Costa Filho
Secretário Geral